PROGRAM AND PROCEEDINGS

NCPV Program Review Meeting 2000

April 16–19, 2000

Adam's Mark Hotel

Denver, Colorado

NREL

Sandia National Laboratories

NOTICE

Available electronically at http://www.doe.gov/bridge

Available for a processing fee to U.S. Department of Energy
and its contractors, in paper, from:

U.S. Department of Energy
Office of Scientific and Technical Information
P.O. Box 62
Oak Ridge, TN 37831-0062
phone: 865.576.8401
fax: 865.576.5728
email: reports@adonis.osti.gov

Available for sale to the public, in paper, from:

U.S. Department of Commerce
National Technical Information Service
5285 Port Royal Road
Springfield, VA 22161
phone: 800.553.6847
fax: 703.605.6900
email: orders@ntis.fedworld.gov
online ordering: http://www.ntis.gov/ordering.htm

TABLE OF CONTENTS

Session 4: Fundamental and Applied Research— Part I, Crystalline Technologies

Concentrator Technologies

Session 5: Fundamental and Applied Research— Part II, Thin-Film Technologies

Session 6: Fundamental and Applied Research— Part III, New Technologies for the Future

Poster Session A

Historically Black Colleges and Universities (HBCUs)

Components

Systems

PV Manufacturing Technology

Concentrators

III-V Material

Future-Generation Technologies

Poster Session B

Miscellaneous

Crystalline Silicon

Amorphous Silicon (a-Si)

Copper Indium Diselenide (CIS)

Cadmium Telluride (CdTe)

The U.S. Photovoltaic Industry Roadmap

A.M. Barnett (AstroPower, Inc.), L. Crowley (Idaho Power), C.M. Davis (Kyocera Solar),
C.A. Farris, Siemens (Solar Industries), L. Kimmerling (Massachusetts Instute of
Technology),R. Little (Spire Corporation), W. Roppenecker (Trace Engineering),
R. Schwartz (Purdue University), H. Shimp (BP-Solarex)

ABSTRACT

The industry-developed roadmap for critical needs of PV technology is discussed. This guide provides and independent assessment of the needs and requriements for PV research, technology, manufacturing, applications, markets, and plocy though 2020.

1. The Roadmap

The U.S. photovoltaics industry is the world leader in research, technology, manufacturing, and market share. In recent years, however, foreign governments have recognized the very large market opportunities that PV systems present. World interest is being fueled by a number of key PV attributes, including its availability as a clean, emission-free, and renewable energy source, its reliability, consumer-friendliness, and ability to be deployed in a variety of applications, and its importance to our national energy security as a fuel-free, distributed energy source. This world interest is reflected in well-coordinated research and deployment programs in various countries, including Japan and Germany, among others, that is leading to establishment of very strong international competition in PV technology.

The U.S. PV industry has recognized that large market opportunities exist for photovoltaics, but understands as well the challenge of emerging international competition.

The roadmap will guide U.S. photovoltaics research, technology, manufacturing, applications, markets, and policy through 2020. Early in 1999, the PV committee established the following vision as a first step in developing the PV industry roadmap:

> *"...to provide the electrical-energy consumer with competitive and environmentally friendly energy products and services from a thriving United States-based solar electric power industry."*

In support of this vision, the PV Roadmap Steering Committee identified an aggressive growth strategy for the PV industry (Fig. 1) that would result in a large projection of cumulative installed PV capacity in the United States and the world. Additionally, four concepts for implementing the vision and these projections have been developed. They are as follows:

- *Maintain the U.S. industry's worldwide technological leadership*
- *Achieve economic competitiveness with conventional technologies*
- *Maintain a sustained market and PV production growth*
- *Make the PV industry profitable and attractive to investors*

3. Targets and Goals

The PV Industry Roadmap Steering Committee articulated a number of goals and targets to support the vision and four concepts. Addressing new electrical generating requirements, the PV Roadmap Steering Committee projected the following "endpoint" for 2020:

> *"For the domestic photovoltaic industry to provide up to 15% (about 3,200 MW) of new U.S. peak electricity generating capacity expected to be required in 2020. The U.S. cumulative PV shipments will be about 30 GWp at this time."*

Overall goals for the U.S. photovoltaics industry align with the 25% annual production growth rate displayed in Exhibit 3. Specific goals are categorized in two major industry target areas—installed volume and cost:

- Total installed volume of at least 6 GW for the U.S. industry in 2020, of which 3.2 GW is used in *domestic* installations. Expected application mix will be

  < 1/2 AC distributed generation
  < 1/3 DC and AC value applications
  < 1/6 AC grid (wholesale) generation

  Installed volume will continue to increase, exceeding 9 GW in 2030.

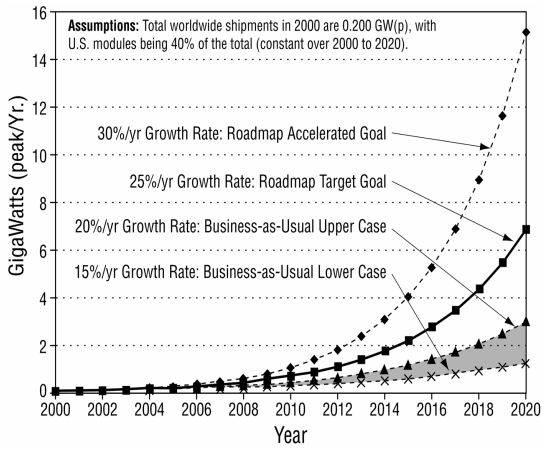

Figure 1 - PV Growth Strategy 2000-2020.

- *Cumulative* U.S. installed capacity in 2020 of about 15 GW, or about 20% of the 70 GW expected worldwide.

- End-user costs, including O&M, of $3 per watt AC in 2010, and approaching $1.50 per watt AC in 2020. Manufacturing costs are projected to be 60% of system costs.

- International markets are significant and will remain a substantial portion of sales for the U.S. PV industry. A strong domestic market for PV systems is necessary in order to keep the international competitiveness of the U.S. PV industry and to obtain the environmental and distributed energy benefits of PV energy for U.S. consumers.

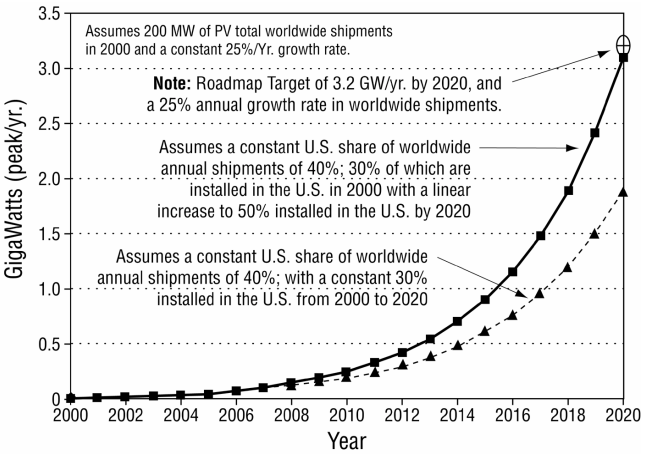

Figure 2 - Projections of U.S. Manufactured PV Modules Installed in U.S. Domestic Applications

To reach these goals, the PV industry and its partners identified four critical **Technology Development Areas,** around which the roadmap process was fashioned. These include:

- Markets and Applications
- PV Components, Systems, and Integration
- Manufacturing, Equipment, and Processes
- Fundamental and Applied Research

4. Workshop and Plans

In June, 1999, forty-four experts from the PV industry, as well as decision-makers from electric utilities, universities, research organizations, system integrators, and marketers gathered to develop the preliminary outlines for the PV Roadmap. The three-day workshop addressed technology and market barriers, and research, marketing, and technology transfer needs of the entire PV industry. The core of the workshop was four facilitated breakout sessions, in which participants explored the primary barriers and needs in the four technology development areas. These breakout sessions resulted in over 140 critical areas, of which about 20 were considered priority. Table 1 lists the priority research and technology transfer needs for each breakout session.

Workshop participants took a further step in each of their breakout sessions to identify a progression of actions that should be taken to best address the barriers and needs related to each Technology Development Area, which included both linkages among the categories of needs as well as time frames for achieving success in carrying out the top priority needs and actions. Each group identified appropriate time frames in which research or market transformation would be expected to yield benefits. Research and technology transfer activities were assigned to one of three time frames: near-term (0-3 years), mid-term (3-10 years), and long-term (beyond 10 years). Participants also identified appropriate roles for industry, government, and educational institutions to support selected research or technology transfer activities. In some instances, industry was identified as the lead; in others, government was so identified. The results of these efforts are described in this report and will undoubtedly shape the comprehensive roadmap for implementing PV technology goals.

5. References

[1] The Industry-Developed PV Roadmap: A Framework for U.S. Industry and Technology Leadership (May, 1999)

[2] U.S. Photovoltaics Industry PV Technology Roadmap Workshop Report (September, 1999).

Table 1. Selected High Priority Research and Technology Transfer Needs for the PV Industry			
Markets and Applications	**PV Components, Systems, and Integration**	**PV Manufacturing**	**Fundamental and Applied Research**
Focus on mechanisms that can advocate and market PV, conduct analysis of competing technologies, and develop alliances with other groups Conduct consumer education programs in cooperation with other organizations, such as DPCA and NAESCO Include photovoltaic technology education as a part of the science curriculum, so that it is a standard component of science learning Improve involvement with government, legislative, and regulatory decision-makers and clearly articulate the impacts of inaction Obtain long-term, low-interest financing for PV systems	Develop national and international standards for PV products and components, including ratings and verification tools for appropriate sized systems Provide wider, more effective public exposure to PV products and their value Design value-added building products using PV Improve reliability, cost-effectiveness, and ease of maintenance for PV products that may be used in buildings and building systems, and quantify externalities associated with these products Demonstrate examples of good building design, and integrated systems, using PV components	Develop manufacturing partnerships so manufacturers can work with suppliers to develop the next generation of PV equipment Develop on-line diagnostic tools and systems to enhance process control and development Conduct equipment demonstrations at high volume (10,000 cells), so that others involved in manufacturing can observe and analyze data Develop high volume, high throughput, high efficiency cell processes Design lower cost module packaging	Research, develop, and demonstrate new materials, such as thin glass, through chemical tempering, thin semi-conducting materials, new encapsulants, low temperature conducting epoxy, optimized transparent conducting oxides, and alternative substrates Improve cell efficiencies to reduce material costs Develop materials and devices with high efficiency and low cost through R&D with specific targets Address issues to increase throughput, including improved automation, process control and scale-up (for cells and module fabrication), high speed interconnect and encapsulation, strategies to improve industry wide throughput, and development of novel technologies such as rapid thermal processing (RTP) and high rate deposition (HRD) Address thin-film manufacturing issues, such as basic R&D, to develop process control needs, process models, in-situ diagnostics, reactor and equipment design, mixed process integration, and better intermediate in-line testing and diagnostics

Sandia's International PV Activities: Sustainable Markets Through Strong Partnerships

C. Hanley, E. Richards, M. Ross
Sandia National Laboratories
P.O. Box 5800
Albuquerque, NM 87185-0704

ABSTRACT

Sandia National Laboratories has teamed with a variety of partner organizations to open new international markets for the U.S. photovoltaic (PV) industry. Emphasis has been on productive-use applications of PV, such as water pumping, in areas not served by an electric grid. Through the provision of technical assistance, training, and the facilitation of large numbers of pilot projects, the Sandia team builds the capacity of in-country organizations and businesses to specify, procure, use, supply, and maintain PV systems. This establishes a local experience and business base, launching growing markets as the pilot projects are replicated outside the immediate program. The Sandia team monitors the activities and uses the information obtained to improve both the program and the technology, as appropriate. Considerable success in opening new markets has been achieved in Mexico with this approach, and the team is now applying the model in Central America.

1. Introduction

Developing international markets for the U.S. photovoltaic (PV) and other renewable energy industries in partnership with the U.S. government is in the best interests of the U.S, a variety of sources have concluded. As examples, the Report of the Photovoltaic Industry Roadmap Workshop stated that it will be necessary to grow both national and international markets in order to reach the vision and goals laid out in the roadmap exercise, and recommends that this be accomplished through partnerships between industry and government [1]. A report by the President's Committee of Advisors on Science and Technology (PCAST) contains strong recommendations that the U.S. government increase it's involvement in international energy issues, especially regarding the use of renewables in developing countries [2]. The Renewable Energy Policy Project recently concluded that using photovoltaic systems for rural electrification in the developing world provides an important contribution to global climate protection [3]. Developing-country markets have been and continue to be key to maintaining the strength of the U.S. PV industry, although increased competition from the PV industries of other developed countries, with strong support from their governments, is now threatening this situation.

The U.S. Department of Energy has supported the development of new international PV markets through activities at both Sandia National Laboratories and the National Renewable Energy Laboratory (NREL). As the competition in the international arena intensifies, the market development efforts supported by the U.S. DOE will become more important to maintaining the position of the U.S. industry. This paper describes the approach, accomplishments, and future directions of the recent international work led by Sandia in partnership with a variety of other government and non-government organizations.

2. Approach

Sandia has developed a model for its international renewable energy (RE) programs that focuses on developing and strengthening local capacity to implement and maintain RE projects [4]. This approach is a direct extension of the PV Systems Assistance Center (PVSAC) philosophy, which has been in effect at Sandia for almost 20 years. The international program model is built around six tenets:

- *Partnerships,*
- *Capacity building,*
- *Technical assistance,*
- *Pilot project implementation,*
- *Monitoring and evaluation, and*
- *Replication.*

Strong partnerships are the key to sustained success in Sandia's international activities. Sandia uses partnerships on several levels. First, at the program implementation level, Sandia manages a multi-institutional team to address the range of technical, cultural, institutional, and economic issues related to the sustainable use of renewables. Key members of Sandia's international program implementation team include Winrock International, the Southwest Technology Development Institute (SWTDI) at New Mexico State University, Enersol Associates, Ecotourismo y Nuevas Tecnologías, and NREL. This team works closely with U.S. industry, and partnerships are also developed in-country with multi-disciplined development organizations, government organizations, local business, and academia.

Capacity building is accomplished through formal training, such as workshops and seminars, as well as through hands-on experience with pilot projects, including project identification, specification, implementation, operation, and ultimately RE program design.

Technical assistance comes in the form of system specifications, assistance in bid reviews, assessment of renewable resources, and the performance of system acceptance tests. In all program areas, the Sandia team works closely with local equipment suppliers to develop their technical capabilities.

The implementation of pilot projects is used as a tool for institutionalizing the use of RE. The hands-on experience gained through these projects provide in-country partners with the institutional ability to develop appropriate RE applications and to procure and maintain systems in the future. They also help establish connections between the U.S. industry and local business partners.

Monitoring is necessary to ensure the long-tern sustainability of individual systems, provide feedback to members of industry for product improvement, and assess the success of the overall program.

While the pilot projects may result in significant numbers of installed systems, the true measure of success of the program is replication. Replication occurs as the success of the pilot projects becomes known, project implementing organizations and end-users become comfortable procuring and using PV, local businesses gain strength, and financing is made available.

3. The Mexico Renewable Energy Program

Since 1994, Sandia has been applying and refining this program model in the implementation of its Mexico Renewable Energy Program, co-sponsored by the USDOE and the U.S. Agency for International Development (USAID). The Mexico program works with established and funded development programs in Mexico to demonstrate the feasibility of RE technologies in off-grid

productive use applications that offer economic returns to the end users of the systems. With its inclusion in a RE annex of the U.S./Mexico Bi-national Agreement in 1998, the program has facilitated the development of a large portfolio of collaborative RE projects between the two countries.

Through several long-term partnerships with Mexican organizations, the Sandia team has facilitated the implementation of more than 300 RE systems (95% of which are PV) in rural Mexico, representing more than 250 kW of installed capacity. Figure 1 shows the total capacity installed over the life of the program. This trend is shifting from program-sponsored pilot projects, which are being phased out, to replication through new programs and market growth.

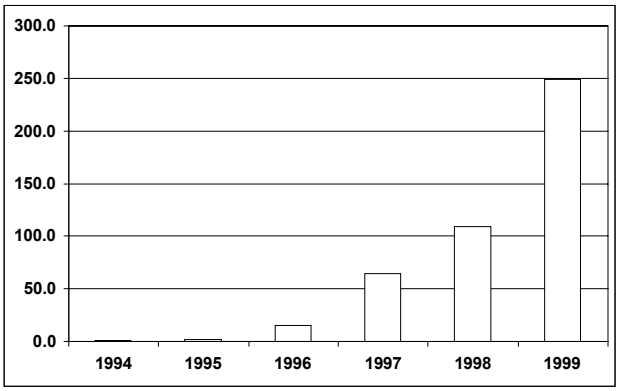

Figure 1: Mexico Program Cumulative Installed kW

Over 175 of these projects are PV water pumping systems, the majority of which are for livestock watering and were installed in partnership with FIRCO, a development organization under the Secretariat of Agriculture. Many other systems (more than 100) have been installed through partnerships with government and non-government organizations involved in the management of protected areas. These include power for ranger stations and research centers, communications systems, and water pumping for communities. In total, more than 100,000 Mexicans are benefiting from these systems.

Through the capacity building and technical assistance activities that have accompanied the implementation of these pilot projects, the Sandia team has trained more than 1600 Mexican engineers, technicians, program implementers, and system suppliers in various aspects of appropriate RE project development. Working with its partners, Sandia has developed technical specifications that have resulted in improved quality and functioning of installed systems. These specifications have been adopted by several organizations throughout Mexico, and are being used in a variety of applications. NREL has developed solar and wind resource maps that have been widely distributed and has used its advanced modeling capabilities to assist in the development of the hybrid systems implemented through the program.

4. Opportunities for U.S. Industry

The Sandia Mexico program has set the stage for significant replication of the pilot projects installed, and U.S. industry is well-positioned to benefit. In the state of Chihuahua, the program has worked with the state government to initiate Mexico's first end-user financing program for both domestic and productive use applications of PV systems. Through a competitively bid award, one U.S. supplier, has already provided more than 150 systems. With assistance from the Sandia team, Winrock International in particular, the Mexican Secretariat of Energy is negotiating with the World Bank and the Global Environment Facility (GEF) to significantly expand on this financing program, with overall investment expected to be in the millions of dollars.

Perhaps the greatest replication success story in Mexico is the first-ever World Bank/GEF program focused on agricultural applications of RE, to be managed and implemented by FIRCO, Sandia's main Mexican partner. This program involves more than $US30 million in investment in RE systems over 5 years. Through the efforts of the Sandia program, several U.S. suppliers have improved their distribution networks and demonstrated their value to FIRCO in many Mexican states. Continued support from the Sandia team will be key to the success of this program.

5. Application of the Model in Central America

The Sandia international program model is now being adapted to provide support to the Central American countries that are still rebuilding in the aftermath of Hurricane Mitch. In April, 1999, Sandia participated in a USDOE/USAID mission to the region to develop a roadmap for sustainable development of the energy sector [5]. The roadmap contains several recommendations for the application of RE technologies, in both on- and off-grid applications. The Sandia team is developing partnerships with government and non-government organizations involved in rural development and local suppliers who wish to develop the capacity to provide technically appropriate, long-lasting systems. This work is sponsored by USAID/Global and the USDOE Office of Technology Access.

Although this Central America program is still in its early stages, several important leveraging opportunities are already under development. Of highest priority are the programs of the USAID missions in the region, which are implementing President Clinton's pledge of $US1B in post-Mitch rebuilding support. Sandia is collaborating with the missions to demonstrate the economic, social, and environmental values of PV and other renewable technologies within their programs. As an example, the Sandia team is providing technical assistance to Fundación Solar, a development organization, and suppliers in Guatemala as they manage the procurement and installation of almost $US1M in PV systems for homes and communities in rural areas. In addition, the World Bank is exploring opportunities for rural electrification in Nicaragua and other countries in the region. Sandia is facilitating informational exchanges between Nicaraguan officials and its Mexican partners involved in the development of the Mexican program. Through its central role in these activities, Sandia plans to build on its successes in Mexico and continue to open new markets for U.S. PV technologies.

6. References

1. U.S. Photovoltaics Industry PV Technology Roadmap Workshop, June 22-25, 1999, Facilitated by the National Center for Photovoltaics (NCPV) for the U.S. PV Industry, (Columbia, MD: Energetics, Incorporated, September 1999).

2. President's Committee of Advisors on Science and Technology (PCAST), Panel on International Cooperation in Energy Research, Development, and Deployment, Powerful Partnerships: The Federal Role in International Cooperation on Energy Innovation, (Washington, DC: Office of Science and Technology Policy, June 1999).

3. Kaufman, S., Et al: Rural Electrification With Solar Energy as a Climate Protection Strategy, (Washington, DC: Renewable Energy Policy Project, January 2000)

4. Richards, E., et al: "Photovoltaics in Mexico: A Model for Increasing the Use of Renewable Energy Systems", Advances in Solar Energy, Vol. 13, (Boulder, CO: American Solar Energy Society, 1999).

5. USAID/USDOE: "Energy Sector Roadmap: Recommendations for the Countries Most Affected by Hurricane Mitch," (July 1999).

The Florida Photovoltaic Buildings Program

Gerard G. Ventre, Ph.D., P.E.

Florida Solar Energy Center
1679 Clearlake Road, Cocoa, Florida 32922

ABSTRACT

The purpose of the Florida Photovoltaic Buildings Program is to establish a sustainable market for grid-tied systems over the next decade, with a goal of 20,000 rooftop installations by 2010. The thrust of the program is to identify and match high value applications with potential end users, and to reduce or eliminate all major barriers to commercialization. Key aspects of the program are quality control, data collection and information dissemination. Florida utilities and other stakeholders have already made major commitments to the program.

1. General Introduction

The Florida Photovoltaic (PV) Buildings Program is a collaborative effort among the Florida Energy Office of the Department of Community Affairs, Sandia National Laboratories, the PV industry, nine end-user groups, and the Florida Solar Energy Center. It complements the federal government's Million Solar Roofs Initiative (MSRI), which calls for one million solar installations in the U.S. by 2010.

2. Underlying Assumptions and Basic Premises

The Florida PV Buildings Program is based on the following underlying assumptions and basic premises:

- PV technology has the potential to make a significant contribution to electric power production in Florida and the U.S. in the twenty-first century.
- Emphasis should be placed on identifying potential end users of the PV technology and delineating high-value applications for each end user, especially for the grid-tied market.
- The development of a sustainable market for grid-tied PV building applications depends on significant price reductions for system installations or equivalent subsidies, and on the removal of other major barriers to commercialization.
- It is important to meet or exceed customer and end user expectations for PV building applications. This requires consistent success in implementing a large number of solar projects.
- The value of PV applications must be readily apparent to potential end users. This requires information and statistically-significant data based on actual experiences.
- For broad acceptance by the building community, new building-integrated products that are attractive and easily assimilated into the building construction process must be developed.
- Widespread markets for grid-tied PV systems will develop most rapidly if the technology is accepted and embraced by the electric utility industry.
- Regardless of economic value, customers should be able to choose PV or other renewable energy technologies to meet a portion of their energy needs.

3. Goals and Objectives

The primary goal of the Florida PV Buildings Program is to establish a solid foundation for a sustainable market for grid-tied systems in Florida. To support this goal, the program has adopted the following objectives:

- Create effective partnerships.
- Generate sufficient revenue and financial resources to support and subsidize applications.
- Overcome major barriers to commercialization.
- Develop a diversity of high-value applications for potential end-user groups.
- Ensure and improve the quality of installed systems.
- Provide sufficient information and data for business planning and decision making.
- Share information, accelerate learning, and improve products and services.

The market for utility-interactive rooftop PV systems is expected to be largely subsidized until significant price reductions are achieved. If price reduction goals can be met, and if major barriers to commercialization can be overcome, it is estimated that as many as 20,000 utility-interactive PV systems may be installed in Florida by 2010. The total number of rooftop solar installations (thermal and PV) in Florida is estimated to be 160,000 by 2010.

4. Approach

During the period of subsidization, the Florida program chooses to invest both time and money in learning and preparing for new markets based on value. Learning will be achieved via application experiments with nine end-user groups. The nine end–user groups include municipal utilities and rural electric cooperatives, commercial building owners and operators, government agencies, school and church organizations, manufactured building corporations, investor-owned utilities and energy service companies, commercial roofing companies, builders and developers, and homeowners and buyers. Of the nine end-user groups, utilities are encouraged to play leading roles in program implementation. Emphasis has been placed on reducing installation and other non-module costs; on determining the impact of distributed generation on the utility grid; on designing energy-efficient PV building systems; on optimizing uninterruptible building power systems; on

evaluating desirable and cost-effective array-roof configurations; on identifying better ways of integrating PV materials into buildings; and on improving the reliability and durability of alternative inverter configurations, including micro-inverters, in warm, humid climates.

5. Ensuring and Improving Quality

To ensure and improve the quality of PV system installations, the Florida plan includes four requirements that must be met to receive buy-down funds, and four other technical support services that can help improve the quality of the products and the capabilities of the practitioners.

The four requirements are:

- Testing and rating of PV modules
- Reviewing and approving PV system designs
- Examining and authorizing PV system installers
- Performing acceptance tests on installed PV systems.

The four technical support services include:

- Offering training programs for PV system designers, installers and code officials.
- Providing assistance in developing technical specifications for procuring PV systems.
- Providing assistance with site surveys and analyses.
- Testing, evaluating and troubleshooting existing PV system installations.

6. Provide Information for Planning and Decision Making

All Florida PV building systems are being monitored for performance, and additional reliability data is being collected. The data and information will allow different end users to assess the value of various PV building applications. It is important to note that the value many end users associate with photovoltaic systems may not be strongly tied to economics. Examples include the value associated with a cleaner environment; the value of less dependence on imported and depletable fossil fuels; the value of a green image; the value of improved public relations; the value of having uninterruptible building power; and, in the case of utilities, the value of providing customers with the option to choose renewable resources to meet a portion of their energy needs. The data and information collected will help market-focused organizations prepare value propositions for a variety of PV building applications. End users will be much better prepared to establish performance expectations and make decisions concerning PV building systems. They will also have much better data upon which to base life cycle cost analyses and business planning.

7. Accomplishments

A number of accomplishments are noteworthy, including the strong partnerships that have been established with Florida utilities, the PV industry and other organizations. Statewide marketing of green pricing programs is underway, and an effective communication network has been established. Over $300,000 has been distributed by FSEC to buy down the cost of over 100 grid-tied PV building systems, and these funds have been leveraged by a factor of four to one.

Interconnection requirements that address the legitimate concerns of both utilities and PV system owners and operators have been recommended to Florida utilities and the Public Service Commission. These recommendations address standards, codes, metering, billing, liability insurance, and the application and compliance process.

Seven PV system installation training courses with examinations have been offered, and forty-nine installers have been authorized to participate in the Florida buydown program.

A PV systems data network has been developed and system performance data for a variety of applications is readily available on FSEC's website.

Florida utilities have committed to 3.8 MW of grid-tied PV systems by 2007, with over half of that coming from municipal utilities.

The Florida program is being used as a model in training workshops for other MSRI partnerships.

In closing, it is important to state that the thrust of this program is to establish value based on data and real experience and to reduce or eliminate all major barriers to commercialization. The intent is *not* to blindly push for large numbers of system installations and promote artificial markets. For scenarios where value and benefits can be clearly established and price reduction goals can be achieved, real markets will follow.

8. Acknowledgements

This work was supported by the U.S. Department of Energy, Sandia National Laboratories, Florida Energy Office of the Department of Community Affairs, and the State of Florida.

Photovoltaics for Buildings: Case Studies of High-Performance Buildings with PV

Sheila J. Hayter, P.E.
Paul A. Torcellini, Ph.D., P.E.

National Renewable Energy Laboratory

1617 Cole Blvd.
Golden, CO 80401

ABSTRACT

Energy efficiency maximizes the value of photovoltaics (PV) in buildings systems. A fixed-sized PV system will offset a much larger part of the electrical load in an energy-efficient building than in a building whose energy design has not been optimized. Integrating an energy-design process when designing buildings helps to evaluate strategies such as daylighting, passive solar heating and cooling, properly engineered heating, ventilating, and air-conditioning (HVAC) systems, improved envelope characteristics, and advanced control systems. These systems – working together – result in substantial energy reduction, making it possible for a reasonably sized PV system to meet a significant portion of the remaining electrical load. This paper focuses on three high-performance buildings whose electricity loads are almost entirely met by modest-sized PV systems.

1. Energy-Design Process

Designing and constructing low-energy buildings (buildings that consume 50% to 70% less energy than code-compliant buildings) require the design team to follow an energy-design process that considers how the building envelope and systems work together. The process requires a design team to set energy-efficiency goals at the beginning of the pre-design phase (Table 1) [1]. Detailed computer simulations used throughout the design and construction phases ensure that the building is optimized for energy efficiency and that changes to the design do not adversely affect energy performance. Properly commissioning the building and educating the building operators are the final steps to successfully constructing a low-energy building.

2. BigHorn Center

The BigHorn Center is a collection of five retail spaces in Silverthorne, Colorado. A design goal for the BigHorn Center was to create a sustainable retail environment. The complex was constructed in three phases. Phase III, completed in April 2000, houses a 17,000-ft^2 (1579-m^2) hardware store and support areas and a 22,000-ft^2 (2044-m^2) building materials warehouse. This phase incorporates the most aggressive sustainable design strategies of the three phases. These strategies include daylighting, advanced lighting technologies, natural ventilation for cooling, transpired solar collector, building-integrated PV, improved envelope features, and integrated controls.

Photovoltaic modules laminated onto the standing-seam metal roof panels were installed on the south-facing roof of the hardware store clerestory and the warehouse dormer [2]. The amorphous-silicon PV modules were wired into three arrays, each serving one phase of the three-phase building power system. The design capacity of the PV system is 8 kW, and the array covers all the available Phase III, south-facing roof area. The BigHorn Center developer/owner has a net-metering agreement with the utility to receive full credit for power that the PV system exports back to the grid.

The design team used the energy-design process to integrate daylighting opportunities, efficient mechanical systems, and improved building envelope features into an optimized building design. It is estimated that the resulting design saves about 21 kW in demand, making it possible for the 8 kW of PV power to meet a significant portion of the annual building electrical load. Designers anticipate that during sunny summer days, it will be possible for the building to export power to the grid during business hours. If daylighting and other design features had not been incorporated, it would not have been feasible to purchase and install enough PV power to offset an equivalent portion of the base-case building load.

The business plan for the project encompassed the ability to sell "green" products in the retail environment. To that end, the building became a statement to the sustainable mission, and the energy features were an integral part of the

Table 1. Energy-Design Process Steps

Pre-Design	Design	Construction/Occupation
1. Simulate a base-case model, establish energy-use targets	5. Prepare preliminary architectural drawings	8. Rerun simulations before construction design changes
2. Complete parametric analysis	6. Design the heating, ventilating, and air conditioning (HVAC) and lighting systems	9. Commission all equipment and controls. Educate building operators to ensure that they operate the building as is intended
3. Brainstorm solutions	7. Finalize plans and specifications	
4. Perform simulations on base-case variants considering economic criteria		

building. Photovoltaic modules integrated into the roofing was an additional cost; however, the marketing value of this investment, coupled with the other features, created a total cost-effective business plan. Even before construction of the BigHorn Center was completed, the owner/developer saw increased sales in his existing facility, which he attributed to the publicity he received for installing the PV system and other sustainable design features.

The BigHorn Center is the first commercial building in the State of Colorado to have a standing-seam metal roof-integrated PV system, and it is the largest building-integrated PV system in Colorado. The grid-tied PV system is one of the first net-metered commercial buildings in Colorado. The BigHorn Center is also one of the first examples in the United States of truly integrated daylighting and natural ventilation cooling systems in a retail space.

3. Zion National Park Visitor Center

The Zion National Park Visitor Center and Comfort Station, under construction at the time this paper was written, will be two of the National Park Service's (NPS) most efficient buildings. The design team optimized the performance of the aggressive low-energy design strategies into the 7600-ft^2 (706-m^2) Visitor Center and 1100-ft^2 (102-m^2) Comfort Station. Design features in both buildings include daylighting, Trombe walls for passive solar heating, downdraft cooling towers for natural ventilation cooling, energy-efficient lighting, and advanced building controls. It is estimated that these features result in about 10 kW of electrical demand savings.

Zion National Park is located in a remote area of southern Utah, where power reliability is an issue. For this reason, the NPS required an uninterrupted power system (UPS) for the buildings. The only additional cost to convert the UPS to a PV-for-buildings system was PV array because the battery storage and balance-of-system components were already a part of the UPS design.

A 7.5-kW roof-mounted PV system is planned to be installed on the south-facing roof of the Visitor Center. Because of the daylighting and natural ventilation cooling systems, designers anticipate that the building's PV system will export power to the utility grid during the summer. During power outages, the building control system will shut down nonessential electrical loads so that the PV/UPS system will be capable of supporting enough building operations to continue business for at least one-half hour without any additional PV power, or all day if PV capacity is available.

Officials at Zion National Park are negotiating a net-metering agreement with the local utility. When an agreement has been reached, this will be the first net-metered system in the State of Utah.

4. Van Geet Residence

The Van Geet Residence is a 3000-ft^2 (279-m^2) home constructed off the utility grid at an elevation of 9200 ft (2804 m) near Idaho Springs, Colorado. The design of the house was optimized to incorporate passive solar heating (including direct solar gain and Trombe walls), natural ventilation cooling, daylighting, and a good thermal envelope. Mass was incorporated into the building shell and some internal walls using dry-stack concrete blocks filled with concrete. Insulation was attached to the external surface of the block. Solar domestic hot-water (SDHW) heating and supplementary space heating needs are met by a solar hot-water system. Energy-efficient lighting and appliances (the refrigerator uses 75% less energy than a conventional refrigerator) minimize electrical loads in the house.

A 1000-W (rated) PV array provides electric power for the house and powers the well pump. Power from the PV array is stored in a battery bank, and an inverter converts the 24V DC from the PV array to 120V AC. An automatic propane generator meets the remaining loads when PV/battery power is not available. During the two years since the house was completed, the occupants have relied on the generator to meet less than 10% of their total power needs.

The Van Geet house is two miles from the power line. It was less expensive to incorporate energy-efficient and renewable energy technologies into the design than it would have been to extend the power line to the house.

5. Summary

In all three examples discussed in this paper, the PV system initial cost and physical size were minimized because aggressive energy-efficiency design measures were first incorporated into the building designs. It is more cost effective to reduce building loads through good design than it is to meet building loads with renewable energy technologies. Photovoltaic and other renewable energy technologies can be viable solutions to meeting today's building energy needs only when combined with measures to minimize building energy loads.

6. Acknowledgements

The National Renewable Energy Laboratory's High-Performance Buildings Research Project and Photovoltaics for Buildings Task provided support for the energy design of the buildings described in this paper. The Department of Energy provides funding for these two activities from the Office of Building Technology, State and Community Programs and from the Office of Power Technologies, respectively.

7. References

[1] Torcellini, P.A., S.J. Hayter, R. Judkoff: "Low-Energy Building Design—the Process and a Case Study," *ASHRAE Transactions*, V 105, Part 2, (1999) 802-810.

[2] Ovonic, *UniSolar* Web Site, www.ovonic.com/unisolar, accessed March 27, 2000.

A Utility Perspective of PV Commercialization

S. Hester, J. Serfass, M. Fioravanti, W. Bensley

Utility PhotoVoltaic Group

Washington, D. C.

ABSTRACT

Utilities and their customers are a significant market for the PV industry. The UPVG's TEAM-UP program has helped develop new energy service business models for PV, including development of dealer networks, joint ventures, and community-based efforts. The UPVG identifies current market development activities that are necessary to accelerate the deployment of PV systems in grid-connected applications. Hardware deployment efforts must continue to expand the business and customer knowledge base.

1. Introduction

The UPVG is a nonprofit association that consists of 100 energy service providers (electric utilities and energy service companies) and over 50 associate members cooperating to develop PV power as a commercial energy option for the benefit of members and their customers. The efforts consist of awareness and education activities and the major hardware deployment effort is the TEAM-UP program.

TEAM-UP (Technology Experience to Accelerate Markets for Utility Photovoltaics) is a partnership of the U. S. electric utility industry and the U.S. Department of Energy to accelerate the deployment of photovoltaic (PV) systems and stimulate the development of a sustainable domestic market. TEAM-UP is an industry managed program to significantly increase PV deployment by cost-sharing PV system installations. The TEAM-UP program is intended to help develop sustainable markets and opportunities for energy service providers and their customers by establishing the needed experience that leads to business opportunities

2. Results of TEAM-UP

The TEAM-UP program has issued funding awards to 36 teams for $15.0 million of DOE funds. Through these efforts they will install 7.4 MW of PV systems in over 1300 installations in 34 states across the U.S. resulting in over $70 million worth of PV projects. There are some 70 utilities involved in the program. hardware deployment efforts, the UPVG can encourage new entrants into the PV market and provide assistance with:

Developing/implementing PV business models;

The TEAM-UP program has been successful in many areas. Federal funds have been significantly leveraged with participant funding. Thirteen different PV manufacturer/technologies are deployed, encompassing almost every available PV material. Nine inverter manufacturers technologies are represented. System configurations include horizontal roof-mounted, fixed roof- and ground- mounted structures, one-axis tracking, polar tracking, and two-axis tracking concentrator designs. The majority of TEAM-UP PV systems are mounted on the roofs of commercial buildings, residential homes, and community facilities such as schools.

The program has helped clarify the relative importance of key issues for PV commercialization. The experiences and lessons captured from the TEAM-UP program have given the UPVG considerable insight into the process and potential of expanding the market and in deploying PV across the nation

3. Utilities Remain Critical to Market Development

There are several reasons why it is important to encourage energy service providers to take the lead in expanding the PV market: 1) simplifying the market by significantly lowering transaction costs; 2) ability to purchase the PV systems or components at a lower cost by purchasing in large quantities; 3) capacity to persuade and convince builders and developers to integrate PV into their designs; and 4) ability to integrate PV with other energy system options. The following market development activities are necessary to expand the commercialization of PV with utilities and energy service providers:

Engage New Utilities and Other Energy Service Providers -- Even with the extensive efforts of the UPVG and TEAM-UP, only a small number of energy service providers in the U. S. have made significant commitments to PV. However, in the age of deregulation and increased competition, new markets will begin to value the qualities that PV electricity provides. In order for new energy service providers to become involved they will need assistance to initiate a PV program within their organization. Building on the current

Green pricing strategies;
Identifying market entry projects; and
Identifying market barriers in their service territories.

Develop More Large-Scale Sustainable PV Programs -- Several energy service providers have developed large PV programs. The UPVG can help develop additional large-scale sustainable PV programs by:

Identifying new marketing strategies;
Assisting with business practices and models;
Identifying large scale commercial projects; and
Addressing and removing market barriers in their service territories.

Encouraging New Delivery Channels for PV -- The TEAM-UP program has helped develop new channels for PV, including development of dealer networks, joint ventures, and community-based efforts. New hardware deployment efforts should continue to push the envelope with respect to delivery channels.

Integration of PV with Buildings and other Distributed Technologies -- Building-integrated PV and integration of PV with other distributed technologies are promising areas that have been identified by UPVG members and by TEAM-UP projects. Efforts to develop these markets should be encouraged in a new PV hardware deployment effort.

4. Future Hardware Deployment Must Address the Continuing Barriers -- TEAM-UP has been a valuable program mobilizing unprecedented utility interest in PV commercialization and sustainability. There are still a number of significant barriers delaying the development of the PV market which future efforts must address:

Cost – Both hardware and non-hardware costs prevent PV from being economically competitive with other energy generation options. Hardware costs have declined somewhat over the last three to four years. Additional items can significantly add to the cost of the PV system including transaction costs, finance, insurance, permitting, etc. and these items should be the focus of continuing hardware deployment efforts by the UPVG.

Technology – Although PV technology has made significant strides over the last few years, reliability is still somewhat of an issue. Inverters are still the primary cause for downtime of a system. While modules have been performing well, overall system ratings are usually less than expected. Future hardware deployment efforts must focus on improvements in these areas. Although PV *components* come with warranties, many system providers do not give PV *system* warranties. Energy service providers may be one way to fill this need.

Infrastructure – Strong infrastructure is imperative for market development. Who do you call if you want to purchase or install a PV system for your house or building? Are they local? Do they have any experience? What if the system needs repairs and maintenance? There is a shortage of sales, supply, and service capability. Utilities and energy service providers can provide customers with a simple contact for this capability, whether it is developed internally or directed to independent businesses increasing customer confidence.

Standards and Codes – PV standards and codes and covenants still remain barriers for PV installations. The recent development of IEEE 929 will be very beneficial for the technical area of interconnection. In the policy and non-technical area much still needs to be done. Building and electrical permitting departments may present unforeseen obstacles if they are unfamiliar with PV. Interconnection contracts historically are cumbersome and burden customers with legal hassles, though some states and other organizations are making significant progress for small systems. The UPVG can help utilities and others address these problems.

Education – Educating utilities and raising consumer awareness remains critical to catalyzing greater demand for PV. Many utilities still need to be convinced that PV represents an opportunity to win new customers and expand business. Tying hardware deployment to grassroots campaigns aimed at schools and local communities creates awareness of alternative energy options, allowing customers to know what to demand from their local energy service provider. Example projects can also be used to make decision makers in the building and energy industry aware of the values PV provides.

5. Conclusions and Recommendations

Continuing hardware deployment, along with UPVG's education and outreach activities will help test and refine practical solutions to PV commercialization. In a new solicitation of cost-shared PV projects, the UPVG expects to see substantial progress in reducing barriers. Increased deployment of standardized systems should improve the technology, the reliability, and performance, and will, most importantly, lower the costs. Support infrastructure will be addressed. The IEEE 929 standard should have a very positive impact on resolving technical interconnection concerns and model interconnection contracts/tariffs can be more widely publicized. Finally, hardware deployment efforts will continue to carry tremendous educational value at all levels.

Jointly with the PV industry and Federal Government agencies, the UPVG will participate in setting a longer term strategy for PV commercialization with the goal of creating unsubsidized multiple-year multiple-megawatt utility markets.

Incentives as a Tool for Stimulating Photovoltaic Market Growth

Christy Herig

National Renewable Energy Laboratory

1617 Cole Blvd. Golden, CO 80401

ABSTRACT

This paper summarizes several studies [1–4] analyzing consumer incentives for the grid-tied domestic photovoltaic (PV) market. Most policy incentives have evolved through state legislative and regulatory utility restructuring activities since 1996. The incentives run the gamut from reducing capital costs, such as buy-downs, grants, and income tax rebates, to optimizing life-cycle benefits, such as net metering and property-tax exemptions. Exemplifying market stimulation, in 1996, only the State of Hawaii's residential break-even turnkey cost (BTC) of $7.50/W exceeded the lowest-reported installed cost of $6.21/W [5]. In 1999, however, nine states' BTCs exceeded the installed system cost of $4.50/W. With installed PV-system costs declining, economic analysis indicates that the market-transition intent of the policy incentives is possible. However, consumer awareness (states typically do not market incentives), PV-industry small-system distribution infrastructure, and utility interconnection are deployment barriers that are causing a slow start to consumer participation, and they may extend the timeframes (currently 4-10 years) for the incentives.

1. Introduction

The domestic market for customer-sited photovoltaics (CSPV) has historically consisted of off-grid systems for which the capital cost of the distribution-line extension offsets the CSPV cost. Grid energy prices ranging from 5¢-14¢/kWh for residential and 5¢-12¢/kWh for commercial do not recover capital investment over the life of the system [5]. However, PV-system installed costs have declined from $6.21/W in 1996 to $3.90/W in 2000,[1] with levelized energy costs of 17¢–12¢/kWh,[2] respectively [5]. Additionally, the PV industry has developed products targeted at the grid-tied residential and commercial market and has developed financing packages to alleviate the up-front cost burden to the consumer. The gap between consumer value and cost for CSPV is close, but not close enough for most U.S. consumers. The final market stimulus for grid-tied CSPV has been the consumer incentives evolving from state utility restructuring, intended to transition the electricity service market toward competition. These include:

- 9 states with income tax rebates
- 30 states with net metering [6]
- 12 states with buy-down or grant programs
- 11 states with property tax exemptions

In addition to the state incentives, the federal 10% tax credit and accelerated depreciation allowance for commercial businesses stimulate the CSPV market. The analysis summary identifies the CSPV consumer value, including incentives for the domestic market, which provides industry with geographic market targets (see Figs. 1 and 2).

2. Approach

The CSPV consumer-value analysis differs for the residential and commercial sectors because of the assumptions [2, 3], data aggregation, and mapping; but the cash-flow analysis resulting in a BTC is a similar indicator. BTC is the iterated system-cost input to a life-cycle benefit and cost cash flow, which is forced to a net present worth of zero. The BTC is the market hurdle price a consumer can pay for a CSPV system without making or loosing money over the life of the system; the consumer breaks even.

3. Results

The first residential BTC analysis was completed in 1996, prior to the establishment of any regulatory incentives. The white columns in Figure 2 show the results of this analysis. The analysis was updated in 1999, with 12 new capital cost-reducing incentives included.

The commercial BTC analysis was first completed in 1998 [3] and was expanded to include the values of material replacement of building-integrated PV products, load-control enhancement, emergency generation, and environmental benefits [4]. The results, shown in Figure 2, are indicative of incentives and energy values only. Building-material replacement values, such as PV replacing spandrel glass, could add $1,70/kW to these values.

4. Conclusions

Though many of the incentives used in the analysis have changed or become obsolete, there is potential for new incentives. Currently, 23 states have initiated or implemented restructuring policies, and 16 states have renewables provisions. The system benefits charges (SBC), included in 13 state restructuring policies, are a source of funding for consumer incentives. Thus far, only 7 of the 13 state SBCs have been implemented, leaving potential for more near-term incentives. Additionally, potential new

[1] These costs are the result of an aggregate long-term purchase for the Sacramento Municipal Utility District Pioneer PV program and represent the lowest reported residential installed costs. These are representative of commercial PV systems of 30 kW or more. The year 2000 cost was estimated from the committed contract price.

[2] Levelized costs are for residential systems with first-mortgage financing and retail-rate compensation for energy production at 10¢/kWh.

arenas for consumer incentives include nine states implementing renewable-portfolio standards, the Million Solar Roofs initiative, 40+ community partnerships that are working on consumer awareness, reducing infrastructure barriers and municipal policies [7], and the 50 utility green-pricing programs, either offered or under development.

Though the potential for market stimulation through incentives is established by analyzing the increased consumer value, the effectiveness as measured by participation of various types of incentives has not been explored and should be a next step to this work.

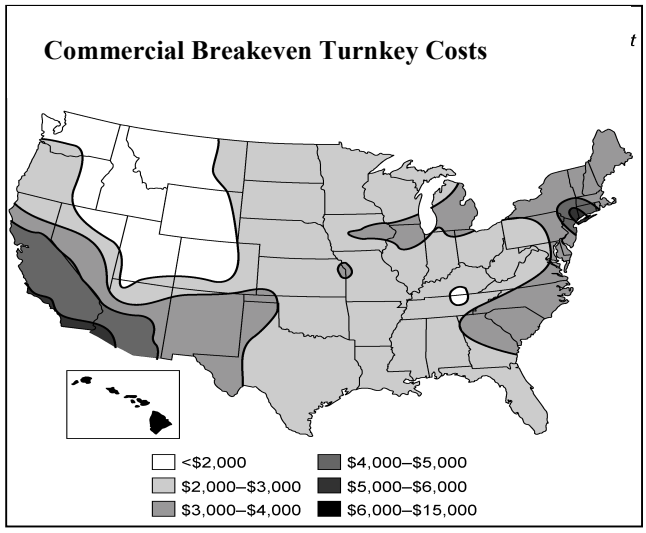

Figure 1. Commercial breakeven turnkey costs.

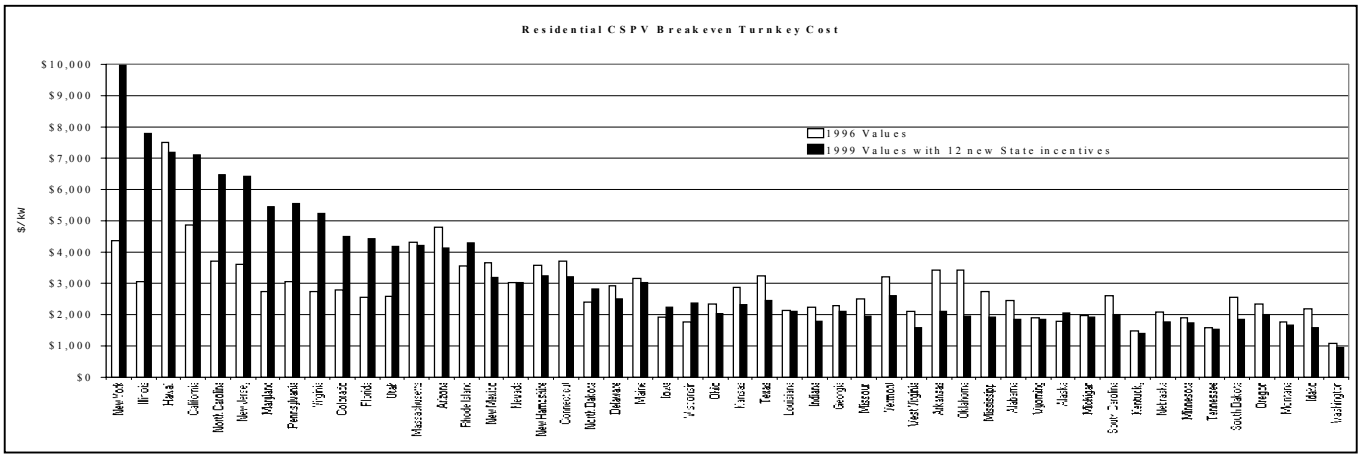

Figure 2. Residential CSPV breakeven turnkey costs.

5. References

[1] Wenger, H., et.al., "Niche Markets for Grid-Connected Photovoltaics," IEEE Photovoltaic Specialists Conference, Washington, D.C., 10/96

[2]Herig, C., et al., "Residential Customer-Sited Photovoltaics Niche Markets 1999," American Solar Energy Society, Portland, Maine, 6/99

[3]Perez R., et al., "Geographical Distribution of the Value of Demand-Side Commercial PV Systems in the United States," Plenary article, 2nd World PV Conference, Vienna Austria, 1998

[4] Perez,R., et al., "Mapping the Value of Commercial PV Installations in the US – Accounting for Externalities," American Solar Energy Society, Portland, Maine, 6/99

[5] Osborn, D., "Sustained Orderly Development and Commercialization of Grid-Connected Photovoltaics: SMUD as a Case Example," A pre-print from Advances in Solar Energy XIV, 2000, Ver. 02/24/2000

[6] Starrs, T. (Mar. 2000), Personal Communications, "Summary of State Net Metering Programs (current)", Kelso Starrs and Assoc., Vashon, WA

[7] President's 1-Million Roof Program, USDOE @ http://www.millionsolarroofs.com, 3/00

A Discussion on Life-Cycle Costs of Residential Photovoltaic Systems

Mike Thomas and Chris Cameron

Sandia National Laboratories*
Albuquerque, NM 87123-0753

ABSTRACT
This paper discusses the characteristics and needed improvements/enhancements required for the expansion of the grid-tied residential power systems market. The purpose of the paper is to help establish a common understanding, between the technical community and the customers of the technology, of value and costs and what is required in the longer term for reaching the full potential of this application.

INTRODUCTION
The decision to invest in PV is based on a unique set of values depending on everything from improvement of the environment, to more personal involvement in energy production, to increased reliability, to energy value. In this paper, we will discuss many of the key technical and non-technical elements that affect values and the purchase of residential PV systems. The intent of the paper is to lay a foundation for common understanding of terms, an understanding that is required for the technology to be understood by all and the lack of which is currently a major barrier toward future expansion of the residential application. We will first look at the rationale commonly used to purchase such a system and combine them into a discussion regarding system value and costs.

The decision to purchase a PV system is affected by a number of issues including:

- What do customers want?
- What is the purchase price?
- Is there a product/system infrastructure available?
- What is required to own and maintain a system?

The following customer specific values and costs are at the heart of the discussion to improve acceptance of PV systems and include

- Enhanced quality (value)
- Training of installers and builders (cost)
- Development of a qualified database (cost)
- Improved building integration (value)
- Reduction in installed and recurring costs (cost)
- Expanded electric utility acceptance (value)
- Improved consumer education (value)

WHAT DO CUSTOMERS WANT?
The consumer buys many things that are seen as good investments because of their quality and because of the perceived benefit from them. While some of these reasons may change in the future, the primary benefits from PV today are substantial. First, the residential consumer can use PV to offset energy production from other more polluting technologies. PV systems can be placed on the roof of virtually any structure and therefore require no additional land space. PV, like solar thermal hot water collectors, can directly defer costs and increase self-reliance. These systems also require very little routine maintenance.

The size in watts of a residential, grid-tied PV system is not really a design issue, but one of preference and match with the structure and its orientation. There is little economy of scale difference between 500 W and 5 kW. So the homeowner can invest a relatively modest amount and still get some of the benefits. Because of the modularity, the consumer can either increase or move their system. This issue is, in fact, critical because of the re-roofing issue (discussed later).

WHAT IS THE PURCHASE PRICE?
It would be convenient to be able to combine all of these concepts and come up with a cost and a value for these types of systems on a national basis. There are many reasons why this is not straightforward. First, the economic value from the systems is, to a first approximation, a function of the amount of sunshine and the utility rates. These two commodities are different for each locale throughout the country, so the energy value will be different. Systems in areas with the high sunshine and highest utility rates will provide the highest energy value. If energy value were the sole reason for purchase, then sales would be limited to those areas of the country where the value is greatest.

Right now with an installed system efficiency of ~10%, 1 kW nameplate of PV modules will produce from about 1050 to 1650 kWh ac depending on location. At an average kWh price of $0.10, that means the total energy value ranges from a little over $100 in the first year to $165. Today's purchase prices vary from about $6.00/W to over $10/W installed. Industry/government goals for 3-5 years out put these costs at about half, and in ten years down to half again -- $1.50-$2.50/W. Even for a system that produced $165/year and cost $1.50/W, that corresponds to a breakeven in less than ten years if there are no recurring costs and if the energy production is

constant. With these small economic benefits, it is likely that the decision to purchase a PV system, especially with energy storage, will be based more on self-reliance and environmental responsibility than on return of investment.

IS THERE A PRODUCT/SYSTEM INFRASTRUCUTRE AVAILABLE?

Today, most of the applications are added to existing structures. Several manufacturers have complete products (kits) that can be added to existing structures, from about 300 W up to several kW. This has resulted in reducing the indirect costs of marketing, distribution, and design. New construction and integration, especially in manufactured and other standard housing, represents a potentially large opportunity for PV in the future. On the other hand, custom design and integration in new housing could potentially decrease reliability and increase costs.

Customer satisfaction is based upon perceived value, a combination of benefits including cost and quality of systems. Quality is dependent upon the design, choice of components, installation, and maintenance. There is currently a dearth of training and certification programs that address the quality issues. The State of Florida has recently begun a certification program for installers through the Florida Solar Energy Center which is also developing a hardware and design approval process through the Florida PV Buildings Program. The manufacturers of packaged systems are attempting to build quality into their products by standardized design and by requiring specific training of its installers.

The weak link currently appears to be in the area of maintaining systems and components that are being sold with a stated 20 to 30 year lifetime. Only a limited number of electrical contractors currently have experience with PV systems. The solar industry and a few states are attempting to improve the situation through certification programs but this is an area that is only now developing. Once this situation is corrected, the cost of the after installation service will still need to be addressed.

WHAT IS REQUIRED TO OWN AND MAINTAIN A SYSTEM?

What can be expected from a PV system after installation? There are simply too few of these systems with a long enough history to answer this question with certainty. Let's look at some of the potential sources of problems.

Most of today's systems are placed over an existing roof structure. The time to replacement of the covering for flat roofs averages about 8 years in the southwestern part of the country, and most pitched roofs with standard materials are re-shingled perhaps every 12-15 years. Because these are the types of roofs that will potentially accommodate the largest numbers of PV systems, the labor cost of removal and re-attachment at least once during the 30-year life of the PV system is a starting point. The expected lifetime of the inverters even with maintenance is no greater than its internal components and has been estimated at 20 years. Thus, there will be the replacement cost of the inverter. Since the average American moves every 8 years, the 30-year concept has limited value until it is included in and increases the value of the structure upon resale. However, depending upon the age of the system and the roof, this could be a liability. We assume that in time the inverter will be a plug and play, but probably hard-wired except for ac modules and that the consumer will be able to perform this action, and that approach will save time and money. The re-roofing is a different matter for most.

Lifetime is a function of reliability and value. Once the cost (real and perceived) to maintain a system exceeds the value (real and perceived), the system is at end of life. Reliability is dependent upon the quality of the components, design, installation, and maintenance. Because the reliability and maintenance data on the residential application are so limited, we have no way to assess how the value of these systems will be impacted over time.

Another issue is general degradation of the system. This takes two forms, reversible and irreversible. An example of reversible degradation is soiling of the array which can reduce the output of an array in a rural or urban setting by as much as 25%. This is reversible because the array could be cleaned….at a cost. Irreversible electrical degradation is seen in almost all modules and represents about 0.5%/yr. A residential customer could ignore this small amount of degradation because it will represent only 50-100 kWh/ten years and the utility is providing back-up. However, it will diminish the energy value from the system.

A potentially large area of future maintenance will result from those systems where energy storage is added. While energy storage represents a very large potential benefit in terms of system availability, batteries do require routine maintenance, a special location, and replacement. Clearly there will be additional costs that must be defined including labor and capital.

SUMMARY

In summary, elements that are unique to the purchaser of future grid-tied residential systems have been discussed to develop a common understanding of the costs and values of these types of systems. Investment value is seen as secondary to self-reliance and environmental concerns. However, these benefits could easily be overshadowed by hassles caused by poor reliability and lack of affordable technical support once the system is installed.

*Sandia is a multi-program laboratory operated by Sandia Corporation, a Lockheed Martin Company, for the U.S. Department of Energy under Contract DE-AC04-94AL85000.

Module 30 Year Life : What Does it Mean and Is it Predictable/Achievable?

T. J. McMahon, G. J. Jorgensen, and R. L. Hulstrom
National Renewable Energy Laboratory, Golden, CO

D. L. King and M. A. Quintana
Sandia National Laboratories, Albuquerque, NM

ABSTRACT

We define what we mean by a 30-year module life and the testing protocol that we believe is involved in achieving such a prediction. However, we do not believe that a universal test (or series of tests) will allow for such a prediction to be made. We can test for a lot of things, but we believe it is impossible to provide a 30-year certification for any arbitrary photovoltaic (PV) module submitted for test. We explain our belief in this paper.

1. Introduction

The photovoltaic (PV) industry wants a module technology that will last 30 years in the field as well as a means by which to certify that a module technology will, indeed, last 30 years. First, we must define what we mean by a 30-year life. Second, we will lay out the accelerated environmental test (AET) protocol involved in such a prediction. Third, we will discuss the time-to-failure calculation and the likelihood of such a certification process. And finally, short of such a certification process, we discuss an approach for rank ordering and testing of failure modes. The rank ordering would be similar to the "Life-Cycle Energy Cost Impact" analysis proposed by R.G. Ross [1].

2. Thirty-Year Life

The language used here is critical. It is clearly impossible to expect that for a given module type, every one will last 30 year without failure. The issue is reliability. What constitutes a failure for one person may not be a failure for others. As a starting point we paraphrase a textbook definition of reliability: [2] "a reliable PV module has a high probability that it will perform its intended purpose adequately for 30 years, under the operating conditions encountered." For simplicity we will say a PV module fails to provide service if its power output decreases by more than 30% after 30 years in its use environment. Also, "a high probability" means that 95% of the modules in the field will achieve this success. By "use environment" we mean any and all use environments that the PV module will experience during service. Site meteorology, handling, and installation are included in use-environment considerations.

3. Accelerated Environmental Testing

A life-prediction approach specifically designed for PV cells and minimodules is outlined elsewhere [3]. Lifetime- prediction tests appropriate for full-sized modules would be possible only when a final module design is defined, all failure modes are identified for that module design, and acceleration parameters for each relevant environmental stress are known. The AET's chosen must use stress or combinations of stresses that will accelerate failure modes that actually occur in the real world. Module lifetime in Florida may be very different than in Arizona. We must decide which performance parameter(s) should be measured to best monitor the failure mode being evaluated and then define what constitutes a failure for that performance parameter.

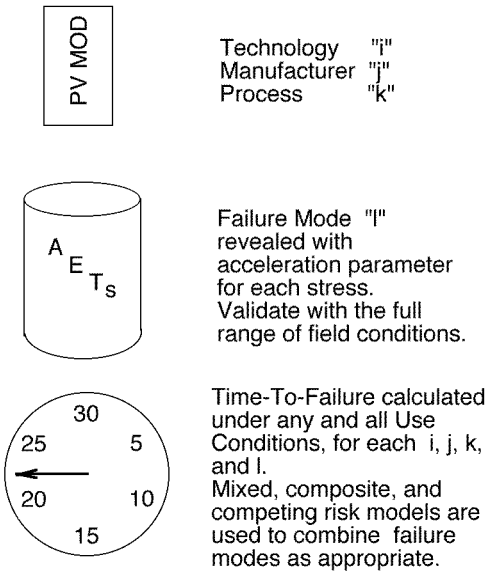

Fig. 1. Diagram of Life Prediction Process

To use AETs for life-prediction testing we divide the protocol into five steps: (1) Identify and isolate all failure modes, e.g., in a c-Si module we might look at solder-bond fatigue or in a thin-film module it might be film adhesion or moisture intrusion.; (2) Design and perform AETs, e.g. thermal cycling with series resistance as a metric or damp heat with visual inspection as a metric; (3) Use appropriate statistical distributions to model specific failure rates; (4) Choose and apply relevant acceleration models to transform failure rates; (5) Develop a total module failure rate as a composite of individual rates to allow service lifetime prediction for each use condition. Fig. 1 outlines this process.

In step (1) above, all of the failure modes designated by "l" must be determined for each module submitted for test. The materials technology and cell design are denoted by the subscript "i". If multiple manufacturers are using that technology, we need a second subscript "j" to denote the manufacturer and probable differences in material processing and/or cell design. If there are different processes or designs used by the same manufacturer, then we need a third subscript "k". For each module, $MOD_{i,j,k}$, the l^{th} failure mode must be identified and, ideally, the underlying failure mechanism (cause) found.

4. Life-Prediction Modeling

Steps (2) through (4) fix the acceleration parameter for the failure model used for the l^{th}-mode under test for each $MOD_{i,j,k}$; call this acceleration parameter $a_{l(i,j,k)}$. The time-to-failure (TTF) under outdoor use is equated to the TTF under accelerated stress by

$$TTF^{use}_{l(i,j,k)} = a_{l(i,j,k)} \bullet TTF^{stress}_{l(i,j,k)}. \qquad (1)$$

If the mechanism changes, the acceleration and failure model need to be changed. A hazard function is developed from the failure model and $a_{l(i,j,k)}$ used for equation (1). If the different TTFs associated with each of M failure modes are statistically independent, then the hazard rate-function, h(t), follows the addition rule [2]:

$$h_{(i,j,k)}(t) = \sum_{l(i,j,k)=1}^{M} h_{l(i,j,k)}(t). \qquad (2)$$

The M failure modes include anything that can fail with the cell, interconnects, bus, encapsulation, leads, J-boxes, etc. A unique hazard function is obtained for each module. Equation (2) combines each failure-mode hazard function into a composite and allows a life prediction. We use the following identity found on p. 118 of reference [2]:

$$1 - F(t) = \exp\left[-\int_0^t h_{(i,j,k)}(t')dt' \right]. \qquad (3)$$

For a 95% survival rate after 30 years equation (3) becomes:

$$Ln(1 - 0.95) \geq \int_0^{30yr} h_{(i,j,k)}(t)\,dt. \qquad (4)$$

For each use condition (site), all of the stress conditions must be known throughout the year. The hazard rate for a given (i,j,k) must be low enough that for all use conditions, equation (4) is obeyed. Is it possible to have a series of tests that could predict h-values for any module (i,j,k) submitted for test under all possible use conditions? In principle this may be possible, but a quick consideration of possible combinations of (i,j,k,l) indicates literally hundreds of potentially unique situations- too many handle in practice.

5. Alternative Approach

It is quite clear that a universal 30-year life prediction protocol will be impossible to obtain. We must look for a testing protocol short of a 30-year certification that will still serve our industry well. A series of AETs need to be developed that produce the most critical yet realistic failure modes. Some AETs will produce failure caused by known failure modes, and other tests will be used to discover new, unknown failure modes. For life prediction, we also need to test for "wear-out" mechanisms, as well as failure mechanisms whose rate decreases with time. The Weibull distribution function [2] has the broadest application for modeling TTFs for rates of failure that increase with time. Other statistical distributions can be used if the mechanism is known [3]. We need to establish the relative importance of the mechanism for which we are testing, i.e. rank order, and determine the TTF distributions to estimate life expectancy for the dominant failure modes. Of course the possibility of unexpected, life-limiting, catastrophic mechanisms must be considered.

The testing we propose will be more involved than the usual standardized qualification tests, which are more appropriate for identifying poor designs and manufacturing flaws [4]. Results of our proposed life-prediction testing need to determine the acceleration factors associated with the failure mechanisms being investigated.

6. Rank-Ordering Failure Mechanisms

As a criterion for rank-ordering failure modes, we can choose those that have the greatest effect on system-energy-output. An approach used by R.G. Ross for crystalline modules [1] and later for thin-film modules [5] is an attempt at doing this. He lists known failure mechanisms and assigns values for "system life-cycle energy cost impact" based on, in his words, 'the author's best judgement in light of likely achievable levels." He assigned a constant rate of system-energy-loss (%/yr) for some mechanisms and a linearly increasing rate of energy loss (%/yr^2) for others. This may be a way to start rank ordering, but ultimately, these are not the functional dependencies typically used to model failure mechanisms [2].

A more objective system of rank-ordering failure modes needs to be developed. We need to understand relative impact to energy production of each failure mode on a module-by-module basis. Then we have to test for those mechanisms that cause the most life-limiting modes in equation (3).

7. Conclusion

Based on known failure mechanisms, we can use AET's to estimate TTF for what we determine to be the most damaging failure modes relative to system-energy output. Unfortunately, appropriate values for acceleration factors in testing will depend on many variables (i,j,k), and TTF will depend on the environmental stresses at the location of use. The development of a universal 30-year pass/fail certification for all PV module types cannot be expected.

8. Acknowledgements

The authors would like to acknowledge the work of previous researchers in this area such as Ron Ross and Al Czanderna, as well as the continuing efforts of module manufacturers and laboratory personnel associated with development of module-test standards.

REFERENCES

[1] R. G. Ross "Technology Developments Toward 30-Year-Life of Photovoltaic Modules", Proc of 17th IEEE PV Spec. Conf . (1984), pp. 464-472.

[2] N. R. Mann, R. E. Schafer, and N. D. Singpurwalla, "Methods for Statistical Analysis of Reliability and Life Data," John Wiley and Sons, NY, 1974.

[3] A. Czanderna, G. Jorgensen, "Service Lifetime Prediction for Encapsulated Photovoltaic Cells/Minimodules", *AIP Conf. Proc. 394, 14th NREL/SNL Photovoltaics Program Review*, Woodbury, NY, 1997, pp. 295-311

[4] "IEEE Recommended Practice for Qualification of Photovoltaic (PV) Modules," IEEE Std. 1262.

[5] R.G. Ross "Crystalline-Silicone Reliability lessons for Thin-Film Modules", Proc of the IEEE PV Spec. Conf. (1985) pp. 1014-1020.

Improving Inverter Quality

R. Pitt

Trace Engineering

5916 195th Northeast, Arlington, WA 98223 U.S.A.

ABSTRACT

This paper summarizes the results to date of the Trace Engineering Quality Improvement Program. This program, partially funded by Sandia National Laboratories, is an ongoing effort intended to improve overall inverter quality for the PV industry. It is important to remember in reviewing these results that the Quality Improvement Program at Trace Engineering is an on-going effort. While the results so far are positive, Trace Engineering continues on a path of constant improvement in quality.

Overall product quality at Trace Engineering, as measured by product return rates, since the program began in mid 1998 has improved by over 400%. In general, the majority of this improvement has been achieved through documenting of processes, training and increased awareness throughout the organization.

1. The Quality Improvement Process

The process used at Trace to implement a state-of-the-art quality system consisted of three phases. Each phase was applied across the entire organization. Sales, Engineering, Procurement, Manufacturing and administrative functions were all included in the process.

Phase 1 of the project consisted of formally documenting the processes currently in use throughout the organization. Over 50 separate business processes were identified and the Trace's implementation of these processes were documented. This "What are we doing now?" step provided a well-defined starting point for improvement.

The second phase of the project involved auditing the current processes against an industry standard quality system. Trace chose the ISO-9000 quality system as the standard upon which our new quality system would be based. In the process of this review, over half of the existing processes needed to be refined and/or changed completely. In addition, 12 new business processes were targeted for implementation as part of the new system.

Phase 3 of the project, the implementation phase, is still under way. This phase includes documenting the new processes, building the necessary infrastructure, training the organization and using the new processes in day-to-day operations.

Trace Engineering's new quality system was audited by Underwriter's Laboratories in January 2000 and was recommended for ISO-9001 certification. The certification process will be completed by the time this paper is published.

2. Cultural Changes

The majority of the gains outlined above were realized due to a fundamental shift in the organization's attitude toward quality. One of the fundamentals of a good quality system is the empowerment of each individual in the organization to affect the quality of the products produced by the company. This empowerment has spawned a cultural change at Trace Engineering.

In the past 18 months Trace has experienced a noticeable shift from top-down driven policies and procedures to a bottom-up proactive approach to problem solving by the organization. In the past, problems would bubble up to senior management who would develop a solution and communicate it down through the organization for implementation. Today, business at Trace is characterized by individuals in the organization solving problems at the lowest levels and communicating the new processes upward to senior management for review and approval.

There have been numerous instances in recent months of quality issues being identified, a solution developed and implemented on the production line in a matter of minutes. Prior to the implementation of the new quality system at Trace, many of these issues would have gone unresolved due to the cumbersome and lengthy process necessary to change the simplest processes.

The consistent and uniform "Can-do" attitude of Trace Engineering's employees has created a quality system and a quality company that benefits Trace, our suppliers, our customers and the renewable energy industry as a whole.

3. Measurable Results

The primary measure of success for any quality system is customer satisfaction as driven by product quality. Analysis of product return data at Trace indicates that return data from the first nine months of product life provides a statistically sample of overall inverter returns. The product defect studies below are summarized from product returns that occurred in the first 3 quarters of product life.

Figure 1 is a basic chart of Trace Engineering's inverter returns since 1993. This chart is plotted using number of units returned in the first three quarters of inverter life. This raw data indicates a clear trend in product quality improvement at Trace in 1998 and 1999.

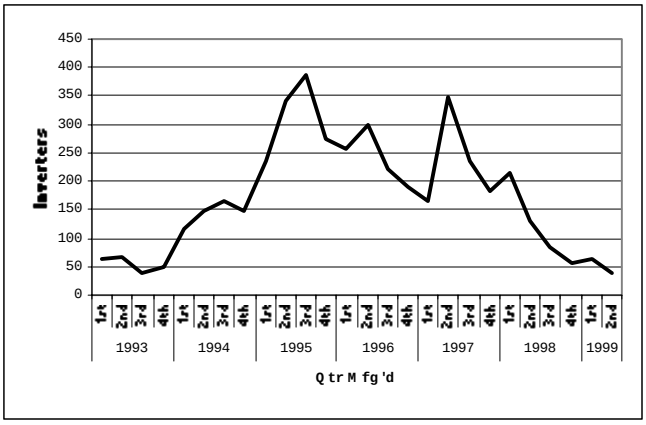

Fig. 1 - Unit Returns by Qtr Manufactured

However, during this same period, inverter production rates at Trace have increased significantly. Therefore, a more useful analysis can be done when the overall production rate of inverters is included in the calculations. Figure 2 illustrates this point.

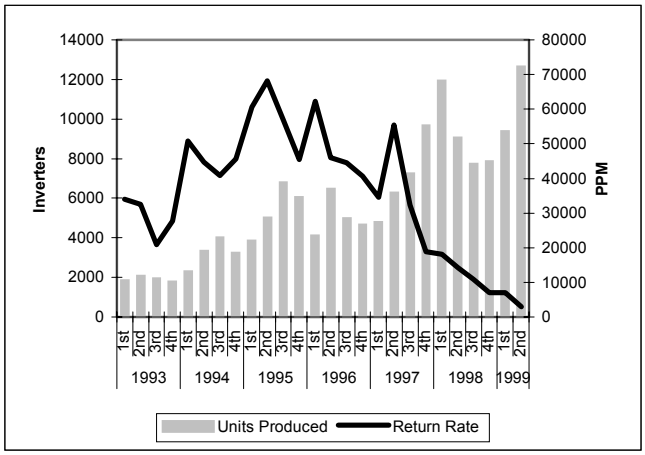

Fig 2 - Return Rate and Unit Production Volume

As measured by product defects in Parts Per Million (PPM) inverters produced, Traces product quality has improved by a factor of four since Q2 1998.

While this data shows a clear trend in improved inverter quality, it does not directly show the value of this trend to the customer. Figure 3 shows the measured Mean Time to First Failure (MTFF) of inverters manufactured over the same period.

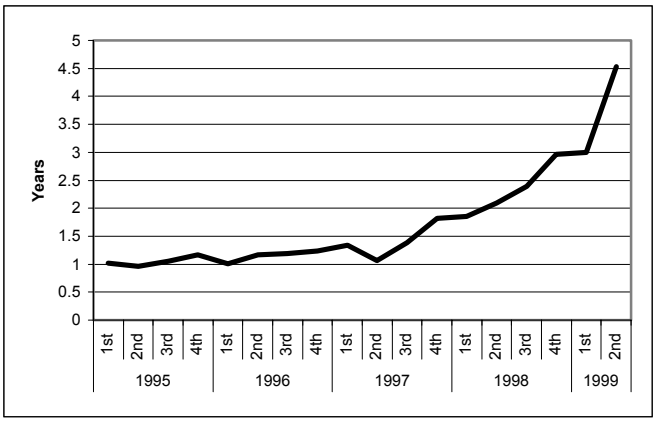

Fig 3 – Mean Time to First Failure (MTTF)

The MTTF is a useful number because it can be used to calculate the total cost of the inverter over the life of the system. Figure 4 plots the average cost of ownership of an inverter as expressed in $ / Watt. This number is calculated assuming a PV system life of 20 years.

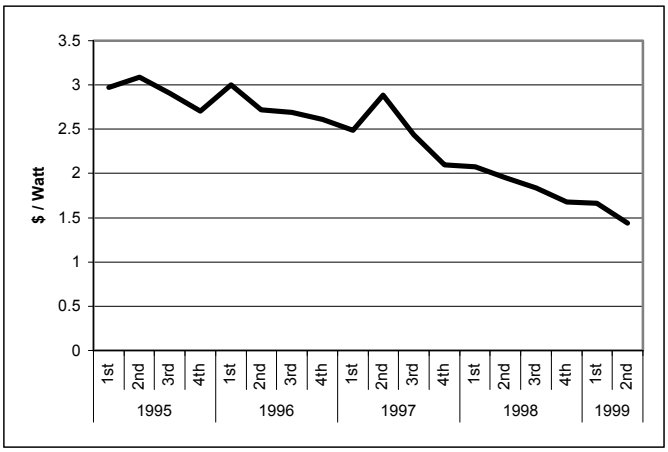

Fig 4 – Total Cost of System Ownership

4. Summary

The Trace Engineering Quality Improvement program has been an unqualified success. The program has created fundamental changes in the way that each and every Trace employee views their role in providing quality products to our customers. As a result, Trace has been able to achieve a significant increase in production volume and simultaneously realize an increase in product quality. The net result of the entire process has been a more reliable product and an average 50% reduction in the cost of system ownership.

IEEE Std 929-2000 – Background, Implications and Requirements

John Stevens
Sandia National Laboratories
P.O. Box 5800, MS 0753
Albuquerque, NM 87185

ABSTRACT

The newly revised standard, IEEE Std 929-2000, has significant positive implications for those designing inverters for utility-interconnected PV systems and for designers and installers of such systems. A working group of roughly 20 people, including PV systems designers/installers, PV inverter manufacturers and utility engineers spent close to 3 years developing a standard that would be useful and beneficial to all.

1. Introduction

IEEE standards are required to be reviewed every 5 years and either reaffirmed or revised. The previous IEEE PV/utility interconnection standard, IEEE Std 929-1988, was originally approved in 1988 and reaffirmed in 1991. In 1996, at the time of the next 5-year review, it was determined that a massive revision would best serve the interests of both the utility and PV communities. This decision was based on the fact that a growing number of utility-interconnected PV systems were being installed, and there was significant disparity between the interconnection requirements of many utilities. It was felt that a single, widely accepted interconnection standard would result in consistent interconnection requirements across much of the country, which would allow PV inverter and PV system designers to standardize their designs.

Such standardization benefits PV system buyers by eliminating the expense associated with customized hardware for each installation. It benefits the PV system installer and the PV hardware manufacturer by allowing manufacture of one product that will fill a specific need in all locations. Standardization benefits the utility, the installer and the buyer by providing components that have been built and tested to a standard, thus reducing the probability of defective hardware.

It was also felt that this standardization would lead to cost savings. These savings would result from allowing inverter manufacturers to standardize on a single design, rather than having different designs for individual utility requirements. Also, a standardized interconnection requirement will eliminate the "soft" costs associated with the sometimes confusing and labor-intensive process of negotiating individual interconnection agreements with individual utilities. Finally, there would cease to be "surprises" when it came time to make the utility interconnection after the PV system is already installed.

It was recognized by the 929 working group that standardization may increase the cost of inverters in some cases, but the potential savings on the items listed above would far out weigh any additional costs associated with the inverter.

2. The Target Standard

At the beginning of the process several goals were established. Foremost was that the standard should be beneficial to both the PV and utility industries. All other goals followed from this one. These other goals included assuring that the PV system will not interfere with utility operation, and providing both the interconnecting utility and the PV system purchaser with a means to be certain that the PV system would be acceptable to the interconnecting utility before the system was installed.

The first of these goals, assuring that the PV system doesn't interfere with utility operation, includes requirements for power quality and safety. The most significant of the safety issues was the definition of a non-islanding inverter, and development of a technique to manufacture, and identify, a non-islanding inverter. A brief discussion of the non-islanding inverter development follows later in this paper.

The second of these goals, providing a method to be certain that the PV system would be acceptable to the interconnecting utility before the system was installed, was realized by a most fortuitous piece of cooperation with Underwriters Laboratories (UL). At the same time that IEEE 929 was being developed, UL took on the task of updating and finalizing UL 1741, the UL test procedure for PV inverters and charge controllers. UL agreed to include all the requirements of the revised IEEE 929 in the test regime for UL 1741. Thus a customer, or a utility, can check to see that the inverter for a PV system meets the requirements of the latest version (May 1999) of UL 1741, and be assured that it then meets the requirements of IEEE 929.

UL allows 18 months between when a new test standard is approved and when it must be used when testing a particular piece of hardware. Thus there is the possibility, until November 2000, that an inverter can be designated as having

passed UL 1741 when it has actually passed an earlier version of 1741 that doesn't include all the requirements of IEEE 929-2000. If there is some uncertainty regarding which version of UL 1741 an inverter has been tested to, one may contact UL directly to confirm which version of UL 1741 a particular inverter was tested to.[1]

3. What is Needed to Meet the Requirements of IEEE 929?

IEEE 929 sets requirements for the utility-interface device. That is, the energy source, the PV array, is not a factor in the standard. The only device that the standard impacts is that device where the utility-interface protection functions are accomplished – the inverter. Thus, the only requirement for meeting IEEE 929 is to use an inverter that is compliant with IEEE 929. Since UL 1741 tests for IEEE 929 compliant inverters, then use of a UL 1741 (May 1999 issue) listed inverter is the only requirement necessary to assure 929 compliance.

Since IEEE 929 does not impact the PV array, it is easy to envision that the energy source could be any of a number of other devices such as batteries or fuel cells, and the requirements of IEEE 929 wouldn't change. Thus IEEE 929 can be used as a model for utility interconnection of other energy sources in addition to PV.

4. A Complete Package

A PV system should be installed in a manner that assures the owner and the interconnecting utility that it is a safe system in all respects. This is particularly important in today's litigious society, and when homeowner's insurance is involved. The combination of IEEE 929, UL 1741, and the National Electrical Code (particularly Article 690) provides a complete package that allows safe and efficient installation of all aspects of utility interconnected PV systems. Furthermore, this package of standards will meet all interconnection requirements in those jurisdictions that have adopted IEEE 929. The list of states that are adopting IEEE 929 as the interconnection standard for PV systems is large and continues to grow.[2]

5. The Non-Islanding Inverter

One of the main concerns of utilities regarding distributed generation is islanding, or the inadvertent energization of a power line that should be de-energized. Islanding can be a significant safety concern, both for the utility line workers and for the public. In addition, islanding can interfere with the utility's normal procedures for bringing their system back into service following an outage. A more complete discussion of islanding and its implications can be found in [1].

To address the issue of islanding, a separate "Anti-Islanding Working Group" was formed at Sandia National Laboratories. This Working Group was composed mostly of representatives of inverter manufacturers, and tackled the development of an anti-islanding scheme that could be applied to any inverter manufacturer's product. The result of the work of this group was development of an active anti-islanding scheme that will result in multiple inverters all working in harmony to detect and de-energize an island.

The Non-Islanding Inverter Test

A key part of the work of the Anti-Islanding Working Group was development of a test procedure that will allow testing of a single inverter to determine if that inverter employs an adequate anti-islanding technique. Such a test was developed, using an RLC load tuned to 60 Hz as the key part of the test. This test, as well as the anti-islanding scheme, is thoroughly discussed in reference 1.

6. Additional Testing

While IEEE 929-2000 was being developed, there was significant activity in various states regarding interconnection standards. One of the most active was New York. Two utility engineers from New York volunteered to serve on the 929 working group because of the high level of activity and these engineers desire to have 929 be a standard that could be adopted in New York. As a result of the New York activity, some specific testing was done at the request of several of the utility engineers in New York. A set of waveforms that was measured during testing of distributed generators in New York during the late 1980's was used for testing. Because of the presence of these unusual waveforms, some conventional protective relays were unable to detect that the utility was experiencing abnormal conditions, and the relays did not remove the distributed generation from the lines. This experience resulted in a requirement in New York that all protective devices be tested to assure that they would perform as required in the presence of these waveforms. Several PV inverters were tested with these waveforms at Sandia National Laboratories, and they had no problem recognizing an abnormal utility condition and disconnecting the inverter.

7. References

[1] Stevens, Bonn, Ginn, Gonzalez, Kern: "Development and Testing of an Approach to Anti-Islanding in Utility-Interconnected Photovoltaic Systems", SAND98-1684, Sandia National Laboratories.

[1]The person to contact at UL at the time of this publication (April 2000) is the engineer in charge of UL 1741, Tim Zgonena. Tim can be reached at (847) 272-8800, ext. 43051, or at Timothy.P.Zgonena@us.ul.com. UL intends to provide either a toll-free phone number or Internet access to allow making such queries in the future.

[2]An update of those states that have adopted IEEE 929 as their interconnection standard can be found on the Internet at www.irecusa.org, then clicking "Connecting to the grid".

REPORT DOCUMENTATION PAGE

Form Approved
OMB NO. 0704-0188

1. AGENCY USE ONLY (Leave blank)	2. REPORT DATE	3. REPORT TYPE AND DATES COVERED
	April 2000	Conference Proceedings

4. TITLE AND SUBTITLE

Program and Proceedings of the NCPV Program Review Meeting 2000

5. FUNDING NUMBERS

C
TA: WO975000

6. AUTHOR(S)

K. Ramanathan, editor

7. PERFORMING ORGANIZATION NAME(S) AND ADDRESS(ES)

8. PERFORMING ORGANIZATION REPORT NUMBER

9. SPONSORING/MONITORING AGENCY NAME(S) AND ADDRESS(ES)

National Renewable Energy Laboratory
1617 Cole Blvd.
Golden, CO 80401-3393

10. SPONSORING/MONITORING AGENCY REPORT NUMBER

NREL/BK-520-28064

11. SUPPLEMENTARY NOTES

12a. DISTRIBUTION/AVAILABILITY STATEMENT

National Technical Information Service
U.S. Department of Commerce
5285 Port Royal Road
Springfield, VA 22161

12b. DISTRIBUTION CODE

13. ABSTRACT *(Maximum 200 words)*

This document serves as the Proceedings for the National Center for Photovoltaics (NCPV) Program Review Meeting 2000, held April 16-19, 2000 in Denver, Colorado. Nearly 150 two-page papers are included that cover both the oral and poster presentations. The main sessions within the meeting were: Markets and Applications; PV Components, Systems, and Integration; Manufacturing; Fundamental and Applied Research—Crystalline Technologies; Fundamental and Applied Research—Thin-Film Technologies; Fundamental and Applied Research—New Technologies for the Future; and Where do We Go from Here?—NCPV's Role in the Future. The work described was performed under the auspices of the U.S. Department of Energy's National Center for Photovoltaics by scientists and engineers from the National Renewable Energy Laboratory, Sandia National Laboratories, universities, and industry.

14. SUBJECT TERMS

photovoltaics; research and development; markets; applications; components; systems; systems integration; manufacturing; crystalline Si; concentrators; thin-films; cadmium telluride; copper indium diselenide; amorphous Si; fundamental and applied research; novel technologies; NCPV

15. NUMBER OF PAGES

16. PRICE CODE

17. SECURITY CLASSIFICATION OF REPORT	18. SECURITY CLASSIFICATION OF THIS PAGE	19. SECURITY CLASSIFICATION OF ABSTRACT	20. LIMITATION OF ABSTRACT
Unclassified	Unclassified	Unclassified	UL

Certification and Standards Update

S. Chalmers
PowerMark Corporation
Phoenix. AZ

Abstract

For the PV industry to fulfill it's potential and avoid the stigma of poor , unreliable products, it needs to have a full array of product standards, manufacturers that have quality systems and certified products tested in accredited laboratories . Why hasn't more been done to promote standards and product certification? Standards provide a minimum hurdle that products sold in the market place must meet. The market place is the World., hence there must be a system of standards and certification in place. One test and standard for a product that is acceptable in all global markets.

National and international standards for Photovoltaic systems and components receives high marks at industry meetings and political forums. Why hasn't more been done to promote standards and product certification? There is no simple one liner to answer this question. We have heard comments such as:

- Is the PV industry profitable ? No it isn't, some would say. Not to the extent necessary to attract investors when the high tech industry stock values are skyrocketing .
- Down sizing, right sizing is a possibility.
- Standards will not improve my product, why spend money on something that will not effect my bottom line

Why is it important to have standards?
Standards provide a minimum hurdle that products sold in the market place must meet.
Customers needs and expectations are met.
Customer confidence in the PV is maintained.
Standards encourage financial institutions to fund PV because the product works and last as advertised.
Over come artificial barriers of interconnection with a standard approach.
You can add to the list.
Why are standards and product certification necessary today?

One world is the international market for PV. Only about 17% of the US production of

Modules are sold in the US. All large US module producers are international corporations.
The market place is the World., hence there must be a system of standards and certification in place so that a product manufactured in one part of the world , built to a standard, in a factory with a recognized quality program and certified product is acceptable in all markets The goal is that this be only done once and that the product will be accepted elsewhere.

Poor quality products are being manufactured, some where out there, that do not last or meet reasonable expectations. The World Bank UNDP ,and may countries have financed and installed systems that failed or did not get the job done. . The World Bank for example, is concerned with the large instances of poor quality products sold in 3rd world countries. The 3rd world is a huge market. Places where conventional electricity is not available, yet were people are poor. Predictions are that the 3rd world will grow to become a dominate market in the near term. The World Bank is considering plans to fund the installation of PV in these areas .to the extent in some years of 15-20% of the current industry manufacturing capability. This will not happen unless we have a product that will be reliable and economically viable. The WB is looking at ways to be assured that the products they fund meet a minimum standard ,tested and produced in a quality manufacturing facility.

What is being done to assure quality?
NREL funded a certification program study a few years ago and the PowerMark (PMC) organization was created to implement a certification process based on IEEE & IEC standards. The first objective was to establish an ISO Guide 25 approved test Laboratory in the US. So that manufactures would have a lower cost shorter turn around time laboratory to send their modules to. rather than to ship to Italy or Germany for testing. Such a facility exists today

in the US at the ASU/PTL laboratory in Mesa Arizona. They are responsive to industry needs. During this process of PMC getting under way PV-GAP was created to address the immediate concerns of poor quality product being built and sold in 3rd world countries. The interests extended further than PV modules to components and small solar home systems. To facilitate the rapid start-up and to use an existing system at low cost an alliance with the IECQ system was formed by PV-GAP. PMC recognized the benefits of using the IECQ system of mutual recognition existing between Supervising Inspectorates, that would achieve the objective having PV products manufactured in one country built to standards suitable in another country. PMC is the administrative body for PV-GAP in the US. It participated on the Board and Technical Committees. The key here is that the WB and possibly others are planning to require that products they will fund be approved/listed by PV-GAP. This involves a product that has been tested in a ISO Guide 25 laboratory and manufactures in a ISO 9000 facility . The PMC organization remains intact and is certification force in the US. To obtain the PV-GAP mark or seal a US manufacturer will need to apply to PMC and pay for the testing and manufacturer plant assessment and the approval process.
IEC standards will be used such as those for modules that are well accepted . Many component and system standards are in the process of being developed. This could take another three years to accomplish. Some 30 countries participate in the photovoltaic standards process and it takes time for comments and approvals. What will happen in the meantime? The IECQ system allows for quicker establishment of an interim Recommended Specification. In approximately one year an acceptable PV-GAP Recommended Specification or an existing national standard can be approved and in use by the Supervising Inspectorats

The IECQ system was developed for electronic OEM components. It is in place but needs modification to address the PV needs which are more consumer oriented. The Telecommunications and Aerospace industries are looking at the possibility of using IECQ for their products and certification. We are in the process of advocating changes necessary to meet the needs of our industry. Based on discussions I have had with may PV industry people these are areas of concern that have been voiced for IECQ modification+

Criteria based on these principles:

- Cost effective / Value added
- Provide international recognition of PV manufactures with acceptable quality systems.
- PV-GAP/IECQ approval process that is simple.
- Avoids duplication.
- Utilize internationally recognized Registrars.
- Approval of audits performed by recognized Registration organizations.
- Accept assessments by accredited Registrars and IRCQA/RAB auditors
- PV-GAP/IECQ assures compliance.
- Cost to the manufacturer as low as feasible

A major challenge will be to have interim IECQ/PV-GAP test procedures in sync with the development of IEC standards and not to delay the process of developing IEC standards. Keeping IECQ procedures in sync with IEC is probably not a major problem for the near term because several of the same technical experts participate in developing IECQ Blank Detail Specification are experts on the corresponding IEC committee. It could be a concern for TC-82 in the future.

When the market place and those who specify and purchase PV require certification there will be a rush on the part of producers to get their products approved and certified. In the mean time a few manufactures have certified products but the rush has not been overwhelming,.nor has it been identified as a must have requirement. I would encourage the industry to get started and certify their PV products to IEC standards where possible.

For the PV industry to fulfill it's potential and avoid the stigma of poor , unreliable products, we need to have a full array of product standards, manufacturers that have quality systems and certified products tested in accredited laboratories. They will be the winners.
One test and standard for a product that is acceptable in all global markets saves money and time.

PVMaT Improvements in Large Area Cell Manufacturing Processes

T. Jester

Siemens Solar Industries

4650 Adohr Lane
Camarillo, Ca. 93011

ABSTRACT

Recent work at Siemens Solar Industries in manufacturing cost reduction has shown highly leveraging benefits in producing thinner solar cells, larger area solar cells, and introducing back surface field processes which increase efficiency. About half of the cost to produce a solar module is incurred by the time a wafer is produced, and another 20% is added in the cell processing steps. In large area wafer and cell production, the manufacturing costs are almost linearly reduced by increasing the area of the wafer, this benefit is compounded as the wafers are made thinner. Siemens Solar Industries has studied, developed and piloted processes for 250 micron thickness cells, in both 103 mm cell and 150 mm sizes. SSI has also started the development efforts for increasing cell size to 200 mm diameter. The yield of each of these processes differs, lowering as the wafers are made larger and thinner, however the electrical efficiency can improve in processing of thin cells. The benefit can be a cost reduction as high as 25-30% on the $/Watt production level. Implementation in manufacturing is the key driver for success in achieving this cost reduction potential.

1. General Introduction

The Photovoltaic Manufacturing Technology (PVMaT) project is sponsored by the U.S. Department of Energy through the National Renewable Energy Laboratory in order to assist the photovoltaics industry in improvement of module manufacturing and reduction of module manufacturing costs. The objective of the DOE/NREL PVMaT subcontract with Siemens solar Industries (SSI) is to continue the advancement of Siemens Solar Industries photovoltaic manufacturing technology in order to achieve a 30% reduction in module cost per watt at the end of three phases of work. The program addresses the reduction in cost per watt with a three part development contract: a significant reduction in wafer thickness from approximately 400 microns at the start of the program to 125 microns at the end of three years, a significant increase in the size of the cells to 200 mm diameter and larger modules, and an additional cost reduction benefit in the recycling and re-use of slurry materials and caustic etching chemicals.

2. Methodology

The first step toward reducing cost in the PVMaT 5 program at SSI is to reduce wafer thickness. The cost for producing photovoltaic modules is almost 50% incurred at the wafer slicing level. (Figure 1). The thinner the wafers are made, the lower the potential cost (Figure 2), however the thinner cells are made, the higher the yield loss, and a competing drop in electrical efficiency will take place, necessitating the use of a Back Surface Field (BSF). For this reason, the approach has been a two step reduction in thickness, from 400 microns to 250 micron cells, with the introduction of a BSF process, and then a wafer thickness reduction from 250 microns to 125 microns.

The larger cells are made, the lower the potential dollar per watt. SSI has initiated the development of 200 mm ingot, wafers and cells to be fabricated into modules. These larger cell designs continue to show the best cost structure as they optimize the watts per kilogram of silicon consumed in producing the cells. Module designs for lower cost contribution have been started.

These three areas of focus: thinner cells, more efficient cells and larger cells and modules have the potential of reducing cost by approximately 30% per watt.

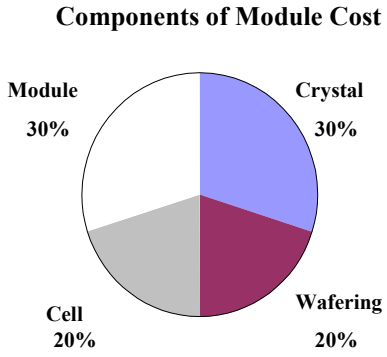

Figure 1. Manufacturing Cost Components

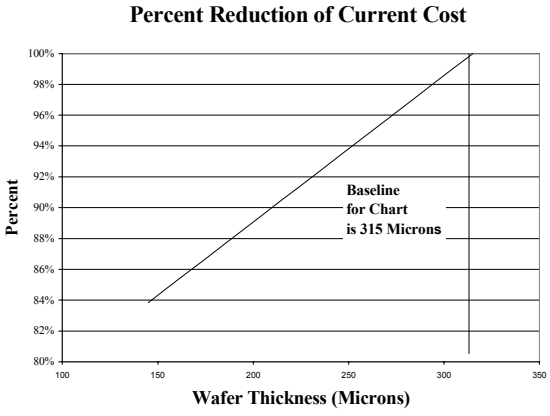

Figure 2. Cost Reduction vs. Wafer Thickness

3. Results

The thinner cells are made, the higher the yield loss, and the larger cell are made, the higher the yield loss. These effects are shown in Figure 3 where yield is contrasted to wafer thickness and size, and and Figure 4 where electrical performance vs. thickness is shown for two different Back Surface Field (BSF) processes. Siemens Solar has introduced the Boron BSF process on a 250 micron, 150 mm diameter cell.

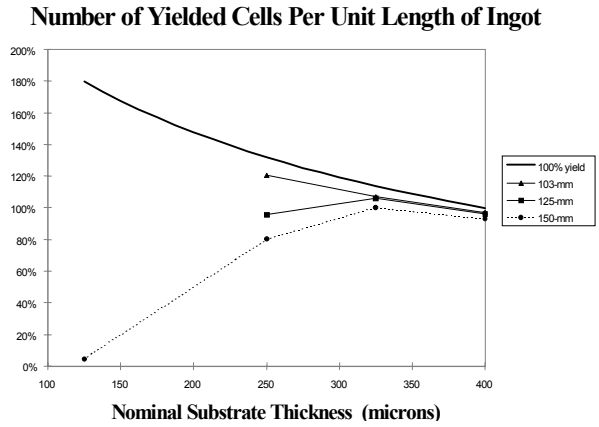

Figure 3. Yield vs. Wafer Thickness and Size

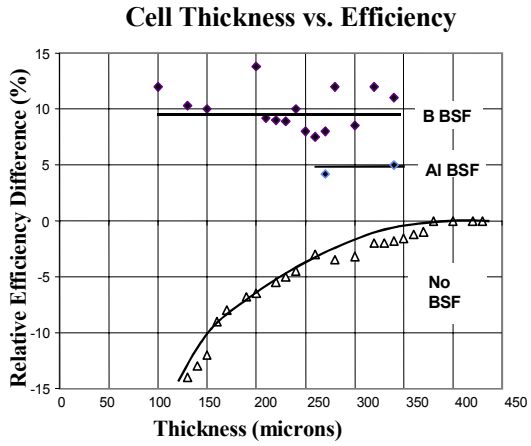

Figure 4. Thickness vs. Electrical Efficiency

Larger area cells have shown greater potential for cost reduction as each process step produces more watts, lowering the labor and overhead contributions directly. Siemens Solar Industries has begun the pilot effort of producing 200 mm ingot, wafers and cells. Figure 5 shows the new cell, and Figure 6, the planned 160 Watt module designed with these new 200 mm diameter cells.

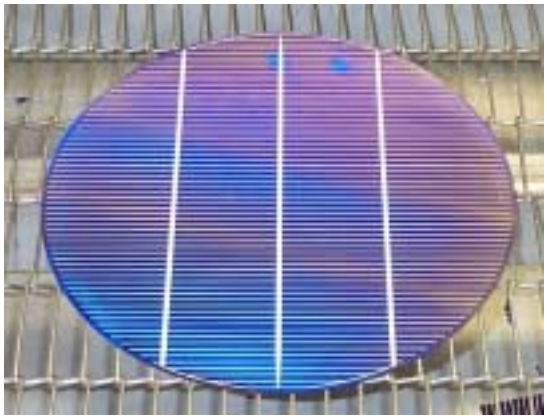

Figure 5. 200 mm diameter Cell

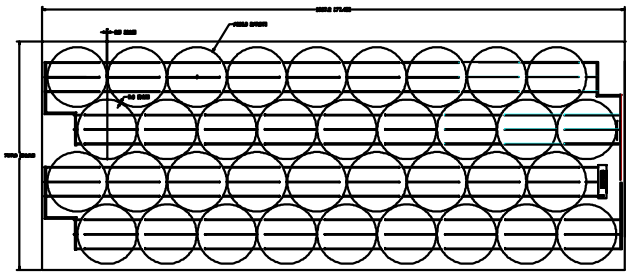

Figure 6. 160 Watt Module

4. Future Work

The combination of reducing wafer thickness, increasing cell and module size and increasing cell efficiency in silicon photovoltaic manufacturing processes continues to show significant cost reduction potential. SSI has introduced high efficiency, 150 mm diameter large area cells into production at a thickness of 250 microns. The continued effort to increase cell area to 200 mm diameter wafers, and to continue lowering costs will demonstrate the 30% reduction program goal.

Research Needs of c-Si Technology Required to Meet Roadmap Milestones

D. S. Ruby
Sandia National Laboratories
MS 0752, Albuquerque NM

T. F. Ciszek and B. L. Sopori
National Renewable Energy Laboratory
1617 Cole Blvd, Golden CO 80401

ABSTRACT

In this paper, we examine the areas in c-Si growth, materials, and processing that require improvement through research to overcome barriers to the implementation of the PV Roadmap's Si goals.

1. C-Si Materials Growth

The key issues in c-Si materials growth for reaching the Roadmap's module production goals are throughput of the growth processes, control of impurities and defects, and effective utilization of silicon-feedstock material. Trade-offs are required in order to achieve an optimum balance between these key issues. Let's look at them in more detail and examine the associated R&D needs.

Throughput of the Growth Processes

To improve PV module throughput to the Roadmap target of 200 MW/factory/year, the typical Si-PV factory must produce >4,000 m^2/day of silicon. This assumes 15% modules capable of generating 150 W_p/m^2, and round-the-clock operation with 10% down time and/or yield losses. For the growth methods currently in use, the throughput per machine and total number of growth machines (growers) required is approximately:

Growth Method	Throughput (m^2/day)	No. of Growers
Dendritic Web	1	4,000
ESP/String Ribbon	1.7	2,350
Capillary Die Growth	20	200
Czochralski (CZ) Growth	30	133
Directional Solidification	70	57
Float-Zone (FZ) Growth	80	50
Electromagnetic Casting	600	7
Substrate Melt Shaping	>1000	<4
Thin-Layer Si Growth	?	?

For ingots, the throughput numbers assume concomitant wire-sawing yielding 20 wafers/cm of ingot. Most thin-layer growth approaches are not at a mature enough stage to estimate throughputs. Research is required to improve the throughput of existing growth methods, to evolve higher-throughput methods, and to demonstrate comparable throughputs with thin-layer growth approaches.

Control of Impurities and Defects during Growth

The growth methods that can sustain a factory with fewer than ten growth machines will generate ingot material with smaller grains than other approaches. Or they generate sheet material with still smaller grains as well as impurities from melt/substrate and melt/ambient interactions. Research is required to improve grain size and perfection, to reduce impurity contents during growth by these fast methods, and to understand defect and impurity behavior in the growth processes, with the goal of in-situ amelioration of adverse effects.

Effective Utilization of Silicon Feedstock Material

In the growth of the PV and integrated-circuit (IC) semiconductor silicon industries, we have, on average, reached the point where the PV demand for low-cost Si feedstock exceeds the IC supply of off-specification and reject Si. One approach that can be taken is to develop alternatives to the silane and chlorosilane processes for creating IC-purity silicon from metallurgical-grade (MG) Si, with the goal of obtaining sufficient, but not excessive, impurity levels for solar-grade silicon at a lower cost. Another approach is to focus on thin-layer Si growth methods that utilize less silicon. Both are daunting research tasks in light of the throughput and module performance requirements of the Roadmap.

2. Material Quality Enhancement in Si Solar Cells

Low-cost silicon wafers used in commercial production of solar cells contain high concentrations of impurities and defects in the as-grown form. The PV industry uses economical processes that have been optimized to upgrade the material quality by incorporating impurity gettering and passivation during cell fabrication. Current solar cells have efficiencies in the 14%-15% range, which is a remarkable achievement. However, higher cell-efficiencies must be reached to meet the future goals of the PV Industry Roadmap. It is imperative that advanced processing methods be developed that can overcome current limitations in the material quality of solar cells. Key issues in the device processing are: developing techniques that can further improve the device performance through quality enhancement of the substrate; implementing these advanced approaches as high-throughput production processes; ameliorating the impurity and defect issues through use of thinner devices; and improving process reliability through efficient monitoring.

Impurity gettering

In solar cell fabrication, impurity gettering is accomplished through phosphorous diffusion and Al alloying employed for junction and contact formation, respectively. These processes are able to remove a majority of dissolved transition-metal impurities from the wafer. Recent research has shown that although the majority of the cell area exhibits strong gettering, large regions (~20%) show low performance. These regions, which have been identified as "defect clusters," are decorated with precipitated impurities. Because precipitated impurities are immobile, it is difficult to getter them by standard solar- cell

fabrication processes. Modeling results have shown that these regions act as shunts to degrade voltage-related cell parameters. Their removal from the wafer necessitates their dissolution with concomitantly long, high-temperature anneals. Thus, the challenge is to invent processes to reduce the time and/or temperature for gettering such precipitates. One approach is to inject point defects during the process.

Modeling results show that successful gettering of precipitated impurities will result in 18%-20% efficient cells on the low-cost material. Alternately, it may be necessary to perform crystal growth with the objective of eliminating impurity precipitation. These new considerations may redefine the as-grown material quality and crystal growth conditions for low-cost Si.

Hydrogen passivation

H-passivation is used as a standard process by many companies in solar-cell manufacturing. Typically, hydrogen is incorporated during plasma-enhanced chemical vapor deposition (PECVD) nitridation followed by a higher temperature drive-in process. The detailed mechanisms of H-diffusion and passivation are still not well understood. Because PECVD can be tailored to include surface passivation, such a process can be very valuable. It is interesting to note that effective passivation also requires that impurities be in a dissolved state. The challenges are to develop simpler, more effective passivation processes based on a comprehensive understanding of passivation mechanisms. An important issue is whether hydrogen can passivate defect clusters.

Processes for increased throughput

It is clear that the processes for upgrading material quality must constitute standard procedures of cell fabrication that are compatible with high throughput, without incurring additional process costs. Forming gas annealing, rapid thermal processing (RTP), continuous optical furnaces, and low-temperature oxidation are potential future processes. New designs are needed to ensure throughputs that are compatible with the needs of the PV industry.

Thinner wafer processing

For the same material quality, thinner wafers can yield higher cell performance. Another important advantage of thin cells is that their passivation and gettering processes can be less time consuming. Thus, much emphasis will be placed on thin cells. However, thinner wafers raise a variety of issues related to the need for:

- Significantly lower interface recombination through surface passivation.
- Reduced stresses due to metallization and asymmetric depositions.
- Automated handling for minimum breakage.

3. Crystalline-Si Cell Processing

The PV Roadmap efficiency goals for c-Si cells call for production-line average efficiencies of 16% in 3 years, 18% in 10 years, and 20% in 20 years. Industrially-produced cells will need to incorporate many of the high-performance features demonstrated by laboratory cells, but use low-cost, high-throughput fabrication techniques.

Low-recombination emitters

High performance requires the use of passivated emitters that have a selectively-doped emitter profile. This allows the Si to remain highly doped beneath the gridlines for low contact recombination and resistance, but more lightly doped between gridlines for reduced emitter recombination. The lightly doped portion of the emitter needs to have excellent surface passivation to avoid losses due to surface recombination. These selective emitter structures have been demonstrated by several research groups, some using single-diffusion techniques amenable to mass production.

Surface passivation

Plasma-deposited silicon-nitride films have been shown to provide excellent emitter and rear-surface passivation. They also double as an effective antireflection coating. In addition, they can provide good bulk-defect passivation by providing a source of atomic hydrogen, which can diffuse into the bulk to passivate defects and impurities. This can allow use of lower-quality feedstock or growth methods. The critical need is to design a high-throughput plasma deposition system with low operational cost.

Thinner wafers

Besides affording lower cost through better material utilization, thin cells are more tolerant of lower-quality bulk Si. However in order to maintain performance, thin cells require excellent light absorbing properties and low back-surface recombination.

Texturing

Lower-cost multicrystalline, sheet, and ribbon Si need affordable texturing to reduce front-surface reflectance and redirect absorbed light obliquely within the cell. This increases optical path length, generates carriers closer to the junction for increased collection, and can trap weakly-absorbed light through total internal reflection.

Self-doping metallizations

Metals which contain appropriate dopants have the potential to form self-aligned selective-emitters and back-surface fields at low cost by avoiding the need for additional diffusion steps. Some new metal deposition techniques also have the potential to reduce contact and series resistance by avoiding the use of oxide frit and organic binders.

Back-contacts

Cells with rear gridlines can benefit from the avoidance of gridline shadowing and may allow significant cost-savings due to simplified cell-interconnection methods.

4. Summary

The challenges for c-Si cells to meet the Roadmap goals are substantial. At the projected production levels, it will be necessary to have sources of low-cost solar-grade silicon or to evolve growth processes that utilize much less material. High-throughput growth processes with low defect and impurity concentrations will also be a necessity. Novel high-throughput cell processing for higher device efficiency and low-cost material upgrading will also be needed.

The Promise and Challenges of Using Multijunction Solar Cells in PV Concentrator Systems

David R. Lillington, Hector L. Cotal, and James H. Ermer

Spectrolab Inc.

12500 Gladstone Ave., Sylmar, CA 91342

ABSTRACT

This paper describes progress toward achieving high efficiency multijunction solar cells for cost effective application in terrestrial PV concentrator systems. Small area triple junction $GaInP_2$/GaAs/Ge solar cells have been fabricated with an efficiency of over 32% when measured by NREL under an AM1.5D spectrum at 47 suns concentration. Large area cells with efficiency approaching 30% have also been fabricated. Small changes to the device design, to achieve efficient operation at concentration ratios of about 500 suns, can achieve cell costs of $0.4 to $0.5/W, at production volumes of approximately 50 MW/year. This makes them highly cost effective in existing concentrator systems, where a substantial increase in module efficiency more than offsets higher cell costs. The future development of new 1 eV materials for space cells, in conjunction with further reduction in Ge wafer costs, promises to achieve solar cells of >40% efficiency that cost $0.38/W or less at these concentration ratios.

1. Introduction

The U.S. PV industry is a world leader in research, development, and manufacturing technology and holds a major share of the world market for PV systems. While the global opportunities for PV are immense, the challenge of emerging international competition has forced U.S. industry to re-evaluate its overall strategy and to define a road map to ensure future industry leadership [1]. High on the list of priorities for competitiveness are cost reduction, and efficiency improvement to reduce end-user system costs to $3/W or less. Concentrators have for many years been recognized as a means to substantially reduce PV system costs, since the cost of optics and a tracker are generally less than the cost of the solar cell itself. However the increased complexity of tracking systems, together with the historical high cost of III-V cells, has limited the widespread application of PV concentrator systems.

Recent performance improvements, and cost reductions achieved in the manufacture of $GaInP_2$/GaAs/Ge latticed matched space solar cells [2] has prompted Spectrolab to re-evaluate the application of this type of cell to terrestrial PV concentrator systems. AM1.5D efficiencies of over 30% can now readily be achieved on triple junction cells using device designs, and high yielding production processes that are only marginally different from space cells. Because of the synergy between space and terrestrial multijunction manufacturing technologies, very low $/W cell costs are obtainable at relatively modest manufacturing rates, making III-V cell technology extremely attractive for achieving near term reductions in PV generation costs. In addition, the leveraging of semiconductor manufacturing capacity afforded by the use of concentration, allows very rapid ramp up to achieve manufacturing capacity in excess of 150 MW per year using existing Spectrolab manufacturing infrastructure, should the need arise in the marketplace.

2. Triple Junction Solar Cell Performance

Triple junction $GaInP_2$/GaAs/Ge solar cells were fabricated using space solar cell device structures modified for optimum performance under the AM1.5D terrestrial spectrum. The cross section of the device structure is shown in Figure 1. Principal differences in the structure compared to a space cell, were a thicker, more heavily doped emitter to reduce distributed sheet resistance losses at high concentration, and a thicker $GaInP_2$ top cell to achieve current matching under an AM1.5D spectrum.

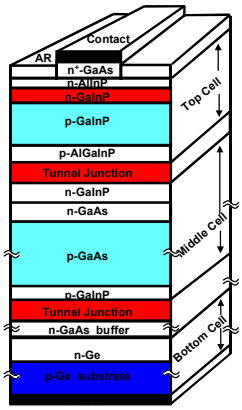

Fig. 1. Cross Section of $GaInP_2$/GaAs/Ge Cell

The solar cell material was grown at Spectrolab in a production MOVPE reactor, and processed at NREL using mask sets specifically designed for concentrator cells. The area of each cell was 0.0139 cm^2. Solar cells measurements were performed by NREL under their High Intensity Pulsed Solar Simulator (HIPSS). Figure 2 shows the measured efficiency of a number of cells vs. concentration ratio. Many of the cells had an efficiency >30% at low to medium concentration. The best cell had an efficiency of 32.3% at 47 suns, and 29% at 350 suns (AM1.5D, 25 ºC). While the subject of the roll-off in performance at >50 suns is the subject of another paper, it

should be noted that this was attributable mostly to series resistance losses and to a "less than ideal" back contact. Tunnel junction performance was believed to be nominal, even at higher concentration levels.

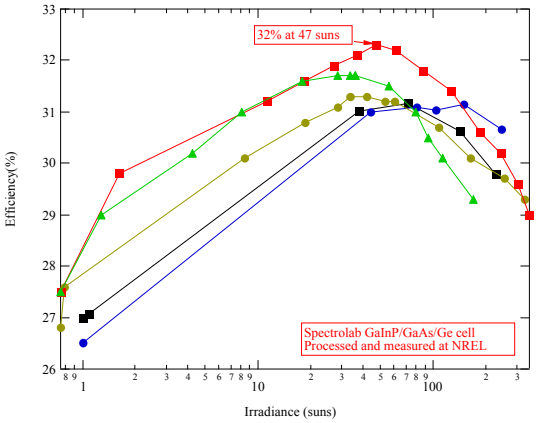

Fig. 2. Triple Junction Efficiency vs Concentration (NREL)

3. Key Challenges for Cost Effectiveness and Growth of Market Share

The key issues to be addressed before industry-wide acceptance of III-V concentrator systems are those of cost, and reliability. Present industry perceptions are that multijunction solar cells are too costly for use in terrestrial systems and that the optics and trackers in which they operate, are complex and unreliable. Furthermore, there is a belief that their application is limited to all but the largest stand-alone utility systems, that are in themselves the most cost-competitive with existing energy sources.

Cost and Manufacturing Maturity

It is true that III-V solar cells have historically been costly, and their use limited to space satellites. However the widespread use of III-V solar cells for commercial and government space applications since 1996, has brought about large reductions in raw materials costs, and increases in manufacturing yields. Today, Spectrolab alone has manufactured over 460 kW of dual junction and over 30 kW of triple junction cells for space application. Over 85 kW of this product is now operating flawlessly on satellites in space. This represents almost 17 million cm^2 of yielded production, equivalent to about 175 MW of terrestrial solar cells at 500 suns concentration ratio!

Spectrolab pricing models indicate that terrestrial concentrator cells can be cost effectively manufactured today at high yield, to provide industry with cells in the range of $0.4 to $0.5/W at 300-500 suns concentration, even at relatively modest manufacturing levels. In addition, the terrestrial industry will benefit greatly from the substantial improvements in performance, planned for space cells. Figure 3 shows Spectrolab's technology roadmap for terrestrial multijunction cells that leverages these improvements to space technology. Whereas state-of-the-art for triple junction solar cells today is a minimum average efficiency of approximately 30%, new 1 eV materials currently being developed for space will allow minimum average efficiencies of over 40% within the next two to three years. This prediction is based on relatively conservative modeling using realistic cell loss mechanisms, and production distributions that allow high manufacturing yields. Indeed, Friedman *et al* [3] have predicted idealized efficiencies (AM1.5D, 500 suns) for improved 3-junction and 4-junction cells utilizing new 1 eV materials, of 47% and 52% respectively. These improvements, together with further planned reductions in Ge wafer cost, and other manufacturing efficiencies will achieve solar cells of >40% efficiency with manufacturing costs between $0.3/W and $0.4/W within the next few years, at relatively modest risk.

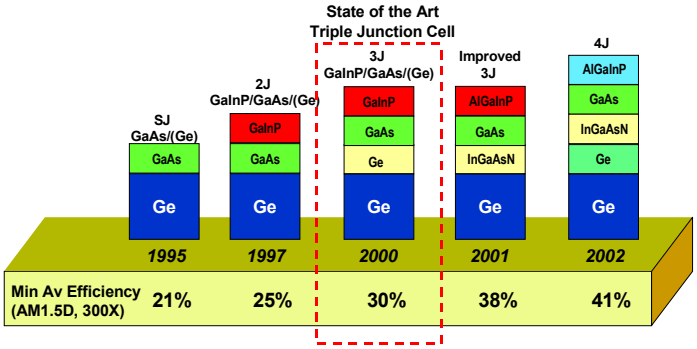

Fig. 3. Spectrolab Technology Roadmap for MJ Cells

Reliability

Both dual and triple junction solar cells have been extensively qualified for space application, and have undergone the rigors of long periods of illumination, temperature-humidity testing, deep thermal cycling, and shock and vibration testing without degradation. However terrestrial environments are extremely challenging, and the effects of long term exposure to concentrated sunlight (i.e. 500 suns or more), and the adequacy of existing cell packaging technology, are not well understood at this time. Each of these issues must be proactively addressed through controlled laboratory, and extensive field tests before multijunction cells can be widely implemented in terrestrial systems. This is an area where both government laboratories and industry must each play active roles.

4. Conclusions

Triple junction concentrator cells, based on very mature space manufacturing technology, have been fabricated with an efficiency of >32% at 47 suns, AM1.5D. Low risk improvements will allow high volume, industry-wide availability of cost effective, 30% efficiency cells in the very near term. Longer term, the opportunity exists for cells costing <$0.3/W through the introduction of improved 4-junction cell technology based on new 1 eV materials.

ACKNOWLEDGEMENTS

The authors are indebted to Sarah Kurtz, Dan Friedman, and Keith Emery of NREL, all of whom played a vital role in processing the cells, and performing the efficiency measurements reported here.

REFERENCES

[1] U.S. Photovoltaics Industry PV Technology Roadmap Workshop, Chicago, Illinois, (June 22-25, 1999)

[2] N H. Karam et al, "Development and Characterization of High Efficiency GaInP/GaAs/Ge Dual- and Triple Junction Solar Cells", IEEE Trans ED (1999) 2116 – 2125

[3] D. J. Friedman et al, "1 eV GaInNAs Solar Cells for Ultrahigh-Efficiency Multijunction Devices", 2nd World PVSEC (1998) Vol 3, 3-7

Science and Technology of Amorphous Silicon Alloy Photovoltaics– Accomplishments and Challenges

S.Guha, J.Yang, A.Banerjee, K.Lord, and B.Yan
United Solar Systems Corp.
1100 W. Maple Road, Troy, MI 48084

ABSTRACT

Significant progress has been made in improving the efficiency of amorphous silicon alloy solar cells and panels. Major expansion of manufacturing capacity has also taken place, and the products are gaining increasing market acceptance. The two major challenges for R&D are to a) further improve the efficiency and b) to increase the deposition rate without lowering the efficiency. The technology challenge is to scale up production further to take advantage of the economy of scale inherent in the manufacturing of these products. The paper reviews the progress that has been made in these areas and the challenges that remain.

1. Introduction

Amorphous silicon (a-Si) alloys have attracted a great deal of attention as a low-cost material for photovoltaics (PV). The worldwide annual manufacturing capacity for a-Si alloy PV is in excess of 30 MW, and several manufacturers have recently announced further expansion plans. The products have been gaining increasing market acceptance, and are being used for a variety of applications from battery charging to grid-connected power generation. Many challenges still remain [1]. The customer acceptance of a PV product depends on efficiency, cost, reliability and aesthetics. Intense efforts are under way to improve all these factors. In this paper, we shall briefly discuss some of these issues.

2. Research Issues

The highest efficiency a-Si alloy solar cells are made [2] using the triple-junction structure in which both a-Si and a-SiGe alloys are used. A key issue is the improvement of the intrinsic layers, and there is a very concentrated effort under the Thin Film Partnership program to achieve higher stable cell efficiency through an improved understanding of the material growth and characteristics. Hydrogen dilution of the active gases during deposition has been proven to be most effective in improving the quality of the intrinsic alloys that have resulted in higher cell efficiency. Hydrogen dilution also promotes growth of microcrystallites, and recent studies [3-5] have shown that the best material is grown just below the threshold of amorphous to microcrystalline transition. The material is characterized by an improved intermediate range order, and this may contribute to improved material quality and stability. This brings us to the question of stability and light-induced degradation. We understand the issue much better today, and know that it is *intrinsic* to the material unrelated to trace amounts of impurities. Several new models have been put forward [6] relating hydrogen motion, collision or bond flipping to light-induced degradation. Although the degradation has been reduced significantly through a combination of superior material characteristics and device design, we still do not have a fundamental solution.

The situation with a-SiGe alloy is more complex. The positional disorder increases the conduction bandtail, impeding transport of the carriers. The microstructure is also poorer since GeH_3 molecules are heavier and do not have adequate adatom mobility. An alternate material is microcrystalline silicon, and is receiving a great deal of attention [7]. There are challenges in terms of improving the deposition rate since the thickness of the microcrystalline film needed to absorb the sunlight is much more than that for the a-SiGe alloy.

An increase of the deposition rate is important for conventional a-Si alloys as well. The high efficiency cells are deposited typically at 0.1 nm/sec. Increase of deposition rate makes the microstructure poorer and results in lowering of efficiency. In order to improve throughput, production processes typically use deposition rates of ~0.3 nm/sec, and there is a gap between efficiency achieved in R&D and production. Table I shows the performance of component cells made at different deposition rates. In addition to conventional *rf* deposition, results are also shown for deposition involving very high frequency (*vhf*). While the difference in performance between the low and high deposition rates is small for a-Si alloy cells, it is much larger when Ge is incorporated in the cells. The poorer efficiency is caused by two factors. The increased power input to the plasma to achieve high deposition rate results in the presence of dihydrides and polyhydrides of silicon in the plasma, which affect the film quality. Moreover, when the impinging species arrive at a very fast rate to the growing surface, there is not enough time for them to find stable sites, causing poorer microstructure. The problem is obviously more in a-SiGe alloys for reasons discussed earlier. An alternative method to increase deposition rate is by *hot-wire* deposition [8]. Understanding the commonality and the differences in the deposition chemistry, growth processes and the material properties of alloys grown by *rf*, *vhf*, and *hot-wire* deposition will play a key role in obtaining high quality material at increased deposition rates.

Table I. Performance of Component Cells at Different Deposition Rates.

		J_{sc} (mA/cm^2)	V_{oc} (V)	FF	P_{max} (mW/cm^2)
top	rf1	8.76	0.990	0.711	6.17
cell	rf3	8.56	0.904	0.646	5.00
on ss	vhf	8.22	0.955	0.664	5.21
middle	rf1	9.06	0.725	0.616	4.05
cell	rf3	8.34	0.694	0.556	3.22
on ss	vhf	7.58	0.720	0.577	3.15
bottom	rf1	11.1	0.609	0.622	4.21
cell	rf3	10.1	0.594	0.564	3.39
on BR	vhf	8.77	0.597	0.535	2.80

P_{max} refers to stable power output under appropriate filter; rf1 1 Å/s; rf3 3-5 Å/s; vhf 6-8 Å/s

3. Manufacturing Issues

a-Si alloy PV products have been in the market now for close to twenty years; first, for consumer applications like calculators and small battery chargers and, for the last three years, for larger applications such as the utility-interconnected power market. Manufacturability is not an issue any more, whether the cells are deposited on a half-a-mile-long stainless steel roll, or stacks of large glass plates. The products show a stable efficiency of about 7.5% and are backed by a twenty-year warranty. Extensive reliability testing have been performed and the products have received both the UL approval in U.S. and ISPRA approval in Europe. The low material cost and the high yield, automated manufacturing process inherent in the a-Si alloy technology have already resulted in the lowering of the manufacturing cost of these products. Further reduction will be achieved through improvement of efficiency, increase of deposition rate and scaleup. The highest total-area cell efficiency is 12%, whereas the average product efficiency is 7.5% – a difference of about 40%. This gap can be minimized by R&D efforts to maintain efficiency constant while increasing the deposition rate, improvement of a non-silver-based back reflector [9], and improved understanding of plasma chemistry in large deposition reactors. Scaling up of production will also lower manufacturing cost. Estimates involving roll-to-roll production technology show that a fivefold increase in capacity can be achieved by increasing the capital cost by only 2.2 times, thereby producing significant economy of scale. The recent announcement by United Solar to build a production machine of annual capacity 25 MW will pave the way for the availability of low-cost a-Si alloy PV products to obtain a larger share of the increasing global market.

4. Conclusion

a-Si alloy PV products are now finding increasing market acceptance. The superior high temperature performance and aesthetically pleasing appearance of these products have created new markets in the building-integrated PV applications. The R&D challenge is to increase the efficiency further and improve the deposition rate. Development of improved manufacturing technology has already resulted in a substantial reduction in production cost, and with the building of large-scale production plant, a-Si alloy technology is expected to play a dominant role in the PV power market.

ACKNOWLEDGEMENT

Support by NREL under Subcontract Number ZAK-8-17619-09 is gratefully acknowledged.

REFERENCES

[1] S. Wagner, D. E. Carlson, and H. M. Branz: "Amorphous and microcrystalline silicon solar cells," Electrochemical Soc. Symp. on Photovoltaics for the 21st Century, 1999 (to be published).

[2] J. Yang, A. Banerjee, and S. Guha: "Triple-junction amorphous silicon alloy solar cell with 14.6% initial and 13.0% stable conversion efficiencies," Appl. Phys. Lett. 70 (1997) 2975.

[3] D. V. Tsu, B. S. Chao, S. R. Ovshinsky, S. Guha, and J. Yang: "Effect of hydrogen dilution on the structure of amorphous silicon alloys," Appl. Phys. Lett. 71 (1997) 1317.

[4] S. Guha, J. Yang, D. L. Williamson, Y. Lubianiker, J. D. Cohen, and A. H. Mahan: "Structural, defect, and device behavior of a-Si:H near and above the onset of microcrystallinity," 74 (1999) 1860.

[5] J. H. Koh, Y. Lee, H. Fujiwara, C. R. Wronski, and R. W. Collins: "Optimization of hydrogenated amorphous silicon *p-i-n* solar cells with two-step *i* layers guided by real-time spectroscopic ellipsometry," Appl. Phys. Lett. 73 (1998) 1526.

[6] H. M. Branz: "Hydrogen collision model: Quantitative description of metastability in amorphous silicon," Phys. Rev. B 59, (1999) 5498; R. Biswas and Y. P. Li: "Hydrogen flip model for metastable structural changes in amorphous silicon," Mater. Res. Symp. Proc. 557 (1999) 371.

[7] A. Shah, U. Kroll, H. Keppner, J. Meier, P. Torres, and D. Fischer: "Potential of VHF-plasmas for low-cost production of a-Si:H solar cells," 9th Int. PVSEC Tech. Digest. (1996) 267.

[8] A. H. Mahan, J. Carapella, B. P. Nelson, R. S. Crandall, and I. Balberg: "Deposition of device quality, low *H* content amorphous silicon," J. Appl. Phys. 69 (1991) 6728.

[9] S. Guha and J. Yang: "Science and technology of amorphous silicon alloy photovoltaics," IEEE ED-46 (1999) 2080.

Early Experience with Manufacturing CIS Products

D. E. Tarrant and R. R. Gay

Siemens Solar Industries
4650 Adohr Lane
Camarillo, California 93010

ABSTRACT

A major milestone in the development of PV was achieved with the commercial introduction of modules based on CIS thin-film technology. First available from Siemens Solar as 5 and 10-Watt modules in 1998, the CIS product line was expanded in 1999 to include 20 and 40-Watt modules. Electrical performance has proven to be quite predictable with aperture efficiencies over 10%. Process development and implementation of production control systems have improved yield and continue to be refined. Accomplishments to date lay the foundation for continued scale-up of the technology. The current challenges are to scale the processes to even larger areas, to reach higher production capacity, to demonstrate in-service durability over longer times, and to advance the fundamental understanding of CIS-based materials and devices with the goal of further efficiency improvements for future products.

1. Introduction

The primary objectives of the SSI "Commercialization of CIS-Based Thin-Film PV" subcontract are to scale-up substrate size and to increase production capacity of the baseline CIS module process while introducing Siemens Solar's first CIS-based products. An additional mid- to longer-term objective is to advance CIS based thin-film technology thereby assuring future product competitiveness by improving module performance, cost per watt produced, and reliability. These combined objectives are pursued to fabricate efficient and stable thin-film modules made by scaleable, manufacturable, low-cost techniques.

2. Long-term Commercialization Criteria

Compared to traditional wafer-based crystalline silicon technologies, monolithic integration of thin film technologies can lead to products of comparable performance but with significant manufacturing advantages [1]: lower consumption of direct and indirect materials, fewer processing steps, easier automation. Monolithic integration is required to achieve these advantages since this eliminates multiple process steps and handling operations during the formation of the absorber and module assembly. This is particularly advantageous for smaller modules that are otherwise produced using partial wafers. The thin-film approach also frees the manufacturer from the threat of shortages of low-cost silicon.

Thin film technologies considered for the reduction of manufacturing costs include alloys of amorphous silicon (a-Si), cadmium telluride (CdTe) and CIS. The basic elements of PV modules produced by these technologies are the same; they have a circuit glass/cover glass laminate, a frame and a junction box. These packaging elements have about the same area-related costs and account for about half the total product cost. The basic circuit elements are also very similar; they each have a base electrode, an absorber, a junction, a top electrode and three patterning steps for monolithic integration. While the details of these costs differ, the basic cost structures are the same on an area-related basis.

If the cost per unit area is the same, then the cost per watt is inversely proportional to the module efficiency. CIS modules have demonstrated the highest efficiencies of any of these candidate technologies. The average aperture-area efficiency of large, ~30x120 cm circuit plates in pilot production at SSI is over 11% and NREL has confirmed over 12% aperture-area efficiency for a champion module (Fig. 1). This performance is comparable to many modules based on crystalline silicon, and is substantially better than the performance reported for other thin-film products. Because the area-based costs are similar, and the CIS modules have a much higher efficiency, CIS will result in the lowest manufacturing cost/watt.

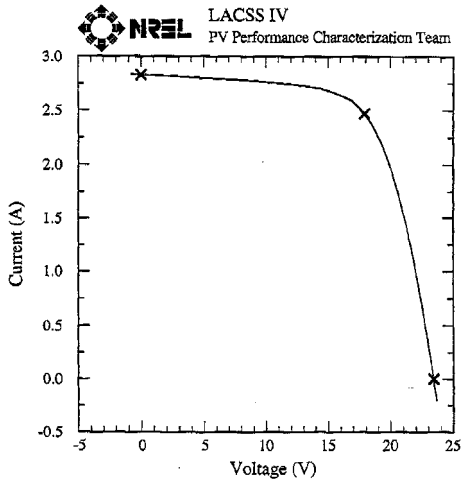

Fig. 1. Champion 12.1% Efficient Large Area Module (3651 cm^2 aperture area).

3. CIS Products

The CIS-based ST5 and ST10 modules were first introduced at the 2nd World Conference on Photovoltaic Solar Energy Conversion, held at Vienna, Austria, in July 1998. The

ST10 module is about 1 square foot in size with a minimum aperture efficiency of 9.6%. R&D Magazine recently recognized the significance of this event by awarding the R&D 100 Award to the Siemens Solar ST family of CIS solar modules. The CIS product line was expanded in 1999 to include 20 and 40-Watt ST20 and ST40 modules. Samples of these commercial products with efficiencies over 11% have been supplied to NREL as contract deliverables.

4. Status

There are a number of prerequisites for commitment of the financial resources needed for large-scale commercialization. The release of inaugural products made using scaleable, manufacturable processes is one, but progress has been made on other fronts. NREL has demonstrated CIS champion solar cells exceeding 18% efficiency [2]. Record breaking efficiencies of over 12 percent have been verified by NREL for a large area ST-40 module [3, 4]. Long-term outdoor stability has been demonstrated at NREL by ~30x30 cm and ~30x120 cm modules from Siemens Solar which have been in field testing for as long as over ten years [3]. Projections based on current processing indicate CIS production costs well below those for silicon-based production costs [1].

The Siemens Solar approach to substrate size and capacity scale-up has been to apply appropriate manufacturing engineering disciplines - Statistical Process Control (SPC), Analysis of Variation (ANOVA), and Design of Experiments (DOE). Circuit plate process data for one year of production (October 1998 through September 1999) exhibits generally good control with an average aperture-area efficiency of 11.2% based on a Gaussian fit to the distribution.

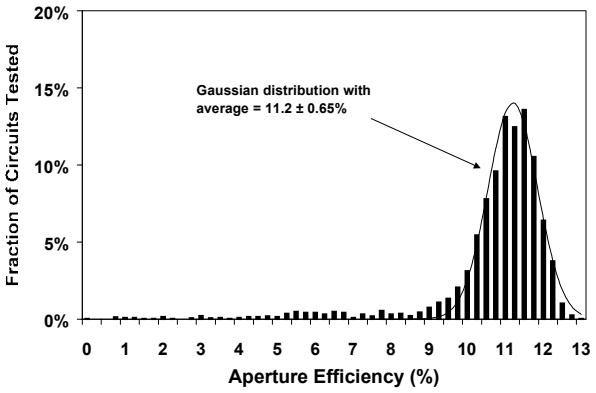

Fig. 2. One Year CIS Circuit Efficiency Distribution.

Judicious tracking of present production using these methodologies has led to a clear definition of near term yield issues. Process development has improved adhesion, decreased breakage, addressed control of raw materials, and decreased failures associated with patterning. In addition to process development aimed at improving efficiency and continual yield improvements, development of manufacturing coordination systems is critical for successful scale-up. Conformance to specification must be checked for incoming raw materials and inventory control is required to prevent shortages. A preventative maintenance system must assure reliable equipment performance. Process consistency requires formal documentation of all procedures, work instructions, and hand-off between production and non-production use. Formal training to written documents and an authorization system are required to assure compliance to procedures.

5. Development for DOE Long Term Goals

The following topics are indicated for long-term process development:

- Improved efficiencies
- Decreased sensitivity to humidity
- Improved large area reactive annealing strategies
- Non-cadmium buffer layers
- Lower cost packaging

Research issues for CIS:

- Role of substrate and base electrode in CIS growth
- Role of sodium in film growth and device performance
- Growth mechanisms for CIS from gas/solid reactions
- Control of adhesion
- Optimization of gallium and sulfur profiles
- Role of buffer layer and junction mechanism
- Understand and control thermal / light soaking transients

6. Conclusions

The cost of electricity from PV is a central issue for DOE program goals; manufacturing costs must decline and module efficiencies must improve for PV to meet these goals. Thin-film technologies offer the greatest promise for cost reduction, and CIS is the highest efficiency of the thin-film options. CIS has demonstrated the prerequisites for a commitment to large scale commercialization – high efficiency, long-term outdoor stability, and attractive cost projections. Remaining R&D challenges are to scale the processes to even larger areas, to reach higher production capacity, to demonstrate in-service durability over even longer times, and to advance the fundamental understanding of CIS-based materials and devices with the goal of further efficiency improvements for future products.

REFERENCES

[1] R. Gay, “Prerequisites to Manufacturing Thin-film Photovoltaics”, Thin Film Photovoltaic Symposium, IEC, May 1997. Published in Progress in Photovoltaics: Research and Applications, 5 (1997) pp. 337-343.

[2] M. Contreras, et. al. “Progress Toward 20% Efficiency in Cu(In,Ga)Se2 Polycrystalline Thin-Film Solar Cells”. Progress in Photovoltaics: Research and Applications. Vol. 7, 1999; pp. 311-316; NICH Report No. JA-520-26111.

[3] U.S. Department of Energy Photovoltaic Energy Program Overview FY 1999. (2000). 24 pp.; NICH Report No. BR-520-26923; DOE/GO-102000-0963.

[4] D. Tarrant, R. Gay, "Thin-Film Photovoltaic Partnership Program – Commercialization of CIS-Based Thin-Film PV, Phase I Annual Technical Status Report”, to be published.

Copper in Contacts to CdTe

T.A. Gessert[1], S. Asher[1], C. Narayansyamy[1], and D. Rose[2]

[1]National Renewable Energy Laboratory, 1617 Cole Blvd, Golden, CO 80401
[2]First Solar LLC, 12900 Eckel Junction Road, Perrysburg, OH 43551

ABSTRACT

Cu from the back contact of a polycrystalline CdS/CdTe solar cell does more than assist in forming a low-resistance contact. In this study we use a sputtered ZnTe:Cu/Ti contact and show that the V_{oc} increases from ~400 mV to >800 mV as the contact deposition temperature increases from ~200°C to ~400°C. High-resolution SIMS analysis shows very little change in Cu within the CdTe layer, yet reveals a systematic increase in Cu within the CdS layer as the deposition temperature increases. Concurrent TLM measurements of specific contact resistance of the ZnTe:Cu/Ti interface shows the fill factor is limited by resistance at this interface for deposition temperatures <~320°C.

1. Introduction

It is well known that most back contacts to polycrystalline CdS/CdTe solar cells contain Cu. Nevertheless, there is very little solid information regarding what function(s) the Cu performs during contacting. It has been suggested that Cu diffusion leads to the formation of a p^+ region near the CdTe outer surface. However, efforts to dope crystalline CdTe to the degenerate levels to enable tunneling have thus far been unsuccessful. Another possibility is that the formation of Cu_xTe is important to contact formation. Although these speculations may shed light on how low resistance is achieved, they do little to explain other observations related to contact formation. These include changes in V_{oc} as the amount of available Cu from the back contact is altered.

In this paper, we describe one study in which the fill factor and V_{oc} of the device increase significantly as the deposition temperature of a ZnTe:Cu/Ti contact is increased from ~200°C to ~400°C. Measurements of specific contact resistance indicate that most of the fill factor increase can be attributed to changes at the metal ZnTe:Cu interface. SIMS analysis of these devices reveals an increase in Cu concentration in the CdS layer with increasing deposition temperature. To our knowledge, this is the first time that this coincident trend has been clearly identified.

2. Experimental

The CdS/CdTe device material used in this study was produced at First Solar LLC. The CdS and CdTe layers are deposited at ~580°C on 5-mm soda-lime glass by the close-space sublimation (CSS) process to thicknesses of ~300 nm and ~4.5 µm, respectively. Following active layer deposition, a wet $CdCl_2$ treatment was performed at First Solar similar to that described elsewhere[1]. Except where noted, all devices used in this study were cut from the same First Solar sample plate (#20746F3).

ZnTe contacting is performed by cutting a small sample (~10 cm^2) from the larger plate, rinsing the sample with methanol, and placing it into a multi-source vacuum deposition system. The system was pumped to ~$5x10^{-8}$ torr, after which the substrate heater (boron-nitride element) is energized at a predetermined and constant voltage. The sample is maintained at the substrate temperatures throughout contacting. The temperatures noted in this study were calibrated by placing a 0.32 cm thick Al block with an imbedded thermocouple onto the deposition platten, and allowing the block to equilibrate for 2 hours at constant heater voltage. Devices were contacted at ten different substrate temperatures ranging between ~200°C and ~400°C. Contact formation was a sequential, three-step process involving ion-beam milling the CdTe surface to a depth of ~100 nm, r.f.-sputter deposition of ~0.5 µm of ZnTe:Cu (~6 at.% Cu), and d.c.-sputter deposition of ~0.5 µm Ti. Following deposition and sample cooling, an array of individual 0.25 cm^2 cells are defined photolithographically on each sample. Cell definition was by chemical etching the Ti layer using TFT etchant (Transene Inc.), followed by ZnTe:Cu- and CdTe-layer etching using an aqueous solution of 39% $FeCl_3$. The front contact is formed with a perimeter of In solder around the entire array of cells (typically six cells per array).

Devices used for secondary ion mass spectroscopy (SIMS) were contacted as above, except that the Ti layer was removed prior to analysis using the TFT etchant. High-resolution SIMS was performed from the contacted side of the devices using a Cameca IMS-5F unit using 12.5 keV O_2^+ as the primary ion (8 keV impact energy). The instrument was tuned for a mass resolution (M/ΔM) of ~4000 to allow for separation of Cu from Te and S species.

3. Results and Discussion

Figures 1 and 2 show the effect of substrate temperature on device fill factor and V_{oc}. The effect of 80-day laboratory storage is also shown, indicating this storage does not significantly alter the light current-voltage (LIV) parameters. These devices were not subjected to accelerated stressing conditions. Figure 1 shows that the substrate temperature during contact formation has a significant effect on the fill factor. To study this dependence, contact-resistance measurements (Transfer-Length Method) were performed on Ti/ZnTe:Cu/glass samples that were deposited at the same time as the devices shown in Figure 1. This analysis revealed that the specific-contact resistance (r_c) at the Ti/ZnTe:Cu interface may become a significant resistance component at substrate temperatures <~320°C (i.e., >0.1 Ohm-cm^2), and the dominant resistance component at substrate temperatures <~290°C C (i.e., >1.1 Ohm-cm^2)[2].

Figure 2 shows a much more surprising result: The substrate temperature has a significant effect on the device V_{oc}. This observation is consistent with anecdotal evidence

from other Cu-containing contact processes and suggests that the junction region may be altered during contacting.

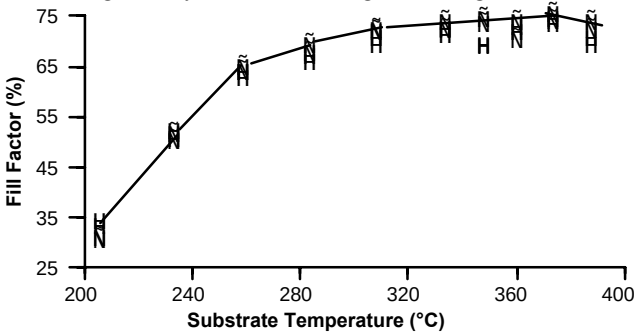

Figure 1. Fill Factor vs. substrate temperature during contact formation. Squares represent range of initial data for the 4 - 6 devices in the array of cells, and triangles represent the range of data after 80-day storage.

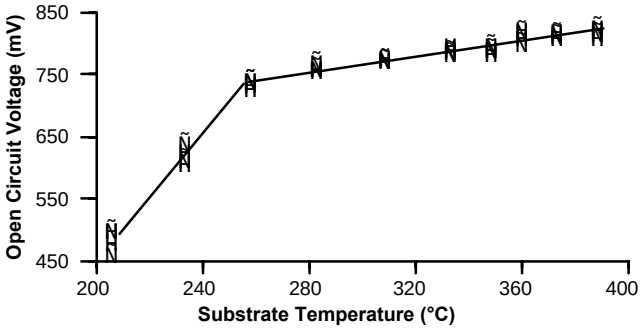

Figure 2. V_{oc} vs. substrate temperature during contact formation. Squares and triangles are same as in Figure 1.

SIMS depth profiles performed at several of the heater temperatures are shown in Figure 3. These data clearly show that, although higher substrate temperatures leads to a systematic increase in Cu concentration in the region of the CdTe layer, there is a much more significant increase in the region of the CdS layer. Indeed, as shown in Figure 4, plotting the device V_{oc} vs. the SIMS-measured Cu concentration in the CdS layer illustrates this coincidence.

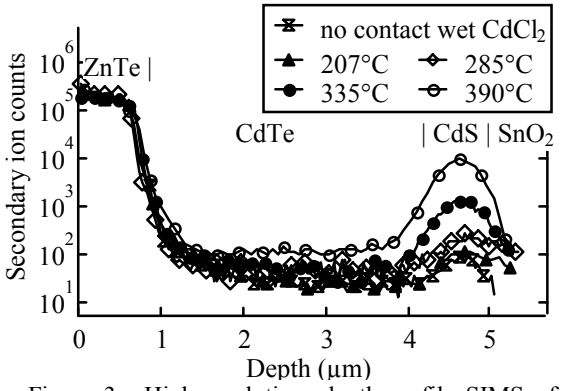

Figure 3. High-resolution, depth-profile SIMS of Cu in devices contacted at various heater temperatures. Note that the control device (with no contact) was produced using vapor-transport deposition at First Solar (#K98072435F6).

At this time, the potential effects of Cu in the CdS layer on the operation of a CdS/CdTe heterojunction are uncertain. It is acknowledged that much of the Cu observed in both the CdS and CdTe layers may reside on grain boundaries.

Unfortunately, at this time, measurement techniques do not exist that have both sufficient spatial resolution and elemental sensitivity to answer this question. It has also been reported that Cu can act as an acceptor in both crystalline CdS and in films grown by CBD[3]. Other possible causes that could relate V_{oc} to substrate temperature include: effects due to the smaller, yet observable, increase in Cu concentration in the CdTe layer; temperature-related changes to defect-complex formation; changes in dopant activation or passivation; or changes at a back-contact barrier. In any event, the findings presented here suggest that one appropriate avenue for future investigations may be to study devices fabricated using Cu-doped CdS and contacted with Cu-free contacts.

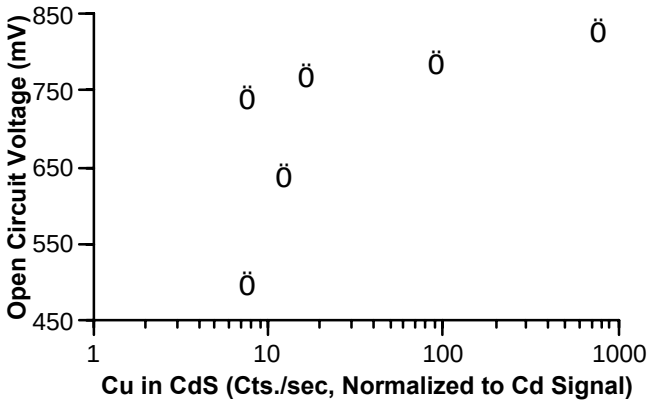

Figure 4. Device V_{oc} vs. SIMS-measured Cu concentration. Data normalized to SIMS Cd signal

3. Conclusions

Numerous observations suggest that Cu from the back contact of a CdS/CdTe device does more than enable the formation of a low-resistance contact. Our studies reveal an increase in Cu concentration in the CdTe and CdS layers from a ZnTe:Cu contact that is coincident with a significant increase in device V_{oc}. The data also reveals that most of the V_{oc} increase is coincident with a very small amount of Cu in the CdS. This study should be viewed as a preliminary step in understanding the role of Cu in device formation in the thin-film CdS/CdTe PV device.

4. Acknowledgements

This research was supported by DOE Contract #DE-AC36-99GO10337.

REFERENCES

[1] D.H. Rose, F.S. Hasoon, R.G. Dhere, D.S. Albin, R.M. Ribelin, X.S. Li, Y. Mahathongdy, T.A. Gessert, and P. Sheldon, "Fabrication Procedures and Process Sensitivities for CdS/CdTe Solar Cells", Prog. In Photovoltaics: Res. And Applic. 7 (1999) 331-340.

[2] T.A. Gessert and T.J. Coutts, Development and Analysis of Cu-doped ZnTe for use as a Back Contact Interface for CdS/CdTe Solar Cells, AIP Conf. Proceedings #306, (1993) 345-353.

[3] N. Pavaskar and C. Menezes, Jap. J. Appl. Physics, 7 (7) (1968) 743-747.

Technical Issues in Large Area CdS/CdTe Thin Film Deposition

R.C. Powell, K. Kormanyos, G. Faykosh, D. Rose, U. Jayamaha, D. Grecu, D. Giolando, G. Dorer

First Solar, LLC.
12900 Eckel Junction Road, Perrysburg, OH 43551

ABSTRACT

This paper reports progress in high-throughput manufacturing of thin-film, CdS/CdTe-based photovoltaic modules at First Solar, LLC. A new production facility that includes thin-film coating equipment capable of depositing semiconductor layers on a 1.2 m-wide web is nearing completion. This equipment was designed to coat glass plates with semiconductor thin films at a rate of ~3 m^2/min. With improvements in module efficiency to 10%, full production targets a goal of 100 MW/yr. Throughputs of >1.7 m^2/min with good film uniformity have already been demonstrated. Module production is scheduled to begin in calendar year 2000. Additional developments in SnO_2 deposition are reported.

1. Introduction

First Solar, LLC. was created in 1999 as a joint venture between Solar Cells, Inc. and True North Partners to commercialize the CdS/CdTe thin-film technology developed by Solar Cells, Inc. Construction of a 75,000 ft^2 factory began in June 1999 and is currently nearing completion. In addition to the significantly larger semiconductor coating system, the new manufacturing facility eliminates most of the batch processes used in pilot production. This paper focuses on the coating processes including imminent improvements.

2. General Process

Commercially available SnO_2:F coated soda-lime glass is used as the starting substrate. CdS and CdTe semiconductor layers are deposited in a vacuum furnace. The resulting film stack is annealed in the presence of $CdCl_2$ to improve electronic properties. The back contact is formed by a multi-step, wet process followed by sputter deposition of metal layers. Monolithic series interconnection is accomplished using pulsed laser ablation. Glass-to-glass encapsulation creates the final module package.

3. Thin Film CdS/CdTe

At the heart of the First Solar process is a high-rate proprietary deposition method known as vapor transport deposition (VTD). This method utilizes flash-sublimation of injected semiconductor powders in an inert carrier gas stream to create a dense vapor cloud in a modest vacuum (~5 Torr) [1]. The inert carrier gas flow directs and controls the dense vapor cloud. The semiconductor films are formed on substrates at temperatures between 500 and 600 ºC with growth rates up to 1 µm/s.

The new production equipment was designed to coat a near-continuous stream of glass 120 cm wide. The coating equipment consists of an entrance load-lock, a glass heating section, a deposition section, an exit load-lock, and a cooling section. The cylindrical geometry of the glass heating and deposition sections is suitable both to support the atmospheric pressure load and to form an excellent radiation cavity to achieve uniform glass temperature. Multiple heating zones allow adjustment of cross-web glass temperature. Glass sheets are supported and moved throughout the system using ceramic rolls that are tangentially driven by a flat chain.

Multiple, redundant coating subsystems are located within the deposition section of the furnace. Injected source material is vaporized, the vapors distributed, and the inert carrier gas exhausted in each coating subsystem. Each vaporizer-distributor is capable of forming one complete layer.

The first version of the 120 cm-wide VTD equipment consists of a direct isotropic increase in size of all the 60 cm-wide pilot deposition components. The increased size of deposition system actually resulted in better temperature uniformity, improved thermometry, and easier film thickness control.

Coating uniformity and consistency are key measures of the deposition system performance and are essential for improved module efficiency. Figure 1 shows several typical CdS cross-web thickness profiles of films deposited on the

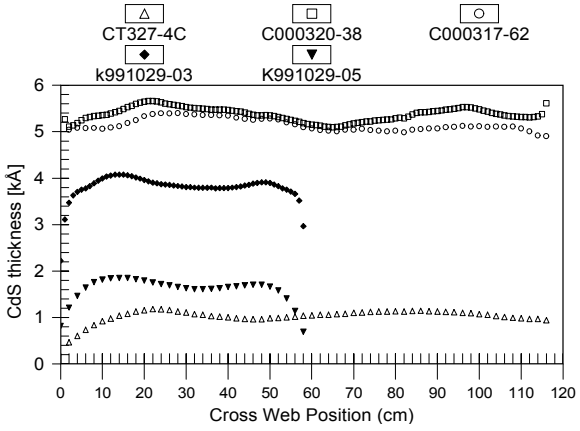

Figure 1. Comparison of average cross-web thickness profiles for CdS films made in the new deposition system (open symbols) and the pilot equipment (solid symbols). Note the similarity in profiles from the different sized equipment.

new deposition system and comparison profiles from the 60 cm web pilot system. Moreover since the new deposition equipment can operate in a continuous steady-state mode, improved consistency is expected.

Critical to production operation is raw material utilization and equipment up-time. To a large degree, these are coupled in the VTD coater as whatever material is not deposited, condenses on cooler components and filters and eventually requires cleaning. Fortunately the components that directly control the coating itself, the vaporizer and distributor, generally remain clean, as they are the hottest components. The experience of the pilot operation indicates that material utilization >70% will be attained and up-time can be extended by proper exhaust design.

With coating rates of up to 3 m^2/min, and CdTe film thickness of up to 4 μm, material consumption could exceed 1 ton/month. We have qualified three vendors for both CdTe and CdS source powder. We have also transferred a cumbersome powder-processing step to our main vendor.

4. Glass Handling and Coater Capacity

The pilot-scale VTD equipment can coat one 60 cm x 120 cm substrate every 3 minutes with throughput limited by glass heating capacity. The production system handles the substrates through the load locks by groups of four 60 cm x 120 cm pieces, and can sequence one group every minute. Ultimately processing one 120 cm x 480 cm sheet of glass every minute is envisioned. Currently the capacity of the semiconductor deposition equipment is significantly greater than the balance of the production line. This was done due to cost and timing consideration in the balance of the line and because the incremental cost of a larger semiconductor coater was not excessive.

Implementation of this large, thin-film manufacturing facility requires the handling of more than a ton of glass substrates every hour. Three 5-axis robots have been installed: two to reproducibly seam, and place glass at the entrance and one to transfer or stack coated plates at the exit.

5. Diagnostics

High-throughput deposition requires constant feedback and control. In addition to over 80 channels of temperature, pressure, position and speed control, the coater is equipped with a scanning infrared imaging system, an internal laser absorption system to measure CdS thickness, an off-line optical system for CdS thickness mapping, and continuous residual gas analysis.

Infrared radiation emitted from the SnO_2-coated glass surface is detected by an imaging system located between the heating chamber and the deposition chamber. The emitted radiation passes through a ZnSe vacuum window. A spinning mirror sequentially reflects radiation from across the web towards a single detector. The imaging system creates a 2-dimensional map of the glass surface temperature. After correcting for some spurious internal reflections, glass temperature uniformity has been measured to be ±5ºC on the 60 cm x 120 cm substrates.

Since the CdS layer is soon buried by the lower bandgap CdTe, CdS thickness detection is best done *in-situ* at deposition temperature. Therefore, an array of fixed-position green lasers and paired detectors have been installed in the deposition system to infer CdS thickness based on optical absorption. Fortuitously, the decrease in CdS bandgap with temperature is sufficient to allow the use of small, readily available, stable solid-state 532 nm lasers.

6. Efficiency

Currently efficiency of devices made from films deposited on the new equipment are similar to those made in the pilot operation: ~10% small area devices which yield ~7% modules. The path to improved module efficiency includes improved uniformity and increased photocurrent through enhanced blue response. Thinning the CdS window layer to < 1000 Å is the best, known method to achieve higher photocurrent in these devices. Figure 1 shows the capability of the VTD deposition equipment to deposit these thin layers.

However, laboratory results have shown that devices with thin CdS suffer from lower voltage unless a higher-resistivity oxide buffer layer between the thin CdS and the SnO_2:F is added. Development of a new chemistry for APCVD of high-resistivity SnO_2 buffer layers is underway. Deposition onto 60 cm x 120 cm substrates using the new chemistry have resulted in films with sheet resistivities of ~5 k Ω/ and good uniformity.

6. Conclusion

Momentous progress has been made on the large-area, high-throughput manufacture of CdS/CdTe thin-film photovoltaics. Semiconductor coating rates > 1.7 m^2/min have already been achieved. Progress on the deposition of both thin CdS and SnO_2 buffer layers is expected to soon result in improved module efficiency. With the higher throughput and improved efficiency combined, the path to a 100 MW/yr plant is clear. Moreover, with production beginning in 2000, the Department of Energy's Thin-Film Partnership program has helped in producing tangible results.

7. Acknowledgements

This work was supported in part by the National Renewable Energy Laboratory under Subcontract ZAK-8-17619-17.

REFERENCES

[1] R.C. Powell, U. Jayamaha, G.L. Dorer, H. McMaster, Proc. 15th NCPV Program Review, AIP Conf. Proc. 462, M. Al-Jassim, J.P. Thornton, J.M. Gee, eds., Denver, CO, 1998, p.31-36.

The National CIS and CdTe R & D Teams

James R. Sites

Physics Department, Colorado State University

Fort Collins CO 80523-1875

ABSTRACT

For the past five years, groups of photovoltaic researchers working with CIS and CdTe technologies under NREL sponsorship have been pooling part of their efforts to collaborate on specific projects. Generally these projects have been both fairly basic and highly relevant to industry. This presentation outlines the structure, the benefits, and the challenges of the team process, and it describes representative examples of results produced in each area.

1. Introduction

The National CIS and CdTe R & D Teams were initiated by NREL in December 1994 following the general model of multiple-institution collaboration in other areas of photovoltaic research. All groups funded by NREL though the Thin-Film Partnership for work with CIS or CdTe cells, as well as the appropriate NREL staff scientists, are automatically members, and others have been added at the discretion of the core group. Each institution names a primary contact, mainly for logistical purposes. The charge to the members is to focus on specific problems, perhaps 20% of total effort, particularly those problems that are likely to have a direct impact on commercial manufacturing. Each team has been meeting approximately twice each year to report on progress and define, or refine, the focus of work for the next period. The number of attendees has ranged from 25 to 60 and has been gradually increasing. Length of meetings has ranged from half a day to two days. Their timing has sometimes been planned to be adjacent to a larger meeting, and other times, they have been hosted by NREL or one of the other member groups.

2. Organizational Structure

There has been some evolution of the organizational structure of the two teams, and some turnover in the individuals involved. The general structure, however, has been to divide into subteams, each with a designated leader and a specific research problem. In some cases the problem has been chosen by vote or consensus of the total membership and in others it has been explicitly defined by one of the industrial members. The subteams have kept in touch through e-mail, conference cells, and pre-meetings. At a full team meeting, each subteam reports its results. The breadth of information reported, number of individuals involved, and amount of general discussion has varied with the length of the meeting. Part of the meeting is often reserved for presenting new ideas and formalizing plans for the next period. A very valuable aspect of each meeting has been the assembly and distribution of a meeting record, which has generally consisted of a summary, brief commentary by each reporter, and copies of the viewgraphs presented.

3. CIS Examples

This section and the following one are not meant to summarize all the work of the two teams, but to present representative examples of results that have been achieved.

One CIS example was the "moly team" whose objective was to look at different combinations of glass substrates and molybdenum back contacts to see whether different choices have an impact on cell performance. Multiple groups participated in the fabrication, measurement, and analysis. The general conclusion was that sodium from soda lime glass moves through the moly layers, perhaps at different rates, but that cell performance is only weakly dependent on the magnitude. Two papers were published, and their conclusions were broader based than would have been likely if only a single laboratory did the study.

A second example, which is more complex and ongoing, involves the CI(G)S junction region. One subteam, known as the "present junction team" defined a project to compare cell performance when the chemical-bath process of CdS-window deposition was modified in various ways to create different buffer layers. NREL absorbers were used. Meanwhile, the "transient team" using Siemens absorbers was looking at reversible time-dependent variations in performance that were related to recent illumination history. Within the past year, these groups have joined forces to ask whether there is a common buffer layer model that provides insight on both base performance and transients and to explore whether such a model is affected by the absorber deposition process.

4. CdTe Examples

One CdTe-cell example was referred to as the "thin CdS project," actually a subset of the "high efficiency team." The increase in photocurrent available as the CdS window is thinned is significant, but the junction quality generally deteriorates substantially when the CdS becomes too thin. The first phase was for several laboratories to make cells with progressively thinner CdS, and a second phase was for

laboratories to complete cells with absorber material from a single source. Cell parameters were plotted against CdS thickness. In most cases the voltage dropped rapidly below 500A, giving a practical target for manufacture. It was also seen that the final thickness of CdS was generally reduced from the deposited thickness due to interdiffusion and that in some cases the final thickness could be near zero if the next layer, a conductive oxide, was highly insulating.

A second CdTe example is the ongoing "stability team" which has in several laboratories been subjecting cells to elevated temperatures to greatly accelerate any changes that may occur in the field. This group has related most such changes to the cells' back contacts, it has documented dependence on cell bias, environmental conditions, and other factors, and it has put together a working model involving copper diffusion. This group more than most has also had to deal with possible commercial consequences from sloppy or incomplete reporting.

5. Benefits of Team Approach

The most obvious benefit of the team approach has been the ability to generalize research results to a much greater extent than likely in a single laboratory. This ability to generalize is particularly important in a field where the material structure is far from the textbook description, hard to characterize at the atomic level, and apt to vary significantly with fabrication procedures. The team process has also provided a rapid-time frame for dissemination of results within the communities focused on CIS and CdTe-based cells.

There are also some clear sociological benefits from the team process. Contact between colleagues, whether it is phone, e-mail, or face-to-face, is more frequent. There is often seen a high level of creativity when the teams or subteams get together to discuss specific issues. The general level of trust in each other is higher, and the balance between NREL guidance and team consensus has, in my opinion, been quite healthy.

6. Challenges to Team Approach

The benefits of the team approach do not happen automatically, and there are several ongoing challenges. Perhaps the biggest has been defining the most appropriate problems for study. Groups of creative people have diverse opinions about how to proceed and both teams had to work through the decision process. A subtext has been whether priorities are primarily determined by the group as a whole or by the needs of specific industries. The CdTe has gone somewhat in the direction of general consensus, and the CIS team has moved more towards industry-focused problems. A related challenge is keeping team meetings focused on the agreed-upon problems when many of the members have other important results they are inclined to talk about. The strategy has been for a smaller group to meet in advance to discuss and then set an agenda with realistic time allotments for presentations and discussion.

An early challenge for the team process was how to deal with confidential information. Truly proprietary information is excluded from the team meetings, but may be part of a subteam's activities. Any confidentiality agreements involved are worked out on an individual basis. The gray area between proprietary information and completely public information was of concern initially, but has largely become a non-issue as the members have become more comfortable working with each other. A somewhat related challenge has been to discourage participation at only a superficial level. It is particularly awkward for industrial colleagues if information is not flowing in both directions. At least a partial solution has come from peer pressure, which has seemed to nudge almost all of the members towards active participation.

7. Participating Institutions

The institutions listed here have been part of the CIS of CdTe teams for at least part of the past five years. The author is indebted to numerous individuals from these institutions for discussion of the team process.

CIS	CdTe
National Renewable Energy Laboratory	National Renewable Energy Laboratory
Florida Solar Energy Center	Florida Solar Energy Center
Daystar Technologies	BP Solar
Energy Photovoltaics	Canrom PV
Global Solar Energy	Golden Photon
International Solar Electric Technology	ITN Energy Systems
Materials Research Group	Solar Cells, Inc/First Solar
Siemens Solar Industries	ALF, Inc.
Solarex	Colorado School of Mines
Unisun	Colorado State University Institute of Energy Conversion
Colorado State University Institute of Energy Conversion	University of South Florida
Pennsylvania State University	University of Toledo
University of Florida	Weizmann Institute of Science
University of Illinois	
Washington State University	

THE ULTIMATE SOLAR CELL: THIN, LIGHT-TRAPPED CRYSTALLINE SILCON

James A. Rand and Allen M. Barnett
AstroPower, Inc., Solar Park
Newark, DE 19716-2000 USA

Abstract

Solar cells formed with thin film polycrystalline silicon offer the potential of capturing the high performance and stability of crystalline silicon while achieving the low cost of thin film manufacturing. Solar cells fabricated from thin silicon active layers (~20 microns) offer significant advantages over thick ingot-based devices. These advantages include higher conversion efficiency than conventional thick devices, and a reduction in material requirements.

1. The Ultimate Solar Cell

The properties of the ultimate solar cell are as follows:

a. High Performance
b. Acceptable Material Cost
c. Stability (High Process Temperatures)
d. Non-Toxic Materials and Processes

High performance begins with the correct choice of bandgap and the ability to form a near-ideal pn junction. Current generation capabilities can be achieved with a combination of material properties (absorption) and device design (non-reflective top surface and light trapping). Acceptable material cost can be achieved through the use of abundant, low-cost materials and low material usage. Stable performance reduces lifecycle costs and is required for optimal system performance. The use of environmentally safe materials and processes are assumed for any modern development effort.

Thin films of silicon supported on a low-cost, environmentally safe substrate meet all the requirements of the ultimate solar cell. The only exception is a performance limit imposed by the less-than-ideal absorption properties of silicon. Significant effort in light-trapping device designs over the past two decades has now eliminated this constraint.

2. Thin Crystalline Silicon Design Rules

Following are the set of design rules used to guide thin crystalline silicon solar cell development:

1. Silicon thickness: 5 to 50 microns.
2. Light trapping (to increase photon absorption).
3. Planar film with single crystal grains at least twice as wide as the film thickness.
4. Minority-carrier diffusion length at least two times the film thickness.
5. Back surface passivation.
6. Benign grain boundaries.
7. A substrate providing mechanical support and back plane conduction.

The significant challenge for a thin crystalline silicon layer acting as a solar cell is the achievement of high levels of light-generated current. Innovative device design must be used to offset weak absorption at the infrared end of the spectrum. As indicated by the device design rules, achieving high light-generated currents require (a) a minority carrier diffusion length equal to or greater than the device thickness, (b) a high level of light trapping achieved with a textured surface and high levels of internal reflection, (c) low recombination surfaces, front and back, and (d) grain boundaries that do not contribute to recombination. Minimizing the grain boundaries through large grain formation can reduce grain boundary electrical activity. Each of the above requirements has been met in different devices. The present challenge is combining them in a single device design.

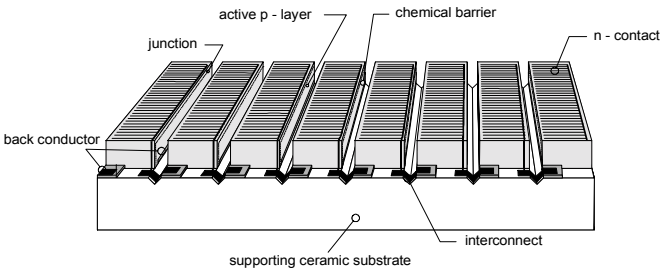

Figure 1. Thin silicon film on a supporting substrate. The benefits of silicon stability and performance are combined with the interconnection properties of thin films in a solar cell that can be readily fabricated using low-cost manufacturing processes.

3. Substrate Considerations

One of the key technological challenges to achieving a commercially viable thin-layer polycrystalline silicon solar cell technology is the development of a low-cost supporting substrate. The requirements for the substrate material are severe. Mechanical strength and thermal-coefficient of expansion (TCE) matching are needed to prevent the film from breaking or deforming during handling and high-temperature processing. The substrate must also provide good wetting and nucleation during the film growth process without contaminating the

film. The substrate can either be conducting or insulating, depending on device requirements. We have chosen an insulating substrate to allow for monolithic interconnection of solar cells (as shown in Figure 1). Finally, the substrate-silicon interface must provide a high degree of diffuse reflectivity and surface passivation.

AstroPower has developed a low-cost ceramic substrate that is thermally well-matched to silicon. The ceramic is fabricated from stable, environmentally benign, high temperature materials. The resulting silicon-ceramic structure can be fabricated into a solar cell using all the processes presently in use for freestanding silicon wafers, including wet chemical steps.

4. Significant Experimental Results

Solar cells fabricated on a ceramic substrate according to the design rules have been tested under solar simulators at both AstroPower and the National Renewable Energy Laboratory. The results show a high short circuit current, 25.8 mA/cm^2, which may be the highest current ever achieved for a silicon layer of this thickness (20 microns) grown on a dissimilar substrate. Quantum efficiency measurements show that the device has a strong response well into the infrared end of the spectrum. This response indicates that the device has achieved many of the important design features identified in the introduction, including good minority carrier properties, surface passivation, and light trapping.

The external quantum efficiency data are shown in Figure 2. Along with the experimental data are curves generated with the PC-1D[1] model. Curve 1 shows the modeled response of a thin silicon layer with excellent minority carrier bulk properties (minority carrier lifetime 3.5 μs), but high levels of recombination at the surfaces (Sb=10^6 cm/s) and no internal reflection. Curve 2 models the same device with excellent rear surface passivation (Sb=0 cm/s). Curve 3 adds light trapping properties to the device. Both front and rear surfaces are modeled with 90% diffuse reflection. A comparison of Curve 3 and the experimental data indicates the device has high lifetime, high levels of surface passivation, and good light-trapping properties to achieve the long wavelength response and high currents that were measured. No other combination of device parameters was able to match the electrical performance. For instance, no value of minority carrier lifetime (no matter how high) could match the spectral response in the red. This strongly suggests that the experimental solar cell benefited from significant light trapping.

5. Conclusion

A thin film of silicon on a supporting substrate is the material needed to build the ultimate solar cell. Two of the critical device properties, light-trapping and back surface passivation, have recently been demonstrated for a 20 micron thick Silicon-Film™ on a ceramic substrate. The achievement of a high short circuit current (25.8 mA/cm^2) from a thin silicon layer represents a major milestone for this technology.

References

[1] P.A. Basore, IEEE Transactions on Electron Devices 37(2), 337 (1990).

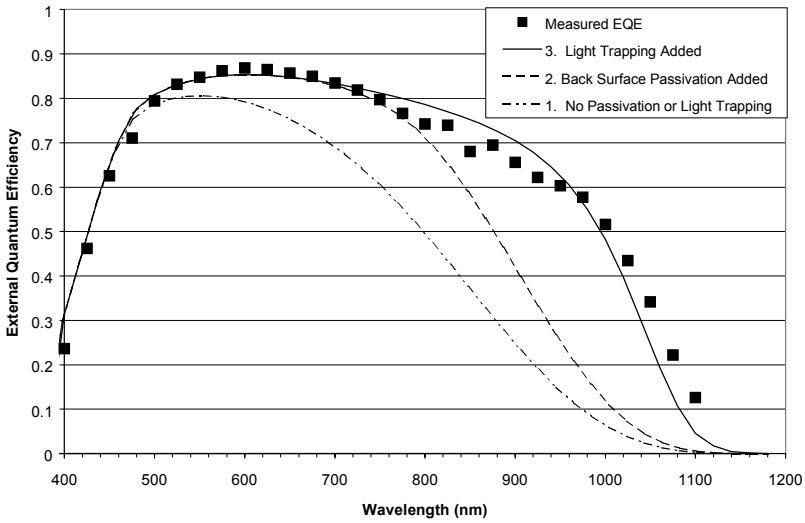

Figure 2. External quantum efficiency of a 20 micron thick silicon solar cell formed on a ceramic substrate. The points represent experimental data. Curves 1 –3 represent models adding important device features to the model. The agreement of the experimental results with curve 3 indicates that the experimental device incorporates all three features.

Executive Summary – Basic Research Opportunities in Photovoltaics Workshop

Angus Rockett

U.S. Department of Energy, Office of Science

This meeting, held May 3, 1999, was organized by J. Benner, S. Deb, and R. McConnell of NREL at the request of James Rannels and the EERE Division in the Department of Energy. The meeting was a follow-on to a meeting organized by A. Zunger under DOE/BES sponsorship in 1992. Teams were selected by the organizers although some changes were made based on input from the invitees. Discussions prior to the meeting varied from team to team. Extended discussions took place during and after the meeting and everyone seemed pleased with the final product. The meeting was divided into topical areas: issues related to crystalline-Si, amorphous Si, chalcopyrites, CdTe, and InGaAsN for PV applications. In addition, novel materials, transparent conductors, and characterization methods were discussed. The workshop proceedings includes team memberships, bulleted lists of the critical issues identified by each team, and papers discussing the points in detail.[1]

Crystalline Si cells benefit from the vast research for the semiconductor industry. However, significant issues remain. Topics specific to PV concern decreasing Si manufacturing cost and energy consumption, and use of polycrystalline materials. Passivation of grain boundaries and impurities, and purification methods are the major science issues. c-Si is the dominant PV technology so even small gains can have a large impact.

Amorphous Si presents many basic science issues, listed in detail in the proceedings. In broad terms these can be grouped as understanding and control of (1) film structure at the atomic and nanoscales, (2) the behavior of H, (3) the physics and chemistry of deposition processes, and (4) doping and carrier mobility. Also, improved (5) simulation of materials and devices, and (6) characterization of short and medium-range order and atomic structure are pivotal. These should lead to a comprehensive understanding of process-property-device performance relationships. The nature and control of instabilities in pure and alloy materials is of critical importance and is a long standing issue requiring detailed experimental and theoretical study.

Chalcopyrite-based solar cells are severely limited by a lack of theoretical and experimental basic science. Issues can be summarized as (1) development of an integrated, predictive understanding of the materials and devices, (2) development of novel processing methods, (3) development of wide-gap materials with adequate properties for devices, and (4) alternative contact materials. Point (1) includes many major subtopics such as the nature of and electron transport at the heterojunction, the chemical, structural, and electronic properties of native point defects, and the factors controlling carrier transport and recombination in the bulk material. These issues will all need to be extended to any alloy materials before optimized devices will be practical to manufacture.

CdTe devices benefit from the literature associated with (HgCd)Te and the availability and studies of bulk single crystals. However, some significant issues remain. Understanding of point defects, impurities, and complexes thereof; the nature of the CdS/CdTe heterojunction, as typically fabricated (far from an ideal single-crystal heterojunction); interdiffusion across the junction; and improved contact technologies require study.

Group III-Nitride solar cell materials, as with other III-Vs, must be grown as single crystals. This technology has significant promise, especially in the high-end high-concentration and space-application areas. It benefits from intense research on short wavelength light emitters. Issues of nitrogen activity, contacts, and doping are important, as for light emitters.

Novel materials hold the possibility for revolutionary advances in PV technology and dramatic reductions in manufacturing cost and increased volume. Significant areas include nano/molecular composites, organic semiconductors, and hot carrier devices. Photoelectrochemical devices[2] have very interesting properties but were not identified in the team report. The science of novel materials is just being established and is a wide-open field.

Transparent conductors are fundamental to all PV technologies and present significant science issues. Current materials are far from optimal and require detailed experimentation and theory to understand limitations to performance and design of new materials. Improved materials would benefit all PV devices and many other fields.

Characterization techniques are important and improved techniques will benefit all semiconductor device technologies. Of particular interest to PV technologies are techniques specialized for optoelectronic properties.

In my opinion, a-Si and chalcopyrite technologies can benefit most clearly from basic science issues. Solving these may also expand the application of these materials outside their current niches. The CdTe community needs to focus on contact technologies. Novel materials and revolutionary concepts such as photoelectrochemical cells are of great interest and potential and include some very interesting and broadly-applicable science possibilities. Finally, transparent conductors are crucial across all technologies and should be studied for possible improvements. Characterization advances are valuable as they are applicable beyond PV.

REFERENCES

[1] V.K. Kapur, R.D. McConnell, D. Carlson, G.P. Ceasar, and A. Rohatgi, eds., Photovoltaics for the 21st Century, Proc. of the International Symp. of the Electrochemical Society, v. 99-11 (Electrochemical Society, Pennington, N.J., 1999).

[2] See Proc. of the Future Generation Photovoltaics Meeting, ed. by R. McConnell AIP Conf. Proc. Ser no. 404 (Amer. Inst. Of Phys., 1997).

Factors Affecting Solar Power Generation

Bettina Adams, Tahida Pierre, William C. Mahone. Dept Natural Sciences, Mississippi Valley State University, 14000 Higyway 82 West, Itta Bena , MS 38941

Abstract: Students and researchers at Mississippi Valley State University have been carrying out a series of research activities designed to develop a familiarity with solar energy generation storage and retrieval. To understand the surface solar energy signature in the Mississippi Delta, a series of measurements of the solar radiation profile were performed. Additionally a series of power measurements with the solar panels were carried out to conditions for optimal power generation. A third objective of our research was to store solar energy as active metals that could be used as elements in batteries or as precursors for chemical hydrogen generation.

Introduction: Energy is a perpetual need of every civilization. In our current society much of our energy comes from pollution producing mechanisms. Even natural gas which is commonly thought of as the cleanest source of combustible energy produces carbon dioxide a green house gas and if used in large enough quantities can result in dramatic climate changes. In the air, other pollutions may take the form of low level ozones and partially consumed hydrocarbons i.e. smog. Additionally fossil fuels are being consumed faster than they are regenerated. Renewable energies hold the promise of the future to supply to supply clean environmentally friendly energy. Additionally renewable energy sources may prove cheaper to implement, which along with deregulation may allow the small businessman to gain a foothold in the energy market. Traditionally energy production has always required high startup costs that priced the small businessman out. Depending on how the renewable energy technology is developed this does not need to be the case with renewable energy. Another avenue of solar energy utilization is in individual application. Increasingly solar energy is finding uses in specialized application. The calculator and other low energy applications have been in use for years. However, more recent applications have been of higher energies. Examples are portable road construction warning signals.

Experimental: The solar radiation experiments involved using wide band photon sensors in three different orientations. One was approximately nine inches inside a cylindrical well which shielded it from diffuse radiation. Another was shielded from direct solar radiation by a semicircular band approximately four inches wide. A third sensor was open to both diffuse and direct radiation. Radiation reaching this sensor was called global radiation. Since global radiation contains both the diffuse and direct component, one expects that the sensor exposed to global radiation should give a response equal to the sum of the sensor response from the other two sensors. The conclusion we reached after two years of observation was as follows. The global mode response, was equal to the sum of the direct plus diffuse response only at noon during the height of the summer solstice. Most of the other time the direct response is larger up to 40 percent larger in some instances (see fig1). Atmospheric scattering could not explain this observation. Therefore we concluded that somehow the direct component was being scattered by the diffuse component at the surface of the detector. This data indicates that solar power output can be increased by nearly 50 percent by using a optical concentrator which would not simply eliminate the diffuse component but will also add to the direct component. Another piece of information learned from the solar radiation experiments was that cloud cover is a crucial factor in determining the feasibility of solar power. Some places have nearly three hundred days of cloud cover per year. Even small clouds can have a significant impact on available solar energy at the surface, while deep cover cloud systems can eliminate all solar power output for weeks. This factor must be considered carefully in reference to any particular application.

The experiments with the solar panel consisted of measuring its open circuit voltage and closed circuit current in several orientations relative the sun and under various weather conditions. We measured the power output of the panel at a vector optimal to solar incidence for the time of the measurement and compared it to measurements with the panel set at optimal for high noon in mid summer. Here again we found that depending on the time of day or year we could achieve from 50 to 100percent increase in power in some cases (see fig 2). Companies now exist that sell rotating arrays designed to maintain optimal orientation to solar incidence. Many of their advertisements claim 50 percent increase in average power output. We have worked out a design for a rotating platform that should be cheap to implement. This should promote the use of island arrays that are much less impactive on their environment. This is the subject of one student's senior project.

A third series of experiments were designed to electro-deposit active metals from aqueous solution using solar panels as an electrical source. Most active metals are produced using a Downs Cell. Commercial downs cells are expensive to build and to operate. They require modification before application to the relatively low energy solar systems. Electro-deposition from a slurry is an alternative that is rapidly supplanting the downs cell. Using a basic buffer solution a student researcher found that he could electro-deposit zinc which had been used in a hydrogen generation experiment. The deposited zinc was again used in the hydrogen generating reaction demonstrating the recycling potential.

In future work we will construct a rotating platform and continue the solar radiation/solar panel experiments. We also will do research into special applications like running well pumps, Irrigation systems, and catfish pond oxygenating systems. These are things important to our region and can find immediate application once demonstrated.

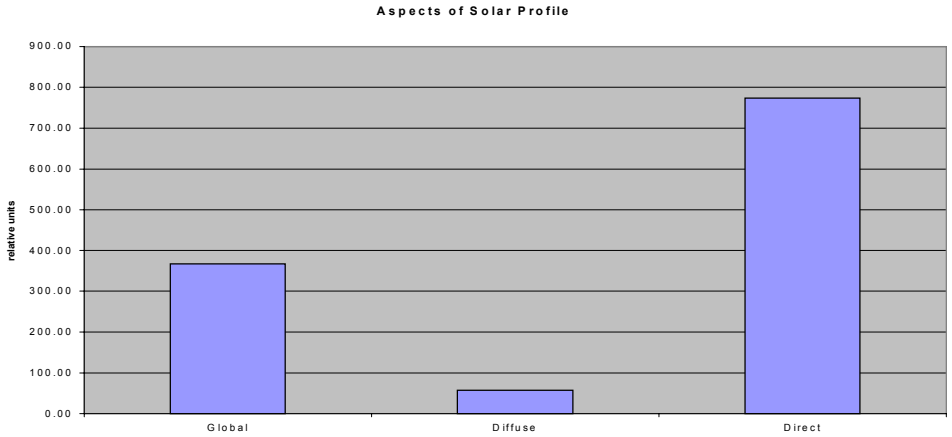

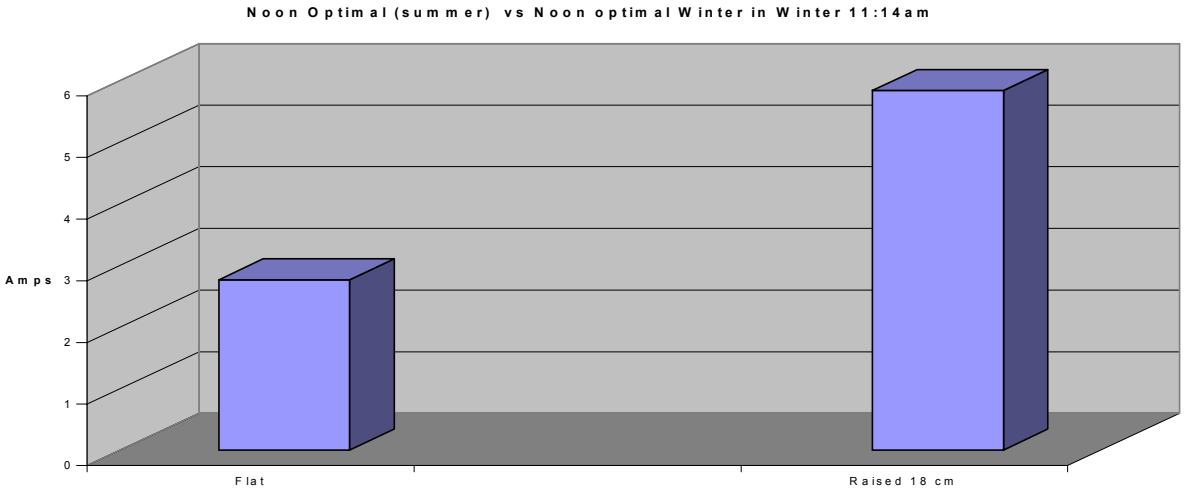

Marketing Renewable Energy Technology In Developing Countries

C. Fuller, H. Evans, C. Hurt

Central State University

1400 Brush Row Road
Wilberforce, OH 45384

ABSTRACT

Since July 1991, Central State University (CSU) has been conducting a water management and development program in West Africa to address critical shortages of safe drinking water. The primary project, designated the Northern Senegal Water Management Project (NSWMP), is a program designed to develop self-sufficiency among Senegalese villagers by providing them with the expertise and materiel to install and maintain their own wind and solar generated water pumping systems. A parallel and supporting project that initially received support from the U.S. Department of Education, Fund for the Improvement of Postsecondary Education (FIPSE) is the Foreign Language/Area Studies Enhancement Project. This parallel and supporting project supports an experience centered, cooperative education program that gives students on-site training in language, culture, and technology. In recent years, student involvement in the West Africa energy program has expanded to include the participation of a select team of CSU students who have combined their renewable energy research and training objectives with resources from the two projects as previously described.

1. Introduction

While under the sponsorship of the HBCU Photovoltaic Research Associates Program (sponsored by the National Renewable Energy Laboratory) and the Consortium for the Advancement of Renewable Energy Technology (CARET, sponsored by the NASA Glenn Research Center) students have conducted various technology development and marketing research projects in West Africa as part of the overall NSWMP water management and development program. The student research has included a variety of hands-on construction and testing of solar and wind energy components in various locations in West Africa and on campus.

2. Approach

The overall goal for the 1996 and 1999 research and observation team visits to West Africa was to investigate the lucrative potential for a new (or existing) renewable energy market in the impoverished rural communities that could benefit the most. The feasibility of a simple hybrid renewable energy system was also investigated.

It was observed that some Aeromotor windmills operating deep within the interior of Senegal did not receive enough wind energy to function during parts of the dry season. The scenario could be potentially disastrous since some villages utilize the Aeromotor windmills as their main method of water procurement. To augment water supply during times of low wind, a hybrid system could be produced using PV panels as a back up power supply. At CSU's on-campus wind energy test site, an amorphous silicon PV module (a module obtained through government surplus) was mounted onto a Windseeker II 250W wind turbine. The wind energy test site also combines the wind turbine with a Solarjack SDS series DC submersible pump for the purpose of simulating water-pumping conditions. The wind turbine along with the PV panel kept the battery bank charged at an optimal level, approximately 12V. An anemometer was used to collect wind speed so that the amount of water produced per period of time could be contrasted with wind speed. The diagnostic tests were conducted so that student research associates could determine the rate of water production at low wind speeds as opposed to power production.

Research associate activities also included examining factors affecting the market governing laws of supply and demand in relation to renewable energy device procurement in poor, rural communities abroad. Those activities included: using the Internet as a primary information resource, visiting a PV module manufacturers and a PV module developers, gathering information from agencies concerned with the dissemination of renewable energy, and attending the regional and national PV conferences. By taking a holistic approach in the examination of the PV industry, from manufacturer to end user, the factors hindering the dissemination of PV to the impoverished areas of Developing Countries were more clearly defined.

3. Observation and Results

Observation of the PV market in West Africa has determined that a major obstacle to the wide scale dissemination of PV devices include a lack of capital and an unwillingness to break away from tradition. There is a need for PV, however, even though many households lack the disposable income to benefit from PV technology. Local affordability of PV devices is a major concern. A few

productive agricultural communities may sell surplus crops to provide down payments on PV systems. Many communities lack food security and must store all surpluses to survive the dry season. Infusions of capital are therefore necessary to provide the villagers with the means to take advantage of PV power. Funds are made available through local banks working in conjunction with international relief agencies and other NGO's. These agencies provide the initial capital that will finance the low interest, long term, revolving credit funds. Monthly payments on the loans are locally affordable, as they are approximately equal to a months supply of batteries or fuel.

Small PV installations in rural communities abroad are typically used for illumination purposes. Systems fabricated for illumination by Senegalese installers cost approximately $1000 (US currency). A basic system consists of a 50W panel, four 10W neon lights, a regulator, a deep cycle battery, distilled water for topping off the electrolyte level and the related cable, wiring, and fuses. Systems fabricated for water pumping are more expensive as depth of water, quality of equipment, and village location are the main determining factors of system price.

A degree of technical know-how is required at the village level. Oftentimes systems break down and ly idle for long periods of time until someone “from outside” comes along to fix it. The problem is addressed through “appropriate” technology transfer and in-country training of village personnel.

Development of the PV market abroad is vitally important to the long-term success of domestic PV manufacturers and the ecology of the village areas abroad. The number of solar panels exported would be greatly diminished if funding strategies were not in place to subsidize the purchase of PV modules and systems. PV installations in the village areas simultaneously provide cheap, green power and reduce environmental degradation. Previous surveys of the surrounding countryside of rural communities in West Africa vividly demonstrated the rampant effects of deforestation. Deforestation continues unchecked because villagers use timber as cooking fuel and construction material and the foliage as animal feed. Small PV systems produce light curtailing the combustion of wood and kerosene and their related health and environmental risks. Where timber is already scarce, programs similar to Port Elizabeth Technikon’s (South Africa) can be developed using local soil in combination with cement mixtures to augment the villages construction needs while keeping costs low.

4. On-Campus Renewable Energy Test Site

To help diversify CSU's renewable energy device marketing efforts, student research associates have completed the installation of a hybrid powered FIASA water-pumping windmill at CSU's renewable energy research site. CSU student researchers also worked closely with student research associates from Wilberforce University. Through a NASA sponsored project called the "Consortium for Advancing Renewable Energy Technology (CARET)", a team of eight CSU students have participated in an Applied Renewable Energy Technology course and laboratory (ENG 450) at neighboring Wilberforce University. Major course objectives have included: assisting in the design and installation of three PV based energy systems at Wilberforce University, Antioch University's Glen Helen Ecological Institute and Springfield South High Scool; the creation of a website that included highlights of work completed on the PV installations; and the completion of individual background reports regarding specific aspects of renewable energy technology.

In order for students to understand the environmental and social challenges of marketing renewable energy products in Developing Countries, CSU students helped expand a renewable energy test site as a replica of facilities found in some Senegal, West African villages. A 100' by 100' area encompasses a 32' FIASA water pumping windmill, a PV solar array, a Windseeker II turbine electrical generating system, and an animal trough and garden area. A gravity feed water storage tank and a custom fabricated PV panel supports are being added. The FIASA windmill has a hybrid power capability and its submersible pump can be operated using wind power or DC power supplied by CSU's PV array. Data collected to date focuses on water pumping rates as a function of wind speed and the discharge and recharge rates of the battery bank to an optimal level of 11V to 13V. The data suggests that the maximum water production for the type system installed would peak at 14 to 15 gallons per 20 minutes of pumping time at an ideal, targeted water depth typical of West Africa.

While it is still in its formative stage of development, the CSU renewable energy test and demonstration site is being further developed to simulate the technological challenges posed by the harsh environment commonly found in the Sahel region of Sub-Saharan Africa. The outcome of these local experiments with various types of appropriate technology may provide the indication of what is economically feasible and sustainable in regions with limited resources and financial assets.

PV Technology Transfer to Remote Area in South Africa

R. Arscott
O. LaFleur

Texas Southern University School of Technology
3100 Cleburne Ave.
Houston, TX 77036

ABSTRACT

The installation of a low maintenance PV system in the remote South African village was to test the durability and efficiency of a stand alone, low voltage PV system. One year later the system's degradation is minimal and does not affect the performance. One problem was encountered three months into the system's operation. The battery could no longer keep a charge. After troubleshooting, it was discovered that the battery used over 80% of its energy due to several cloudy days and the owners lack of energy moderation. To prevent this situation from reoccurring, a deep cycle battery was used to replace the old car battery in the system's battery bank. The system was back in operation at full efficiency. Since then, the owner has been using the PV system to benefit the village.

Introduction

Many remote areas in South Africa lie outside of the country's utility grid. Extending the grid to most of these areas could possibly cost millions of South African Rand (South Africa's currency). Due to this cost factor there are thousand of homes and schools that go without power each year. PV power is a solution to the problem. By participating in the Rural Electrification Program of South Africa, TSU School of Technology provides hands on experience for students by visiting some of the remote villages and installing a low maintenance off-grid PV system. The installer gains training in PV field installation and the homeowner receives a durable, long-lasting non-polluting source of electricity.

Site Selection

The PV installation project was through the contributions of TSU's School of Technology, PE Technikon and ESKOM, the South African National Utility. PE Technikon worked with ESKOM to identify a building in need of electricity. ESKOM has installed several PV systems in rural schools to provide lights, and therefore, selected a home in one of these remote villages outside of East London (a coastal town approximately 400 km north of Port Elizabeth also in the Eastern Cape) as the site for the installation. The house is located in the village of Siqitini in the Nqamakwe District and Silinxa Administrative Area. The owner of the home was a young man chosen because of accomplishments in school.

System Layout

The house was approximately 900 feet with rooms and a porch. The house was constructed of earthen brick with a layer of plaster on the inside and outside wall, and dirt floors maintained with wet manure (commonly used technique). The PV system was designed to supply electricity to four 18-watt fluorescent lights (one in each room and one for the porch). Two 75-watt panels were connected to supply a 24-volt system. A distribution board was installed on the wall of the living room with a battery cabinet located underneath. The distribution board consisted of switches (connected to the panels, lights and batteries), a load shed device (preventing battery over-discharging), and a solar regulator. String-pulled switches were installed at each room doorway entrance for each light.

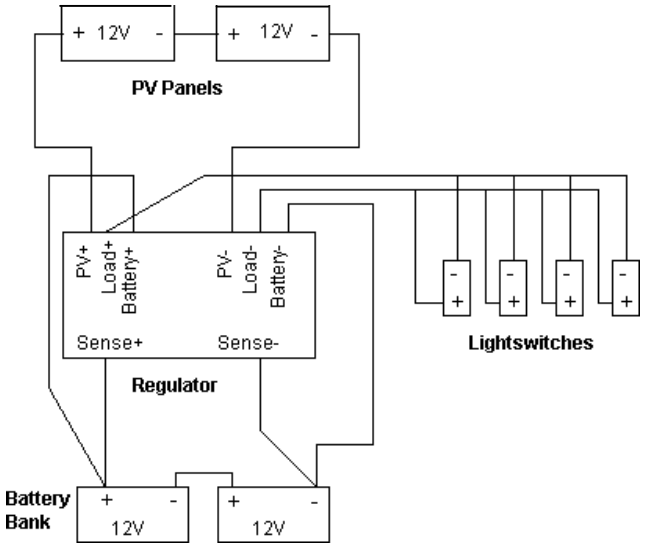

Fig. 1. Layout of 24 volt Remote PV System Installed in South Africa

Participants

There was a division of duties on the PV installation due to the number of students participating on the project. Participants consisted of high school and college students with and without technical background. Duties for the PV installation includes; PV panel wiring and assembly, PV panel frame assembly, pole cable mounting, ditch digging, batteries and distribution board assembly, installing and wiring the lights and pull switches and pole installation. However, everyone was able to move

between groups and participate in all aspects of the project.

Installation

The installation began at approximately 10:00 am and many unexpected obstacles were encountered during the installation.

No power was available in the village so a gasoline generator had to be brought to the site. The installation started with the wiring, assembling and mounting the solar panels. The panels were first connected to an aluminum alloy frame to hold the panels together. The aluminum alloy frame was used to prevent rusting and corrosion in the South African climate. Once the two 75-watt solar panels were firmly fitted to the frame, they were connected in series to produce voltage at 24-volts.

When the time came to dig the hole for the pole, several difficulties were encountered. The soil was extremely hard and dry. There was also a layer of rock approximately two feet into the ground. A pick ax was used to break the rock into pieces and the students were able to continue digging the three-foot hole. A trench was also dug to run the underground conduit to the house.

It was now time to install the interior portion of the PV system. Drilling holds in the wall proved to be very difficult because the house was constructed of earthen brick that break very easily. Three holes were drilled in the wall, one to bring in the electrical conduit and the other two were installed for the ventilation of the battery bank. All holes drilled into the wall had to pass completely through because the walls were made of mud.

Once the location of the battery bank was determined, the distribution board was mounted on the wall. At the same time, the pull switch light fixtures were installed in the three rooms inside the house and one on the outside porch. After the light fixtures were installed the solar panels and battery bank were connected to the distribution board.

This installation was completed in one day; a site orientation was conducted the previous day, with the input of students, staff and PE Technikon faculty and students. Individuals from ESKOM were on site and assisted in the installation as well. The installation ran very smoothly and was well organized. At the end of the day, the lights were finally tested under overcast skies. Apparently the batteries lost some of their charge and were below the cutoff level of the regulator and, therefore, the batteries could not supply power to the lights. However, since ESKOM will be primary caretakers of the system, PE Technikon is keeping in close contact with the utility to ensure a successful installation.

Phone Card Business

Upon a return visit to South Africa it was discovered that the home has been turned into a very profitable but necessary business. This village now has the opportunity to make contact with friends and family in the city by buying phone card and making phone call from the phone card business that was set up in this home because of the energy that is supplied by the PV system installed by students in TSU School of Technology renewable energy program.

References

[1] M. Hankins: "Small Solar Electric Systems for Africa" Motif Creative Arts Ltd., Nairobi, Kenya (1991)

[2] Harris, Miller, Thomas: "Solar Energy Systems Design" John Wiley and Sons Inc., (1985)

[3] PE Technikon: "Solar Training Manual" Port Elizabeth Technikon, (1997)

TSU Battery Free Solar Refrigerator Project

C. Chang
O. LaFleur

Texas Southern University School of Technology

3100 Cleburne Ave.
Houston, TX 77004

ABSTRACT

As the internship continues with Solus at NASA, the battery free solar refrigerator project at Texas Southern University School of Technology Research and Demonstration Laboratory continues to benefit with the transfer of knowledge from the manufacturer to the actual research project in the School's lab. In the Photovoltaic Lab, we are discovering that a good match exists between the available amount of solar energy and the solar refrigerator load demand on an annual basis. The battery free solar refrigerator appears to be performing well. However, new and better variable speed compressors will be on the market soon and this will allow for larger battery-free solar refrigerator and freezer designs.

Introduction

Currently there is a need for research to increase the efficiency of the solar cell and as some researchers fight to find solutions to this problem, others are searching to increase the storage capacity of batteries. The School of Technology's quest for research in this area has lead to a battery free solar refrigerator with NASA and a private company called Solus. The battery free solar refrigerator is manufactured by Solus and the School of Technology conducts the field test with funding from NASA.

Project Objective

The objective of the project is to test the battery free solar refrigerators in various locations under different settings and conditions to see if performance in the field will equal in house performance

Application

In many applications, 90 to 120 Watts of rated panel power is all you need. During cloudy weather, internal thermal storage keeps your product cold up to 7 days, even in a warm tropical climate. The four cubic feet cabinet uses a super quiet compressor and fan, which allows nearly silent operation. Indicator lights on the front of the refrigerator let you know the state of your thermal reserve.

What are the System Design Issues?

The refrigerator is designed to maintain cold temperature up to 7 days without sun. Ratio of thermal storage to refrigerator heat leak must be high for seven days. Compressor must perform 100% of daily cooling requirement in 4 hours (commercial as compared to residential designs). A solar powered vapor compression refrigeration system is made practicable with thermal storage and novel control techniques. In one embodiment, the refrigeration system includes a photovoltaic panel, a capacitor, a compressor, an insulated enclosure, and a thermal reservoir.

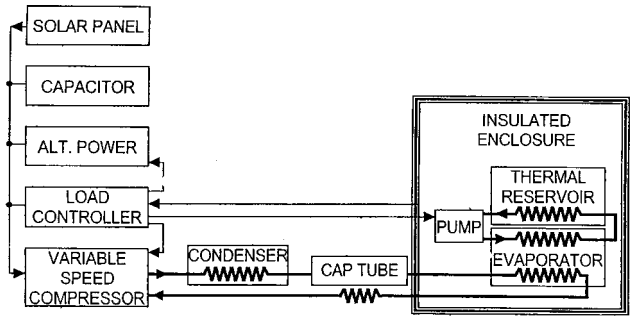

Fig. 1. Diagram of Battery Free Solar Refrigerator Operating System

How does it perform?

Figures two and three show the test result of the battery free solar refrigerator in the Photovoltaic Research and Demonstration Laboratory. The solar refrigerator ran for three (3) days at 30°F then the power was disconnected for two days during which time 8 warm cans of cokes were inserted. On the fourth day, the temperature raise to 50°F then dropped to 30°F in a few hours without any power support.

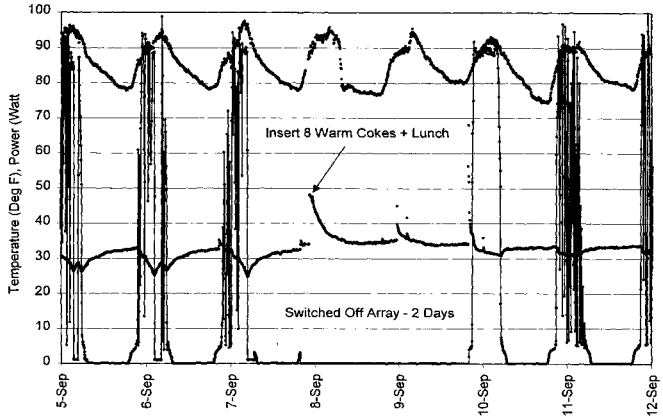

Fig. 2. Battery Free Solar Refrigerator Performance Chart

Collected Data (1999)

For the past few months, the battery free solar refrigerator has been on test in the solar lab. The chart in figure two is showing some test results of the solar refrigerator at Texas Southern University in the Photovoltaic Research and Demonstration Laboratory. The solar refrigerator was tested while running for 6 months from July 21 to December 8, 1999. The inside temperature of the refrigerator remained at an average of 30°F for all weather conditions for the six months period even though there were high variations of temperature change on the outside. At different times, the refrigerator was moved to the outside of the lab and left exposed to the naked sunlight.

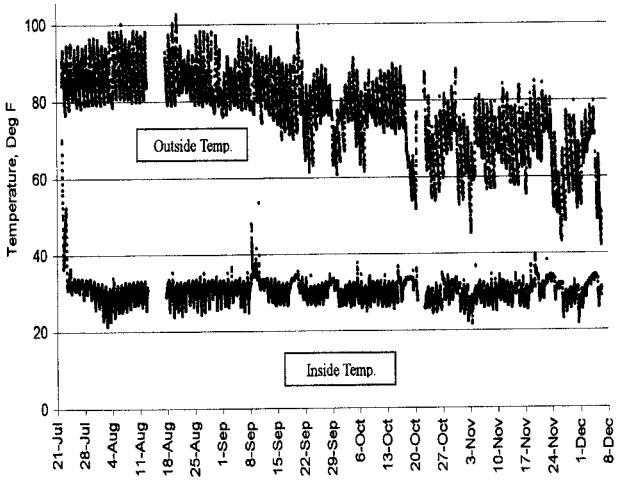

Fig. 3. Performance of Battery Free Solar Refrigerator during the Six Months Test at TSU

With this battery free solar refrigerator, we believe that there is no need to waste time maintaining and replacing heavy lead-acid batteries, when you could be enjoying the freedom of solar living with a battery-free refrigerator. Manufactured by Solus field tested by Texas Southern University School of Technology Photovoltaic Research and Demonstration Laboratory.

What are the Advantages of a Battery-Free Design?

Eliminating the battery saves money and time over the life of the refrigerator. If a standard solar refrigerator operates 15 to 20 years it will typically use 5-6 sets of batteries. These batteries represent a liability in terms of cost, time, and pollution potential.

Fig. 4. The Battery Free Solar Refrigerator on Test Outside the Photovoltaic Research and Demonstration Laboratory

The Solus battery-free solar refrigerator can provide years of zero maintenance off-grid refrigeration for your residential or commercial application. The Solus design provides true plug and play operation by eliminating the need for batteries and charge controllers. Simply wire your arrays to the unit and it begins cooling.

References

[1] D. Bergeron III. "Solar-Power Refrigeration System", NASA Case Number: MSC- 22970-1-SB.

[2] "Direct Current Compressor for 134a 12 V and 24 V", Danfoss Compressors 8 (1998) 1-7

The Historically Black Colleges and Universities Photovoltaic Research Associates Program at Clark Atlanta University

Gerald W. Grams, Kofi B. Bota, and Randal L. N. Mandock

Clark Atlanta University

223 James P. Brawley Drive, N. W.
Atlanta GA 30314

ABSTRACT

This program provides financial support and research opportunities for undergraduate students to enhance their knowledge in the field of photovoltaic research and to encourage them to pursue careers in photovoltaics. A primary goal of the research part of this program is to determine the effects of atmospheric variability on the production of solar energy by photovoltaic sources. Another goal is to provide our students with opportunities for obtaining a background in modeling and design optimization of solar cells. Other activities are underway to promote the use of photovoltaic technology for providing electric power to remote areas in developing countries.

1. General Introduction

By providing research opportunities and financial support for undergraduate students, the Clark Atlanta University (CAU) Historically Black Colleges and Universities (HBCU) Photovoltaic Research Associates Program enhances the students' knowledge in the field of photovoltaic research and encourages them to pursue careers in photovoltaics.

2. Atmospheric effects on production of solar energy

The goal of this project is to determine the effects of atmospheric variability on the production of solar energy by photovoltaic devices. A combination of solar radiation measurements, meteorological observations, and computer modeling work is being used to carry out an assessment of the efficiency of operation of photovoltaic modules under different atmospheric conditions. The CAU Earth System Science (ESS) program operates an Atmospheric Optics Observatory (AAO) on the roof of the Research Center for Science and Technology. The AAO provides a platform for instruments used to monitor the amount of solar energy reaching Earth's surface throughout the day. An Ascension Technology Rotating Shadowband Pyranometer (RSP) measures the global, direct, and diffuse radiation at the surface for visible wavelengths. In addition, a NOAA automated weather station operated at the AAO site provides meteorological data on atmospheric pressure, temperature, humidity, wind speed , and wind direction.

To improve our ability to interpret data obtained by the RSP and the meteorological instruments, we are developing a simple, inexpensive atmospheric haze sensor that uses an LED (light-emitting diode) as a narrow-band detector. Six different LED wavelengths are available, and data from such a device operated throughout the day at multiple wavelengths can be used to determine the fraction of incident solar energy that has been lost due to the presence of haze (aerosol particles) in the atmosphere. Successful operation of this device will improve our ability to model atmospheric effects on the solar resource.

Two students (Bryant Pierson and Akil Sutton, Physics majors from Morehouse College) began work on the development of the LED haze sensor during the summer of 1999. A working model was completed and preliminary measurements were obtained prior to the REAP (Renewable

Energy Academic Partnership) Conference sponsored by NREL and held at Southern University in Baton Rouge, LA, August 9 - 13, 1999. Both students attended the REAP conference and presented their results.

3. Modeling and Design Optimization of Solar Cells

This activity is being conducted as a collaborative project with Dr. Godfrey Augustine of the Northrop Grumman Science and Technology Center, who has a background in modeling and design optimization of Indium Phosphide solar cells. Dr. Augustine volunteered to mentor one of our students for the project - Mr. Robert Easley, a Physics and Mathematics major from Morehouse College, who began working with him during the Fall 1999 semester. A research effort has been initiated to carry out literature searches and to update an existing model for optimizing the design of InP solar cells for higher efficiency and greater radiation tolerance.

4. Solar power for remote areas in developing countries

Another goal of this project has been to promote the use of photovoltaic technology to provide electric power to remote areas in developing countries. Specific plans for activities to promote the use of photovoltaic energy in Ghana are being developed as part of this project.

5. Future Plans

Work is underway to optimize the performance of the LED haze sensors and to develop the computer software required for analysis of data. Our work on atmospheric effects on the production of solar energy will be incorporated into a summer project for an NSF-sponsored summer research program that will be conducted at CAU during Summer 2000. This project will involve ten undergraduate students from different universities working on various aspects of the problem of developing a model for the effects of aerosol particles and meteorological parameters on the amount of atmospheric radiation reaching Earth's surface. Computer models and databases that are being developed by our PV Associate students during the Spring 2000 semester will be used as part of this summer research program.

Work on the model for optimizing the performance of InP solar cells will continue. We purchased the PC1D computer program from the Photovoltaics Special Research Centre at the University of New South Wales in Sydney, Australia. This program solves the fully-coupled nonlinear equations for the quasi-one-dimensional transport of electrons and holes in crystalline semiconductor devices, with emphasis on photovoltaic devices. The program has been installed on a computer in our laboratory, and Mr. Easley will be working with the program under the guidance of Dr. Augustine to extend his previous research on photovoltaic devices.

Activities associated with our interest in promoting the use of photovoltaic technology for electric power for remote areas in developing countries such as Ghana are just beginning. The Ghana PV energy project will be developed as soon as a search for a qualified student is completed.

6. Conclusions

This program is designed to provide research opportunities for selected students at CAU and other schools associated with the Atlanta University Center to enhance their knowledge in the field of photovoltaic research and to encourage them to pursue careers in photovoltaics. Most of the plans to develop research activities for our students have been formulated, and their work has begun. As the work carried out by the students selected for this program continues, their research efforts are expected to attract the attention of other students who, in turn, may also be encouraged to pursue careers in photovoltaics.

Improved PV System Reliability Results from Surge Evaluations at Sandia National Laboratories

Russell H. Bonn and Sigifredo Gonzalez
Sandia National Laboratories
P.O. Box 5800, Albuquerque, NM 87185-0753

Abstract

Electrical surges on ac and dc inverter power wiring and diagnostic cables have the potential to shorten the lifetime of power electronics. These surges may be caused by either nearby lightning or capacitor switching transients. This paper contains a description of ongoing surge evaluations of PV power electronics and surge mitigation hardware at Sandia.

1. General Introduction

Direct lightning strikes are expected to cause extensive damage to PV equipment and are not the subject of this effort. However, electronics equipment can be hardened to the damaging effects of nearby lightning. Nearby lightning couples to wires through magnetic and electrical fields that are radiated and conducted from the area of a lightning strike. Surges due to nearby lightning are much more frequent than those from direct lightning strikes. Electrical surges that result from load transients, commutation notching, fault clearing, capacitor switching, and system faults can also adversely effect grid tied inverters.

At the request of inverter manufacturers, Sandia National Laboratories (SNL) has recently begun evaluating the response of PV inverters to such nearby surges. At this time most PV inverters do not have surge protection and there is evidence that electrical surges are reducing inverter reliability. Failures, in turn, result in increased repair cost and higher inverter cost. Additionally, the continued ability to avoid islanding after such surges is a utility requirement. Because of reports of field failures due to nearby lightning strikes, this effort is expected to improve the reliability of PV hardware as well as remove barriers to installation on US electric utility lines.

IEEE C62.41-1991 defines the source and frequency of potentially damaging surges and defines the standard surge testing waveforms. IEEE C62.45-1992 discusses the low-voltage equipment test conditions and test methodology in detail. It defines a location category C that includes inverters that are located outside and specifies test pulses with up to 10-kV charge voltages. Location category B (pulses up to 6 kV) includes the building service entrance and has been selected by SNL as the most appropriate location category for typical PV inverter evaluations. Location category B specifies test pulses with up to 6-kV charge voltages. The selection of 6 kV as a peak voltage for indoor systems results from the fact that conductors for indoor systems are spaced such that voltages greater than 6 kV will generally arc. Similarly the value of 10 kV for category C results from dimensions in outdoor wiring that would generally arc. Two pulses are described in the IEEE documents: (1) a .5 µs rise time -100 kHz ring wave (Figure 1), and (2) a 1.2 x 50 µs (rise time x pulse width) –8 x 20 µs combination wave (Figure 2). The combination waveform is a 1.2 x 50 µs voltage pulse into an open circuit and an 8 x 20 µs current pulse into a short circuit. The pulse shape and the charge voltage applied to capacitors inside the surge generator determine the energy in the applied pulse. Charge voltages for location B are variable up to 6 kV. Surviving these pulses does not ensure that an inverter would survive nearby lightning. In fact, the levels of the pulse are negotiable by the parties involved in the evaluations. Surviving the pulses does confirm a certain desirable level of hardening of the inverter.

2. Laboratory Test Capability

A Velonex Model 587 high voltage surge generator and a Velonex V-2734 isolation unit are used in the SNL evaluations. An additional 1.2 x 50 µs waveform is available to pulse high impedance circuits. If, as is typical, the inverter inputs have low impedance then the 8 x 20 µs pulse, defined for a short circuit, is the more severe stress. The respective source impedance of the three SNL waveforms are 9.2, 215, and 2.2 ohms.

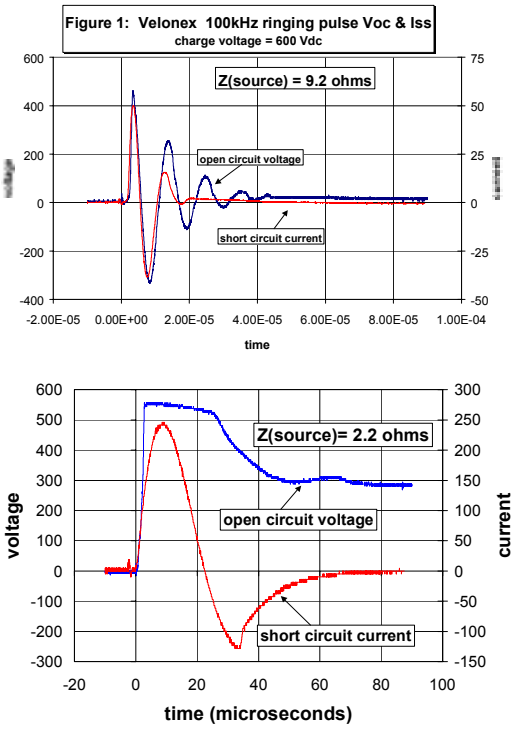

Test Philosophy: The test philosophy includes the following elements:

a. Incremental Application of Stress. Pulses result from the discharge of a surge generator capacitor through the impedance presented by the inverter. Thus the actual output voltage may differ significantly from the capacitor charge voltage. The initial charge voltage is chosen as 500 volts. Subsequently, to determine the level of hardness of the equipment under test (EUT), the charge voltage is

incremented in steps of 1000 Vdc from 1 to 6 kV. As the charge voltage is increased it is probable that a protecting device will suddenly be activated. This may result in less coupled energy at higher voltages than at lower voltages where the protective device is still inactive. Thus the EUT may prove to be more susceptible to a lower or intermediate voltage than to a higher voltage.

b. Dual Polarity Testing. Both negative and positive pulses are applied.

c. Repetitive Pulses. High voltage pulses can incrementally weaken components with no apparent damage after the initial pulse. Thus for an inverter which survives all voltage increments three pulses are applied at the highest charge voltage level. Repetitive pulses are at least one minute apart.

d. Unpowered Evaluations. When external power is provided to the EUT there is the potential for greater stress to components. Breakdowns due to surges can be exacerbated by the large amount of energy available from either the dc or ac lines. This extra current, supplied by the equipment under test, is referred to as "follow" current. Since the stress is lower in the unpowered EUT case, unpowered evaluations may be completed prior to powered up evaluations.

e. Powered Evaluations. Powered evaluations are necessary because of the likelihood of "follow" current and because of the need to evaluate the survivability of anti-islanding features of grid-tied inverters. Because of the possibility of latent damage to these critical circuits, an anti-islanding test should always be conducted after each significant voltage increase in a surge test. Filters are required between the EUT and other power sources to protect the power source and to present a high impedance to the surge.

f. Evaluation of Transfer Functions. A transfer function that defines the current that passes through the protection circuitry is useful for designers. Care must be taken to avoid significantly changing the circuit configuration or damaging instrumentation. This is accomplished by monitoring the signal with a current probe. The monitored wire is wrapped in mylar to prevent arcing and centered in the current probe, to minimize capacitive coupling. The signal from the current probe may be fed to a battery-operated oscilloscope and thus isolated from ground.

The transfer function also provides a means for detecting flashover or breakdown in the applied signal. Initially the signals are applied at low voltage where no possibility of flashover exists. As the charge voltage is increased, the coupled signal envelopes will be identical and will scale in magnitude unless a nonlinear effect occurs. Thus a change in the coupled signal envelope or a failure to scale linearly implies that a nonlinear event has occurred.

3. Evaluations of Surge Mitigation Devices

The evaluations of a typical metal-oxide varistor (MOV) and a silicon spark gap are presented below. Note that the ring wave, which has a faster rise time, rises to a higher voltage prior to being clamped. As the charge voltage is increased a higher amplitude of peak voltage is coupled past the MOV to potentially vulnerable electronics. This particular MOV was pulsed more than 12 times with no obvious degradation.

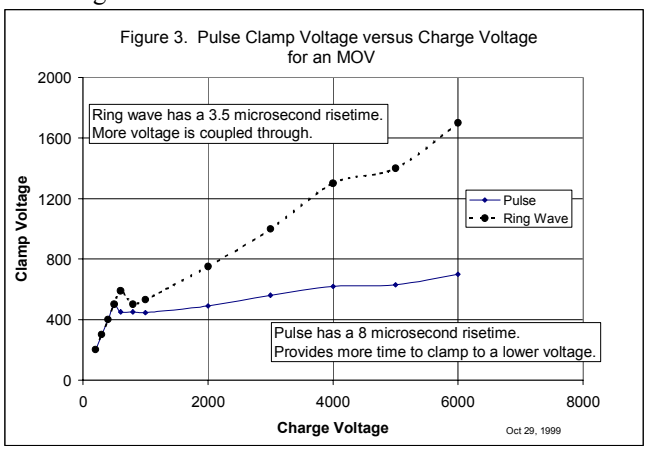

A Delta Model LA 302-RG was also evaluated. This unit has been used in many PV applications; it is not clear that the users understood its proper application. Delta's description defines the clamping voltage but does not define the initiation voltage. The initiation voltage, the voltage required to start an arc is usually much larger than the clamping voltage. The LA 302RG had no effect at surge voltages up to 6 kV. A physical examination of the arrestor revealed that it is a silicon-filled (sand) spark gap.

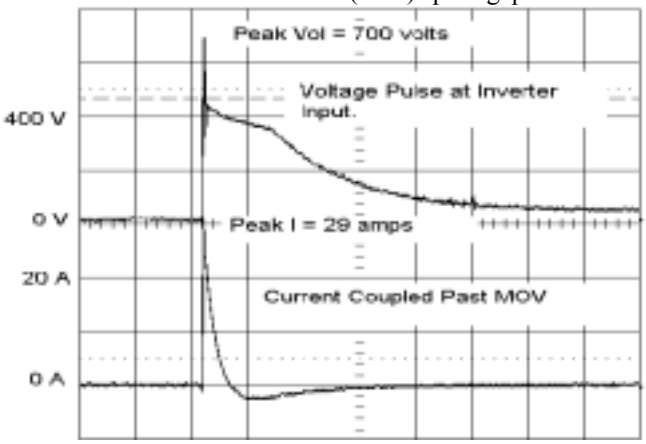

Figure 4. Test Data from the Omnion Inverter

This clamping effect is clearly seen in data from a pulse test of an Omnion inverter that uses an MOV. In Figure 4 the 6000 volt 8 x 50 μ second output of the surge generator is limited to a peak of 700 volts. This is quickly clamped to a voltage of about 400 volts. The current spike (current into the inverter) is limited to 29 amps peak and is of very short duration. The current is measured after the MOV and its shape is affected by other inverter components.

Conclusions

The surge testing of power electronics and surge protection devices at SNL will continue with emphasis on providing practical guidelines for manufactures and users.

References

[1] IEEE Std C62.41 91, IEEE Recommended Practice on Surge Voltages in Low-Voltage AC Power Circuits.

[2] IEEE Guide on Surge Testing for Equipment Connected to Low-Voltage AC Power Circuits.

PV Hybrid Battery Testing

Tom D. Hund
Sandia National Laboratories
PO Box 5800, Albuquerque, NM 87185-0753

ABSTRACT

A laboratory PV hybrid battery test procedure has been defined and tested at Sandia to evaluate and improve battery performance. Test results have identified several battery designs with improved performance. In addition, common battery management strategies have been shown to result in significant premature capacity loss in many cases. The test data has also been very useful in identifying hybrid battery management strategies that are more effective in maintaining battery capacity. The objective is to improve battery cycle-life and thus lower system life-cycle costs.

1. Introduction

PV hybrids represent a relatively large group of renewable energy power systems with multiple power sources that vary considerably with respect to system design, size, load characteristics, and possible battery management strategies. Previous laboratory and field test results at Sandia for stand-alone PV systems, using vented (flooded) and valve regulated lead-acid (VRLA) batteries, indicated that battery capacity can fade prematurely in PV systems [1,2]. This premature capacity loss stems primarily from an operational mode known as deficit-charge cycling. Deficit-charge cycling occurs when a discharged battery is not fully recharged after each discharge. This is a common occurrence that results from cost-reduction practices, themselves a result of the high cost of sizing the photovoltaic array to fully recharge the battery or the added engine generator runtime required to finish-charge the battery. The work presented here will attempt to identify the maximum deficit-charge interval time and charging requirements for specific lead-acid battery technologies used in PV hybrids.

2. Laboratory Test Procedure

The essential premise of the PV hybrid test procedure is that the battery cannot be fully charged every cycle. The questions that this test procedure attempts to answer are: 1) How often does the battery need a finish-charge to maintain capacity? 2) What charge parameters are needed to maintain capacity? 3) What PV hybrid controls are needed to maintain battery capacity? and 4) What battery is most appropriate for a given system design? The test parameters include; 1) charge and discharge rate, 2) bulk-charge termination voltage, 3) discharge termination voltage, 4) finish-charge regulation voltage, 5) finish-charge interval, 6) finish-charge time, and 7) number of deficit and finish-charge intervals required to obtain battery capacity trends.

The PV hybrid test procedure in this case makes an assumption about "typical" charge and discharge rates. It is important to understand that if system rates deviate significantly from the chosen rates, then the results may change. These rates are specified in hours required to charge or discharge the rated battery capacity. The charge and discharge currents are specified by the capacity (C) in amp-hours (Ah) divided by the required charge or discharge hours. In this case, a charge rate of C/24 and a discharge rate of C/35 were chosen to simulate a "typical" PV hybrid. If 60% of the battery capacity is discharged, then in theory, the battery would require 14.4-hr to charge and 21-hr to discharge every cycle. The resulting total cycle time would be about 1.5 days. The actual cycle time did vary due to changes in actual capacity and finish-charge time.

The other test parameters, such as voltage, were chosen based on the battery manufacturer's recommendations, previous battery test experience, and PV hybrid system design requirements. Below in Figure 1 is a typical PV hybrid cycle test profile with a 30-day deficit-charge interval showing battery voltage and cycle Ah. The test sequence includes 20-deficit-charge cycles discharging to 1.98 vpc and charging to 2.35 vpc with a 12-hr finish-charge at the end of 20-cycles. This sequence is repeated three times.

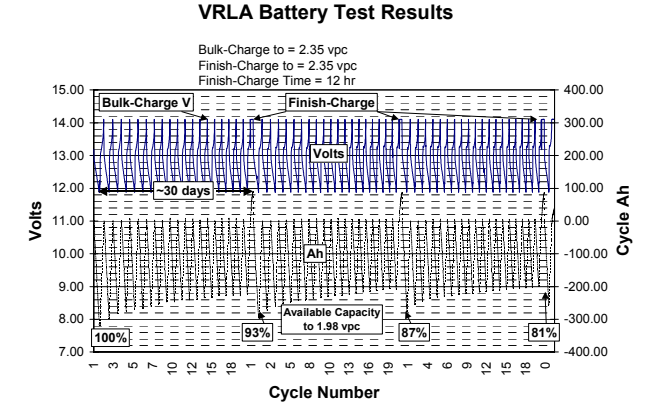

Fig. 1. PV Hybrid Battery Test Procedure

In this case the results clearly show that the available battery discharge capacity to 1.98 vpc after the finish-charge is dropping at a consistent rate of about 6 to 7% per deficit-charge interval (30-days). If the battery maintains this capacity loss rate, a 50% capacity loss would occur in 7 to 8 months. Modification of the test parameters would be indicated for this VRLA battery. Such modifications could include reducing the deficit-charge interval to 7-days and/or increasing the bulk termination voltage and finish-charge regulation voltage to 2.40 vpc. In either case the objective is

to maintain a stable battery capacity which implies a longer cycle-life.

3. Test Results

In Figure 2, the percent of initial capacity for the above VRLA battery is plotted as a function of the number of finish-charges. In the last three cases, a 12-, 6-, and 3-hr finish-charge was provided every cycle instead of every 5-, 10-,or 20-cycles. The battery capacity measured as percent of initial capacity for the last three cases is recorded at every 5th cycle as would be the case for the ~7-day deficit-charge interval test. The ~15-day deficit-charge interval measurement was made every 10th cycle after the finish-charge and discharge to 1.98 vpc.

The results demonstrate that deficit-charge intervals of ~7-days or less are required to maintain the capacity of this VRLA battery. If finish-charges are conducted every cycle, then a 3- to 6-hr finish-charge is required for the given test

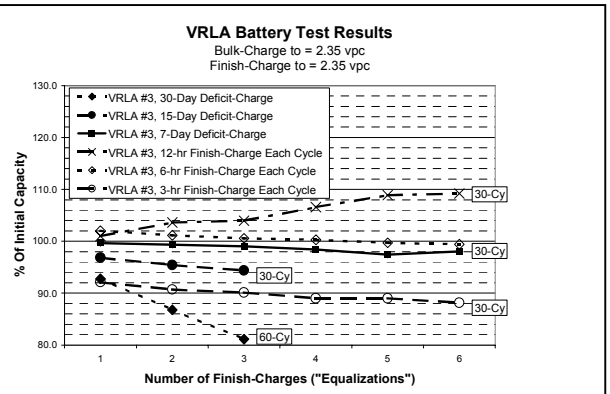

Fig. 2. PV Hybrid VRLA Battery Test Results

conditions vs the 12-hr finish-charge used in the deficit-charge cycle tests. This clearly indicates that longer deficit-charge intervals require a longer finish-charge time.

Test results from a vented industrial motive power deep-cycle battery, are in Figure 3, and show a much greater tolerance to deficit-charge cycling. A key factor in this

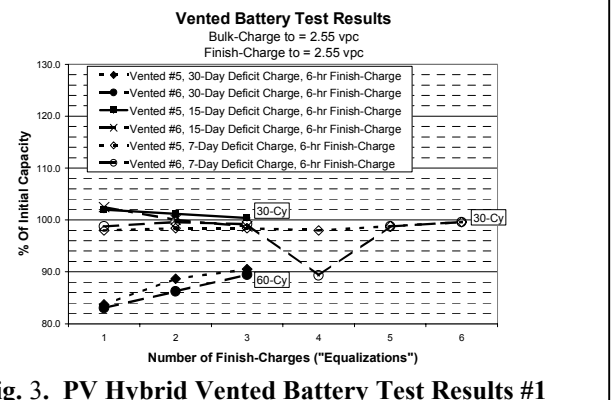

Fig. 3. PV Hybrid Vented Battery Test Results #1

battery's performance is the grid alloy content, positive plate active mass, bulk-charge termination voltage (2.55 vpc) and the finish-charge voltage and time (2.55 vpc, 6-hr). The bulk-charge termination voltage recovers the electrolyte from excessive stratification and the finish-charge voltage and time recovers the battery from sulfation and other degradation mechanisms in the grid and positive active mass [1].

In Figure 4 are other test results from a popular PV hybrid vented deep-cycle battery. The results show that deficit-charge intervals of ~7-days will result in a continued loss of battery capacity. If capacity loss continues, this vented deep-cycle battery would be at 50% of its initial capacity in about 4.5 to 5.0-months. This battery would probably not be the best choice for a PV hybrid system.

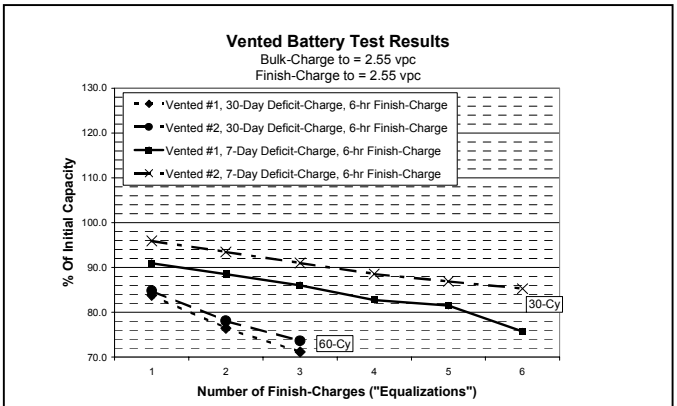

Fig. 4. PV Hybrid Vented Battery Test Results #2

4. Summary

The questions of how often does a PV hybrid battery need to be finish-charged or "equalized", and what regulation voltages should be used and/or which battery is most appropriate for PV hybrids can be answered by this test. The answer to the above questions based on the test results is dependent on the battery and how that battery is used. Since different lead-acid batteries and different system designs may require different voltages for charging, the system should have adjustable voltages and time setpoints. In addition, the system must provide a means to finish-charge or "equalize" the battery at regular intervals based on battery and system design requirements.

In some cases the net affect of using appropriate battery technology and the necessary battery controls may increase system capital costs. This possible increase in capital costs should be offset by lower life-cycle costs resulting from a significant increase in battery cycle-life and the resulting lower system repair costs.

REFERENCES

[1] T. Hund: "Capacity Loss In PV Batteries And Recovery Procedures", Sandia National Laboratories PV Web site, http://www.sandia.gov/pv/bos/batteries.htm (1999).

[2] T. Hund: "Test Results From The PV Battery Cycle-Life Test Procedure", Sandia National Laboratories PV Web site, http://www.sandia.gov/pv/bos/batteries.htm (1999).

A Database Prototype Has Been Developed to Help Understand Costs in Photovoltaic Systems

Larry M. Moore

Sandia National Laboratories

Abstract

High photovoltaic (PV) system costs hinder market growth. An approach to studying these costs has been developed using a database containing system, component and maintenance information. This data, which is both technical and non-technical in nature, is to be used to identify trends related to costs. A pilot database exists at this time and work is continuing. The results of this work may be used by the data owners to improve their operations with the goal of sharing non-attributable information with the public and industry at large.

The published objectives of the DOE PV program are to accelerate the development of PV as a national and global energy option, as well as ensure U.S. technology and global market leadership. Our approach to supporting these objectives is to understand what drives costs in PV applications. This paper and poster session describe work-in-progress in the form of a database that will help identify costs in PV systems.

In an effort to address DOE's Five-Year PV Milestones, a program was established in the summer of 1999 to study system costs in three PV applications - solar home lighting, water pumping, and grid-tied systems. This work began with a RFQ requesting data from these types of systems. Creating a partnership with industry and other system organizations such as Non-Government Organizations (NGOs) was the approach chosen to maintain a close tie to the systems in the field. Nine participants were selected as partners, who provided data on their systems. Two activities are emphasized in this work. For the first, an iterative approach of developing baseline reliability[1] and costs information with the participants was taken. This effort led to identifying typical components in these systems as well as the specific data (metrics) that would be needed in any analysis used to understand total systems costs. This data came to be defined in terms of system characteristics and component attributes in addition to how and why the system failed. The second major effort, which is still in progress, is the creation of a relational database for storage, review and analysis of this data. A database model was created using the following database requirements as a framework for present and future use:

- Modular structure to support future additions
- Each System has one owner
- Make simple associations at the component level
- Allow multiple components to be tracked with a system
- Allow multiple failures to be documented as a result of a maintenance visit

and future additions are expected to be:

- New applications and/or components
- Inspections to be documented for a system
- Owner may be associated with more than one system
- System may be associated with more than one owner
- Track history of specific system
- Spanish language version

The cost drivers in these systems are technical as well as non-technical in nature. Technical

[1] Here reliability is used in a 'soft' interpretation of the definition. The initial analysis is expected to provide trend information and set in place efforts to provide more accurate information for future studies.

costs include system design, installation, maintenance and component design. Was the system well-designed given state-of-the-art practices for this application? Anecdotal stories circulate describing installations by the inexperienced. Can these problems be identified using available data? Maintenance includes the results of not maintaining a system as well as providing incorrect care. In addition, fielded systems show some components perform better than others. Can quantitative support for this experience be developed? A substantial effort was taken to define categories of how a system failed. This work relied on the experience of the nine participants in the study with the realization that these definitions and categories will evolve as our experience with the data increases. The non-technical issues are sometimes described as institutional in nature. In some applications such as solar home lighting, experience has shown these issues can dominate system costs. Education, training, usage patterns, gender and customs create a collection of problems that can sometimes overwhelm the technical aspects of fielding the PV system.

At this time a minimum set of metrics is being used in the analysis to identify trends in the data. This data can be summarized as follows:

- System Identification
- System Installation Date
- Date System Failed and Repaired
- Costs (labor, parts, travel)
- Failure Mode
  - What failed?
  - Why did the failure occur?

The most complete data sets are being used at this time in the pilot data analysis. Initial discussions with the data owner(s) have provided a guide to focus the early analysis efforts. As development of the analysis routines proceeds the iterative process of sharing information with the data owners will focus the evolving charts and tables that identify the information needed to understand the costs in these systems. The eventual goal will be to combine information from various applications and provide public information that will help the PV community and yet protect the proprietary interests of all who participate in the project.

A collection of lessons-learned has emerged from the work-in-progress. This experience is non-technical in nature at this time and reflects the difficulty in establishing a useful database. The lessons-learned can be summarized as follows:

- Customer understanding of their systems and feedback are critical to helping minimize system maintenance
- Data collection is sometimes very difficult-simple worksheets are best because they are used
- Attention to non-technical issues may be important to cost reduction
- Small data sets exist at this time for some partners-there is general interest in developing this information for future collaboration
- Ability to track system history is believed to be valuable for tracking cost contributions
- Additional up-front planning for data collection and sharing reduces effort of translating data for entry into database. Translating data from owner for input to database is tedious and time consuming.

In summary, reducing costs can accelerate the market expansion of PV systems. An approach to studying these costs has been developed using a database containing system, component and maintenance information. This data, which is both technical and non-technical in nature, is to be used to identify trends that help understand costs in the systems. A pilot database exists at this time and work is continuing. The results will be available to data owners to improve their operations with the goal of sharing non-attributable information to the public and industry at large.

Development of an Accelerated Weathering Protocol using Weatherometers for Reliability Study of Minimodules and Encapsulation Materials

F. J. Pern

Engineering and Reliability Division, National Center for Photovoltaics,
National Renewable Energy Laboratory, 1617 Cole Blvd., Golden, CO 80401

ABSTRACT

This paper is condensed from a full report [1] that describes the needs, reasoning, approaches, and technical details to establish a practical accelerated weathering test (AWT) protocol for indoor testing of the photothermal stability of encapsulation materials and encapsulated solar cells and minimodules. Essentially the AWT Protocol resembles ASTM methods and is designed solely to better utilize the capabilities of user-programmable systems such as the Atlas Model Ci4000 weatherometers (WOMs). The important part of the Protocol is on determining the parameters of the test cycles, total radiant exposure, and exposing duration.

1. The Need for an AWT Protocol

Strict requirements on the long-term weathering durability of all component materials and assembly integrity are necessary for PV modules to achieve a desired 30-year service life. Weathering-induced degradations of the ethylene-vinyl acetate (EVA) encapsulants, metallic components, and delamination have been observed for modules in the field and laboratories. The degradations resulted in performance loss and/or premature module failure [2,3]. Testing PV modules outdoors under natural weathering for 20-30 years is obviously impractical if one wants to determine and improve material stability in a span (life cycle) of 1-3 years. Thus, a practical and dependable test method that can *accelerate* the test conditions in a realistic manner over a reasonably short period of time is clearly needed. As shown in **Table 1**, only a few ASTM and one IEEE test standards are available for testing PV modules. AWT with exposure to (UV) light greater than 1 sun is clearly absent. A qualification test of PV modules in the IEEE 1262 specifying a 54 MJ/m^2 of UV exposure will most likely not qualify the modules and their comprising materials to be immune from long-term UV-induced degradation. The 54 MJ/m^2 can be accumulated in ~2 months outdoors or ~150 hours in a WOM using a Xe light intensity of 100 W/m^2 (300-400 nm broadband), which will hardly result in any observable physical or chemical changes on the presently existing module component (other than a-Si cells). Hence, the criterion of UV radiant exposure (e.g., total accumulated UV dose) is better established on the basis of actually known physical and/or chemical facts.

2. Weatherometer Systems and Capabilities

In this work we used two user-programmable Atlas Model Ci4000 WOMs. The systems use a water-cooled Xe arc lamp rated at 6500 W with a typical lamp life of 2000 h. Pre-aged type-S borosilicate inner and outer filters are selected for a light emission spectrum that best simulates the solar spectrum. The light intensity can be monitored and feedback-controlled by either a 340-nm narrow band filter or a 300-400 nm broad band filter. Development of the AWT Protocol involved determining the test conditions of variable parameters in light intensity, chamber dry bulb temperature (DBT), black panel temperature (BPT), relative humidity (RH), specimen spray (front side, to simulate rain), number of segments, and test duration control.

3. Samples, Sample Configurations, and Analytical Characterization

Encapsulated minimodules (and laminated encapsulation materials) are used as a miniaturized model of large-size PV modules. This allows the component materials in any type of PV module to be tested in an integrated, functional format. The sample configuration is designed in such a way that it permits independent spectroscopic characterization of the encapsulant and electrical characterization of the solar cell [3].

4. Development of the AWT Protocol

The following briefly summarizes the approaches and procedures to establish the AWT Protocol. Detailed reasonings and descriptions are given in ref. [1].

Step 1: Compiled 12 years of climatological data, provided by South Florida Test Center, for the hot-humid Miami, FL, and hot-dry Arizona areas. Derived the averaged values of radiant exposures and rain periods for each climate region.
Step 2: Compiled the most relevant test standards including the few existing for PV modules (Table 1), and compared the test conditions of those standards.
Step 3: Determined the WOM-deliverable operating parameters on light intensity, BPT, chamber DBT, RH%, light/dark cycles, specimen spray, segment time, etc. under different lamp operating wattage.
Step 4: Determined the physical/chemical reference from previous experiment results the approximate times required for EVA films to discolor, for example, by a net change of yellowness index of 4–4.5.
Step 5: Measured and determined the integrated UV intensity and the equivalent UV-suns in the 300-400 nm range of the Xe lamp emission spectra at different operating wattage.

Step 6: Determined from Steps 4 and 5 the approximate radiant exposures needed for A9918 and 15295 EVA discoloration. A total radiance of ~675 MJ/m^2 was obtained for a light yellow-brown EVA A9918 exposed to a solar simulator at a BPT of ~45^{o}C.

Step 7: Compared the 675 MJ/m^2 in Step 6 to the UV-test set points described in test standards.

Step 8: Determined the daily radiant exposure and light cycle time comparable to the average daily UV radiance from the EMMAQUA systems operated in Arizona. Obtained an acceleration factor of ~5.7 for UV exposure alone. Calculated the total daily spray time and compared the result to the average daily rain time in Miami. Spray in the middle of a light cycle is to simulate rain and to induce a thermal shock. A 120-min "specimen spray time" was obtained versus a 72-min "rain time" per day.

Step 9: Determined the number of light/dark segments per cycle, specimen spray time, BPT, and chamber DBT for each light and dark segment. A BPT of 85^o-90^{o}C in the light cycle is about 20^o-30^{o}C higher than the typical operating temperatures of crystalline-Si PV modules on racks or on rooftops.

Step 10: Established and revised the AWT Protocol parameters per test results. After a number of test-runs and recent system hardware and software upgrades, the working AWT Protocol has been revised several times as following:

- Irradiance monitored and controlled at I(300-400 nm) = 125 W/m^2; corresponding I(340 nm) ~1.05 W/m2.
- Xe lamp operating power ~6.07 kW (safe under the nominal rating of 6.5 kW maximum).
- BPT Control: active (BST control inactive).
- Chamber DBT Control: active.
- Test Duration Control: by desired radiant exposure.
- Five Test Segment Parameters:
  1. Light, 125 W/m^2, 1.385 MJ/m^2 (~185 min), BPT = 85^{o}C, DBT = 65^{o}C, RH = 35%, Spray Off
  2. Light, 125 W/m^2, 150 KJ/m^2 (~20 min), BPT = 55^{o}C, DBT = 60^{o}C, RH = 50%, Spray On
  3. Light, 125 W/m^2, 1.385 MJ/m^2 (~185 min), BPT = 85^{o}C, DBT = 65^{o}C, RH = 35%, Spray Off
  4. Dark, 70 min, BPT = 40^{o}C, DBT = 40^{o}C, RH = 85%, Spray Off
  5. Dark, 20 min, BPT = 40^{o}C, DBT = 40^{o}C, RH = 95%, Spray On
  6. Three cycles per every 24 hours

5. Conclusions

A practical AWT Protocol has been established on the basis of numerous instrumental testing and observations. The radiant exposures for the overall test duration are established using the extent of actual EVA discoloration as a criterion rather than from an arbitrarily chosen number. The AWT Protocol is presently employed to test samples of a matrix experiment. The results will be compared with the previous tests using UV solar simulators. Test duration (of radiant exposures) may be adjusted because the AWT Protocol combines high BPT in the light cycle, low and high RH%, periodic specimen spray, and light/dark cycles. All of these were not available in previous AET experiments using solar simulators.

ACKNOWLEDGEMENT

The author wants to thank S. Glick, who was instrumental in setting up the two Ci4000 WOM systems and making them operational, for his assistance in this work. This work was performed at NCPV, NREL under U.S. Department of Energy Contract No. DE-AC36-99-G010337.

REFERENCES

[1] F.J. Pern, "Accelerated Weathering Test (AWT) Protocol for PV Module Encapsulation Materials and Encapsulated Solar Cells," a task milestone report for Task PV80.6201, NREL, June 1998.

[2] A.W. Czanderna and F.J. Pern, "Encapsulation of PV Modules using Ethylene-Vinyl Acetate Copolymer as a Pottant: A Critical review," *Solar Energy Materials and Solar Cells*, 43 (1996) 101-183.

[3] F.J. Pern and S.H. Glick, "Photothermal Stability of Encapsulated Si Solar Cells and Encapsulation Materials upon Accelerated Exposures, *Solar Energy Materials and Solar Cells*, 61 (2000) 153-188.

Table 1. A List of Some Standard Test Methods and Practices for PV Cells and Modules

Standard No.	Title Description of Standard
ASTM E1038-93	Test method for determining resistance of PV modules to hail by impact with propelled ice balls
ASTM E1171-93	Test method for PV modules in cyclic temperature and humidity environments
ASTM E1462-95	Test method for insulation integrity and ground path continuity of PV modules
ASTM E1524-93	Test method for saltwater immersion and corrosion testing of PV modules for marine environments
ASTM E1596-94	Test methods for solar radiation weathering of PV modules
ASTM E1597-94	Test method for saltwater pressure immersion and temperature testing of PV modules for marine environments
ASTM E1799-96	Practice for visual inspection of PV modules
ASTM E1802-96	Test methods for wet insulation integrity testing of PV modules
IEEE 1262-95	Recommended practice for qualification of PV modules (with short UV conditioning; under revision)
NREL	Interim qualification test procedures for thin film PV modules (similar to ASTM E1171)

Effects of Accelerated Exposure Testing (AET) Conditions on Performance Degradation of Solar Cells and Encapsulants

S. H. Glick and F. J. Pern

National Center for Photovoltaics, Engineering and Reliability Division
National Renewable Energy Laboratory, 1617 Cole Boulevard, Golden, CO 80401

ABSTRACT

This paper briefly summarizes the results from several accelerated exposure tests (AET) studies. A range of light intensities (~1.2 to 9 UV suns) and heating at different black panel temperatures (BPT, 65° to 145°C) were used to evaluate optical and electrical materials performance and photothermal stability of laminated photovoltaic (PV) cells of various configurations. The results show that optical changes (transmittance (%T), and yellowness index (YI)) of encapsulants were strongly affected by the AET conditions. In contrast, irregular changes in I-V parameters (J_{sc}, J_{max}, V_{oc}, V_{max}, fill factor (FF), and efficiency) of solar cells were observed, which could not be fully attributed to observed optical changes in transmittance (%T) or yellow-browning of superstrate/pottant materials. Causes responsible for the photothermal instability of the encapsulated Si solar cells appear to be multiple and complex.

1. Introduction

The long-term objective of achieving a 30-year service life for PV systems compels application of reliable and durable materials-systems for current PV technologies in order to realize a clean, economically competitive, reliable, and efficient power delivery alternative. Attaining increased module performance, reliability, and durability in an effective, timely manner predicates use of accelerated test methods to help identify and quantify the complex degradation mechanisms. In this study, we employed various AET conditions to evaluate performance stability of solar cells and encapsulation materials.

2. Experimental

Several sample sets were studied for changes before, during, and after various AET exposures. Sample configurations incorporating most features found in typical c-Si PV modules are given in Table 1 and reference [1]. Details of analytical methods are described in [1]. The values in Table 1 are calculated changing rates of electrical and optical parameters per exposure hour. This allows direct comparison with an assumption that the changes are linear, upon completion of AETs.

3. Results and Discussion

Optical Changes of Superstrate/Encapsulant Layer

As seen in Table 1, applied AET conditions strongly affect encapsulant discoloration rates and %T changes in the samples. Following AET, all encapsulant samples typically show a net %T loss in the UV-visible (290-800 nm) range. Ethylene-vinyl acetate (EVA) discoloration rates resulting from AET with ultraviolet (UV) light and heat are generally faster and greater than the rates of samples heated in a dark oven. Discoloration rates of EVA typically depend on the formulation. For example, the regular-cure A9918 discolors to a greater extent than fast-cure 15295 EVA; the latter to a greater extent than NREL-V11 EVA [1]. No discoloration of EVA pottants was observed on the samples that are laminated with stable polymer films such as Tefzel or Tedlar that are permeable to oxygen and permit photobleaching [1]. Instead, the polymer/EVA laminates produced small increases in %T at wavelengths in the UV-region, due to photodepletion of UV absorbers if used in the EVA formulation. When an opaque white substrate layer, such as Tedlar/polyester/Tedlar (TPT), was used, then following AET, a low level of TPT discoloration contributed to the total %T and YI changes observed. Furthermore, light reflection from the white TPT layer enhanced the measured solar cell efficiency.

Electrical Changes of Encapsulated Solar Cells

Although %T loss is generally seen for the glass superstrate laminated EVA upon AET treatments, few changes in the solar-cell I-V parameters were observed which were logically consistent with the %T losses alone. Based on the measurement uncertainty of ~2%, which were established using a working reference solar cell, the measured I-V parameters and calculated changing rates resulting from AET treatments appear to be irregular as indicated in Table 1. The values of V_{oc} for all cell samples did not show significant changes and thus are not shown here. Only those samples with substantial EVA browning would clearly show a corresponding efficiency loss. For example, samples (ECIS-09, 18) subjected to ~9 UV suns at 145°C exhibited a %T loss rate of 4.07-4.66 x 10^{-2}/h with a corresponding, but not proportional, 1.80-2.90 x 10^{-2}/h loss rate in efficiency. Similar results are obtained for the c-Si solar cell samples exposed to ~6.5 UV suns at 65°C and heated in a 105°C oven. In contrast, several of the cell samples exposed to 7.5 UV suns at 85°C (ECIS-06, 22), 1.2 UV suns at 65°-85°C (ECIS-04, 17), and heating at 85°C (ECIS-07, 19) show an increase in J_{sc} and efficiency, while their %T shows net losses. Interestingly, most of these cells exhibit a net loss rate in FF. Other samples show a mix of either an increase or decrease in efficiency and FF with a net %T loss. A particular case was observed for Tedlar/silicone/Tedlar-laminated c-Si solar cells (e.g., D1-2 and D2-1)

exposed to a 1.2 UV suns at 60°-65°C. The cells showed a net %T gain rate of 4.22 and 5.66 x 10^{-3}/h due to photobleaching of the silicone thin layers, but a net loss rate of 1.34 and 2.39 x 10^{-2}/h in efficiency, respectively. This was tentatively attributed to a yet-unidentified chemical attack on cell contacts by photodecomposition compounds from silicone upon AET exposure [1].

To separate electrical (I-V) change of the solar cells from optical change of the encapsulant, NREL-developed V11 EVA was used for its greatly improved photothermal stability against discoloration [1]. Even so, the cells (BP-C4 and HT-C1) still show a net loss in J_{sc}, FF, and efficiency while the %T loss rates are low. More details are described in references [1] and [2].

4. Conclusions

Optical properties for layered superstrate/encapsulant were shown to typically decrease upon AET treatments, except for those with a polymer superstrate or substrate that allows photobleaching of the encapsulant. Changes in solar cell performance are found to be irregular. The irregularity appears to be independent of the AET conditions and optical changes. Transmission losses alone are insufficient to explain all the observed electrical performance losses. Causes responsible for photothermal instability of the encapsulated Si solar cells in this study appear to be multiple and complex. To provide a cohesive explanation of the irregular changes in solar cell I-V performance, more detailed studies and analysis of electrical degradation mechanisms are required.

ACKNOWLEDGEMENTS

The authors thank J. Raaff, D. Tomek, and G. Watson for assistance in performing the work. B. von Roedern of NREL is thanked for the partial support of the technicians through a CRADA fund. The work was performed at NREL under U.S. Dept. of Energy Contract No. DE-AC36-99-G010337.

REFERENCES

[1] F. J. Pern and S. H. Glick, "Photothermal Stability of Encapsulated Si Solar Cells and Encapsulation Materials upon Accelerated Exposure", Solar Energy Materials and Solar Cells, 61 (2000) 153-188.

[2] F. J. Pern and S. H. Glick, "Photothermal Stability of Encapsulated Si Solar Cells and Encapsulation Materials upon Accelerated Exposure - II", short and review abstracts submitted to 28th IEEE PVSC.

Table 1. Changing Rates of Electrical and Optical Parameters for Some Encapsulated c-Si Cells upon AET Treatments

	Measurement Uncertainty (±%):			2.35	1.11	1.75	0.63	4.79 [1]
	Standard Deviation/Average (%):			1.87	0.66	1.39	0.35	3.23 [1]
Sample ID	**Super-strate**	**Pottant Type**	**Substrate**	**Δ J_{sc} (mA/cm^2-h)**	**Δ FF (%/h)**	**Δ Eff. (%/h)**	**Δ %T (%T/h)**	**Δ YI (YI/h)**
AET Condition: 0.0 UV Sun (Oven) at BPT = 85°C (Glass = 3.175-mm (1/8-in.) thick borosilicate plate)								
ECIS-03	Glass	15295P	Glass	-1.82E-3	-1.29E-3	-3.40E-3	-4.55E-4	6.47E-4
ECIS-07	Glass	15295P	Glass	9.62E-3	-4.61E-3	4.36E-3	-1.83E-3	4.59E-4
ECIS-19	Glass	A9918P	Glass	7.14E-3	2.16E-4	7.44E-3	-8.22E-4	2.08E-4
AET Condition: 0.0 UV Sun (Oven) at BPT = 105°C (TPT = opaque white Tedlar/Polyester/Tedlar trilaminate)								
HT2-A1	Glass	15295	TPT	-2.57E-3	-2.76E-3	-4.21E-3	-1.23E-3	2.82E-3
HT2-B1	Glass	15295	Glass	-1.14E-3	-4.36E-3	-5.30E-3	-1.59E-3	4.50E-4
HT2-C1	Glass	NREL-V11	TPT	-1.48E-3	-6.35E-3	-7.65E-3	-2.09E-3	2.67E-3
AET Condition: ~1.2 UV Suns at BPT = 60°-65°C								
ECIS-04	Glass	15295P	Glass	9.87E-3	-1.06E-3	8.58E-3	-1.26E-3	-1.41E-5
ECIS-16	Glass	A9918P	Glass	5.50E-3	-1.72E-2	-1.37E-2	-7.51E-4	3.87E-4
A2-2	Tedlar	EVA	Tedlar	7.74E-3	-1.09E-3	6.06E-3	9.26E-4	-
D1-2	Tefzel	Silicone	Tefzel	-1.91E-2	8.33E-3	-1.34E-2	5.56E-3	-
D2-1	Tefzel	Silicone	Tefzel	-2.02E-2	-4.59E-3	-2.39E-2	4.22E-3	-
AET Condition: ~1.2 UV Suns at BPT = 80°-85°C								
ECIS-05	Glass	15295P	Glass	1.12E-2	-2.67E-3	7.86E-3	-9.53E-4	3.17E-4
ECIS-17	Glass	A9918P	Glass	4.98E-3	-2.72E-3	1.29E-3	-1.87E-3	1.86E-3
AET Condition: ~6.5 UV Suns at BPT = 65°C								
BP-A4	Glass	15295P	TPT	-5.88E-3	-1.42E-3	-7.70E-3	-4.22E-3	2.23E-3
BP-B4	Glass	15295P	Glass	-3.95E-3	-1.42E-3	-4.99E-3	-3.29E-3	1.69E-3
BP-C4	Glass	NREL-V11	TPT	-2.90E-3	-4.82E-3	-7.85E-3	-2.07E-3	1.62E-3
BP-D4	Glass	A9918P	TPT	-4.99E-3	-1.22E-3	-6.50E-3	-1.08E-2	2.05E-2
AET Condition: ~7.5 UV Suns at BPT = 85°C								
ECIS-06	Glass	15295P	Glass	7.51E-3	-5.30E-4	6.82E-3	-2.05E-2	3.15E-2
ECIS-22	Glass	A9918P	Glass	3.34E-3	4.29E-3	4.41E-3	-1.07E-2	2.17E-2
AET Condition: ~9.0 UV Suns at BPT = 145°C								
ECIS-09	Glass	15295P	Glass	-1.49E-2	-2.68E-3	-1.80E-2	-4.66E-2	5.66E-2
ECIS-18	Glass	A9918P	Glass	-2.83E-2	1.88E-3	-2.90E-2	-4.07E-2	4.80E-2

Forward-Biased Thermal Cycling: A New Module Qualification Test

C.R. Osterwald, J. Pruett, S. Rummel, A. Anderberg, and L. Ottoson

National Renewable Energy Laboratory

1617 Cole Boulevard
Golden CO 80401

ABSTRACT

Following a proposal by BP Solarex to modify the standard module qualification sequence, we performed forward-biased thermal cycling on three types of commercial modules to evaluate the procedure. The total number of thermal cycles was doubled to 400 and maximum power measurements were made every 50 cycles. During this test, we discovered several technical pitfalls that should be avoided. The results showed that current commercial modules are able to pass this proposed modification.

1. Introduction

Silicon modules deployed outdoors in systems are known to exhibit slow fill-factor degradation on the order of 1% per year. This has been attributed to gradual increase in series resistance associated with solder bonds [1]. In an attempt to test for susceptibility to such degradation, BP Solarex has proposed that a forward-bias current equivalent to the current at the maximum power point under 1-sun conditions be passed through modules during the thermal cycling portions of the standard qualification sequence [2].

The standard thermal cycling test consists of either 50 or 200 cycles (depending the sequence) of -40°C to +90°C module temperature excursions in 4- to 6-h cycles, with the test modules open-circuited [3]. Because modules in use have current flowing through them during daily temperature excursions, it was thought that a current bias during thermal cycling would simulate this degradation. We have therefore attempted to evaluate this procedure by performing biased thermal cycling on several types of commercial modules.

2. Test Design

We decided to evaluate biased thermal cycling by performing the test on three models of medium-power commercial modules. The models chosen were the Siemens Solar M55 Si, the ASE Americas 50-AL Si, and the USSC US-32 a-Si. In order to exaggerate the effects of the test, we chose to extend the test to 400 cycles total (this is double the number of the standard test), while stopping the test every 50 cycles to measure the performance. Rather than compare the effects against untested control modules, we compared them against modules that were thermal cycled at the same time, but were left open-circuited. The modules were cycled in a BMA Corp. 81-cu. ft. environmental chamber. Forward biasing was done with Kepco bipolar power supplies-amplifiers, operated in the current mode. Current-voltage (I-V) measurements were done using a Spire Corp. model 240A solar simulator at standard reporting conditions (25°C, 1000 W/m^2 global irradiance).

3. Technical Issues

The test program immediately showed a number of issues that must be dealt with if current biasing is to be included in the standard qualification test. First, the current biasing dissipates power that results in heating of the modules. Even though E 1171 specifies the temperature profile in terms of the actual module temperature, this heating makes it difficult to reach the -40°C low point of the cycle. We found that the temperature could be 6° to 8°C higher than the unbiased modules. Because of this, it is recommended that the biasing be turned off when the temperature is less than 0°C. The heating also affects the +90°C high point, although to a lesser amount (we noted a 2° to 4°C difference between the biased and unbiased modules). It is therefore important to measure the actual module temperatures and adjust the programming of the environmental chamber controls so that the correct profile is obtained.

Second, the dark current-voltage characteristics of a-Si modules changes greatly between -40°C and +90°C. In this test, the changes were so large that the power supply was unable to provide the correct amount of current to the USSC module during the low temperature excursion and changed over to voltage limit mode. This resulted in a much smaller amount of forward-bias current through the module. Fortunately, this issue can also be resolved by simply turning off the bias current during the low temperature portion of the cycle.

4. Results

Figures 1-3 show the normalized maximum power results for each of the three types of modules. The M55 showed little or no detectable difference between the biased and unbiased cases, with an 8% drop for the entire test. At the 200-cycle point, the drop was less than half of this amount, only 2-3%. This is much different from the a-Si US-32, which dropped 6% within the first 50 cycles when biased, with little additional degradation thereafter. The unbiased module changed very little. For the 50-AL case, the unbiased module dropped only a slight amount, while the biased module was about twice as much, to 2% overall.

The most striking result in Figures 1-3 was the initial a-Si drop. This was attributed to a forward-biased degradation mode similar to light-induced degradation in a-Si, but one that acts much faster [4]. If this were the case, it should be possible to anneal the modules and recover the lost power. IEEE 1262 has an annealing procedure that is intended to remove light-induced degradation from a-Si modules that are exposed to light during the qualification sequences [2]. This procedure consists of successive 24-h, +90°C anneals each followed by an I-V measurement. The steps are ceased when the performance changes by less than 1% from the previous step. Figure 2 shows the results of this procedure on the US-32 modules. Note that the biased module recovered almost half of its initial power.

5. Conclusions

This initial evaluation of the biased thermal cycling test showed, first of all, that the commercial modules tested are able to pass well within the degradation limits of IEEE 1262 [2]. Second, two of the three module types showed increased degradation when forward-biased. This implies that the procedure does stress the module interconnections more than unbiased test, and therefore meets the original objective. While none of the modules failed the qualification limits, we

believe this test should cause failures in modules that have poor interconnections. Finally, the current biasing introduces a few complications over the standard test, but these can be overcome with some simple precautions.

6. Acknowledgements

This work was supported by the U.S. Department of Energy under contract Nos. DE-AC36-83CH20093 and DE-AC36-99GO10337.

REFERENCES

[1] J. Wohlgemuth, BP Solarex, personal communication.
[2] IEEE Standard 1262, "IEEE Recommended Practice for Qualification of Photovoltaic (PV) Modules," IEEE, New York, NY, ISBN 1-55937-586-8, 1995.
[3] ASTM Standard E 1171, "Standard Test Methods for Photovoltaic Modules in Cyclic Temperature and Humidity Environments," ASTM Annual Book of Standards, Vol. 12.02, ASTM, West Conshohocken, PA, 1999.
[4] T. McMahon, NREL, personal communication.

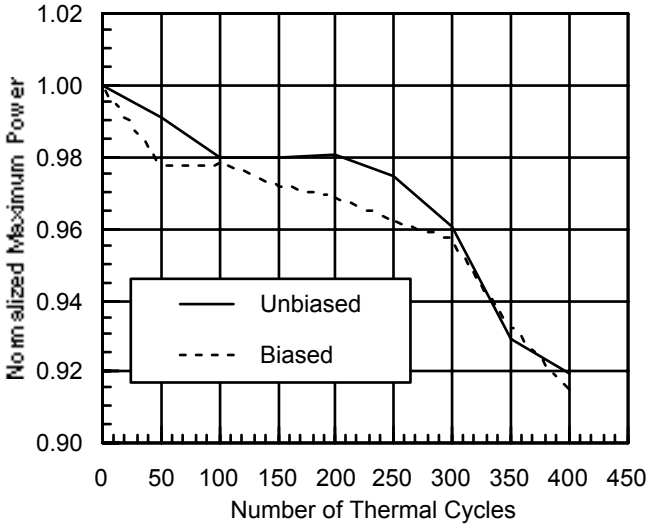

Figure 1. Normalized maximum power versus the number of thermal cycles for the Siemens M55 modules.

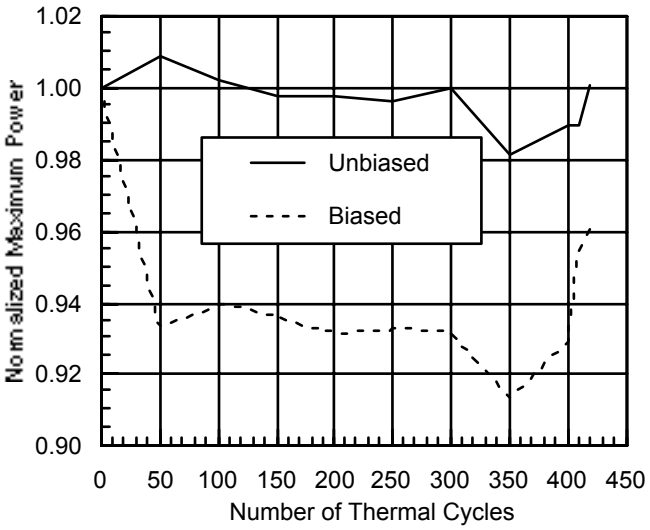

Figure 2. Normalized maximum power versus the number of thermal cycles for the USSC US-32 modules. The last two points are annealing steps.

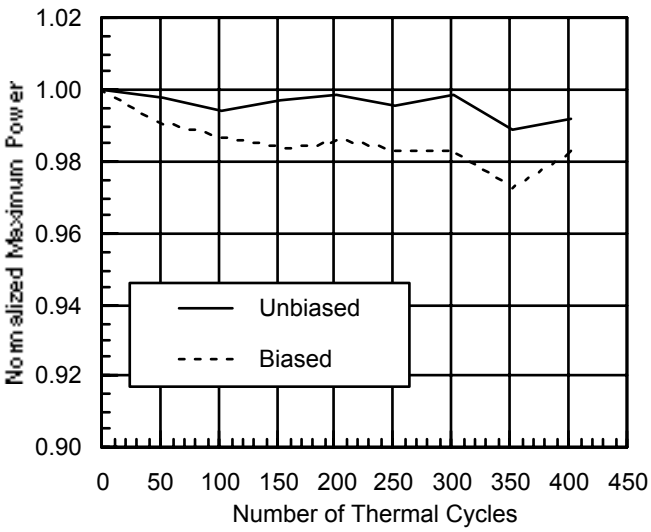

Figure 3. Normalized maximum power versus the number of thermal cycles for the ASE Americas 50-AL modules.

Photothermal Stability of Various Module Encapsulants and The Effects of Superstrate and Substrate Materials Studied for PVMaT Sources

F. J. Pern and S. H. Glick

Engineering and Reliability Division, National Center for Photovoltaics,
National Renewable Energy Laboratory, 1617 Cole Blvd., Golden, CO 80401

ABSTRACT

This paper briefs the photothermal reliability studies we conducted on different encapsulation materials for some U.S. PV companies that are subcontractors of the Photovoltaic Manufacturing Technology (PVMaT) program. The results indicate that the photothermal stability of two foreign ethylene vinyl acetate (EVA) films is dependent on the formulation, curing method and condition, as well as accelerated exposure condition and time. With a Tefzel or Tedlar superstrate or substrate, no EVA discoloration was observed. Delamination and/or wrinkling were observed for some thin-film superstrate materials and non-EVA encapsulants. Silicone adhesive caused notable electrical degradation on crystalline and amorphous silicon (c-Si and a-Si) solar cell samples.

1. Introduction

Upon request by several U.S. PV manufacturers, we have conducted accelerated exposure tests (AET) in the past three years for two foreign EVA formulations, non-EVA encapsulants, and polymer superstrates and substrates. These PV manufacturers are subcontractors to the PVMaT program administrated by NREL; they are not identified in this paper for obvious reasons. The studies were to evaluate the photothermal stability of the various encapsulant materials in laminated forms that can be indicated by discoloration (e.g., yellowing), delamination, and wrinkling. Some studies also involved testing the special encapsulated solar cells supplied by the participants. All of these studies were/are carried out in line with our own research and development task activities and within our capabilities.

2. Experimental

Samples and Configurations

The samples received from the PV manufacturers varied in form, thickness, lamination, and solar cell type. The encapsulant materials included EVA of peculiar formulations and pre-cross-linking, non-EVA polyolefin, and thin layers of non-EVA adhesives. The superstrate and substrate materials used on the laminates included borosilicate glass plates and various polymer films, such as Tefzel, Tedlar, and polyester. Three laminate configurations were used: glass/encapsulant/glass (G/E/G), glass/ encapsulant/polymer (G/E/P), and polymer/ encapsulant/ polymer (P/E/P), with or without a c-Si solar cell or a-Si minimodules. Most of the encapsulant laminates without solar cells were prepared in our laboratory using a custom-built double-bag vacuum laminator. Laminates of commercial EVA formulations, the slow-cure EVA A9918 and fast-cure 15295, and NREL-developed V11 EVA formulations were also studied in parallel for comparison.

Accelerated Exposure Tests (AET)

The samples were studied using the various test equipment as described in [1]. The AET conditions were designed individually depending on the sample characteristics and agreed to by the participating companies prior to initiation of the experiments.

Analytical Characterization

The two foreign EVA formulations (Sov-NA and BS EVA) were analyzed for the presence and concentration of UV absorber (UVA) and gel content before and after particular curing conditions. Details of the analytical methods were described in [2]. The laminate samples were characterized before, during, and after the selected periods of exposure tests with several spectroscopic analyses for the encapsulant and superstrate materials and efficiency measurements for the solar cell.

3. Results and Discussion

Photothermal Stability of Encapsulants and Their Laminates

Samples of G/E/G configuration of the various encapsulants were used in this study. Results show that the discoloration rate is strongly dependent on the encapsulant's formulation, curing method, and condition under a given AET condition and exposure length. Figure 1 shows the net changes in yellowness index (YI) for five different EVA formulations. As expected, the slow-cure A9918 EVA discolored faster and greater than other [1]. The Sov-NA EVA formulation contains UVA and antioxidants identical to that of fast-cure 15295 EVA and was previously cross-linked with e-beam to ~50-55 gel% rather than using a curing agent in the latter for a ~80 gel%. The Sov-NA EVA samples show an earlier yellowing, but a more stable discoloration rate than the 15295 EVA after 1000 h exposure. A fast curing of Sov-NA EVA in the G/E/G lamination process produced a relatively better stable laminate than that from a 3-step, longer curing process. The fast-cure BS EVA, which contains an UV absorbing compound that is different from the UVA in the A9918, 15295 and Sov-NA EVA, was stable against discoloration within our test time frame. The BS and V11 EVA were comparable in the short-term AET study (~700 h). But a recent field observation indicated the

BS EVA turned yellow-brown after a dormant eight years. For the non-EVA encapsulant that used a polyolefin, the laminates were stable against photo-induced yellowing, much better than A9918 and 15295 EVA and similar to that of V11 EVA under a very stringent AET condition [1]. However, the encapsulant delaminated severely at a test temperature of ~110°C while G/EVA/G laminates remained adhesive [1]. The polyolefin is said to have a melting point of 100°-110°C as compared with the ~70°C m.p. for EVA.

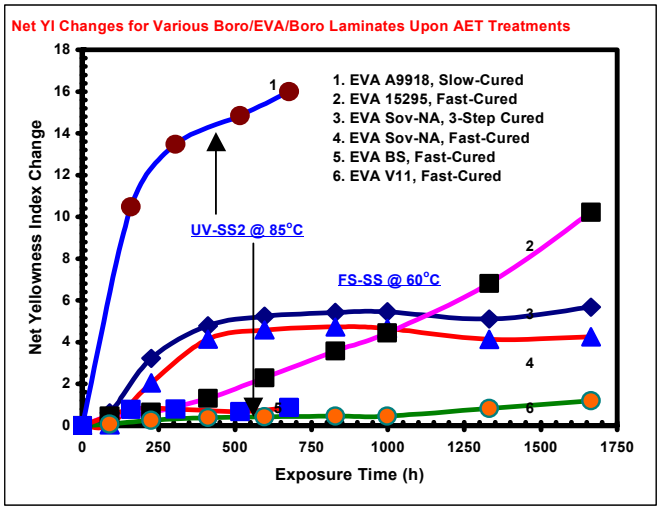

Figure 1. Net changes in yellowness index (YI) for five different EVA formulations in G/E/G configuration.

Effect of Superstrate and Substrate Materials on Encapsulant Photodiscoloration

When the laminates were in the G/E/P or P/E/P configurations, with P used either as a superstrate or substrate, low to no EVA discoloration was observed under various AET conditions. This is attributed to the photobleaching reactions when air (oxygen) was allowed through the permeable polymer films, such as Tefzel and Tedlar. For laminates using polyester or nylon superstrate, light-to-dark yellowing, delamination, and/or wrinkling were observed [1].

Degrading Effect of Silicone Adhesives on Solar Cell Performance

As seen in Table 1, significant efficiency degradation was observed for c-Si cells and a-Si minimodules encapsulated with silicone adhesives in the P/E/Si cell/E/P configurations upon AET treatments [1]. The degrading effect is tentatively attributed to the yet-unidentified chemical compounds from silicone adhesives that induced harmful reactions on the solar cell/metallic components during the photothermal exposures.

4. Conclusions

We have studied various encapsulation materials for several PVMaT subcontractors in an effort to help on the mission objectives of NCPV at NREL. This work has permitted us to make timely contributions to the advancement or development of new encapsulant materials by the U.S. PV industry. The results, also reported individually to each of the PV manufacturers, have allowed them to evaluate or determine the usefulness of, or to improve, their chosen materials.

ACKNOWLEDGEMENTS

The authors thank the temporary technicians, J. Raaff, D. Tomek, and G. Watson for their assistance in performing the work. B. von Roedern of NREL is thanked for the partial support of the technicians through a CRADA fund. This work was performed at NREL under U.S. Department of Energy Contract No. DE-AC36-99-G010337.

REFERENCES

[1] F.J. Pern and S.H. Glick, "Photothermal Stability of Encapsulated Si Solar Cells and Encapsulation Materials upon Accelerated Exposures, *Solar Energy Materials and Solar Cells*, **61** (2000) 153-188.

[2] F.J. Pern, "Factors That Affect the EVA Encapsulant Discoloration Rate Upon Accelerated Exposure," *Solar Energy Materials and Solar Cells*, **41/42** (1996) 587-615.

Table 1. Percent Changes of I-V Parameters for Polymer Films-Encapsulated c-Si Cells and a-Si Minimodules after AET Treatment in DSET Tabletop Exposure System #2 with ~1.2 UV Suns at BPT = 60° - 65°C [1].

Sample ID	Polymer Film	Pottant Type	Voc (%)	Vmax (%)	Jsc (%)	Jmax (%)	FF (%)	Pmax (%)
(a) c-Si cells at 1188 h								
B1-1	Tefzel	EVA	0.00	-1.26	4.63	6.04	0.12	4.74
B2-1	Tefzel	EVA	-0.36	-2.32	7.30	8.02	-1.35	5.48
D1-2	Tefzel	Silicone	-1.04	-0.65	-22.69	-15.43	9.90	-15.95
D2-1	Tefzel	Silicone	-0.36	-0.14	-23.96	-28.24	-5.46	-28.37
(b) a-Si minimodules at 1235 h								
F57S6-1	PES[1]	EVA	-1.81	-4.68	-9.38	-3.83	3.04	-8.34
F57S18-3	UV-PES[1]	PE[1]	-4.20	-7.33	-10.80	-10.76	-2.95	-17.11
F55S28-4	Nylon	Silicone	-1.69	-7.27	-14.10	-14.40	-6.00	-20.61

[1] PES: polyester; UV-PES: UV-screen polyester; PE: polyethylene thermoset adhesive.

Preliminary Investigations of Outdoor Meteorological Broadband and Spectral Conditions for Evaluating Photovoltaic Modules and Systems

D.R. Myers, S.R. Kurtz
National Renewable Energy Laboratory
1617 Cole Blvd, Golden CO 80401

C. Whitaker, T. Townsend
Endecon Engineering
2500 Old Crow Canyon Rd. San Ramon CA 94583

ABSTRACT

Historically, flat-plate photovoltaic (PV) modules have been rated at "peak-output" for power generated under Standard Reporting Conditions (SRC) of 1000 Watts per square meter W/m^2 global irradiance at a standard temperature (25°C) and reference spectral distribution. We examine the direct-normal irradiance, spectral distribution, ambient temperature, and wind speed to be used for evaluating flat-plate and concentrator module performance. Our study is based upon the 30-year U.S. National Solar Radiation Data Base for conditions observed when the global irradiance on a 2-axis-tracked surface is 1000 W/m^2. Results show commonly-used values for concentrator testing of 850 W/m^2 for direct-normal irradiance and 20°C for ambient temperature are appropriate. Wind speed should be increased from 1 m/s to a more frequently observed 4 m/s. Differences between the reference direct-normal spectrum and spectra measured at three sites when broadband direct-normal irradiance and global-normal irradiance are near SRC irradiances suggest revisions to the reference spectra may be needed.

1. Performance Reporting Conditions

Various existing standards address the performance of PV devices, as shown in Table 1. Device performance is commonly reported with respect to a fixed set of conditions for total irradiance, device temperature, and reference spectral distribution. Note that only PV for Utility Scale Applications (PVUSA) test conditions and this work address PV concentrator test conditions.

DNI and GNI correspond to Direct Normal Irradiance and Global Normal Irradiance, respectively. Standard Test Conditions (STC) or Standard Reporting Conditions (SRC) are defined only for flat-plate collectors as 1000 W/m² irradiance on the module at 25° C Cell temperature, under a reference spectral distribution (American Society for Testing and Materials, ASTM E891 and ASTM E892). The 1000 W/m² irradiance is an arbitrary but convenient achievable "peak" performance condition.

Flat-plate PV devices are often tested indoors, under simulated sunlight near SRC per ASTM Standard Test Method 1036. Indoor testing of PV-concentrator modules is difficult. There are currently no consensus standards for reporting PV-concentrating collector performance so the PV-concentrator industry reports performance based on conditions (PVUSA test conditions, or PTC) developed as part of technology procurements.

Table 1. Summary of Standard PV Test Conditions.

Standard Name	Irradiance W/m^2	Temp.	Wind speed	Comments
STC or SRC (Standard Test/Reporting Conditions) [1]	1000 global AM1.5 Spectrum E892	25°C cell	Not applic-able	Indoor peak performance (most catalogues)
PTC (PVUSA test conditions) [2,3]	1000 global 850 DNI	20°C ambient	1 m/s at 10 m	Outdoor peak performance (utilities)
Nominal operating conditions [1]	800 global	20°C ambient	1 m/s at module height	nominal operating cell temperature (NOCT) [1]
This work	***1000 global 836 ± 44 DNI***	***23.7 ° ±8.8 °C ambient***	***4.5 ± 2.8 m/s at 10 m***	***Observed when GNI is 1000 W/m^2.***

2. Technical Approach

This study provides a technical basis for choosing outdoor-rating conditions, compatible with existing SRC, as described in references [4] and [5]. Hours from the 30-year (1961-1990) NREL National Solar Radiation Database (NSRDB) with the GNI at 1000 W/m^2 ± 25 W/m^2 were selected. We analyzed the direct-normal irradiance, turbidity, temperature, total column water vapor, and wind speed for these hours. NSRDB does not contain GNI. We modeled GNI using the Perez Anisotropic Model [6] with an albedo of 0.2. Two years of modeled and measured GNI showed the model unbiased with root-mean-square error of 2.5%, similar to measurement uncertainty.

We are investigating comparisons of the ASTM E892 reference spectrum to measured spectra extracted from the Solar Energy Research Institute (SERI) Solar Spectral Data Base [7] for GNI and DNI within 10 W/m² of 1000 W/m² and 850 W/m², respectively.

3. Results

Table 2 compares SRC, PVUSA, and the mean results of our analysis for 37 NSRDB sites in the American southwest with outdoor conditions near SRC. The frequency distributions of DNI, ambient temperature, wind speed, atmospheric turbidity, and precipitable water vapor were found to be non-Gaussian and site dependent. Figure 1 shows the distribution of median DNI for all sites when outdoor conditions approximate SRC. Individual distributions are discussed in detail in references [4] and [5].

Table 2. Prevailing Conditions Near SRC

Parameter	Average Median	Standard Deviation	SRC	PVUSA
DNI W/m²	834.4	22.8	N/A	850
GNI W/m²	1001.0	1.3	1000	1000
Temp °C	24.4	4.0	25*	20
Wind Speed m/s	4.4	1.1	N/A	1.0
Total Water cm	1.4	0.5	1.42	N/A
Aerosol Optical Depth	0.08	0.27	N/A	N/A
Air Mass	1.43	0.09	1.50	N/A

* Cell temperature

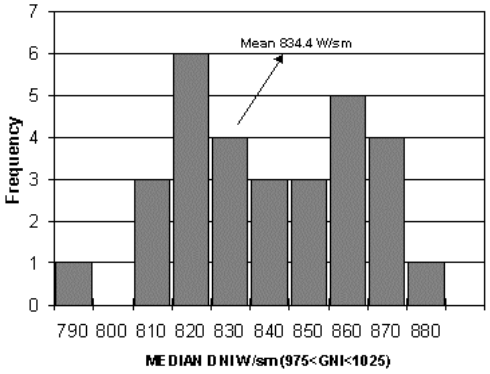

Fig 1. Histogram of median DNI for GNI ~1kW/m², all sites. Median for all sites = 834.4 W/m²

Correlation between observed temperature and wind speed at outdoor conditions near SRC, and annual average temperatures and wind speed are shown in figure 2. In the future these correlations may be used to relate outdoor conditions representing SRC to readily available meteorological data.

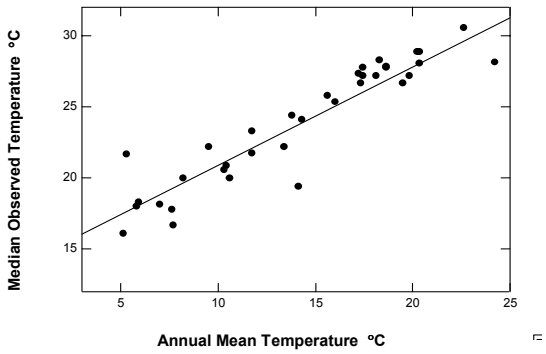

Figure 2. Correlation of observed temperature for outdoor conditions near SRC with Annual Average Temperatures

The frequency of occurrences of DNI greater than of 800 W/m² for all hours between 8 a.m. and 6 p.m. are being examined. As shown in figure 3, these conditions occur more than 30% of the time for five of the six sites shown.

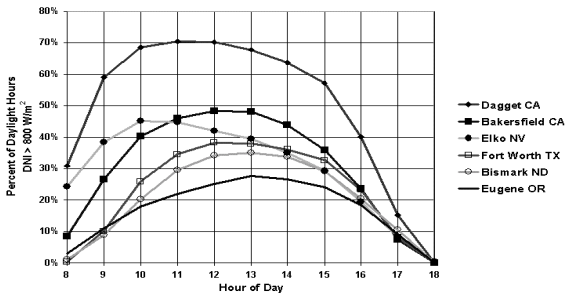

Figure 3. Relative percentage of time by hour between 8 a.m. and 6 p.m. (1961-1990) when DNI exceeds 800 W/m² for six sites.

We searched the NREL/SERI Solar Spectral Data Base, available at http://rredc.nrel.gov/solar/old_data/spectral/, for measured DNI spectra when DNI was near 850 W/m² and GNI was near 1000 W/m². Figure 4 compares measured spectra at Cape Canaveral, Florida, San Ramon, California, and Denver, Colorado with the ASTM E892 DNI Spectrum.

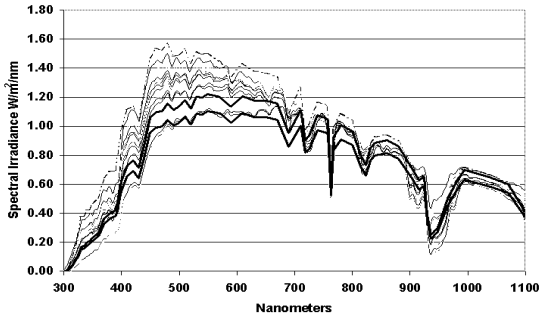

Fig. 4. ASTM E 892 AM 1.5 DNI (thick line) and measured DNI spectra (thin lines) for DNI and GNI near 850 W/m² and 1000 W/m².

References

1. Standard Test Methods for Electrical Performance of Nonconcentrator Terrestrial Photovoltaic Modules and Arrays Using Reference Cells, E1036M, ASTM, in Vol. 12.02. (1998)

2. Whitaker, C. M., T. U. Townsend, J. D. Newmiller, D. L. King, W. E. Boyson, J. A. Kratochvil, D. E. Collier, and D. E. Osborn, "Application and Validation of a New PV Performance Characterization Method," in *Proceedings of the 26th IEEE Photovoltaic Specialists Conference*, 1253-1256 (1997)

3. Stultz, J. W., and L. C. Wen, Thermal Performance Testing and Analysis of Photovoltaic Modules in Natural Sunlight, 5101-31, 1977.

4.Kurtz, S.R., D. Myers, C. Whitaker, T. Townsend, A. Maish, "Outdoor Rating Conditions for Photovoltaic Modules and Systems" *Solar Energy Materials and Solar Cells (*In press).

5. Myers; Kurtz, S.; Whitaker, C.; Townsend, T.; Maish, A. "Objective Method for Selecting Outdoor Reporting Conditions for Photovoltaic Performance" Solar 99, Proceedings of American Solar Energy Society 1999 Annual Conference, Portland Maine, Jun 12-16, 1999, p 267-272

6. Perez, R., R. Seals, P. Ineichen, R. Stewart, and D. Menicucci, "A New Simplified Version of the Perez Diffuse Irradiance Model for Tilted Surfaces,"*Solar Energy* **39,** 221-231 (1987).

7. Riordan, C., "Joint EPRI-SERI Spectral Solar Radiation Database Project," *Solar Cells*, **21**, pp. 337-342. (1987)

Procedures at NREL for Evaluating Multijunction Concentrator Cells

T. Moriarty and K. Emery

National Renewable Energy Laboratory

1617 Cole Blvd., Golden, CO

ABSTRACT

The procedures for evaluating the performance of multijunction-concentrator cells at the National Renewable Energy Laboratory are described. The accurate measurement of the performance of multijunction cells requires accurate relative-quantum-efficiency-measurements, "matched" reference cells, and a spectrally adjustable solar simulator.

1. Introduction

The procedures for evaluating multijunction cells are a generalization of single junction measurement procedures developed in 1985 [1]. The procedures were first documented in 1986 [2] and adopted by various groups [3-5]. The procedures involve adjusting the spectrum of the solar simulator until each junction is operating at its correct photocurrent. This is accomplished for an n-junction solar cell by satisfying the following set of equations

$$I^{R_1,S} = \frac{I^{R_1,R}}{M_1}$$

$$I^{R_2,S} = \frac{I^{R_2,R}}{M_2}$$

$$\bullet \quad \bullet \quad \bullet$$

$$\bullet \quad \bullet \quad \bullet \qquad (1)$$

$$\bullet \quad \bullet \quad \bullet$$

$$I^{R_n,S} = \frac{I^{R_n,R}}{M_n}$$

where I is the short-circuit current and M is the spectral mismatch. The superscript R_n,R denotes the reference cell for junction n under the reference spectrum while the superscript R_n,S denotes the reference cell for junction n under the simulator spectrum.

The spectral mismatch or correction factor M_n for junction n is given by

$$M_n = \frac{\int_{\lambda_1}^{\lambda_2} E_s(\lambda) * S_{tn}(\lambda) d\lambda}{\int_{\lambda_3}^{\lambda_4} E_s(\lambda) * S_{rn}(\lambda) d\lambda} * \frac{\int_{\lambda_3}^{\lambda_4} E_{ref}(\lambda) * S_{rn}(\lambda) d\lambda}{\int_{\lambda_1}^{\lambda_2} E_{ref}(\lambda) * S_{tn}(\lambda) d\lambda} \qquad (2)$$

where $S_{tn}(\lambda)$ is the spectral response of junction n and $S_{rn}(\lambda)$ is the spectral response of the reference cell for junction n. The reference spectral irradiance is $E_{ref}(\lambda)$ and the simulator spectral irradiance is $E_s(\lambda)$. The spectral response for each junction of a multijunction device is determined by using filtered constant-light bias to turn on all of the junctions not being measured and illuminating the cell with chopped monochromatic light. Applying a voltage bias may also be required for multijunction devices with voltage-dependent quantum efficiency such as amorphous silicon. This is generally accomplished by applying a forward bias until the responsivity is a maximum. For two identical junctions in series this would be one half of the open-circuit voltage. This allows the cell being measured to operate at 0 volts while the junction not being measured is operating near its open-circuit voltage.

These procedures have been followed since 1987 for 1-sun multijunction cells. Ideally these procedures should be followed for measurements under concentrated light. The spectrum of NREL's High Intensity Pulsed Solar Simulator (HIPSS) could be altered by placing filters close to the lamps but this has not been done yet. Currently, procedures determine the concentration ratio from the 1-sun short-circuit current. A separate set of measurements are performed to determine if the current is linear with total irradiance. The 1-sun multi-source simulator; and concentrator results are compared to determine if there is a large difference in the fill factor. A difference in the fill factor could indicate that a different junction is current limiting under the HIPSS light than under the standard spectrum.

2. Example

The spectral responsivity for the individual junctions for the GaInP/GaAs/Ge triple-junction concentrator cell is shown in Figure 1. The cell was developed and grown at Spectrolab and processed at NREL.

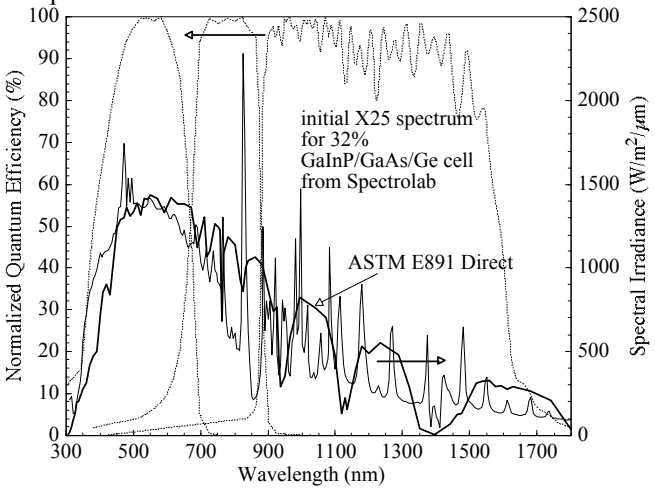

Figure 1. Spectrolab / NREL GaInP/GaAs/Ge triple-junction concentrator showing the normalized quantum efficiency for each junction, the direct-reference spectrum and the initial Spectrolab X25 spectrum.

Primary reference cells with an uncertainty of ±1% were available for the top and middle junction and a secondary reference cell of GaAs filtered Ge was calibrated for the

bottom junction with an uncertainty of ±5%. The spectrum of NREL's Spectrolab X25 solar simulator was adjusted until the three-junctions' photocurrent was within ±1% of their calibrated value. The filtering of the X25 solar simulator was complicated by a lack of appropriate filters for the bottom junction. Ideally the filters should allow light for only one of the three junctions to pass through, allowing independent adjustment of the light to each junction. In reality, the filter's transmissions overlapped and, because of inadequate filters (Figure 2), the simulator could only achieve 750 W/m^2 without adversely affecting the spatial uniformity. Figure 2 shows the final filters used for the 32% for the cell in Figure 1.

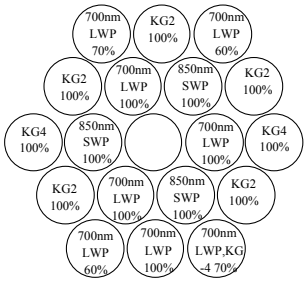

Figure 2. Position of the filters placed in front of the Spectrolab X25 solar for the GaInP/GaAs/Ge triple-junction cell.

Once the nominal 1-sun characteristics under the multi-source X25 are established, the sample is taken to the HIPSS and measured as a function of concentration as shown in Figure 3. The linearity of I_{sc} with total irradiance was

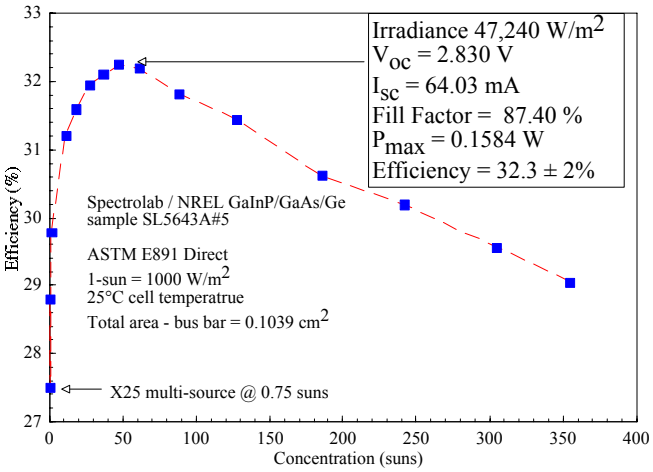

Figure 3. Efficiency *vs.* concentration assuming linearity for the cell described in Figures 1 and 2.

determined by measuring I_{sc} as a function of attenuation and plotting the ratio as a function of I_{sc}. The intensity was changed by adjusting apertures close to the lamp and by changing the lamp voltage. This maps the slope of I_{sc} *vs.* irradiance and is constant for linear devices. Figure 4 illustrates that, within experimental error, the slope is zero.

3. Summary

The procedures at NREL for evaluating the performance of multi-junction cells have been presented. Because of the urgent need to determine the spectral sensitivity of multi-junction devices over the period of a standard day, procedures to more rapidly determine the performance under varying spectral conditions are under development. The spectrum of the HIPSS must be made adjustable to properly evaluate the spectral sensitivity of concentrator cells. This has not been a major problem in the past because the current-limiting junction has been the same under the HIPSS and standard spectrum. The HIPSS must be able to measure irradiance directly so linearity assumptions and checks are not needed. Finally, the proper way to determine the linearity of a device is to measure its absolute spectral responsivity over the irradiance range of

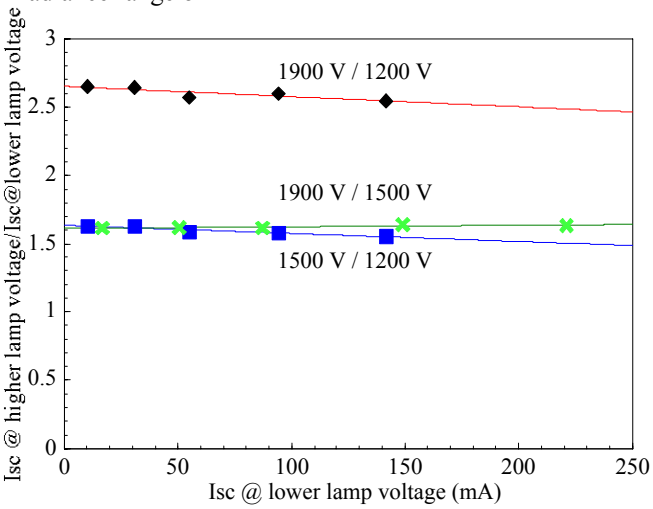

Figure 4. Variation in the slope as a function of current for the cell in Figure 3. showing linear behavior within experimental error.

interest. This is because simulator-based measurements, as a function of total irradiance are a function of the spectrum of the solar simulator that may not have the same functional dependence as the reference spectrum.

4. Acknowledgement

This work was supported under DOE contract DE-AC36-99GO10337. Thanks to Don Dunlavy for the QE measurements.

REFERENCES

[1] K.A. Emery, C.R. Osterwald, T.W. Cannon, D.R. Myers, J. Burdick, T. Glatfelter, W. Czubatyj, and J. Yang, "Methods for Measuring Solar Cell Efficiency Independent of Reference Cell or Light Source," *Proc. 18th IEEE Photovoltaic Spec. Conf.*, Las Vegas, NV, October 21–25, 1985, pp. 623–628, IEEE, New York, 1985.

[2] T. Glatfelter and J. Burdick, "A Method for Determining the Conversion Efficiency of Multiple-Cell Photovoltaic Devices," *Proc. 19th IEEE Photovoltaic Spec. Conf.*, New Orleans, LA, 1987, pp. 1187-1193

[3] K.A. Emery, "Multi-Junction Amorphous Silicon Solar Cell Calibrations and Testing," *Proc. of the 1989 Amorphous Silicon Contractors Review meeting*, June 19-20, 1989, pp. 253-262, SERI tech. rep. CP-211-3514.

[4] G. Virshup, "Measurement Techniques for Multijunction Solar cells," *Proc. 21st IEEE Photovoltaic Spec. Conf.,* Kissimimee, FL, 1990, pp. 1249-1255.

[5] M. Bennett and R. Podlesny, "Two Source Simulator for Improved Solar Simulation," *Proc. 21st IEEE Photovoltaic Spec. Conf.,* Kissimimee, FL, 1990, pp. 1438-1442.

Procedures for Determining the Performance of Stand-Alone Photovoltaic Systems

P. McNutt, B. Kroposki, R. Hansen, and R. DeBlasio
National Renewable Energy Laboratory, 1617 Cole Blvd, Golden, Colorado 80401 USA

K. Lynn and W. Wilson
Florida Solar Energy Center, 1679 Clearlake Rd., Cocoa, Florida 32922 USA

P. Boulanger
GENEC CEA Cadarache, Bldg. 351, 13108 Saint Paul Lez Durance, France

Introduction

Standard test procedures are being developed to assess the performance of stand-alone photovoltaic (PV) systems. This paper will present an overview of the latest procedures.

The procedures being developed fill the need for a short-term (approximately one month) test that can assess the performance of a stand-alone PV system. The majority of PV systems being installed around the world are small lighting systems that consist of an array, a lighting load, a controller, and a battery. These systems are essentially PV-powered battery chargers with a small load. With this in mind, we wanted procedures to indicate how well the PV system can charge the battery.

To date, most PV "system" performance test procedures have only looked at the performance of the individual components and have not addressed how the integrated system worked as a whole. The performance tests being developed verify that the system and load operate as expected, ensure the PV array is capable of recharging the battery, determine the usable battery capacity (UBC), and determine if there is any significant change in the UBC measured at three different times during the performance tests.

Background

The procedures outlined in this paper fill a void and establish the technical foundation needed to reduce uncertainty that a system's performance will be what its designers and builders claim. The need for this document was recently made more apparent with the initiation of a PV Global Approval Program at the international level. These tests will serve as the basis for national and international stand-alone PV system test standards.

In July 1998, the National Renewable Energy Laboratory (NREL) published "Interim Test Methods and Procedures for Determining the Performance of Small PV Systems" [1]. This document provided an initial performance test for stand-alone PV systems. Validation testing was conducted at four U.S. laboratories: NREL, Florida Solar Energy Center (FSEC), Southwest Technology Development Institute (SWTDI), and Photovoltaics for Utility-Scale Applications (PVUSA). Based on this testing, NREL updated the test procedures and published "Procedures for Determining the Performance of Stand-Alone PV Systems" [2] in September 1999. This test document was used as the basis for IEEE P1526/D1 "Recommended Practice for Testing the Performance of Stand-Alone PV Systems." The procedures presented in this paper describe the latest version of the IEEE P1526 document.

The Procedures

Figure 1 is a graphical representation of the testing in terms of battery voltage and time. The time periods shown are approximate. During the test, the battery temperature is kept at an average 30±5°C. This is meant to simulate a tropical climate where many stand-alone PV systems are being installed.

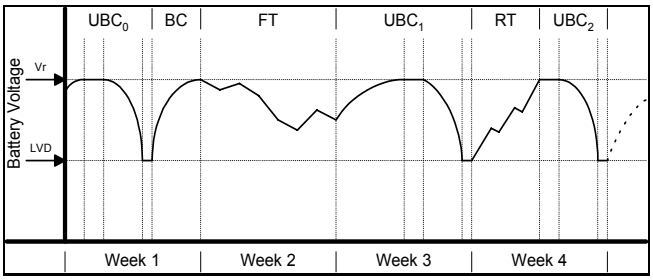

Figure 1 – Sample test profile for the stand-alone PV system performance test

UBC_0 - Initial Capacity Test

This test establishes a baseline capacity measurement for the battery. First, the battery is charged by the PV array with the load disconnected. Next, with the array disconnected, the battery is discharged by operating the load continuously until the system reaches its low-voltage disconnect (LVD). The initial usable battery capacity (UBC_0) is measured during the discharge.

The three battery capacity tests, UBC_0, UBC_1, and UBC_2, are conducted the same way. The change in UBC is determined by comparing UBC_0 to UBC_2.

BC – Battery Charge

The battery is recharged using the array before starting the functional test.

FT – Functional Test

The functional test is run at least 7 days to determine if the system and load can operate as designed. The load is set to operate 4 hours per night. For at least 2 consecutive days, the array should receive "low" solar insolation (≤ 2 kWh/m^2 per day). For at least 2 days, not necessarily consecutive days, the array should receive "high" solar insolation (≥ 5 kWh/m^2 per day).

RT – Recovery Test

The recovery test determines the ability of the array to charge the battery from its LVD state to voltage regulation (Vr) while the load is enabled. After reaching LVD in the UBC_1 test, the system is set for normal operation with the load set to operate 4 hours per night. The system is operated until the battery reaches Vr and then for at least another 3 days. The battery Ah and sun hours to regulation are measured.

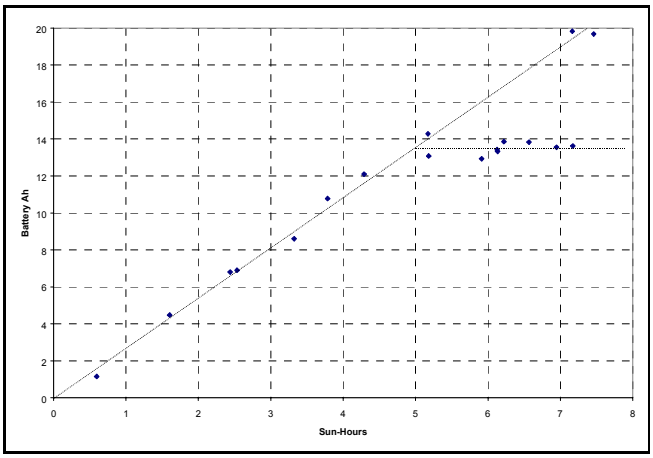

Figure 2 – Sample P-Chart displays daily battery Ah vs. sun hours

The Performance- or P-Chart in Figure 2 is generated using the daily battery-Ah and the sun-hour data from both the functional and recovery tests [3,4,5]. The P-Chart gives a graphical representation of how many Ah the array can deliver to the battery for a given number of sun hours. It also displays at what point the charge controller begins regulating the array output. The data should tend to fall along two lines similar to those shown in Figure 2. In this example, it takes about 5 sun hours for the battery to reach regulation voltage after the load has operated for 4 hours. The steeper the diagonal line, the quicker the array will charge the battery. The level of the horizontal line indicates at what point the charge controller will begin regulating the array current. The level of this line depends on the array size and load run time.

Validation of the Procedures

The latest procedures are being validated at four U.S. labs (NREL, FSEC, PVUSA, and SWTDI) on two PV-lighting systems manufactured in the United States. A lighting system manufactured overseas will also be validated at NREL and at GENEC in France. All three lighting systems consist of a silicon module, a fluorescent lighting load, a lead-acid battery, and a charge controller. The validation is being conducted primarily to determine if the procedures can be followed and, secondarily, to compare the system test results run at different labs in different climates. Results of the testing will be presented at the 28th IEEE Photovoltaic Specialists Conference in September 2000.

Conclusion

These procedures have been submitted to IEEE for use in the IEEE document, P1526 "Recommended Practice for Testing the Performance of Stand-Alone Photovoltaic Systems." A standardized stand-alone PV-system performance test will help in the verification of systems design. Future work will include developing qualification tests to evaluate the design of stand-alone PV systems.

References

[1] "Interim Test Methods and Procedures for Determining the Performance of Small Photovoltaic Systems." NREL/TP-520-25077, July 1998. Golden, Colorado.

[2] "Procedures for Determining the Performance of Stand-Alone Photovoltaic Systems." NREL/TP-520-27031, September 1999. Golden, Colorado.

[3] "Interim Procedures for Determining the Performance of a Photovoltaic System." December 1999. GENEC, Cadarache, France.

[4] A. Reinders, "Performance Analysis of Photovoltaic Solar Energy Systems." Ph.D. thesis, Utrecht University, Netherlands.

[5] J.M. Servant, J.C. Aigullon, "Test of PV Lighting Kits." 11th EC Photovoltaic Solar Energy Conference, 1992, Montreux, Switzerland.

Radiometric Measurements and Data for Evaluating Photovoltaics

D.R. Myers, A. Andreas, M. Rymes, T. Stoffel, I Reda, S. Wilcox, J. Treadwell

National Renewable Energy Laboratory
1617 Cole Blvd, Golden CO 80401

ABSTRACT

The National Renewable Energy Laboratory (NREL) Photovoltaic Radiometric Measurements Task addresses the impact of solar and optical radiation on photovoltaic (PV) devices. The task maintains spectral and broadband calibration capability directly traceable to the National Institute of Standards and Technology (NIST) and the World Radiometric Reference (WRR) of the World Meteorological Organization (WMO). Radiometric resource data and analysis are brought to bear on issues relating to PV performance. Current activities include monitoring the spectral drift in pulse solar simulators, characterizing radiometers, accurate interpolation of averaged radiation and weather data, identifying typical prevailing conditions for PV applications, evaluation of consensus standard spectral references, and technical support for development of PV-related consensus standards.

1. Introduction: Task Objectives

The objective of the NREL PV Radiometrics Measurements Task is to perform traceable calibrations, measurements, and research regarding the influence of optical and solar radiation on photovoltaic devices and systems.

2. Spectral Calibrations and Measurements

The task provides traceable calibrations and measurements and solar resource data collection and analysis to evaluate the impact of optical and solar radiation on PV-device performance. 1000 Watt NIST standards of spectral irradiance are the references for calibrating reference and user spectroradiometers. NREL spectroradiometers are shown in figure 1.

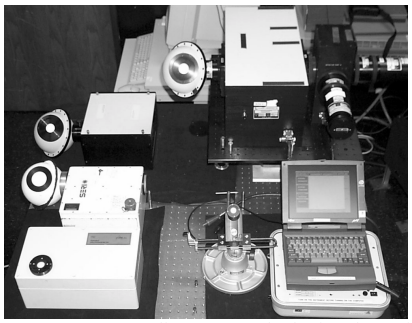

Figure 1. NREL spectroradiometers. Clockwise from front left: Li-1800 [0.3-1.1 um], Geophysical Environmental Research (GER) [0.35 -2.4 um] , Optronic Laboratories (OL) OL-754 [0.18-0.8 um], OL-750 [0.25 -2.4 um], Analytical Spectral Devices (ASD) FieldSpec FR [0.35 -2.4 um]

Reference spectroradiometers calibrate filter radiometers over their response range. Figure 2 shows an OL-754 Ultraviolet (UV) spectrometer calibrating the radiometer monitoring UV exposure in the NREL UV test chamber, and the spectral distribution of the exposure lamps

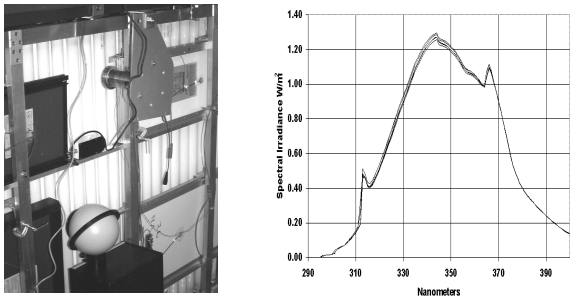

Figure 2a. UV exposure chamber UV monitor calibration against OL-754 spectrometer. 2b. Spectral distribution of exposure lamps.

The UV-exposure tests are run at elevated temperatures (65°C). We characterized the temperature response of the UV monitor to be 5%/°C (25°C to 45 °C). Figure 3 shows relative changes in spectral distribution for the NREL Spire 240 Pulse solar simulator from April 1999 to February 2000.

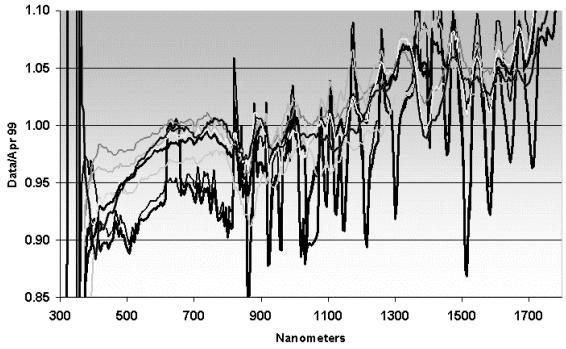

Figure 3. Relative spectral distribution changes in Spire 240 with respect to baseline measurement in April 1999. Light lines are for May - Nov. 1999, heavy gray lines are for Jan. and Feb. 2000

3. Broadband Radiometric Calibrations

NREL broadband pyranometers and pyrheliometers are calibrated against NREL reference absolute cavity pyrheliometers traceable to the WMO WRR. In October, 1999, NREL conducted an intercomparison of absolute-cavity pyrheliometers at the Solar Radiation Research Laboratory (SRRL) to maintain the WRR factors of the NREL and other participating cavity radiometers. Table 4 shows the WRR factors and uncertainty with respect to *System Internationale* (SI) units for NREL cavity radiometers used as the standard for PV reference cell

calibrations and at the outdoor test Facility Reference Meteorological and Irradiance System (RMIS).

Table 1. OCT 1999 Intercomparison Results for NREL Working Cavity Pyrheliometers

Cavity Radiometer	WRR Factor	Uncertainty With Respect to SI units
23734 (PV ref)	0.99855	0.35%
29794 (RMIS)[+]	0.99485	0.50%

[+]RMIS cavity radiometer operated continuously with window in place.

The task coordinates calibration of radiometers used in PV-performance testing with respect to the NREL working-standard absolute cavity pyrheliometers, assuring traceability of calibrations to WRR.
Our Broadband Outdoor Calibration (BORCAL) procedures produce maps of pyranometer responsivities as functions of zenith and azimuth angle. Calibrations on clear days throughout the year result in a sparse matrix of responsivities. We have developed an interpolation technique to produce a detector angular responsivity map as shown in figure 4

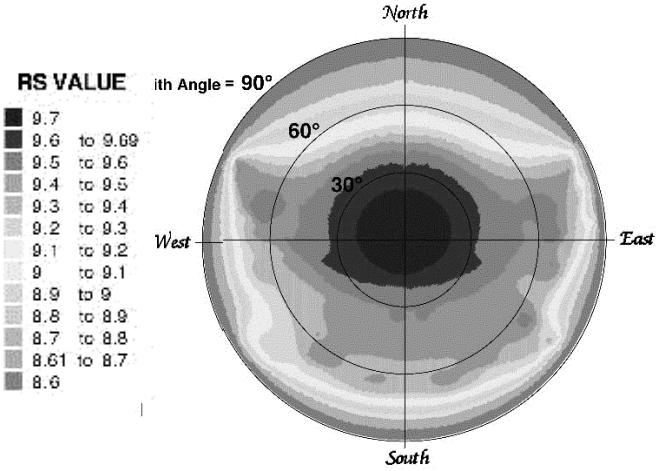

Figure 4. Pyranometer angular-response map derived from outdoor calibration data.

4. Solar Radiation Resources and PV Performance

We began a study [3] to provide a technical basis for evaluating PV-rating conditions. We selected direct-normal irradiance (DNI), turbidity, temperature, total column water vapor, and wind speed from the 30-year (1961-1990) National Solar Radiation Database (NSRDB) when the global normal irradiance was 1000 W/m^2 ± 25 W/m^2 [1,2,3].
The frequency of occurrence of DNI values by hour to determine what DNI values may represent "typical" conditions for various sites is being studied. Figure 5 is a contour plot of the frequency distribution of DNI by hour from 8 a.m. to 6 p.m. for Elko, NV showing representative results.

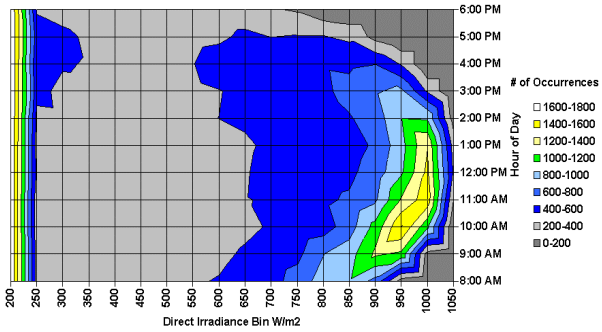

Figure 5. Frequency distribution by hour of DNI for hours 8 a.m. to 6 p.m. for Elko, NV. 1961-1990 hourly data. See also ref [1,2].

We developed a simple algorithm to convert averaged data into data with higher resolution.[4] Figure 6 is an example showing one minute DNI values derived from 24 hourly average DNI.

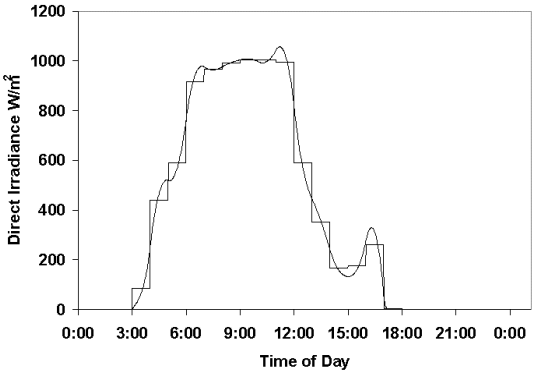

Figure 6. One minute DNI (smooth curve) derived from hourly average DNI (step curve) by a mean preserving interpolator.

5. PV Standards and Codes Support

We are evaluating the American Society for Testing and Materials (ASTM) E892 reference spectrum with respect to measured spectra extracted from the SERI Solar Spectral Data Base [5] for GNI and DNI within 10 W/m² of 1000 W/m² and 850 W/m², as described in [1]

References

1. Myers, D.; S.R. Kurtz, C. Whitaker, T. Townsend. "Preliminary Investigations of Outdoor Meteorological Broadband and Spectral Conditions for evaluating PV Modules and System" These Proceedings.
2.Kurtz, S.R., D. Myers, C. Whitaker, T. Townsend, A. Maish, "Outdoor Rating Conditions for Photovoltaic Modules and Systems" *Solar Energy Materials and Solar Cells* In press.
3. Myers; Kurtz, S.; Whitaker, C.; Townsend, T.; Maish, A. "Objective Method for Selecting Outdoor Reporting Conditions for Photovoltaic Performance" Solar 99, Proceedings of American Solar Energy Society 1999 Annual Conference, Portland Maine, Jun 12-16, 1999, p 267-272
4. Rymes, M.D. and D. Myers "Mean Preserving Algorithm for Smoothly Interpolating Averaged Data to Higher Resolution" Draft for *Solar Energy*
5. Riordan, C., "Joint EPRI-SERI Spectral Solar Radiation Database Project," Solar Cells, Vol. 21, 1987, pp. 337-342.

The NREL Outdoor Accelerated-Weathering Tracking System Photovoltaic Module Exposure Results

T. S. Basso

National Renewable Energy Laboratory (NREL)

1617 Cole Blvd., Golden, CO, 80401-3393

ABSTRACT

Status results are presented for the Outdoor Accelerated-Weathering Tracking System (OATS) first study on photovoltaic (PV) modules. Studies began in November 1997 on pairs of commercially available crystalline silicon and amorphous silicon (a-Si) PV modules kept at constant resistive load. The modules do show weathering, but there were no module failures. Through February 2000, the PV modules under OATS reflector conditions received 1286 MJ/m^2 of total ultraviolet (TUV) exposure, and the modules under the covered reflectors received 809 MJ/m^2.

1. General Introduction

The OATS system [1] provides accelerated stress testing, and this study's purpose is to assess PV module durability to ultraviolet (UV) radiation and outdoor exposure, focusing on degradation of module encapsulants and other polymer components, the PV device structures, and general module components. Test protocol was based on existing standards [2,3]. Pairs of commercially available crystalline silicon and a-Si PV modules (Table 1) were deployed in the two OATS test planes. One test plane has its reflectors covered so the irradiance is nominally equal to that of a two-axis tracker, and the second test plane experiences sunlight concentration by four flat-plate aluminum reflectors at 45° to the sun (3X concentration theoretical maximum). Each module is at a resistive load calculated to provide one-sun maximum power-point operation. In-situ monitoring is back-of-module temperature, load current and voltage, and once a day, the module short-circuit current and open-circuit voltage are measured when total-irradiance tracking is near 1000 W/m^2. This OATS study will continue to 2000 MJ/m^2 TUV exposure or until failure, defined as module power having decreased to 25% of its initial value. The TUV exposure level is defined as the UV irradiance integrated below 400 nm. At varied intervals, the PV modules are removed from OATS for visual inspection and solar-simulator performance measurements. When modules pass the rated power criteria, they are returned to OATS; otherwise, they will undergo failure analysis.

2. Results

Status results and comments follow. There were no module failures and visual inspections show minor anomalies. The reported exposure levels include a 1.26 multiplier to account for the TUV radiometer (TUVR) instrument spectral response ending at 385 nm. Measurements at NREL's Solar Radiation Research Laboratory were used to establish that multiplier [4].

The current-voltage (I-V) power performance data are compared to the 3/97 baseline (Table 2), not the 11/97 values. From the table, one can see that module #10 at OATS one-sun exposure was at 96.3% power in 2/00 after 809 MJ/m^2 TUV exposure, and the same model PV module #2 at concentration exposure was at 94.5% in 2/00 after 1286 MJ/m^2. Only the a-Si modules showed any substantial change, which is primarily attributed to the Staebler-Wronski effect.

The OATS cumulative TUV exposure through 2/00 for the PV modules under reflector conditions was 1286 MJ/m^2, and for modules in the test plane with the reflectors covered, it was 809 MJ/m^2.

This initial PV module study is ongoing. When failures or substantial visual anomalies are noted, they will be compared to results of other exposure methods. Further, for this ongoing PV module exposure study, the data, results, and the OATS system description will be documented in a detailed NREL report planned for Fall 2000.

TABLE 1. OATS Test Photovoltaic Module Descriptions

Manufacturer	**Module Models**	**Technology**
Siemens Solar Industries	M10 & Pro 1JF	crystalline silicon
Solarex Corp.	MSX10 & MSX20	crystalline silicon
United Solar Systems Corp.	UniSolar 1206 & 1212	Dual-junction amorphous silicon

TABLE 2. Photovoltaic Module Relative Power [(a)] after OATS Exposure[(b)]

OATS TUV Exposure[(b)] Levels in MJ/m^2 (Date) for Modules #2 - #7 and Modules #10 - #15							
#2 - #7	0 (11/97)	54 (1/98)	165 (3/98)	260 (5/98)	392 (7/98)	1100 (9/99)	1286 (2/00)
#10 - #15	0 (11/97)	54 (2/98)	158 (5/98)	240 (8/98)	-----	703 (10/99)	809 (2/00)
Module Model - #	**Relative Power[(a)] (% @ standard reporting conditions)**						
M10 #2	98.2	96.3	97.6	98.0	95.8	95.6	94.5
M10 #10	98.2	98.3	98.9	97.5	-----	96.5	96.3
Pro1JF #3	97.2	95.9	96.2	97.0	95.7	94.6	93.5
Pro1JF #11	97.3	96.1	94.9	94.8	-----	94.0	93.3
MSX10 #4	99.2	98.2	98.5	98.7	97.6	95.5	95.6
MSX10 #12	98.5	97.7	97.2	97.1	-----	95.5	85.2
MSX20 #5	99.2	97.3	98.3	98.8	97.1	96.8	95.2
MSX20 #13	98.7	98.2	98.1	99.8	-----	96.5	96.9
1206 #6	85.6	77.8	71.7	71.0	72.8	69.8	64.5
1206 #14	84.3	67.1	64.7	65.7	-----	67.4	64.4
1212 #7	86.1	80.0	74.2	74.6	74.3	72.3	66.5
1212 #15	89.2	71.4	68.2	68.9	-----	72.2	67.8

(a) Module power % is relative to 3/97 measurement.
(b) All modules were exposed to 1-sun conditions outdoors, about 30 days during 3/97 to 11/97.
Modules #2 - #7 @ OATS reflector conditions.
Modules #10 - #15 @ OATS covered-reflector conditions.

3. Acknowledgments

The following NREL colleagues are acknowledged for their support: A. Anderberg, R. Hansen, D. Myers, and S. Rummel. The National Center for Photovoltaics at NREL funded this work. The National Renewable Energy Laboratory is a U. S. Department of Energy Laboratory operated by Midwest Research Institute•Battelle•Bechtel, under Contract no. DE-AC36-99-GO10337.

4. References

[1] T. S. Basso, "The NREL Outdoor Accelerated-Weathering Tracking System and Photovoltaic Module Exposure Results," *NCPV Photovoltaics Program Review Proceedings of the 15th Conference*, American Institute of Physics AIP Conference Proceedings 462 (1998) 643 - 648.

[2] *ASTM E 1596 Standard Test Methods for Solar Radiation Weathering of PV Modules*, American Society for Testing and Materials, West Conshohocken, PA (1994).

[3] *ASTM E 1799 Standard Practice for Visual Inspections of Photovoltaic Modules*, American Society for Testing and Materials, West Conshohocken, PA (1996).

[4] D. Myers, NREL interoffice memo, Computing UV integral dose from TUVR data, NREL, Golden, CO (February 4, 1997).

Thermal Characteristics of Flat-Plate Photovoltaic Modules Deployed at Fixed Tilt

J.A. del Cueto

National Renewable Energy Laboratory

1617 Cole Blvd., Golden, CO 80401

ABSTRACT

The thermal characteristics of flat-plate photovoltaic modules, deployed at fixed tilt, are investigated in order to characterize their behavior against meteorological elements. For all modules above ½-sun irradiance, the difference between module and air temperatures is proportional to the solar irradiance and related by a constant of proportionality, whose specific value appears preordained by module construction—ranging 27°C to 41°C per kW/m^2. At high irradiance, these thermal characteristics are driven by the radiant power. When low irradiance occurs under clear-sky conditions, the average temperature differences per unit irradiance become small and can exhibit negative values. Greater module reflectance, resulting from larger angles of incidence to the sun, coupled with radiant heat loss to the sky determine the thermal properties in this regime. Conversely, when low irradiance conditions arise from the obscuration of the sun by clouds, the thermal characteristics are similar to or larger than those at high irradiance.

1. Introduction

Because operating conditions typically encountered in the field rarely emulate standard reporting conditions, determining realistic energy-production capacities for photovoltaic (PV) modules remains a challenge. Recently, methodologies for deriving energy ratings have been developed at the National Renewable Energy Laboratory (NREL) and at Sandia National Laboratories. Operating module temperature is a critical parameter that enters these energy-ratings methods. Hence, accurate characterization and prediction of the thermal behavior of PV modules from the prevailing meteorological conditions become essential tasks in determining energy production capacities.

2. Experimental

Eleven PV modules, representing all existing flat-plate terrestrial technologies were studied: four crystalline silicon (c-Si) modules; two amorphous silicon (a-Si) modules (one a single-junction and the other a triple-junction); two cadmium telluride (CdTe) modules; one poly-crystalline silicon (poly-Si) module; and two copper indium diselenide (CIS) modules. These modules are deployed on the Performance and Energy Ratings Testbed (PERT) situated on the roof of the Outdoor Test Facility at NREL. PERT modules are mounted on a steel structure at fixed plane-of-array (POA) tilt with respect to the horizontal, set to latitude (40°±1°), facing due south (±2°). The mounting structure resembles one-half side of an A-frame roof, in which the roof angle is 40° and defined by the modules. It allows air to circulate on both sides of the modules, albeit, airflow on the backside is partially obstructed by the building. PERT modules are connected to data acquisition systems that monitor their I-V characteristics, module temperatures and concurrent meteorological conditions including POA irradiance and wind speed. Another meteorological measurement station—located in the array field about 60 m away—was used to augment the PERT data. For this analysis, wind speed and irradiance data were measured about a half-meter or less in elevation above the modules; air temperatures were measured 60 m away.

3. Results

Fig. 1 portrays the difference between module and air temperatures ($\Delta T = T_{MOD} - T_{AIR}$) plotted against wind speed in any direction along the horizontal plane, and for data within two irradiance ranges about 1000 and 500 ±25 W/m^2. The straight-line fits to these data are also depicted as either dashed or solid lines. This figure illustrates two tenets of module thermal characteristics: ΔT is a decreasing function of wind speed and an increasing function of solar irradiance. For all data measured at or above 500 W/m^2, the intercept of ΔT at zero wind speed is very nearly a linear function of irradiance—the intercepts in Fig. 1 are ~18° C and ~39° C at 500 and 1000 W/m^2, respectively. Henceforth, it is useful to characterize thermal characteristics by temperature difference divided by POA solar irradiance (ΔT/Irr) and to analyze its behavior against meteorological conditions.

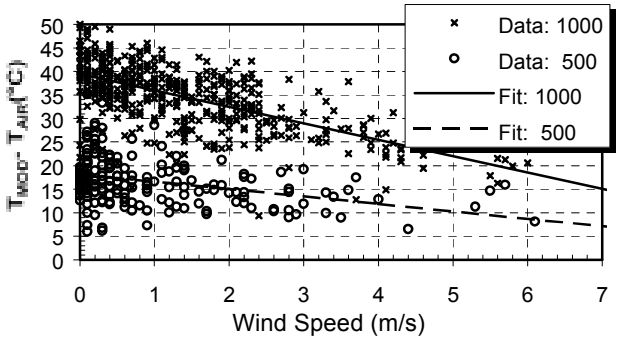

Fig. 1. Difference between module and ambient temperatures versus wind speed, for two data sets within two irradiance windows centered about 500 and 1000 ±25 W/m^2.

The module thermal characteristics (ΔT/Irr) were analyzed by segregating the data into 50 W/m^2-wide irradiance bins and performing least-squares fitting of the data within each bin to a linear function in wind speed. The constant term from this fit represents the intercept of ΔT/Irr with zero wind speed. These data are depicted in Fig. 2 along the abscissa, plotted against irradiance along the ordinate, for seven out of the eleven modules investigated.

Additionally, the data in Fig. 2 have been filtered to reflect largely clear-sky illumination conditions, using a statistical filtering method. Fig. 2 shows that above 500 W/m^2 irradiance for all modules, the intercept values of ΔT/Irr are primarily constant and span 27°–41°C/(kW/m^2) in values. Each module type develops a specific preordained value that is only slightly moderated by radiant thermal emission. Average module (zero wind) temperatures can be obtained from this graph: the product of respective ΔT/Irr values times the irradiance plus the air temperature. For a-Si #4737 for example, at 1000 and 500 W/m^2, the module is ~40°C and ~20°C hotter than the air temperature, respectively, at zero-wind speed. Toward lower irradiance, ΔT/Irr values diminish and can become negative, which can be ascribed to a combination of greater module reflectance at larger angles of incidence—angle between the direction to the sun and the vector normal to module surface—coupled with relatively high (in comparison to incident irradiance) radiant thermal emission from the module under clear-sky conditions.

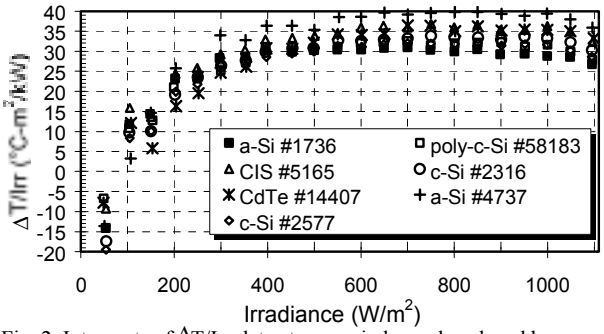

Fig. 2. Intercepts of ΔT/Irr data at zero-wind speed analyzed by irradiance bins, versus average irradiance within each bin, under predominantly clear-sky conditions, for seven PV modules.

The linear slopes of ΔT/Irr with wind speed, computed within 50 W/m^2-wide irradiance bins for the same seven PV modules, are portrayed in Fig. 3, plotted against irradiance. These data were filtered in order to include predominantly clear-sky conditions. Wind data include all directions in the horizontal plane. These data show that above 400 W/m^2, the slopes are negative and range –2.5° to –5 °C per kW/m^2 per m/s. For example, a slope of –3 units indicates that for every 1 m/s increment in wind speed, ΔT/Irr diminishes by 3°C/(kW/m^2)—equivalently, cooling the modules by 3°C and 1.5°C at 1000 and 500 W/m^2, respectively. These slopes represent the low-wind speed, linear approximation to the convection coefficients, since for moderately to very high

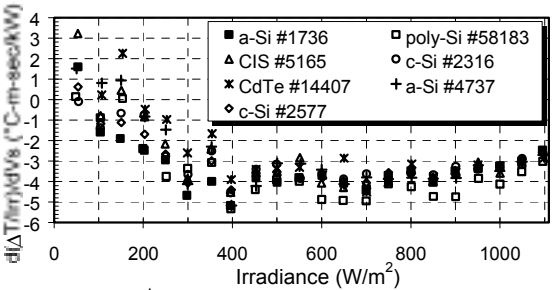

Fig. 3. Slopes of ΔT/Irr with wind speed analyzed by irradiance bins, versus average irradiance in each bin, under predominantly clear-sky conditions, for seven PV modules .

wind speeds (>10 m/s), their application predicts increasingly negative ΔT, contrary to expectation. Negative ΔT does occur as depicted in Fig. 2, but generally only at very low irradiance when under clear skies—corresponding to high angle of incidence between the modules and the sun. Toward lower irradiance in Fig. 3, the slopes appear to increase to positive values—which is likely an artifact of the linear approximation that reflects the decrease and change in sign of ΔT/Irr at low irradiance. Because increasing wind speed must oppose increases in the magnitude of ΔT, the slopes appear to mirror the behavior of ΔT/Irr.

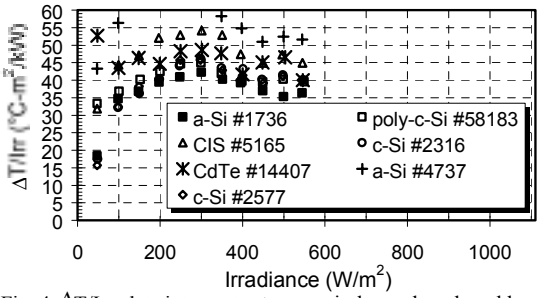

Fig. 4. ΔT/Irr data intercepts at zero-wind speed analyzed by irradiance bins, versus average irradiance in each bin, under predominantly cloudy-sky conditions, for seven PV modules.

Fig. 4 depicts ΔT/Irr intercepts at zero wind speed for the same seven PV modules, when the analysis is carried out for data that portrays predominantly cloudy-sky conditions by using a statistical filtering method. These data are generally limited to low-irradiance values, because cloudy-sky conditions primarily diminish the irradiance. Fig. 4 shows that when low irradiance conditions are produced in this manner, the corresponding values of ΔT/Irr are much larger than those obtained at low irradiance under clear-sky conditions, and similar to or larger than those obtained under clear-sky conditions at high irradiance.

4. Analysis and Conclusions

For modules deployed at fixed tilt, radiant solar power drives their thermal characteristics (ΔT/Irr) above 500 W/m^2 irradiance, forcing average differences between module and air temperatures to be directly proportional to the irradiance and related by constants ranging from 27° to 41°C/(kW/m^2) in values dependant upon module construction. Coefficients were presented that indicate cooling effects spanning 2.5°–5 °C/(kW/m^2) per 1 m/s wind speed for all modules above 400 W/m^2. At lower irradiance, the thermal behavior depends upon the cause of low illumination. If it is due to cloudy versus large angle-of-incidence conditions, the ΔT/Irr values will be 10°–20 °C/(kW/m^2) larger, or 10°–40 °C/(kW/m^2) smaller, respectively, than values at high irradiance. This distinction is likely because of the importance of radiant thermal emission from the modules and ground up to the sky. Under clear skies, a large fraction of radiant heat is lost into space, leading the modules to cool off faster than the ambient air and resulting in negative ΔT/Irr values. When skies are cloudy, more of this thermal emission—long-wavelength IR largely invisible to the pyranometers—is reflected back, resulting in much larger ΔT/Irr values.

Tracking Optimal Operating Point For A Faulted PV System Using ANN and Genetic Algorithm

James A. Momoh Sahar S. Kaddah Hassan Greene
IEEE Fellow Graduate Student Undergraduate Student
Howard University, Washington DC, 20059, USA

1. Abstract

This paper represents A Genetic Algorithm optimization technique for a photovoltaic power system under a faulted condition. The Artificial Neural Network is used to forecast the solar radiation as an input to the PV power system. The proposed PV system-based ANN and GA scheme is tested on actual solar radiation data from the NREL website and the simulation results shown in the paper.

2. Introduction

Photovoltaic, PV, system continues to gain wide acceptance as one of the energy solutions in the future. This has necessitated the need for research efforts aimed at improving the performance of such systems. As the photovoltaic power system is a free-fuel source of electric power, tracking the optimal operating point is a very important issue. Many researchers have discussed this in a normal operating condition. But this paper concentrates on the optimal tracking of the PV system at abnormal conditions.

The power characteristic of PV panel is dependent on the *Insolation* level, cell temperature and array voltage. The power output increases with a steep gradient, proportional to solar *radiation*. At constant temperature, the higher *irradiance* level results in higher power and higher voltage. Temperature increase on the other hand has negative effect on the power generation of a PV system. Higher cell temperature results in lower open circuit voltages. The PV rating is usually specified at insolation level of $1000W/m^2$ and cell temperature of 77^0 F

The proposed PV system-based ANN and GA scheme is innovative and it involves: (a) Forecasting of solar radiation using artificial neural network as input for PV system, (b) Photovoltaic system model as series parallel of PV cells subject to abnormal conditions, (c) GA optimization model to track the optimal operating point of the total power under different conditions.

The proposed scheme is tested on a faulted three-array power system based on actual radiation data and the detailed results are shown in the paper.

Funded by NREL grant No. "AAK-9-18675-06"

3. Solar Radiation Forecasting Using ANN Technique

To have a reliable PV system, we need previous information about the solar radiation. Trained Artificial Neural Networks using historical solar radiation data, minimum five years data, will be able to forecast the solar radiation as function of time. Then we can run a more predictable and reliable PV power system.

An ANN is a software designed to model the performance of the brain in dealing within a particular task of interest. ANN possesses the ability to learn from experience, generalize from previous examples to new ones, and abstract pertinent information from examples containing irrelevant or incomplete data. ANN is best suited to problems where voluminous data and a complex non-linear relationship exists between the input and output patterns, such as the solar radiation problem. Training algorithms can be classified as supervised or unsupervised. Supervised training requires pairing each input vector with a desired output, or target vector, together these are called a training pair. Here, we are using the supervised training.

4. Genetic Algorithm and Power Tracking of A Faulted PV system

Whereas classical optimization techniques suffer from localization based on the initial point, GA is not subject to the initial point. GA searches for the global optimal solution in the entire range of feasible solutions and is insensitive to localized solutions. The GA routine involves the following four stages: Selection of initial population, Crossover and mutation to get new population, Reproduction, and Evaluation of the fitness function. The routine is repeated until the termination criterion is satisfied.

4.1 Formulation

The PV panel is modeled as a current source consisting of parallel arrays each of series connected solar cell modules. A bypass diode is usually placed across each module to short out a cell that fails by opening it. The output of our mathematical model can be approximated by a 5^{th} order polynomial as a function of the array voltage. The GA optimization problem is therefore stated as:

$$Max \quad P(V) = \sum_{i=1}^{N} \sum_{j=1}^{5} \alpha_i V_i^{j-1}$$

$$Subject \quad to \quad 0 \le V_i \le V_{oci}$$

Where

$P(V)$: The total power generated

α_i : The polynomial coefficients

V_{oci} : is the array open circuit voltage of array *i*.

N : is the number of parallel-connected solar arrays.

5. Case Study

Figure 1 shows a PV panel consisting of three parallel arrays each with 30 series cell modules. Each of the series modules is shunted by a bypass diode. The shunt diode serves to complete the array connection circuit when the

shunted solar modules experience open circuit failures. The panel is rated at an open circuit voltage of, V_{oc} = 21.1V, and I_{SC} has a proportional relationship with the solar radiation. This panel was used to test the proposed scheme. Possible cell open circuit failures were taken into consideration ranging from 5% to 75% of the 3-arrays being faulted.

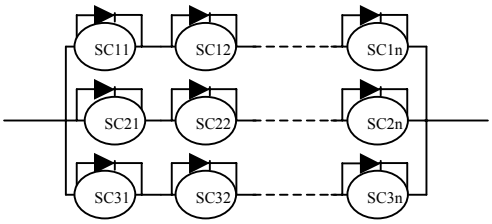

Figure 1: Arrangement of solar cells in the solar panel

The first step was to find accurate measurements of solar radiation levels. Files were downloaded containing Hourly Synoptic Data for Sterling, VA from NREL website *"http://www.nrel.gov/solar/pubs"*. Using data for one twenty-four hour period for a specific day, say March 2nd, in ten different ten years (1981-1990) an ANN was trained to forecast the global solar radiation. Using the values for year and hour as inputs and the hourly values for Global Horizontal Radiation (Wh/m^2) as target outputs a training file for an ANN of two inputs, ten hidden nodes, and one output node. The output was an estimate of the global solar radiation (Wh/m^2) for every hour of that day, starting at 1 AM. The suggested ANN design is shown in Figure 2.

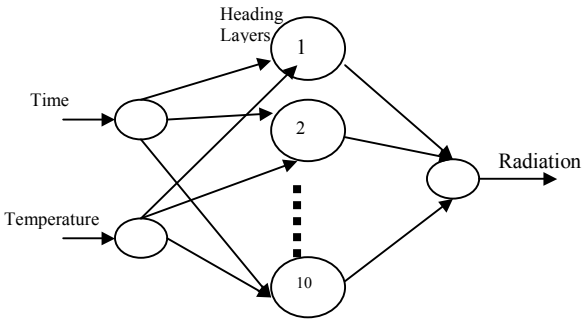

Figure 2 Suggested ANN Design

There are nine different targets, representing the data of years 1991 up to 1999, have been used as training files for the ANN, Figures 3&4 represent sample of Howard ANN output for March 2nd.

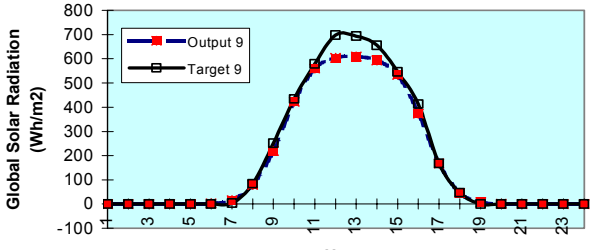

Figure 3 ANN Prediction of Solar Radiaiton for target 9

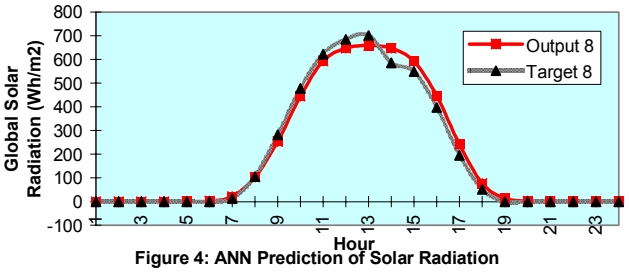

Figure 4: ANN Prediction of Solar Radiation

As shown from the previous two figures, our ANN model is almost matching the actual data and it will be more accurate if we get the full information about the cloud cover and the temperature, which we are trying to get now.

The PV mathematical model is exposed to the ANN output, solar radiation. The output of that model will be power vs. voltage curves, our goal now is to evaluate or estimate the optimal array voltage, which produce the optimal power at each specific case. GA is going to be used to overcome the multi-peak problem resulting from the fault criterion. Thousands of cases has been tested, Figure 5 represents a specific case.

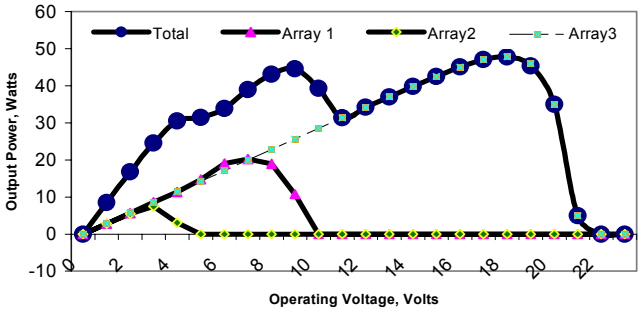

Figure 5: P-V characteristic of PV Panel at Insolation of 750 W/m^2 and T= 273° K

This particular case can be represented by a 5th order polynomial for each array and the summation of those curves have been used as an input the Genetic algorithm model, which estimates the optimum operating voltage to be 18.93 (V) and the corresponding optimum power was 48.0154 (W).

6. Conclusions

A new Artificial Neural Network based Genetic Algorithm scheme of optimal tracking of a faulted power system is introduced in this paper. The ANN was predicting the solar radiation in a sufficient manner and the GA was tracking the optimal operating point of the multi-peak power curve successfully.

7. References

[1] Mohamad H. Hassoun, " Fundamentals of Artificial Neural Networks", MIT Press, 1995.

[2] Yongho Kim; Hyunmin Jo; Deokjunj Kim: "A new Peak Power Tracker for cost-effective Photovoltaic Power system", IEEE 1996.

[3] L. Davis, "Hand book of Genetic Algorithms," Van Nostrand Reinhold, 1991.

[4] Danie B Snyman; Johan HR Enslin: "Simplified Maximum Power Point Controller for PV Installations", IEEE 1993.

Twenty Years of Service at NBNM--Analysis of Spectrolab Module

N. G. Dhere, M. B. Pandit, S. R. Ghongadi

Florida Solar energy Center

1679 Clearlake Road, Cocoa, FL 32922-5703

M. A. Quintana, D. L. King and J. A. Kratochvil

Sandia National Laboratories

P.O. Box 5800, Albuquerque, New Mexico 87185-0752

ABSTRACT

This study of adhesional strength and surface analysis of encapsulant and silicon cell samples from a Natural Bridges National Monument (NBNM) Spectrolab module is an attempt to learn from its success. The module was fabricated using polyvinyl butyral (PVB) as an encapsulant. The average adhesional shear strength of the encapsulant at the cell/encapsulant interface in this module was 4.51 MPa or ~18% lower than that in currently manufactured modules. Typical encapsulant surface composition was as follows: C 75.0 at. %, O 23.2 at. %, and Si 1.6 at. %, with Ag ~0.2 at. % (over grid lines) and small amounts of Pb ~0.5 at. % and tin over the solder bond. Representative silicon cell surface composition was: K 1.4 at. %, C 20.8 at. %, Sn 0.94 at. %, O 15.1 at. %, Na 2.7 at. % and Si 59.0 at. %. The presence of tin detected on the silicon cell surface may be attributed to corrosion of solder bond. The module differs from typical contemporary modules in the use of PVB, metallic mesh type interconnection, and silicon oxide AR coating.

1. Introduction

Amongst the three types of PV modules initially deployed at the Natural Bridges National Monument (NBNM) in southeastern Utah, those manufactured by Spectrolab have experienced performance degradation of about 1%/year maintained a fill factor of ~70% [1]. This study of adhesional strength and surface analysis of encapsualnt samples from a NBNM Spectrolab module is an attempt to understand the success as well as how the modules are degrading. The climate at Natural Bridges is hot and dry in the summer and cold and dry with some snow in the winter.

2. Morphology and Adhesional Strength Analysis

The module was fabricated using polyvinyl butyral (PVB) as an encapsulant. One hundred twenty 5.1-cm diameter silicon solar cells were arranged in six rows with twenty cells in each row. The electrical circuit had been formed by soldering short broad pieces of a metallic mesh from the ends of bus lines of one cell to the back side of the next cell (Figure 1). Most other modules manufactured after 1979, cells have been connected with solid continuous ribbons that cover most of the bus line by soldering at multiple spots or continuously. The mesh used on the Spectrolab modules appears to have accommodated the differential thermal expansion better. On the other hand, solder at multiple spots or continuously over most of the length of the bus provides benefit of redundancy.

Cell and encapsulant surfaces were examined by optical and scanning electron microscopy. Pyramidal texture was observed on the cell. Marks from a grid line of the solar cell and impressions of the pyramidal texture of the cell were seen on the encapsulant.

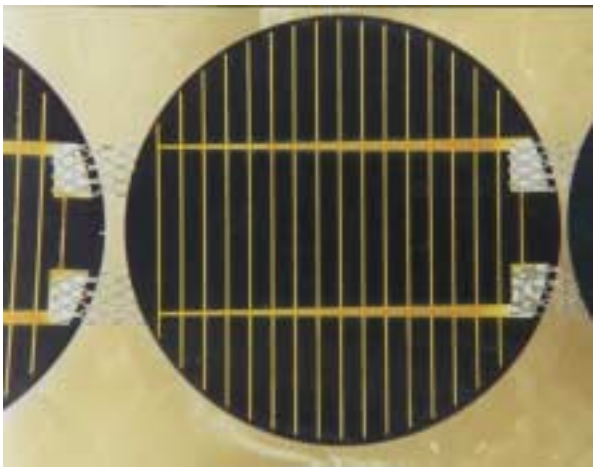

Fig 1. Front view of silicon cells in NBNM Spectrolab Module.

Coring and extraction of samples from module DA was carried out following the standard procedure using a coring drill of 1.9 cm O. D [2,3]. Aluminum nuts were glued on to samples using an ultra-high vacuum (UHV) compatible conductive epoxy glue. Because of the small diameter (5.1 cm) of the solar cells and relatively large diameter (1.9 cm) of the coring tool, only four samples could be extracted from a given cell. In spite of this limitation, a large number of samples were extracted from several cells. Moreover, the area of the sample extended from near the periphery to near the center. Hence, in the following, no distinction is made based on location of samples. Samples were twisted to failure and failure always occurred at the cell/encapsulant interface. Average adhesional shear strength was approximately 4.51 MPa.

Encapsulant samples were analyzed by X-ray photoelectron spectroscopy (XPS) and after coating with a AuPd thin layer by energy dispersive analysis of X-rays (EDAX). Silicon cell samples were analyzed by Auger electron spectroscopy (AES). The UHV compatible conductive epoxy glue and larger sample diameter were dictated by sample requirements of XPS and AES analysis.

3. XPS, EDAX and AES Analysis

Atomic concentrations of elements identified on the cell side of encapsulant sample DA39P1 that included the region over the solder bond and the bus line were as follows: C (1s), 300 eV, 75.8 at. %, O (1s), 550 eV, 21.6 at. %, Si (2p3), 110 eV, 1.7 at. %, Ag (3d5), 400 eV, 0.3 at. % and Pb (4f7), 138 eV, 0.5 at. % (Figure 2). Concentrations of elements identified

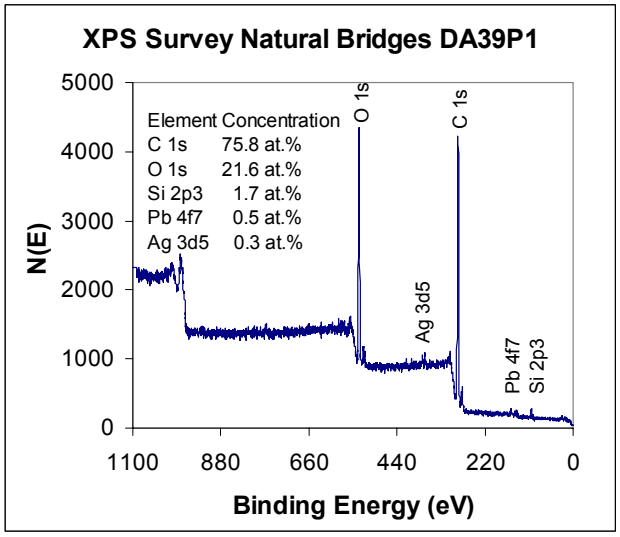

Fig. 2. XPS spectrum of encapsulant surface including the soldered contact over cell DA39 in the Spectrolab module.

on the cell side of a typical encapsulant sample DA39P3 away from solder bond were as follows: C (1s), 300 eV, 73.7 at. %, O (1s), 550 eV, 24.6 at. %, Si (2p3), 110 eV, 1.5 at. %, Ag (3d5), 400 eV, 0.1 at. % (Figure 2). Careful investigation of encapsulant surface by EDAX showed that the presence of silver, lead was restricted respectively to regions covering grid lines and solder bonds (Fig. 3). Tin was also detected on the encapsulant sample covering the solder bond region (Fig. 3).

Concentrations of elements identified on surface by AES survey of the silicon cell sample DA86AR were as follows: K 243 eV, 1.4 at. %, C 267 eV, 20.8 at. %, Sn 430 eV 0.94 at. %, O 505 eV, 15.1 at. %, Na 988 eV, 2.7 at. % and Si 1605 eV, 59.0 at. %(Figure 4). Tin must have resulted from solder bond corrosion. There was a layer of SiO_2 antireflection (AR) coating on the cell surface. SiO_2 beneath the solder bond pads was considerably thinner.

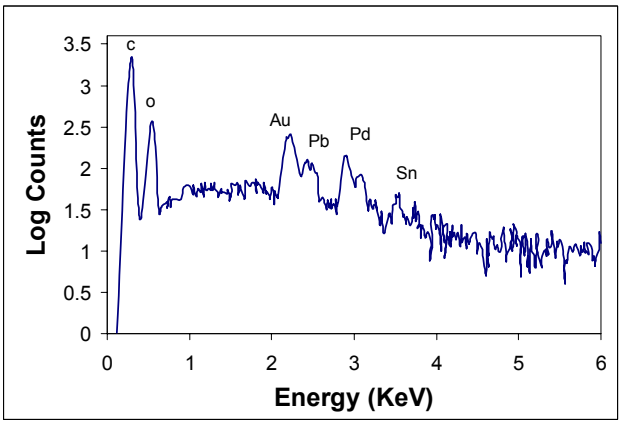

Figure 3. EDAX survey of a encapsulant surface directly over the bus line and soldered contact (Au, Pd from coating).

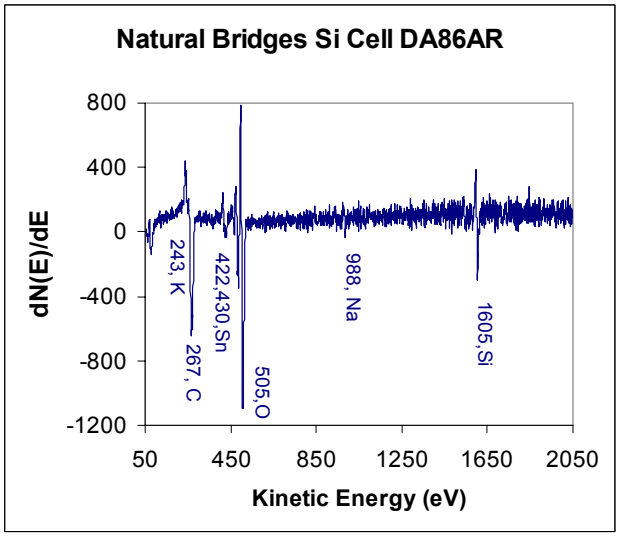

Figure 4. AES survey of a silicon cell sample surface.

4. Conclusions

The average adhesional shear strength of 4.51 MPa at the cell/encapsulant interface of the Spectrolab PV module was ~18% lower as compared to that (5-6 MPa) of new modules studied earlier at FSEC but much greater than field deployed modules with EVA encapsulant. Typical elemental concentrations on the encapsulant surface were carbon 75.0 at. %, oxygen 23.2 at. %, silicon 1.6 at. % and silver 0.2 at. %. Small amounts of lead (~0.5 at. %) and tin were detected on samples extracted from solder bond locations. The presence of silver, lead and tin was found to be restricted respectively to regions covering grid lines and solder bonds. Typical Si cell surface composition was K 1.4 at. %, C 20.8 at. %, Sn 0.94 at. %, O 15.1 at. %, Na 2.7 at. % and Si 59.0 at. %. Corrosion of solder bonds is indicated by the presence of tin on the cell surface. The module differs from typical contemporary modules in the use of PVB, metallic mesh type interconnection, and silicon oxide AR coating.

5. Acknowledgements

This work was supported by the Sandia National Laboratories.

REFERENCES

[1] S. E. Forman, M. P. Themelis, "Reliability of Terrestrial Photovoltaic Modules at Various DOE/MIT Lincoln Laboratory Test Sites", 15th IEEE PV Specialists' Conference, (PVSC), Orlando, Fl, (1981), 1106-1110.

[2] N. G. Dhere, K. S. Gadre, and A. M. Deshpande, "Durability of Photovoltaic Modules", Proc. 14th European PV Solar Energy Conf., Barcelona, Spain, (1997) 256-259.

[3] N. G. Dhere, M. E. Wollam, and K. S. Gadre, "Correlation between surface carbon concentration and adhesive strength at the Si Cell/EVA interface in a PV Module", Proc. 26th PVSC, Anaheim, CA, (1997) 1217-1220.

Validation of a Photovoltaic Module Energy Ratings Procedure at NREL

B. Marion

National Renewable Energy Laboratory

1617 Cole Boulevard, Golden, CO 80401

ABSTRACT

A procedure was developed to assign energy ratings to a photovoltaic (PV) module for five reference days that represent different climates. The procedure uses indoor tests to characterize the electrical performance of a PV module and hourly meteorological conditions from the reference days to model PV module energy. PV performance measurements from NREL's Outdoor Test Facility during the calendar year 1998 were used to validate the procedure by comparing modeled and measured energy for seven PV modules representing different technologies.

1. Introduction

This paper is a brief summary of work [1] performed to develop and validate a PV module energy rating procedure for incorporation into IEEE PAR1479, "Recommended Practice for the Evaluation of Photovoltaic Module Energy Production." The energy rating procedure may be applied to five reference days that represent a range of climatic conditions for the United States. The reference day names depict their type: Hot Sunny, Hot Cloudy, Cold Sunny, Cold Cloudy, and Nice (Cool Sunny).

The procedure uses indoor tests to characterize the electrical performance of a PV module and to determine factors to correct for non-linear performance when the irradiance and PV module temperature vary. Meteorological data from the reference days are used to calculate PV module irradiances and temperatures, from which PV module current-voltage (I-V) curves are generated, one for each hour of a reference day. The calculated PV module irradiances and temperatures are used to account for the PV module's spectral response and thermal characteristics.

2. Energy Rating Methodology

Three technical areas address implementing the procedure: (1) determining PV module temperature and irradiance correction factors and functions, (2) determining the irradiance and PV module temperature for each reference day hour, and (3) translating a reference I-V curve to the irradiance and PV module temperature conditions.

Based on Annex A2 of ASTM E1036-96 [2], the PV module temperature and irradiance correction factors and functions are determined from a matrix of short-circuit current (Isc) and open-circuit voltage (Voc) values resulting from I-V curve measurements over a range of six irradiances and six operating temperatures. Three correction factors and functions are determined: α, the Isc correction factor for temperature; $\beta(E)$, the Voc correction for temperature as a function of irradiance, E; and $\delta(T)$, the Voc correction for irradiance as a function of the PV module temperature, T.

The solar radiation and meteorological data for the reference days are used to model hourly values of the incident irradiance and the PV module temperatures. The incident irradiance is determined by:

$$E = \frac{\int_a^b E_{INC}(\lambda) SR(\lambda) d\lambda}{\int_a^b E_{REF}(\lambda) SR(\lambda) d\lambda} \cdot 1000\ \mathrm{W/m^2} \qquad (1)$$

where:

λ	=	wavelength
$E_{INC}(\lambda)$	=	incident spectral irradiance
$E_{REF}(\lambda)$	=	AM1.5 spectral irradiance [3]
$SR(\lambda)$	=	module spectral response per [4]

For series-connected multi-junction modules, the spectral response of the junction that gives the smallest numerator (current at actual conditions) is used to evaluate the numerator, and the spectral response of the junction that gives the smallest denominator (current at reference conditions) is used to evaluate the denominator. Spectral responses for two junctions are required to evaluate equation 1 if one junction is the current limiting factor at reference conditions and the other junction is the current limiting factor at actual conditions. The model SEDES2 [5] is used to calculate the incident spectral irradiance.

A model developed by Fuentes [6] for use in the simulation program PVFORM is used to determine PV module temperature.

Using the incident irradiance and the PV module temperature, Isc and Voc are calculated and a reference I-V curve is translated to determine maximum power and the current at a fixed voltage. These procedures are based on modifications to ASTM E1036-96 and use equations 2 and 3 for Isc and Voc. In equations 2 and 3, the zero subscripts denote Standard Reporting Conditions (SRC).

$$Isc = \frac{E}{E_0} \cdot Isc_0 \cdot \left[1 + \alpha \cdot (T - T_0)\right] \qquad (2)$$

$$Voc = Voc_0 \cdot [1 + \beta(E_0) \cdot (T - T_0)][1 + \delta(T) \cdot \ln(E / E_0)] \quad (3)$$

For determining the I-V curve for desired conditions, a reference I-V curve is selected for translation from the matrix of I-V curves measured to determine the correction factors and functions. The I-V curve selected for the reference is the one measured under the conditions of irradiance and temperature closest to those desired. This minimizes errors caused by the I-V curve translation not accounting for changes in fill factor with changes in temperature and irradiance.

Each I-V data pair of the reference I-V curve is then translated to the desired conditions using equations 4 and 5. The subscript R refers to the reference I-V curve, and Isc and Voc are determined with equations 2 and 3.

$$I = I_R \cdot \frac{Isc}{Isc_R} \quad (4)$$

$$V = V_R \cdot \frac{Voc}{Voc_R} \quad (5)$$

Because the translation procedure does not change the fill factor, the reference I-V curve data pair for maximum power becomes the translated I-V curve data pair for maximum power. To determine the current at a specified voltage, the current may be interpolated using the two adjacent I-V curve data pairs from the translated I-V curve with voltages above and below the specified voltage.

3. Comparison of Modeled and Measured Energy

The energy rating procedure was validated by comparing modeled and measured values of energy for seven PV modules for the calendar year 1998. The PV modules are located on the lower roof of NREL's Outdoor Test Facility, face south with a tilt from horizontal of 40°, and are operated at their peak-power point.

Table 1 provides root-mean-square-error (RMSE) and mean-bias-error (MBE) statistics for comparing hourly values of modeled and measured PV module energy production. RMSEs and MBEs are expressed as a percent of the average. The RMSEs are indicative of modeling accuracy for hourly data. Twice the RMSE gives a 95% confidence interval. The MBEs indicate the modeling accuracy for the year.

Table 1. RMSEs and MBEs for Modeled Hourly Energy

PV Module	Energy	
	RMSE (%)	MBE (%)
a-Si/a-Si/a-Si:Ge, S/N 1736	9.5	4.5
CdS/CuInGaSSe , S/N 5165	5.4	-1.8
CIS, S/N 114	5.7	1.2
Mono-Crystal Si, S/N 0442	5.8	-1.7
Multi-Crystal Si, S/N581836	5.4	-1.6
a-Si/a-Si:Ge, S/N SYS49	5.6	-1.2
CdS/CdTe, S/N 14407	5.4	1.5

Comparison of daily values of modeled and measured energy is the best indicator of the suitability of the procedure for rating PV modules for daily energy production. These comparisons were performed for the 1998 days that were similar to the reference days. The results (Table 2) were used to estimate the uncertainty of the procedure in predicting the relative performance of PV modules of different technologies. Uncertainties are higher when the a-Si PV modules are included because of the increased difficulty in modeling their spectral dependencies. Also, the procedure does not account for annealing effects and long-term degradation that may have occurred during the test period.

Table 2. Estimated Percent Uncertainty in Predicting Relative Performance by Reference Day Type

PV Module Group	Cold Cloudy	Cold Sunny	Nice	Hot Cloudy	Hot Sunny
All	7	11	8	3	6
Not a-Si	3	4	3	1	5

Because different facilities will probably perform the characterization tests and energy ratings, the overall uncertainty estimate should account for the reproducibility limit of 6.7% [2] in the measurement of electrical performance by different facilities. By defining the overall uncertainty as the square root of the sum of the squares of the reproducibility limit and the maximum uncertainties from Table 2, a statement such as the following applies: "Because of errors in measurements and energy-rating methodology, differences of 8% or less in the energy ratings of two PV modules are not significant. If one of the PV modules is amorphous silicon, differences of 13% or less in the energy ratings of two PV modules are not significant."

4. Acknowledgments

NREL staff Joe del Cueto, Keith Emery, Ben Kroposki, Daryl Myers, Carl Osterwald, and Steve Rummel were instrumental in the completion of this work.

REFERENCES

[1] Marion, B.; Kroposki, B.; Emery, K.; del Cueto, J.; Myers, D.; Osterwald, C., *Validation of a Photovoltaic Module Energy Ratings Procedure at NREL*, NREL/TP-520-26909, Golden, CO: National Renewable Energy Laboratory, 1999.

[2] ASTM E 1036-96, *Standard Test Methods for Electrical Performance of Nonconcentrator Terrestrial Photovoltaic Modules and Arrays Using Reference Cells*, West Conshohocken, PA: American Society for Testing and Materials.

[3] ASTM E 892-92, *Standard Tables for Terrestrial Solar Spectral Irradiance at Air Mass 1.5 for a 37° Tilted Surface*, West Conshohocken, PA: American Society for Testing and Materials.

[4] ASTM E 1021-95, *Standard Test Methods for Measuring the Spectral Response of Photovoltaic Cells*, West Conshohocken, PA: American Society for Testing and Materials.

[5] Nann, S.; Emery, K., "Spectral Effects on PV-Device Rating." *Solar Energy Materials and Solar Cells*, 27, pp. 189-216, 1992.

[6] Fuentes, M.K., *A Simplified Thermal Model for Flat-Plate Photovoltaic Arrays*, SAND85-0330, Albuquerque, NM: Sandia National Laboratories, 1985.

Automation for Photovoltaic Module Edge Trimming, Edge Sealing, and Framing

M. J. Nowlan, J. M. Murach, E. R. Lewis, S. F. Sutherland, and S. J. Hogan

Spire Corporation, One Patriots Park, Bedford, MA 01730

ABSTRACT

Automated systems are being developed at Spire for photovoltaic (PV) module processing, under the National Renewable Energy Laboratory's PV Manufacturing Technology project. The systems consist of two automated machines: an edge trimmer for removing excess encapsulant and back cover film from module edges after lamination, and an edge sealer and framer for dispensing edge sealant and installing frames on trimmed modules. The mechanical layout, process flow, and electrical and software approaches for these systems have been defined. Detailed design work is nearing completion, and system fabrication has begun.

1. Introduction

The PV module edge trimming, sealing, and framing processes are done after solar cells are laminated, typically to a glass sheet which forms the front cover and structural support for the module. Lamination is normally done with the module face down in a heated vacuum laminator. Both the edge trimmer and the edge sealer-framer are designed to process modules face down, eliminating the need to turn them over after lamination. Both machines use powered conveyors for module transport and a standard interface protocol, allowing them to be placed together or separately to suit the manufacturing process sequence. These machines complement the automated module testing and buffer storage systems developed earlier in this program.

The edge trimmer and the sealer-framer will handle a range of module sizes, from 30 cm x 91 cm to 102 cm x 162 cm. They will process one module every 60 s or less.

2. Edge Trimming System

The edge trimmer's main components include module transport conveyors, a module aligner, a module lift, and a robotic edge trimmer. The design is shown in Figure 1, with panels removed to show the system's components.

The module aligner is built into the input conveyor. Modules are lifted up above the conveyor by two sets of wheels that are perpendicular to the roller direction, and an arm driven by an air cylinder gently snugs the module against a pair of stops on the opposite edge of the conveyor.

After alignment, the module is transported into the trimming section on belt conveyors. Large rubber vacuum cups mounted on guided air cylinders grip the module securely and lift it up above the belt surface for trimming.

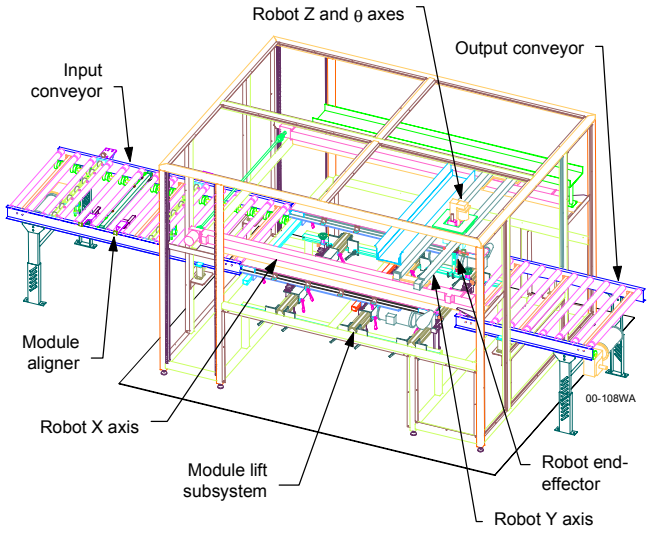

Fig. 1. Edge trimmer with panels removed.

A four axis (x, y, z, and θ) Cartesian robot transports an end-effector with two fiber optic sensors for detecting glass edges and a hot knife for trimming excess encapsulant and back cover film from the module edges. A mechanical clutch is installed between the end-effector and the robot to protect the robot from damage should a collision occur. The end-effector travels at high speed to each corner of the module. The robot moves the two optical sensors at slow speed across two adjacent glass edges at each corner. Servo position data is captured as each sensor crosses its reflectance threshold. Position data is used to calculate the location of the glass perimeter.

The perimeter data is compared against user-specified tolerances for glass size and angle of each corner. If the glass perimeter fails this dimensional inspection, the specific fault condition is displayed and the module is passed out of the system without being trimmed. If the glass perimeter passes the dimensional inspection, and if the hot knife is within a specified temperature range, the robot trims the four sides of the module with the hot knife, at a specified distance (typically 0.5 mm) from the glass edge. The robot moves the knife blade vertically in a periodic motion while trimming, to extend blade life.

After the trimming process is complete, the belt conveyors are run at high speed to remove any material that may fall on them during trimming. The lift vacuum is then turned off and the module lift retracts to place the module down on the conveyor. If the downstream process is ready

to receive a module, the belt conveyors and the output roller conveyor transport the module out of the trimming station.

3. Edge Sealing and Framing System

The edge sealer and framer's main components include module transport conveyors, a module aligner, a module lift, a robotic frame transport, a long frame feeder, a short frame feeder, corner key feeders, corner key presses, and a two-axis frame press. The design is shown in Figure 2, with panels removed to show the system's functional elements.

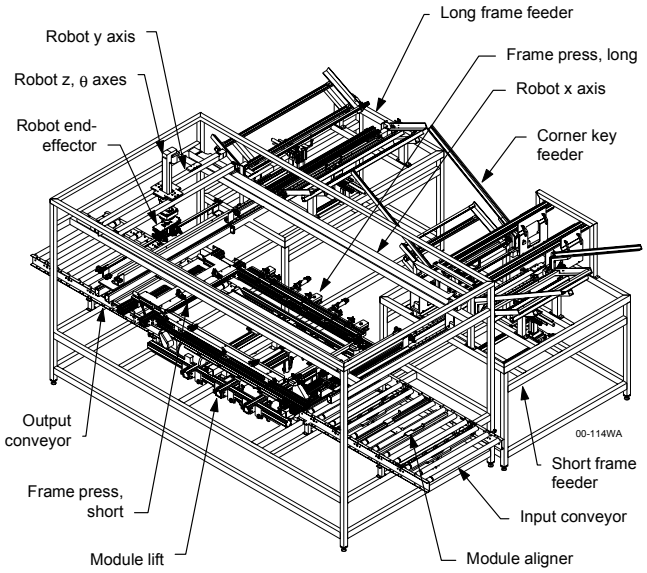

Fig. 2. Edge sealer and framer with panels removed.

The edge sealer-framer has module conveyor, aligner, and lift systems that are similar to those in the edge trimmer. The long frame feeder subassembly automatically dispenses long frame members from two stacks. Two pneumatic pick-and-place mechanisms, each with three motion axes and vacuum cups to grip the frame members, transport frames from the stacks to the carriage. The carriage drives two long frame members at constant velocity past two hot melt sealant nozzles which dispense a bead of sealant into a channel in each frame member. The frame members are then picked up by the robot and transported to the long frame press.

The short frame feeder subassembly includes similar frame feeders, carriage, and hot melt sealant dispensers as those used in the long frame feeder. Four corner key feeders and four key presses are provided to dispense L-shaped corner keys and press them into both ends of two short frame members. Two pneumatic pick-and-place mechanisms, each with four motion axes and vacuum cups to grip the frame members, transports frames from each stack to the key press, and, after the keys are inserted, from the key press to the carriage. The carriage drives two short frame members at constant velocity past two hot melt sealant nozzles which dispense a bead of sealant into a channel in each frame member. The frame members are then picked up by the robot and transported to the short frame press.

The four axis (x, y, z, and θ) Cartesian robot transports an end-effector with four mechanical grippers for holding two frame members. Frame members are picked up from either the long or short frame carriage and placed in one of four positions in the frame press: the press and static sides of the long frame press, and the press and static sides of the short frame press. The long frames are rotated 90° before placement in the press.

Vertical and horizontal compliance have been designed into the robot end-effector to reduce the tolerance requirements for frame placement in the press. A mechanical clutch is installed between the end-effector and the robot to protect the robot from damage should a collision occur.

The frame press uses air actuated clamps to hold the frame members in place prior to pressing. Pneumatic cylinders press the frame members up against the edge of the module laminate. A higher force cylinder is used for the short frame members because it also presses the corner keys (previously attached to the short frame members by the key presses) into the ends of the long frame members. After pressing, the two moving sides of the press retract and ejection pins push the framed module away from the two static sides of the press. The module is now free to be lowered down onto the belt conveyors when the lift cylinders retract. If the downstream process is ready to receive a module, the belt conveyors and the output roller conveyor transport the module out of the trimming station.

4 Controls and Software

The main controller for each system is an industrial PC running Microsoft Windows NT. An ethernet connection links the PC with process controllers for servo motor control and handling digital Input/Output. Machine control software is written in Visual Basic. A touch screen provides the user interface.

Both systems are guarded and interlocked to protect personnel from crushing and cutting hazards due to the robot and other mechanisms. Emergency stop buttons are installed around the perimeter of the machine.

5 Acknowledgment

This work was supported by the US Department of Energy under the National Renewable Energy Laboratory's Photovoltaic Manufacturing Technology (PVMaT) project.

Automation of the String Ribbon Process

R. E. Janoch, A. P. Anselmo, and J. I. Hanoka

Evergreen Solar

211 Second Avenue, Waltham, MA 02451, USA

ABSTRACT

A method for producing crystalline silicon ribbon grown in a continuous process known as String Ribbon is now undergoing automation. A newly designed String Ribbon machine and some automated features it contains are described.

1. Introduction

Evergreen Solar is now commercializing a vertical silicon ribbon growth method termed String Ribbon. This commercialization effort will be operating in the latter part of the year 2000. String Ribbon [1,2] produces silicon ribbon in a process illustrated in Figure 1.

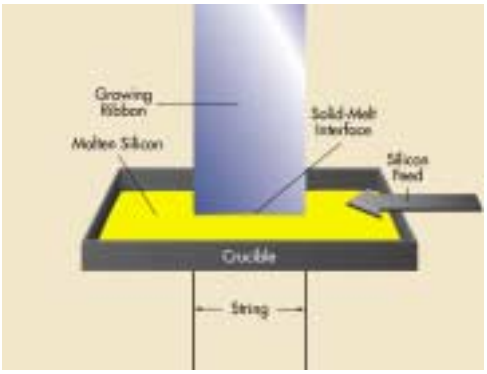

Figure 1. The String Ribbon process.

Spools of high temperature string material are used to feed the strings continuously to provide edge stabilization for the growing ribbon. In June, 1998, Evergreen Solar began a three year PVMaT subcontract from NREL, having as one of its principal goals the automation of the String Ribbon process.

The String Ribbon process is an inherently robust one wherein the ribbon is grown on a continuous basis, 24 hours a day, by production operators. Each ribbon machine produces a single ribbon. Machine throughput is then determined by the speed of growth and the ribbon width. For a 10 MW plant, Evergreen is planning on installing 120 ribbon machines according to the new design described below.

2. New Furnace Design

As part of the PVMaT work, the ribbon machine was completely redesigned. This was done in order to facilitate automation and operator productivity, and to reduce the capital cost per machine. While the size and cost of an individual machine was small in comparison to any other known ribbon techniques, the drive to lower costs even further was behind this redesign effort. A photograph of the new machine is shown in Figure 2.

Figure 2. Furnace with ribbon growing from the machine.

The newly designed machine has these features: the outer, water cooled chamber, is 1/3 the cost of the previous machine; all the feedthroughs and access openings are now much more tightly sealed; the feeder for the continuous supply of the feedstock silicon is more compact; the spool size for the strings has been enlarged such that spools are changed about three times less frequently; all controls are run from a single PLC that can be inputted into a central computer; viewports have been enlarged to make the

machine more user friendly; and growth of wider ribbon can be accommodated quite readily.

3. Automation

At present, ribbon that is grown and used for our production line is 300 μm thick. Uniformity of ribbon thickness across the width of the growing ribbon is important for high yields. Prior to this PVMaT contract, thickness was measured manually and temperature adjustments were made manually when warranted based on operator input. Both inputs and outputs are highly subjective from operator to operator.

The first task in the automation project was the design and implementation of an automatic thickness measurement system. This method was found to improve repeatability and substantially reduce the standard deviation of the thickness measurement in comparison to the manual procedure. The new system also found subtle variations in the growing ribbon which were not able to be detected via manual measurement of the ribbon.

The second task was to develop an algorithm for controlling ribbon thickness. Ribbon thickness is typically maintained by manually varying the inputs to the system (four elements which modify the thermal environment of the system), in response to the outputs of the system (the thickness of the ribbon taken intermittently by hand at three points).

In order to automate this process, a model of how the system reacted at each of the output points as a function of each input was developed. An objective process function was also created based on the outputs (the thickness of the ribbon at three points) and the desired target thickness; this function minimizes as the process improves towards the target thickness. The model, coupled with the objective process function, allowed the prediction and ranking of which input changes would achieve the best output. By implementing this prediction and ranking scheme on programmable logic controller (PLC), control changes were then made to the system in a consistent manner. Figure 3 shows how the thicknesses at three points on the ribbon change with time, while the objective function is reduced during the automatic control of a furnace.

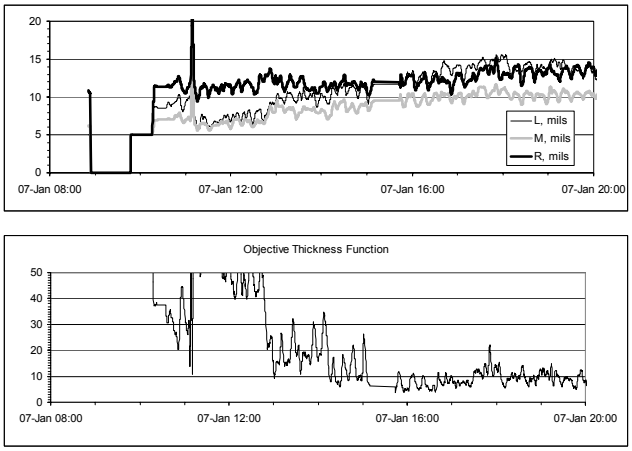

Figure 3. Thickness and objective function as a function of time (under automatic control) showing how the ribbon proceeds towards the target thickness.

Summary

A new ribbon growth machine, designed and built under a PVMaT subcontract has been successfully operated in production and will be replicated in Evergreen's new factory. Automation of ribbon thickness control has been attained for this furnace.

REFERENCES

[1] Wallace, R.L, Janoch, R. E. , and Hanoka, J. I. Second World Conference And Exhibition on PV Solar Energy Conversion, Vienna, July 1998.

[2] Wallace, R.L., Hanoka, J. I., Narashimha, S., Kamra, S. and Rohatgi, A. 26th PVSC Anaheim, CA 1997.

Acknowledgement

This work is funded under a PVMaT subcontract, ZAX-8-17647-07. We wish to thank Dr. Martha I. Symko-Davies, our contract monitor, for her support and encouragement.

Development of Commercial Building Products Using Solarex Thin Film Photovoltaics

John H. Wohlgemuth
BP Solarex
630 Solarex Court
Frederick, MD 21703

ABSTRACT

This paper reports on the work performed by BP Solarex under DOE Cooperative Agreement #DE-FC36-97GO10245. The objective of this PV:Bonus program is to develop building integrated photovoltaic (BIPV) products using tandem junction amorphous silicon modules produced in the Solarex factory in Toano, VA. BP Solarex is supported in this effort by Kawneer, Solar Design Associates and Viracon. The team is developing a photovoltaic spandrel curtain wall panel, a sunshade with integrated PV module and a semi-transparent, photovoltaic viewglass panel.

1. Introduction

The design of these BIPV products required a number of modifications to the thin film plates including:

- Size flexibility - The ability to produce PV plates in smaller sizes than the one size available at the beginning of the program.
- Strengthened Glass - Several of the products, particularly the view glass product, require the use of heat strengthened glass.
- Semi-transparency - The potential market for BIPV will be much larger if the PV plates can be made to transmit a significant fraction of the incident light.

Product development efforts include Viracon work to integrate PV module insulated glass (IG) units, Kawneer efforts to design a PV sunshade and the need for a module edge connector.

2. Size Flexibility

The Toano factory was originally designed to produce only one size modules (~2 ft. by 4 ft.). This size inflexibility severely limits applying these plates to buildings, where size is often a function of the building design and structure. A process has been developed that allows plates to be cut after fabrication, thereby allowing for flexibility in size. This process has been implemented on a commercial basis with various sizes of plates now available for sale.

3. Heat Strengthened Glass

The standard product made in the Toano plant is a glass-EVA-glass laminate made from annealed glass. The high-temperature processes used to deposit the TCO and to fire the frit used for electrical connections, precludes the use of tempered or heat strengthened glass. However, many BIPV applications require the use of heat strengthened glass because of building codes and because of technical demands on the structure. Efforts during this program have lead to the development of a process for using heat strengthened as the superstrate onto which the thin film layers are deposited. This process must now be optimized for use in manufacturing.

4. Semi-transparency

Our marketing analysis indicated that a BIPV product that allows light transmission could have a large market. While the standard thin film plates are not semi-transparent, a process has been developed that allows light through. As long as the percentage of light is held fairly low (5 to 10%) the power loss is approximately the same percentage. These modules can work very well in overhead glazing where the main issue with standard glass is often reducing the amount of transmitted light in order minimize the heat load.

Besides the standard pattern with uniform transmission, the process also works to provide for a variety of interesting patterns. Several are shown in Figures 1 and 2.

Figure 1. Department of Energy Crest on a working PV module.

There are many possible ways that this technology can be utilized in building design. It gives the architect a new tool for design in terms of cosmetics and functionality. This technology also integrates well into IG units as will be discussed in the next section.

Figure 2. A commercial application

5. Insulated Glass Units

PV modules can be integrated into IG units. A critical factor involved in this integration is the backsheet of the module. Since these thin film modules normally use a glass substrate, they can be incorporated into IG units in the same way that a standard piece of glass is incorporated into such a unit. The major issue with this construction is how to get the electrical power out of the module without violating the seal of the IG unit. This has been solved by the use of an edge connector. The connector brings the electrical power out between the two pieces of glass and therefore does not interfere with the manufacture or performance of the IG unit.

In their work on development of PV IG units, Viracon has found that one of their IG units with a semitransparent PV module on the front and a low e-coating on the third glass surface, has thermal properties similar to their standard "SuperWindow" construction.

6. Sun Shades

Many architects and designers use sunshades to differentiate their wall elevation aesthetically, as well as to reduce solar heat gain. For some, this is a more desirable method of reducing glare without employing reflective glass while still allowing a high degree of natural daylighting. Most sunshade systems are custom and therefore expensive design options. A pre-engineered sunshade system that has design flexibility engineered into the product will provide a balanced approach to cost and aesthetics. Additionally, a pre-engineered sunshade system that is packaged as part of the curtain wall system allows the architect/owner the confidence of single source responsibility.

As part of the PV:Bonus program Kawneer has designed a PV sunshade system that integrates into their 1600 Curtain Wall System. Each blade of the sunshade carries a thin film module. The system is designed to allow installation at the proper angle for optimum shading and PV collection. Figure 3 shows a set of blades with PV modules attached. Figure 4 shows how the sunshade is attached to the curtain wall.

Figure 3. Sunshade blades with thin film modules attached.

Figure 4. Sunshade structure from underneath.

7.Future Efforts

The team is now designing and building the first working prototypes of the sunshade and a curtain wall system incorporating vertical and overhead glazing semi-transparent PV IG units. These prototypes will be used to verify construction details, as models and for testing. These systems must meet the structural requirements of building codes as well as the electrical requirements of the NEC. Our plan is to get each system reviewed, tested and listed by UL.

Acknowledgements

The author would like to acknowledge the work of Bob Oswald and Mark Gasson at BP Solarex, Richard Braunstein at Kawneer, and Peter Anderson at Viracon.

High-Performance Building Design: Keys to Success

Sheila J. Hayter, P.E.
Paul A. Torcellini, Ph.D., P.E.

National Renewable Energy Laboratory (NREL)

1617 Cole Blvd.
Golden, CO 80401

ABSTRACT

The energy-design process optimizes the interaction between the building envelope and systems. Buildings designed and constructed using this process can save between 30% and 75% in energy costs. In addition, these buildings can be constructed for the same, or nearly the same, first cost as a non-energy-efficient building with no sacrifice of comfort or functionality. A design team must set energy efficiency goals at the beginning of the pre-design phase. Detailed computer simulations are used throughout the design and construction phases to ensure the building is optimized for energy efficiency, and that changes to the design do not adversely affect the energy performance. Properly commissioning the building and educating the building operators are the final steps to successfully constructing a low-energy building. This paper defines the energy-design process and shows actual projects in which energy costs were reduced by more than 60%.

1. Energy-Design Process

To successfully realize a low-energy building, the design team, which consists of the owner, architect, and engineer, must make cost-effective energy minimization a high-priority design goal. Low-energy design is not intuitive. The building's energy use and energy cost depend on the complex interaction of many parameters and variables that can only be effectively evaluated with hourly building energy simulation tools. The nine-step energy design process described here is a guideline for designing, constructing, and commissioning low-energy buildings [1]. The design team must fully execute each step to ensure the successful design of a low-energy building. At least one team member should act as the energy consultant and evaluate all design decisions using computerized tools.

Pre-Design Steps

1. Simulate a base-case building model and establish energy use targets
2. Complete parametric analysis
3. Brainstorm solutions with all design team members
4. Perform simulations on base-case variants considering economic criteria

Design Steps

5. Prepare preliminary architectural drawings
6. Design the heating, ventilating, and air-conditioning (HVAC) and lighting systems
7. Finalize plans and specifications

Construction/Occupation Steps

8. Rerun simulations before making construction design changes
9. Commission all equipment and controls. Educate building operators to ensure that they operate the building as is intended.

2. Thermal Test Facility

NREL's Thermal Test Facility (TTF) is a 10,000-ft^2 (929-m^2) open laboratory building with office and support areas. A stepped building design accommodates clerestory windows for the mid- and high-bay laboratory areas and maximizes the building's daylighting potential. Daylighting meets all the TTF lighting needs except in the minimal-use areas of the building's core (e.g., restrooms, electrical rooms). Daylighting-occupancy sensors control operation of the electric lighting in the daylit areas, maintaining 50-foot-candles (538 lux), and occupancy sensors govern electric lighting use in other areas. The total lighting load of this building is approximately 75% less than in an equivalent, non-daylit building.

Reducing unwanted summer solar gains with engineered window overhangs and lowering internal gains by offsetting electrical lighting with daylighting, reduced the building cooling load by 43%. Installing a direct/indirect evaporative cooling system, which is less expensive to operate compared to a conventional chilled-water or DX system, further reduced cooling costs.

The heating loads in the building increased slightly when the lighting internal gains were eliminated. Storing winter passive solar gains in the high thermal mass of the building envelope offset some of this increase.

Figure 1 shows that the total energy cost of the TTF was reduced by 63% compared to a code-compliant base-case building [1].

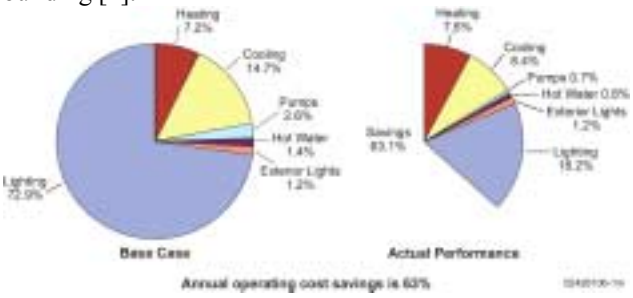

Fig. 1. TTF energy cost savings

3. BigHorn Center

The BigHorn Center is a collection of five retail spaces in Silverthorne, Colorado. The complex was constructed in three phases. Phase III houses a 17,000-ft^2 (1579-m^2) hardware store and support areas and a 22,000-ft^2 (2044-m^2) building materials warehouse. This phase incorporates the most aggressive sustainable design strategies of the three phases. These strategies include daylighting, advanced lighting technologies, natural ventilation cooling, transpired solar collector, building-integrated photovoltaics (PV), improved envelope features, and integrated controls.

Daylighting combined with energy-efficient lighting fixtures and advanced lighting system control is expected to reduce building lighting loads 79%. Decreasing lighting loads has the added benefit of reducing the internal gains on the building during the summer when the cooling loads are the highest. Glazing selection and overhang lengths were engineered to work with the daylighting and thermal requirements of the building. These features minimized the cooling load so that natural ventilation can meet the load. Natural ventilation occurs when the building control system automatically opens the clerestory windows to induce the stack effect in the building.

Radiant heating systems meet heating loads in the store and warehouse. A transpired solar collector preheats ventilation air for the warehouse. The building control system maximizes the ability of the roof-integrated PV system to reduce building electrical demand.

Figure 2 shows simulation results indicating that the BigHorn Center Phase III energy costs are expected to be 62% less than the base-case building [2,3].

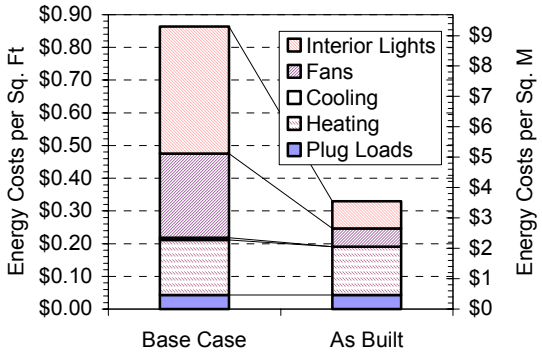

Fig. 2. Energy cost performance of the code-compliant base-case building compared with the as-built building.

5. Zion National Park

The Zion National Park Visitor Center and Comfort Station will be two of the National Park Service's (NPS) most efficient buildings. The design team optimized the performance of aggressive low-energy design strategies into the 7600-ft^2 (706-m^2) Visitor Center and 1100-ft^2 (102-m^2) Comfort Station. Design features in both buildings include daylighting, Trombe walls for passive solar heating, downdraft cooling towers for natural ventilation cooling, energy-efficient lighting, and advanced building controls.

The NPS plans to install a 7.5-kW, grid-connected PV system on the roof of the Visitor Center. Because of the low-energy design, designers anticipate that the PV system will export power to the grid after meeting all building electrical loads.

The optimized Visitor Center is smaller than the initial building. Designers saved space by moving permanent exhibits outdoors and eliminating building mechanical systems. The estimated construction cost of the optimized building is 40% less than the initial design and 10% less than a non energy-efficient building whose floor area is the same as the optimized design (Fig. 3).

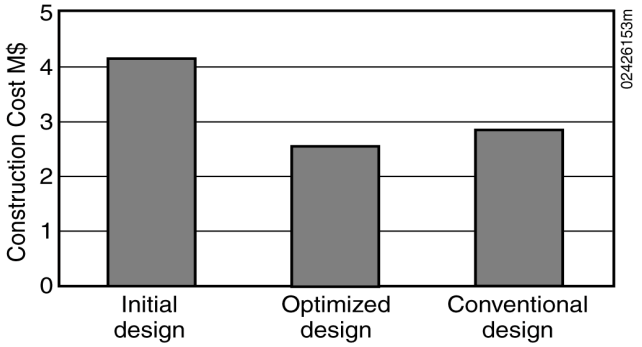

Fig. 3. Visitor Center construction cost comparison

6. Performance Monitoring

The TTF performance reported in this paper is based on actual data recorded for the building. Construction for the BigHorn Center and the Zion National Park Visitor Center will be completed in April and May 2000, respectively. Upon completion, researchers will monitor and evaluate their performance as well. The performance data will help researcher verify the accuracy of the simulations used to design the buildings. Researchers will also use the data to perfect the building control strategies and further improve performance.

7. Acknowledgements

The National Renewable Energy Laboratory's High-Performance Buildings Research Project provided support for the energy design of the buildings described in this paper. The U.S. Department of Energy provides funding for this activity from the Office of Building Technology, State and Community Programs.

8. References

[1] Torcellini, P.A., S.J. Hayter, R. Judkoff: "Low-Energy Building Design—the Process and a Case Study," *ASHRAE Transactions*, V 105, Part 2, (1999) 802-810.

[2] Hayter, S.J., P.A. Torcellini, R. Judkoff: "Effective Use of Daylighting in a Retail Space," 2000 ACEEE Summer Study on Energy Efficiency in Buildings (2000), to be published.

[3] Hayter, S.J., P.A. Torcellini: "A Case Study of the Energy Design Process Used for a Retail Application," 2000 ASES National Passive Solar Conference Proceedings (2000), to be published.

High Rate CIGS Processing on Flexible Substrates

Jeff Britt, Scott Wiedeman, Doug Mason, and Robert Wendt

Global Solar Energy
5575 So, Houghton Rd.
Tuscson, AZ

ABSTRACT

GSE has developed sources and control techniques for high rate co-evaporation of CIGS on moving substrates. Device quality CIGS has been deposited at rates that are up to an order of magnitude greater than typical laboratory-scale evaporation processes. Resultant CIGS films deposited at high rates are uniform, large grain and single phase. Average small area device performance for controlled runs is between 9 and 11%.

1. INTRODUCTION

Multi-source co-evaporation has proven to be the best process to deposit CIGS for high efficiency devices. Evaporated CIGS films exhibit a uniform, large grain structure conducive to high efficiency. Even with the excellent results achieved in laboratory-scale reactors, most industrial companies have elected either selenization of binary metallic stacks or sequential selenization for depositing the CIGS layer. This in largely due to the engineering and control issues associated with transitioning evaporation processes to large-scale manufacturing.

GSE has designed and built large area evaporation sources for depositing CIGS. Reproducible device quality CIGS has been deposited with efficiencies approaching 12% using these large area evaporation sources in production-based roll-to-roll equipment. Additionally, GSE has been able to deposit large-grain uniform CIGS films with total deposition times of up to an order of magnitude less than typical times reported for laboratory-scale evaporation processes.

In this paper, results for CIGS deposited in production-based equipment will be presented. Included are the effects of deposition time on film morphology, through-thickness composition, and device performance. Results presented are for a specific source sequence and material delivery profile and show the effect of reaction time but do not necessarily represent the best results achieved in production equipment.

2. CIGS DEPOSITION APPROACH

In production based-equipment, CIGS is deposited by roll-to-roll movement of continuous flexible Mo coated substrate over spatially located effusion sources. Material delivery rates of the effusion sources are held constant but the forming CIGS film undergoes composition evolution as a consequence of the source ordering and spacing. To date CIGS has been deposited on roll lengths of up to 500-ft. Typical lengths are 200 to 300-ft.

Resultant CIGS films were characterized by cross-section SEM examination of grain structure, EDS composition analysis, and by device J-V measurements. In some cases, X-ray diffraction measurements and Auger depth profiles were conducted, courtesy of the characterization group at NREL.

3. RESULTS

3.1 CIGS Uniformity

Compositional uniformity through the CIGS film thickness is important to optimize device efficiency. The rapid film growth rates and low substrate temperatures required for high rate manufacturing on the flexible web limit both the time and temperature normally available to assure thorough mixing and reaction through diffusion.

However, in production-based equipment with the web moving at 15 cm/min and substrate temperatures near 400°C, fairly uniform compositional profiles through the thickness were achieved (Fig. 1). The near surface region of the CIGS film exhibits a significant gradient in Ga/(In+Ga). Modifications are planned to further alleviate undesirable compositional gradients.

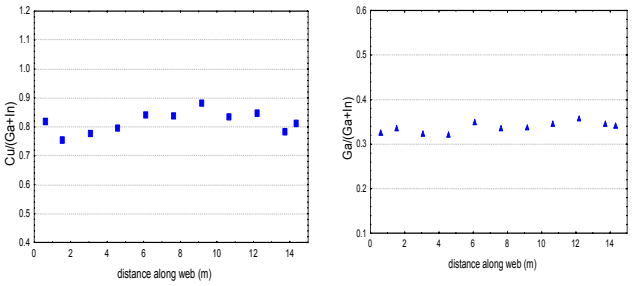

Figure 1. CIGS composition uniformity

3.2 CIGS Film Properties

CIGS has been deposited at web speeds of up to 60 cm/min. It should be noted that the deposition rate includes the metals deposition (Cu, In and Ga) and exposure to Se. No post deposition heat treatment was performed.

A SEM cross-section of a CIGS film deposited at 30-cm/min is shown in Figure 3.2a, and can be compared to material deposited at the standard rate of 15-cm/min shown in Figure 3.2b. Morphology of the film appears to be excellent with a large, dense grain structure. In fact, the morphology of the film deposited at 30-cm/min appears to be better than films deposited for slower web speeds. The film thickness is approximately 1.8 µm.

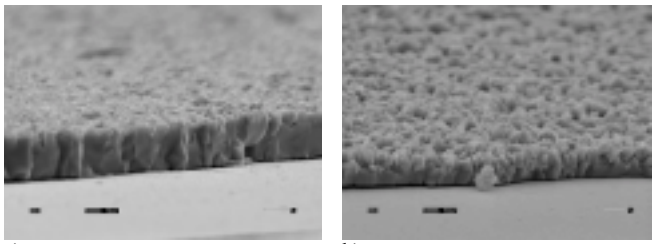

a) b)

Figure 2. Cross-section SEMs of a CIGS films deposited at a) 30 and b) 15-cm/minute.

Utilizing the capability of the evaporative sources under development at GSE, we have deposited CIGS films **at web speeds of up to 60 cm/min**. Absorber formation in such brief times might be expected to affect the polycrystalline material growth and film morphology. Additionally, composition gradients that occur as a result of the source sequence during the deposition may be expected to be affected given such short time in the high temperature Se environment. However, the XRD data shown in Figure 3 appears to indicate little difference in the crystalline orientation and phases formed at web speeds between 15-45 cm/min.

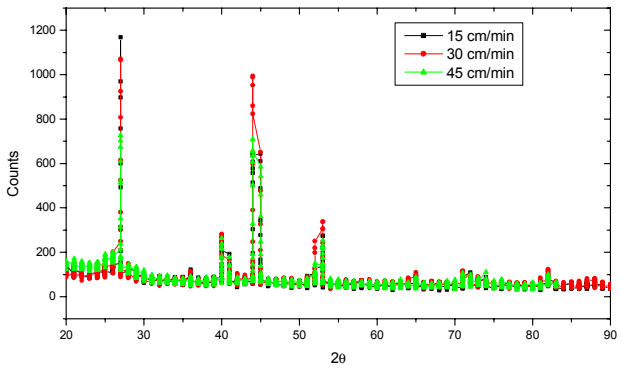

Figure 3. XRD spectra of CIGS deposited at high rates.

Critical composition ratios from Auger depth profiles have been measured on CIGS deposited rates of 15, 30, and 45 cm/min. (Figure 4). There are no major qualitative differences in the elemental profiles between the films. Taken together with the x-ray data, diffusion processes do not appear to limit the formation rate of CIGS.

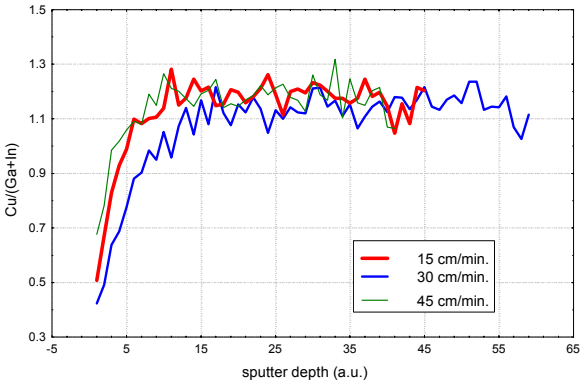

Figure 4. Cu/(Ga+In) Auger profiles for CIGS deposited at hi-rates

3.3 Device Properties

The device results for the web speed tests described here, conducted in close time proximity, are shown in Fig. 5. While the conversion efficiencies are similar (between 8-9%) at 15 and 30 cm/min., characteristic parameters are substantially different. The reasons for the differences are not yet understood.

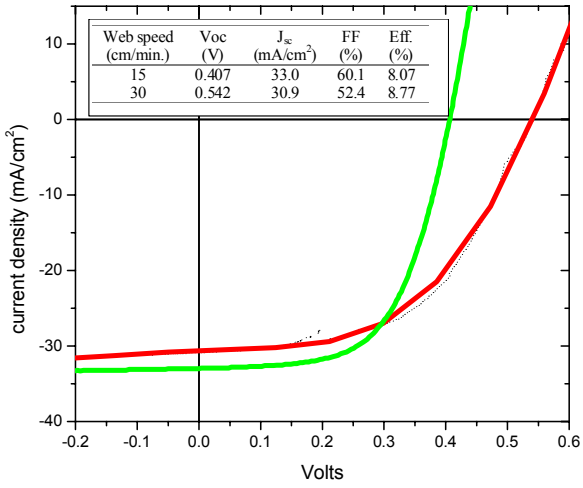

Figure 5. J-V Characteristics of devices from CIGS films deposited at 15 and 30 cm/min.

4. CONCLUSION

GSE has developed sources and control techniques for high rate co-evaporation of CIGS on moving substrates. Resultant CIGS films deposited at high rates exhibited large equiaxed grains similar to laboratory-scale processes. XRD indicated single phase material and Auger indicated reasonably uniform through thickness composition. Using the above effusion sources, GSE is currently depositing up to 1000-ft/week of CIGS with run lengths averaging 200-ft.

5. ACKNOWLEDGEMENTS

The authors would like to acknowledge funding support from DARPA Agreement MDA972-95-C-0036, NREL Subcontracts ZAX-8-17647-11 and ZAK-8-17619-04, and Unisource Energy.

Monolithically Interconnected Silicon-Film Module Technology

P.E. Sims, E.J. DelleDonne, A.E. Ingram, D.H. Ford, J.P. Yaskoff, J.A. Rand, R.B. Hall, and A.M. Barnett
AstroPower, Inc. Solar Park, Newark, Delaware 19716-2000, U.S.A

Abstract

AstroPower is employing Silicon-Film™ technology toward the development of an advanced thin-silicon-based, photovoltaic module product. This module combines the design and process features of advanced thin-silicon solar cells, is light trapped, and integrated in a low-cost monolithic interconnected array. This advanced product includes the following features:

- silicon layer grown on a low-cost ceramic substrate.
- a nominally 50 micron thick silicon layer with minority carrier diffusion lengths exceeding 100 microns.
- light trapping due to back- surface reflection and random texturing.
- back surface passivation.

These performance design features, combined with low-cost manufacturing using relatively low-cost capital equipment, continuous processing and a low-cost substrate, will lead to high performance, low-cost photovoltaic panels.

Approach/Background: Thin film polycrystalline silicon grown on a low cost substrate is one of the most sought after paths to low cost photovoltaic power. Cost reductions can be realized in module fabrication through the use of large-area, series-interconnected submodules. This design incorporates a method of partitioning the thin-film photovoltaic layer into sub-elements and reconnecting them as a series array. The sub-element device design consists of a thin (35-50 μm) polycrystalline silicon layer grown on a low-cost substrate. The thin silicon device structure allows the use of imperfect materials and increased doping levels, and lowers cost by minimizing the use of relatively expensive feedstock material. Diffusion lengths equivalent to twice the device thickness are required to assure high carrier collection through the bulk of the base layer.

The solar cell device structure incorporates light trapping and back surface passivation to improve energy conversion efficiency. Light trapping is achieved by using diffuse reflection from a randomly textured back surface resulting in enhanced optical absorption of weakly absorbed light and improved current generation. Electrical passivation of the back surface is achieved by minimizing surface recombination velocity at the barrier/silicon interface. Back surface passivation results in improved voltage, fill factor, and current.

Status/Accomplishments: Accomplishments for FY99 include the following:

Ceramic: A ceramic substrate has been developed that meets the chemical, mechanical, electrical, thermal, and economic criteria required for the growth and device processing of thin films of silicon. The size of this ceramic is presently 15 x 15 cm and the materials cost is on the order of $10 per square meter. The reflectance for a ceramic-air interface is near 100%. There is no evidence of contaminants in silicon films due to the ceramic after high-temperature processing. The ceramic-silicon structure is compatible with standard laboratory wet processes.

Silicon Deposition: Three new deposition systems were constructed during FY99. A small prototype CVD system was constructed based on a tube geometry. This system was capable of depositing silicon on 2 x 4 cm substrates. A larger CVD system was then constructed using a modification of the Silicon-Film™ technology. This system is capable of depositing on 15 x 15 cm substrates. A semi-continuous proprietary deposition system was constructed which is capable of high-speed deposition of silicon on multiple 15 x 15 cm ceramic substrates. AstroPower is also collaborating with the Institute of Energy Conversion at the University of Delaware to evaluate the potential of using hot-wire CVD to deposit silicon on ceramic substrates.

Silicon Solar Cell Fabrication: Standard laboratory procedures have been employed to evaluate silicon-on-ceramic layer quality. These processes have been found to be adequate and do not require modification due to the presence of the ceramic. Work has commenced on the identification and evaluation of high-temperature conductive inks that can be screen printed on the ceramic prior to the silicon deposition process.

Solar Cell Device Results:

- Achieved a short-circuit current density of 25.8 mA/cm^2 on a 0.6 cm^2, 20 micron thick silicon-on-ceramic device (NREL measurement). The quantum efficiency characteristic for this device suggests that a high level of light trapping and back surface passivation has been achieved (AstroPower measurement).
- Demonstrated a 9.1% efficient, 0.988 cm^2 silicon-on-ceramic device. The solar cell parameters for this device were: Voc = 0.567 V, Isc = 0.0207 A, Jsc = 20.8 mA/cm^2, FF = 76.9%, Imax = 19.0 mA, Vmax = 0.472 V, Pmax = 8.99 mW (NREL measurement).
- Demonstrated a four element interconnected silicon-on-ceramic array which did not display any degradation due to the interconnection process (AstroPower measurement).

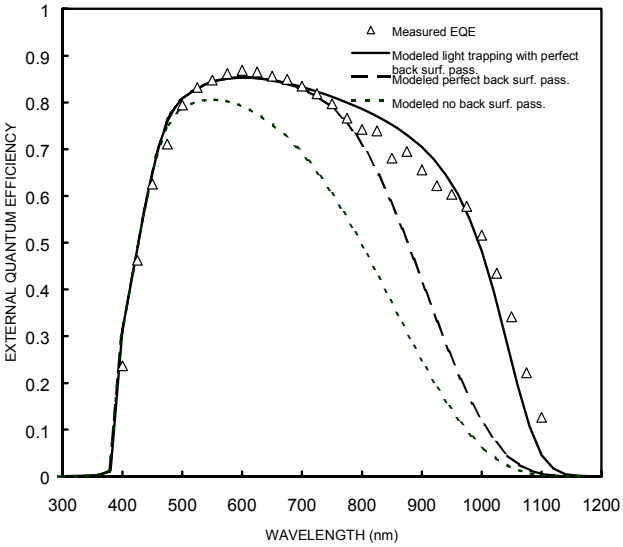

Figure 1. External quantum efficiency curve containing both experimental and modeled data for the high-current solar cell discussed above.

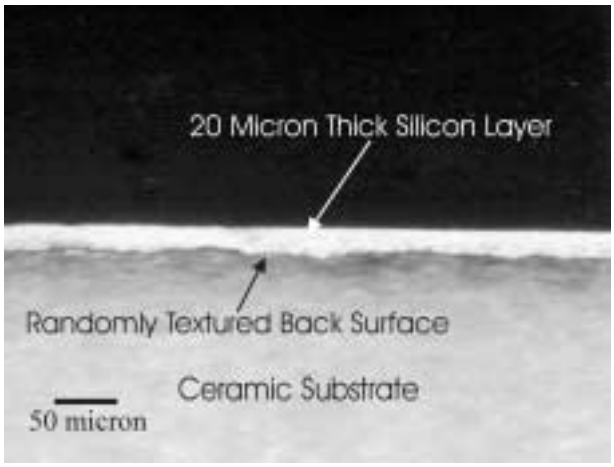

Figure 2. Cross-sectional micrograph of a thin-film polycrystalline silicon layer on a ceramic substrate.

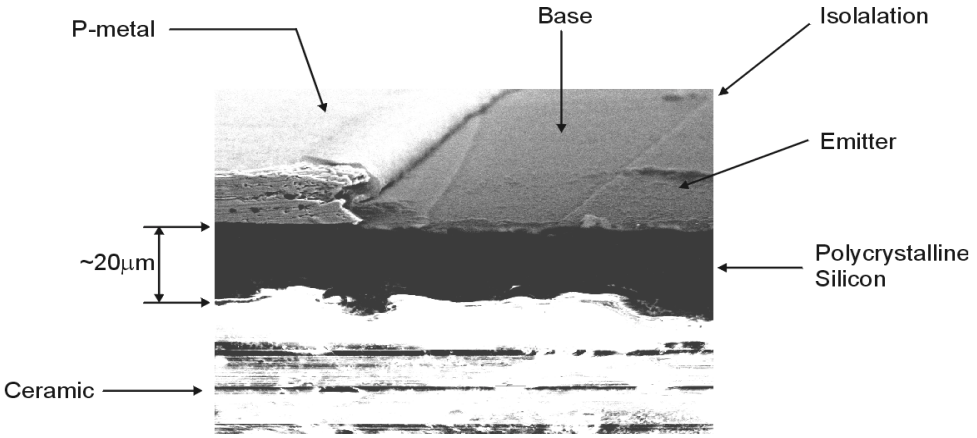

Figure 3. Cross-sectional SEM micrograph of a 20μm thin-film polycrystalline silicon layer with a p-contact and isolation region on a ceramic substrate

Production of Solar Grade Silicon by Upgrading MG Silicon in Charges up to 140 Kg

C. P. Khattak, D. Joyce and F. Schmid

Crystal Systems, Inc.

27 Congress Street, Salem, MA 01970

ABSTRACT

Upgrading commercially available as-received metallurgical grade (MG) silicon using refining in the molten state followed by directional solidification has resulted in reduction of all impurities including boron (B) and phosphorus (P). The most difficult element, B, was reduced to 1-ppma level for a 1-kg charge. Based on this result, the charge size was scaled up to 140 kg and B and P were reduced to <10 ppma each and other impurities to <1 ppma. The simple refining procedures were very effective, and can lead to production of solar grade silicon feedstock for photovoltaic applications.

1. Introduction

Photovoltaics for power generation are based on crystalline silicon technologies. The growth rate would increase if low-cost solar grade silicon feedstock were commercially available. Almost all feedstock used by the photovoltaic industry relies on excess capacity, rejects and scraps from the semiconductor industry. Therefore, the supply and price of silicon feedstock are profoundly affected by the demand of the semiconductor industry. The purity of silicon feedstock required by the photovoltaic industry is not as high as that needed by the semiconductor industry. The alternative to semiconductor silicon feedstock - metallurgical-grade (MG) silicon - is not sufficiently pure for solar cell applications. Several technologies were adapted in the 1970's to produce low-cost silicon feedstock, but none of these technologies was commercialized. Now that it is recognized that crystalline silicon will be the mainstay for the photovoltaic community, it is imperative to develop a solar-grade silicon feedstock that eliminates the need for the photovoltaic community to compete in availability and price with the semiconductor industry.

Upgrading MG silicon is attractive because the starting material is available in very large quantities and at low cost. The photovoltaic community even at GW levels will use only a very small portion of the entire production of MG silicon. Based on chemical analysis of MG silicon, it is clear that most impurities could be effectively reduced by directional solidification. Two impurities that cannot be reduced by directional solidification are boron (B) and phosphorus (P) whose segregation coefficients are 0.8 and 0.35, respectively. Therefore, the simplest approach for upgrading MG silicon is to carry out refining of the molten state and follow it with a directional solidification step. The U. S. Department of Energy through the National Center for Photovoltaics funded a Photovoltaic Manufacturing Technology (PVMaT) program for refining MG silicon in the molten state to produce solar grade silicon. This paper reports the work carried out so far using refining processes to reduce impurities, especially B and P. In addition to B and P, other impurities have also been refined. The charge size has been scaled up to 140 kg MG silicon and the B and P have been reduced to <10 ppma levels.

2. Background

For solar grade silicon it is necessary to reduce each metallic impurity, especially B and P, to <1 ppma level,. It is expected that this feedstock will be used initially for ingot growth where further directional solidification will reduce all impurities except B and P to much lower levels. Typical concentrations of B and P in MG silicon are 20 – 60 ppma. The emphasis was to use thermo-chemical reactions that have been proven in laboratory scale experiments[1]. The approach pursued involved purging moist reactive gases through the melt and reactions of the melt with slag compositions. After the refining step, the melt was directionally solidified. This approach was used with a 2-3 kg charge and all metallic impurities were reduced to <1 ppma level. This approach was different from the Elkem[2], Kawasaki[3] and other approaches, even though the goal for all these technologies was to develop solar grade silicon feedstock.

3. Theoretical Analysis

Thermodynamic calculations were performed using a database involving silicate and silicon liquid solution models to delineate kinetic from equilibrium effects. Gas speciation reactions were analyzed to delineate local equilibrium effects. Initially, the system Si-B-P-H_2O-Ar was studied. Subsequently, components were added, and the Si-B-P-O-H-Cl-Ca-Al-Fe system was evaluated. Refining approaches such as volatilization, slagging and segregation were analyzed for removing impurities from liquid MG silicon[4]. Experimental results and further modeling support the concept that the removal of impurities from liquid silicon can be a multi-step process involving several sequential speciation reactions that produce impurity-enriched phases. Transport of these phases away from liquid silicon is crucial, and if care is not exercised, the reverse reactions could undo the refinement achieved. It is also evident that the sequence of refining steps has a major impact on the results.

4. Experimental Results

Commercially available MG silicon, as received from the supplier, and without any cleaning or surface treatments, was loaded in a fused silica crucible and placed in a modified (Heat Exchanger Method) HEM furnace[5] for refining experiments. The HEM furnace is set up to operate under vacuum or overpressure and for reactive gas purging through the molten charge. After the refining steps are completed, the charge is directionally solidified.

A typical experiment involved heating the charge under vacuum until molten and stabilizing the melt at approximately 1500°C. The furnace was backfilled to 1 atm using Argon gas and the first sample of the melt was extracted. Thereafter, refining steps can be carried out and a sample of the molten bath is extracted after each refining step. One of the key ingredients for B removal is by reaction with H_2O(v)/steam/water vapor[4]. Therefore, all gases purged through the furnace were passed through a constant temperature water bath to incorporate moisture before entering the furnace chamber. Slags were also added to the charge. Mixed oxide slags were initially added to the crucible with the MG silicon charge or added to the melt.

Typically, refining experiments were carried out for about 4-6 hours; the melt was left in the crucible overnight and an additional 4-6 hours refining carried out the following day. After refining, the charge was directionally solidified. Iterative procedures were used to improve the efficiency of refining based on experimental data. These procedures were followed and the charge size was increased from 1 kg to 140 kg. The B and P levels achieved for each charge size are shown in Figure 1. It can be seen that both B and P have been reduced significantly as the charge size has been increased. The refining of B for various samples taken from a 140 kg charge is compared with the data for 1-kg charge refinement in Figure 2. This data shows that effective B reduction was achieved with scale up. In addition to B and P, all other impurities were reduced to <1 ppma levels.

5. Conclusions

Upgrading of MG silicon for use as feedstock for photovoltaic applications requires refining of B and P impurities prior to directional solidification. A modified HEM furnace was set up to refine molten MG silicon using moist reactive gases, slagging, stirring and volatilization as refining tools followed by directional solidification. Charge sizes have been increased up to 140 kg and B and P have been reduced below 10 ppma levels each and other impurities have been reduced to <1 ppma. The simple refining procedures have been effective when the charge size was increased from 1 kg to 140 kg.

Further improvement in B and P is required, but this kind of processing is expected to produce low-cost solar grade silicon feedstock, because of the low-cost of materials, the simplicity of the equipment and significant economies of scale.

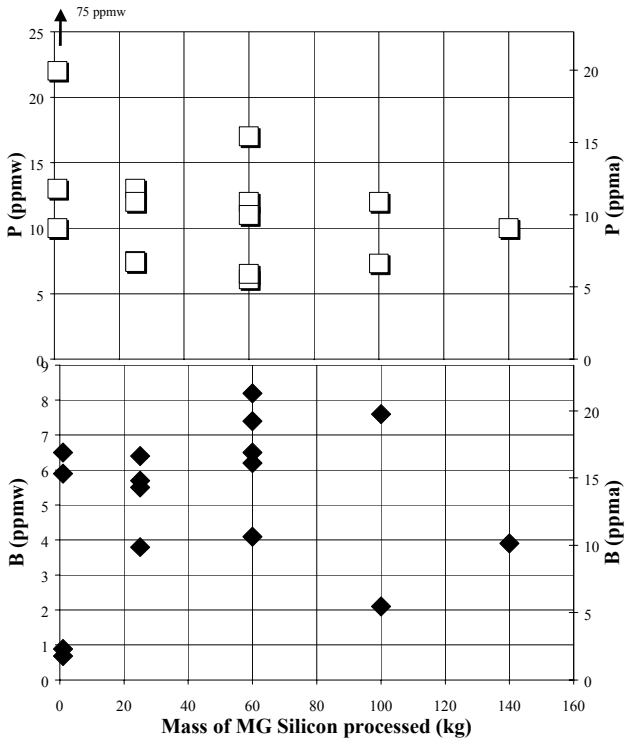

Figure 1. Characterization of B and P for different charge sizes

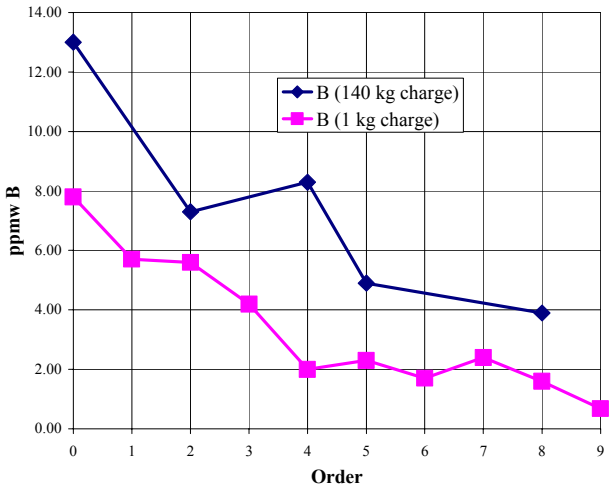

of MG silicon between 1 kg and 140 kg.

Figure 2. Reduction of B concentration with refining for a 1 kg charge and a 140 kg charge of MG silicon.

REFERENCES

[1] C. P. Khattak and F. Schmid, Proc. Electrochemical Soc. Vol. 83-11 (1983) p. 478.
[2] J. A. Amick, et al, Proc., Electrochemical Soc. Vol. 83-11 (1983) p. 67.
[3] H. Baba, et al, Proc. 14th E.C. Photovoltaics Conference, Vol. I (1997) p. 157.
[4] C. P. Khattak, et al, AIP Proc. Vol. 462, (1998) p. 731.
[5] C. P. Khattak and F. Schmid, Silicon Processing for Photovoltaics II, (North Holland, New York, 1987) p. 153.

PVMaT Advances in CdTe Product Manufacturing*

A. McMaster, J. Bohland, K. Smigielski, C. Zarecki, J.J. Hanak
First Solar, LLC – Technology Center, 12900 Eckel Junction Road, Perrysburg, OH 43551

ABSTRACT

Three items are addressed in Phase II. The first one follows from the need to achieve matching rates for all manufacturing steps. A time-consuming and costly step addressed in Phase II is the finalization of the modules, including lamination and contact termination. The second item is to prepare the product for the passage of the UL 1703 qualification tests; it follows from the failed IEEE 1262 qualification tests of the PV modules in Phase I. In anticipation of a large-scale production in the near future, the third item addressed in Phase II is the Environmental, Health and Safety program. A near completion of the finalization-line project has been achieved, including new contact termination, improved pressure lamination, and preparation of a new, 100 MW/year facility and workforce for safe and environmentally sound PV module production.

1.0 Introduction

Just prior to the beginning of Phase II of the PVMaT project, major changes occurred in the company's corporate structure. Beginning February 1, 1999 Solar Cell, Inc. (SCI) formed a joint venture partnership with True North Partners of Scottsdale, AZ. The new company was named First Solar, LLC. This event has led to the immediate start of construction of a major, 75,000 square-foot manufacturing facility in Perrysburg, a suburb of Toledo, Ohio. The facility was designed for producing PV modules, based on cadmium telluride solar cells at a rate of 100 MW per year. Some of the engineering plans for this facility had been developed by SCI during the preceding PVMaT Subcontract ZAI-4-11295-02. The facility was completed by the end of 1999. First 8 ft^2 modules were coated in a new, high-speed coater by March 2000, at a rate of 30 s each, equivalent to 50 MW/year, assuming continuous operation and 100% yield. This turn of events resulted in a dramatic change of emphasis on the goals of the PVMaT project. The effort on the PVMaT project has been expanded to include the former SCI team in Toledo, Ohio, and an additional team from an engineering subcontractor, Product Search, Inc., in Scottsdale, Arizona.

A plan developed to identify and correct the issues of the module design and lamination process for achieving UL certification are to: (a) review and improve the *pressure-lamination process using EVA*; (b) test the *cold-cure liquid resin* process begun in Phase I; (c) test the *insulated glass encapsulation* finalization; (d) develop an alternative process for *contact termination and mounting* of modules.

2.0 The EVA pressure-lamination system

Two failure modes have been identified. The first one is migration of moisture from the edges of the module along the interface of the front substrate glass and of the EVA laminate to the metal and semiconductor layers, causing their corrosion and failure. The migration is facilitated by a 1-cm wide, "edge-delete" region along the periphery of the coated substrate, which is actually a small step in the glass, formed by grit ablation of the deposited layers. Another cause of failure was found to be the deionized water used to wipe off the dust following the edge deletion. By changing to isopropanol, the modules survived the test, thereby removing the main cause of failures.

In an attempt to find another solution to the moisture-ingress failure mode, development of *an edge-potting technique* was attempted, similar to that used in the crystalline silicon modules. The modules were failing the damp-heat test. The likely reason that edge potting works for the crystalline silicon and not for thin-film modules is that with silicon modules use two layers of EVA, whereas the thin film modules use only one layer.

Several test failures in pressure-laminated modules using EVA have been traced recently to the autoclave, the racks on which the modules rest, the means of applying vacuum between the plates, and the non-uniform heating of the modules. A thorough review of these issues was made followed by modifications in the laminating system. Substantial improvements have been achieved in the module performance and durability, as well as in increased production capacity.

3.0 The cold-cure liquid polyester resin laminate system

Work on the cold-cure liquid polyester resin laminate system had been initiated during Phase I. The process involves placing a cover glass over the substrate plate bearing the solar cell layers, placing a double-sided tape on all four sides, leaving a release liner in place on the fourth side, dispensing the resin in it, removing the liner and closing the glass envelope.

Three modules were made with each of three types of cold-cure liquid polyester resin supplied by Zircon, Inc. They were subjected to an in-house environmental testing. In the best cases the modules passed the severe damp-heat test. All three gave indications of exceeding the high temperature/high humidity requirements of the IEEE qualification testing.

The advantages to this system, include process simplicity, low equipment cost, one half the material cost, compared with the EVA process, and the use of flat, annealed back glass. The process also achieved two goals of Phase II, namely, a 25 percent materials cost reduction, and a throughput of 60 modules per hour. Furthermore, there is no degradation in conversion efficiency upon lamination, compared with a relative loss of about 5% in the EVA pressure lamination process. The main disadvantage of the cold-cure process is that it was designed to cure in 24 hours. This lengthy cure would impose a requirement of providing

enough space to carry a day's inventory and for allowing the product to cure before it is shipped.

4.0 The insulated glass concept for module finalization

Insulated glass technology, originally developed by Pittsburgh Plate Glass, is a concept widely used in commercial building and residential home windows as a means for thermal insulation. A company named Glass Equipment Development uses an improved process called *glass-intercept system,* capable of processing 16,000 square feet of glass in one 8-hour shift. It is a well-proven system, having been put through a very extensive and rigorous environmental testing. Golden Photon used this concept in its PV module finalization; their modules passed both the IEEE 1262 and UL 1703 testing.

Arrangements were made for finalization of three First Solar prototype PV modules to be done by this process. All three modules finalized by the insulated-glass process passed the damp-heat test readily, showing relative decreases in efficiency of 0.1, 4.8 and 9.4%, respectively, thus indicating a viable process for a durable product.

The advantages of the insulated glass product are that it is a proven concept and that the cost of finalization is lower by factors of two and four compared with the polyester resin system, and the EVA system, respectively.

5.0 Contact termination and mounting

The objectives of this task are to: (a) increase manufacturing throughput by a factor of four, (b) reduce labor costs by a factor of ten, and (c) improve overall quality. The existing method of contact termination potting and module mount application uses a two-part, polyurethane-reaction, injection molding process to form in place four circular mounting feet and an oblong lead-wire, potted terminal. A galvanized "T" nut is molded in the mounting feet. The potted terminal houses the ends of a pair of high-voltage wires, along with a bypass diode, soldered to tin-coated copper buss foils connected to the positive and negative ends of the module. Because of the failure in the qualification tests, the time-consuming nature, and the high cost of the process, the potting method has to be replaced by alternative approaches.

5.1 Alternative mounting methods

From the interaction with customers it has been established that variants of roof-mounting methods might be required, based on site application. One practical alternative method of mounting has been identified, patented by Powerlight, Inc. This method, developed for horizontal mounting on rooftops, utilizes modules bonded to a solid foam material and interlocked together, much like a puzzle, in cushioned frames. This method does not require either mounting pads or fastening of the modules to the frame. A search for other methods is also continuing.

5.2 Alternative designs for contact termination

In considering the projected production line improvements, potential cost-reduction measures have been identified in potting, labor and material and increased throughput. Two different designs have been generated and subjected to in-house testing, in succession, to be followed by their submission to Underwriter Laboratories (UL) for testing. One of them was the *Top-Hat* design, utilizing a small, injection-molded part for electrical termination. In-house testing of PV modules incorporating this design detected some strain-related problems, which led to a redesign of this part.

The redesign resulted in a fixture called the *Cord Plate,* which uses EVA as the encapsulant and a new line layout for the termination process. A hot-melt potting material is applied to all termination locations. The new design utilizes commercially available connectors. In-house tests of PV modules included the damp-heat and humidity-freeze tests, followed by hi-pot and current leakage tests. All of the modules came out of the damp-heat test with no breakage. They also performed well in the wet hi-pot test and with only one failure of a total of 24 modules tested.

By the end of January, 2000, a new round of finished modules, incorporating improved EVA lamination and the Cord plate contact termination, were sent to the Arizona State University (ASU) test lab for UL testing. This accomplishment marks the near completion of the finishing-line project.

6.0 Environmental, Health and Safety Programs

The formation of the First Solar LLC partnership has added a major new responsibility on the EHS activity. It is to prepare environmentally sound and a safe working environment in the new Cedar Park manufacturing facility, and to provide training of new employees in accepted EHS practices. Since its formation, the number of employees has more than doubled.

The goal of the EHS program is to conduct an extensive review of its current programs and address issues that need improvement. Altogether over thirty different activities have been conducted in the EHS program over the period of 10 months of Phase II. Among these activities were: development and implementation of fifteen EHS-related plans and programs; obtaining permits concerning PV manufacture; generating reports to municipal and state agencies; cooperating with said agencies in conducting inspections; environmental sampling of R&D and production equipment and facilities for hazardous substances; installation and monitoring of EHS equipment; conducting safety inspections of all manufacturing equipment; periodic evaluation of employees for baseline cadmium; establishing first aid medical supply station for the Cedar Park facility; training of new employees on the EHS Handbook; conducting first aid training; establishing "Safety Council" meeting to address and assign controls to hazards in the start-up of the Cedar Park facility. The ultimate goal of the EHS program is to place First Solar in a leadership position relative to comparable businesses within and outside of the photovoltaic industry.

*This work is supported in part through the NREL PVMaT Subcontract No. ZAX-8-17647-06.

PVMaT Enabled In-line Chemical Processing of Silicon-Film™ Solar Cells

I. Goncharovsky, J.S. Culik, G.A. Addison, P.E. Sims, and J.A. Rand
AstroPower, Inc. Solar Park, Newark, Delaware 19716-2000, U.S.A

Abstract

A major technical goal of our PVMaT 5a contract is the elimination of all batch production processes in AstroPower's solar cell manufacturing line. The Silicon-Film™ sheet generation process produces large-area planks in a continuous manner which is compatible with in-line processing. New solar cell manufacturing processes are being developed that can accommodate these large-area Silicon-Film™ planks. We are investigating in-line chemical etching systems for surface preparation prior to diffusion and for removal of post-diffusion oxides. Our PVMaT program also includes advances in sheet fabrication, solar cell processing, and module assembly. Only developments in chemical processing are covered here.

Pre-getter Clean

As the first step in moving toward in-line wet chemical processing equipment, AstroPower purchased and installed a Rinser-Dryer system (Figure 1) in the new production facility. This apparatus is being used to clean Silicon-Film™ wafers immediately before the getter process. The dryer employed in the system has proven successful in completely drying both sides of a wafer with minimal breakage. Compared to the cassette-based box dryer systems currently employed at other points of the process, the throughput has been significantly increased, and drying quality has been improved.

Figure 1. High throughput in-line rinser-dryer which accepts a wide range of wafers sizes.

Sodium Hydroxide Etch Bath Monitoring

Conversion of the sodium hydroxide etch process from batch to continuous is presently under development. In order to gain a better understanding of the sodium hydroxide etch process and solution chemistry we developed several analytical techniques for monitoring sodium hydroxide and silica concentrations in our etch tanks. Using these techniques, we performed etch bath monitoring experiments. The data for such an experiment is shown in Figure 2. We found that both sodium hydroxide and silica concentrations increased as the first thousand wafers were etched and then dropped down to steady state concentrations. As a result of the initial bath monitoring experiments, the refresh rate of sodium hydroxide in our production scale batch process was cut in half. These techniques will be used to optimize process parameters for the in-line system under development.

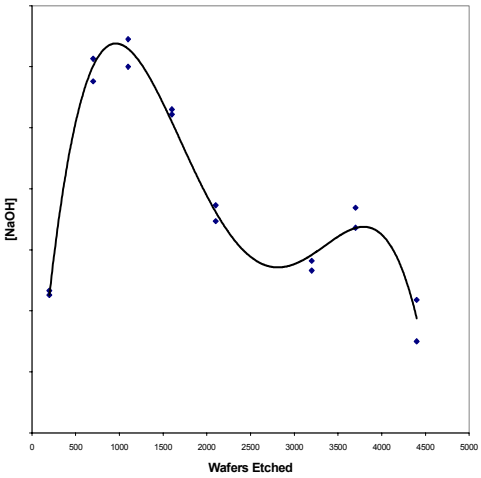

a. Sodium hydroxide concentration

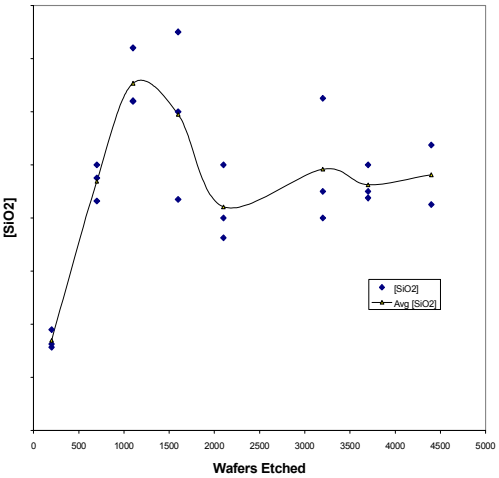

b. Silica concentration

Figure 2. Bath monitoring experiment with reduced sodium hydroxide usage indicates that concentrations of both sodium hydroxide and silica fluctuate during batch operation.

Continuous Sodium Hydroxide Etch

The continuous in-line surface etch system will be based on our current tank-based process sequence. However, in the continuous etch system individual wafers will travel through the process sequence without cassettes. The advantage of this, in addition to eliminating the individual load and transfer steps, is that larger Silicon-Film™ wafers and planks can be processed by the same equipment with minimal handling and virtually no need for fixturing.

The equipment used for continuous in-line wet processing will be based on individual process modules that perform a particular step in the process sequence and are combined into a complete system. For the continuous surface etch process, the individual modules consist of: (1) pre-etch rinse; (2) sodium hydroxide etch; (3) etch stop rinse; (4) acid neutralization; (5) cascading water rinse; and (6) dry. Figure 3 shows schematically the modules that would combine to make up a surface etch system.

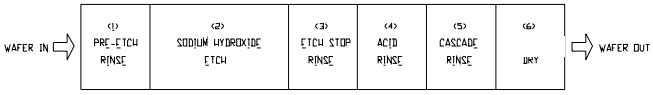

Figure 3. Block process diagram of the in-line surface etch system under development.

Continuous Diffusion

Prior to the PVMaT-4 program, Silicon-Film™ wafer gettering and emitter junction diffusion were performed as batch-type processes using large, 8-inch bore diffusion tubes with $POCl_3$ as the dopant source. As the area of Silicon-Film™ wafers has increased, the effort and cost required to obtain high performance junctions in a tube furnace-based system also increased. We have engineered a new continuous “rapid thermal” process and manufacturing system for diffusing n-type junctions onto large-area Silicon-Film™ wafers and planks. The width of the diffusion furnace belt is 36 inches. The throughput of this system exceeds 1000 Silicon-Film™ wafers per hour.

In-line Deglazing System

During the diffusion process a thin layer of phosphorus-doped silicon dioxide grows on the surface of the wafer. This oxide must be removed prior to the contact metallization steps by briefly etching the wafers in a dilute hydrofluoric (HF) acid solution. This is followed by several deionized (DI) water rinses and a drying step. At present the diffusion oxide etch is performed in chemical process tanks in a fume hood. The diffused wafers must be individually loaded into plastic cassettes for this type of batch processing. The largest cassette available for square wafers holds 15x15 cm wafers. Groups of four cassettes are processed through the "diffusion glass etch" sequence, moving them from tank to tank by hand. Once the diffusion oxide is etched, the wafers are unloaded from the cassettes so that they can proceed to the next process step.

Converting this process from batch to continuous would have the following advantages:

- process large-area Silicon Film™ planks;
- eliminate cassette loading and handling;
- increase the areal throughput rate by more than a factor of five;
- eliminate operator exposure to the process chemicals; and
- reduce material and labor cost.

During PVMaT-5 a continuous phosglass etch system was designed and built. This 27 inch wide prototype is currently being evaluated in our manufacturing facility. From preliminary experiments we predict a throughput of nearly 1500 Silicon-Film™ wafers per hour and a material cost reduction of two thirds or more.

Conclusion

We have achieved significant progress in developing in-line, continuous processes and equipment to increase the manufacturing productivity of large-area Silicon-Film™ wafer cleaning, pre-diffusion surface preparation, junction diffusion, and phosglass removal. Manufacturing equipment for several of these processes has been installed for Silicon-Film™ solar cell production on the new AstroPower production line. Under the AstroPower PVMaT-5 program, we will continue development of new in-line continuous processes and production equipment.

Acknowledgements:

The work presented here was supported by:
J. Furch, K.Kruger, G. Collins, R. McDade, and R. Fortner

PVMaT Improvements in the Solarex PV Module Manufacturing Technology

John H. Wohlgemuth and Stephen Shea
BP Solarex
630 Solarex Court
Frederick, MD 21703

ABSTRACT

This paper reports on the work performed by BP Solarex under NREL Subcontract #ZAX-8-17647-05. The objective of this three year PVMaT program is to continue the advancement of Solarex PV manufacturing technologies in order to design and implement a process which produces polycrystalline silicon PV modules that can be sold profitably for $2.00 per peak watt or less and which increases the production capacity of the Frederick plant to at least 25 megawatts per year. Progress has been achieved in the areas of silicon feedstock development, casting, wire sawing, cell processing, faster cure encapsulation, handling and measurement and control.

1. Introduction

Achieving the overall objectives of the program is based on the following components:

- Developing a solar-grade silicon feedstock.
- Optimizing and improving process control in casting.
- Reducing wire diameter and wafer thickness to reduce silicon feedstock requirements.
- Reducing wire saw operating costs.
- Developing a faster cure encapsulant to reduce labor and equipment requirements.
- Increasing cell efficiency and using more robust processes.
- Improving handling and eliminating non-value added handling steps.
- Improving measurement and control throughout the production line.

2. Silicon Feedstock

In this task, BP Solarex is working with subcontractor, SiNaF Products, Inc. to develop a process to produce silicon feedstock from H_2SiF_6. The overall process for Si production includes generation of the high purity SiF_6 gas and then its reduction via Na to form Si. Progress to date involves the development of processes to produce the high purity gas from a number of available sources.

The primary feed material for gas generation is produced in excess by the phosphate fertilizer industry, but in quantities insufficient to meet the current as well as the future needs of the photovoltaics industry. This led SiNaF to identify other inexpensive starting materials that can supplement its need for a raw material supply to be used in its technology. SiNaF has identified two additional silicon-containing materials for the production of the gaseous intermediate. They are spent catalyst from the petroleum industry and mine tailings, generated from hard rock mining activities that have accumulated over the last 150 years. These technologies developed by SiNaF for added gas production have established an unlimited raw material base for the production of PV grade silicon.

3. Casting

In this task effort BP Solarex is improving control of and optimizing the casting process. This will increase the process yield (kilograms of silicon out divided by kilograms of silicon in) by 3% and improve material quality to result in a 1% increase in average cell efficiency.

We first designed replacement control systems for the casting stations. These are now almost fully implemented in production. The new systems provide a much higher level of automated control and data acquisition than did the old systems. The operator interface, alarm and troubleshooting functions have all been significantly improved. Actual yields in this area increased by 4% in 1999.

Process improvement is tracked by routine measurement of minority carrier lifetime for each production casting. This data can be correlated with later cell results for that cells made from that casting, as shown in Figure 1 below.

Figure 1
Efficiency and Current vs Lifetime

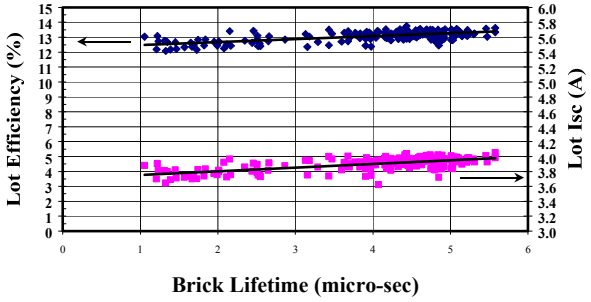

4. Wire Sawing

BP Solarex is working to reduce the center-to-center cut distance, ("pitch") on the production wire saws to below 450 microns. We have successfully reduced this pitch from 500 microns to 450 microns with no loss of downstream yield, and a further reduction to 440-micron pitch is planned.

We are also introducing slurry and silicon carbide recycling to significantly reduce the operating cost of the saws. Equipment was put into production in 1999 and handoff completed in early 2000.

We are presently evaluating on one saw the use of a "double" table mounting structure to mount twice as much material for each wire saw run. Although the cut rate must be reduced, the overall output of the saw is increased by some 40%.

5. Cell Processing

In this task BP Solarex is developing, demonstrating and implementing a cost-effective, robust cell process that produces a minimum average cell efficiency of 15% and improves the cell line electrical yield.

To-date, an aluminum paste Back Surface Field (BSF) process has been successfully implemented in each of the company's screen-print production lines, resulting in a 5% increase in average power.

PECVD silicon nitride has been evaluated as a replacement for either LPCVD nitride or TiO_2 anti-reflection coatings. PECVD silicon nitride can produce dramatic cell efficiency improvement through the passivating effect of the plasma-enhanced process on both surface and bulk defects. We have demonstrated 8% improvement in average power on pre-production trial lots, and we plan to introduce the new process into one of the BP Solarex production lines in 2000.

6. Faster Cure Encapsulation System

Solarex is developing and qualifying, through a lower-tier subcontract with Specialized Technology Resources, Inc. formerly Springborn Testing and Research (STR), an encapsulation system that meets technical and reliability requirements and can be laminated and cured in less than 6 minutes in the present Solarex laminators. The first step in the process was a literature review that determined that EVA based systems offered the best opportunity to meet the goals. A number of research studies were then conducted to determine what cure level is required for PV modules and what parameters effected the level of cure.

These research studies indicated that the present fast cure EVA systems 15295 or X33561 could be cured in a 6 minute process, but that this required the use of a lamination temperature that is not consistent with manufacturability. STR experimented with the use of additional cure agent, different cure agents and co-curative agents. A number of formulations have now been tested that provide adequate cure in less than six minutes as shown in Table 1.

Table 1
Cure Levels of Formulations Cured at 140° C

Formulation	Cure Time (min)	Gel Toluene (%)	Gel Chloroform (%)	Oven Test (%)
X33561	6	44	49	<70
X33562	6	63	70	<70
X34646-4	4	70	78	>70
X34646-4	5	80	84	>80
X34646-4	6	85	87	>80
X34646-10	4.5	72	77	>70
X34646-10	5	74	77	>70
X34646-10	6	83	85	>80
X34646-14	5	75	80	>70
X34646-14	6	80	88	>80
X34646-16	5	72	78	>70
X34646-16	6	78	84	>80

Because of the differing chemistries 2 different gel tests and an oven creep test have been employed to evaluate the formulations. As long as all of the tests are above 75% the material should be adequately cured. As the Table shows, Several of the candidates each this level in less than 6 minutes at 140° C. Modules have now been fabricated with 4 of these formulations and are undergoing qualification testing.

7. Handling

In the handling effort, BP Solarex is developing improved product and materials handling techniques (including efforts in at least three separate areas) to increase line yields by 3% and reduce handling labor to save $0.05/watt. BP Solarex is supported in this effort through a lower-tier subcontract with ARRI, the Automation and Robotics Research Institute of the University of Texas at Arlington.

The first area addressed was module assembly. A completely new, U-shaped assembly line was designed, purchased and installed in the BP Solarex plant in Frederick, Maryland. The new line provides automated handling of large modules, starting with tabbed cells and producing a fully assembled, tested and packaged product for shipment.

Defects caused by mechanical abrasion have been a significant cause of rework in assembly lines that rely on manual handling of modules. In the new line, the incidence of this type of defect has been reduced essentially to zero. Labor productivity was improved by over 50% relative to the manual line, and labor cost was reduced by more than the goal of $0.05 per Watt.

Additional handling projects are under way involving the movement of large ceramic pieces and in the loading and handling of large silicon ingots in the casting stations.

8. Measurement and Control

BP Solarex is developing process measurement and control procedures for use on the production line (including efforts in at least three separate areas) to improve yield by 3% and reduce rework by 50%. ARRI also provides support in this area.

A prototype data collection and tracking system was designed and installed in the diffusion area of the Frederick plant. The system provides a count of wafers entering the furnaces, recording of several control parameters, and an operator interface that alerts the operator to potential or actual out-of-control conditions and provides on-screen procedures to correct the condition. Implementation of this system was halted after successful pre-production trials pending completion of a new production data collection and communication system.

The new system, now operational, provides a wide range of operational and process data on local-area web pages. For example: wafer thickness; cell coefficient of variation (COV); solder joint pull strength; output; and many other parameters are tracked in real-time and available through the local network. The data collection system at diffusion will be interfaced to the network system later in 2000.

Research on Amorphous Silicon Solar Cells and Modules at BP Solarex

D. Carlson, G. Ganguly, G. Lin, M. Gleaton, M. He, J. Newton, G. Wood, R. Arya, M. Bennett, F. Willing
BP Solarex
3601 LaGrange Parkway, Toano, VA 23168

ABSTRACT

In the past year, the amorphous silicon (a-Si) R&D program at BP Solarex has focused on reducing the manufacturing costs and improving the manufacturing throughput of a-Si/a-SiGe tandem modules. We have shown that the deposition rate of the a-Si:H i-layer can be tripled and the utilization of silane and germane feedstock gases doubled without any loss in stabilized efficiency. We have also determined that the device performance can be reduced by the presence of contaminants such as oil or dopant gases during the i-layer deposition or by variations in the electrode geometry.

1. Introduction

BP Solarex is continuing to ramp up the production of a-Si/a-SiGe tandem modules at its TF1 plant in Toano, VA. In this paper, we present some recent results on increasing throughput and gas feedstock utilization. We also show how contaminants and reactor grid spacing can affect stabilized performance. We also present some data on the temperature behavior of various types of a-Si based solar cells.

2. Increasing the Deposition Rate of a-Si:H

As shown in Fig. 1, we have been able to increase the deposition rate of the a-Si:H i-layer to ~ 3 Å/s without any significant loss in stabilized performance (Fig. 1 shows the fill factor after 600 hours of light soaking at ~0.8 suns).

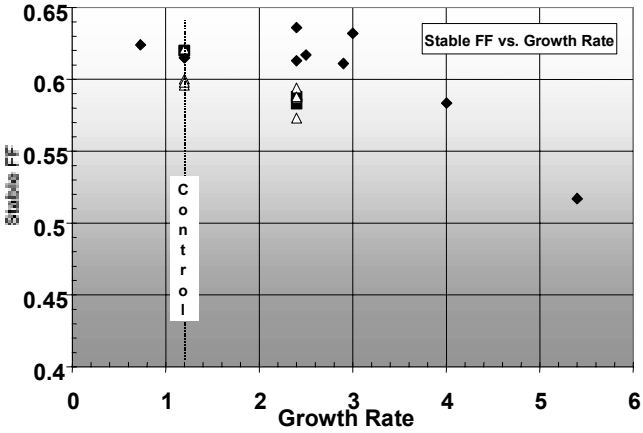

Fig. 1 The stabilized fill factor of a-Si single-junction cells for i-layers prepared at different growth rates. The cells were fabricated with similar short-circuit current densities.

3. Development of a Fast Tunnel Junction

Since the formation of the tunnel junction has been one of the rate-limiting steps in the manufacturing of a-Si/a-SiGe tandem modules, we have developed a new process that reduces the tunnel junction process time by a factor of three. As shown in Fig. 2, the average performance of tandem cells made with the new fast process is similar to those made with the standard process.

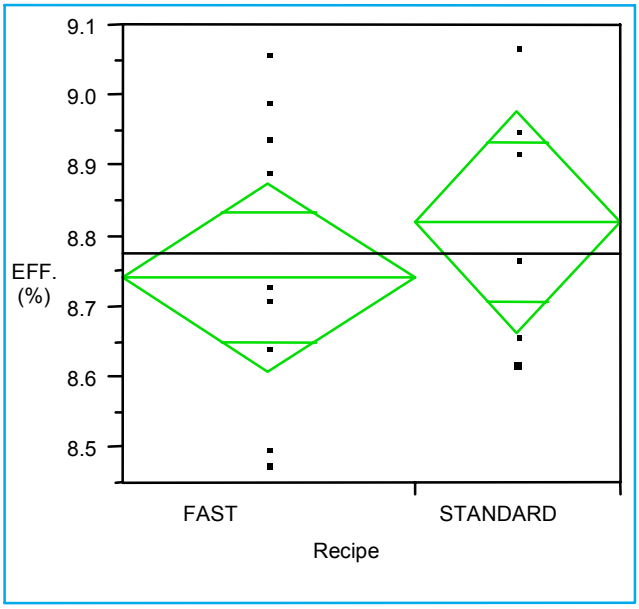

Fig. 2 The statistical variation of the efficiency for multiple runs of a-Si/a-SiGe tandem cells using the fast and standard tunnel junction processes.

4. Effect of Contaminants on Performance

A series of experiments were conducted to examine the effects of oil and dopant contamination on the initial and stabilized (light-soaked) performance of a-Si p-i-n solar cells. In these experiments, controlled amounts of diborane, phosphine and three different oil contaminants were added to the discharge chamber of a DC PECVD reactor during the deposition of the i-layers. The concentration levels of boron, phosphorus and carbon in the i-layers were determined by Secondary Ion Mass Spectroscopy (SIMS). As shown in Table 1, the presence of oil in the deposition system did not have a strong effect on the initial performance; the greatest loss in initial efficiency was about 5% for machine oil located on the discharge electrode. However, as also shown in the table, the light-induced degradation (600 h, ~ 0.8 suns) increased significantly when oil contamination was present inside the plasma region.

We also fabricated single-junction a-Si solar cells where we added either 1.2 vppm of diborane or phosphine to the discharge atmosphere during the deposition of the i-layer, and the initial performance was lowered by ~ 15-20% by the presence of these dopants. A surprising result was that most of the light-induced degradation was irreversible for cells contaminated with boron. Fig. 3 shows that

annealing at 170°C for 90 minutes did not reverse the degradation of boron-contaminated cells caused by illumination with 60 suns for 730 minutes; a similar effect was observed after exposure to ~ 0.8 suns for 600 hours.

Table 1. Effects of Oil Contamination on Single-Junction Device Performance

Type of Contam.	Position of Application	Carbon ($x10^{18}cm^{-3}$)	Initial Eff. (%)	% Degrad
None (controls)	-	5	7.87 ±0.10	25-26
Pump Oil	Outside plasma region	50	7.74 ±0.19	27
Vacuum Grease	Outside plasma region	-	7.61 ±0.15	24-26
Machine Oil	Inside plasma region	10	7.49 ±0.15	38
Pump Oil	Inside plasma region	80	7.67 ±0.14	37

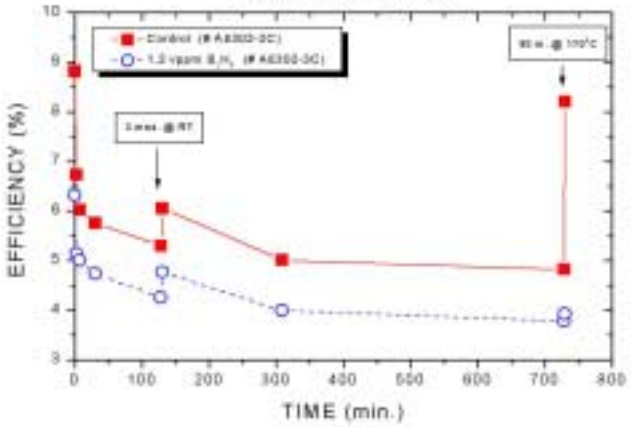

Fig. 3. The efficiency of boron-contaminated and control p-i-n cells vs. time exposed to 60 suns at 60°C.

5. Effect of Electrode Spacing on Device Performance

In another series of experiments, we examined the effect of changing the spacing beween the grid and the substrate in one of our DC discharge reactors. As shown in Fig. 4, the amount of light-induced degradation increases as the spacing increases.

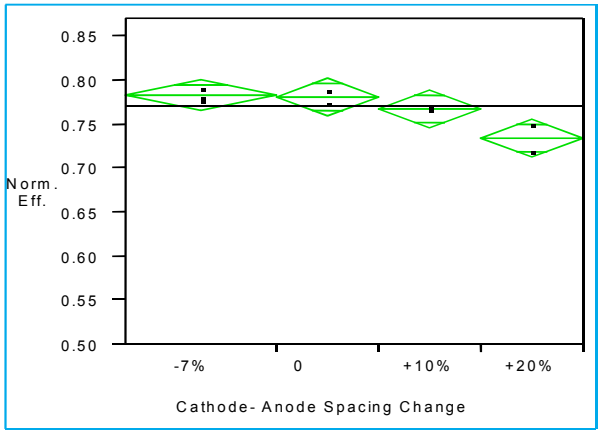

Fig. 4 The normalized efficiency of a-Si single-junction cells prepared at different cathode-anode spacings after 1000 hours of light soaking at 1 sun.

6. Temperature Behavior of a-Si Cells

Since a number of recent studies [1-4] have shown that amorphous silicon PV modules exhibit much better performance at elevated temperatures than other types of PV modules, we decided to examine the temperature dependence of different types of a-Si based cells. As shown in Fig. 1, the temperature behavior of a-Si based cells varies over a wide range depending on the fabrication and treatment conditions, and it is not possible to assign a single temperature coefficient for the efficiency.

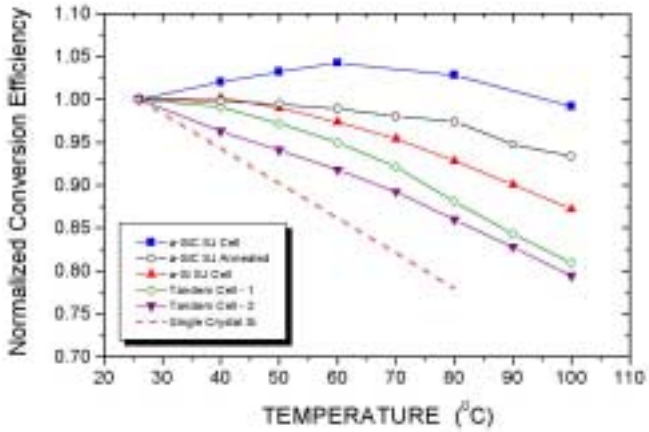

Fig. 5. The normalized initial efficiency as a function of temperature for five different types of a-Si solar cells. The dashed line is typical of a crystalline Si cell (-0.40%/°C).

7. Utilization of Feedstock Gases

We have also been able to increase the utilization of both silane and germane feedstock gases by 50% without any loss in performance. For example, we were able to obtain an average initial efficiency of 8.91 ± 0.08% for tandem devices made with a 50% reduction in germane as compared to 8.82 ± 0.13% for devices made with the standard process.

ACKNOWLEDGEMENTS

This work was partially funded by the NREL under DOE Subcontract ZAK-8-17619-02.

REFERENCES

[1] M. Kameda, S. Sakai, M. Isomura, K. Sayama, Y. Hishikawa, S. Matsumi, H. Haku, K. Wakisaka, M. Tanaka, S. Kiyama, S. Tsuda and S. Nakano, Proc. 25th IEEE PVSC (1996) 1049-1052.

[2] K. Akhmad, A. Kitmura, F. Yamamoto, H. Okamoto, H. Takakura and Y. Hamakawa, Solar Energy Materials and Solar Cells 46 (1997) 209-218.

[3] K. Fukae, C. C. Lim, M. Tamechika, N. Takehara, K. Saito, I. Kajita and E. Kondo, 25th IEEE PVSC, (1996) 1227-1230.

[4] M. Kondo, H. Nishio, S. Kurata, K. Hayashi, A. Takenaka, A. Ishikawa, K. Nishimura, H. Yamagishi, Y. Tawada, Solar Energy Materials and Solar Cells 49 (1997) 1-6.

Development & Commercialization of a 4.5-Sun, Flat-Plate Concentrating PV System

John R. Tuttle, Aaron Szalaj and Kelly Beninga

DayStar Technologies, Inc.

600 Corporate Circle, Suite L, Golden, CO 80401
303.279.9505 / 303.742.1899 fax / info@daystartech.com

ABSTRACT

The design features of a patented 2-8 sun, "flat-plate" concentrating module are presented. Optical characterization indicates Ag is the reflecting material of choice. Thin-film Cu(In,Ga)Se_2 (CIGS) solar cells on metallic substrates out-perform non-optimized wafer-Si in reflectivity and performance under concentration. Wafer-Si cells are easily incorporated into the module with minor variability in performance. An 8.0% active-area submodule is reported.

1.0 Introduction

In conventional flat-plate module designs, cell components represent 60-70% of the total module costs. In order to reduce module and system costs, whether it's for a 100 W system or 100 MW project, it makes sense to replace expensive semiconductor with cheaper optical components. In conventional concentrator products, however, new manufacturing technology is required to handle the "open-package" design, i.e., separate optical and cell-receiver components. DayStar Technologies has developed a unique and patented "closed-package" module design that reduces cell costs by 60-80% with 4-5 Suns of concentration. The product form-factor, which is identical to that of a conventional flat-plate module, enables compact system designs and only slight modifications of standard manufacturing practices. In this paper, we discuss progress towards commercialization of this technology.

2.0 Module Design

DayStar's concentrator module consists of a lens/optical package, series connected cell components, laminates, encapsulates, and frame. The unique components are described in detail below. Preliminary module and system specifications are provided in Table 1.

Table 1 Module and system description

Item	Description
Cell Material	Wafer-Si or CIGS
Module Size	0.72-m^2 (0.6m x 1.2m)
Module Output Power	80W (40V x 2.0A)
System Output Power	11.1 kW

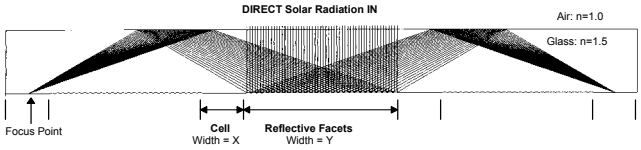

Fig. 1 Ray-trace diagram of concentrating optics.

2.1 Optics

The patented optical design for this concentrator product is based upon reflection off of angled prisms and total-internal-reflection (TIR) off of the front optical surface (Fig. 1). Hence, the solar cells and primary optical component are coplanar, thus creating a solid package. The angular sensitivity for a 4.5-Sun design is $\pm 2.5^{\circ}$. The design creates normal and off-normal incidence of incoming light to the cell receiver. The module dimensions (cell width X, spacing Y, and thickness Z) and concentration ratio ((Y+X)/X) are all interrelated and scalable. The TIR property of the optical package decreases the thickness required for a desired concentration ratio by a factor of two.

There are several options on how the full optical package is manufactured. They include full-thickness acrylic or similar plastic, or a thin-plastic lens / coverglass couple. The former is easier to manufacture, but has unknown field reliability due to the potential for surface abrasion and creep. The latter enables conventional down-stream module manufacturing, but introduces thermal expansion mismatch issues between the coverglass and plastic lens. DayStar is working with vendors and has identified robust solutions to these problems.

2.2 Cell components

The original module design incorporated thin-film cell materials as the receiver. At present, both wafer-Si and thin-film CIGS are being used in the module. Cell material is manufactured either as wafers (12.5cm x 12.5cm) or sheets (30cm x 30cm) with appropriate modifications to the emitter and grid designs for 5 x J_{sc} current flow. The cell material is subsequently cut into strips (2mm wide) and series interconnected. At these cell dimensions, the density of contacts increases 16-fold. This presents a challenge for conventional serial cell-interconnect tooling. In contrast, however, die-attach and bonding tooling that supports the electronics industry is well suited for this application.

3.0 Module Component Development Progress

Development work to date has focused primarily on fabricating and characterizing the optical package and on cell modification and interconnects.

3.1 Optical Package

The module optical package consists of the front surface, internal transparent medium and interfaces, reflecting facets, and the cell receiver. The performance of any concentrator module depends on efficient redirection of the *direct component* of sunlight to the cell. We have characterized the optical package as a whole and in part, where possible. The reflective surface has been studied using both Al and Ag. Al and Ag films were deposited on 0.45cm acrylic and glass. Previous studies [1] on the optical properties and durability of each reflector material on acrylic suggest that Ag is best applied to acrylic with a 200 Å SiO_x intermediate and 200Å Cu cap layer for protection. In Fig. 2, we contrast the optical performance of the different material combinations. We conclude that Ag is the superior reflector, and that acrylic exhibits absorption and could contribute to current loss in the final product.

We have additionally characterized the reflective properties of wafer-Si and thin-film CIGS cell components (Fig. 2, (A) & (B)) and found there to be significant losses associated with as-received wafer-Si in comparison to thin-film CIGS, which shows very low reflectivity. Upon assembling a full module package and using outdoor light for characterization, our findings for Ag-coated acrylic translate into high optical transfer functions (85-90%) with thin-film cells, and lower (75-80%) with wafer-Si cells.

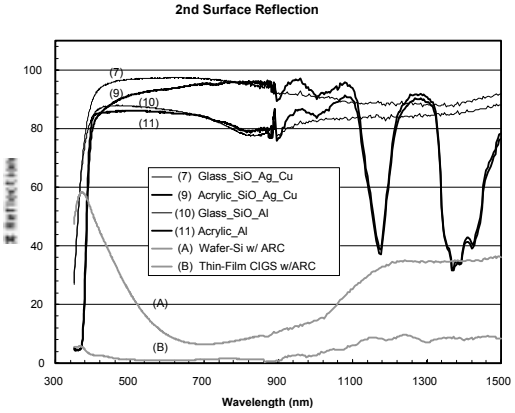

Fig. 2 Reflectivity measurements for Ag- and Al-coated acrylic and glass and for thin-film CIGS and wafer-Si cell

3.2 Cell Performance and Interconnect

We have previously reported on the performance of thin-film CIGS under concentration [2]. In order to test wafer-Si, 12.5cm x 12.5cm cast poly-silicon wafers were cut along grid lines into strips 3.04mm wide. In Fig. 3, we present the uniformity of cell-strip performance across an entire wafer after cutting. In Table 2, the performance of 10- and 13-cell strings is presented. When these cell strings are subsequently integrated into the module and measured at the NREL outdoor test facility (Fig. 4), the results confirm the substandard performance of the optical package in conjunction with non-optimized wafer-Si cell components.

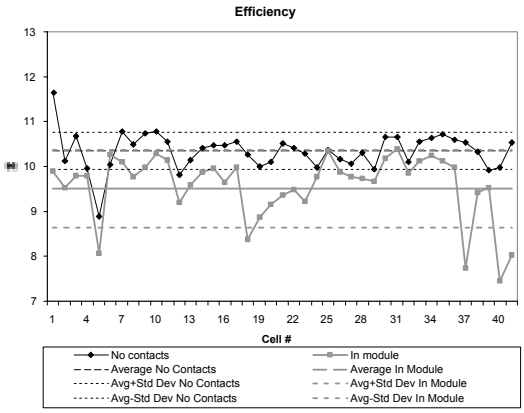

Fig. 3 Performance variability with poly-Si

Table 2 Performance of 10- & 13-cell strings.

String #	# of Cells in string	Voc (V)	Jsc (mA/cm^2)	Fill Factor (%)	Efficiency (%)
1	10	5.403	2.44	63.94	8.431
2	10	5.449	2.59	66.58	9.385
3	10	5.479	2.62	69.71	10.019
1	13	7.214	1.99	67.04	9.601
2	13	7.226	2.02	69.00	10.055

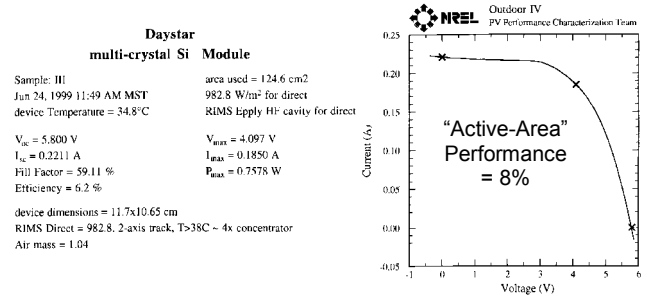

Fig. 4 Performance of concentrator module with wafer-Si as the cell component.

4.0 Conclusion

Optical package and solar cell characterization has provided insight into required technology improvements necessary for manufacturing and commercialization of DayStar's flat-plate concentrating PV module technology. Work in the coming year will focus on field-testing and reliability.

References

[1] P. Schissel, C. Kennedy, and R. Goggin, "Role of Inorganic Oxide Interlayers in Improving the Adhesion of Sputtered Silver Film on PMMA', J. Adhesion Sci. Technol., 4(1995) 413-424.

[2] J.R. Tuttle, E.D. Cole, T.A. Berens, A. Szalaj, J.Keane, and J. Alleman, "A Novel "Flat-Plate" PV Concentrator Package", NCPV Photovoltaics Program Review (1999) 315-319.

Acknowledgements

This work was performed with the support of the National Renewable Energy Laboratory under subcontract ZAK-8-17619-25.

Highly Efficient 32.3% Monolithic GaInP/GaAs/Ge Triple Junction Concentrator Solar Cells

H.L. Cotal, D.R. Lillington, J.H. Ermer, R.R. King, N.H. Karam
Spectrolab, Inc., 12500 Gladstone Ave., Sylmar, CA 91342 U.S.A

S.R Kurtz, D.J. Friedman, J.M. Olson, S. Ward, A. Duda, K.A. Emery, T. Moriarty
National Renewable Energy Laboratory, 1617 Cole Blvd, Golden, CO 80401

ABSTRACT

Results from Spectrolab-grown $Ga_{0.5}In_{0.5}P$/GaAs/Ge structures optimized for the AM1.5D spectrum are described along with progress toward developing next-generation multijunction solar cells for high concentration ratios (X). The structures were processed into small-area cells at NREL, and I-V tested vs. X. Many cells were tested, with the best cell eff. at 32.3% at 47X and 29% at 350X. The FF limited the devices above 60X. The V_{oc} vs. X showed its log-linear dependence on I_{sc} up to ~75X; a decrease in Voc at higher X is attributed to a bucking junction at the back of the Ge bottom cell. Based on recent cell improvements for space applications, multijunction cells appear to be ideal candidates for high eff., cost effective, PV concentrator systems.

1. Introduction

Recent performance improvements along with cost reductions carried out in the manufacture of $GaInP_2$/GaAs/Ge lattice-matched space solar cells has prompted Spectrolab to re-evaluate the application of this type of cell for use in terrestrial PV concentrator systems [1]. AM1.5D efficiencies of over 30% can now readily be achieved on triple-junction (3J) cells using device designs and high-yield production processes that are only marginally different from space cells. Since space and terrestrial multijunction cell technologies share the same manufacturing operations, cells with very low dollars per watt can be produced at modest manufacturing rates. This makes multijunction cells extremely attractive for achieving near-term reductions in PV generation costs.

$GaInP_2$/GaAs/Ge 3J cell layers were grown at Spectrolab in a production MOVPE reactor incorporating high-efficiency cell structures suitable for the high current densities encountered at concentration and the terrestrial spectrum. These epitaxially grown layers were then metallized and fabricated into concentrator cells by NREL for performance evaluation under an AM1.5D spectrum. A major difference in these devices compared to that of a space cell is a thicker, more heavily doped emitter to reduce sheet resistance across the surface that might otherwise cause significant performance losses at high concentration. Other layers of the cell were also adjusted to achieve current matching under an AM1.5D spectrum. Two device structures were modeled, and the grid design for both pace and terrestrial cells were optimized for each application.

2. Procedure

Light I-V measurements were performed at NREL on small area devices of 0.1039 cm^2 under their High Intensity Pulsed Solar Simulator (HIPSS) at 1 sun and under concentration. It should be pointed out that NREL has sent this cell to the Fraunhofer ISE in Freiburg, Germany for 1-sun measurements and performance verification. The short-circuit current (I_{sc}) and the maximum power agreed to within 0.2% of NREL's results. Further measurements for performance evaluation under concentration are underway by Fraunhofer ISE.

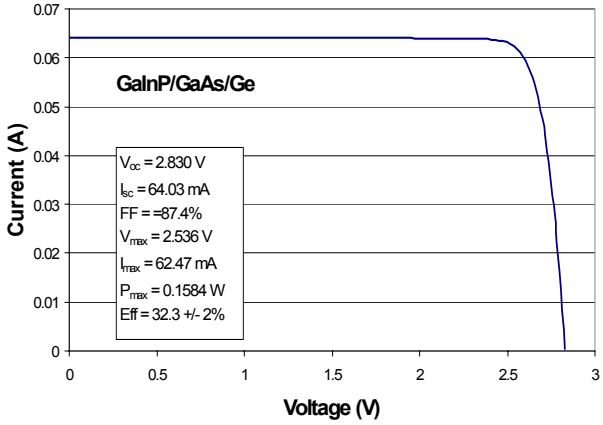

Figure 1: Light I-V characteristics of the best $GaInP_2$/GaAs/Ge TJ solar cell measured at AM1.5D and 47 suns by NREL.

3. Results and Discussion

Figure 1 shows a representative I-V curve for an early generation of small-area cells with the best cell yielding an efficiency of 32.3%. The other photovoltaic parameters of the cell are displayed in the figure. Many other cells were measured as a function of concentration level and gave efficiencies greater than 30%. All of their photovoltaic parameters were well-behaved with increasing concentration, and only the fill factor decreased.

In Fig. 2 is shown such a set of efficiency curves versus concentration for these initial cells, which were tested at NREL with remarkably high values. Just recently, other cells were processed and tested, and their device performance at concentrations greater than 200 suns was higher than the performance of the earlier cells. Figures 3 and 4 show their open-circuit voltage (V_{oc}) and fill factor characteristics for one of these high-concentration cells as a function of concentration ratios. The V_{oc} of the high-concentration 3J cells increased linearly on a logarithmic scale as expected from the sum of V_{oc} values for each subcell using the simple ideal-diode relation in forward bias::

$$V_{oc,3J} = V_{oc,c1} + V_{oc,c2} + V_{oc,c3} \approx \frac{kT}{q} \ln\left(\frac{J_{ph,c1} J_{ph,c2} J_{ph,c3}}{J_{o,c1} J_{o,c2} J_{o,c3}}\right)$$

where J_{ph} and J_o are the photogenerated and the saturation current density, respectively, for a given subcell, and c1, c2,

and c3 designate subcells 1, 2, and 3 in the multijunction stack. As the incident intensity increases by a factor of ten, the J_{ph} in each subcell increases by a factor of 10 and the change in V_{oc} for the 3-junction solar cell is $(kT/q)\ln(10^3)$ = 177 mV/decade at 25°C for a diode-ideality factor of 1 for each subcell. For the high-concentration cells, the V_{oc} perform according to Eqn. (1) to concentration levels over 1000 suns, as shown in Fig. 3.

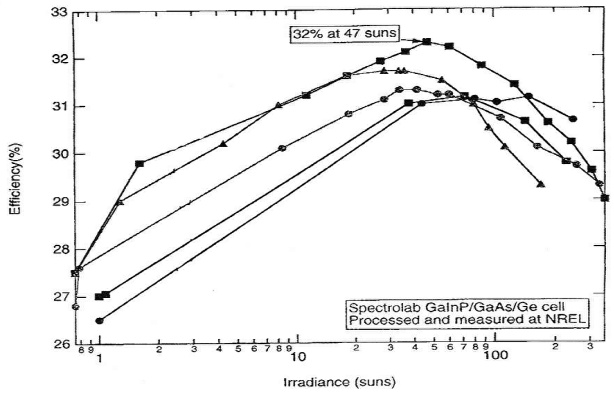

Figure 2: Spectrolab $GaInP_2$/GaAs/Ge TJ efficiencies versus concentration for 5 cells processed from the same wafer by NREL.

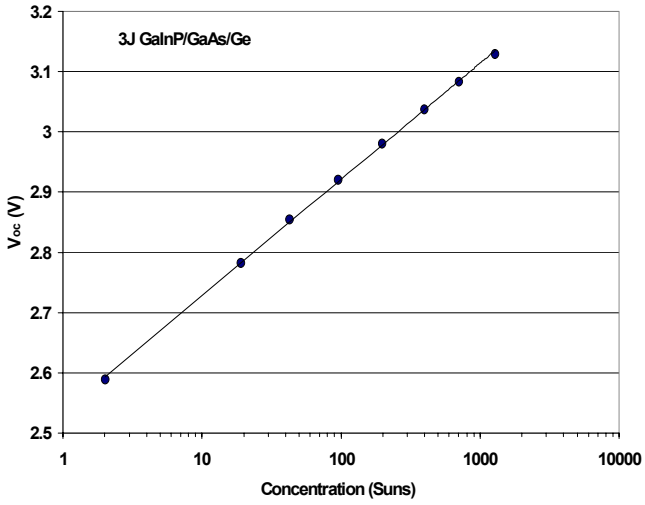

Figure 3: $GaInP_2$/GaAs/Ge TJ open-circuit voltage versus concentration ratio for high-concentration device (not shown in Fig. 1).

A wide-bandgap tunnel junction was used in between the GaInP top cell and the GaAs middle cell, in order to increase photogeneration in the middle cell [1,2]. The wider bandgap of the semiconductors used can increase the energy barrier for tunneling and thereby increase the resistance and lower the peak tunneling current for wide-bandgap tunnel junctions. However, a wide-E_g tunnel junction structure was chosen that has been found to be robust on thousands of cells at one-sun and at low concentration ratios, and which appears to have acceptably low voltage drops for over 500 suns.

Figure 4 shows more detailed features of the fill factor as a function of concentration for the cell of Fig. 3. The FF exhibits a maximum near 20 suns and then decrease steadily from 20 suns to over 1000 suns. The drop in FF is due to the increased role of the series resistance at higher concentrations.

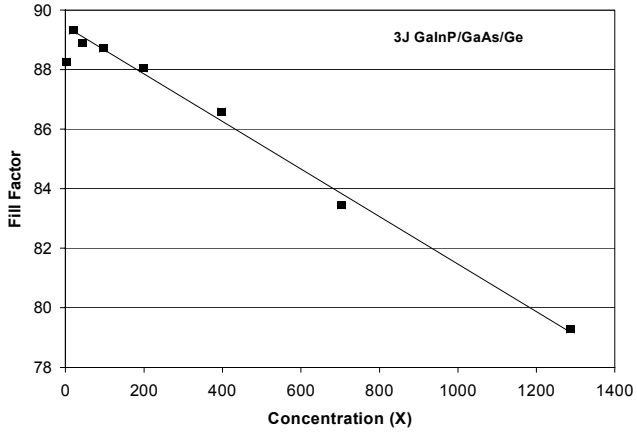

Figure 4: $GaInP_2$/GaAs/Ge TJ fill factor dependence on the concentration ratio.

Cell efficiencies as high as those shown in Fig. 2 present a remarkable message: in their present state, TJ cells can work effectively in a PV concentrator system and generate power in excess of 10 MWhr/yr for a system populated with only 500 cm^2 of cell aperture area! Even with the anomalous roll-off in V_{oc}, the efficiency was 29% at 350 suns, indicating that a concentrator system populated with such cells would yield a power output twice as high as that of commercial Si cells with 15% efficiency.

3. Conclusions

In conclusion, results from well-established, 3J space-based solar cell growth technology at Spectrolab showed efficiencies for the best device from an early generation of cells of 32.3% at AM1.5D. IV testing of improved cells is currently underway and will be presented in the paper. In the near future, low risk improvements will give rise to high-volume, industry-wide availability of cost effective cells above 30%. Several years from now, the opportunity will exist for cell costs to be less than $0.3/W with the introduction of improved 4-junction cell technology based on 1-eV materials.

ACKNOWLEDGEMENTS

The authors extend their thanks to K. Edmondson and D.K. Krut for useful discussions and all whom directly contributed to the progress of this work.

References

[1] N.H. Karam, R.R. King et al., "Recent Development in High-Efficiency GaInP/GaAs/Ge Dual- and Triple-Junction Solar Cells: Steps to Next Generation PV Cells," *Solar Energy Materials and Solar Cells,* 2000.

[2] D.J. Friedman et al., "Ge Concentrator Cells for III-V Multi-Junction Devices," submitted to this conference.

Large Installations of High-Concentration PV Systems

D. Roubideaux, V. Garboushian

Amonix, Inc., 3425 Fujita Street, Torrance, CA 90505

H. Hayden

Arizona Public Service, 400 North 5th, Phoenix, AZ 85072

ABSTRACT

This paper presents practical considerations for large installations of high-concentration PV systems, including site planning and installation. The current generation of Amonix's Integrated High-Concentration PV (IHCPV) system has been optimized for large-scale deployment through a modular configuration known as a MegaModule™.

1. General Introduction

Prior installations of high-concentration PV systems have been limited to single site systems primarily for demonstration and utility evaluation. In 1999, Amonix, Inc. contracted with Arizona Public Service (APS) to install 300 kW of its Integrated High-Concentration PV (IHCPV) systems in APS's service area. This project represents the largest deployment of high-concentration PV in the world. This paper discusses some of the practical considerations in fielding large installations of high-concentration PV systems.

2. System Configuration

The IHCPV system is a Fresnel lens concentrating system operating at approximately 250X. Several system design iterations have been made to significantly increase reliability and reduce cost. Much of this activity was presented in previous papers [1,2]. The current system consists of highly modular MegaModules™ mounted onto a newly designed drive. Each MegaModule™ contains 48 receiver plates with corresponding Fresnel lens parquets. Each receiver plate contains 24 AMX-10 solar cells connected in series capable of producing a nominal 120 W_{DC} under PVUSA test conditions. This configuration makes the MegaModule™ a nominal 5 kW building block. A photograph of a two MegaModule™ IHCPV system is shown in Figure 1. An earlier generation 168-panel system is shown in the background.

3. Site Planning

Concentrating solar collectors track the Sun. In planning site layout for multiple systems, consideration must be given to potential shadowing effects on the overall field performance. Newly developed computer modeling programs enable the optimum placement of individual systems for maximum utilization of real estate and minimum interference (shadowing) from adjacent systems. Sample computer images are shown in Figures 2 and 3.

Figure 1: Two MegaModule IHCPV System

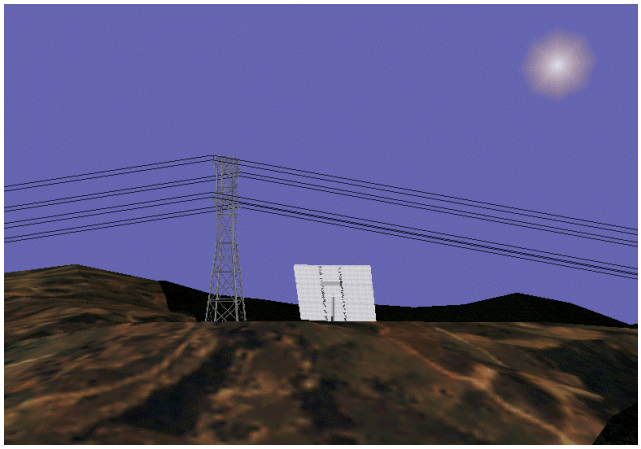

Figure 2: Single IHCPV System Model

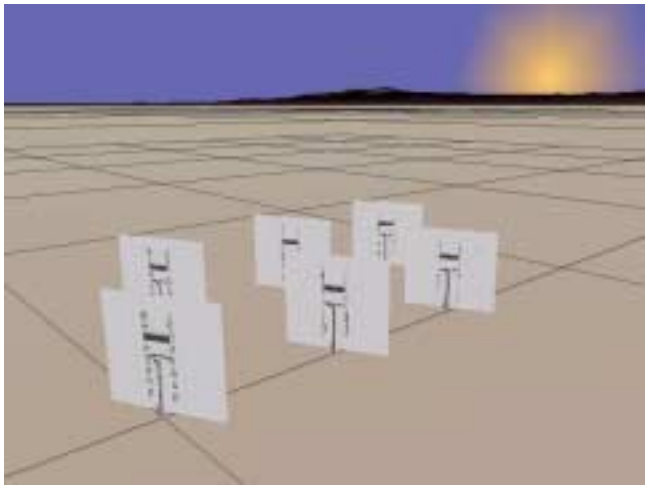

Figure 3: IHCPV Model Used For Shadow Interference Analysis

4. System Configuration Modularity

The MegaModule™ concept offers several advantages for configuration of multiple systems matched to the requirements of a particular site. Differing system sizes ranging from a single 5 kW MegaModule™ to five MegaModules™ may be easily configured for different applications. A photograph of a four MegaModule™ and a two MegaModule™ system is shown in Figure 4. Again note the earlier generation monolithic system in the background.

Figure 4: Different Configurations of MegaModule Systems

5. Installation Requirements

An extremely important issue for large installations is the ability to rapidly deploy and install the systems. Again, the MegaModule™ concept allows flexibility in managing the installation sequence. The MegaModules™ are pre-assembled, inspected and tested in a controlled indoor environment. The foundation, pedestals, and drives can be pre-installed along with all wiring, trenching and interconnectins. The completed MegaModules™ are then transported to the job site and quickly mounted to the drive support tube. A photograph of megamodules on a truck is shown in Figure 5. A photograph of final wiring is shown in Figure 6.

Figure 5: MegaModules™ on Truck

Figure 6: Final Interconnections

REFERENCES

[1] V. Garboushian, D. Roubideaux. S. Yoon: " Integrated High-Concentration PV; Near-Term Alternative for Low-Cost Large-Scale Solar Electric Power", Invited Paper at the International Photovoltaic Science & Engineering Conference, November 1996

[2] V. Garboushian, D. Roubideaux, S. Yoon, J. Allen Gunn: "An Evaluation of Integrated High-Concentration Photovoltaics for Large-Scale Grid Connected Applications", 25th IEEE Photovoltaic Specialists Conference, May 1996

Outdoor Measurement of 28% Efficiency for a Mini-Concentrator Module

M.J. O'Neill and A.J. McDanal

ENTECH, Inc

1077 Chisolm Trail, Keller, TX, 76248 USA

ABSTRACT

This brief paper presents outdoor test results, measured in Keller, Texas, for a mini-concentrator module comprising a stretched-membrane line-focus Fresnel lens and a prism-covered triple-junction solar cell. While this lens and this solar cell were developed for space power applications, they also function extremely well under ground test conditions. Indeed, this mini-module has routinely achieved overall module (combined lens and cell) solar-to-electric conversion efficiency levels from 25% to 29% under a variety of conditions. This mini-module's performance is more than double the performance of ENTECH's conventional silicon-based terrestrial concentrator module. These results may indicate the proper direction for future development of a new generation of terrestrial concentrator modules.

1. Introduction and Background

ENTECH has been involved in photovoltaic concentrator technology for terrestrial applications for the past 22 years [1-3]. ENTECH's latest terrestrial concentrator module uses a large (85 cm wide aperture) acrylic lens to focus sunlight at 21X concentration onto air-cooled silicon photovoltaic cells. The performance of these terrestrial concentrators has been excellent, as shown in Fig. 1, which compares the long-term performance of leading photovoltaic technologies as measured by the independent PVUSA project [4].

ENTECH has been involved in photovoltaic concentrator technology for space applications for the past 15 years [5-7]. ENTECH's latest space concentrator module uses a small (8.5 cm wide aperture) silicone Fresnel lens to focus sunlight at 8X concentration onto radiation-cooled triple-junction photovoltaic cells. These space concentrators provide outstanding performance and reliability. The most recently launched ***SCARLET*** (solar concentrator array using refractive linear element technology) array powers both the satellite and the ion engine on the NASA/JPL Deep Space One probe, shown in Fig. 2. Deep Space One is currently 160 million miles from earth, on its way to a comet rendezvous in 2001.

Over the past two years, ENTECH has developed a new space concentrator array technology, called the stretched lens array (SLA) [8]. This new SLA provides higher performance at dramatically reduced mass. Recent SLA prototype tests in space simulators have confirmed over 300 W/sq.m. areal power generation and over 300 W/kg specific power at the fully functional panel level. As part of this new space array development, several prototype mini-concentrator modules have been tested under terrestrial sunlight by ENTECH in Keller, Texas. Somewhat surprisingly, these units have provided outstanding performance, although the triple-junction cells were optimized for the space solar spectrum, which is much different from the terrestrial solar spectrum. The following paragraphs highlight these terrestrial performance results.

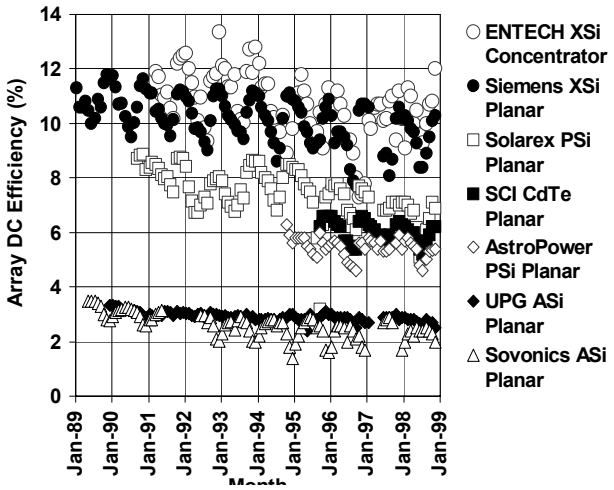

Fig. 1 – PVUSA Test Data for 20 kW Arrays in Davis, CA

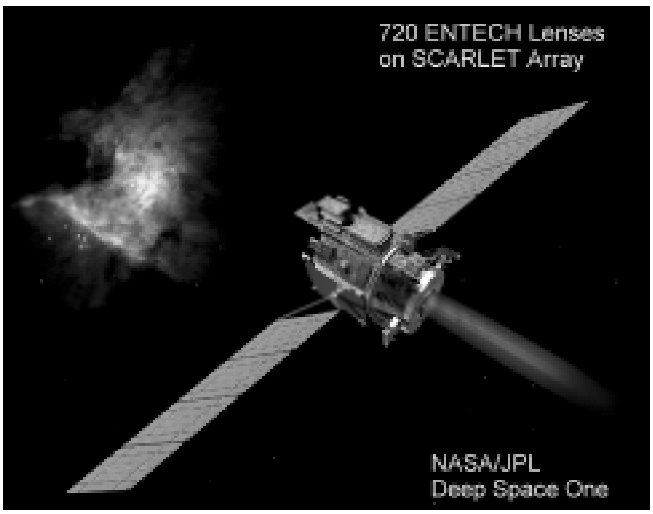

Fig. 2 – Deep Space One Probe Launched October 1998

2. Stretched Lens Mini-Module Performance Testing

Fig. 3 shows a stretched lens mini-concentrator module. The lens is a stretched membrane Fresnel lens made from a space-qualified silicone (DC 93-500).

The arched lens has an aperture width of 8.5 cm, and a focal length of 9.2 cm measured from the top of the arch. The line-focus lens is smooth on the outer convex surface, and has microscopic prisms on its inner surface. The solar cell at the focus of the lens is a Spectrolab triple junction GaInP/GaAs/Ge device (Cell 5L5), with an active width between busbars of 0.8 cm and a length of 4.0 cm. The cell is equipped with an ENTECH prism cover to minimize gridline shadowing losses, and is electrically contacted using electrically conductive adhesive and a copper/polyimide flex circuit. The flex circuit is attached to a 190 micron thick graphite composite radiator sheet, using a silicone pressure sensitive adhesive.

Fig. 4 shows a typical measured IV curve for the mini-concentrator module. The module efficiency of 28.1% is based on a lens aperture area of 34 sq.cm. and a direct normal irradiance of 947 W/sq.m., as measured with an Eppley normal incidence pyrheliometer (NIP).

The module efficiency was measured under a variety of conditions for a number of different days from December 1999 until February 2000, with typical variations shown in Fig. 5. The major reason for the wide variation in module efficiency, from about 25% to about 29%, is due to the same level of variation in the ratio of short circuit current (ISC) to direct normal irradiance (DNI). When this ratio is high (420 mA per kW/sq.m.), the module efficiency is high (28%). When this ratio is low (380 mA per kw/sq.m.), the module efficiency is relatively low (26%). The variations in this ISC/DNI ratio are due to spectral variations in the direct solar irradiance. Fig. 5 shows that the direct solar spectrum varies with both irradiance level during the day, and atmospheric conditions from one day to another. A second cell (9154L5), with a 1 cm width between busbars, was also tested in the mini-concentrator on 2/4/00, with nearly identical performance.

REFERENCES

[1] M.J. O'Neill, "Solar Concentrator and Energy Collection System," U.S. Patent No. 4,069,812, 1978.

[2] M.J. O'Neill, "Silicon Low-Concentration, Line-Focus, Terrestrial Modules," Chapter 10 in ***Solar Cells and Their Applications***, John Wiley & Sons, 1995.

[3] M.J. O'Neill and A.J. McDanal, "Photovoltaic Manufacturing Technology Improvements for ENTECH's Fourth-Generation Concentrator Systems," NCPV Review Meeting, 1996.

[4] PVUSA Project Team, "1998 PVUSA Progress Report," USDOE Contract No. DE-FC04-96AL89774, 1999.

[5] M.F. Piszczor and M.J. O'Neill, "Development of a Dome Fresnel Lens/Gallium Arsenide Photovoltaic Concentrator for Space Applications," 19th IEEE-PVSC, 1987.

[6] M.J. O'Neill, "Line-Focus Optics for Multijunction Cells in Space Power Arrays," 25th IEEE PVSC, Washington, 1996.

[7] M.J. O'Neill, "Color-Mixing Lens for Solar Concentrator System and Methods of Manufacture and Operation Thereof," U.S. Patent 6,031,179, 2000.

[8] M.J. O'Neill, "Ultralightweight Fresnel Lens Solar Concentrators for Space Power - the Stretched Lens Aurora (SLA) Array," 2nd Technology Interchange Meeting for Space Solar Power Exploratory Research and Technology, NASA MSFC, 1999.

Fig. 3 - Mini-Concentrator Module Under Test Outdoors

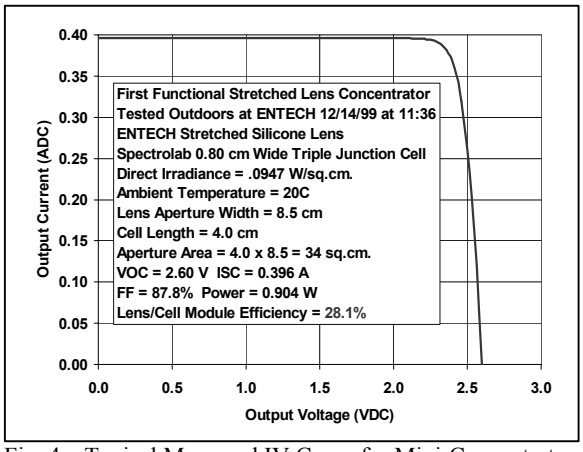

Fig. 4 – Typical Measured IV Curve for Mini-Concentrator

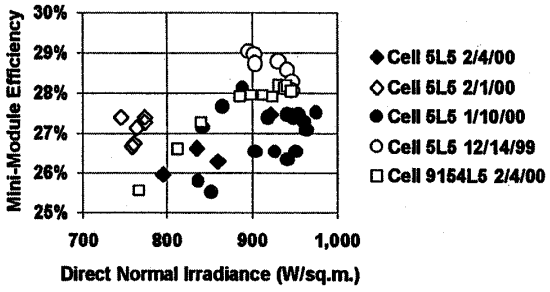

Fig. 5 - Mini-Concentrator Module Efficiency Variation

Standards for New Generation Technologies: CONCENTRATORS

G. Tamizh-Mani, Bob Hammond and Liang Ji
Arizona State University East, Photovoltaic Testing Laboratory
7349 E. Unity Avenue, Mesa, AZ 85212

ABSTRACT

Flat-plate crystalline and amorphous silicon PV (photovoltaic) modules have been well investigated and their design/safety qualification standards have already been developed by IEEE (Institute of Electrical and Electronics Engineers), IEC (International Electrotechnical Commission) and UL (Underwriters Laboratories). New generation technologies such as concentrators, CdTe (cadmium telluride) and CIS (copper indium diselenide) are being or have already been introduced in the market place. The current work at ASU, in collaboration with NREL and DOE, deals with the development of design qualification standards and test equipment, and validation of test procedures for the "Concentrator" technologies.

Introduction

Crystalline and amorphous silicon flat-plate PV modules are currently certified or listed as meeting test standards: IEEE 1262, IEC 61215/61646 and /or UL1703. The tests involved in these test standards provide confidence that the modules are durable, reliable and safe. The existing test specifications in these test standards generally exclude or are inappropriate for the new technologies such as concentrators, CdTe and CIS. As a result, existing specifications must be extended, or new test specifications developed, for each new technology. This paper deals with the development of a qualification test standard for the concentrator technologies.

Arizona State University – Photovoltaic Testing Laboratory (ASU-PTL) has been testing and certifying the crystalline and amorphous silicon flat-plate modules as per four standards mentioned above since 1994. The current work, related to the standards development for the concentrator technologies, is being carried out in collaboration with NREL and industrial partners. This paper presents the current status of test standard development, test equipment development and test procedures validation.

Development of Test Standard

A qualification test standard, IEEE 1513, for concentrator modules has been under development by an IEEE working group since 1997 [1]. This standard includes all the flat-plate module qualification tests, with only a few exceptions. This standard recommends the parallel qualification test sequences for both concentrator receivers and modules. A few more tests unique to the concentrators are also included in this standard. These unique tests include thermal shock and off-axis beam damage tests. ASU-PTL is assisting the IEEE working group for the implementation of successful balloting of IEEE 1513 by September 2000. This document, draft 8, is currently being reviewed by the PV industry and it will be sent out to the IEEE Working Committee by April 1, 2000.

Development of Test Equipment

The equipment/instruments necessary to carry out the concentrator module qualification testing are being procured/installed/developed at ASU-PTL. These include the development and/or installation of a thermal shock chamber, two-axis trackers, water spray station and weather monitoring station. A used environmental chamber (donated by Astropower) is being retrofitted to meet the shock chamber specifications which include high heating and cooling rates (7.5^{o}C/min) and specific temperature/humidity profiles (-40 to 110^{o}C, 85%RH). Figure 1 shows a photograph of a two-axis tracker with no modules installed and Figure 2 shows a photograph of a two-axis tracker with two concentrator modules installed. Figure 3 shows a photograph of a water spray station developed at the ASU-PTL. This station will be used to carry out the field wet resistance test (FWRT). The concentrator modules/receivers, generously offered by PVI (Photovoltaic International) and Amonix, will be used for the validation of IEEE 1513 test procedures.

Validation of Test Procedures

This work is in the initial stage and hence no conclusive results are available yet. At this current stage of the project, the validation work is focused on two key test procedures: (i) side-by-side performance comparison of stressed and reference/control modules, and (ii) series resistance measurement (via dark I-V curves) of the modules/receivers before and after each stress test.

REFERENCES

[1] IEEE 1513/D8: "Draft Recommended Practice for Qualification of Photovoltaic (PV) Concentrator Modules", Institute of Electrical and Electronics Engineers, 2000.

Figure 1: Photograph of a two-axis tracker with no concentrator modules installed

Figure 2: Photograph of a two-axis tracker with two concentrator modules installed

Figure 3: Photograph of a water spray station

System Performance of a 30.5 kW AC SunFocus PV Linear Concentrator Rooftop Array at SMUD

W. Bottenberg, N. Kaminar, P. Carrie, K. Chen, D. Gilbert, P. Guzman, D. Lehmicke, C. Sherring

Photovoltaics International, LLC

171 Commercial Street
Sunnyvale, CA 94086

ABSTRACT

PVI has installed a 30.5 kW AC concentrator array on the roof of a warehouse building at the Sacramento Municipal Utility District (SMUD). This system is the first installation of an advanced, new generation of line-focus, Fresnel lens concentrator modules. A system description and performance data is presented. The data show that the system performs as expected based on a new performance model.

Introduction

PVI has been developing a next generation, linear focus, one-axis tracking PV concentrator system during the last two years [1,2]. The modules employ an extruded plastic, Fresnel lens to focus the direct beam radiation on a string of 36 solar cells in series. The solar cells are mounted on an aluminum receiver that functions as a support and heat sink. The solar cells are encapsulated in ethylene vinyl acetate with a fluoro-polymer cover. A bypass diode protects the solar cells in groups of nine. The module is assembled as a rigid framework for mounting the lens by attachment of two roll-form aluminum sides and two cast aluminum end caps.

The concentration ratio of the system is 8.5 at standard conditions. This allows the use of specially designed cells manufactured on a standard one-sun cell line. This has a strong advantage in lowering the cost of concentrator solar cells.

The module is mounted on a frame support that provides the tracking function. An electric motor/gear box is actuated by a sun-following sensor. The motor drives a linkage that rotates the twelve modules on the frame from east to west.

System Description and Installation

The system consists of 240 SunFocus linear concentrator modules mounted on 20 tracker panels. The modules are wired into 10 source circuits of 24 modules in series. The inverter is a Trace Technology PV40-GTI rated at 40 kW AC.

Each panel frame is attached to the roof through a roof mounting system that penetrates the roof and is securely attached to the roof structure beams.

The SMUD 59th Street warehouse is oriented 15 degrees to the west because of its alignment to an adjacent set of railroad tracks. To optimize summer peaking performance the array structure is tilted at 29 degrees, which is about 9 degrees less than the latitude of 38.5 degrees.

Fig. 1. 30.5 kW AC PVI Array at SMUD

System Performance Modeling

We modeled the performance of the array using a modification of the method developed at Sandia by King et al. [3]. The system installation includes a data acquisition system (DAS), which measures DNI and POA irradiance, Vmp, Imp, Pac, Tambient and wind speed every 10 minutes during the day. Since Isc and Voc were unavailable, we used Imp as the indicator for system response to irradiance. This method is described in an upcoming paper [4].

In this method, measured values of Imp are used to calculate the angle of incidence function and the response to a reduced air mass function. An estimate of the effective irradiance is calculated from the Imp values. The power response is modeled using the effective irradiance, ambient temperature and wind speed.

Figures 2 and 3 show the comparison of the measured response for Imp versus the calculated response for consecutive sunny and cloudy days in November.

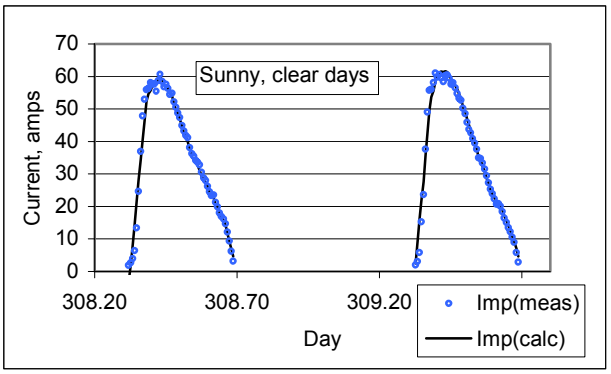

Fig. 2. Array Current at Max Power, Sunny Days

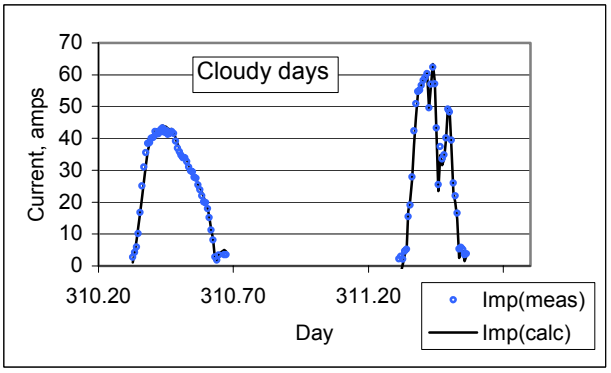

Fig. 3. Array Current at Max Power, Cloudy Days

The fall-off in the afternoon is due to the expected response to high angle of incidence in the afternoon winter hours. As mentioned previously, the building is tilted 15º to the west. During the winter the output is maximum in the morning. The panel will peak in the afternoon during the months from March through September.

The model adequately accounts for all of the features of performance: shadowing by clouds, varying irradiance, and angle of incidence.

System Energy Delivery

We have developed a system prediction model to estimate PV linear concentrator performance using solar resource data, for example as found in the Solar Radiation Data Manual [5]. This model uses a more complete version of the model described in the previous section. Module response data was measured on a two-axis tracker for Isc, Imp, Voc and Vmp. Response functions for angle of incidence, effective air mass, diffuse irradiance and temperature were developed. Figure 4 shows the measured system AC energy delivered compared to the expected energy delivered. The expected monthly values are calculated using an array size of 30.5 kW and the monthly capacity factor evaluated using Red Book data for Sacramento [5]. The agreement is found to be very good, indicating overall consistency in the methodology.

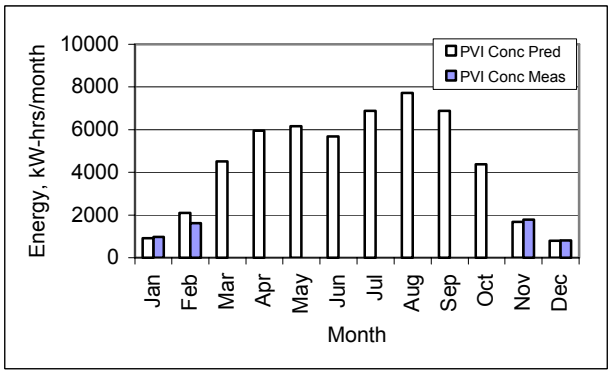

Fig. 4. Monthly Energy Delivery, Measured vs. Model

Conclusions

A 30.5 kW AC array based on a next generation linear concentrator module has been deployed as a rooftop system on a SMUD warehouse in Sacramento, California. Initial measurements of system performance indicate that the system is performing to expectation and progress has been made on validating a useful performance model for linear concentrators.

REFERENCES

[1] The authors wish gratefully to acknowledge support from the Department of Energy through the PVMaT Program under subcontract ZAF-6-14271-11. This support enabled the development of manufacturing technology for significant reduction of manufacturing cost.

[2] N. Kaminar, et al., "Manufacturing Technology Development of the Powergrid Linear Focus Photovoltaic Concentrator System", NCPV Photovoltaics Program Review, 16th Conference, AIP Conference Proceedings 462, (1998).

[3] D. King, et al., "Field Experience with a New Performance Characterization Procedure for Photovoltaic Arrays", 2nd World Conference and Exhibition on Photovoltaic Solar Energy Conversion Proceedings, Vienna, Austria (1998) 1947-1952.

[4] To be published later.

[5] "Solar Radiation Data Manual for Flat Plate and Concentrating Collectors", NREL/TP-463-5607 (1994).

An STM Survey of As/Ge(mnn) and P/Ge(mnn) Surfaces

W.E. McMahon and J.M. Olson

National Renewable Energy Laboratory

1617 Cole Boulevard, Golden, CO 80401

ABSTRACT

This paper contains a few representative results of a scanning tunneling microscope (STM) survey of Ge surfaces after exposure to arsenic and phosphorous. PH_3 (phosphine)- and As_4-exposed surfaces remain flat, whereas AsH_3 (arsine)-exposed surfaces can become nano-facetted due to etching. Some examples are given, and more general trends are discussed.

1. Introduction

Currently, high-efficiency GaAs/GaInP tandem cells are grown on Ge substrates. However, little is known about the nucleation of the initial layers on the Ge surface. One complication is that the initial nucleation surface is not clean Ge, but either arsenic- or phosphorous-exposed Ge. For this reason, we have conducted a study of the effect of arsenic and phosphorous exposure on Ge surfaces. In order to understand a range of technologically-relevant miscut directions, we have studied Ge(mnn) surfaces between (100) and (111).

2. Experimental Details

All surfaces were prepared in a metal-organic chemical vapor deposition (MOCVD) chamber under 50–70 torr of H_2 carrier gas flowing at 6–8 L/min. The group V source was either PH_3, AsH_3 or background As_4.

After preparation in the MOCVD chamber, samples were quenched to room temperature and transferred under vacuum to an ultra-high vacuum (UHV) chamber for study with low-energy electron diffraction (LEED), Auger electron spectroscopy (AES) and scanning tunneling microscopy (STM). All surfaces were studied as-quenched, with no additional surface preparation after leaving the MOCVD chamber.

3. Definitions

In this paper, the index (mnn) is limited to surfaces between (100) and (111), in other words, m > n. Figure 1 shows the relative orientations of the crystal surfaces to be discussed in this paper.

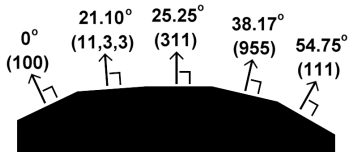

Figure 1. Schematic diagram of the facets discussed in this paper, with angles referenced to (100).

As/Ge refers to an arsenic-exposed Ge surface, while P/Ge refers to a phosphorous-exposed Ge surface, regardless of the source of arsenic or phosphorous. To specify the exact source of arsenic or phosphorous, a slightly different nomenclature is used. PH_3:Ge, AsH_3:Ge and As_4:Ge denote a Ge surface which has been exposed to (respectively) phosphine, arsine and elemental arsenic. In this paper the As_4:Ge surfaces were prepared by exposure to the background As_4 in our MOCVD chamber.

4. Results

We have found that PH_3:Ge(mnn) and As_4:Ge(mnn) surfaces remain flat for the conditions we have studied, while AsH_3:Ge(mnn) surfaces can be either flat or nano-facetted, depending upon the exact sample-preparation conditions. Here we will provide three specific examples, then discuss general trends.

4(a). PH_3:Ge(311)

Figure 2 is an STM image of PH_3:Ge(311). It is very flat, and has adopted an $n \times 2$ reconstruction. The "2" refers to the width of the obvious rows, which have a spacing of 13.3 Å, while the "n" refers to the regularly-spaced breaks along each row. LEED analysis indicates that these breaks occur every 6 to 7 atoms (n = 6 or 7). In the literature, similar gaps in surface reconstructions have been attributed to strain relief [1-4].

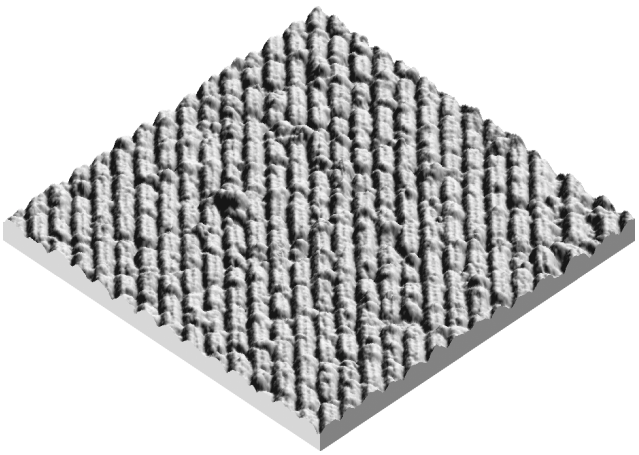

Figure 2. P/Ge(311) prepared by annealing a Ge(311) surface in an MOCVD chamber under 1.2 torr PH_3 at 570°C for 5 min.
Image size: 400 Å × 400 Å.

4(b). As_4:Ge(311)

Figure 3 is an STM image of As_4:Ge(311). This surface was prepared by annealing a Ge(311) surface in an MOCVD chamber under H_2 and background As_4. It also remains flat, but with a 2×3 reconstruction. The "3" indicates that the row spacing is 19.9 Å. Note that this is different from the row spacing seen for PH_3:Ge(311). The "2" indicates that a subtle two atom periodicity along the rows is observed with LEED.

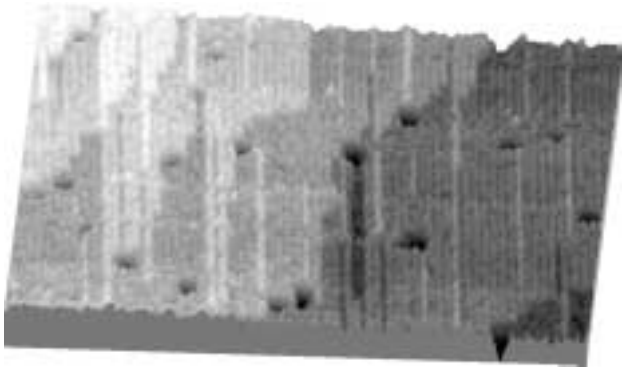

Figure 3. As/Ge(311) prepared by annealing a Ge(311) surface in an MOCVD chamber under background As_4 for 50 min. while slowly lowering the temperature from 640° to 470°C. Some steps are observed, due to a slight unintentional misorientation of the substrate away from (311).
Image size: 2000 Å × 2000 Å.

4(c). AsH_3:Ge(311)

Figure 4 is an STM image of AsH_3:Ge(311). In contrast to the previous two examples, this surface is nano-facetted. This nano-facetting is a result of AsH_3-etching of the surface. (No etching of Ge is observed for either PH_3 or As_4.) Two preferred facetting directions are observed: (11,3,3) and (955).

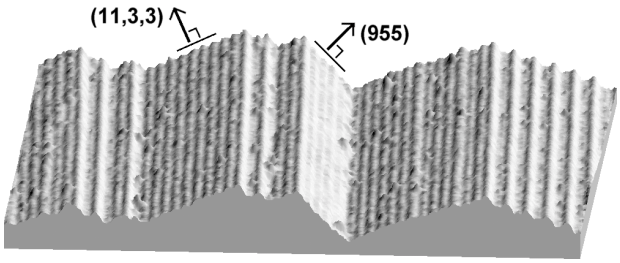

Figure 4. As/Ge(311) formed by annealing a Ge(311) surface under 1.2 torr AsH_3 for 30 min. at 640°C. An (11,3,3) and a (955) facet have been labelled. The rightmost facet can be formed by interlacing (11,3,3) and (955) surface unit cells.
Image size: 1500 Å × 1500 Å.

5. Discussion

The preceding (311) examples serve as a basis for discussing the entire range of As/Ge and P/Ge (mnn) surfaces. Similar results have been obtained for Ge(211), Ge(311), Ge(411), Ge(511), and vicinal Ge(100) [5, 6] miscut 2, 6 and 9° toward (111).

For the conditions we have studied, PH_3:Ge(mnn) surfaces always remain flat. This suggests an energetic driving force, such as surface tension, which tends to make the surfaces flat.

As_4:Ge(mnn) surfaces also remain flat for the conditions we have studied. Moreover, it is possible to flatten a previously nano-facetted Ge(mnn) surface by heating it under As_4. This indicates that subsurface Ge can rise to the surface and travel great distances before relocating in a more desirable location.

Because AsH_3 etches Ge, the AsH_3:Ge(mnn) surfaces are more complicated. As with the As_4 case, thermal energy still causes subsurface Ge to rise to the surface. However, the etching process removes some fraction of this Ge before it has a chance to relocate. If all of the Ge is removed, and none relocates, the resulting surface can become completely facetted. If most of the Ge relocates (compared to the etching rate), the resulting surface will be flat. The As_4 case represents one extreme in which all of the Ge relocates (none is etched).

This balance between the supply, removal, and relocation of Ge during AsH_3 etching is consistent with our observations, but more work needs to be performed before it is understood in detail. Nonetheless, we are now able to describe the general trends, and have identified three principle nano-facetting directions: (100), (11,3,3) and (955).

6. Conclusions

The effects of arsenic and phosphorous exposure on Ge(mnn) substrates has been studied. We find that As_4- and PH_3-exposed Ge surfaces remain flat, whereas AsH_3 exposure can induce nano-facetting. This behavior was observed for a range of Ge(mnn) surfaces between (100) to (111).

Acknowledgments

This work would not have been possible without the help of J. Geisz, A. Kibbler, D. Friedman, S. Kurtz, C. Kramer, M. McCarthy and K. Jones. This work is supported by the Office of Energy Research, Basic Energy Sciences, U.S. Department of Energy.

REFERENCES

[1] R.S. Becker, T. Klitsner and J.S. Vickers: "Arsenic-terminated silicon and germanium surfaces studied by scanning tunneling microscopy", J. of Microscopy 152 (1988) 157-165.

[2] X. Chen, F. Wu, Z. Zhang and M.G. Lagally: "Vacancy-vacancy interaction on Ge-covered Si(100)", Phys. Rev. Lett. 73 (1994) 850-853.

[3] L. Kipp, R.D. Bringans, D.K. Biegelsen, J.E. Northrup, A. Garcia, and L.-E. Swartz: "Phosphine adsorption and decomposition on Si(100) 2×1 studied by STM", Phys. Rev. B 52 (1995) 5843-5850.

[4] D.-S. Lin, T.-S. Ku and R.-P. Chen: "Interaction of phosphine with Si(100) from core-level photoemission and real-time scanning tunneling microscopy", Phys. Rev. B 61 (2000) 2799-2805.

[5] W.E. McMahon and J.M. Olson: "Atomic-resolution study of steps and ridges on arsine-exposed vicinal Ge(100)", Phys. Rev. B 60 (1999) 2480-2487.

[6] W.E. McMahon and J.M. Olson: "Atomic-resolution STM study of a structural phase transition of steps on vicinal Ge(100)", Phys. Rev. B 60 (1999) 15999-16005.

BGaInAs Alloys Lattice Matched to GaAs for High-Efficiency Solar Cells

J.F. Geisz, D.J. Friedman, J.M. Olson, Sarah R. Kurtz, R.C. Reedy, A.B. Swartzlander, B.M. Keyes, A.G. Norman

National Renewable Energy Laboratory

1617 Cole Boulevard, Golden, CO 80401

ABSTRACT

A novel alloy, BGaInAs, may prove useful in high-efficiency III-V multijunction solar cells. We report the epitaxial growth of zinc-blende $B_xGa_{1-x-y}In_yAs$ and $B_xGa_{1-x}As$ on GaAs substrates with boron concentrations (x) up to 3%-5% by atmospheric-pressure metal-organic chemical-vapor deposition. The band gap of $B_xGa_{1-x}As$ increases by only 4-8 meV/%B with increasing boron concentration in this concentration range. We demonstrate an epitaxial zinc-blende $B_xGa_{1-x-y}In_yAs$ layer with a band gap of 1.34 eV nearly lattice matched to GaAs and a BGaInAs solar cell with an electron diffusion length greater than 0.4 μm.

1. Introduction

The high-efficiency GaInP/GaAs/Ge cascade solar cell is the current state-of-the-art device for space applications and is highly promising for terrestrial concentrator applications. Yet the combination of these three semiconductor materials does not consist of the optimal band gaps necessary for maximum efficiency. By reducing the band gap of the 2nd junction in a two- or three-junction cell or inserting a 1 eV junction between the GaAs and Ge junctions [1], the overall efficiency of the device can be significantly increased. In order to maintain high crystalline quality, we are attempting to band-gap engineer a new semiconductor material that would have a band gap in the range of 1.0-1.35 eV that can be grown lattice matched to GaAs or Ge. Although GaInNAs lattice matched to GaAs has been grown with band gaps ranging from 0.95 to 1.4 eV [2], no GaInNAs material grown to date has been demonstrated to provide sufficiently long diffusion lengths for high-quality solar cell devices [3].

We propose $B_xGa_{1-x-y}In_yAs$ as another material with the potential to be grown lattice matched to GaAs with band gaps below 1.4 eV [4]. The contraction of the crystal lattice by the addition of boron can be used to offset the expansion due to indium. Assuming Vegard's law and a BAs lattice parameter of 4.777Å [5], $B_xGa_{1-x-y}In_yAs$ should be lattice matched to GaAs when y = 0.46 x.

2. BGaAs

We have grown a series of $B_xGa_{1-x}As$ layers with varying boron concentrations by atmospheric-pressure metal-organic chemical vapor deposition (MOCVD) using diborane as a boron source [4]. These layers have specular morphology and a distinct epilayer peak in the double-crystal X-ray diffraction (DCXRD). Compositional analysis by DCXRD and secondary-ion mass spectrometry (SIMS) reveal boron compositions up to $1.4x10^{21}$ cm^{-3} (x = 3%-5%), the highest reported to date. Photoluminescence (PL) and absorption measurements indicate that the band gap increases by 4-8 meV/%B with increasing boron concentration in this concentration range. Figure 1 shows how the band gap of $B_xGa_{1-x}As$ varies with lattice constant. We have estimated an optical bowing parameter of 1.6-2.3 eV from these data. This estimate of the bowing parameter is much closer to other typical III-V alloy systems than the large bowing parameters observed in GaNAs alloys [6]. The lack of large bowing in the BGaAs alloys may allow for higher electrical quality material to be produced than is possible for GaNAs alloys.

3. BGaInAs

Figure 1 also shows an estimated ternary line for $B_xIn_{1-x}As$ alloys based on a similar bowing parameter to the $B_xGa_{1-x}As$ system. This assumption predicts that $B_xGa_{1-x-y}In_yAs$ alloys could potentially be lattice matched to

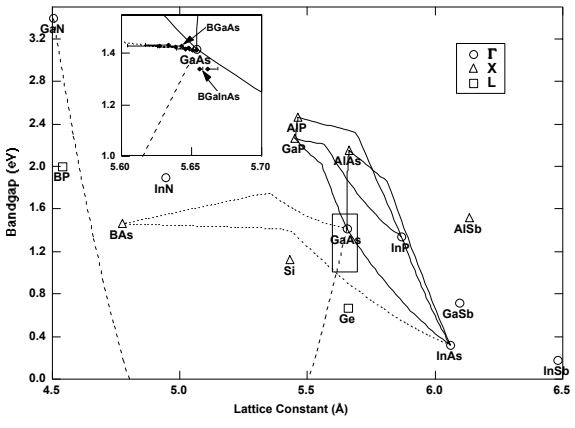

FIG. 1. Band gap vs. lattice constant of III-V semiconductors including boron and nitride alloys. The points in the inset show data for actual BGaAs and BGaInAs alloys grown to date.

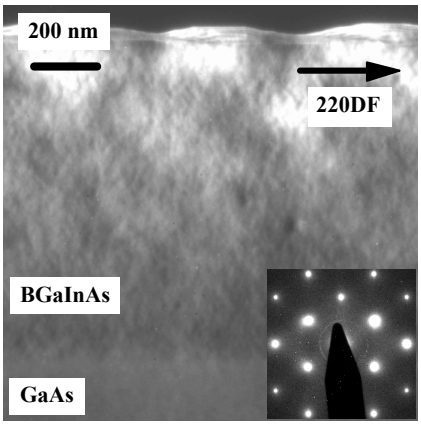

FIG. 2. <220> dark-field TEM image of $B_xGa_{1-x-y}In_yAs$ sample also characterized in Figures 2, and 4. Inset is <110> pole electron diffraction pattern from layer showing only spots expected for zinc-blende.

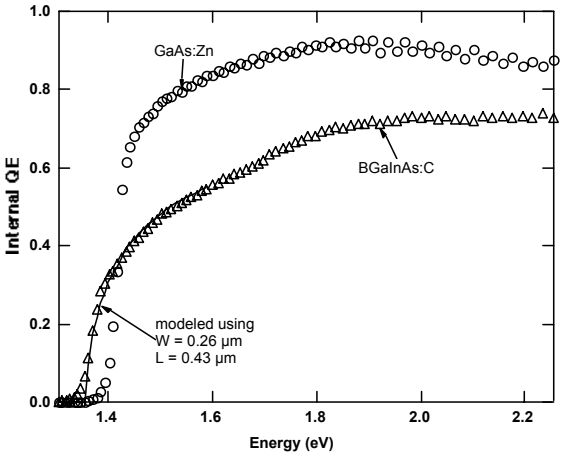

FIG. 3. Internal quantum efficiency (QE) spectra of BGaInAs and GaAs cells.

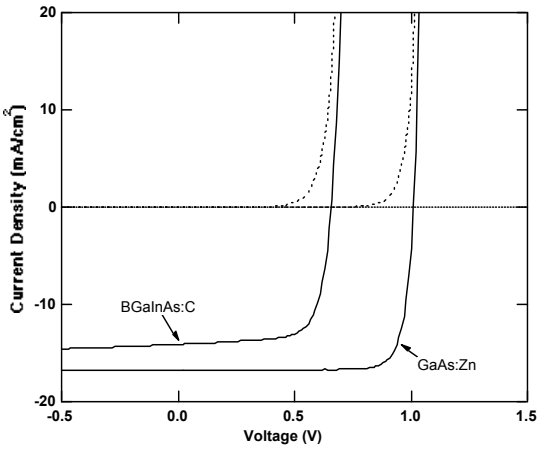

FIG. 4. IV curves of BGaInAs and Ga As cells under AM1.5D, one–sun conditions (solid lines) and dark (dashed lines).

GaAs with band gaps ranging from 0.9 to 1.42 eV depending on the extent of boron that can be incorporated onto group III sites within a zinc-blende structure. We have demonstrated a $B_{0.02}Ga_{0.92}In_{0.06}As$ layer nearly lattice matched to GaAs with a 1.34 eV band gap [4]. The composition was determined by SIMS, DCXRD, and Auger electron spectroscopy (AES). The transmission electron microscopy (TEM) image in figure 2 demonstrates that the layer is dislocation-free and zinc-blende in structure. Strong room-temperature PL emission indicates that this is a direct-gap material.

4. BGaInAs Solar Cells

Using BGaInAs with a band gap of about 1.34 eV (assuming sufficient electrical quality) could increase the efficiency of a two- or three-junction device by almost 2% absolute if it were used as the second junction. Towards such an end, we have fabricated and characterized the first BGaInAs solar cell. The single-junction n-on-p device consists of an 0.1-μm-thick Se-doped GaAs emitter, a 1.5-μm-thick C-doped $B_{0.03}Ga_{0.91}In_{0.06}As$ base, and GaInP window and back-surface-field layers.

Figure 3 shows the quantum efficiency (QE) of this device in comparison with a nearly identical structure that contains a Zn-doped GaAs base. The QE demonstrates that the BGaInAs material has a lower band gap (1.36 eV) than GaAs. The internal QE of this first BGaInAs device with a base carrier concentration of 1.5×10^{16} cm^{-3} exceeds 70% and is comparable to the best GaInNAs cells grown to date. Modeling of the QE indicates that the material has an electron diffusion length greater than 0.4 μm.

Figure 4 shows a comparison of the IV curves under AM1.5D conditions. The low Voc and FF of 0.66V and 73%, respectively, of the BGaInAs cell require considerable improvement before this cell can be used to improve on the GaAs cell in a multijunction device, but represent a significant first step. A better understanding of boron incorporation, doping of the material, and important defects should be helpful in improving this cell.

5. Summary

We have proposed the use of BGaInAs alloys for high-efficiency III-V multijunction solar cells, estimated the bowing parameter of BGaAs, demonstrated the first BGaInAs material lattice matched to GaAs with band gaps as low as 1.34 eV, and fabricated the first BGaInAs solar cell.

REFERENCES

[1] S. R. Kurtz, D. Myers, and J. M. Olson, "Projected Performance of Three- and Four-Junction Devices using GaAs and GaInP." Proceedings of the 26th IEEE Photovoltaic Specialists Conference, 875 (1997).

[2] M. Kondow, K. Uomi, A. Niwa, T. Kitatani. S. Watahiki, and Y. Yazawa, "GaInNAs: A novel material for long-wavelength-range laser diodes with excellent high-temperature performance." Jpn J. Appl. Phys. **35**, 1273 (1996).

[3] J. F. Geisz, D. J. Friedman, J. M. Olson, S. R. Kurtz, and B. M. Keyes, "Photocurrent of 1 eV GaInNAs lattice-matched to GaAs." J. Cryst. Growth (1998).

[4] J. F. Geisz, D. J. Friedman, J. M. Olson, S. R. Kurtz, R. C. Reedy, A. B. Swartzlander, B. M. Keyes, an A. G. Norman, "BGaInAs alloys lattice matched to GaAs." Appl. Phys. Lett. **76** 1443 (2000).

[5] J. A. Perri, S. LaPlaca, and B. Post, "New group III-group V compounds: BP and BAs." Acta Cryst. **11,** 310 (1958).

[6] M. Weyers and M. Sato, "Growth of GaAsN alloys by low-pressure metalorganic chemical vapor deposition using plasma-cracked NH_3." Appl. Phys. Lett. **62**, 1396 (1993).

BAs–GaAs Semiconductor Alloys as a Photovoltaic Alternative to Nitride Alloys

G. L. W. Hart and A. Zunger

National Renewable Energy Laboratory, Golden CO 80401

ABSTRACT

Nitrogen alloyed III–V semiconductor compounds have been intensely studied in recent years due to unusual effects caused by nitrogen alloying. These effects are exploited in band gap engineering for specific applications such as solar cells and blue lasers. However, alloying with *boron* instead of nitrogen may offer similar effects while mitigating the difficulties associated with nitride semiconductors. Using the full-potential linearized augmented planewave implementation of density functional theory within the local density approximation, we have studied* BAs as well as boron alloying in GaAs. We find that BAs is unusual with respect typical III–V semiconductors in that it resembles Si, not III–Vs: it has an indirect gap; has the *p*-like conduction band below the *s*-like state; and the valence density is distributed equally on the 2 atoms in the cell. We find in this first theoretical study of BAs–GaAs alloys that the band gap bowing of $B_xGa_{1-x}As$ is much smaller than in $GaAs_{1-x}N_x$ and the bulk mixing enthalpy for boron in GaAs is significantly lower than for nitrogen. We conclude that boron alloying presents new opportunities in band gap engineering.

1. Introduction

Nitrogen alloying of semiconductors leads to unusual effects such as (i) localization of states near the conduction band minimum (CBM) (ii) giant band gap bowing, and (iii) composition dependent bowing. By exploiting these effects, the properties of an alloy (band gap, etc.) can be tuned for specific applications. However, there are also difficulties associated with nitride alloys such as poor transport, limited solubility, etc.

Boron alloying of GaAs has been proposed. [1–5] Both boron and nitrogen form exceptionally strong bonds in the alloys and cause large size mismatches. In the case of boron, however, the size mismatch is slightly less severe and the bonding somewhat weaker. Also the B–As bonds are very covalent whereas the Ga–N bonds have a strong ionic component. Until now, how these similarities and differences between nitrogen and boron would affect the properties of semiconductor alloys was an open question. Historically, the difficulty in fabricating boron alloys experimentally[2] and the computational burden of modeling dilute alloys have made studies of boron semiconductor alloys difficult. However, the development of advanced experimental techniques for fabricating nitride alloys (which can be applied to boron alloys) and significant advances in computational approaches have now made the study of boron alloys easily accessible. We have examined a typical III–V boron alloyed semiconductor, BAs, and have studied the effects of boron alloying in GaAs. Our results are as follows:

2. Zinc-blende BAs

BAs has an indirect band gap of ~1.6 eV near the X point, and the direct band gap is ~4.2 eV (as calculated by the GW method; reliable measurements do not exist).[6] The band structure of BAs is unusual compared to "conventional" III–V materials in that the Γ_{15c} *p*-like conduction state is *below* the *s*-like Γ_{1c} state. As a result of this reversal of conduction band states and the indirect gap, the band structure of BAs closely resembles that of silicon. The similarity to silicon is due in part to the very covalent nature of the bonding in BAs which results from the very similar electronegativities of boron and arsenic. Consequently the cation and anion states mix very strongly at the valence band maximum (VBM), the anion/cation distinction becomes blurred, and BAs resembles a covalent IV–IV semiconductor like silicon rather than a typical III–V semiconductor.

3. BAs–GaAs band offsets

Figure 1 shows our calculated band offsets for the group III–As family including BAs. Despite the much smaller bond length of BAs, its VBM is significantly higher than that of AlAs and close to that of GaAs. In contrast, in the Ga–group V family, the VBM of GaN lies more than 2.0 eV below that of GaAs and more than 1.5 eV below that of GaP. The height of the VBM in BAs results from the strong mixing of boron and arsenic *p* states at the VBM. This feature which is unusual compared to other III–Vs draws the VBM up towards the *p* orbital energy of boron. Notice the very small predicted band offsets in BAs–GaAs.

4. Band gap bowing in $B_xGa_{1-x}As$

The band gap bowing for $GaAs_{1-x}N_x$ alloys is very large, and even for relatively small concentrations of nitrogen, the bowing is composition-dependent, varying between ~10 to ~20 eV. Surprisingly, our calculations show that, unlike $GaAs_{1-x}N_x$, the bowing of $B_xGa_{1-x}As$ alloys is relatively small

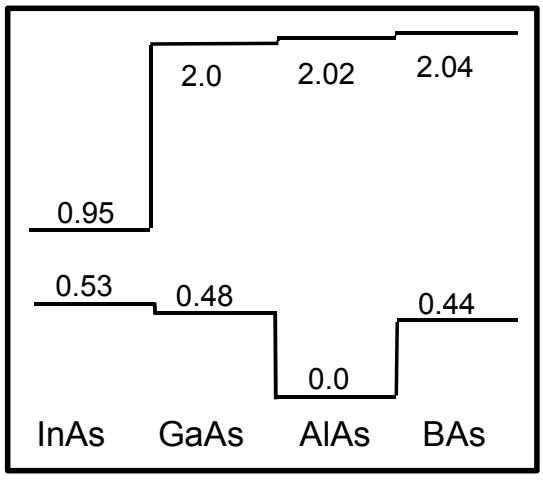

Figure 1. Valence and conduction band offsets for the group III–As family. The VBMs are calculated while the CBMs are determined from the minimum measured band gap (indirect near X for BAs and AlAs; direct for GaAs and InAs).

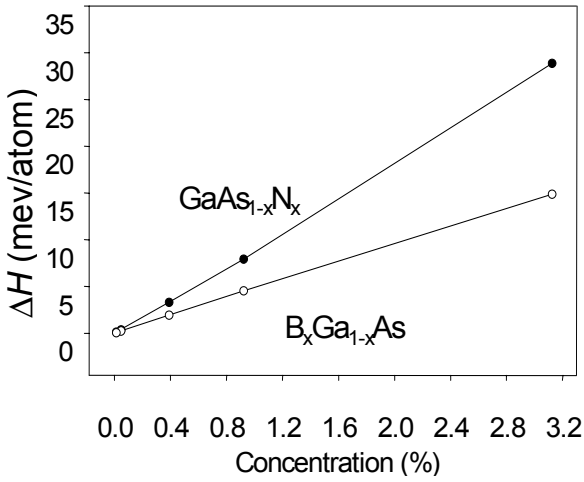

Figure 2. Mixing enthalpy of boron and nitrogen in GaAs as a function of concentration

(~3 eV) and fairly composition independent, in agreement with the experimental results of Ref. 5. This is somewhat unexpected given that both boron and nitrogen cause large size mismatches and both form very strong bonds with their neighbors. Nitrogen alloying very strongly perturbs the electronic structure of GaAs whereas the effects of boron alloying are much more "gentle."

5. Bulk mixing enthalpy of $B_xGa_{1-x}As$

The calculated bulk mixing enthalpy of $GaAs_{1-x}N_x$ versus $B_xGa_{1-x}As$ (Fig. 2) is also unexpected. The mixing enthalpies are much higher (~60%) for the $GaAs_{1-x}N_x$ alloy. If the differences in the bulk mixing enthalpies are indicative of the differences in the solubilities for boron and nitrogen alloying of GaAs, we can conclude that the boron containing alloy can be grown with a larger composition range than the nitride alloy.

6. Wavefunction localization in $B_xGa_{1-x}As$

An unusual feature of the nitride alloys is the localization of wavefunctions Ψ for states in or below the conduction band. In a 3% BAs–GaAs alloy (see Figure 3 below), Ψ^2 for the valence band maximum is completely delocalized and has a strong As *p*-like character. On the other hand, the CBM is "semi-localized", i.e. it is strongly localized near the boron atom but extended at longer distances. Similarly, the state just above the CBM is also localized around the boron atom and some of the gallium atoms.

7. Conclusions

Despite the fact that boron and nitrogen are both small, first row atoms that have a tendency to form strong bonds in compounds, their effects on III–V alloys show very pronounced differences. (i) The band gap bowing is large and composition-dependent for $GaAs_{1-x}N_x$ but relatively small and composition-independent for $B_xGa_{1-x}As$, and (ii) the bulk mixing enthalpy of boron in GaAs is much smaller than for nitrogen. Despite these differences, both alloys share the feature of wavefunction localization. Two implications of this study are immediately obvious. (i) Boron alloys may allow larger composition ranges than the nitrides, and (ii) the boron alloys offer new opportunities in band gap engineering.

REFERENCES

[1] S. Sakai, Y. Ueta, and Y. Terauchi, Jpn. J. Appl. Phys. **32**, 4413 (1993)
[2] S. M. Ku, J. Electrochem. Soc. **113**, 813 (1966).
[3] M. A. Tischler, et al., J. Appl. Phys. **71**, 984 (1992).
[4] C. H. Wei and J. H. Edgar, J. Cryst. Growth **208**, 179 (2000)
[5] J. Geisz, et al., Appl. Phys. Lett. **76**, 1443 (2000)
[6] M. P. Surh, S. G. Louie, and M. L. Cohen, Phys. Rev. B **43**, 9126 (1991)

* Details of the calculations are given in our paper " BAs and Boron III–V Alloys," G. L. W. Hart and A. Zunger, to be published (2000).

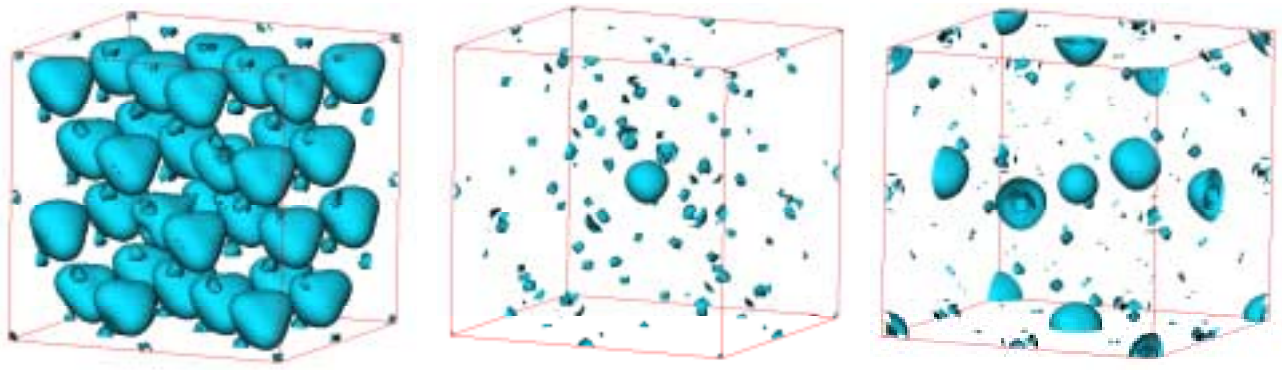

Figure 3. Isosurface plots of the square of the wavefunction for the VBM, CBM, and the first state above the CBM. The VBM is completely delocalized with As *p*-like character. In contrast, the first state states in the conduction bands shows effects of localization.

GaAsP/InGaAsN Strained Layer Superlattices for Solar Cell Applications

S. M. Bedair[1)], J. C. Roberts[1)] and N. A. El-Masry[2)]

[1)]Department of Electrical & Computer Engineering, North Carolina State University, Box 7911, Raleigh, NC 27695
[2)]Department of Materials Science & Engineering, North Carolina State University, Box 7907, Raleigh, NC 27695

ABSTRACT

GaAsP/InGaAsN strained layer superlattices (SLSs), lattice matched to GaAs are proposed to extend the long wavelength absorption of the bottom cell in a cascade solar cell structure. In the proposed SLS structure, the In content can be higher than in conventional InGaAsN bulk films and the N content maintained near 1% while still maintaining the lattice matching condition to the GaAs substrate. Data are presented for GaAsP/InGaAs SLSs that validate this approach and which lay a framework for the successful development of the GaAsP/InGaAsN SLS structure.

1. Introduction

The cascade solar cell may be the only promising approach to achieve conversion efficiencies greater than 30%. However, there are several problems that have to be addressed before such high efficiencies can be realized. One of these problems is the lack of lattice matched material systems having the optimum bandgap combinations. This combination is about 1.8 eV for the high bandgap junction (top cell) and about 1.2 eV for the lower bandgap junction (bottom cell).

Previous efforts have been based on using combinations of lattice mismatched heterostructures such as AlGaAs for the top cell and InGaAs for the bottom cell [1]. A high density of defects is always present between the GaAs substrate and the InGaAs film and also between the bottom and the top cells. These defects will reduce the current collection efficiency of this solar cell structure. The other option is to use an AlGaAs/GaAs (top cell/bottom cell) combination to avoid this lattice mismatch problem. The main problem with this structure is that the bandgap of the GaAs (E_g = 1.43 eV) is too high for optimum collection of solar radiation. The AlGaAs/GaAs structure has open-circuit voltage, $V_{oc} \cong 2V$, thus an increase of 1% in the short-circuit current, I_{sc} will result in an increase of 2% in the solar cell collection efficiency. Therefore, any slight increase in the ability of this structure to absorb long wavelength photons (longer than 0.86 μm) will result in a significant improvement in the collection efficiency. Strained layer superlattices (SLSs) can be useful in several solar cell structures such as cascade solar cells.

2. Potential of GaAsP/InGaAs Strained Layer Superlattices

Strained layer superlattices such as GaAs/InGaAs [2] and GaAsP/GaAs [3] have been studied extensively. However, these superlattices and other binary-ternary structures suffer from major limitations. The average lattice parameter of these binary-ternary structures does not lattice match to that of the typical substrate such as GaAs. For example, an $In_xGa_{1-x}As$/GaAs SLS will have a lattice parameter which corresponds to bulk $In_{x/2}Ga_{(1-x)/2}As$ as shown in Figure 1. Thus, when grown on a GaAs substrate, defects in the form of misfit dislocations appear at the SLS/substrate interfaces [4]. These difficulties can be avoided if binary-ternary SLSs are replaced by other material systems. What is needed is a superlattice composed of two materials having equal but opposite lattice mismatches such that the average lattice constant matches that of GaAs. For example, a SLS made of $GaAs_{1-y}P_y$-$In_xGa_{1-x}As$ ternary alloys can satisfy these requirements [5].

$GaAs_{1-y}P_y/In_xGa_{1-x}As$ SLSs can be grown directly on a GaAs substrate with an average lattice constant equal to that of GaAs. In such a structure, with $y \cong 2x$, the InGaAs will

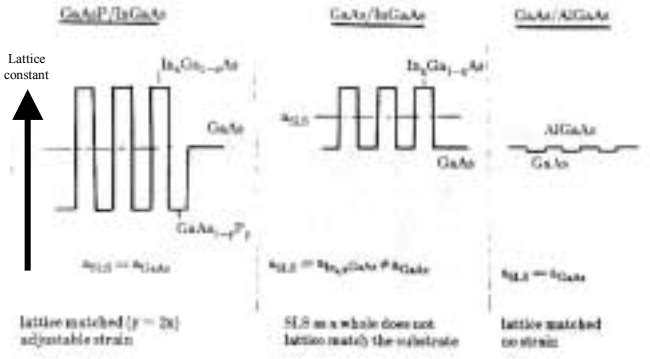

Figure 1. Schematic of the lattice constant of several SLS structures (left to right): GaAsP/InGaAs, InGaAs/GaAs, AlGaAs/GaAs.

be under compression, whereas the GaAsP layer will be under tension and the lattice parameter of the SLS as a whole will be equal to that of GaAs as shown in Figure 1. In this case, no defects are generated between the SLS and the substrate and no limitations are imposed on either the value of strain between the individual layers or the number of SLS periods. Such a structure will thus allow the use of GaAs or AlGaAs as buffer or confining layers since all layers including the SLS have the same lattice constant in the growth plane.

3. MOCVD Growth and Characterization of GaAsP/InGaAs SLSs

The MOCVD approach [6] uses trimethylgallium (TMG), triethylindium (TEI), arsine (AsH_3), and phosphine

(PH_3) as sources of Ga, In, As, and P respectively. Both AsH_3 and PH_3 are 5% in H_2. The growth temperature was 630 °C, which is a compromise between ideal growth temperature for the two ternary alloys. For GaAsP a relatively high temperature is required to obtain a wide range of GaP composition since phosphorous incorporation is low at reduced temperature [7]. On the other hand, for InGaAs, a low growth temperature is preferable because InAs incorporation decreases as the growth temperature increases. Details of the growth process were previously described [6]. Epitaxial layer thickness and superlattice structures were examined using an x-ray diffraction technique. From the (400) diffraction pattern for 45 periods of a $GaAs_{0.8}P_{0.2}/In_{0.1}Ga_{0.9}As$ SLS grown on a GaAs substrate we obtained the zero-order diffraction peak (n = 0) that gave the lattice parameter of the SLS as a whole, with a lattice mismatch of less than 0.1% to the GaAs substrate. Satellite peaks, due to the periodicity of the SLS, imply a period of 350 Å, which is consistent with that predicted from the growth rate and that obtained from the total thickness measurement of the SLS on a cleaved sample.

4. GaAsP/InGaAs SLS Solar Cell

A superlattice p-n junction bottom cell was grown with doping levels for both p- and n-type in the 10^{17} cm^{-3} range [8]. The SLS was made of alternating layers of $GaAs_{0.72}P_{0.28}$ and $In_{0.14}Ga_{0.86}As$ with equal thicknesses of about 150 Å each. The total thickness of the n-type and p-type superlattice are about 0.3 μm each. The slope of the log (current) vs. voltage characteristics of these superlattices junctions gave a diode factor of about 2, indicating that the current transport is controlled by generation and recombination processes in the depletion region. Current-voltage characteristics of test device structures have been made with and without illumination. The value of V_{oc} for illumination at about 1 Sun is close to 0.85 V. The spectral response for a GaAs cell with part of the active region made of a GaAsP/InGaAs superlattice is shown in Figure 2. As shown in this figure, the bottom cell spectral response can be extended to wavelengths longer than those achieved in GaAs cells without the superlattice structure. It should be emphasized that this is achieved without introducing any defects that are present in a lattice-mismatched system. This test structure was not optimized for maximum absorption; however, the great flexibility of this ternary alloy strained-layer structure provides the ability to design a solar cell optimized for high efficiency [8]. This extended absorption can be achieved by using the GaAsP/InGaAs SLS as a part of the bottom cell [8]. It is thus expected that about 70% of the photons in the energy range from 1.25 to 1.43 eV may be collected by the SLS which has an effective bandgap of 1.25 eV and a total thickness of about 1 μm. The efficiency of minority carrier diffusion through the superlattice layers can be improved by reducing the width and height of the GaAsP barrier layers..

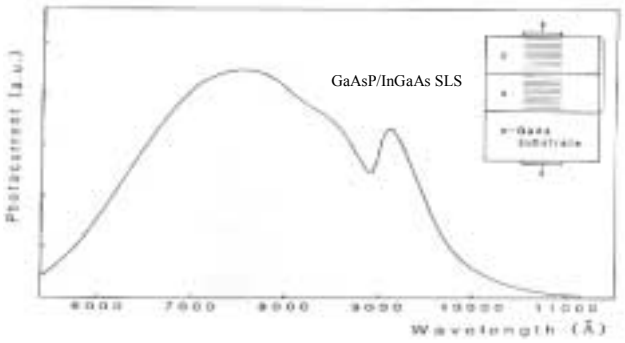

Figure 2. Photocurrent response of GaAsP/InGaAs SLS test cell with device structure inset.

5. Potential of GaAsP/InGaAsN for 1 eV Bottom Cell

Recent reports have shown that InGaAsN-based solar cell structures can reduce the bandgap to that required for bottom cells to about 1 eV. However, development of this material system presents significant problems. First, achieving a fairly high N concentration of about 3% is needed but this gives material with very poor electrical and optical properties such as poor carrier lifetime and fairly short diffusion length. The second problem is a result of the limited amount of In that can be used (≅6%) to maintain lattice matching to the GaAs substrate. The above two problems can be mitigated by using the structure GaAsP/InGaAsN, where a lessened restriction on the amount of In% to maintain the lattice matching condition and the $E_g \cong 1$ eV can be achieved with a N content of ~1%, Recent data have demonstrated that this fairly low N% does not result in any substantial deterioration of the quality of the InGaAsN material system. A quick estimate can show $E_g \cong$ 1eV can be achieved in this SLS with In = 20%, Ga= 80%, As = 99% and N = 1% that will be part of the GaAsP/InGaAsN SLS structure.

6. Conclusions and Future Work

GaAsP/InGaAs SLSs have been successfully grown and characterized, showing extended absorption to longer wavelengths. Work is underway to add N to the InGaAs component of the SLS to extend the absorption edge to ~1 eV.

7. References

1. S. M. Bedair, S. B. Phatak and J. R. Hauser, IEEE Trans. Electron Devices **ED-27**, 822 (1980).
2. L. R. Dawson et al., J. Vac. Sci. Technol. **B2**, 179 (1984).
3. R. M. Biefeld, J. Electron. Mater. **15**, 193 (1986).
4. S. M. Bedair, T. P. Humphreys, N. A. El-Masry, Y. Lo, N. Hamaguchi, C. Lamp, A. Tuttle, D. L. Dreifus and P. Russel, Appl. Phys. Lett. **49**, 942 (1986).
5. S. M. Bedair, T. Katsuyama, P. K. Chiang, N. A. El-Masry, M. A. Tischler and M. Timmons, J. Cryst. Growth **68**, 477 (1984).
6. T. Katsuyama, S. M. Bedair, N. C. Giles, R. R. Burns and J. F. Schetzina, J. Appl. Phys. **62**, 498 (1987).
7. G. B. Stringfellow, J. Crystal Growth **62**, 225 (1983).
8. T. Katsuyama, M. A. Tischler, D. Moore, N. Hamaguchi, N. El-Masry and S. M. Bedair, Solar Cells **21**, 413 (1987).

Structural Studies of 1-eV Solar Cell Materials Lattice-Matched to GaAs

A. G. Norman, M. M. Al-Jassim, D. J. Friedman, J. F. Geisz, J. M. Olson, and S. R. Kurtz

National Renewable Energy Laboratory

1617 Cole Boulevard, Golden, CO 80401

ABSTRACT

Structural studies using transmission electron microscopy have been made on 1-eV band-gap materials, lattice-matched to GaAs and Ge substrates, grown by metal-organic vapor-phase epitaxy for use in multijunction, high-efficiency solar cells. $(GaAs)_{1-x}(Ge_2)_x$ alloy layers exhibited pronounced phase separation during epitaxial growth. $Ga_{1-x}In_xN_yAs_{1-y}$ layers grown under a wide range of conditions, using both hydrazine and dimethylhydrazine as nitrogen sources, have also been investigated. Layers grown at high temperatures (650˚C) using dimethylhydrazine contained a high density of "comet"-like precipitates that are associated with a high concentration of carbon and hydrogen, as revealed by secondary ion mass spectrometry. GaN_yAs_{1-y} layers grown with hydrazine at 550˚C were observed to undergo a transformation from single-crystal epitaxial layers at low hydrazine/III flow ratios to nanocrystalline or amorphous layers at high hydrazine/III flow ratios.

1. Introduction

By inserting a 1-eV junction between the GaAs and Ge junctions of the current state-of-the-art high-efficiency GaInP/GaAs/Ge cascade solar cell, it is predicted that the overall efficiency of the device may be significantly improved [1]. Several 1-eV band-gap materials, such as $(GaAs)_{1-x}(Ge_2)_x$ and $Ga_{1-x}In_xN_yAs_{1-y}$ alloys, lattice-matched to GaAs and Ge substrates to maintain high crystalline quality, are being investigated for incorporation into these multijunction solar cells. Structural studies of these materials have been performed using transmission electron microscopy (TEM) and diffraction (TED).

2. Results

2.1 $(GaAs)_{1-x}(Ge_2)_x$

Although GaAs and Ge are size-matched, they are mutually insoluble in the equilibrium bulk state, leading to almost complete phase separation into GaAs- and Ge-rich regions at all temperatures below the melting point. Despite this strong tendency toward phase separation, relatively homogeneous epitaxial $(GaAs)_{1-x}(Ge_2)_x$ alloy layers have been reported, grown by non-equilibrium techniques such as metal-organic vapor-phase epitaxy (MOVPE), sputter deposition, and molecular-beam epitaxy (MBE). In this work, $(GaAs)_{1-x}(Ge_2)_x$ alloy layers were grown by MOVPE under a wide range of growth conditions using trimethyl gallium, arsine, and germane as source materials. All the layers grown with these source materials exhibited pronounced phase separation into regions of GaAs-rich zinc-blende material and Ge-rich diamond cubic material [2,3]. Fig. 1 shows a 002 dark-field (DF), chemically sensitive, (110) cross-section TEM micrograph of a $(GaAs)_{0.90}(Ge_2)_{0.10}$ layer grown at 640˚C. The phase-separated microstructure in this layer is remarkably regular, with thin sheets of Ge-rich material lying on both sets of {115}B planes and is associated with a faceting of the growth surface on these planes [2,3]. In some areas, the Ge-rich material is in the form of closely spaced clusters or rods lying on {115}B planes. As the growth temperature was increased to 690˚C, the phase-separated microstructure evolved into large, irregular-shaped Ge-rich plates lying roughly parallel to the (001) plane in a GaAs-rich matrix [3]. Growth on a {115}B orientation substrate resulted in the spontaneous formation of a GaAs-rich/Ge-rich superlattice along the [115]B growth direction [3]. The occurrence of this phase separation was associated with substantial band-gap narrowing. Recent results have suggested that we may be able to kinetically suppress the phase separation by growth at low temperatures and high growth rates.

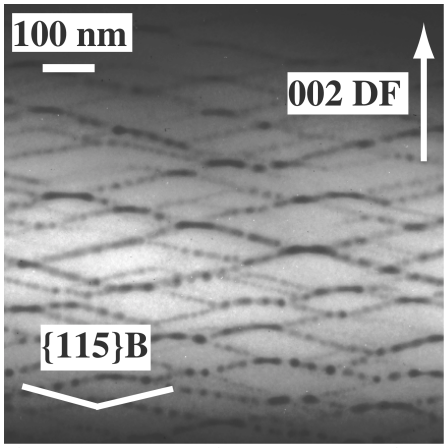

Fig. 1. (110) cross-section, 002 DF TEM image showing phase-separated microstructure of $(GaAs)_{0.90}(Ge_2)_{0.10}$ layer grown at 640˚C.

2.2 $Ga_{1-x}In_xN_yAs_{1-y}$

$Ga_{1-x}In_xN_yAs_{1-y}$ can be grown lattice-matched to GaAs or Ge substrates with a band gap of ≈ 1 eV for x ≈ 3y and a N content of about 2% [4]. MOVPE growth of the above 1-eV band-gap alloy has been performed using dimethylhydrazine (DMHy) as a nitrogen source at growth temperatures of 580˚ and 650˚C. However, the grown layers typically exhibit low minority-carrier diffusion

lengths, high junction recombination, and a high p-type background doping concentration, which are serious problems for their application in solar cells [5]. The reason for these poor electrical properties is not well understood, but may be due to spatially localized band fluctuations associated with the presence of isolated clusters of GaN in the alloy, possibly as a result of the large miscibility gap predicted for this alloy.

TEM studies of layers grown at 580˚C revealed the alloy to be of good structural quality, with a low defect density and no detectable sign of significant N clustering. In layers grown at 650˚C, however, a region of pronounced strain contrast was visible in the lower part of the layers, suggesting that phase separation had occurred, as shown in Fig. 2. More detailed examination revealed this strain contrast to be associated with a band of precipitates lying at the top of the region of strain contrast. These "comet"-like precipitates appeared to have left behind a tail of material of different composition during layer growth, hence resulting in the band of strain contrast observed in the layer below the precipitates. A high density of threading dislocations ($\approx 10^8$ cm^{-2}) was nucleated at this band of precipitates. The position of the band of precipitates correlated with the presence of broad spikes in the hydrogen and carbon contents in the layers, as revealed by SIMS depth profiles. This suggests that the precipitates may be related to hydrocarbon contamination or a gas-phase reaction occurring at high growth temperatures. Similar precipitates were also observed in GaN_yAs_{1-y} layers grown at 650˚C.

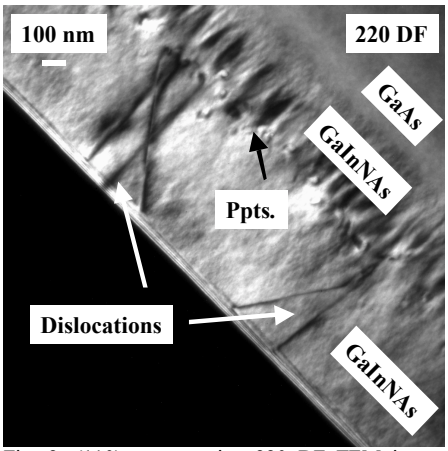

Fig. 2. (110) cross-section 220 DF TEM image showing "comet"-like precipitates (ppts.) and associated band of strain contrast and dislocations in $Ga_{1-x}In_xN_yAs_{1-y}$ layer grown at 650˚C.

Alternative nitrogen sources to DMHy, e.g., hydrazine (Hy), are also being investigated for the growth of these alloys. This is to enable growth at higher temperatures and arsine flows which is expected to lead to an improvement in the minority-carrier properties of the alloy layers [6]. A reduction in the background carrier concentration of the semiconductor alloy was also desired [6].

With Hy, significant N incorporation was obtained at much lower nitrogen source/III flow ratios than would be required using DMHy, although no improvement in background carrier concentration has so far been observed [6]. GaN_yAs_{1-y} layers were grown using AsH_3/III flow ratios of 4.4 and 44, with the Hy/III flow ratio varied over several orders of magnitude at both of these values [6]. At each AsH_3/III flow ratio, layers grown with a Hy/III flow ratio below a critical value were single-crystal epitaxial layers containing a few percent N with well-defined band gaps. Above the critical Hy/III flow ratio at each AsH_3/III flow ratio, the GaN_yAs_{1-y} layers became nanocrystalline or amorphous [6], as shown in Fig. 3, and contained a high N content.

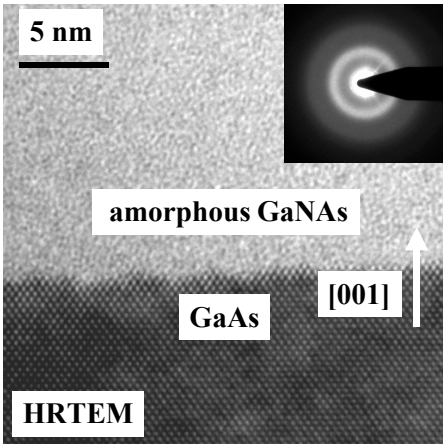

Fig. 3. High-resolution TEM image of GaNAs layer grown at 550˚C with AsH_3/III = 4.4 and Hy/III = 8.6. Inset is TED pattern from GaNAs layer showing that it is amorphous.

REFERENCES

[1] S. R. Kurtz, D. Myers, and J. M. Olson: "Projected performance of three- and four-junction devices using GaAs and GaInP," *Proceedings of the 26th IEEE Photovoltaic Specialists Conference* (1997) 875-878.

[2] A. G. Norman, J. M. Olson, J. F. Geisz, H. R. Moutinho, A. Mason, M. M. Al-Jassim, and S. M. Vernon: "Ge-related faceting and segregation during the growth of metastable $(GaAs)_{1-x}(Ge_2)_x$ alloy layers by metal-organic vapor-phase epitaxy," *Appl. Phys. Lett.* **74** (1999) 1382-1384.

[3] A. G. Norman, J. M. Olson, J. F. Geisz, H. R. Moutinho, A. Mason, M. M. Al-Jassim, and S. M. Vernon: "Phase separation and facet formation during the growth of $(GaAs)_{1-x}(Ge_2)_x$ alloy layers by metal organic vapour phase epitaxy," *Inst. Phys. Conf. Ser. No.* 164 (1999) 171-174.

[4] M. Kondow, K. Uomi, A. Niwa, T. Kitatani, S. Watahiki, and Y. Yazawa: "GaInNAs: a novel material for long-wavelength-range laser diodes with excellent high-temperature performance," *Jpn. J. Appl. Phys.* **35** (1996) 1273-1275.

[5] D. J. Friedman, J. F. Geisz, S. R. Kurtz, and J. M. Olson: "1-eV solar cells with GaInNAs active layer," *J. Crystal Growth* **195** (1998) 409-415.

[6] D. J. Friedman, A. G. Norman, J. F. Geisz, and S. R. Kurtz: "Comparison of hydrazine, dimethylhydrazine, and t-butylamine nitrogen sources for MOVPE growth of GaInNAs for solar cells," *J. Crystal Growth* **208** (2000) 11-17.

Identification of metal – oxygen complexes as lifetime limiting defects in solar cell materials

E.R.Weber[1], S.A.McHugo[2], A.A.Istratov[1], C.Flink[1], and H.Hieslmair[1]

University of California at Berkeley(1) and Advanced Light Source, Lawrence Berkeley National Laboratory(2)

Dept. of Materials Science and Engineering, 577 Evans Hall, University of California, Berkeley CA 94720-1760

ABSTRACT

A combination of traditional characterization tools with synchrotron radiation based x-ray microprobe technique enabled us to demonstrate that the difficulties of gettering of transition metals from the bulk of mc-Si wafers are associated with strong binding of metals to oxygen and silicon by the formation of metal-oxides and metal-silicates. Experimental observations of iron-oxides and iron-silicates in the bulk of mc-Si material are reported. It is concluded that the key for improving minority carrier lifetime in mc-Si lies in understanding of the interaction between transition metal contaminants and oxygen during crystal growth and subsequent heat treatment.

1. Introduction

Transition metals easily decorate dislocations, grain boundaries, and intragranular microdefects in mc-Si, thereby significantly enhancing their recombination activity and decreasing the minority carrier diffusion length. Gettering treatments which work well with crystalline silicon proved to be inefficient for improving lifetime in mc-Si [1]. To understand the reasons for the poor efficiency of gettering, we examined the physics of processes involved in gettering, and recombination properties of precipitated metals [2-7, 12]. We found no indications that the kinetics of diffusion of metals to the sinks may explain the poor efficiency of gettering in mc-Si solar cells. Hence, the dissolution of metal clusters must be the limiting factor for gettering.

Most previous studies assumed that the metal clusters in silicon consists of either pure metals, or metal silicides. In this presentation, we report the results of studies of the chemical state of metal impurities in mc-Si by using advanced techniques of x-ray analysis. We demonstrate that the metals, which cannot be gettered, are bound in oxides and silicates. These compounds have very high negative formation energy and are very difficult to dissolve by heat treatment.

2. Experimental techniques

Boron-doped polycrystalline silicon (polysilicon) grown by a casting technique was used in this work. Areas with low diffusion length were identified by SPV and EBIC. X-ray fluorescence (XRF) and X-ray absorption spectroscopy (XAS) were performed at the Advanced Light Source, Lawrence Berkeley National Laboratory in order to ascertain elemental distribution and chemical state, respectively, of metals in the silicon material. Both XRF and XAS analysis were performed with X-rays focused to a spot size of 1-2 μm^2, with scan areas typically over hundreds of microns. By monitoring the absorption of the impinging X-ray beam as the energy of the beams varied, we obtain from μ-XAS a fingerprint of the chemical state of the element, which is compared to standard samples of known chemical state. Since the valence band electrons are sensitive to variations in chemical binding, this technique provides an excellent means for chemical identification.

3. Results

Fe Kα and Kβ X-ray emission was detected in as-grown polysilicon with the μ-XRF system. The absorption spectra of the Fe precipitates in the polysilicon sample shown in Fig. 1 is the summation of 19 spectral scans taken with the μ-XAS system. Multiple XAS scans are also shown in Fig. 1

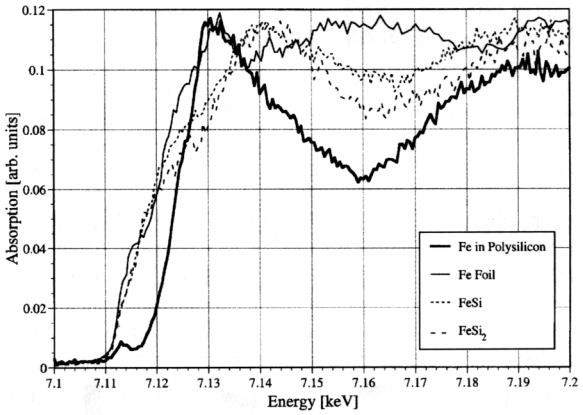

Fig. 1. X-ray absorption spectra from Fe in polysilicon, FeSi, $FeSi_2$ and metallic Fe.

for Fe, FeSi and $FeSi_2$ standards. Unexpectedly, we observe little similarity between the absorption spectra obtained on mc-Si and those obtained on standards, indicating that Fe in the polysilicon is not Fe, FeSi nor $FeSi_2$.

The shift of the absorption edge for the Fe spectra suggests the Fe atoms have been elevated to a higher valence state. This is common for metal oxides and metal silicates but not for metallic iron or Fe silicides. Furthermore, the presence of the pre-edge structure (at approx. 7.115 keV in Fig. 1) indicates that the local environment of the Fe atoms in this compound is highly asymmetric, which again is common for oxides and silicates but not for metallic Fe or Fe silicides. Further indications of Fe-related complexes comes

from other research, which has indicated that Fe may complex with oxygen precipitates in silicon [8].

With these possibilities in mind, we analyzed standard powders of α-Fe_2O_3 and Fe_2SiO_4 with the μ-XAS beamline for comparison to the Fe in the polysilicon. Results are shown in Fig. 2. We observe some similarity between the absorption spectra of the metal oxides, silicates, and Fe in polysilicon. In particular, the pre-edge structure is

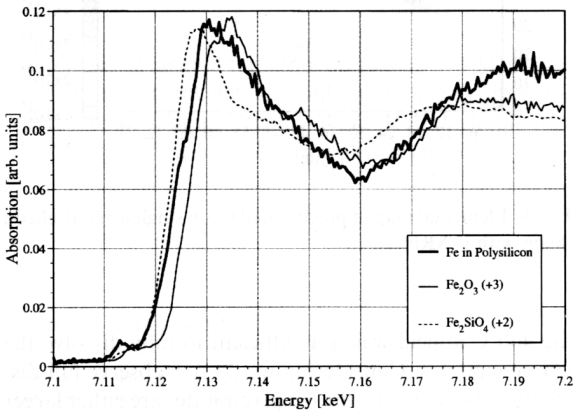

Fig. 2. X-ray absorption spectra from Fe in polysilicon, α-Fe_2O_3 (+3 charge state) and Fe_2SiO_4 (+2 charge state).

remarkably similar. Furthermore, the absorption edge of Fe in polysilicon falls between α-Fe_2O_3 and Fe_2SiO_4. Considering that Fe in α-Fe_2O_3 is in a +3 charge state and Fe_2SiO_4 is in a +2 charge state, the Fe in polysilicon seems to be a mix of +2 and +3 charge states. From these comparisons, one may suggest the Fe in polysilicon is a mixed state of oxide and silicate. These results compare well with Kitano [8] who observed the formation of a mixed +2, +3 state of Fe_2SiO_4 with Fe reaction at a Si-SiO_2 interface.

Table 1. Enthalpies of formation of Fe related compounds.

Compound	ΔH (KJ/mol)
FeSi	-39.3
$FeSi_2$	-30.6
1/2 Fe_2O_3	-412.1
1/3 Fe_3O_4	-372.8
1/2 Fe_2SiO_4	-740

With the iron in an oxide or silicate state, the ability to remove or getter the ironis greatly hindered by the high binding energy of iron to oxides and silicates relative to iron silicides. Table 1 lists the standard molar enthalpy of formation for iron silicides, oxides, and silicates at 298 K, data from [9,10]. The data has not been corrected for compound formation within a silicon matrix, however, these numbers provide a relative indication of binding energy. From the data, the thermodynamic formation energies of iron oxides and silicate is significantly higher than iron silicides, thus, the binding energy of an iron atom to an oxide or a silicate precipitate is higher than to a silicide precipitate. With a higher binding energy, the solubility of Fe in the presence of an oxide or silicate precipitate will be low, compared to that in the presence of a silicide precipitate. Since dissolution is a flux-limited process, this lower solubility decreases the dissolution rate, i.e., the gettering rate. This result has significant impact on solar cell improvements via gettering.

4. Conclusions

Based on our results we can conclude that Fe in polysilicon solar cells can be in the form of an oxide or a silicate. This is contrary to common thought, where a Fe silicide is expected to form. With the iron being in the form of an oxide of silicate, the rate of impurity removal is significantly reduced due to higher binding energy of Fe atoms to oxides or silicates as compared to silicides. Hence, the key to understanding the effect of metals on degradation of solar cell efficiency lies in the reactions of metals with oxygen during growth of mc-Si and its subsequent thermal treatment. Rapid solidification of melt, containing certain concentrations of transition metals and high concentration of dissolved oxygen, may stimulate the formation of complexes between iron and oxygen. The fact that these complexes are found predominantly in areas with low minority carrier diffusion length suggests that they are detrimental recombination centers.

REFERENCES

[1] S.A. McHugo, H. Hieslmair, E.R. Weber, Mater. Sci. Forum 196-201 (1995) 1979.
[2] A.A. Istratov, C. Flink, H. Hieslmair, E.R. Weber, T. Heiser, Physical Review Letters 81 (1998) 1243.
[3] A.A. Istratov, H. Hieslmair, E.R. Weber, Applied Physics A 69 (1999) 13.
[4] H. Hieslmair, A.A. Istratov, S.A. McHugo, C. Flink, T. Heiser, E.R. Weber, Applied Physics Letters 72 (1998) 1460.
[5] H. Hieslmair, A.A. Istratov, S.A. McHugo, C. Flink, E.R. Weber, J. Electrochem. Soc. 145 (1998) 4259.
[6] A.A. Istratov, C.F. Flink, H. Hieslmair, S.A. McHugo, E.R. Weber, Mater. Sci. Engineering B 72 (2000) 99.
[7] A.A. Istratov, H. Hedemann, M. Seibt, O.F. Vyvenko, W. Schröter, T. Heiser, C. Flink, H. Hieslmair, E.R. Weber, Journal of the Electrochemical Society 145 (1998) 3889.
[8] T. Kitano, Journal of Electronic Materials 21 (1992) 1027.
[9] D.R. Lide (ed.), CRC handbook of chemistry and physics (CRC press, Boca Raton, 1998).
[10] M.E. Schlesinger, Chem. Rev. (1990) 607.
[11] M. Takiyama, S. Ohtsuka, S. Hayashi, M. Tachimori, in: H.R. Huff, W. Bergholz, K. Sumino (Editors), Semiconductor Silicon - 1994 (The Electrochem. Soc., Pennington, 1994), p. 346.
[12] C.Flink, H.Feick, S.A.McHugo, A.Mohammed, W.Seifert, H.Hieslmair, T.Heiser, A.A.Istratov, and E.R.Weber, Physica B 273-274 (1999) 437.

Improving Properties of GaInNAs with a Short-period GaInAs/GaNAs Superlattice

Y. G. Hong and C. W. Tu

Dept. of Electrical and Computer Engineering, University of California, San Diego, La Jolla, CA 92093-0407

Tel: (858) 534-3014, Fax: (858) 534-2486, E-mail: yghong@ucsd.edu

ABSTRACT

We have investigated short-period superlattices of GaInAs/GaNAs as a digital alloy of GaInNAs. Hall measurements show electron mobility is improved by a factor of almost two. The photoluminescence (PL) intensity is improved by rapid thermal annealing. The PL intensity for digital alloys is 2.5 to 3 times higher than that of random alloys at room temperature and a factor of about 12 at low temperature (10K). High temperature (above 850°C) anneal causes In and N interdiffusion and forms GaInNAs at superlattice interfaces. PL spectra show separation between the quantum confined level and the GaInNAs state.

1. Background

Recently, the quaternary $Ga_{1-x}In_xN_yAs_{1-y}$ alloy system has attracted a great deal of attention due to its potential applications in next-generation ultra-high-efficiency multijunction solar cells as well as in optoelectronic devices for optical communications [1],[2]. A problem with GaInNAs is its low carrier mobility and short minority carrier lifetime due to alloy scattering and degradation of material quality with nitrogen incorporation. To minimize alloy scattering, we have investigated short-period superlattices of GaInAs/GaNAs as a digital alloy of GaInNAs. We report the growth and characterization of these short-period superlattices (SL) and comparison of random alloy vs. digital alloy. Rapid thermal anneal (RTA) was preformed to improve the superlattice quality.

The layers in the superlattices are strain-compensated, i.e., GaNAs is under tension and GaInAs is under compression. Thus, thick $GaIn_{0.08}As/GaN_{0.03}As$ superlattices can be grown lattice-matched to GaAs substrates.

2. Experimental Procedure

Short-period superlattices of GaInAs/GaNAs were grown by gas-source molecular beam epitaxy with different period thicknesses from 16 Å to 100 Å. The number of periods was selected so as to keep the total thickness 0.4 μm constant. RTA study was carried out in a 100% N_2 ambient and a temperature range from 650 °C to 900 °C. Photoluminescence (PL) and high-resolution X-ray rocking curve (XRC) measurement were used to characterize samples. Indium and nitrogen compositions were determined by dynamical-theory simulations of the measured x-ray rocking curves on calibration samples.

3. Results and Discussion

All the samples studied here have a mirror-like surface and streaky RHEED pattern throughout growth. The zeroth order peak is closed to the GaAs substrate peak with lattice mismatch less than 0.05%. The satellite peaks can be observed clearly.

For as-grown samples, no detectable room-temperature PL was obtained, indicating the presence of a high concentration of nonradicative centers. We annealed the SL samples and the reference bulk $GaIn_{0.04}N_{0.015}As$ sample at the same time at 700 °C for 10 sec in N_2 ambient. Low-temperature PL spectra of the two investigated SL structures are shown in Figure 1. The PL intensity of SL is much stronger than that of bulk layer. The PL intensity increase about 12 times at the low temperature (10K) and 3 times at room temperature.

A series of RTA study were carried out to optimize RTA conditions, which are 700 °C and 10 sec in N_2 ambient. The PL linewidth for sample annealed below 650

°C is broad, presumably due to composition non-uniformity. 700°C annealing increases the PL intensity and narrows the PL linewidth. High-temperature anneal (above 850 °C) results in a splitting of the PL emission into two peaks, the quantum confined level and the GaInNAs state which is formed by the interdiffusion of In and N [3]. The PL spectra exhibit a rather strong dependence on excitation power and measurement temperature.

Hall measurements were carried out on SL samples with different period thicknesses and the reference sample (4000Å-thick bulk $GaIn_{0.037}N_{0.017}As$ layer). The electron mobility for SLs is improved by a factor of almost two [see table 1]. This mobility improvement is presumably due to reduced alloy scattering. All the as-grown n-type samples change to highly p-type (~$2x10^{18}$ cm^{-3}) after anneal. Secondary ion mass spectroscopy (SIMS) measurement shows high hydrogen concentration ($3x10^{19}$ cm^{-3}) on these samples, but low carbon concentration ($1x10^{16}$ cm^{-3}). We are still investigating the reasons for the type conversion and high p-type doping.

4. Conclusions

In summary, strain-compensated thick short-period $GaIn_{0.08}As/GaN_{0.03}As$ SLs were grown on GaAs substrates by gas-source MBE. As compared to the bulk $GaIn_{0.04}N_{0.015}As$, the PL intensity for SLs is improved by a factor 12 at low temperature (10K) and by a factor of 3 at room temperature. The electron mobility is improved by a factor almost two. RTA improves PL intensity and reduces PL linewidth. Optimized RTA conditions for short-period

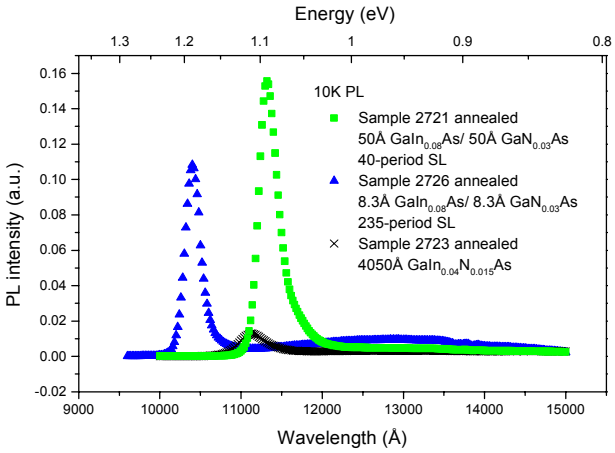

FIG. 1. Low temperature (10K) photoluminescence on superlattice samples and reference sample

SLs are 700 °C and 10 sec in N_2 ambient. High-temperature (above 850 °C) RTA results in a splitting of PL emission into two peaks, where the low-energy peak comes from GaInNAs alloys formed by high temperature annealing.

5. Acknowledgments

The authors gratefully acknowledge D.J. Qiao and Professor S.S. Lau at UCSD ECE department for their help on RTA and M.Geva of Bell Lab, Lucent Technology, for SIMS measurements. This work was supported by National Renewable Energy Laboratory (AAD-9-18668-07).

Reference

[1] M. Kondow, K.Uomi, A.Niwa, T. Kitatani, S.Watahiki, and Y.Yazawa, Jpn. J. Appl. Phys., Part 1, 35, 1273 (1996)

[2] S.R. Kurtz, A.A. Allerman, E.D. Jones, J.M.Gee, J.J.Banas, and B. Hammons, Appl. Phys. Lett. 74, 729 (1999)

[3] Y. Narukawa, Y. Kawakami, M. Funato, S. Fujita, S. Fujita, and S. Nakamura, Appl. Phys. Lett. 70, 981 (1997)

TABLE 1. Hall measurement on SL and reference sample.

		#2721: (50Å $GaIn_{0.08}As$/ 50Å $GaN_{0.03}As$) 40-period SL	#2726: (8 Å $GaIn_{0.08}As$/ 8 Å $GaN_{0.03}As$) 235-period SL	#2723: 4000Å $GaIn_{0.04}N_{0.015}As$ bulk layer
As-grown	n (cm^{-3})	$1.1x10^{14}$	$4.0x10^{14}$	$3.2x10^{14}$
	μ(cm^2/V-sec)	230	240	130
Annealed	p (cm^{-3})	$1.9x10^{18}$	$1.9x10^{18}$	$2.3x10^{18}$
	μ(cm^2/V-sec)	160	190	90

Lifetime Characterization of Polycrystalline PV Materials

A. Romanowski, L. Kordas, and G. Rozgonyi

Materials Science & Engineering Dept.
North Carolina State University
Raleigh, NC 27695-7916.

ABSTRACT

Contactless microwave photoconductance μ-PCD and microwave frequency resolve photoconductance FR-PC methods have been used for PV material characterization. The relation between the ac microwave reflectance and grain parameters has been found and the impact of grain size on microwave reflectance spectra has been analyzed. Activation energy E_a and ratio of electron/hole capture cross sections σ_p/σ_n have been used for material characterization and they have been evaluated for p-type polycrystalline silicon. It has been found that multilevel recombination centers control carrier kinetics at room temperatures. They become unstable at elevated temperatures.

1. Introduction

It was previously demonstrated [1,2,3] that material parameters could be evaluated from their lifetime characteristics. However, described methods have only been applied to CZ or FZ silicon wafers, used in IC technology. In this paper the lifetime technique has been implemented for the characterization of PV wafers. Contrary to monocrystalline silicon wafers, PV materials exhibit higher conductivity and shorter lifetimes. Therefore, μ-PCD used for PV characterization should have a high sensitivity and a fast response time. Our new lifetime system, JANUS 300 has an enhanced sensitivity and can measure the minimum lifetime of 200 ns. Also the FR-PC method developed at NCSU can be used for characterization of solar silicon due to the sensitive lock-in technique. The serious limit of our FR-PC technique that was the low lock-in amplifier bandwidth of 150kHz has been overcome. We have developed a New Frequency Resolved Photoconductance System (FR-PC-1M) expanding the bandwidth to 1 MHz.

2. AC microwave reflectance in a polycrystalline silicon

The electron/hole generation function in frequency domain has the form [4]:

$$g_{ij}(z;t) = g_{ij}^0 + \alpha \tilde{G}_{ij}^t \exp(-\alpha z + i\omega t) \qquad (1)$$

The quadrature component $Y(\omega) = \mathrm{Im}\, R(\omega)$ of the reflectance has the Lorentzian profile with the full width at half maximum (FWHM) [4]:

$$FWHM = \frac{\sqrt{3}}{\pi} \frac{1 + 2(\pi L/a)^2}{\tau} \qquad (2)$$

where L, τ are the diffusion length and the electron recombination lifetime, while a is the grain size. FWHM increases with increasing L/a ratio and decreasing carrier lifetime τ. For large diffusion lengths (L >> a), FWHM depends on diffusivity and the grain surface S. It does not depend on the diffusion length or carrier lifetime. For a large grain size (a >> L) FWHM takes the lowest value and the FWHM for polycrystalline and monocrystalline materials are equal.

3. Lifetime Measurements

The lifetime image, of the polycrystalline PV silicon, measured by our new μ-PCD JANUS-300 is shown in Fig. 1. The map has been measured at room temperatures with laser injection level of 10^{14} cm^{-2}. The lifetimes varies from 2μs

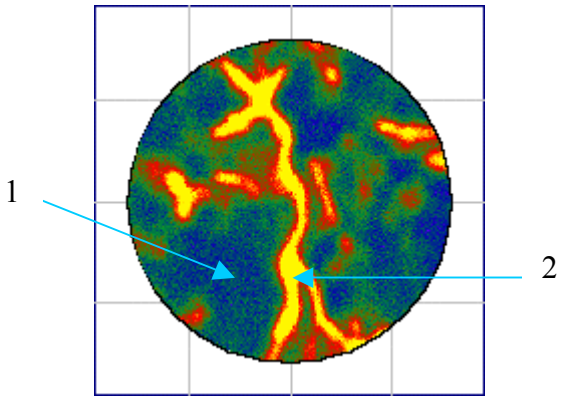

Fig. 1. Lifetime image of the polycrystalline silicon measured at 25^0C, injection level of 10^{14} cm^{-2}, radius = 16 mm

(region 2) to 2.4μs (region 1). Lifetime variations in the labeled (1, 2) areas vs. injection or temperature are shown in Fig. 2 and 3, respectively. The lifetime increases with the

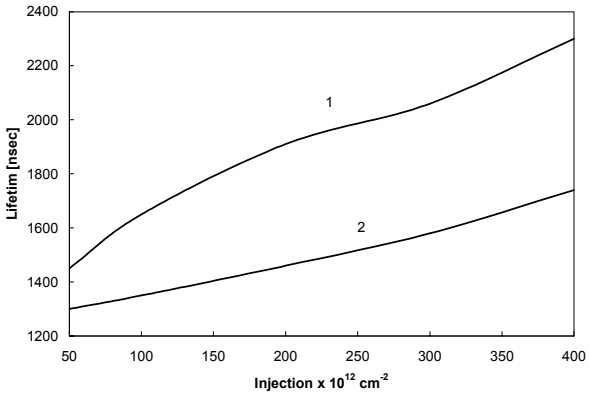

Fig. 2. Lifetime vs injection level

injection level indicating operative recombination center in the semiconductor middlegap [5]. The lifetime deterioration in the temperature range between 90^0C and 200^0C reveals complicated nature of the recombination level, where two

levels are active, resembling iron recombination center in p-type monocrystalline silicon [6]. Both characteristics are

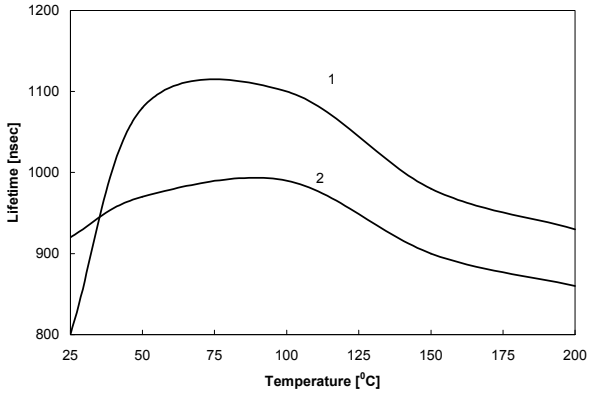

Fig. 3. Lifetime vs. temperature

typical for iron contaminated c-Si materials [6]; therefore, one can expect the presence of iron impurities in measured materials. A deep level has also been detected by the newly implemented FR-PC-1M system. A broad spectrum measured at the room temperature is generated by multilevel recombination centers. At moderate temperatures, above 200^0C, unstable trapping/recombination levels dissociate and spectrum fits Lorentzian profile characteristic [2,3] for a single recombination center. Figures 4 and 5 show experimental and simulated spectra for temperatures 180^0C and 240^0C. The simulated curves match the experimental

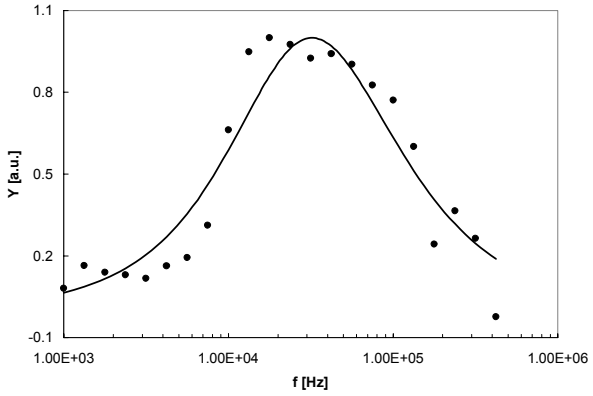

Fig. 4. Measured and simulated (solid line) FR-PC spectrum of polycrystalline silicon at 180^0C

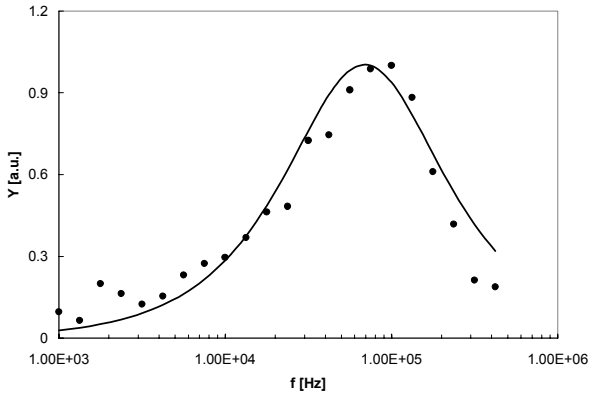

Fig. 5. Measured and simulated (solid line) FR-PC spectrum of polycrystalline silicon at 240^0C

ones; however, evaluated parameters are different. Surface recombination velocity, for example, is equal to $1.5x10^3$ cm/s and 0 for 180 and 240^0C, respectively. The activation energies are 0.48eV and 0.43eV, while the ratio σ_p/σ_n is of $5.8x10^{-3}$ and $9.7x10^{-3}$, respectively (σ_n, σ_p are electron/hole capture cross sections). Evaluated E_r and σ_p/σ_n are smaller than the same parameters determined for c-Si containing iron [4]. Wide spectrum measured at 180^0C is generated by a two level recombination center rather than single level, with high surface recombination velocity, in agreement with previous discussion (see Fig. 3). Measured at 240^0C spectrum has Lorentzian profile, indicating single recombination level. It should be emphasized here, that the procedure, which has been used for PV wafer evaluation, assumes monocrystalline properties of the wafer. However, good fitting between experimental and "monocrystaline" Lorentzian spectra at 240^0C reveal low recombination process at GB.

4. Summary and Conclusions

A 3D model has been developed and has been used for determining the relation between the ac microwave reflectance and grain parameters. Activation energy of 0.43eV and σ_p/σ_n = 0.01 ratio have been evaluated for PV polycrystalline silicon indicating an operative interstitial iron center. Multilevel recombination centers control carrier kinetics at the range of temperature from 25^0C to 180^0C. They are unstable at elevated temperatures. The recombination process at GB can be neglected at high temperature.

REFERENCES

[1] O. Hahneiser and M. Kunst, "Theoretical and experimental study of charge carrier kinetics in crystalline silicon", J. Appl. Phys. 85 (1999) 7741-7754.

[2] A. Romanowski, A. Buczkowski, A. Karoui and G. Rozgonyi, "Contacless Frequency Resolved Photoconductance (FR-PC) Measurement of Iron Contaminated p-type Silicon", in *Silicon Recombination Lifetime Characterization Methods*, ASTM STP 1340, F.Bacher and W.H.Hughes Eds. (1998), pp. 68-79.

[3] A. Romanowski, A. Buczkowski, A. Karui, and G. Rozgonyi, "Frequency-Resolved Microwave Reflection Photoconductance: Recombination Lifetime and Surface Recombination Velocity Evaluation", J. Appl. Phys., **83**, 7730 (1998).

[4] "Characterization and Ti Gettering of PV Substrates", Annual Report 1999, Contract #: NREL XAF-8-17607-03, NCSU, Raleigh, 2000.

[5] AD.K. Schroder, "Recombination Lifetimes in Silicon" in *Silicon Recombination Lifetime Characterization Methods*, ASTM STP 1340, F.Bacher and W.H.Hughes Eds. (1998), pp. 5-17.

[6] Y. Hayamizu, T. Hamaguchi, S. Ushio, and T. Abe, F. Shimura, "Temperature dependence of minority-carrier lifetime in iron-diffused p-type siliconwafers", J. Appl. Phys. 69 (1991) 3077-3081.

THE LOCATION OF VERY SMALL PARTICLES IN SILANE RF DISCHARGES

K. Rozsa, G. Bano and A. Gallagher
JILA, NIST and University of Colorado, Boulder, CO 80309

Silane rf discharges are ubiquitous in the deposition of hydrogenated amorphous silicon (a-Si:H) photovoltaics and thin film transistors. Particles grow rapidly in these discharges, due to the trapping and growth of negative ions. A copious flux of small particles also incorporate into films, and are believed to play important roles in the electronic properties of a-Si:H devices. Due to rapid gas flow across typical reactors, only small (<50 nm) particles are important to devices. Particle locations within a rf discharge determine where they incorporate into devices. These locations depend on gas-drag and ion-wind forces, sheath location and small variations in plasma potential. We have measured the dependence of particle density and location on a variety of factors, such as particle size, discharge power and electrode shape. Particle size is determined from their behavior in the afterglow, as described in Ref.1.

1) M.A.Childs and A. Gallagher, J. Appl. Phys. **87**, 1076 (2000).

Low Temperature (200-600°C) Metal-Induced Nucleation and Solid Phase Crystallization of Silicon for Large Grained Polycrystalline Si PV Materials

C. M. Chen, S. Okada, H. A. Atwater
Thomas J. Watson Laboratory of Applied Physics
California Institute of Technology

ABSTRACT

We have studied two regimes for making polycrystalline thin-films of silicon, both using metal-induced nucleation and metal-mediated crystallization. Nickel, implanted into patterned silicon layers, nucleated crystals in amorphous silicon (*a*-Si), and crystallized the *a*-Si by silicide-mediated growth, producing <110> textured substrates. Growth rates of 8 nm/s were attained for anneals at 610°C. Also, an *a*-Si layer deposited onto a tin layer, annealed at 200°C, 220°C, or 500°C yielded crystalline Si particles interspersed with silicon-tin alloy and tin globules.

1. Introduction

The drive for lower cost efficiency has stimulated research into thin-film silicon technology coupled with low-cost substrates, of which the paragon is soda-lime or borosilicate glass. The low thermal stability (<650°C) of these glasses has motivated low temperature approaches for making crystalline Si thin films. Two promising processes for application in low-cost thin-film crystalline silicon solar cells are selective nucleation and solid phase epitaxy (SNSPE) of Si with Ni implanted sites as nucleation seeds, and metal mediated crystallization with Sn.

2. Nickel-Induced Nucleation and Crystallization

Formation of large-grained polycrystalline silicon films at low temperatures by selective nucleation and solid phase epitaxy followed by silicon vapor phase epitaxy is reported. In this process, selective crystallization of an initially amorphous silicon film enables grain sizes larger than those observed from random crystallization.

Amorphous Si films, 75 nm thick, were deposited by low-pressure chemical vapor deposition onto 100 nm thick thermally grown SiO_2 films on (100) Si. Selective heterogeneous nucleation centers were created on the amorphous silicon films by masked implantation of nickel islands. Photolithography and wet etching were used to define *a*-Si islands of different shapes and sizes on the SiO_2. The nucleation seed regions were defined by windows in the photoresist, through which the nickel was implanted into the *a*-Si at an energy of 40 keV. Two types of structures were studied: 2 μm Ni-implanted circles with a dose of 5×10^{15} cm^{-2} and various Si patterns, and Si rectangles with a 2 μm wide band of implanted Ni with a dose of 1×10^{15} cm^{-2} at one end, seen in Fig. 1. The implantation energy was chosen to give the peak of Ni atoms at a depth of half the *a*-Si film thickness.

All the samples were cleaned with solutions to remove surface particulates and metal contaminants, and annealed in a vacuum furnace, operating at 1×10^{-7} Torr and at temperatures ranging between 550-610°C. Seeded crystallization begins at the metal islands and propagates by nickel mediated crystallization, resulting in fast propagation of branching needle-like structures, seen in Fig. 2, led by silicide particles[1]. This gives rise to crystallized regions with area of several tens of square microns in one hour. At 610°C, for a Ni implanted dose of 1×10^{15} cm^{-2}, the crystallization rate was about 8 nm/s.

Transmission electron microscopy analyses showed a large grain size but a high density of sub-grain boundary defects in the crystallized Si film. X-ray fluorescence microprobe analysis showed that after annealing, the Ni remains within the crystallized Si. Following completion of crystallization, the average Ni concentration is 7×10^{18} cm^{-3}.

The crystallized samples were used as templates for Si epitaxial deposition of 1 μm thick Si films. Prior to epitaxy, the templates were cleaned in solutions to remove surface particulates and metal contaminants, and in a $HF:H_2O$ solution to remove the surface oxide. The deposition was performed at 550°C with a deposition rate of 0.1 nm/s, at a pressure of about 8×10^{-9} Torr.

Transmission electron microscopy analysis showed a strong microstructural correlation between the substrate grain structure and the grain structure in the deposited layer, indicating local epitaxial growth. The final layer exhibited a large-grain morphology, with grain sizes larger than 4 μm.

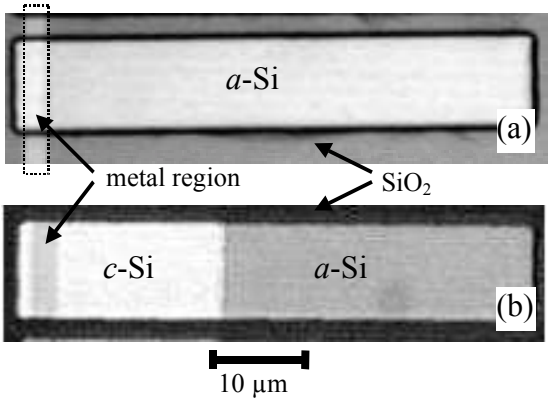

Figure 1. (a) Optical image of Ni as-implanted sample. The rectangular pattern is the *a*-Si film deposited on the SiO_2 substrate. The region indicated by the dotted rectangle represents the Ni implanted region. (b) Optical image after annealing at 610°C for 35 min. The bright region indicates the crystallized Si.

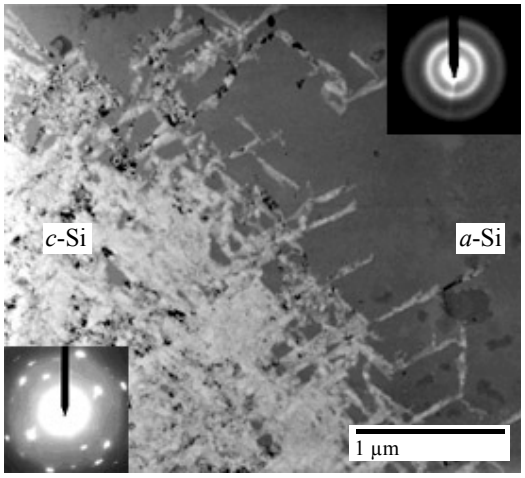

Figure 2. Bright field plan view TEM image of the growth front of a Ni implanted sample, with a dose of 5×10^{15} cm^{-2}, annealed at 610°C for 65 min. The lighter region is the crystallized region, the darker area is the *a*-Si.

3. Tin-mediated Crystallization of Silicon

An a-Si on Sn layer structure was deposited by vapor deposition in ultrahigh vacuum on a 100 nm thick silicon oxide layer thermally grown on a <100> silicon substrate. Both a-Si and Sn layers were 50 nm thick each. The substrates were cleaned and then vacuum annealed with a pressure of 10^{-7} Torr at 200°C, 220°C, or 500°C, for an hour, and then imaged by TEM, , and atomic force microscopy (AFM).

The samples at all three annealing temperatures had similar morphology: monocrystalline Si particles and Sn particles interspersed in a Si-Sn alloy matrix as seen in Fig. 5. Though it is difficult to discern the individual grains and therefore the grain size in the plan view TEM images, the features appear to scale with annealing temperature, with ~50 nm particles for the 200°C anneal, ~80 nm particles for the 220°C anneal, and ~100 nm particles for the 500°C anneal. Some Sn-rich globules segregated to the surface, which correlate to the large mounds, around 100 nm high, seen in the AFM image, in Fig. 3. The surface has an rms roughness of 4 nm. From the cross sectional image in Fig. 4, voids can be seen underneath some of the bumps. The Sn probably migrated to the surface, catalyzing the Si crystallization, leaving voids in some areas. Composition was determined by energy dispersive x-ray analysis.

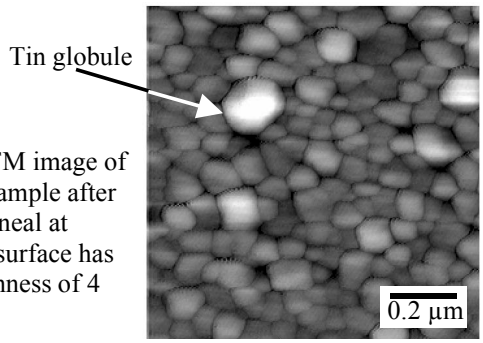

Figure 3. AFM image of a Si-on-Sn sample after an 1 hour anneal at 220°C. The surface has an rms roughness of 4 nm.

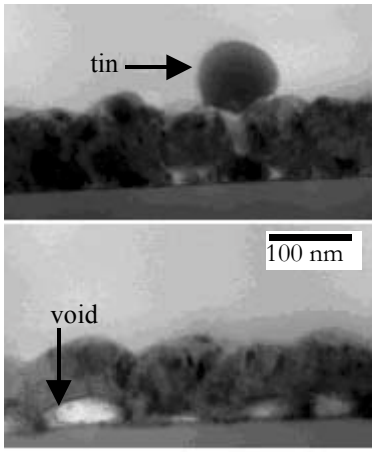

Figure 4. Bright field, cross-sectional TEM images of a Si-on-Sn sample after an 1 hour anneal at 220°C. Visible in this image are voids present under the crystallized layers, and tin that segregated to the surface.

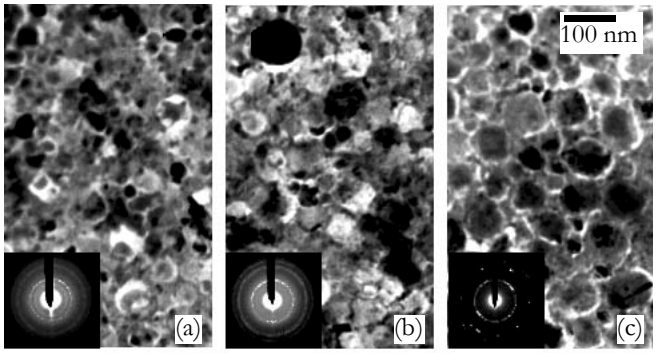

Figure 5. Bright field, plan view TEM of Si-Sn samples annealed at (a) 200°C with grain features ~50 nm, (b) 220°C with grain features ~80 nm, and (c) 500°C with grain features ~100 nm. Selected area diffraction patterns displaying polycrystalline diffraction rings are shown in the insets.

REFERENCES

[1] C. Hayzelden and J. L. Batstone: " Silicide Formation and Silicide-Mediated Crystallization of Nickel-Implanted Amorphous-Silicon Thin-Films ", J. Appl. Phys. 73 (1993) 8279-8289.

Manipulation and Control of Nucleation and Growth Kinetics with Hydrogen Dilution in Hot-Wire CVD Growth of Poly-Si.

Maribeth Swiatek, Jason K. Holt, David G. Goodwin, Harry A. Atwater

Thomas J. Watson Laboratories of Applied Physics
California Institute of Technology
Pasadena, CA 91125

ABSTRACT

Hot-wire chemical vapor deposition (HWCVD) has been shown to be a method for high quality polycrystalline silicon growth at high deposition rates and at temperatures under 500ºC, and is a promising method to produce large-grained thin films for photovoltaic applications [1]. In the SiH_4:He gaseous ambient, polycrystalline silicon films with 400Å grain size have been deposited at a rate of 1.7Å/s. With H_2 dilution in the ratio 20:1 (H_2:SiH_4), polycrystalline films of 850Å grain size were obtained at growth rates of 0.6Å/s, due to concurrent etching by atomic H. Further investigation of nucleation kinetics as a function of hydrogen dilution indicated a decrease in Si nucleation density during the early stages of nucleation and growth on SiO_2. The nucleation density was found to vary sublinearly with time.

1. Experiment

For all HWCVD experiments, an 0.25 mm diameter W wire was resistively heated to 2000ºC and positioned at a distance of 2.5 cm from the substrate. The wire was used to radiatively heat the SiO_2 substrate to a temperature of 300ºC. H_2 dilutions are referenced to 1 mTorr of SiH_4 in 99 mTorr He. A translatable shutter between the wire and substrate was used to enable several growth experiments at identical gas ambient and wire temperature on each substrate at low Si coverage.

2. Results

The net Si growth rate was measured using a quartz crystal oscillator with H_2 dilution between 0 and 150:1. As seen in Figure 1, the net growth rate decreases with increasing H_2 partial pressure, which was attributed to Si etching by atomic H. In a separate experiment, the SiH_4 flux, measured at the same H_2 dilutions with a differentially-pumped quadrupole mass spectrometer, with orifice located at the substrate position, was observed to increase with the addition of H_2. This observation was attributed atomic H etching Si species from the chamber walls and recombining with these species in the gas phase. A transition from net growth to net etching is observed with the addition of 80 mT H_2. Transmission electron microscopy confirmed that, at an H_2 dilution of 20:1, Si films are fully polycrystalline; no initial amorphous layer is observed during film growth due to this etching process.

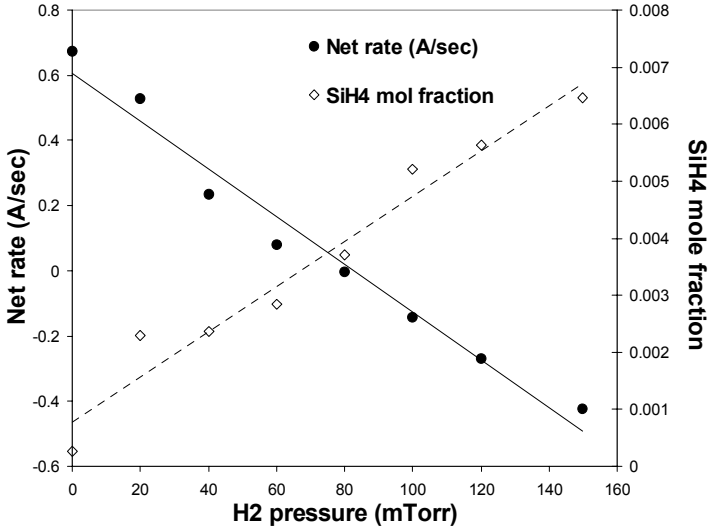

Fig. 1. Net deposition rate and SiH_4 flux, as a function of H_2 dilution.

The nucleation density at low Si coverage on a 1000Å thick SiO_2 layer was determined using atomic force microscopy, as illustrated in Figure 2, for dilutions between 0 and 80 mTorr of H_2 in the region nearest the wire. As seen in Figure 3, the nucleation density increased with time, and was highest for no added H_2. The nucleation density decreased with H_2 dilution. The nucleation density measurements are consistent with the AFM measurements in Figure 4, which indicate an increase in grain size in thick, continuous films from 400 Å with no H_2 dilution to 850 Å at an H_2 dilution of 20:1. The nucleation density increases sublinearly with time. The nucleation rate is initially high until a critical density of nuclei is reached, at which time the nucleation rate is sharply reduced and grain growth begins.

To determine the role of atomic hydrogen etching in the growth process, an SiO_2 substrate was exposed to 60 mT H_2 for 20 minutes, after which growth was allowed to

proceed with an undiluted silane mixture. The resulting nucleation densities were similar to those for undiluted growth without previous H_2 exposure, suggesting that the effect of H_2 is to promote the growth of crystalline Si by preferentially etching amorphous Si and smaller nuclei rather than surface cleaning or roughening the SiO_2 substrate.

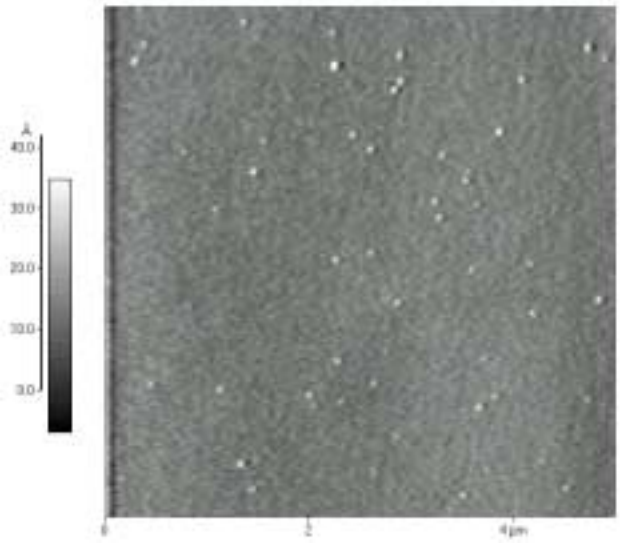

Fig. 2. AFM image of film grown at 20:1 H_2 dilution for 90 s, illustrating the nucleation phase.

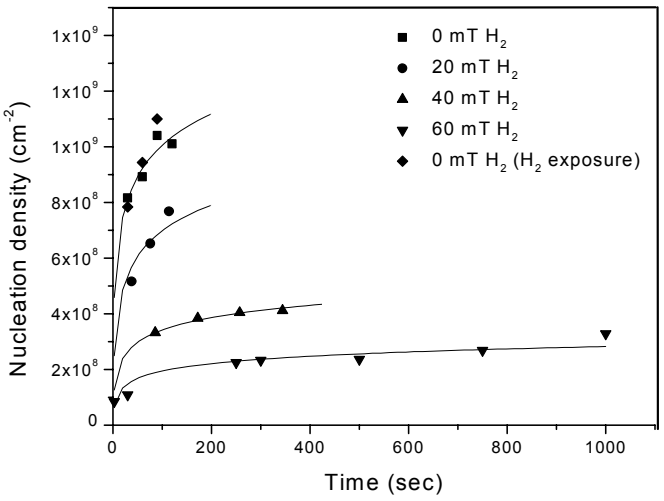

Fig. 3. Effect of hydrogen dilution on nucleation density of Si on SiO_2.

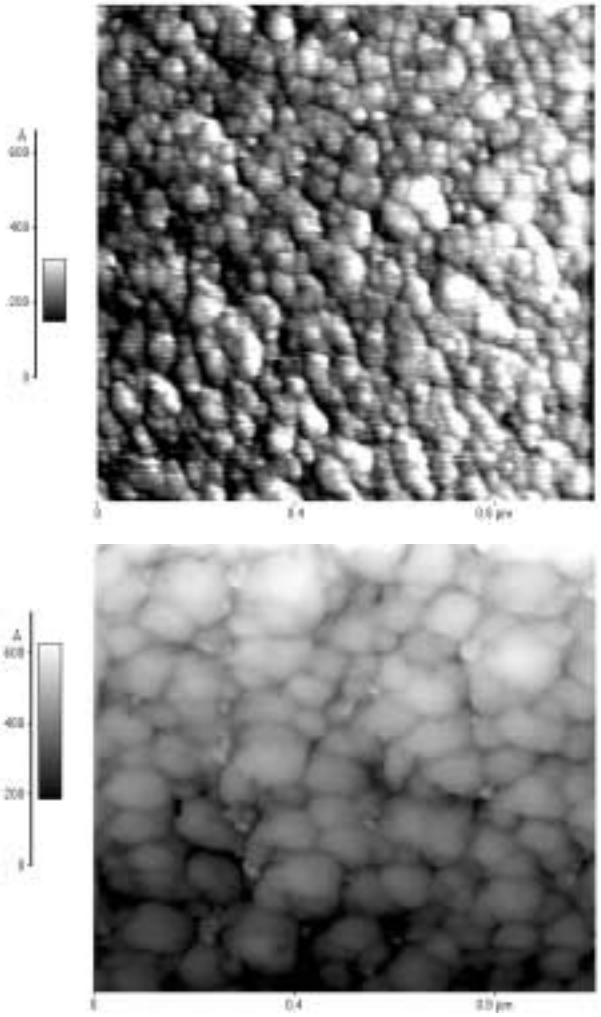

Fig. 4. AFM images. Top: 0 mT H_2, average grain size 400 Å. Bottom: 20 mT H_2, average grain size 850 Å.

3. Conclusions

Polycrystalline films have been grown on SiO_2 by hot-wire CVD at 1.7 Å/sec yielding a 400 Å grain size without the addition of H_2. The addition of 20 mT H_2 decreases the growth rate but produces films with grains of 850 Å in size. This increase in grain size is attributed to atomic H etching of amorphous Si and small crystalline nuclei, decreasing the nucleation density. The nucleation density increases sublinearly with time, implying a fast nucleation rate until a critical density is reached, after which grain growth begins.

4. References

[1] H.N. Wanka, R. Zedlitz, M. Heintze, and M.B. Schubert. *Mat. Res. Soc. Symp. Proc.* 420, 1996.

Materials Issues For CdSe Nanocrystal Activated Polymer Photovoltaics

A Kadavanich[1,2], D Underwood[1], M Erwin[1], T Kippeny[1], R Ward[1], J McBride[1], S Pennycook[2], S Rosenthal[1]
[1]Vanderbilt University, Dept. of Chemistry, Nashville, TN 37235
[2]Oak Ridge National Laboratory, Solid State Division, PO Box 2008, MS 6030, Oak Ridge, TN 37831-6030

Abstract

We present charge carrier dynamics and surface chemical information for CdSe nanocrystals and chemical analysis for poly-(3-hexylthiophene) (P3HT) polymer. We also discuss preliminary results on our own prototype devices.

1. Introduction

Nanocomposites have shown promise as active layer materials for photovoltaic energy conversion. One example is the CdSe nanocrystal/P3HT composite demonstrated by Hyunh et.al.[1] In this paper we investigate the baseline properties of the materials used in a such a device. These properties will be important as we extend the work of Hyunh et. al. by incorporating a dedicated electron-transport material into the active layer.

2. Excited State Carrier Dynamics From Fluorescence Upconversion

CdSe nanocrystals were synthesized using standard techniques.[2] Carrier Dynamics were investigated with a home-built fluorescence upconversion system. Decay profiles for CdSe nanocrystals (NC's) ranging in sizes from 27 to 72 Å were collected and fit to a sum of three exponentials. Independent of size, each band edge trace contains an ultrafast rise component of less than 300 fs, followed by a sub-3 ps decay and finally a long-lived ~nanosecond component. For a given size NC, the band edge dynamics shows no wavelength dependence for emission monitored at 15 nm to the blue and red side of the static fluorescence peak. The band edge kinetics show no dependence on excitation polarization.

The dynamics of the hole are especially important to the overall efficiency of photovoltaic devices utilizing CdSe quantum dots because holes may become localized at the nanocrystal surface. Tight-binding studies of CdSe nanocrystals by Pokrant and Whaley [6] indicate Cd dangling bonds lie in the conduction band while Se dangling bonds give rise to mid-gap states. We attribute the red-shifted emission feature in the static emission spectra to carrier recombination involving holes localized in these surface states. Our RBS data indicates that 30% of the NC surface contains Se atoms with dangling bonds, giving a measure of the surface density of states. To the best of our knowledge, we have obtained the first data on the hole trapping dynamics to these surface states with femtosecond fluorescence upconversion. Two sizes of NC's were studied (Fig. 1) with radii of 27 and 31 Å. The 27 Å NC's had risetimes of 318 fs, and 1.61 ps, whereas the 31 Å sample had longer risetimes of 929 fs and 9.7 ps; both samples contained a long-lived nanosecond decay component.

The size dependence of the long time band edge emission is illustrated in Fig. 2 for 30- and 72 Å CdSe. The smaller NC's fit to a sum of three exponentials with time constants of 155 fs (rise), 1.7 ps (decay), and 19 ps (decay); the larger NC's fit to time constants of 327 fs (rise), 3.2 ps (decay), and 35.5 ps (decay). It is clearly evident that the

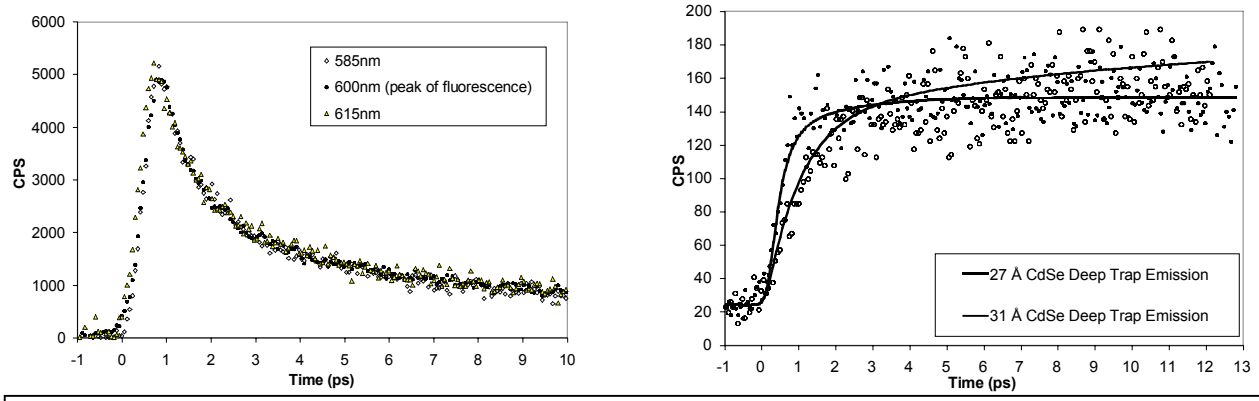

Fig. 1. Band edge and surface emission profiles for CdSe nanocrystals. The band edge emission for 34 Å CdSe (left) shows no wavelength dependence on the kinetics. The surface emission (right) shows a size-dependence on the rise time of the emission, measured at 885 nm.

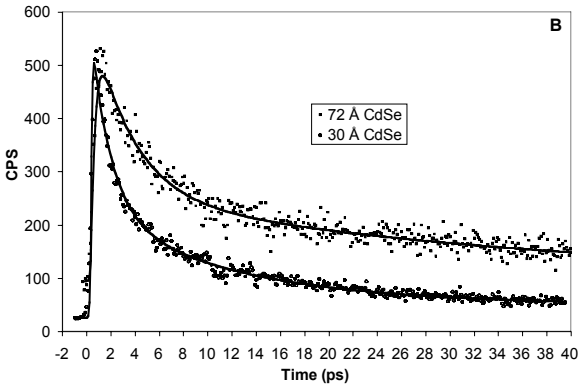

Fig. 2. Comparison of the size dependence on the band edge emission for 30- and 72 Å CdSe in toluene.

larger NC's contain a longer rise and decay time than those of the smaller. A study to determine the excitation wavelength dependence of the rise time is underway.

3. Surface Analysis Using STEM/EELS

The structure and composition of individual nanocrystals were investigated in a pair of Vacuum Generators Scanning Transmission Microscopes (STEM). Atomic resolution imaging confirms the wurtzite structure of the nanocrystal core and provides information on the lattice polarity. Electron Energy Loss Spectroscopy (EELS) on ensembles of nanocrystals previously indicated oxygen associated with nanocrystals. An EELS linescan on a single nanocrystal (Fig. 3) suggests that the oxygen appears in the form of a thin surface oxide. We are attempting to combine atomic resolution imaging with spatially resolved EELS to map out the oxygen distribution as a function of crystal surface.

4. Chemical Analysis of the polymer matrix.

Rutherford Backscattering Spectroscopy (RBS) on thin films of commercially available P3HT indicates the presence of several heavy metal impurities, most likely Zn and Fe and/or Ni. Purification of the as-received polymer reduces the amount of impurities dramatically but as of yet does not remove it completely. This is of concern as the work functions of these metals may permit them to act as carrier traps in a CdSe/P3HT device. Further investigations are ongoing.

5. Prototype devices

We have constructed prototype devices using an active layer of 80% by weight CdSe nanocrystals (~45% by volume) in P3HT sandwiched between aluminum and ITO (or SnO_2:F) on glass electrodes. Under approximated AM 1.5 illumination the maximum photovoltage observed to date was 350 mV. However, current extraction was extremely poor. We anticipate that the addition of an

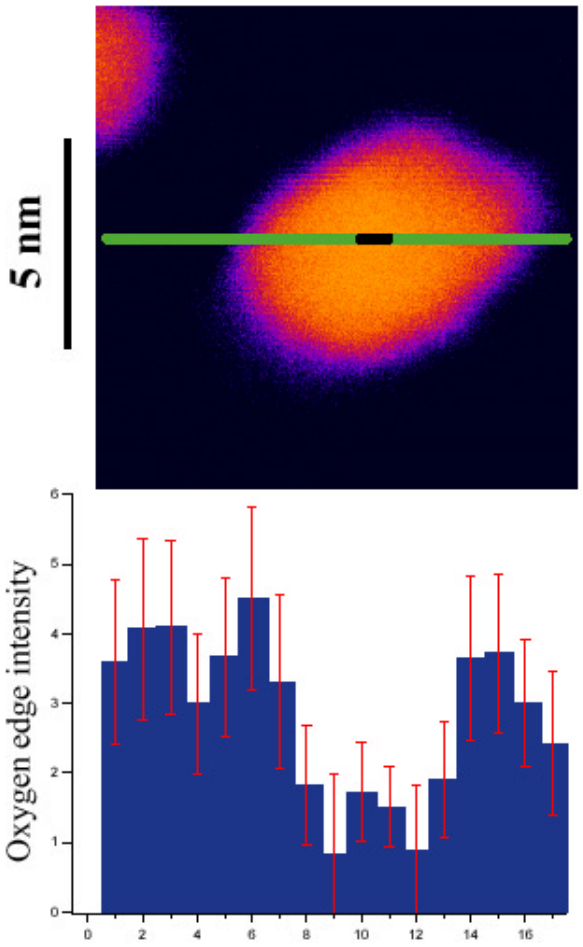

Fig. 3. Top: STEM-dark field image of a single CdSe nanocrystal with the linescan indicated by the horizontal line. The marker in the center indicates the length of each scan step and thus the area integrated for each EELS measurement Bottom: The oxygen concentration profile calculated from the EELS oxygen K-edge intensity. The oxygen concentration is smallest at the center and largest at the edges as would be expected for a thin shell of oxide. (The background oxygen level is due to the MEH-PPV polymer matrix).

electron-transporting material (soluble C_{60} derivatives) to the composite will improve current extraction.

REFERENCES

[1] Huynh, W.U., Xiaogang, P., and Alivisatos, A.P., CdSe nanocrystal rods/poly(3-hexylthiophene) composite photovoltaic devices. Advanced Materials, 1999. 11 (11): p. 923-7.

[2] Peng, X.G., Wickham, J., and Alivisatos, A.P., Kinetics of II-VI and III-V colloidal semiconductor nanocrystal growth: "Focusing" of size distributions. Journal Of the American Chemical Society, 1998. 120 (21): p. 5343-5344.

Medium-Range Order in Hydrogenated Amorphous Silicon Measured by Fluctuation Microscopy

P. M. Voyles[1,2], M. M. J. Treacy[2], H-C. Jin[1], J. R. Abelson[1], and J. M. Gibson[1,3]

1. Departments of Physics and of Materials Science and Engineering, University of Illinois at Urbana-Champaign
2. NEC Research Institute, Princeton NJ
3. Argonne National Laboratory, Argonne IL

ABSTRACT

We have characterized with fluctuation electron microscopy the medium-range order of hydrogenated amorphous silicon thin films deposited by a variety of methods. Films were deposited by reactive magnetron sputtering, hot-wire chemical vapor deposition, and plasma enhanced chemical vapor deposition with and without H_2 dilution of the SiH_4 precursor gas. All of the films show the signature of the paracrystalline structure typical of amorphous Si. There are small variations in the degree of medium-range order with deposition method and H content. The PECVD film grown with high H_2 dilution contains Si crystals ~ 5 nm in diameter at a density of ~ 10^9 cm^2. The amorphous matrix surrounding these crystals shows no difference in medium-range order from the standard PECVD film. Thus the reported improvement in electronic metastability for H_2 diluted films may be associated with the grains or grain boundary regions rather than with the structure of the amorphous matrix.

INTRODUCTION

Fluctuation electron microscopy is a technique for characterizing medium-range order (MRO) in disordered materials. It has been used previously to demonstrate a reduction in MRO in a-Ge thin films on thermal annealing [1] and in hydrogenated amorphous silicon (a-Si:H) thin films on light soaking [2]. It has also lead to the development of the paracrystalline model for the structure of as-deposited amorphous semiconductor thin films [3].

EXPERIMENT

We have examined six different a-Si:H thin films on aluminum foil substrates. Three films were deposited by reactive magnetron sputtering (RMS) from a Si target in an Ar/H_2 atmosphere. One film was prepared by hot-wire chemical vapor deposition (HWCVD) in the National Renewable Energies Laboratory (NREL) reactor. Two films were deposited by radio-frequency plasma-enhanced chemical vapor deposition (PECVD) by United Solar Systems Corporation. One of these films was grown with high H_2 dilution of the SiH_4 precursor gas, and the other is standard material.

RESULTS AND DISCUSSION

Figure 1 shows $V(k)$ for the RMS films, the HWCVD film, and the standard PECVD film. All of the films show a characteristic double-peak pattern in $V(k)$. The first peak lies at $k = 0.31$ Å^{-1} and the second peak at $k = 0.55$ Å^{-1}. These correspond to the first and second diffraction maxima [4] of amorphous silicon [5]. The magnitude of the peaks for all the materials is similar.

This suggests that all of the materials share the same underlying structure, which we have proposed is paracrystalline (PC) [3]. A paracrystal is made up of small strongly strained grains that are topologically crystalline [6] with an amorphous matrix between them. Such a structure has more MRO than a continuous random network (CRN). $V(k)$ calculated from PC molecular dynamics model structures provides a better match for experimental $V(k)$ measurements than $V(k)$ calculated from CRN model structures [3].

There are some very subtle differences in MRO among the films. Figure 1(a) shows the three RMS films with varying H content. The film with 15 at. % H, which has been optimized for use in thin film transistors and other devices, shows slightly more MRO than the films with either higher or lower H content. **Figure 1**(b) compares the 15 at. % H RMS film, the HWCVD film, and the standard PECVD film. The RMS film shows slightly more MRO, while the HWCVD and the PECVD films the same lower degree of MRO. We have also PECVD material grown at USSC under "standard" and "H_2 diluted" conditions. The latter material contains small Si crystals. However, fluctuation microscopy detects no difference in the MRO of the bulk amorphous matrix between these samples.

CONCLUSIONS

We conclude from the data presented here that a-Si:H films grown by reactive magnetron sputtering (RMS), hot-wire chemical vapor deposition (HWCVD) and plasma-enhanced chemical vapor deposition (PECVD) all share the paracrystalline structure. This makes the paracrystalline structure surprisingly universal, as it is also shared by evaporated a-Ge and a-Si [3] and a-Si formed by self-ion-implantation [7]. We postulate that the paracrystalline structure is a residual effect of sub-critical crystal nuclei formation during the deposition.

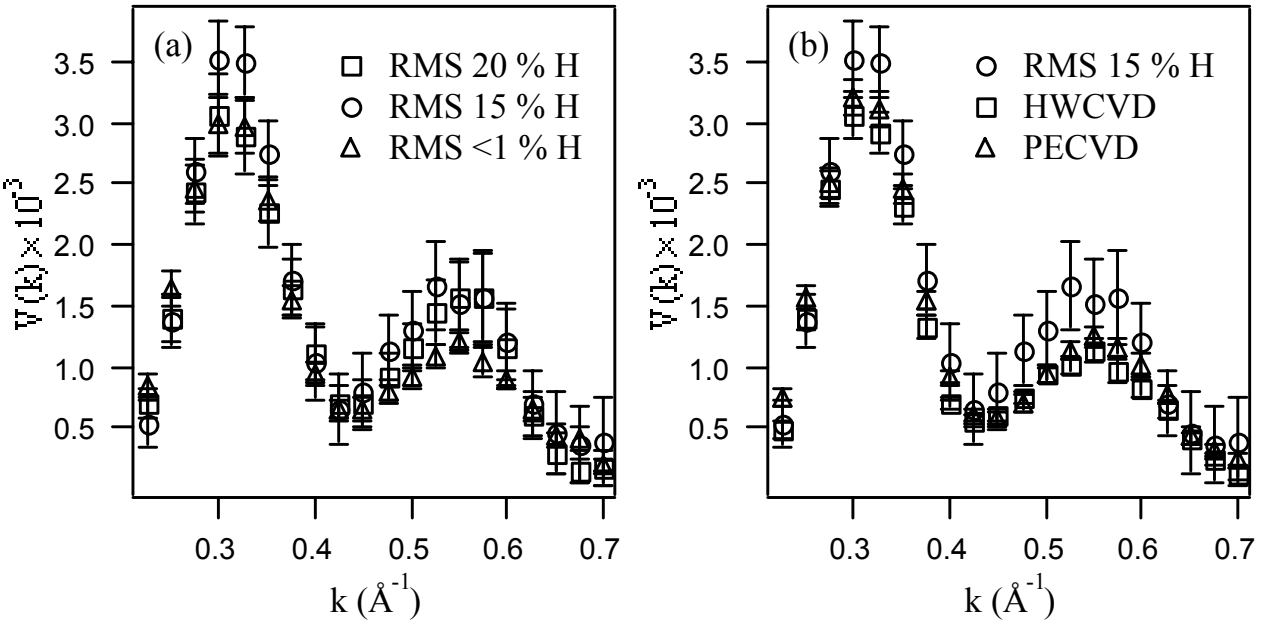

Figure 1. $V(k)$ for (a) the three RMS films with varying H content and (b) the device-quality RMS, HWCVD, and standard PECVD films.

Only small differences in the MRO of a-Si:H thin films have been found with changes in H content and deposition method. High H_2-dilution PECVD material from USSC contains crystals ~ 5 nm in diameter at a concentration of 10^9 cm^{-2} in a matrix which has MRO indistinguishable from that of PECVD a-Si grown without H-dilution. However, this does not necessarily mean that there is no strain reduction in films grown under H_2-dilution, as it may be possible to have a bond reconstruction which affects short range order and strain only without changing MRO. And recent work suggests that such small crystallites may indeed enhance stability [8]. Thus the present work, which is based on the most direct measurement of medium range order in a-Si:H, raises new questions about the microscopic origins of the improved electronic stability in films grown by hot wire CVD or H_2-diluted PECVD.

ACKNOWLEDGMENTS

P.M.V. acknowledges the support of the National Science Foundation (DMR 97-03906). H.C.J. and J.R.A. acknowledge the support of NREL (ADD-9-18668).

REFERENCES

[1] J. M. Gibson and M. M. J. Treacy, Phys. Rev. Lett. **78**, 1074 (1997).

[2] J. M. Gibson, M. M. J. Treacy, P. M. Voyles, H-C. Jin, and J. R. Abelson, Appl. Phys. Lett. **73**, 3093 (1998).

[3] M. M. J. Treacy, J. M. Gibson, and P. J. Keblinski, J. Non-Cryst. Solids **231**, 99 (1998).

[4] For historic reasons, electron microscopists define $k = 1/\lambda$ instead of $k = 2\pi/\lambda$, so the units here are 2π smaller than those used in x-ray diffraction.

[5] K. Laaziri, S Kycia, S. Roorda, M. Chicoine, J. L. Robertson, J. Wang, and S. C. Moss, Phys. Rev. Lett. **82**, 3460 (1999); Phys. Rev. B **60**, 13520 (1999).

[6] M. M. J. Treacy, P. M. Voyles, and J. M. Gibson, to be published in J. Non-Cryst. Solids.

[7] J. M. Gibson, J-Y. Cheng, P. M. Voyles, M. M. J. Treacy, and D. C. Jacobson, in *Microstructural Processes in Irradiated Materials,* S. J. Zinkle, G. Lucas, R. Ewing, and J. Williams, eds., Mat Res. Soc. Symp. Proc. **540**, 1999, p. 27.

[8] Y. Lubianiker, J. D. Cohen, H.-C. Jin and J. R. Abelson, Phys. Rev. B **60**(7), 4434 (1999).

Modeling of Au outdiffusion from Si due to Al gettering

S. Joshi, U. Gösele and T. Tan

Department of Mechanical Engineering and Materials Science, Duke University

Durham, NC 27708-0300

ABSTRACT

Experiments and modeling of Au indiffusion in Si in the literature have shown that the indiffusion process is dominated by the Kick-Out (*KO*) mechanism, involving the interaction of Au atoms with Si self-interstitials (I). Our experiments and modeling of Au outdiffusion from Si due to Al gettering indicate that the outdiffusion of Au is dominated by the Frank-Turnbull (*FT*) mechanism, involving the interaction of Au atoms with vacancies (V).

1. Introduction

Aluminum gettering is a promising technology for improving performance of crystalline Si solar cells by removal of metal impurities from the Si [1]. For proper application of Al gettering, it is important to understand and accurately model the impurity diffusion and gettering processes. The diffusion behavior of Au in Si has been extensively studied [2-4] and makes it an ideal impurity for studying Al gettering.

Gold is a substitutional-interstitial impurity in Si, i.e., nearly all Au atoms reside on substitutional sites (Au_s), but diffusion occurs through fast-moving interstitial Au atoms (Au_i). Interchange between Au_s and Au_i needs participation of the native point defects in Si, viz., I and/or V. Thus, Au diffusion tends to create non-equilibrium concentrations of I and V. In dislocation-free Si, these non-equilibrium concentrations can be relaxed only by diffusion to or from free surfaces, which are infinite sinks or sources of I and V. Indiffusion of Au into dislocation-free thin Si wafers yields characteristic U-shaped profiles even when the Au source is on only one side of the wafer. Fast-diffusing Au_i easily diffuse through the wafer thickness, but incorporation of Au into substitutional sites is controlled by proximity to wafer surfaces rather than by proximity to the Au source.

Modeling and experiments in the literature have shown that Au indiffusion is dominated by the *KO* mechanism [2-4], wherein an Au_i yields an Au_s and an I or the reverse:

$$Au_i \Leftrightarrow Au_s + I. \tag{1}$$

Thus, indiffusion of Au leads to generation and supersaturation of I, which is relieved by outdiffusion of I to the wafer surfaces. The competing *FT* mechanism [5] does not have much contribution during Au indiffusion. Here, an Au_i combines with a V to give an Au_s or the reverse:

$$Au_s \Leftrightarrow Au_i + V. \tag{2}$$

Indiffusion of Au would lead to consumption and undersaturation of V, which would be relieved by indiffusion of V from the wafer surfaces.

Earlier modeling of Al gettering of Au assumed that the *KO* mechanism also dominated Au outdiffusion. This implies that outdiffusion of Au to the gettering layer would be controlled by proximity to the wafer surfaces. Outdiffusion of Au would lead to undersaturation of I, which would have to be relieved by indiffusion of I from the wafer surfaces. Even with an Al gettering layer on only one surface, the outdiffusion of Au would proceed to progressively greater depths from both surfaces as diffusion of Au_i species to the Al gettering layer would not be the limiting process. Experimental results on Al gettering of Au in Si have been previously obtained by us [6], which qualitatively support these modeling results. Qualitatively speaking, the same phenomenon would be seen for the *FT* mechanism as well, with outdiffusion of supersaturated V controlling Au gettering. The purpose of this work was to quantitatively fit our experimental data.

2. Modeling

For modeling of gold diffusion simultaneously by the *KO* and *FT* mechanisms, the I-V reaction must also be taken into account :

$$\phi \Leftrightarrow I + V, \tag{3}$$

where, ϕ represents a Si atom on a lattice site. The complete set of coupled, 1-dimensional partial differential equations to describe the Au diffusion process is [2,4] :

$$\frac{\partial C_s}{\partial t} = k_b^{KO} C_i^{eq}\left(\frac{C_i}{C_i^{eq}} - \frac{C_s}{C_s^{eq}}\frac{C_I}{C_I^{eq}}\right) + k_b^{FT} C_i^{eq} C_V^{eq}\left(\frac{C_i}{C_i^{eq}}\frac{C_V}{C_V^{eq}} - \frac{C_s}{C_s^{eq}}\right), \tag{4}$$

$$\frac{\partial C_i}{\partial t} + \frac{\partial C_s}{\partial t} = \frac{\partial}{\partial x}\left(D_i \frac{\partial C_i}{\partial x}\right), \tag{5}$$

$$\begin{aligned}&\frac{\partial C_I}{\partial t} - k_b^{KO} C_i^{eq}\left(\frac{C_i}{C_i^{eq}} - \frac{C_s}{C_s^{eq}}\frac{C_I}{C_I^{eq}}\right)\\ &- k_b^{IV} C_I^{eq} C_V^{eq}\left(1 - \frac{C_I}{C_I^{eq}}\frac{C_V}{C_V^{eq}}\right) = \frac{\partial}{\partial x}\left(D_I \frac{\partial C_I}{\partial x}\right),\end{aligned} \tag{6}$$

$$\begin{aligned}&\frac{\partial C_V}{\partial t} + k_b^{FT} C_i^{eq} C_V^{eq}\left(\frac{C_i}{C_i^{eq}}\frac{C_V}{C_V^{eq}} - \frac{C_s}{C_s^{eq}}\right)\\ &- k_b^{IV} C_I^{eq} C_V^{eq}\left(1 - \frac{C_I}{C_I^{eq}}\frac{C_V}{C_V^{eq}}\right) = \frac{\partial}{\partial x}\left(D_V \frac{\partial C_V}{\partial x}\right),\end{aligned} \tag{7}$$

where, C_i, C_s, C_I, C_V are the concentrations of Au_i, Au_s, I, V species respectively with the superscript "eq" representing the corresponding equilibrium concentrations. C_i^{eq} is taken to be 1% of C_s^{eq}. D_i, D_I, D_V represent the corresponding diffusivities with the species Au_s having negligible diffusivity, while k_b^{KO}, k_b^{FT} and k_b^{IV} represent the backward reaction rate constants of the *KO*, *FT* and *IV* reactions respectively, which are kept large enough to ensure dynamic equilibrium of the respective reactions. If only the *KO* mechanism is to be modeled, Eqns. (4)-(6) are used with k_b^{FT} and k_b^{IV} set to zero and if only the *FT* mechanism is to be modeled, Eqns. (4), (5) and (7) are used with k_b^{KO} and k_b^{IV} set to zero. The Al gettering process is ac-

counted for by a suitable boundary condition, whereby dynamic equilibrium is maintained at the boundary between the Si and the Al at all times for Au [6] :

$$\left.\frac{C_i}{C_{Al}}\right|_{Si/Al} = \frac{C_i^{eq}}{C_{Al}^{eq}}, \tag{8}$$

where C_{Al} is the Au concentration in the Al and is assumed to be uniform through the thin Al layer thickness X_{Al}. The Au concentration in the Al increases as gettering proceeds, which is accounted for by increasing C_{Al} as per [6] :

$$\frac{dC_{Al}}{dt} = -\frac{D_i}{X_{Al}} \left.\frac{\partial C_i}{\partial x}\right|_{Si/Al}, \tag{9}$$

where the flux $\partial C_i/\partial x|_{Si/Al}$ is computed at the *Si/Al* boundary on the Si side.

3. Results

The experimental work consisted of Au indiffusion at $950^o C$ for 16 h into 530μ thick *FZ* Si, an etch to remove 15μ from both sides of the wafer samples and Al gettering at $1000^o C$ for 30 min with a 1μ thick Al layer on only one surface [6]. The Au outdiffusion profile measured by Spreading Resistance Profiling (*SRP*) is truncated about 50μ from both surfaces as the surface concentration of Au was too low to measure by *SRP*. Fig. 1 shows the fitting of the experimental profile by the *KO* mechanism alone. The gettering/outdiffusion process is too slow for normal values of $D_I C_I^{eq}$, and this value needs to be increased 10 times to get a reasonable fit. Fig. 2 shows the fitting by the *FT* mechanism alone where it is seen that a normal value of $D_V C_V^{eq}$ gives a satisfactory fit even when the individual D_V and C_V^{eq} values are varied over a few orders of magnitude. Fig. 3 shows the fitting by the *KO* and *FT* mechanisms together, which is very close to the fit by the *FT* mechanism alone.

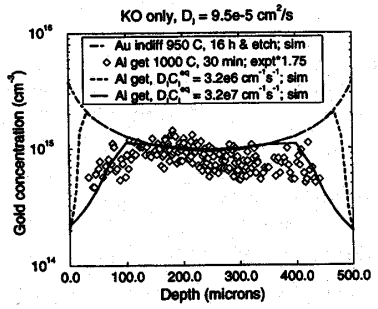

Figure 1. Fitting of experimental profile by *KO* mechanism only with two different values of $D_I C_I^{eq}$.

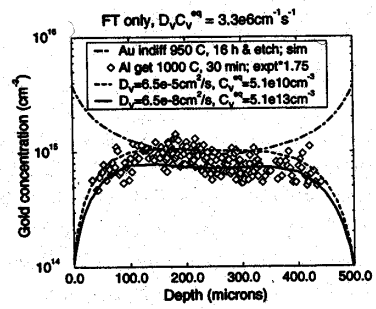

Figure 2. Fitting of experimental profile by *FT* mechanism only with $D_V C_V^{eq}$ kept constant and D_V varied.

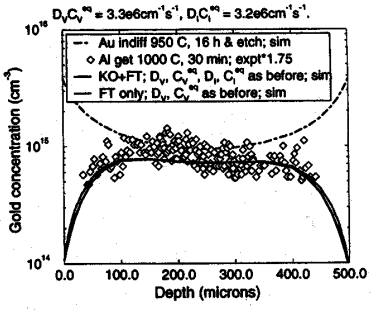

Figure 3. Fitting of experimental profile by *KO* and *FT* mechanisms combined.

4. Discussion

Since the value of $D_I C_I^{eq}$ is well-established, the fit obtained by the *KO* mechanism alone is not reasonable, as it requires $D_I C_I^{eq}$ be increased by one order of magnitude. In contrast, the *FT* mechanism gives a good fit to the experimental profile with a value of $D_V C_V^{eq}$ close to established values in the literature. Even though the $D_V C_V^{eq}$ value is very close to the $D_I C_I^{eq}$ value at the temperature in question, the *FT* mechanism clearly has a dominant contribution to Au outdiffusion, in direct contrast to the domination of the *KO* mechanism for Au indiffusion at the same temperature. Vacancies get supersaturated during Au outdiffusion, and the diffusion of V to the surfaces limits Au outdiffusion or gettering.

5. Summary

Gold outdiffusion during gettering is controlled by the *FT* mechanism. Modeling by the *KO* and *FT* mechanisms combined clearly shows that the *FT* mechanism has a dominant contribution to Au outdiffusion.

6. Acknowledgements

This work is supported by the US Department of Energy via National Renewable Energy Laboratory Subcontract No. XAF-7-17607-1. Computational facility support by the North Carolina Supercomputing Center is acknowledged.

REFERENCES

[1] S. M. Joshi, U. M. Gösele and T. Y. Tan, J. Appl. Phys. 77 (1995) 3858-3863.
[2] U. Gösele, W. Frank and A. Seeger, Appl. Phys. 23 (1980) 361-368.
[3] N. A. Stolwijk, B. Schuster and J. Hölzl, Appl. Phys. A 33 (1984) 133-140.
[4] D. Mathiot, Phys. Rev. B 45 (1992) 13345-13355.
[5] F. C. Frank and D. Turnbull, Phys. Rev. 104 (1956) 617-618.
[6] S. Joshi, U. Gösele and T. Tan, MRS Proc. 490 (1998) 117-122

Modeling of Electrical Activity of Metallic Precipitates in Silicon Based on Schottky Effect

P. S. Plekhanov and T. Y. Tan

Department of Mechanical Engineering and Materials Science, Duke University

Durham, NC 27708-0300

ABSTRACT

A quantitative model of the electrical activity of metallic precipitates in Si is presented. An emphasis is made on the Schottky junction effects in the precipitate-Si system as well as the carrier diffusion and drift in the Si space charge region. Carrier recombination rate is found to be determined by the thermionic emission charge transport process across the Schottky junction rather than the surface recombination process. It is shown that the precipitates can have a very large minority carrier capture cross-section.

Metal and metal silicide precipitates can be prominent carrier recombination centers in Si. They are abundant in multicrystalline Si used for manufacturing low cost solar cells. Hence, it is important to understand the mechanism of recombination at the precipitates and to obtain the associated carrier capture cross-section (CCS) values. In this paper, we present a model for calculating the precipitate CCS based on the Schottky effect. Previously, Schottky barrier effects associated with metallic precipitates were quantitatively considered in EBIC contrast calculations, but the Si carrier lifetimes due to the precipitates were assumed [1,2] rather than calculated based on the properties of the interface with Schottky barrier.

A metal or silicide precipitate forms a Schottky junction with Si, and therefore is charged and surrounded by a Si space charge region. The supply of carriers is determined by their diffusion and drift in the electric field, which is due to the charge on the precipitate and the space charge. In most cases, the charges attract minority carriers and hence increase their supply and repulse majority carriers and hence decrease their supply. With these two effects, it cannot be qualitatively judged the diffusion of which type of carriers will be the limiting factor of the recombination process. Once the carriers reach the precipitate, they can recombine either in Si at the precipitate interface states or inside the precipitate. In the former case, the local carrier recombination rate is determined by the surface recombination velocity due to interface states, while in the latter case it is governed by the thermionic emission mechanism for charge transport across the Schottky junction. Upon entering the precipitate, an electron-hole pair can be considered recombined. Generally, in the case of direct current across the Schottky junction, only the transport of majority carriers across the junction is involved, and thermionic emission potential exists only for majority carriers. In the case of recombination current, there is transport of both types of carriers, and the thermionic emission potentials are essential for both majority and minority carriers. These potentials have opposite signs for electrons and holes, and their absolute values are generally not equal. At the surface of the precipitate, the carrier concentrations are determined by the Schottky barrier height φ_b, which is an intrinsic property of the material, and the thermionic emission potentials, which vary with the recombination current. Away from the precipitate surface, the carrier concentrations are controlled by diffusion, drift, generation, and background recombination due to centers other than precipitates, e.g. dissolved metal atoms.

To find out whether carrier recombination occurs primarily inside the precipitate or at the surface states, the interface recombination velocity of an ideal metal-semiconductor junction having no interface states was calculated based on the Schottky model. For p-type Si under the weak generation condition $n_0 << \delta n << p_0$, we obtain that the surface recombination velocity $s = A m_e^* T^2 / (emN_c) = 5.0\text{x}10^{-6}$ cm/s at room temperature. Here A is the Richardson constant, m_e^* is the effective mass of an electron in Si, m is electron mass, T is the absolute temperature, e is the elementary charge, and N_c is the density of states in the conduction band. Since the interface recombination velocity due to interface states is usually much less than $5.0\text{x}10^6$ cm/s, it can be neglected. Furthermore, our modeling showed that even if the interface recombination velocity due to interface states exceeds this value by a few orders of magnitude, the capture cross-section of the precipitate is affected only slightly.

The numerical modeling of recombination at precipitates was carried out using a variety of material parameter values. Examples of electron and hole concentration profiles around the precipitate for p-type Si and FeSi precipitate are shown in Fig. 1. The CCS plots versus precipitate radius are shown in Fig. 2 along with the precipitate cross-section area, and the total CCS of dissolved metal atoms in Si of a number equal to that in the precipitate. The precipitate CCS is roughly proportional to its diameter, as predicted by the diffusion-limited model [3]. A smaller generation rate or a higher precipitate concentration leads to a larger CCS. The dependence of CCS on φ_b and background recombination constant is relatively weak. Under the conditions considered, the supply of minority carriers is the limiting factor. The supply of holes becomes influential only at lower p-doping levels and higher generation rates, for which the weak generation condition no longer holds.

In order to verify the model, some available experimental data are fitted. The minority carrier diffusion length was calculated based on the published measured parameters for platelet-shaped $NiSi_2$ precipitates in n-type Si [4] using the model, Fig.

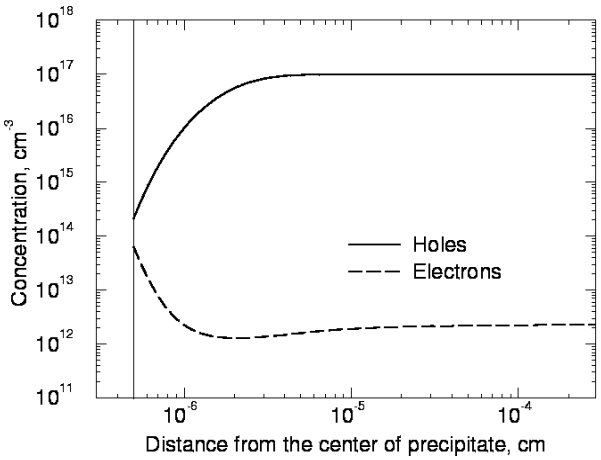

Fig. 1. Electron and hole concentration profiles around the precipitate. Parameters used: background recombination constant 10^5 s^{-1}, generation rate 10^{19} s^{-1} cm^{-3}, precipitate concentration 10^{10} cm^{-3}, precipitate diameter 10^{-6} cm, p-type doping level 10^{17} cm^{-3}, φ_b = 0.68 eV (FeSi)

3. For each sample, two values of precipitate concentration were reported, as measured by TEM and EBIC, along with the precipitate dimensions. Accordingly, two values of minority carrier diffusion length were calculated and then compared to the experimental data. The generation rate and the background recombination constant were not known and were used as fitting parameters. The same fitting values were used for all samples. Variations of these values within an order of magnitude do not change the picture qualitatively. The measured diffusion length lies between the two calculated values or within experimental error from them, which can be considered a confirmation of the validity of the model.

In conclusion, a model of the carrier recombination process due to a precipitate with metallic properties in Si has been developed. It shows a good apparent agreement with experimental data. It was found that such precipitates can serve as very efficient recombination centers with minority carrier CCS in great excess of their geometric cross-section area and under certain conditions as large as, or slightly larger than the total CCS of their constituent metal atoms dissolved in Si. Under the weak generation conditions, the supply of minority carriers, via diffusion and drift, is the limiting factor of the recombination process.

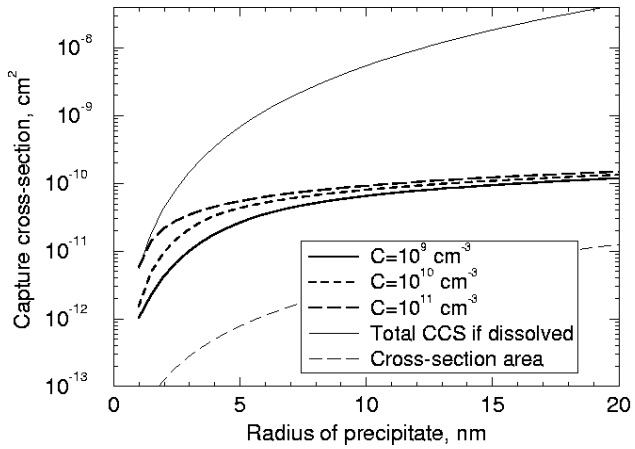

Fig. 2. Dependence of precipitate capture cross-section on its diameter at various precipitate concentrations. Other materials parameters used are the same as in Fig. 1.

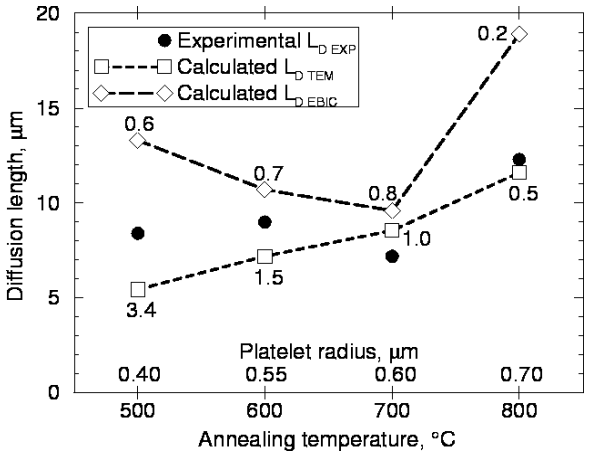

Fig. 3. Experimental and calculated hole diffusion lengths in n-type Si with $NiSi_2$ platelet-shaped precipitates. For each experimental sample, two values were calculated in accordance with two precipitate concentration values observed by TEM and by EBIC. The concentrations are indicated at each calculated point, in 10^9 cm^{-3}. Other parameters used are: background recombination constant 10^5 s^{-1}, generation rate 10^{18} s^{-1} cm^{-3}, n-type doping level $4x10^{14}$ cm^{-3}, φ_b = 0.79 eV (B-$NiSi_2$)

ACKNOWLEDGEMENTS

This work is supported by US Department of Energy via National Renewable Energy Laboratory Subcontract No. XAF-7-17607-1. Computing facility support by North Carolina Supercomputing Center is acknowledged.

REFERENCES

[1]. C. Donolato, Semicond. Sci. Technol. 7, 37 (1992).
[2]. W. Seifert, M. Kittler, M. Seibt, and A. Buczkowski, Solid State Phenomena **47-48**, 365 (1996).
[3].P. S. Plekhanov, R. Gafiteanu, U. M. Gösele, and T. Y. Tan, J. Appl. Phys. **86**, 2453 (1999).
[4]. M. Kittler, J. Larz, W. Seifert, M. Seibt, and W. Schroter, Appl. Phys. Lett. **58**, 911 (1991).

Multifunctional Antireflective/Gettering Coating Ti Film

A. Romanowski, J. Kasichainula, J. Muth*), and G. Rozgonyi

Materials Science & Engineering
North Carolina State University
Raleigh, NC 27695-7916.
*Electrical & Computer Engineering
North Carolina State University
Raleigh, NC 27695-7916.

ABSTRACT

Electrical, optical and structural parameters of Ti film deposited using magnetron sputtering with Ar plasma are investigated. It is shown that gettering efficiency of the Ti thin film is comparable with that of Al thin film and nitrogen diluted Ar plasma deteriorates gettering efficiency. Unstressed Ti thin film has been obtained using oxygen and nitrogen diluted Ar plasma. The film has good optical quality.

1. Introduction

It is well established that thin film layers deposited by magnetron sputtering are structurally and optically uniform. In order to form and investigate Ti AR/Gettering films, we have equipped our magnetron sputtering system with the hydrogen, nitrogen, oxygen and argon lines. A precise two-needle valve connected in series to the main valve controls the oxygen flow. The distance between target and substrate is about 20 mm. Such a small distance allows us to increase the deposition rate but also introduces two inconveniences; (i) plasma heating of the sample, and (ii) ion bombardment [1,2]. During plasma treatments molecular oxygen and nitrogen atoms are negatively ionized and reach film surface with the kinetic energy of several hundreds eV [1]. Both effects generate surface stress that can be compressive or tensile. The tensile process is additionally generated by the film recrystallization and substrate/metal interface formation [3].

2. Material preparation

The p-type CZ silicon wafers (doping concentration of 10^{15} cm^{-3} have been intentionally contaminated with iron (10^{12} cm^{-3}). The JTB procedure has been used for wafer cleaning and next Ti thin films have been deposited using magnetron sputtering method for 15 min prior to 3 min target annealing. The Ar pressure has been kept constant at 1 μTorr. Four different plasma gases have been used during magnetron sputtering: (1) Ar, (2) Ar + N_2, (2) Ar + N_2(50%) + O_2(50%), (3) Ar + O_2. The optical/structural parameters have been tested using SEM and reflectance spectroscopy. Two samples with Ti or Al films, deposited using (1) or (2) plasma were gettered in 700^0C for 150min in N_2 atmosphere. The samples were electrically characterized using μ-PCD and DLTS techniques after stripping metal films by CP-4 solution.

3. Results

Gettered samples: The lifetime rate κ (= τ_G/τ) ≈ 30 (τ_G, τ are lifetimes of gettered and non-gettered samples) was measured for the gettered Ti film, and it was lower than the lifetime rate of Al getterd film of 35. The Al getter is well-established external getter in IC and PV technology; therefore, has been used as reference material. The DLTS-concentration spectra for Ti and Al getters are shown in Fig. 1. The separating peaks due to the donor-Au, the Au-Fe complexes and Fe-4 level for Ti-getter, as well as the Fe-B pairs and donor-Fe for Al-getter are shown in the spectrum. The Al getter spectrum varies continuously, indicating continuous distribution of the deep levels in the lower Si bangap. In the case of Ti and Al getters, the Fe concentration does not surpass $3x10^{11}$ cm^{-3} which is ~100 lower than initial Fe-B concentration. Measured iron concentration; however, can be masked by iron precipitation process. In the case of Ar + N_2 plasma used for sputtering a low lifetime rate of κ = 14 has been found. DLTS spectrum for the above sample is shown in Fig. 2. The five peaks, clearly seen in the spectrum are Fe-B pair, donor/acceptor Au, Au-Fe complex and Ni. Peaks are not overlapping as in the case of Ti(Ar) or Al getters shown in Fig. 1. Dominating donor-Au peak is responsible for lifetime deterioration. Au related defects were easily created by vacancy injection from the surface during nitridization processes and interaction between nitride and oxygen atoms.

Optical /Structural Characterization of the Non-Gettered Films: The presence of the stress is observed on SEM images of the cleaved samples, as shown in Fig. 3. Large located defects have been seen only for samples with Ti film deposited in Ar + O_2 (Fig. 3a) or Ar + N_2 (Fig. 3b) plasma. The above defects have not been visible for the film deposited using Ar plasma (not shown in figure) or Ar+N_2+O_2 (Fig. 3c) plasma. We expect that these defects could be eliminated during gettering processes at 700^0C. The film reflectivities are presented in Fig. 4. The reflectivities were measured in wavelength range from 200nm to 800nm. The long-wavelength reflectivity of ~30% can be seen for reference, TiO_xN_y, and TiO films. In the case of Ti, TiO(150^0C) and TiN films the reflectance increases with wavelength and reaches the value of 60% for Ti film due to the presence of the metal atoms. The higher reflectance of TiO film deposited at 150^0C than that deposited at room temperature is probably due to enhanced metal recrystallization. Small TiO, TiO_xN_y film reflectivities in the range between 200 and 350nm are due to the high oxygen concentration. At 150^0C, oxygen solubility in Ti enhances, while O-N complexes are formed for TiO_xN_y film. We also believe that in both cases compressive stress is released due to enhanced temperature or small nitrogen ion size (0.015nm) compared to oxygen ion size (0.137nm).

4. Summary and Farther Work

The reflectance of the Ti films deposited by the pulsed dc sputtering process has been investigated. Ti film can be used as external getter; however, its gettering efficiency is lower than Al film. Formation of TiNSi complexes reduces impurity segregation at interface. Nitrogen and oxygen diluted Ar plasma give unstressed AR coating films. Their reflectance is comparable with TiO_x coatings.

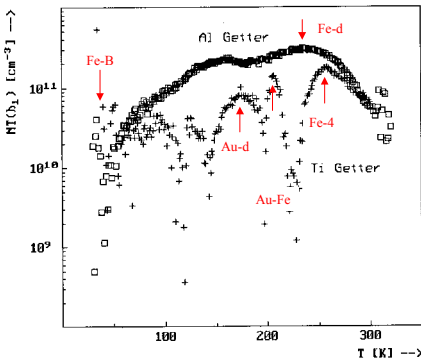

Fig. 1. Deep level concentrations measured by DLTS for Fe contaminated p-type Si CZ wafers with Ti and Al getters (700^0C, 150 min).

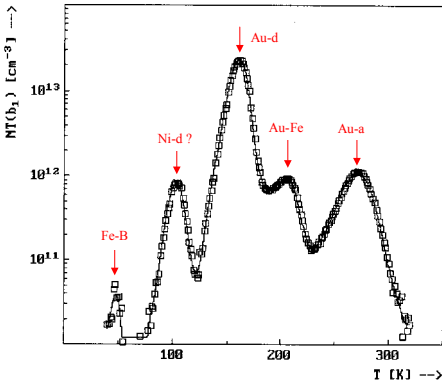

Fig. 5. Deep level concentrations measured by DLTS for Fe contaminated p-type Si CZ wafers with Ti (Ar + N_2 plasma) getter (700^0C, 150 min).

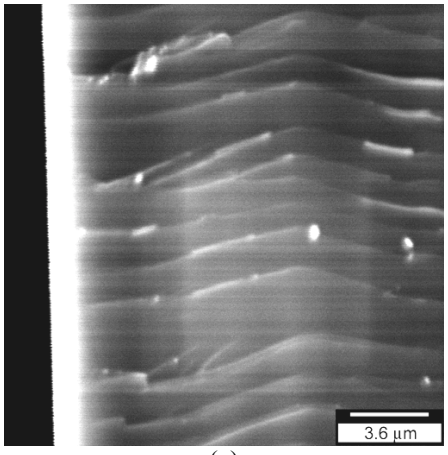

(a)

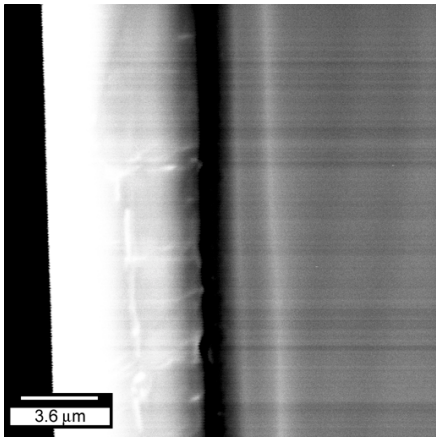

(b)

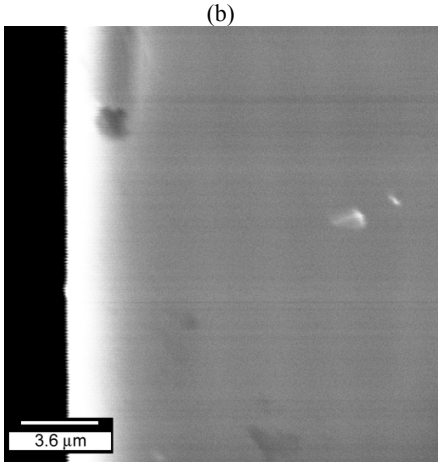

(c)

Fig. 3. SEM images of cleaved wafers with (a) TiO_x, (b) TiN_x and (c) TiO_xN_y films

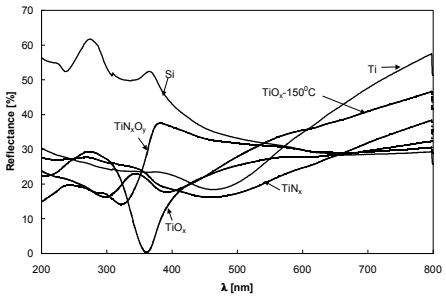

Fig. 4. Reflectance of the Ti films deposited on Fe contaminated CZ silicon

REFERENCES

[1] H. Ohsaki, Y. Tachibana, A. Hayashi, A. Mitsui, and Y. Hayashi, "High rate deposition of TiO_2 from TiO_{2-x} target", Thin Solid Films 351 (1999) 57-60.

[2] M. Vergohl, N. Malkomes, T. Staedler, T. Matthee, and U. Richter, "Ex situ and in situ spectroscopic ellipsometry of MF and DC-sputtered TiO_2 and SiO_2 films for process control", Thin Solid Films 351 (1999) 42-47.

[3] P. Oberhauser, and R. Abermann, "Influence of substrate properties on the growth of titanium films: part III", Thin Solid Films 350 (1999) 59-66.

Nanocrystal/Polymer Composite Photovoltaic Devices

W. Huynh, L. Manna, A. P. Alivisatos

Department of University of California, Berkeley
Material Sciences Division, Lawrence Berkeley National Laboratory

Berkeley, CA 94720(USA)

ABSTRACT

Unlike conventional solar cells, novel polymeric photovoltaic devices have flexibility, large area processibility and potential low costs. We have constructed devices consisting of a composite of CdSe nanocrystals and poly(3-hexylthiophene). The resulting monchromatic power conversion efficiency is 0.7 %. Since the efficiency in these devices is limited by poor electron transport, we seek to improve the mobility of electrons in the CdSe with nanorods in place of nanocrystals. Devices fabricated with small aspect ratio CdSe nanorods and poly(3-hexythiophene) have conversion efficiencies up to 2 %. Soluble nanorods of CdSe were synthesized with aspects ratios reaching 10:1 by controlling the kinetics of nanocrystal growth in lyothermal solutions.

Introduction

Thin film electronic devices with polymeric active components have been intensely studied because of the possibility of constructing large area, flexible devices with simple processing [1,2]. The first photovoltaic devices fabricated from single layer, thin films of semiconducting polymer were inefficient [3]due to poor separation and collection of the generated electron-hole pairs (excitons). It was subsequently recognized that enhanced charge separation occurs at an interface between two materials with disparate electron affinities, allowing for transport of the carriers in separate materials with a low probability of recombination. Substances introduced into the polymer to create heterojunctions for improved device performance include, C_{60}[4], small organic molecules[5], and other conjugated polymers[6,7]. In this paper we report the fabrication and characterization of nanocrystal/polymer composite photovoltaic devices as well as the synthesis of nanorods of CdSe and their incorporation in photovoltaic devices.

CdSe Nanoparticle/Poly(3-hexylthiophene) Devices

Photovoltaic cells were fabricated by spin casting a chloroform solution of pyridine passivated 5 nm diameter CdSe nanocrystals and poly(3-hexylthiophene) (P3HT) onto an indium-tin oxide (ITO) coated glass substrate and evaporating aluminum top contacts. Films were of thickness typically between 50 to 100 nm[8]. From the current-voltage response of 90 % wt. CdSe in P3HT(Fig 1), a quantum efficiency of 5 %, a open circuit voltage of 0.57 V and a fill factor of 0.51 can be calculated. The resulting power conversion efficiency is 0.7 %

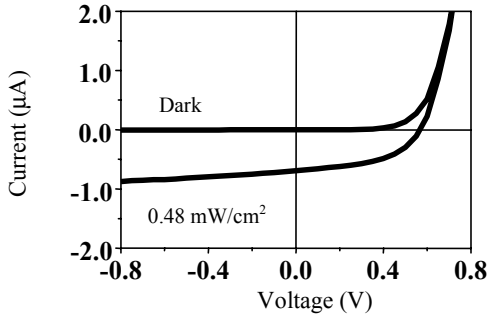

Fig. 1Current-voltage response of 90 % wt. 5 nm CdSe in P3HT device.

As compared with previous nanocrystal/polymer composite photovoltaic devices constructed from CdSe and the polymer MEH-PPV(poly(2-methoxy,5-(2'-ethyl-hexyloxy)-*p* phenylenevinylene), the devices reported here show a factor of three improvement in power conversion. This is mainly attributed to the higher fill factor and open circuit voltage. We can explain this in the context of reduced recombination rates due to a higher hole mobility in P3HT which is of the order 10^{-2} cm/(sV) as compared with MEH PPV which is of the order 10^{-4}. Observation of TEM images of films of the polar CdSe and the non-polar P3HT indicate that there is microphase separation such that CdSe nanocrystals form a percolation path through the polymer. Measurements of the intensity dependence of the external quantum efficiency indicates an almost linear relation. This is consistent with recombination at a fixed number of sites corresponding to "dead-ends" in the nanocrystal network.

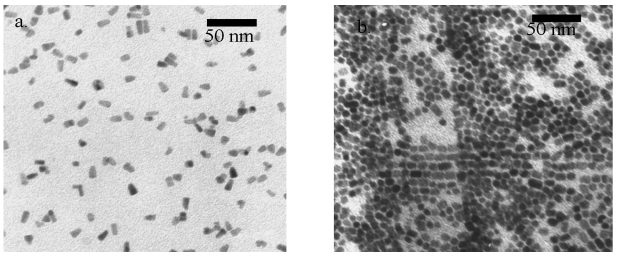

Fig. 2. a) Transmission electron micrograph of 8 x 13 nm CdSe nanocrystal rods. b) TEM of chains of 5 x 8 nm CdSe particles stacked along the c-axis.

Elongated rod-shaped CdSe nanocrystals were synthesized using a slightly modified nanocrystal synthesis (Fig. 2a) . From TEM images, it can be seen that rods have a

tendency to organize along their long axes, possibly forming a directed pathway for electron transport.(Fig. 2b). Films of 80 % by weight 8 x 13 nm CdSe rods in P3HT were used in photovoltaic devices and we observe an increase in quantum efficiency by a factor of three. The fill factor and open circuit voltage is essentially unchanged from devices made of spherical nanocrystals. An overal power conversion efficiency of 1.9 % at 514 nm is obtained for the improved devices. This is comparable to the most efficient of the recent polymer composite devices reported.

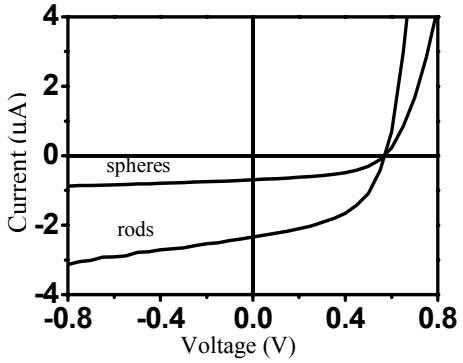

Fig. 3 Current-voltage response of 80 % wt. 8 x 13 nm CdSe in P3HT device.

CdSe Nanorods

We seek to further improve these composite devices by incorporating wires to transport electrons rather than a network of discreet nanoparticles. Recently the kinetic control of CdSe nanocrystal growth has been used to vary the shapes of particles from a nearly spherical morphology to rod-like with aspect ratios as large as ten to one[9].

In a classical CdSe nanocrystal synthesis Cd and Se precursors in solution are rapidly injected into hot (340-360 °C), surfactant, usually tri-octyl phosphine oxide (TOPO). Nucleation occurs immediately, followed by growth. At the growth temperature, surfactant molecules adsorb and desorb rapidly from the nanocrystal surface, enabling the addition (as well as removal) of atoms from the crystallites, while aggregation is suppressed by the presence, on average of one monolayer, of surfactant at the crystallite surface. The reaction can be stopped at any time with heat removal producing nanocrystals of a desired average size.

A modification of this preparation leads to shape control of CdSe nanocrystals. According to this new protocol, Cd and Se precursors are injected into a binary surfactant mixture composed of TOPO and hexylphosphonic acid (HPA), with a well defined ratio of HPA/TOPO. Moreover, the amount of precursos injected is much higher than used in conventional CdSe nanocrystals synthesis. In this system the growth of CdSe nanocrystals is very fast and highly anisotropic, resulting in a rod-like shape where the long axis is the c-axis of the wurtzite crystal structure (Fig. 4).

The aspect ratio of the rods increases quickly just after injection, while the the short axis shows only a slow increase . This stage is considered to be strongly over-driven growth, since the monomer concentration is high after the initial injection. As the monomer concentration depletes during growth, the aspect ratio gradually decreases to nearly one (ordinary quantum dots), but the short axis grows significantly. This stage is considered to be thermodynamically controlled, since a near-equilibrium spherical morphology of the nanocrystals would minimize their surface area. The rod morphology can be maintained by additional (slow) injections, which replenish the monomer, resulting in longer quantum rods (up to 50 nanometers, Fig. 4). Nanorods synthesized with multiple injections also show high monodispersity of the short axis, as confirmed by optical absorption and emission sprectra and low-resolution transmission electron microscopy.

Quantum rods of any desired size and aspect ratio can be systematically obtained by varying several parameters, like the reaction time, the amount of precursors injected, and the numer of injections.

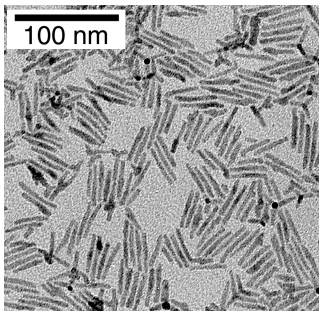

Fig. 4 Low resolution transmission electron microscopy image of CdSe nanorods.

Conclusion

In this work we have demonstrated that rod-shaped CdSe nanocrystals blended with P3HT conducting polymer can be used to construct efficient photovoltaic devices. High aspect rods have been synthesized to increase the efficiency of electron transport for future composite devices.

References

[1] Greenham, N. C.; Moratti, S. C.; Bradley, D. D. C.; Friend, R. H.; Holmes, A. B. *Nature* **1993**, *365*, 628-630.

[2] Ho, P. K. H.; Thomas, D. S.; Friend, R. H.; Tessler, N. *Science* **1999**, *285*, 233-236.

[3] Marks, R. N.; Halls, J. J. M.; Bradley, D. D. C.; Friend, R. H.; Holmes, A. B. *Journal of Physics-Condensed Matter* **1994**, *6*, 1379-1394.

[4] Yu, G.; Gao, J.; Hummelen, J. C.; Wudl, F.; Heeger, A. J. *Science* **1995**, *270*, 1789-1791.

[5] Janssen, R. A. J.; Christiaans, M. P. T.; Hare, C.; Martin, N.; Sariciftci, N. S.; Heeger, A. J.; Wudl, F. *Journal of Chemical Physics* **1995**, *103*, 8840-8845.

[6] Halls, J. J. M.; Walsh, C. A.; Greenham, N. C.; Marseglia, E. A.; Friend, R. H.; Moratti, S. C.; Holmes, A. B. *Nature* **1995**, *376*, 498-500.

[7] Granstrom, M.; Petritsch, K.; Arias, A. C.; Lux, A.; Andersson, M. R.; Friend, R. H. *Nature* **1998**, *395*, 257-260.

[8] Huynh, W. U.; Peng, X. G.; Alivisatos, A. P. *Advanced Materials* **1999**, *11*, 923-927,886.

[9] Peng, X. G.; Manna, L.; Yang, W. D.; Wickham, J.; Scher, E.; Kadavanich, A.; Alivisatos, A. P. *Nature* **2000**, *404*, 59-61.

Nanostructure Arrays for Multijunction Solar Cells

B. Das, S. McGinnis, P. Sines, C. Garman, D. Gray and W. Zhang

West Virginia University

Nanostructures Research Group
Department of Computer Science & Electrical Engineering
Morgantown, WV 26506-6109

ABSTRACT

This paper presents the results of the Phase I effort of a three-year project to develop low cost high efficiency solar cells using semiconductor nanostructure arrays. The Phase I effort included the identification of the substrate material, identification of semiconductor nanostructure material and size, optimization of fabrication process parameters, template characterizations by AFM, SEM, capacitance-voltage and current-voltage techniques, and the development of theoretical models. A summary of the Phase I results is presented in this paper together with an outline of the on-going research and the collaborations developed for this project.

1. Introduction

While photovoltaic cells based on thin film technologies are among the most promising for commercial applications, many technical challenges still remain such as reduced cell efficiency, poorer material quality, spatial non-uniformity, material stability and manufacturing costs [1-4]. In order to address these limitations, we are developing a new *inexpensive* photovoltaic cell technology based on the electrochemical fabrication of semiconductor *nanostructures*. Nanostructure based PV cells have the potential to provide very high energy conversion efficiencies resulting from the following effects: (a) nanostructure *crystallite sizes* are comparable to the *carrier scattering lengths*, which significantly reduces the carrier scattering rate, thus *increasing the carrier collection efficiency*; and (b) the *strong absorption coefficient* of nanostructures due to the increased density of states. In addition, by varying the size of the nanostructures, the band gap can be tuned to absorb in a particular photon energy range [5]. The major impediment to the development of a nanostructure based PV technology has been the inability to fabricate large arrays of nanostructures with the required periodicity and size control at low cost. We have developed a unique low cost technology for the fabrication of periodic arrays of semiconductor nanostructures with very good size control (± 10%) and periodicity. This technique uses electrochemical synthesis on a preformed template of anodized aluminum to form the nanostuctures (Figure 1a). This technology is also ideally suited for the formation of multijunction structures which will further increase the photo-conversion efficiency [6]. The photovoltaic cells fabricated using this technique can be formed by stacking layers of nanostructure arrays as shown in Figure 1b, where the multi-junction feature is achieved by using band gap tuning through nanostucture size control.

2. Results and Analysis

Test silicon wafers were identified as the best choice for the initial development work. This provides a relatively inexpensive substrate material (~$8 per wafer), and provides the ability to characterize both the template and the fabricated nanostructures through standard MOS capacitance-voltage measurements. The long range goal is to fabricate the aluminum oxide template on commerical plate glass. This will provide the ability to fabricate transparent large area photovoltaic cells without substantially increasing material handling costs. The primary concern with this material is roughness and material nonuniformity. However, after reviewing the relevant technical standard (ASTM 1036-91), this does not appear to be a significant limitation. To facilitate template formation on insulating substrates, a process was developed and verified for anodization without the need for a back contact. In addition, the ability to fabricate multilayer stacks of templates was demonstrated.

The standard thin film deposition process used in this research was thermal evaporation. However, we also investigated the effect of sputter deposited aluminum films on template properties. This deposition technique is attractive since it is commonly used for high volume commercial thin film deposition and provides superior film adhesion. The primary difficulty with this technique for our application is that high energy (1kW) magnetron sputtering produces a significantly rougher film than thermal evaporation. However, even with 5 nm RMS film roughness, AFM measurements revealed uniform pore formation.

To improve the anodization process and to provide flexibility for a wide range of substrate materials and sizes, a new anodization apparatus was designed and fabricated. The details of the design and performance are discussed in an article submitted to the Review of Scientific Instruments.

The quality of the template material and the silicon/aluminum oxide interface was verified by performing standard MOS capacitance-voltage measurements using the aluminum oxide as the insulating material. The results of these measurements are shown in Figure 2 along with the anodization potential-time profile

for this device. This measurement shows that the aluminum oxide provides a high quality insulating material without substantial interface states or traps. Repeated stressing of the aluminum oxide film with a potential of up to 1.5 MV/cm revealed no breakdown of the insulator. This result is significant for long term operational stability of the PV cells. Standard charge-to-breakdown measurements will be conducted to quantify the breakdown strength of the oxide.

For the initial work, the composition of the semiconductor nanostructures was restricted to the ZnCdS family with Cu and Mn doping. This choice was made since these materials have the ability to cover the solar spectrum, and the fact that the electrochemical fabrication techniques for these materials have been well developed. To determine the size and composition of the nanostructures to be synthesized, a model of the optical properties of the materials as a function of alloying and quantum wire diameter was developed. This was accomplished using a one-electron model in the effective mass approximation for the acceptor energy levels in quantum confined wires. The results of this model demonstrates that through alloying and quantum confinement, this material system can cover wavelengths between 375-950 nm. This current model will be extended to include the effect of dopant concentration, and nonlinear effects associated with changing alloy composition.

The alloyed ZnCdS quantum wires are synthesized by galvanostatic co-deposition using a dimethylsulphoxide (DMSO) solution containing elemental sulfur, and the appropriate choloride salt of the cation and the dopant material. This approach has been previously demonstrated to fabricate high quality CdS thin films [7].

In addition to the work conducted at WVU, we have developed a number of collaborations to significantly enhance this research. We are currently working with Dr. P.N. Kumta at Carnegie-Mellon University and have had discussions with Dr. R. Bhattacharya at the National Renewable Energy Laboratory to extend the electrochemical deposition process to other compound semiconductors. In addition, we have a collaboration with Dr. B. Carter at the University of Minnesota and Dr. P. Boolchand at the University of Cincinnati to perform nanoscale material and surface characterization and Raman spectroscopy measurements respectively. We are currently working with Dr. M. Cahay of the University of Cincinnati to develop a model for the electron transport in the quantum wires including interface effects. In addition, we have an ongoing collaboration with Dr. Ricardo Aroca of the University of Windsor on a related project to perform Surface Enhanced Raman Spectroscopy (SERS) on our templates.

3. Discussion

The Phase I objectives of this project were to determine the substrate material, nanostructure dimensions, material composition for the p-type semiconductor quantum wires, and the initiation of semiconductor nanostructure fabrication and characterization. As described in the previous section, the Phase I objectives of the project have been successfully accomplished and the project is well positioned to progress to the next phase. The substrate materials as well as the nanostructure composition/dimensions have been identified. Theoretical models have been developed to correlate nanostructure parameters to absorption energy in order to have improved match to the solar spectrum. The template characterization and semiconductor nanostructure fabrication have been initiated and the project is ready for the Phase II effort.

REFERENCES

[1] Photovoltaic – The Power of Choice: The National Photovoltaic Program Plan for 1996-2000; *NREL Report.*
[2] Photovoltaic Technologies; *NREL Report.*
[3] K. Zweibel, Thin Film Technologies Project FY96 Summary, NREL.
[4] M. Gratzel, Coord. Chem. Rev. 111, 176 (1991). A. Kay and M. Gratzel, J. Phys. Chem., 97, 6272 (1993).
[5] A. Zunger, S. Wagner, and P.M. Petroff, J. Electronic Materials, 22, 2 (1993).
[6] S.R. Kurtz, D. Myers, and J.M. Olson, 26th IEEE PV Specialist Conference, Anaheim, CA Sept 29-Oct 3, 1997.
[7] T. Edamura, J. Muto, Thin Solid Films, 235, 198 (1993).

FIGURES

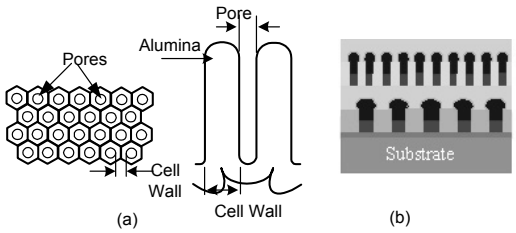

Fig. 1 (a) Top and cross-sectional views of template, and (b) schematic cross-section of nanostrcuture multijunction PV cell.

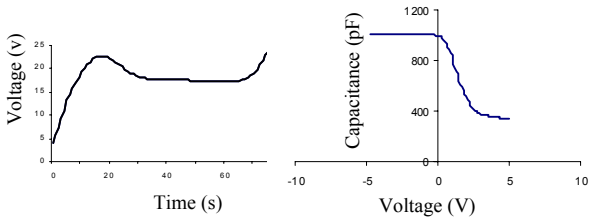

Fig. 2 Voltage-time and Capacitance-Voltage characterstics

Nondestructive Characterization of Atomic Profiles in Layer-Structured Photovoltaic Materials Using the Method of Angular Dependence of X-ray Fluorescence(ADXRF)

S. Kim, Y.L. Soo, G. Kioseoglou, S. Huang, Y.H. Kao,
State University of New York at Buffalo

K. Ramanathan and S. Deb,
National Renewable Energy Laboratory

Abstract

Angular dependence of x-ray fluorescence technique has been applied to the study of atomic density profile in composite systems. This method is shown to be useful for probing the microstructures and intermixing of constituent elements in layer-structured photovoltaic materials.

I. **Introduction**

It is well known by now that further development of advanced photovoltaic (PV) technology will make extensive use of layer-structured materials. This approach will depend crucially on the technical capability to prepare layer structures with high quality interfaces. To this end, a clear understanding and quantitative characterization of the microscopic structure and density profile around the inferfacial region would seem highly desirable. A basic problem in this area of research still remains unsolved is the intermixing of constituent elements across the interfaces. An example can be found in the case of CdS/Cu(In,Ga)Se_2 heterojunctions. This class of PV materials has already demonstrated a record high efficiency of 18.8%; however, the problem of microstructure and intermixing of atoms around the heterointerface is still poorly understood.

Recent development of the technique of angular dependence of x-ray fluorescence (ADXRF) using synchrotron radiation has shown that it is very useful for nondestructive characterization of layer-structured CdS/CdTe PV materials.[1, 2] This method is element-specific and nondestructive, it can provide valuable information about the density profile of selected elements in a composite system, thus is particularly useful for the study of element intermixing across the interfaces. In essence, when an x-ray beam impinges on a layer structure, its penetration depth varies from nanometers to micrometers as the grazing incidence angle passes through the critical angle of the material, the fluorescence yield (FY) of a specific element measured as a function of angle can therefore provide information on the depth profile of that selected element in the material. For a multilayer material consisting of very thin films, the x-ray FY can be described by the following equation[3]:

$$I_{aj} \propto C_{aj} \rho_j D_j \mid E^t_j + E^r_j \mid^2 \qquad (1)$$

where I_{aj} is the primary x-ray fluorescence intensity of a particular element a in layer j, C_{aj} the mass fraction of element a in layer j, ρ_j the density of layer j, D_j the thickness of layer j, E^t_j and E^r_j the transmitted and reflected fields at the top of layer j, which are functions of the roughness σ, and the incidence angle θ. By a comparison of the calculated and measured FY, information about the depth distribution of selected elements in the layer material can be obtained.

II. **Examples of ADXRF Applications**

A typical ADXRF result is shown in Fig. 1. In this figure, the Ge-K_α FY is plotted as a function of grazing incidence angle for a SiGe layer grown on Si(100) by molecular beam epitaxy. The nominal concentration of Ge is 80%, and the nominal thickness is 150Å. The data were taken at Beamline X3B1 at the National Sybchrotron Light Source using x-ray photon energy of 12 keV. The solid line

Fig.1. Typical ADXRF for a SiGe layer grown on Si(100). The raw data (open circle) are fitted with theoretical calculation (solid line) based on equation (1).

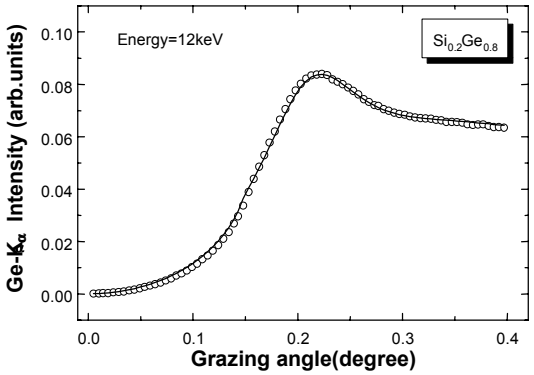

in Fig.1 is a fit to the raw data by using Eq. (1). From the close agreement between theory and experiment, the actual Ge concentration of the SiGe layer has been determined to be 56% throughout the entire SiGe layer. This corrected Ge concentration is also consistent with other experimental results including x-ray diffraction and x-ray absorption fine structure (XAFS) obtained with the same sample.

The problem of element intermixing in a CdS/$CuInSe_2$ junction has been investigated using the ADXRF method.[4] Figure 2 shows some preliminary data taken with x-ray energy at 28keV.

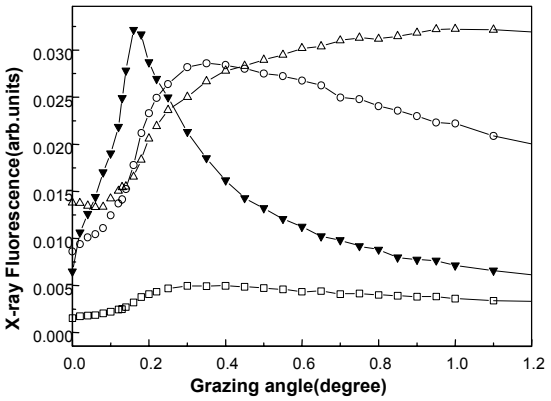

Fig.2. ADXRF data for different elements in a CdS/$CuInSe_2$ heterojunction taken with incident x-ray energy at 28keV: In(triangles), Se(circles), Cu(squares), and Cd(inverted triangles). All the data are subject to a geometrical factor correction.

While detailed quantitative analysis of these results are in progress, it is useful to compare the experimental results with a simulation of the Cd FY in this system. In Fig. 3, the angular dependence of Cd-K_α FY is shown for the cases with and without a 10% Se diffusion from the bulk $CuInSe_2$ to the CdS top layer. For simplicity, the Se atoms are assumed to be uniformly distributed in the CdS layer. The gross feature of these curves are seen to be similar to the Cd FY data shown in Fig. 2 (after a geometrical factor correction). This example also shows the sensitivity of the

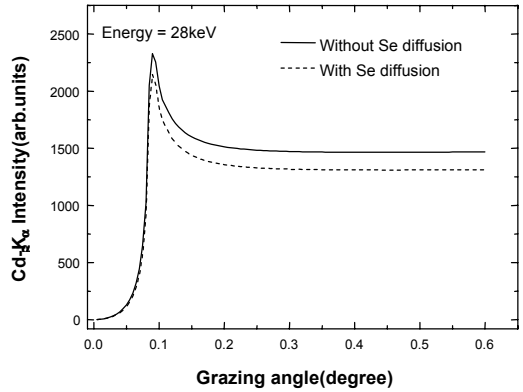

Fig.3. Simulation for Cd-K_α FY profile in a CdS/$CuInSe_2$ heterojunction : (a)without Se diffusion into the CdS layer (b)with 10 % Se diffusion into the CdS layer.

ADXRF method for detecting changes in the density profile of selected elements. When this plot is analyzed in conjunction with a similar plot for Se FY, more detailed information about Se diffusion can be obtained. Likewise, the same technique can be applied to probing the density profiles related to the diffusion of Cu or In into the CdS layer, and S or Cd into $CuInSe_2$.

III. **Conclusion**

In summary, we have demonstrated by way of examples that the ADXRF technique can be conveniently applied to studying the changes in density profiles of selected elements in a composite system. This method is therefore specifically useful for investigating the problems of atomic profile and element intermixing in layer-structured PV materials.

The present research is supported by DOE and NREL.

IV. **References**

1. Y. L. Soo, S. Huang, Y. H. Kao, and A. D. Compaan, J. Appl. Phys. **83**, 4173 (1998).
2. Y. L. Soo, S. Huang, Y. H. Kao, and A. D. Compaan, Appl. Phys. Lett. **74**, 218 (1999).
3. D. K. G. de Boer, Phys. Rev. B **44**, 498 (1991).
4. Y. L. Soo, S. Huang, Y. H. Kao, S. K. Deb, K. Ramanathan, and T. Takizawa, J. Appl. Phys. **86**, 6052 (1999).

« Novel Cd – Sn – In – based Bulk and Thin Film Transparent Conducting Oxides »

R.P.H. Chang[+], T.J. Marks[+*], T.O. Mason[+] and K.R. Poeppelmeier[*]

[+] Department of Materials Science and Engineering

[*] Department of Chemistry

Northwestern University, Evanston, IL 60208

ABSTRACT

This research focuses on next - generation transparent conducting oxides (TCOs) for improved photovoltaic (PV) performance. More specifically, there are two research foci : 1) improved Sn – based, n – type TCOs aimed at enhanced CdTe PV cell performance, and 2) novel Cu – based, p – type TCOs applicable to a variety of PV designs. An integrated interdisciplinary bulk and thin film team is engaged discovering, synthesizing, characterizing, and optimizing novel TCOs phases in promising Sn and Cu – based compounds. The objective of the research is to identify, explore, evaluate, and develop new materials for future generations of PV technologies.

A key result of our study has been to demonstrate that the reactions in bulk, and probably in thin films, between the oxides $CdO – SnO_2 – In_2O_3$ are dominated by the formation of solid solutions which can be represented by the double substitution reaction : $2\ In^{3+} \rightleftharpoons Sn^{4+} + Cd^{2+}$. Furthermore, a new series of volatile, thermally stable Cd complexes have been prepared which will enable efficient $CdO – SnO_2 – In_2O_3$ – films to be grown by metal – organic chemical vapor deposition (MOCVD).

Progress in Bulk Studies

The discovery of exceptionally high mobilities in thin films of n – type Cd_2SnO_4 and $CdIn_2O_4$ at NREL and elsewhere prompted us to undertake an investigation of phase space in the $CdO – SnO_2 – In_2O_3$ system. Although this study is partially complete and ongoing, a number of important findings have emerged. Two extensive solid solutions have been found : a spinel phase extending from $CdIn_2O_4$ to between 75% and 80% Cd_2SnO_4 (see Fig. 1.) and a co – substituted bixbyite phase extending from pure In_2O_3 to about x = 0.34 in $In_{2-2x}Cd_xSn_xO_3$ at 1175°C. One important ramification of the phase relations along the $CdIn_2O_4 – Cd_2SnO_4$ vertical section is that beyond the solubility limit, the spinel phase is in equilibrium with a substantially lower doped orthorhombic Cd_2SnO_4 (having the Sr_2PbO_4 structure). This implies that spinel Cd_2SnO_4, which forms in thin films, is metastable and forms because of the synthetic pathway.

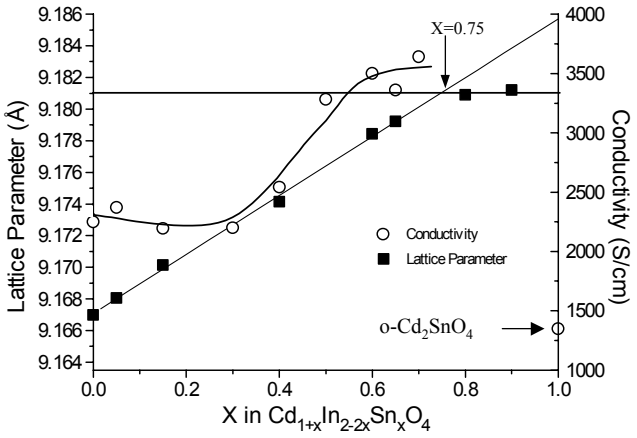

Fig. 1. Quenched 1175°C lattice constant (as-fired samples) and 4-point DC conductivity (reduced samples) on bulk $Cd_{1+x}In_{2-2x}Sn_xO_4$.

Electrical property measurements (4 – point conductivity) and optical measurements (diffuse reflectance) were made on pellets of samples in both $CdIn_2O_4 – Cd_2SnO_4$ (see Fig. 1.) and $In_{2-2x}Cd_xSn_xO_3$ solutions. Conductivity (corrected for porosity) in both as – fired and reduced (annealed 6h at 400°C in forming gas, in parentheses)

specimens increases from 1600S/cm (2300S/cm) to 2600S/cm (3600S/cm) as x increases from 0 to 0.70. These values extrapolate at x = 1 (spinel Cd_2SnO_4) to values comparable to those reported in films, and are decidedly larger than we obtain for orthorhombic phase of Cd_2SnO_4. There is a precipitous rise in conductivity at x = 0.40 and a similar drop in optical band gap at x = 0.20 as determined by diffuse reflectivity in $In_{2-2x}Cd_xSn_xO_3$ solid solution. We are investigating the possibility of a concurrent change in the distribution of the cations. At the same time, we are carrying out room temperature thermopower measurements to ascertain whether the rise in conductivity is due primarily to increased carriers, mobilities, or both.

The bixbyite, $In_{2-2x}Cd_xSn_xO_3$, solid solution may also be of interest for potential PV applications. Conductivity in as – fired specimens remains relatively constant (≈ 100S/cm) over $0 \leq x \leq 0.16$, whereafter it increases rapidly to 700S/cm at x = 0.20. It should be cautioned that the ultimate solubility limit has yet to be firmly established for this phase. Nevertheless, given that these materials are neither intentionally Sn – doped or hydrogen – reduced, the values obtained are encouraging.

Progress in Thin Films Studies. Metal – Organic Precurcors

In an effort to replace dimethylcadmium as the current cadmium precursor used in MOCVD applications, a volatile, less toxic Cd precursor family is desired. For MOCVD of Cd_2SnO_4 – based TCO films, new Cd and Sn precursors are required.

We have recently designed and investigated several new precursors (see Fig. 2.). Furthermore, several Cd precursors were tested in our cold – wall CVD system. Using Cd(mmm – miki)$_2$ (see Fig. 2.) with oxygen as the oxidant, films obtained are typically dark with significant carbon contamination (20 – 30 at %), most likely caused by the required low growth temperatures (< 350°C). However, using Cd(hfa)$_2$TMEDA (see Fig. 2.), with O_2/H_2O as oxidant to remove carbon, CdO films with low carbon content (< 5%) were grown at 350° - 380°C. These films have good transparency (~ 85%) with good conductivity (~ 3100S/cm).

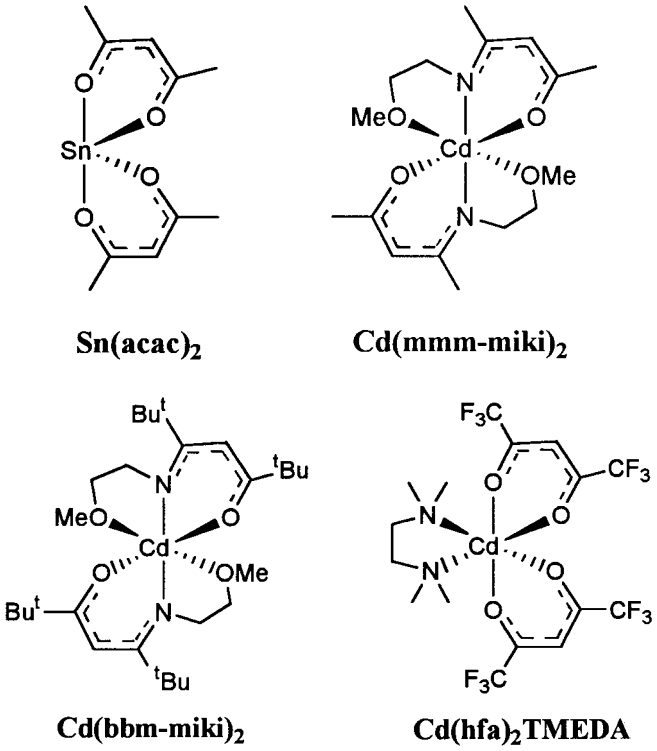

Fig. 2. Molecular structures of the precursors used.

Although SnO_2 and CdO films have been successfully deposited by MOCVD using our newly designed Sn and Cd precursors, the deposition of Cd_2SnO_4 has not yet been achieved owing to the deposition temperature gap between the Sn and Cd species and incompatibility of the Sn precursor with water. We are currently pursuing : a) a more thermally stable Cd precursor for higher temperature growth so that Sn(acac)$_2$ (see Fig. 2.) can be used for the final Cd_2SnO_4 deposition, and b) a less stable Sn precursor with possible use of O_2/H_2O as oxidant for low carbon contamination. Also under study is plasma enhancement during the CVD process to lower the growth temperature of SnO_2.

Novel Glass-Ceramic Substrates for Thin Film Polycrystalline Silicon Solar Cells

N. Nemchuk*, S. Krasulya*, J. Couillard#, D. Ast*, F. Fehlner #, L. Pinckney #

* Dept. of Materials Science and Engineering, Cornell University, Ithaca, NY 14853
# Corning Incorporated, Corning, NY 14831

ABSTRACT

Novel transparent glass-ceramic substrates suitable for the economical fabrication of thin film polycrystalline silicon solar cells are being developed by Corning Incorporated and Cornell University under the NREL contract. The substrates match the thermal expansion of silicon and can be processed at temperatures as high as 900 ºC. To prevent out-diffusion of glass components into the polysilicon film, low cost barrier layers are being developed and characterized.

To verify the suitability of the barrier coated glass-ceramics to serve as substrates for thin film solar cells, we fabricated at 900 ºC test p-i-n structures and thin film transistors. The later permits to quantitatively measure the density of gap states (DOS) of polysilicon films deposited on these novel glass-ceramic substrates and to compare it to the DOS of polysilicon film deposited on established control substrates such as fused silica and oxidized silicon. The results show that the DOS of polysilicon film deposited on glass-ceramic substrate is comparable to that of films deposited on fused silica and oxidized silicon substrates.

Introduction

The economical fabrication of polycrystalline silicon thin film solar cells requires low cost transparent substrates that can be processed at high (T>700ºC) temperatures to achieve the high deposition rates and quality necessary for mass production. The most heat resistant commercial glass substrates soften at temperatures above 650 ºC. Fused silica is transparent and meets the temperature requirements but is expensive. Its thermal expansion coefficient is 1/5 of that of silicon, leaving a polysilicon film deposited at high temperature under a high tensile stress that can lead to the cracking of the film.

An attractive alternative to glass is glass-ceramic. Glass-ceramics are commercially used in products such as range tops. They withstand high temperatures and can be engineered to be transparent and to match the thermal expansion of silicon. But the substrates need to be coated with a barrier layer to stop the out-migration of glass components from the substrate.

Glass-ceramic substrates

The glass-ceramics that are being investigated have the composition SiO_2-Al_2O_3-ZnO-MgO-TiO_2, ZrO_2 [1] and their final microstructure consists of 10-15 nm-sized spinel crystals, dispersed uniformly in a siliceous glass matrix.

To obtain a surface as similar as possible to that of oxidized silicon or fused silica and to minimize the effect of surface roughness on the device performance we polished the glass-ceramic wafers to 0.7 nm rms using Chemical Mechanical Polishing (CMP).

To prevent the out-migration of substrate components into the thin film a low cost barrier layer was developed. The barrier layer, consisting of 1000 Å of SiN_x followed by 1000 Å of SiO_2, was deposited by Plasma Enhanced CVD (PECVD). The ability of this layer to act as a diffusion barrier was confirmed by SIMS profiles which showed that none of the glass elements penetrated the layers during a 4-hour anneal in nitrogen at 900 ºC.

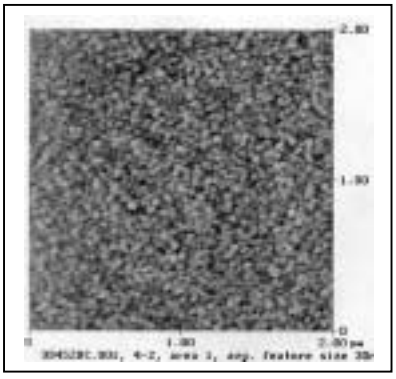

Figure 1. AFM image of the surface of a glass-ceramic with the PECVD barrier layer.

The optical transparency of 1mm thick glass-ceramic wafer coated with this barrier layer is greater than 95%. The high optical transparency of the substrates may be of interest not only as a 'superstrate' cover for solar cells but also useful in other thin film devices such as flat panel displays.

It should be noted, however, that coating the glass-ceramic with this PECVD barrier layer increased the surface roughness from 0.7 to 1.21 nm rms. Detailed analysis of the surface coated with the barrier layer using Atomic Force Microscopy revealed features with an average lateral size of 30 nm (fig.1). These features were found on the surfaces of different substrates coated with the barrier layer. The fact that the size of the features does not depend on the surface on which the layer was deposited can be explained by considering the nature of the PECVD process, which is far from the thermal equilibrium. The structure of the deposited film therefore is more likely determined by the deposition parameters rather than surface features. The roughness of the initial (bare) substrate contributes only in a minor way to the final surface roughness.

Glass-ceramics coated with this barrier layer were used to fabricate p-i-n test structures (see our poster for details) and thin film transistors to validate the investigated glass-ceramic/barrier layer system as a substrate for thin film solar cells.

DOS of poly-Si film

Thin film transistors (TFTs), minority carrier devices that permit quantitatively characterize electronic structure of thin polysilicon film, were fabricated on glass-ceramic, fused silica and oxidized silicon substrates. A detailed description of the fabrication process can be found in [2]. These TFTs were used to map out the density of the midgap states (DOS) of the polysilicon films deposited on different substrates. Figure 2a shows the DOS plots of non-hydrogenated polysilicon films deposited on barrier layer coated glass-ceramics, fused silica and oxidized silicon substrates. As can be seen from the fig. 2a the DOS of non-hydrogenated film is very high (~10^{19} $cm^{-3}eV^{-1}$) and the curves can hardly be distinguished from each other. To probe on a more sensitive scale for differences, the polysilicon films were hydrogenated and re-measured (fig.2b). Hydrogenation passivated grain boundaries states and reduced overall DOS by two orders of magnitude. The higher DOS of polysilicon films on glass-ceramic and fused silica substrates compared to polysilicon films on oxidized silicon is currently

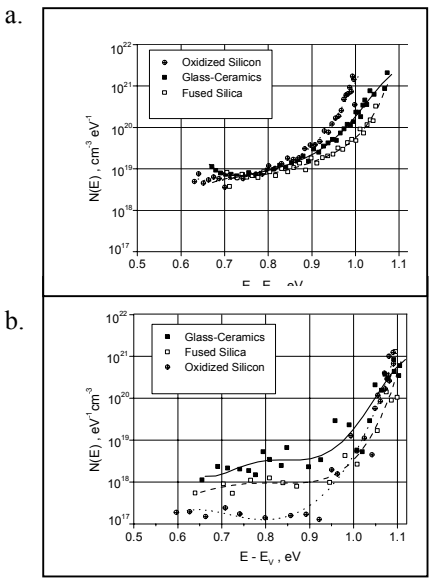

Fig. 2. DOS of non-hydrogenated (a) and hydrogenated (b) polysilicon films deposited on barrier layer coated glass-ceramics, fused silica and oxidized silicon substrates

attributed to the different structure of this films due to the variation in substrate surface roughness. Our aim is to lower the DOS to 10^{17} $cm^{-3}eV^{-1}$ and then to probe, by DLTS, for the presence of chemical impurities.

Conclusions

A low cost, effective and highly optically transparent diffusion barrier layer was developed for high temperature glass-ceramics. However further work is required to obtain substrates with lower surface roughness.

Polysilicon films with density of gap states as low as 10^{17} $cm^{-3}eV^{-1}$ were obtained on oxidized silicon substrates. DOS of the polysilicon films deposited on rougher glass-ceramic and fused silica substrates is of order 10^{18} $cm^{-3}eV^{-1}$.

TFTs of comparable high performance were fabricated on oxidized silicon, fused silica and barrier layer coated glass-ceramics.

Acknowledgements

This work was funded by NREL under contract XAF-8-17607-06. Experimental work was performed in part at the CNF supported by the NSF under Grant ECS-9319009, Cornell University and industrial affiliates.

References

[1] L.R.Pinckney, J. Non-Cryst. Solids 255 (1999) 171

[2] N.I. Nemchuk et. al. Proc. 5th Int. Sem. Dev. Res. Symp., Charlottesville, VA, 1999, pp. 45-48

Novel Synthesis and Capacitance Measurements of Copper Indium Gallium Diselenide Alloys

J. Heath, J. D. Cohen, J. Thompson and D. C. Johnson

Materials Science Institute, University of Oregon

Eugene, Oregon 97403

ABSTRACT

The objective of this reasearch is to characterize optimized samples of $CuIn_{1-x}Ga_xSe_2$, both from our synthesis approach and from other related research teams at NREL. We anticipate following trends in the number of total defects, the growth and or suppression of particular defect levels, and the relative importance of defects at grain boundaries as a function of both synthesis approach and annealing conditions. Growth and measurement studies have both been initiated. We first discuss the results of our growth efforts followed by our initial measurement results.

1. General Introduction

We are exploring the use of elementally modulated reactants as a cost effective technique for the production of large area, high efficiency $CuIn_{1-x}Ga_xSe_2$, films for thin film solar cells. In this approach, we use high vacuum deposition techniques to repeatedly deposit alternating layers of the desired elements. The individual elemental layers are on the order of 5-50Å in thickness. The thickness of each layer controls the diffusion distances and composition within each reactant resulting in the ability to control the reaction pathway and the sequence of compound formation. [1] We are following trends in the number of total defects, the growth and or suppression of particular defect levels, and the relative importance of defects at grain boundaries as a function of both synthesis approach and annealing conditions for samples produced by us at Oregon and by other NREL research teams using the transient photocapacitance method.

2. Synthesis

Samples were made by sequential and co-deposition of elements from thermal sources in a vacuum deposition chamber. Deposition targets included pieces of silicon wafer for low angle XRD analysis, off angle polished quartz for high angle XRD, and polymethylmethacrylate (PMMA) coated silicon as a source for freed sample used for differential scanning calorimetry (DSC) and high angle XRD analysis. Samples are annealed under a dry nitrogen atmosphere at atmospheric pressure. Samples are analyzed on a Scintag XDS 2000 or a Philips X-pert MRD x-ray diffractometer using a Cu kα source.

3. Synthesis Results Using Modulated Elemental Reactants

Seventeen samples have been prepared to date at Oregon with compositions near the stoichiometry of copper indium diselenide. On deposit the films all contain small crystallites of $CuInSe_2$. Grazing angle x-ray diffraction data of the as deposited films was used to estimate the thickness uniformity of the films. Wainfain and Parratt suggested that the presence of strong interference maxima between the front and the back of a film is indicative of film "smoothness". [2] They proposed that the variation in thickness, Δt. that would broaden the nth fringe maxima at θ_n so that it could no longer be observed would be given by

$$\Delta t = \lambda / [4(\theta_n^2 - \theta_c^2)^{1/2}] \qquad (1)$$

where λ is the x-ray wavelength and θ_c is the critical angle for total reflectance of x-rays. In general, the highest fringes for our films fall below 2.3° 2θ corresponding to a Δt of approximately 20 to 25 Å. The film "smoothness" does not change on annealing the films below 300°C. Above 300°C, the interference fringes completely vanish, implying that the films rapidly coarsen.

On annealing the as-deposited films, the crystals of $CuInSe_2$ rapidly grow as evidenced by the increase in intensity and decrease in linewidth of the x-ray diffraction maxima. The $CuInSe_2$ crystallites have a preferred 112 orientation with respect to the substrate. In contrast to the stacked elemental layer process for the formation of $CuInSe_2$, [3] we observe only $CuInSe_2$ growth below 300°C. The $CuInSe_2$ crystallites appear to extend completely from the front to the back of the films after extended annealing at 300°C resulting in rapid coarsening of the film surface. Annealing above 300°C results in the formation of small amounts of a number of impurity phases.

To understand secondary phase formation, we prepared films with a range of diffusion distances and repeat layer

sequences including Cu-In-Se, Cu-In-Se-In and Cu-In-Se-In-Se-In-Se. The sample with a Cu-In-Se-In-Se-In-Se repeat sequence showed the formation of InSe on annealing at 300°C. The InSe formed was crystallographically aligned suggesting templated growth off $CuInSe_2$ crystallites. Preliminary results on a thinner Cu-In-Se repeat sequences with an intentional excess of Se show a reduction in secondary phase formation.

4. Measurement of Electronic Properties

The transient photocapacitance method (TCP) has been used to measure the sub-bandgap defect states of working CIGS devices. TPC probes the occupation of sub-bandgap states after a voltage "filling" pulse. The TPC signal originates from trapped charge which is optically excited into mobile conduction and valence band states so that it can escape the depletion region near the barrier.

After a voltage "filling" pulse, the sample evolves back to its equilibrium carrier occupation through optical and thermal excitations. This change in gap state occupation can be measured as a transient capacitance signal whose sign indicates whether carrier motion is occurring predominantly in the conduction or valence band. In this case it is a predominantly majority carrier process, ie. trapped holes being excited into the valence band.

The difference between the dark transient signal and that measured in the presence of sub-bandgap light gives the purely optical component of the release of trapped gap state charge. This difference signal, when normalized to the photon flux and integrated over an appropriate time window, is identified as the TPC signal. We take care to operate in the low light intensity limit, where the normalized signal is intensity independent. The TPC method has been described in more detail elsewhere [4].

Figure 1 displays a 150K TPC spectrum, measured at the University of Oregon, of a CIGS device provided by Energy Photovoltaics, Inc. This spectrum clearly shows a band edge at 1.1 eV and an Urbach energy, E_0, less than 20 meV. The value of E_0 provides a measure of the degree of disorder in a sample, and can be as low as 7 meV for single crystal samples [5]. In contrast, in one study of fairly disordered $CuInSe_2$ thin films grown by annealing of evaporated stacked elemental layers, the value of E_0 was found to be over 100 meV [6]. Since the degree of disorder should correlate with the efficiency of the device, we believe TPC spectra will provide a valuable characterization tool of working CIGS devices.

The spectrum of figure 1 also reveals a distinct shoulder of deep defect transitions extending between 0.75 and 1.0 eV. Additional experiments are needed to identify these deep defect states and relate them to those previously observed in CIGS samples. We are beginning to examine a series of samples provided by the University of Deleware to find out how the spectrum of deep defects changes with Ga content. The preliminary results, to be reported at the meeting, are providing insight into the role of Ga in these CIGS alloys.

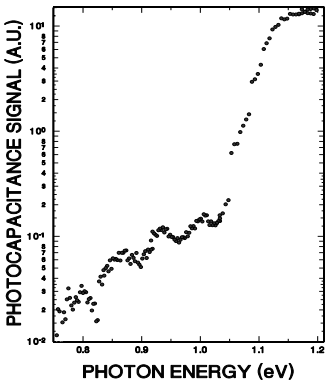

Fig. 1. Transient photocapacitance spectrum of a CIGS thin film device showing a sharp band edge with Urbach energy less than 20 meV and a distinct shoulder of deep defect transitions. (Note that small scale structure is believed to be due to interference fringes)

REFERENCES

1. Johnson, D.C., Controlled Synthesis of New Compounds Using Modulated Elemental Reactants. Current Opinion in Solid State and Materials Science, 3 (1998) (: p. 159-167.
2. Wainfan, N. and L.G. Parratt, J. Appl. Phys., 31 (1960) p. 1331-1337.
3. Probst, V., *et al.*, *Advanced Stacked Elemental Layer Process for Cu(InGa)Se$_2$ thin film Photovoltaic Devices*, in *Thin Films for Photovoltaic and Related Device Applications*, D. Grindley, Editor. 1996, Materials Research Society: Pittsburg, PA. p. 165-176.
4. Cohen, J.D. and A.V. Gelatos, Transient Photocapacitance Studies of Deep Defect Transitions in Hydrogenated Amorphous Silicon, in *Amorphous Silicon and Related Materials Vol A*. 1988, World Scientific: Teaneck NJ. p. 475-512.
5. Shioda, T., *et al.*, Influence of nonstoichiometry on the Urbach's tails of absorption spectra for $CuInSe_2$ single crystals. J. Appl. Phys., 80 (1996) (: p. 1106-1111.
6. Kavcar, N., Study of the sub-bandgap absoprtion and the optical transitions in$CuInSe_2$ polycrystalline thin films. Solar Energy Materials and Solar Cells, 52 (1998) (1-2): p. 183-195.

Patterned Selective Nucleation of Large Grained (30-40μm) Polycrystalline Silicon Thin Films Using Ni Nanoparticle Seed Arrays Fabricated by Ink-Jet Printing

Satoshi Okada and Harry A. Atwater

Thomas J. Watson Laboratory of Applied Physics
California Institute of Technology
Pasadena, CA91125

ABSTRACT

Selective nucleation and solid phase epitaxy to form polycrystalline Si was demonstrated using ink jet printing of a Ni nanoparticle ink. The solvent chosen for the Ni ink was isopropanol. Crystallization induced by Ni was observed, with grain sizes of ~30-40 μm. In each crystallized grain, needlelike structures with the same crystal orientation were observed that originated from a Ni nucleation site. The location of the crystallized Si regions can be defined with ink jet printing. Ink jet printed feature resolution for Si crystallization was comparable to simple printing on paper.

1. Introduction

For making low-cost crystalline thin film Si photovoltaic device materials, selective nucleation and solid state epitaxy of Si is a promising process. Metal induced crystallization of amorphous Si with Ni has been shown to occur below 600 ºC [1], making it compatible with the use of conventional low cost soda-lime glass substrates. Previous work with masked deposition or implantation of metals to form nucleation sites, however, required photolithography and resulted in nucleation of multiple grain orientations in crystal growth at each site [2].

In contrast, Ni nanoparticles can be nucleation sites for single Si grain nucleation. Ink jet printing is already established as a method to fabricate prototype ceramic objects ready for sintering [3] and it is low-cost ambient pressure process with the possibility for commercial production.

In this paper, we show fabrication of Ni nanoparticle seed arrays to form single grain nucleation sites, and the results of selective nucleation of Si using ink jet printing.

2. Experiment

Experiments were performed with 200 nm amorphous Si films, deposited by electron beam evaporation at 100 ºC onto SiO_2 films on Si substrates in ultrahigh vacuum. Ni nanoparticle seed arrays patterns were printed by a HP Deskjet 970Cxi printer on amorphous Si films. After drying the inks, the samples were annealed at 600 ºC for 1 hour to induce selective nucleation of amorphous Si.

3. Ni ink

Ni "inks" were prepared by mixing Ni nanoparticles with solvents. The Ni nanoparticles, produced by Nanophase Technologies Corp., had particle sizes under 200 nm. Requirements for the solvent for Ni ink were to be inert to Ni, to wet amorphous silicon substrates, and to be easy to evaporate with little residue. The solvents investigated included methanol, hexane, methanol/ethylene-glycol, isopropanol/ethylene-glycol, isopropanol, and water. With inks including methanol or hexane, the printheads of the ink jet printer leaked and did not print well. Water was not used because it could oxidize the Ni particles, and isopropanol with ethylene glycol took for ~2-3 days to completely dry at room temperature though it dispersed nanoparticles well. Finally, isopropanol was adopted as the solvent for the Ni ink, with nanoparticle concentration of 20 mg/ml.

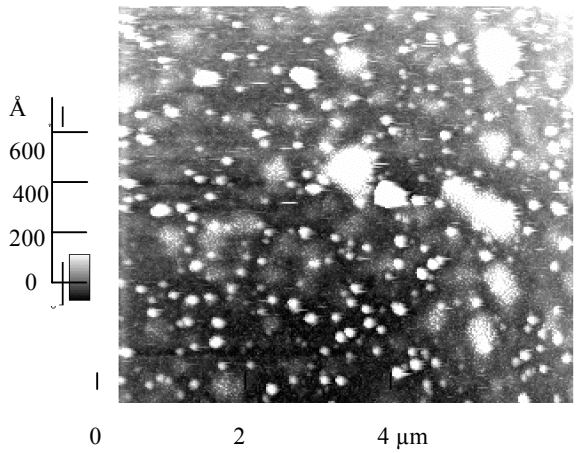

Figure 1. Atomic force microscope image of amorphous Si film printed with Ni ink before annealing (Ni:iso-propanol = 20 mg : 1 ml) Numerous individual Ni nanoparticles with a mean density of 8 /μm^2 and some agglomerates can be seen.

4. Results

An atomic force microscope image of the amorphous Si film printed with Ni ink before annealing is shown in Fig. 1. Numerous individual Ni nanoparticles with a mean density of 8 /μm^2 and some agglomerates were observed on the surface. If all particles were nucleation sites, the crystal grain sizes should be approximately 125 nm.

Figure 2.(a) is an optical micrograph of polycrystalline Si crystallized by ink jet printing of Ni nanoparticles. Homogenous grain growth was observed from Ni particles visible in this magnification. The grain sizes observed, before coalescence obscured the grain boundary, were estimated to be ~30-40 μm. The growth rate was estimated to be over 90Å/s at 600 ºC, which is significantly larger than ~9 Å/s at 660 ºC of the previous report [4]. A bright field transmission electron micrograph and a diffraction pattern of a single Si grain are shown in Fig. 2.(b). In the center, agglomerated Ni

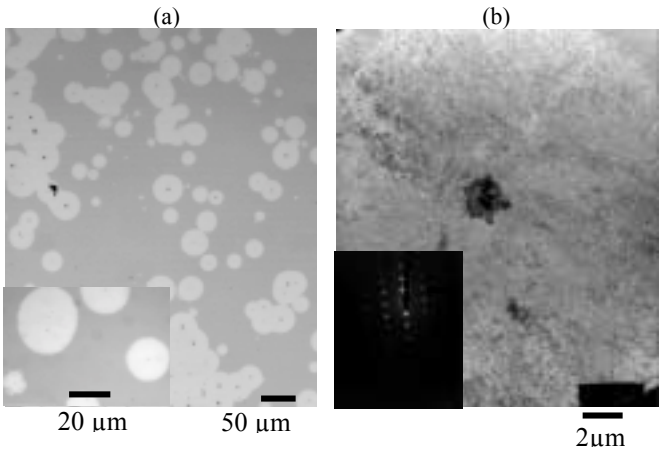

Figure 2. (a)Optical micrographs of polycrystalline Si crystallized by ink jet printing after 1 hr at 600ºC ; insert is an image at a higher magnification, (b) bright field transmission electron micrograph of polycrystalline Si crystallized by ink jet printing after 1 hr at 600ºC; a Ni agglomerate in the center and the needlelike structure due to migration of nickel silicide can be seen, insert is a diffraction pattern of single Si grain ,which indicates needlelike structure is oriented the same direction.

nanoparticles and the needlelike structure due to migration of nickel silicide can be seen.

The diffraction pattern taken in Si area around Ni indicates creation of a silicon monocrystalline regular network with needlelike subgrain defects.

Further experiments that employed an ink with low Ni particle density of ~ 0.3 mg/ml with few agglomerates induced only partial crystallization. The nucleation results did not depend on the pre-treatments for removing organic substances and the native oxide on the amorphous Si film.

These results suggest that agglomerated Ni particles, not isolated nanoparticles, are the nucleation sites. This could be a reason why such large grains, over 30 µm, are seen in spite of the high areal density of Ni particles on the Si film, as seen in Fig. 1.

In Fig. 3, feature resolutions are compared. Figure 3 (a)-(c) are printed lines crystallized on Si. Individual crystalline Si grains coalesce continuous lines as the annealing time increased, due to grain impingement at the final stages of grain growth. Figure3 (d) is an example of the same feature printed on paper with commercial blue ink. These lines are continuous polycrystalline silicon after annealing although the crystallized Si linewidth is broadened due to grain growth outward from the line edges.

5. Conclusions

Selective nucleation by Ni nanoparticles deposited by inkjet printing leads to grain sizes of ~30-40 µm at 600 ºC for 1hr. Agglomerated Ni particles of about 1 µm, with present experimental conditions of 200 nm thick amorphous Si film and annealing at 600 ºC for 1 hr, are nucleation sites.

The possibility of ink jet printing for selective nucleation of polycrystalline Si was demonstrated. This approach is a potentially low-cost non-vacuum method for patterned and unpatterned crystallization.

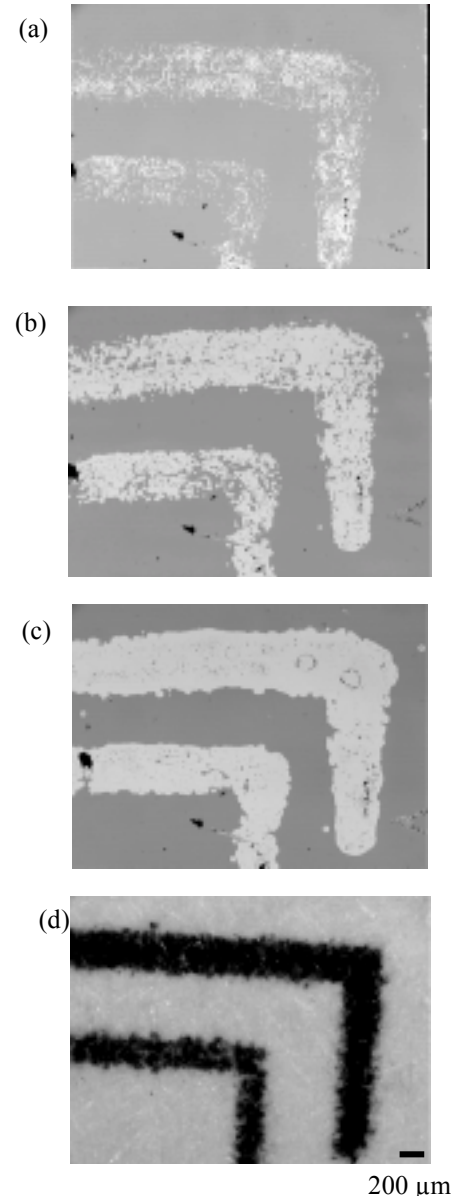

Figure 3. Optical micrographs of (a) crystallized Si lines by printed Ni annealed at 600 ºC for 20 min; (b) 1 hr; (c) 2 hrs and (d) simple printed lines on paper.

REFERENCES

[1] Z.Jin, G.A.Bhat, M.Yeung, H.S.Kwok and M.Wong: "Nickel induced crystallization of amorphous silicon thin films", J. Appl. Phys. 84(1998) 194-200.

[2] C. M. Chen and H.A. Atwater:" Polycrystalline Si Films Fabricated by Low Temperature Selective Nucleation and Solid Phase Epitaxy Process", Mater. Res. Soc. Proc. 485(1998) 67-72.

[3] J. Windle and B. Derby:"Ink jet printing of PZT aqueous ceramic suspensions", J. Mat.Sci.Lett. 18(1999) 87-90.

[4] C.Hayzelden and J.L. Batstone:"Silicide formation and silicide-mediated crystallization of nickel-implanted amorphous silicon thin films", J. Appl. Phys. 73(1993) 8279-8289.

A PLASMA-CHEMICAL MODEL OF PARTICLE GROWTH AND ESCAPE IN SILANE RF DISCHARGES

Alan Gallagher
JILA, NIST and University of Colorado, Boulder, CO 80309

Particle-in-plasma models for laboratory rf plasmas have normally considered non-attaching gases, in which particles carry many negative charges and are trapped in the quasi-neutral-plasma region. In contrast, semiconductor processing and thin film deposition plasmas normally utilize attaching gases. I will describe the very different character of particle charge in attaching gases, and the major consequences for particle escape from rf discharges in attaching gases. This difference results from a typical ion/electron density ratio of 100 in attaching gases. A quantitative plasma and chemistry model for particle growth and escape from silane rf plasmas will be presented, to provide a concrete example of particle behavior in an attaching gas.

Porous Silicon Texturing of Polysilicon Substrates

C. Striemer, F. Shi, and P. Fauchet

Department of Electrical and Computer Engineering
University of Rochester
P.O. Box 270231
Rochester, NY 14627-0231

ABSTRACT

A light trapping surface layer formed by the electrochemical etching of Low Pressure Chemical Vapor Deposited (LPCVD) polysilicon has been studied. Encouraged by our recent success in producing a 10.1% efficient porous polysilicon (PPS) solar cell, a systematic set of experiments is being conducted to further enhance efficiency by developing greater control over film morphology. The goal of this study is to maximize light trapping while maintaining the electrical properties of our devices, potentially leading to thin film photovoltaic applications of this technique.

1. Introduction

Porous silicon has been widely studied since the early 1990's, due primarily to interest in its development as an efficient light emitting material for optoelectronic applications [1]. The light trapping and anti-reflection properties of porous silicon, in addition to its simplicity of formation and broadly tunable morphology, make it particularly well suited for photovoltaic applications.

Porous silicon results from the electrochemical dissolution of a silicon substrate in the presence of a hydrofluoric acid (HF) solution and positive charge carriers (holes). Initially pits form in the substrate surface, and under the correct conditions, dissolution is favored at the bottoms of these pits, which allows the formation of pores that can propagate into the substrate [2]. Porosity (the percentage of empty space) is controlled by the current density, HF concentration in the electrolyte, etching time, ambient light, and substrate doping. Since the etching process is driven by holes diffusing toward the substrate surface, nearly all dissolution occurs at the bottom of the porous layer, leaving the upper, hole-depleted porous region unaffected. Therefore porosity can be modulated as the etching progresses by varying the current density, and highly uniform multilayer structures can be produced [3].

Porous silicon has been applied to solar cell research since the early 1980's [4]. It has been used as a single or multilayer antireflective coating by exploiting the tunability of the film's effective index of refraction [5, 6]. Improvements of 50% in I_{SC} have been demonstrated while maintaining fill factor and V_{OC} [7]. Demonstrated reflectivity tends to average between 10%-15% over the spectral range 300nm-1200nm using single or double porous silicon layers, but average reflectivities as low as 2% have been shown with graded index multilayers [8].

Our approach is to utilize the light trapping characteristics of a thicker porous silicon film to improve efficiency. Similar to the effect achieved by pyramidal and inverted pyramidal structures formed by the alkaline etching of (100) crystalline silicon substrates [9], normally incident radiation striking the roughened porous surface is refracted and forced to take a longer path through the space charge region of the solar cell [10]. Therefore, absorption in the active region is increased and internal reflection within the solar cell is enhanced. Porous silicon texturing can also be applied to a broad range of crystalline, microcrystalline, and multicrystalline silicon substrates [11], unlike anisotropic alkaline etching which is specific to (100) oriented substrates for pyramid-like structuring. Our goal is to find an optimal compromise between the light trapping optical characteristics of the film and the electronic transport properties of the resulting structure [12].

2. Experiment

Our most recent study has focused on the etching characteristics of LPCVD polysilicon films deposited on n-type and p-type silicon wafers. The n-type substrates had resistivities in the range of 10-20 Ω-cm and the p-type substrates ranged from 0.01-0.1 Ω-cm.

Substrate preparation began with an RCA cleaning step, followed by an HF dip to remove any native oxide. A thick intrinsic polysilicon layer was deposited by LPCVD at 610°C. The back sides of the n-type wafers were heavily phosphorous doped using a spin-on glass procedure to allow for an ohmic contact to aluminum at the end of the substrate processing. The front sides of the n-type substrates were then implanted with a 1E15 dose of boron, while the p-type substrates received a 1E15 phosphorous dose. Dopant activation and drive-in was completed with a 20 minute, 900°C anneal in nitrogen. Finally, an aluminum back contact was sputtered on all the substrates, followed by a 15 minute, 450°C sinter step.

A matrix of samples was electrochemically etched to form PPS. The primary variables in this study were the electrochemical current density and the etching time. This matrix consisted of samples etched at current densities ranging from 5- 20 mA/cm^2, and etching times of 30-120 seconds. The only other variable was the introduction of

light from a 50 Watt tungsten lamp during the etching of the n-type substrate samples. Light was required to allow current flow through the reverse biased n-i-p structure. All other etching variables remained constant.

Reflectivity spectra of all samples were taken. Each sample was also cleaved, and scanning electron microscope (SEM) cross sectional analysis was performed. Aluminum contacts were deposited on some samples and preliminary I-V analysis was conducted.

3. Results

The samples prepared on the n-type and p-type substrates showed considerable differences in every aspect of this study, due primarily to the reverse bias condition of the n-i-p structure. As a result, the n-type substrate samples exhibited high voltages during the etching procedure, and the introduction of light into the electrochemical cell was necessary to keep the voltage below the 110V limit of the current supply. Under illumination, the cell voltage ranged from 3V - 70V for current densities of 5 mA/cm^2 – 20 mA/cm^2. For the same current densities, the p-type substrates etched easily in the dark with voltages of 0.5V – 2V.

Reflectivity spectra clearly show that the integration of a PPS layer substantially reduces the reflection losses in all samples. For n-type substrates, the total reflectivity is reduced by a factor of 2 across the spectral range from 200nm – 1200nm, relative to crystalline silicon. P-type substrates exhibit a factor of 4 reduction in reflectivity over the same range.

The SEM cross sectional analysis provided information about the various PPS layer thicknesses and film morphology. These images reveal that the substrates have a textured surface that is a natural result of the thick LPCVD. In the cross sections, the porous layer is easy to observe when compared to unetched samples, generally appearing lighter in color and exhibiting more damage from cleaving. Thicknesses ranging from 150nm to over 5000nm were measured in the films etched in this study. In thicker films, the emitter thickness could also be determined from the SEM micrographs by observing the porosity gradient resulting from the dopant profile. Emitter thickness averaged ~1μm, which is reasonable for the processing conditions of the implant and anneal.

Preliminary dark I-V analysis of these samples has also been conducted which shows slight ohmic degradation in the current flow for thin and low porosity films, indicating an increase in the series resistance of these samples. Samples etched with larger current densities and longer times exhibit more drastic degradation of their I-V characteristics. With appropriate optimization, it appears that an overall increase in photovoltaic efficiency can be achieved with the integration of PPS layers in polycrystalline solar cells.

5. Conclusion

The most advanced crystalline silicon solar cells have achieved efficiencies well above 20%, using inverted-pyramid type structuring, $Si0_2$ passivation of the front and back surfaces, back side fields, laser grooved buried contacts, and high purity silicon wafer substrates [13]. Although porous silicon based photovoltaics have not achieved these benchmark efficiencies, their simplicity of formation, and compatibility with both crystalline and randomly oriented polysilicon materials make these devices an economically viable solution for low cost, large area photovoltaic applications [10].

The work discussed in this paper is the initial stage of study that seeks to explore the parameter space of polysilicon electrochemical etching for future application in thin film silicon photovoltaic devices produced on inexpensive substrates. It has been demonstrated that the incorporation of a porous layer on the surface of a photovoltaic device can substantially reduce optical reflection losses while maintaining reasonable I-V characteristics. Future work will focus on the improvement of the front contact characteristics of these devices, as well exploring the light I-V and photonic response characteristics.

REFERENCES

[1] P.M. Fauchet, IEEE J. Select. Topics in Quantum Electron., 4 (1998) 1020.
[2] R.L. Smith and S.D. Collins, J. Appl. Phys. 71 (1992) R1.
[3] S. Chan and P.M. Fauchet, Appl. Phys. Lett., 75 (1999) 274.
[4] A. Prasad, S. Balakrishnan, S.K. Jain, and G.C. Jain, J. Electrochem. Soc. 129 (1982) 596.
[5] S. Strehlke, S. Bastide, J. Guillet, C. Levy-Clement, Mat. Sci. and Eng. B69-70 (2000) 81.
[6] A. Krotkus et al., Solar Energy Materials and Solar Cells 45 (1997) 267.
[7] P. Vitanov et al., Thin Solid Films 297 (1997) 299.
[8] S. Uehara, K. Kurose, and T. Matsubara, Porous Semiconductors-Science and Tech. (2000) 167.
[9] A. Goetzberger, J. Knobloch, and B. Vob, Crystalline Silicon Solar Cells, Wiley (1998) 118-120.
[10] L. Stalmans et al., Prog. Photovolt. Res. Appl. 6 (1998) 233.
[11] V. Yerokhov et al., Porous Semiconductors-Science and Tech. (2000) 151.
[12] S.P. Duttagupta, P.M. Fauchet, et al., Solar Energy Materials and Solar Cells 52 (1998) 271.
[13] W. Wettling, Solar Energy Materials and Solar Cells 38 (1995) 487.

Transparent Conductors (TCO's) and Barrier Layers for Thin film Solar Cells

R. G. Gordon, R. Broomhall-Dillard, X. Liu, D. Pang and J. Barton

Harvard University

Cambridge, MA 02138

ABSTRACT

Task 1. Chemical Vapor Deposition (CVD) of Zinc Stannate Films. Zinc stannate is predicted to form lower resistance contacts to amorphous silicon solar cells. A CVD process was developed for forming zinc stannate films on substrates heated to temperatures between 400 and 600 ^{o}C.

Task 2. CVD of Fluorine-doped Zinc Oxide Films. Amorphous silicon solar cells grown on etched, fluorine-doped zinc oxide films showed 11% higher efficiencies and currents, compared to those grown on standard fluorine-doped tin oxide or on non-etched ZnO:F. The etching apparently removes a damaged layer on the surface of the zinc oxide that had interfered with making low-resistance electrical contact with the cells. Subsequent experiments to reproduce these results have produced many more shunted cells and lower efficiencies. The cause for this difference between different runs is being sought.

Task 3. CVD of Aluminum Oxide Films. Aluminum oxide films placed between soda-lime glass substrates and ZnO:F films reduced the sheet resistance of the ZnO:F by about 10% form films deposited near 500 ^{o}C. The aluminum oxide acts as a barrier preventing diffusion of sodium from the glass into the ZnO:F. When the ZnO:F was deposited at lower temperatures, 400 to 470 ^{o}C, no effects of a aluminum oxide barriers had been seen. The aluminum oxide promotes efficient nucleation of the ZnO:F, resulting in smoother films with lower haze levels. Etching of the ZnO:F increases the texture and haze levels, allowing for more efficient light-trapping in solar cells made on the ZnO:F.

Task 4. CVD of High-Resistance Tin Oxide Films. Nominally undoped films of tin oxide were grown by CVD. They had resistivities around 0.1 ohm-cm. In order to grow films with higher resistivities for potential applications as a buffer layer in thin-film solar cells, zinc doping was used to compensate the native donors arising from oxygen vacancies in the tin oxide.

1. CVD of Zinc Stannate Films

For a TCO to form a low-resistance contact to p-Si, the TCO should have a high work function (corresponding to a low Fermi energy). Work functions for some transparent conductors are given in the following table.

TCO	Work Function (eV)	Electron Concentration (cm^{-3})
ZnO:F	4.2	2×10^{20}
ZnO	4.5	7×10^{19}
In_2O_3:Sn	4.8	$> 10^{20}$
SnO_2:F	4.9	4×10^{20}
$ZnSnO_3$	5.3	6×10^{19}

Table 1. Work Functions of Transparent Conductors [1]

The work function for fluorine-doped tin oxide is indeed higher than that of fluorine-doped zinc oxide, confirming the observations [2] that it is more difficult for zinc oxide to make a low-resistance contact to p-Si. The work function for sputtered $ZnSnO_3$ is even higher than that of SnO_2:F. Thus, if the work function argument is correct, an even lower-resistance contact to p-Si should be obtained by $ZnSnO_3$.

Therefore we developed a CVD method for making zinc stannate films that would be compatible with our CVD processes for making ZnO:F. We used zinc bis(2,4-pentanedionate), also called zinc acetylacetonate, $Zn(C_5H_7O_2)_2$, as a source of zinc and dimethyltin diacetylacetonate, $(CH_3)_2Sn(C_5H_7O_2)_2$, as a source of tin. These compounds were dissolved in di(ethylene glycol) methyl ether, $CH_3OCH_2CH_2OCH_2CH_2OH$. This solution was nebulized ultrasonically with a Sonotek nozzle into a stream of nitrogen gas preheated to about 200 ^{o}C, mixed with oxygen and passed over substrates heated to temperatures from 400 to 600 ^{o}C. RBS analysis of deposited films found tin, zinc and oxygen, with the zinc/tin ratio increasing along the direction of gas flow in the CVD reactor. They have high optical transparency, provided the temperature and oxygen content of the deposition atmosphere are high enough.

2. CVD of Fluorine-doped Zinc Oxide Films

Fluorine-doped zinc oxide films are more transparent than fluorine-doped tin oxide films with the same sheet resistance [3]. Amorphous silicon solar cells grown on ZnO:F superstrates in fact show higher currents than cells grown under the same conditions on SnO_2:F. However, this advantage has not translated into improved efficiencies, because the voltages and fill factors of cells grown on ZnO:F have been smaller than those grown on SnO_2:F, typically by 3 to 5%. Apparently, a higher-resistance contact formed between the ZnO:F and the top p-silicon layer of the cells [4].

One possibility for the poor contact with ZnO:F is that its surface was damaged or contaminated. In order to remove any such defective layer, ZnO:F films were etched in a concentrated ammonium chloride solution for times up to one minute. The thickness of the material removed varied from 0.1 to 0.2 microns out of films initially 0.8 to 1 micron thick. Removal of 0.1 micron increased the light transmission in the blue end of the spectrum and increased the sheet resistances by a few per cent. Removal of 0.2 micron increased the haze levels of the films, as well.

The cells grown on these etched ZnO:F samples showed 10% higher open circuit currents, compared to cells grown in the same runs on commercial SnO_2:F from AFG. These results confirm the high transmission and light-trapping ability of these etched ZnO films. Remarkably, the fill factors and voltages of the cells on etched ZnO:F were identical to those made on SnO_2:F in the same runs. The decreases in FF and Voc previously seen on all ZnO:F-based cells were not seen for the etched ZnO:F. As a result, the efficiencies of the etched ZnO:F cells were more than 10% higher than those of the cells made on SnO_2:F. These improved results for the cells on etched ZnO:F were found for ZnO:F films grown directly on bare soda-lime glass, as well as those grown on alumina- and silica-coated glass.

TCO Superstrate	Voc	FF	Jsc	Efficiency
Without ZnO:F Etch	0.97	0.95	1.05	0.97
With ZnO:F Etch	1.01	1.00	1.10	1.11

Table 2. Ratios of Parameters for Solarex Tandem Cells Grown on ZnO:F to those on Standard SnO_2:F Superstrates

The haze levels of the etched ZnO:F films could be adjusted to any desired value by adjusting the etching time. Haze levels from 8 to 22% were obtained. The resulting etched surfaces of the films do not have sharp edges that might be likely to cause shunts in solar cells grown on them. Samples of etched films with various haze levels were supplied to Solarex for use as superstrates for amorphous silicon solar cells. The resulting cells did not show any more shunted cells than are normally found with tin oxide superstrates. This result is a marked improvement over previous results on zinc oxide films with highly faceted textures that showed more frequent shunting problems. Unfortunately, subsequent attempts to repeat these results have resulted in many shunted cells and lower efficiences. Possible causes for this non-reproducibility are being investigated.

3. CVD of Aluminum Oxide Films

Soda-lime glass contains a high concentration of sodium, which can out-diffuse into TCO layers during their deposition and increase their resistance. In the case of tin oxide, deposition normally takes place at temperatures of 550 ^{o}C or higher, and a sodium barrier of silica or alumina is normally employed between the soda-lime glass and the tin oxide. In the case of ZnO:F, we have in the past not used any barrier layers because the deposition temperature was only 470 ^{o}C or less, so the sodium mobility was lower, and we did not see any effects of using a diffusion barrier.

In more recent ZnO:F depositions, we increased the substrate temperature up to around 500 ^{o}C, so we decided to re-investigate the possible effects a sodium diffusion barrier. Alumina films were deposited on soda-lime glass, and then ZnO:F films were grown on the alumina. The samples with barriers had resistances about 10% lower than those deposited directly on soda-lime glass under the same conditions. This result suggests that sodium diffusion from the glass was having some deleterious effects on the conductivity of the zinc oxide films deposited at substrate temperatures around 500 ^{o}C.

The alumina barrier layers had the additional effect of providing good nucleation of the zinc oxide, so that the ZnO films grown on alumina films were reproducibly smooth. Etching in concentrated ammonium chloride solution increased their texture and haze to values sufficient for efficient light trapping in amorphous silicon solar cells [5].

4. CVD of High-Resistance Tin Oxide Films

Some undoped tin oxide films were deposited from lower concentrations of dibutyltin diacetate. They are, however, still fairly conductive, with sheet resistances in the ten kilo-ohm range for thicknesses of 100 nm, corresponding to resistivities of 0.1 ohm-cm. Presumably this conductivity arises from oxygen vacancies in the lattice. In order to increase the resistance to the 10^4 level that may be optimal for buffer layers in solar cells, it is necessary to introduce acceptor doping to trap some of the free electrons.

Zinc-doping can be used to trap free electrons in tin oxide, and increase its resistance. The CVD process developed under Task 1 for zinc stannate was adapted to this purpose by using only a small proportion of zinc in the precursor solution. Samples of high-resistivity zinc-doped tin oxide were produced by CVD from the vapor of these solutions, with sheet resistances higher than 10^5 ohms per square (the upper limit of our 4-point probe). More sensitive instrumentation is being acquired to make measurements of the sheet resistances and carrier concentrations of these high-resistivity films.

REFERENCES

[1] T. Minami et al., Surface Coating Technology 108-109 (1998) 583-587 and personal communication.

[2] J. Hu and R. G. Gordon, Solar Cells 30 (1991) 437-450.

[3] R. G. Gordon, American Institute of Physics Conf. Proc. 394 (1997) 39-48.

[4] R. G. Gordon, 1996 Annual Report, NREL Subcontract XAN-4-11318-05, Bolko von Roedern, technical monitor.

[5] For similar etching procedure using hydrochloric acid etch, O. Kluth, A. Loffl, S. Wieder, C. Beneking, W. Appenzeller, L. Houben, B. Rech, H. Wagner, S. Hoffmann, R. Waser, J. A. Anna Selvan and H. Kepper, Conf. Rec. 26th IEEE Photovoltaic Spec. Conf., (1997) 715-718.

Comparison of Dye-Sensitized Rutile- and Anatase-Based TiO_2 Solar Cells

N.-G. Park, J. van de Lagemaat, and A. J. Frank
National Renewable Energy Laboratory, Golden, Colorado 80401

ABSTRACT

The objective of this work is to develop and optimize the new dye-sensitized solar cell technology. For the first time, crack-free nanocrystalline rutile TiO_2 films with thicknesses of up to 12 μm were prepared and characterized. The photoelectrochemical properties of the rutile-based solar cell were compared with those of the *conventional* anatase-based cell. Intensity-modulated photocurrent spectroscopy and scanning electron microscopy studies indicate that electron transport is slower in the rutile layer than in the anatase layer due to differences in the extent of inter-particle connectivity associated with the particle packing density. In view of the infancy of rutile material development for solar cells, the PV response of the dye-sensitized rutile-based solar cell is remarkably close to that of the anatase-based cell.

1. Introduction

Dye-sensitized solar cells based on nanocrystalline porous films of TiO_2 are a promising new kind of PV cell. Technological interest in these cells stems from their demonstrated solar efficiencies of 10% – 11% (AM1.5), stability of the semiconductor material, potentially inexpensive manufacturing and materials cost, use of environmentally friendly components, and potential unique applications (transparent, various possible colored dyes). The most extensively studied cell consists of a monolayer of a Ru-bipyridyl-based charge-transfer dye adsorbed onto the surface of a thin nanocrystalline TiO_2 film supported on transparent SnO_2 conducting glass. The particles of the film are in contact with an electrolyte solution containing iodide and triiodide ions as a redox relay and are sandwiched by a second plate of electrically conducting glass covered with platinum. The metal oxide is the recipient of injected electrons from optically excited dye molecules and provides the conductive pathway from the site of electron injection to the transparent back-contact. The redox species in solution transports the hole from the oxidized dye to the counter electrode, thus regenerating the original form of the dye and completing the oxidation-reduction cycle. The metal oxide can strongly influence the photovoltage, the fill factor, and the photon-to-current conversion efficiency (IPCE), which is determined by the light-harvesting efficiency of the dye, the quantum yield of electron injection, and the efficiency of collecting the injected electrons. Although most work on dye-sensitized nanocrystalline metal oxide solar cells has focused on the anatase form of TiO_2, rutile TiO_2 is potentially cheaper to produce and has superior light-scattering characteristics, which is a beneficial property from the perspective of effective light-harvesting. Recently, we showed that dye-sensitized solar cells based on rutile TiO_2 exhibit photovoltaic characteristics at one-sun light intensity comparable to those of conventional anatase TiO_2-based solar cells [1]. Nanocrystalline rutile films were directly deposited onto the transparent tin oxide back-contact from the ambient hydrolysis of $TiCl_4$ and subsequently annealed. High-quality films prepared by this method were limited to thicknesses of less than 5 microns, which is well below the requisite thickness for a commercially viable solar cell using the sensitizing dye $Ru(LL')(NCS)_2$ (where L = 2,2'-bypyridyl-4,4'-dicarboxylic acid, and L' = 2,2'-bipyridyl-4,4'-ditetrabutylammoniumcarboxylate).

We have refined our methodology to synthesize relatively thick (1- μm), crack-free, nanocrystalline rutile TiO_2 films. In this paper, we characterize these rutile-based solar cells and compare their photoelectrochemical properties with those of the anatase-based cell [2].

2. Results and Discussion

Scanning electron microscopy (SEM) shows that the rutile films consist of homogeneously distributed rod-shaped particles with an average dimension of 20 × 80 nm. Incident monochromatic photon-to-current conversion efficiency (IPCE) measurements imply that a significant fraction of light with wavelengths below 600 nm is absorbed in the first few microns of the dye-covered films due to strong absorption by the dye. In the longer-wavelength region, where the dye molecules absorb weakly, the short-circuit photocurrent increases in direct linear proportion to the film thickness, suggesting that the electron-injection rate throughout the cell is essentially homogeneous. Changing the thickness of the rutile films has only a small influence on the open-circuit photovoltage due to the offsetting effect associated with the dependence of the number of dye molecules and recombination centers on the surface area. The photocurrent–voltage responses of the dye-sensitized rutile and anatase films at one-sun light intensity are remarkably close in view of the early stage of rutile material development for solar cells. The photovoltage of the materials is essentially the same, whereas the short-circuit photocurrent of the rutile-based cell is about 30% lower than that of the anatase-based cell. The difference in photocurrent is found to be related to the smaller surface area of the rutile film compared with that of the anatase film per cell volume. Intensity-modulated photocurrent spectroscopy and SEM studies indicate that electron transport is slower in the rutile layer than in the anatase layer due to differences in the extent of inter-particle connectivity associated with the particle packing density. Possible ways to improve both the photocurrent and electron transport rate in the rutile films are discussed.

REFERENCES

[1] N.-G. Park, G. Schlichthörl, J. van de Lagemaat, H. M Cheong, A. Mascarenhas, and A. J. Frank: "Dye-Sensitized TiO_2 Solar Cells: Structural and Photoelectrochemical Characterization of Nanocrystalline Electrodes Formed from the Hydrolysis of $TiCl_4$," *J. Phys. Chem. B* 103 (1999) 3308.

[2] N.-G. Park, J. van de Lagemaat, and A. J. Frank: "Comparison of Dye-Sensitized Rutile- and Anatase-Based TiO_2 Solar Cells," submitted.

How Porosity Modifies the Photovoltaic Effect in Nanocrystalline Solar Cells

Brian A. Gregg and François Pichot

National Renewable Energy Laboratory

1617 Cole Blvd., Golden, CO 80401

ABSTRACT

The porosity of the nanocrystalline semiconductor affects many aspects of the photoconversion process in dye-sensitized solar cells, thus distinguishing them mechanistically from conventional photovoltaic and photoelectro-chemical cells. We discuss several examples from our recent work.

1. Electric Fields

The porosity influences the location and magnitude of equilibrium, photogenerated, and applied electric fields because ion motion throughout the film neutralizes electric fields over a short range (nanometers). [1] This results in having no macroscopic (only nanoscopic) electric fields in the device either at equilibrium or under illumination. Therefore, charge carrier motion occurs via diffusion rather than drift. Photoinduced charge separation induces a transient electric field that is rapidly neutralized by ion motion in the conventional cell. But solid state versions often lack supporting electrolyte and thus exhibit rapid charge recombination. Thus, a viable solid state cell will require excess mobile electrolyte.

2. Potential of Sensitizing Dye

Because the adsorbed sensitizing dye sits in the electrochemical double layer, its redox potential is not fixed relative to either the semiconductor or the solution. When the dye is mostly inside the double layer, its potential will tend to follow the semiconductor; when it is mostly outside, its potential will be almost independent of the semiconductor.[2]

3. Photovoltage-Determining Mechanism

To distinguish experimentally between two competing models of the photovoltage-determining mechanism in nanoporous solar cells, we deposited dye-sensitized TiO_2 films on four different substrates having vacuum work functions spanning a 1.4 eV range. We then measured the photovoltage obtained from these films in three different redox electrolyte solutions. No significant differences in photovoltage were obtained on the different substrates, showing that the photovoltage is determined by photoinduced chemical potential gradients, not by equilibrium electric fields,[3] (see Figure 1).

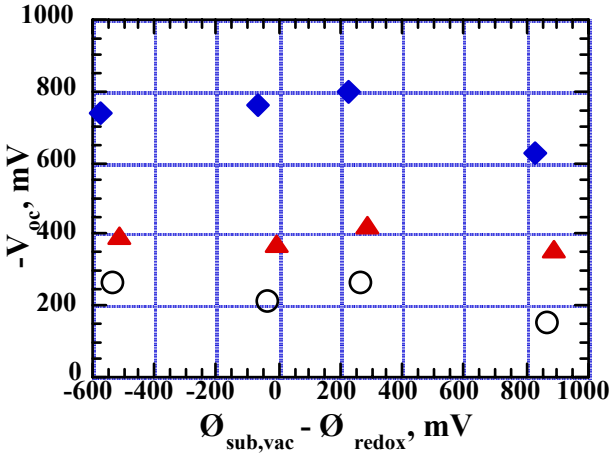

Figure 1. V_{oc} plotted vs the difference between the work function of the substrate (for 4 different substrates) and the

solution redox potential (3 different solutions). This shows that V_{oc} is not determined by the equilibrium electric field.

4. Passifying Recombination Sites

The high surface area of the nanocrystalline film puts severe constraints on the hole conductor, because the hole can only escape recombination with electrons in the TiO_2 if the recombination rate is unusually slow. The conventional hole conductor, I_2/I_3^-, has very slow kinetics for reduction and thus allows holes to escape recombination, but some of its other properties are less than ideal. Figure 2 shows J-V curves for a cell made with the conventional I_2/I_{3-} electrolyte and also for a cell made with the much faster redox couple ferrocene/ferrocenium. A faster redox couple eliminates the photovoltaic effect because of the rapid recombination reaction. We discuss two strategies for passifying recombination sites in nanocrystalline solar cells in order to facilitate the use of other redox couples, such as those needed for solid state versions of the dye cells.

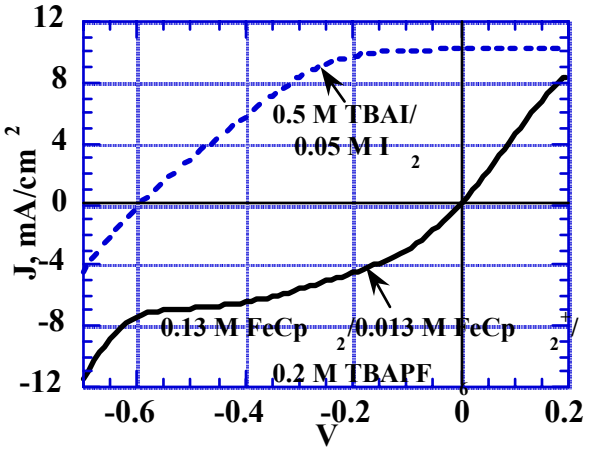

Figure 2. J-V curves under illumination of a standard dye cell using the I^-/I_3^- couple and one using a faster redox couple, ferrocene$^{+/0}$. The faster couple shows no PV effect but one can be induced with proper surface treatments.

REFERENCES

(1) Zaban, A.; Meier, A.; Gregg, B. A. *J. Phys. Chem. B* **1997**, *101*, 7985-7990.

(2) Zaban, A.; Ferrere, S.; Gregg, B. A. *J. Phys. Chem. B* **1998**, *102*, 452-460.

(3) Pichot, F.; Gregg, B. A. *J. Phys. Chem B* **2000**, *104*, 6-10.

Non-linear Electron Transport Kinetics in Nanocrystalline TiO_2-Based Solar Cells

J. van de Lagemaat and A.J. Frank

National Renewable Energy Laboratory

1617 Cole Boulevard, Golden, Colorado 80401

ABSTRACT

An analytical model describing electron transport in dye-sensitized nanocrystalline TiO_2 solar cells is shown to account for the non-linear dependence of the electron transport rate on the electron concentration. Equations relating the influence of an exponential distribution of surface states to electron transport are derived and verified by intensity-modulated photocurrent spectroscopy measurements. A slope of 69 meV is inferred for the surface-state distribution curve.

1. Introduction

Injected electrons from optically excited dye can either traverse the TiO_2 particle network and be collected at the transparent conducting glass back-contact or can recombine with redox species (e.g., I_3^-) or dye molecules at the particle/electrolyte interface. Because the collection of electrons competes with recombination, slow electron transport (with respect to recombination) leads to a low charge-collection efficiency, and hence, to a low conversion efficiency [1,2].

Recently, we introduced a statistical model relating the time constants for recombination and charge collection to the charge-collection efficiency (η_{cc}) and the incident photocurrent conversion efficiency (IPCE) over a wide range of applied biases [2]. Electrical impedance spectroscopy and intensity-modulated photocurrent spectroscopy (IMPS) were used to measure the time constants for the recombination and collection of photoinjected electrons. As the applied bias is varied from short-circuit to open-circuit conditions at one-sun illumination, recombination becomes faster, the collection of electrons becomes slower, and the IPCE strongly decreases. The drop-off of IPCE was shown to correlate with the decline of the charge-collection efficiency as calculated from the model. Although the strength of the statistical model is its predictive value, it does not provide detailed information on the mechanism of charge transport.

In this paper, we introduce an analytical model [3] to understand quantitatively the mechanism of charge transport. It is assumed that electrons undergo multiple trapping-detrapping events, involving an exponential distribution of surface states, during their transit through the film. The predictions of this model are compared with experimental results obtained by IMPS.

2. Results and discussion

The conduction-band electron concentration profile $n_{cb}(x)$ can be calculated by solving the continuity equation:

$$\frac{\mathrm{d}n_{cb}(x)}{\mathrm{d}t} = \alpha\eta_{inj}I(x) + \frac{1}{q}\frac{\mathrm{d}J_n(x)}{\mathrm{d}x} - U_t(x) + U_e(x) \qquad (1)$$

The concentration of electrons in surface states, however, depends on the energy distribution of traps. A single exponential describes the energy distribution of the density of surface states ($N_{SS}(E) = N_{SS0}e^{\frac{E-E_{F0}}{m_c}}$) in nanocrystalline TiO_2 films [4]. From this equation, one can calculate the concentration profile for trapped electrons $n_t(x)$:

$$n_t(x) = m_c N_{SS0}\left[e^{\frac{E_F(x)-E_{F0}}{m_c}} - 1\right] = m_c N_{SS0}\left[\left(\frac{n_{cb}(x)}{n_{cb}(0)}\right)^{\frac{kT}{m_c}} - 1\right] \quad (2)$$

Because the density of trapped electrons is much larger than that of free electrons [1], the electron concentration $n(x) = n_{cb}(x) + n_t(x)$ in the film is essentially equal to $n_t(x)$ (Eq 2). Thus, $n_{cb}(x)$ is related to $n(x)$ by the expression $n_{cb}(x) \propto n(x)^{m_c/kT}$. Validation of the power-law dependence of n_{cb} on n has been obtained by IMPS measurements [1].

The total number of electrons in the film Q can be obtained by integrating Eq. 2 with respect to x:

$$Q = m_c N_{SS0} n_{cb}(0)^{\frac{m_c}{kT}} \left(\frac{\eta_{inj} I(0)}{\alpha D_n}\right)^{\frac{kT}{m_c}} \int_0^d \left[1 - \alpha x e^{-\alpha d} - e^{-\alpha x}\right]^{\frac{kT}{m_c}} dx \quad (3)$$

Q is, therefore, related to the incident light intensity by the relation $Q \propto I(0)^{kT/m_c}$. Alternatively, because the short-circuit current density J_{sc} depends linearly on the light intensity, one can obtain the expression:

$$J_{sc} \propto Q^{\frac{m_c}{kT}} \quad (4)$$

Figure 1 shows the relationship between J_{sc} and Q, measured by IMPS, for a typical dye-sensitized nanocrystalline TiO_2 solar cell.

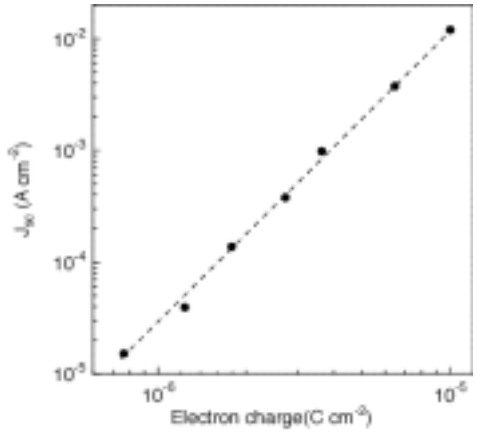

Fig.1 The relation between the short-circuit photocurrent density and electronic charge for a typical dye-sensitized cell. The dashed line is a fit to Equation (4).

Equation (4) describes well the experimental data in Figure 1. From the fit of the data, the slope of the surface-state distribution curve is obtained as m_c = 69 meV, which is in good agreement with values determined from time-of-flight [5] and electrical impedance spectroscopy [2] in the light intensity range (<1-sun) used in the present study.

3. Conclusions

Expressions that relate an exponential distribution of surface states to electron transport are derived and verified by intensity-modulated photocurrent spectroscopy measurements. A slope of 69 meV is inferred for the surface-state distribution curve.

REFERENCES

[1] G. Schlichthörl, N.-G Park, and A. J. Frank, J. *Phys. Chem. B* 103 (1999) 782.

[2] J. van de Lagemaat, N.-G. Park, and A. J. Frank, J. *Phys. Chem. B* 104 (2000) 2044.

[3] J. van de Lagemaat and A. J. Frank, *J. Phys. Chem. B* submitted.

[4] G. Schlichthörl, S.Y. Huang, J. Sprague, and A. J. Frank, *J. Phys. Chem B* 101 (1997) 8141.

[5] N. Kopidakis, E. A. Schiff, N.-G. Park, J. van de Lagemaat, and A. J. Frank, *J. Phys. Chem. B*, in press.

Crystalline Silicon Materials Research

T.F. Ciszek, T.H. Wang, M. Page, M. Landry, J. Casey, R. Bauer, and E. Good

National Renewable Energy Laboratory

1617 Cole Boulevard, Golden, CO 80401

ABSTRACT

Our recent silicon photovoltaic (PV) materials research activities are summarized. We developed a novel iodine-vapor transport technique that produces polycrystalline Si layers of 10-40 µm thicknesses on glass substrates, and at a high growth rate of ~3 µm/min. The layers exhibit large grain sizes of 5-20 µm and 5 µs minority carrier lifetime. Results from our on-going study of metal impurity and impurity-dopant pair defect effects on lifetime indicate strong recombination at Fe-Ga pair defects. Transient photoconductance simulations by finite element analysis were carried out for our surface probe lifetime measurement approach. Several cooperative research activities with Si-PV companies are discussed.

1. Introduction

Our recent research activities have focused on three topics: thin-layer silicon growth on foreign substrates; understanding the effects of transition metal impurities on minority charge-carrier lifetime and Si material performance in PV devices; and assisting the c-Si PV industry with selected materials research problems. The sections below elaborate on these research areas.

2. Thin-Layer Silicon Growth

Nucleation on non-Si substrates requires a growth process with sufficient driving force to overcome a substantial nucleation barrier. We originated a chemical-vapor transport method that achieves this using an iodine disproportionation reaction [1]. It offers the possibility of atmospheric operation in an open system and is capable of depositing large-grain polycrystalline Si layers on foreign substrates at a fast rate and an intermediate temperature.

Our system consists of a vertical reactor with iodine and source silicon placed at the bottom. The source silicon temperature is maintained at 1000°-1200°C. The top of the reactor is kept slightly above the melting point of iodine and is capped with a removable purge inlet and outlet assembly that blankets the region above a gravitationally confined iodine column with either inert gas or hydrogen. A movable sample holder suspends the substrate near the top of the reactor during purging and precursor formation. The substrate is then lowered to a position where the temperature is about 900°C for thin layer Si growth. We have used several high-temperature glass ceramics as substrates, as well as heavily doped silicon.

During the entire purge and run cycle, the heavier iodine and silicon iodide gas species stay in the lower section of the reactor tube and are trapped at the top by a cooler cloud of condensates. A hydrogen purge gas forms a gas curtain between the reacting gases and the atmosphere, allowing open system operation without significant loss of iodine or reduced iodine partial pressure as is the case in a normal open system involving a carrier gas.

Our experiments show that the disproportionation reaction between SiI_2 and SiI_4 is responsible for silicon transport from high to low temperature in the atmospheric pressure reactor. Fig.1 illustrates the reaction mechanism.

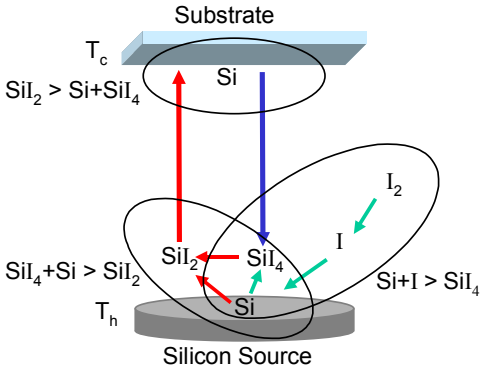

Fig. 1. Iodine vapor transport reaction mechanism

Grains as large as 20 µm are easily obtained, as shown in Fig. 2. Higher temperature favors larger grains. The typical growth rate is 3 µm/min and strongly depends on the substrate and source temperatures. A minimum substrate temperature of about 800°C is needed to start the deposition. Growth rates as high as 10 µm/min are observed for a source/substrate temperature of 1200°/1000°C. An effective minority-carrier lifetime of about 5 µs was measured, implying a diffusion length far exceeding the 10-40 µm layer thickness.

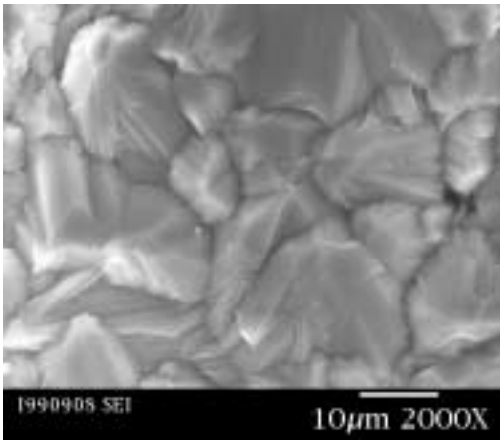

Fig. 2. SEM photo of the surface of the Si layer

3. Impurity Effects and Lifetime

There are dramatically different effects on minority-carrier lifetime (τ) and PV device performance for different transition metal impurities. For example, Cu is relatively benign, Ti has a very strong degrading effect, and Fe has an intermediate effect. In addition, transition metal impurities participate with the typically-used boron dopant to form pair defects. There is increased interest in alternative p-type dopants because boron has been linked to short-term, slight efficiency degradation. There are also increased efforts to "upgrade" metallurgical-grade Si (MG-Si) for solar-grade feedstock use. Thus, there is a need to better understand differences in Shockley-Read-Hall recombination of the different metallic impurities and to characterize defect-pair behavior with other p-type dopants such as Ga.

We have initiated a systematic study of Fe, Ti, and Cu behavior in otherwise high-purity silicon, with and without Ga doping. Dislocation-free, float-zoned Si was deliberately doped with Fe and Ga during growth. Crystal properties were documented by deep-level transient spectroscopy and annealing studies [2]. The typical τ of Fe-Ga co-doped crystals (0.4 μs) was dramatically lower than that of crystals doped with similar amounts of either Fe alone (12 μs) or Ga alone (1,400 μs), contrary to the τ behavior at low injection of Fe-B pair defects (see Table I). Thermal dissociation of Fe-Ga pairs increased τ, confirming a stronger carrier-recombination activity at Fe-Ga pairs than at interstitial Fe. Defect energies (relative to the valance band) equal to 0.10 and 0.21 eV were observed for Fe-Ga co-doped samples. The corresponding hole-capture cross-sections were found to be 3×10^{-16} cm^2 and 6×10^{-15} cm^2.

Table I. Minority-Carrier Lifetime of Dislocation-Free <100> FZ Single Crystals Doped with Fe and Ga

Crystal	Resistivity (Ω-cm)	Ga (cm^{-3})	Fe (cm^{-3})	Lifetime (μs)
41121 a	3.5	3.8×10^{15}	0	>1400
51129-1	24,000	0	1.2×10^{14}	12
70515	6	2.2×10^{15}	4.8×10^{11}	2.2
51212-la	4.1	3.3×10^{15}	1.3×10^{14}	0.40
51212-lb	1.4	1×10^{16}	1.3×10^{14}	0.34

Localized photon excitation and photoconductance detection on a silicon ingot surface are a convenient and cost-effective means to measure minority-carrier lifetimes, and we reported on an industrially-rugged surface-probe system for the measurement at the last review meeting [3]. Using the classical drift-diffusion-recombination model, we successfully performed three-dimensional transient photo-conductance simulations by finite element analysis to examine the correlation between measured effective lifetime and true bulk lifetime. For two-probe detection and localized photon excitation, we found that the majority carriers determine the ambipolar diffusion and drift with a small spatial separation between the minority and the majority carriers. Various combinations of surface-recombination velocity and bulk lifetime were calculated using specified values for absorption coefficient, minority carrier diffusivity, and excitation-spot size to enable the derivation of an empirical formula for practical lifetime measurements.

4. Research on Industry Si Materials Problems

We completed activities under a cooperative research and development agreement (CRADA) with EBARA Solar, Inc. (ESI) on the dendritic-web ribbon-growth process. An ESI web-growth furnace was set up and operated at NREL. The research resulted in major improvements in the success rate of the web-growth start-up procedure, an intricate process involving coplanar propagation of two dendrites from a single seed dendrite. An improved crucible design for better shallow-melt stability and thermal isolation of the melt replenishment process from the ribbon-growth region was also achieved. The other aspect of the work involved x-ray topographic analysis of ribbon defects and stresses. In the course of the work, the production rate of silicon dendritic web at ESI more than doubled. Overcoming start-up problems and gaining greater insight into the web-growth initiation process has lead to increased throughputs.

Another collaborative project is underway with GT Equipment Technologies, Inc. in the area of silicon feedstock deposition. This work is examining modified chemical-vapor deposition (CVD) techniques with the potential of greatly enhanced deposition rates. In addition, we are engaged at NREL in several approaches for purifying MG-Si to useful levels for solar-grade feedstock.

5. Summary

Our project emphasizes silicon materials research that will complement work in industry by examining next-generation silicon growth technologies (such as iodine vapor transport), by understanding the effects of grown-in defects and impurities (such as transition metals and metal-dopant pair defects) on silicon minority-carrier lifetime and material performance, and by assisting the c-Si PV industry with selected silicon materials problems (such as the pending feedstock availability problem or specific crystal-growth issues). Some of our recent progress in these areas has been presented. Additional details about our research can be found on our website at http://www.nrel.gov/silicon/.

REFERENCES

[1] T.H. Wang and T.F. Ciszek, "Growth of Large-Grain Silicon Layers by Atmospheric Iodine Transport," to be published in May, 2000 J. of the Electrochem. Soc.

[2] T.F. Ciszek, T.H. Wang, W.A. Doolittle, and A. Rohatgi, "Iron-Gallium Pair Defects in Float-Zoned Silicon," in: High Purity Silicon V, Eds. C.L. Claeys, P. Rai-Choudhury, M. Watanabe, P. Stallhofer, and H.J. Dawson (The Electrochemical Soc., Proceedings Volume 98-13, New Jersey, 1998) pp. 230-240.

[3] T.H. Wang, T.F. Ciszek, M. Landry, A. Matthaus, and G. Mihalik, "A Silicon Ingot Lifetime Tester for Industrial Use," in: NCPV Photovoltaics Program Review, Proceedings of the 15th Conference, Eds. M. Al-Jassim, J.P. Thorton, and J.M. Gee, Denver, CO, Sept. 8-11, 1998 (AIP Press, Woodbury, NY, 1999) pp. 443-452.

Defect Monitoring in Multicrystalline Silicon

Using Scanning Room-Temperature Photoluminescence Spectroscopy

I. Tarasov and S. Ostapenko,

Center for Microelectronics Research, University of South Florida
4202 Fowler Ave., Tampa, Florida 33620, USA

ABSTRACT

Scanning room temperature photoluminescence (PL) was applied to cast multicrystalline Si to assess defects in regions with degraded lifetime. The intensity of band-to-band PL correlates with minority carrier lifetime. An intense "defect" PL band at about 0.8eV is found in regions with degraded lifetime. The mapping of the 0.8eV PL band revealed a linkage to areas of a high dislocation density. Dislocation topography was obtained independently using light scattering technique and PL mapping of the dislocation D-lines at 77K. PL spectroscopy down to 4.2K was performed at areas with high and low "defect" band intensity. The origin of the 0.8eV band is related to contaminated dislocations in multicrystalline silicon wafers and solar cells.

1. Introduction

Development of reliable diagnostics for photovoltaic multicrystalline (mc) Si and application them to as-grown and solar cell processed wafers is valuable for assessing electronic quality upgrading. We report here using of scanning room-temperature photoluminescence (PL) spectroscopy to explore defects contributing to lifetime degradation in solar grade mc-Si prepare with block-casting technique. Experimental details of PL mapping system are published elsewhere [1].

2. Results and Discussion

PL spectrum at room temperature is generally composed of two bands shown in Figure 1a: band-to-band (I_{bb}) and "defect" (I_{def}) band. First, we mapped the band-to-band PL and compared this to a mapping of the effective minority carrier lifetime (τ_{eff}) performed using μ-PCD technique. In Figure 2a and 2b, we presented a distribution of both values. It is obvious, that the low-lifetime regions of the wafer (dark contrast) correspond to a noticeably reduced I_{bb} and the opposite, high lifetime areas (white contrast) match to the increased band-to-band PL. For illustration, one of "bad" regions is depicted by a frame.

We further observed in some regions of mc-Si a new "defect" PL band with the maximum at about 0.8eV (Fig. 1a, curve 2). Using PL mapping technique we proved that the 0.8eV band is strongly localized in "bad" regions showing a reverse contrast to τ_{eff} and I_{bb} (Fig. 2c). Complimentary to PL and μ-PCD mapping, we performed at the same wafer mapping of the dislocation density using light scattering technique. The data in Figure 2d document a positive correlation of I_{def} and a distribution of the dislocation density. Specifically, the 0.8eV PL band is observed in areas with dislocation density ranged (1 to 8)E+6 cm^{-2}. We performed low-temperature PL spectroscopy down to 4.2K. The PL spectrum at 77 K of a "bad" region is presented in Figure 1b (thick line). The entire spectrum was numerically deconvoluted at four lines, which are very close in maximum positions to dislocation D-lines in Cz-Si [2]. As temperature increased, one of these lines, D1', is shifted and can be tracked to the "defect" PL band at room temperature. A principal difference between D1' line in mc-Si versus dislocation D-lines in Cz-Si is a substantial broadening of the D1' line, which accompanied by a different temperature

quenching tracing to the "defect" PL at room temperature. This is accounted for interaction of the dislocations in mc-Si with impurities and defect precipitates. Therefore, the low-temperature PL spectroscopy additionally confirmed a linkage of the "defect" luminescence in mc-Si to dislocations.

3. Conclusions

Defect PL band is observed in cast, EFG and ribbon wafers and solar cells. The scanning monitoring of its intensity with PL mapping can be used to assess active dislocations, which degrade lifetime in PV silicon. Important that PL mapping at room temperature using different spectral features allows selective control of recombination centers in solar-grade multicrystalline silicon. We can postulate that improved passivation of the contaminated dislocations may lead to high-efficiency mc-Si solar cells.

4. Acknowledgements

This work was supported by NREL grant XD-2-11004-5.

5. References

[1] Y. Koshka, S. Ostapenko, I. Tarasov, C. McHugo, J. P. Kalejs, Appl. Phys. Lett., **74**, (1999) 1555-1557

[2] R. Sauer, J. Weber, J. Stolz, E. R. Weber, K.-H. Kusters, H. Alexander, Appl. Phys, **A36** (1985) 1-13

[3] S. Ostapenko, I. Tarasov, J. P. Kalejs, C. Haessler, E. Reisner, Sem. Sci. Technology (in press)

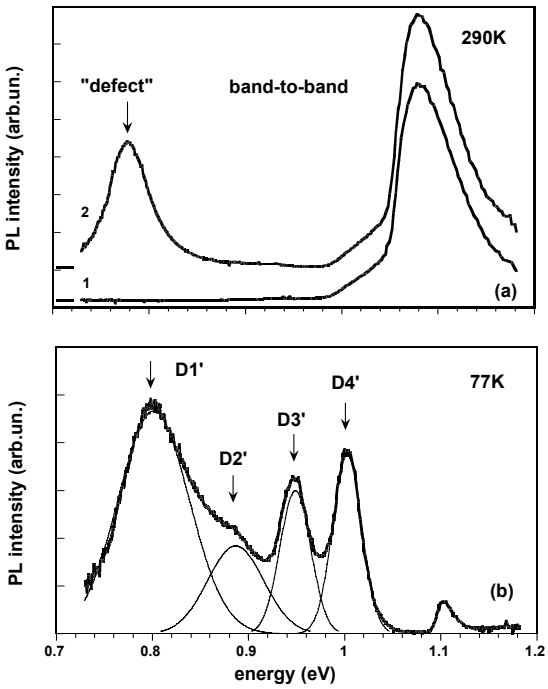

Figure 1. (a) - Room-temperature PL spectrum measured in high lifetime region (1) and low lifetime region (2) of mc-Si wafer. (b) – PL spectrum at 77K and deconvolution on four individual sub-bands. D1' line corresponds to the "defect" PL band at room temperature.

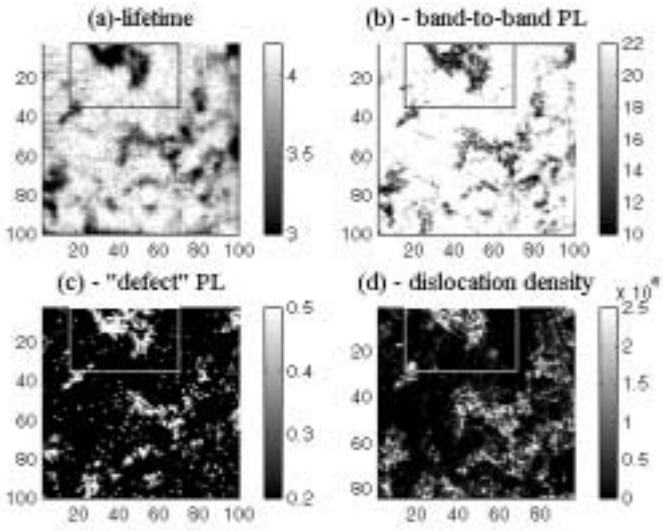

Figure 2. (a) map of minority carrier lifetime using laser-microwave reflection, (b) map of band-to-band PL intensity, (c) map of "defect" PL intensity, and (d) map of dislocation density.

Detailed Characterization of Si Substrates and Solar Cells with High-Speed PVSCAN

B. L. Sopori, W. Chen, Y. Zhang, and J. Madjdpour
National Renewable Energy laboratory,
1617 Cole Boulevard, Golden, CO

V. Yelundur, J. Jeong, and A. Rohatgi
Georgia Institute of Technology, Atlanta, GA

ABSTRACT

This paper describes some applications of PVSCAN– an instrument developed for rapid characterization of photovoltaic (PV) materials and devices. It measures defect distribution, reflectance, and external and internal responses of light beam induced current at two wavelengths of optical excitation.

1. Introduction

PVSCAN is an optical scanning system that has many applications in the PV industry, including high-speed mapping of material and cell parameters such as defect density, reflectance, and light-beam-induced current (LBIC). In response to the PV community's needs, we have recently made improvements on the system that give it the capability to scan larger substrates and cells, with higher speeds and finer resolution, and provide statistical information that can be very valuable for analyzing low-cost solar cells.

This paper briefly describes the operation of the instrument and presents some examples to illustrate recent improvements and how they can be used to characterize some important issues in PV technology.

2. A brief description of PVSCAN

PVSCAN uses the optical scattering from a defect-etched sample to statistically count the density of defects. A defect-etched wafer is illuminated with a laser beam and the (integrated) intensity of the reflected (scattered) light is measured by a photodetector. The detector signal is proportional to the number of scattering centers—providing a signal that is proportional to the local dislocation density [1]. By scanning over the sample, the instrument can map the defect distribution. In multicrystalline materials, PVSCAN can distinguish between various crystallographic defects using their scattering-patterns to simultaneously generate maps of grain boundary and dislocation distributions in a wafer. Figure 1 is a schematic of the optical system. The various symbols used are identified in the figure caption. A detailed description of the system is given elsewhere [1]. Some important features of the system are: (i) provides mapping capability at two different wavelengths, λ_1=0.633 μm, λ_2=0.980 μm; (ii) monitors dislocations and grain boundaries simultaneously by detectors DDi and GBi, respectively; (iii) has capability to measure diffuse as well as specular components of reflectance simultaneously; and (iv) the incident light power illuminating the test wafer or cell is continually monitored.

PVSCAN also provides a quantitative means of measuring the LBIC response of a solar cell at two different wavelengths (0.633 and 0.980 μm) of light excitation. This enables the instrument to separate the near-surface and the bulk recombination characteristics of the cell. The photo-current response for each excitation can be measured and saved by the computer as the external response. PVSCAN's capability of mapping reflectance provides an important step toward identifying losses in the cell because reflectance is a major cause of "efficiency loss" for solar cells. By combining the LBIC reading with reflectance losses, the instrument calculates the cell performance as a function of the light that is actually transmitted into the cell to get an internal photoresponse; this is the core information needed to improve cell performance.

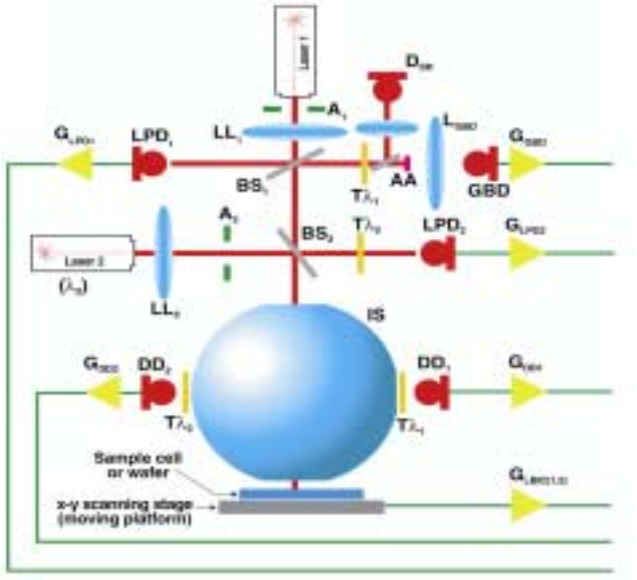

Figure 1. A schematic of the optical system of PVSCAN.

A_i = aperture, BSi = beam splitter, DD_i = dislocation density detector, GBD = grain boundary detector, Gi = amplifier gain, IS = integrating sphere, Lli = laser focusing lens.

3. Characterization

Because PVSCAN can perform analysis of both materials and devices parameters, we can illustrate some examples of each of these.

The efficiency of a Si solar cell is controlled by the impurity and the defect content in the substrate. Because gettering removes most of the dissolved lifetime-killing impurities, one finds a direct correlation between dislocation density and the local cell performance. Thus, it is necessary to measure the local variations in the defect density of the wafer. Defect maps are also important to improve the crystal growth because defect distributions reflect the nature of thermal stresses during the growth. The standard procedure for defect mapping involves polishing the wafer by a chemical-mechanical procedure before defect etching [2]. This procedure is time consuming and particularly difficult for ribbon samples. We have recently developed a procedure that abates this step. Figure 2 shows a defect map of a ribbon that uses our new procedure of chemical polishing and defect etching.

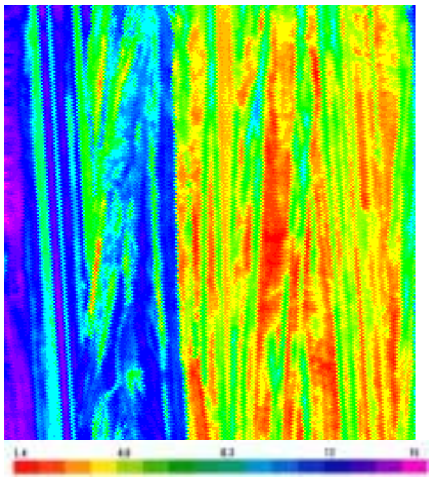

Figure 2. A defect map of a ribbon sample. Sample size: 1.4-in. x 1.5-in. The defect density values are those shown in the legend x10^6 cm^{-2}.

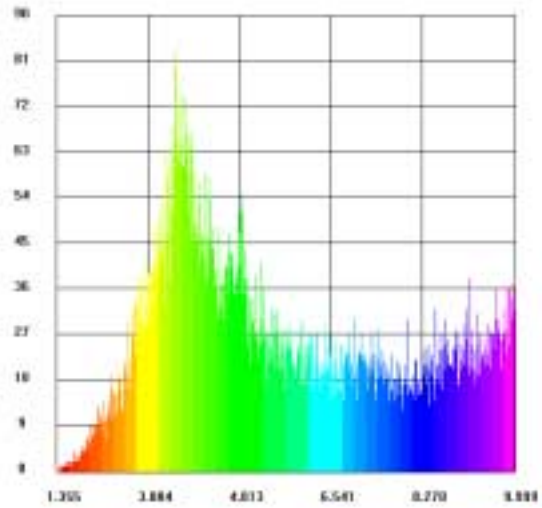

Figure 3. Distribution of defects in the sample shown in Figure 2.

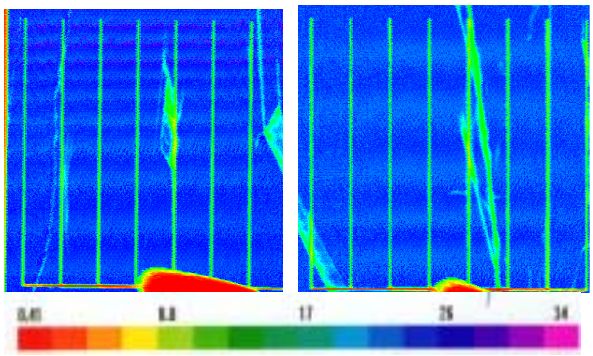

Figure 4. LBIC response maps of two ribbon cells

Another feature recently added to the system is the display of the statistical parameters. Figure 3 shows the distribution of defect density in the ribbon shown in Figure 2 which has an average value of 7.3x10^6 cm^{-2}.

The average value is also important to compare the performance of non-uniform solar cells. It is a common experience that small-area spectral responses or minority-carrier diffusion-length measurements do not correlate well with the cell performance. However, the averaged LBIC at □ = 0.980 □m, determined by PVSCAN, correlates well with cell performance. Figures 4a and 4b show LBIC maps of two ribbon cells—the averaged responses of the cells and their cell parameters are given in Table 1.

Table 1. Cell parameters and the averaged LBIC response of two devices shown in Figure 4.

Cell ID	Cell A	Cell B
Jsc, mA/cm2	29.65	28.96
Voc, mV	558.5	550
FF	0.744	0.74
Response, mA/cm2	24.05	23.57

4. Summary

The capabilities of PVSCAN have recently been extended to meet the current requirements of the PV community. These include: (i) Larger scan area—up to 8-in. x 8-in., (ii) higher-speed scanning—up to 4 in/s, (iii) improved system software with capabilities that help characterizing mc-Si cells, and (iv) improved procedures for faster and more convenient sample preparation [3].

REFERENCES

[1] National Renewable Energy laboratory, Technology Brief, NREL/MK-336-21161.

[2] B. L. Sopori, J. Elctrochem,. Soc. **131**, 667 (1984)

[3] Bhushan Sopori, Wei Chen, Yi Zhang, Tess Hemschoot, and Jamal Madjdpour, "Extending PVSCAN to Meet the Market Needs for High-Speed, Large-Area Scanning," Proc. 9th workshop on Silicon Solar Cell Materials and Processes, Breckenridge, CO, 135 (1999).

Emitter-Wrap Through Solar Cells with Screen-Printed Contacts

D. Smith

Sandia National Laboratories*
Albuquerque, NM

ABSTRACT

The Emitter-Wrap Through (EWT) solar cell is a back contact solar cell design that has potential for high efficiencies using poor quality silicon and simplified module assembly. This paper reports on a version of this device utilizing screen printed contacts. An efficiency of 15.2 % under AM1.5G illumination has been demonstrated for a 41 cm^2 cell.

1. Motivation

Back contact cells have the potential for increased efficiencies compared to front contacted cells. They also allow for simplified module assembly due to co-planar contacts. The Emitter-Wrap Through cell is a back contact cell that uses laser-drilled holes to connect the emitter from the front to the back, as seen in Figure 1. Double-sided collection gives an additional advantage of reducing demands on material quality due to double-sided collection. There are several design variations currently under development[1,2,3].

The EWT has demonstrated 18 % efficiency with a laboratory fabrication process involving photolithography[4]. Current efforts are focused on fabricating this device using low-cost processes. The process addressed in this paper is screen printed contacts.

2. Device Design

The laser-drilled hole spacing of the EWT determines the contact spacing (as seen in Figure 1). For screen printed metal, tolerances must be large enough for ease of alignment. A hole spacing of 2 mm x 0.5 mm was used for this device. Grid line width was chosen at 400 µm for both N and P contacts. The percentage of p-type surface at the back was chosen at 40 %. This results in 200 µm spacing between the edge of the P contact to the nearest N-type region on either side, and hence, this is the alignment tolerance.

The emitter was formed by the deposition and patterning of CVD oxide on the back. This glass acts as a phosphorous diffusion mask. The patterning of the mask oxide is done by photolithography. Laser hole drilling occurs after deposition of the mask oxide and before patterning of the mask oxide.

3. Contacts

The N-contact metal used in these devices was screen printed silver paste, DuPont 4943. P-contact was formed either by aluminum or silver/aluminum paste. In both cases, an acceptable contact was formed as demonstrated by fill factors of 73 %. Contacts were co-fired in a belt furnace at temperatures ranging from 700 to 750C with time at peak temperatures approximately one minute.

After emitter diffusion, the contact metal pastes were printed directly on the N and P type regions without removal of either mask oxide or phosphorous diffusion glass. This was a key feature of this device. It is well known that screen printed contacts can be fired through oxides and nitrides, due to the aggressive glass frit in the screen printed metal pastes. In this device, it was also found that contamination was occurring during the belt furnace firing cycle. With only thin oxides on the silicon surfaces, contaminants were able to diffuse into the cell and decrease the lifetime near the cell surfaces. Also, it was found that the shunt conductance was unacceptably high when contacts were fired through only a thin surface oxide. The high shunt conductance was caused by contact spiking through the junction. Maintaining the thick surface oxides reduced the high shunt conductance and also acted as a diffusion barrier to contaminants during the firing cycle.

4. Device Results

Figure 2 shows I-V curves of 41 cm^2 EWT cells with screen printed contacts under AM1.5G illumination. The base material used is 0.5 ohm-cm float zone silicon. Base lifetimes are typically 5-10 µsec after a high temperature step with deposited oxides on the surface, while 100 µsec has been measured with samples receiving just a

* Sandia is a multi-program laboratory operated by Sandia Corporation, a Lockheed Martin Company, for the U.S. Department of Energy under contract DE-AC04-94AL85000.

phosphorous diffusion. Lifetimes are measured by RF-PCD on a control sample using a light N+ diffusion for surface passivation. It has been determined that the deposited oxide is harming the bulk lifetime of the base material. Minimal effort has been expended to eliminate the lifetime problems, since the EWT cell demonstrates its potential most clearly with low-quality material.

5. Future Work

The EWT cell described here still has the disadvantage of one photolithography step for patterning of the emitter. It has been demonstrated that bare silicon surfaces give an unacceptable device quality for the EWT cell. Therefore, any emitter formation technique will have to result in oxidized silicon surfaces. Also, polycrystalline materials would benefit greatly from a gettering step. If these two process requirements can be met in a high efficiency device, then the EWT cell will become an attractive back contact cell.

Acknowledgements

The author would like to thank Fernando Uribe and James Gonzalez for screen printing and firing, Beverly Silva for cell processing, and Jeannette Moore for cell measurements.

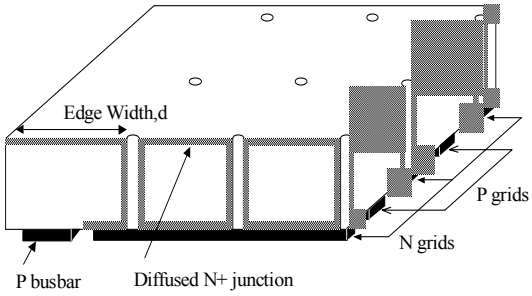

Figure 1. Emitter-Wrap Through solar cell geometry

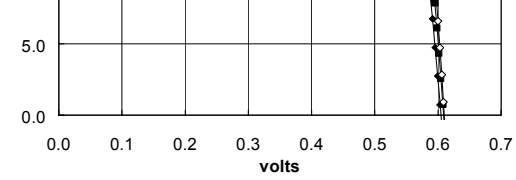

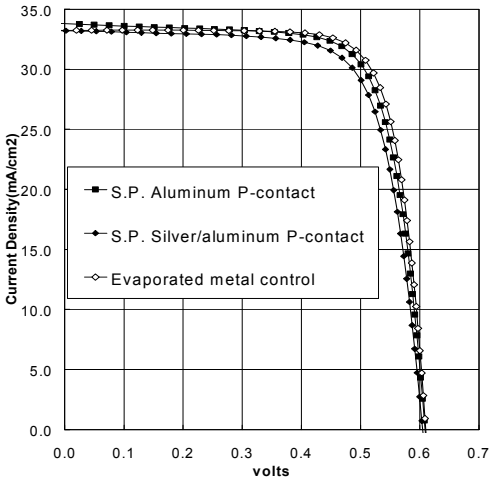

Figure 2. Illuminated current-voltage characteristics, EWT cells with screen-printed contacts and evaporated metal control. AM1.5G efficiencies of these three cells are 15.6 % for the control, 15.2 % for the screen-printed aluminum contact, and 14.6 % for the screen-printed silver/aluminum contacted sample.

References

[1] J.M. Gee, *et al.*, "Emitter-Wrap Through Solar Cell," 23rd IEEE Photovoltaic Specialists Conference, p. 265 (1993).

[2] A. Kress, *et al.* , "Low-Cost Back-Contact Silicon Solar Cells Applying the Emitter-Wrap Through Concept," 2nd World Conference on Photovoltaic Solar Energy Conversion, July 1998.

[3] A. Schoenecker, *et al.* , "Attacking Limiting Factors in 10 x 10 cm^2 Multicrystalline Silicon, Emitter-Wrap Through Solar Cell Design and Processing," 2nd World Conference in Photovoltaic Solar Energy Conversion, July 1998.

[4] D. Smith, *et al.,* Circuit Modelling of the Emitter-Wrap-Through Solar Cell," IEEE Transactions on Electron Devices, ED-46, No. 10, pp. 1993-1999.

Gettering and Passivation of PV grade Silicon Materials

A. Rohatgi, A. Ebong, V. Yelundur and J. Jeong
University Center of Excellence for Photovoltaic Research and Education,
School of Electrical and Computer Engineering, Georgia Institute of Technology, Atlanta, GA 30332-0250

Abstract

As-grown lifetime in the three ribbon silicon materials was found to be quite low. In order to improve the lifetime for achieving ≥ 16% efficient 100 μm thick screen-printed silicon solar cells, low-cost and manufacturable gettering and passivation techniques using lamp heated belt furnace were employed. SiN heat treatment alone, without prior gettering, does not produce much hydrogenation. The hydrogenation effect from SiN on phosphorus gettered ribbon silicon was also very small. The Al gettering alone was found to be somewhat effective. However, the effect of Al and SiN co-firing is much greater than the additive effects of individual process because vacancy generation due to Al alloying enhances the diffusion and incorporation of atomic hydrogen in Silicon.

1. Dendritic web ribbon silicon

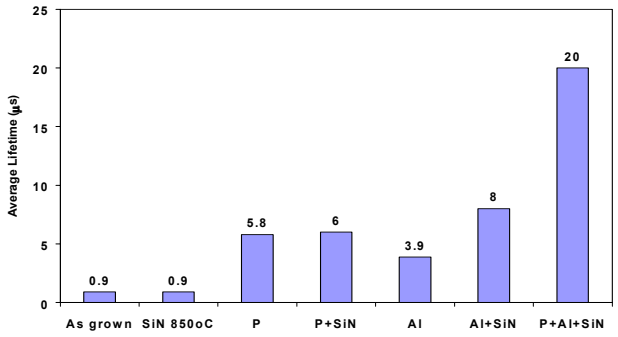

Fig. 1 Phosphorus and Al gettering and SiN hydrogenation of dendritic web ribbon silicon

As grown lifetime in a 16 Ω-cm p-type dendritic web Si was found to be 0.9 μs. SiN deposition followed by a 850°C/2 min anneal showed no improvement in bulk lifetime. Phosphorus gettering at 925°C for 6 min, which produces a 45 Ω/□ spin-on doped emitter in a belt furnace, raised the bulk lifetime to 5.8 μs. A subsequent SiN deposition and 850°C/2 min anneal did not show any improvement in bulk lifetime. Al gettering or BSF formation alone at 850°C/2 min increased the as-grown bulk lifetime from 0.9 μs to 3.9 μs. SiN deposition and 850°C/2 min anneal after the Al process increased bulk lifetime from 3.9 μs to 8 μs. Thus if phosphorus gettering, SiN deposition, and Al gettering are done sequentially and their effect was additive, then the web lifetime should be at best 14 μs. However, Fig. 1 shows that combined effect of phosphorus gettering followed by simultaneous Al and SiN heat treatment at 850°C for 2 min resulted in 20 μs lifetime. It should be noted that the temperature cycles (925°C/6 min for phosphorus diffusion plus 850°C/2 min for Al BSF + 730°C/ 30 seconds for contact firing) used in this study simulate the emitter diffusion, BSF formation, and screen-printed contact firing cycles used in actual cell fabrication.

2. EFG Sheet silicon

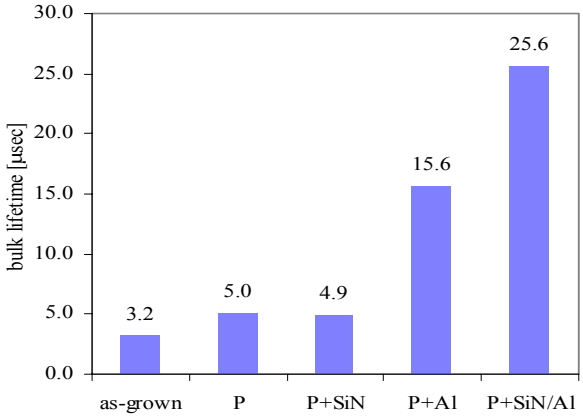

Fig. 2: Bulk lifetime improvement in EFG silicon due to P, Al gettering treatments and SiN induced hydrogenation.

A systematic study was conducted to determine the effect of a post-deposition anneal of PECVD silicon nitride in conjunction with the screen-printed aluminum on the back surface. Figure 2 shows change in bulk lifetime of EFG silicon due to individual and combined gettering and SiN hydrogenation treatments. The P treatment alone improved the as-grown bulk lifetime from 3.2 to 5.0 μsec and the

subsequent Al treatment (850 ^{o}C/2min) raised the bulk lifetime from 5.0 to 15.6 μsec. In addition to P and Al gettering, we studied the effect of PECVD SiN-induced hydrogenation of EFG silicon. After the P gettering, when a PECVD SiN was deposited on the front followed by an 850 ^{o}C/2 min anneal in a conveyor belt furnace, without the presence of Al on the back, no improvement in bulk lifetime was observed. This indicates that either PECVD SiN film without the Al does not efficiently passivate the defects in EFG silicon at 850 ^{o}C/2min or the lifetime is being dictated by some other mechanism. However, when the PECVD SiN on the front was annealed in conjunction with screen-printed Al on the back, a very significant improvement in bulk lifetime was obtained. In this scheme, after the P diffusion at 930 ^{o}C/6 min, a PECVD SiN film was deposited on the front followed by screen printing of Al on the back. Annealing of the PECVD SiN film and gettering of the screen-printed Al were performed simultaneously at 850 ^{o}C/2 min in a conveyor belt furnace. This resulted in a very significant improvement in the bulk lifetime of EFG silicon from 5.0 μsec to 25.6 μsec, as shown in Figure 2. Recall that P and Al gettering raised the bulk lifetime from 3.2 μsec to 15.6 μsec and PECVD SiN by itself did not show any hydrogenation. Therefore, 10 μsec (25.6 μsec – 15.6 μsec) increase is attributed to the synergistic effect of Al and SiN.

3. String Ribbon Silicon

String Ribbon is another promising PV material. Fig. 3 shows that the combination of phosphorus gettering and SiN_x hydrogenation at 850°C improved the lifetime by 7 μs, which is nearly equal to the sum of the enhancement provided by individual phosphorus gettering and hydrogenation treatments. A similar additive effect is observed in the combination of phosphorus and aluminum gettering in which the lifetime improved by over 11 μs. In contrast, a noteworthy average lifetime of over 38 μs, an improvement of over 30 μs, was observed when the SiN_x induced hydrogenation treatment and aluminum gettering treatment were combined in one heat treatment at 850°C for 2 min. This improvement in lifetime is far greater than the sum of the 850°C hydrogenation and aluminum treatments alone. This result suggests that there is a positive synergistic interaction between the hydrogenation from the front surface and the aluminum alloying process simultaneously occurring at the back surface of the substrate at 850°C.

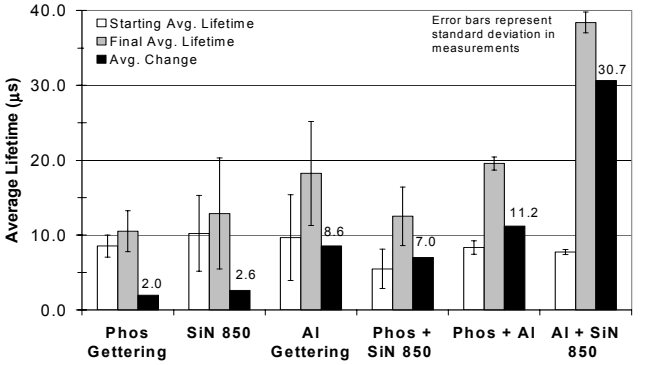

Fig. 3: Effectiveness of gettering and passivation treatments in String Ribbon silicon.

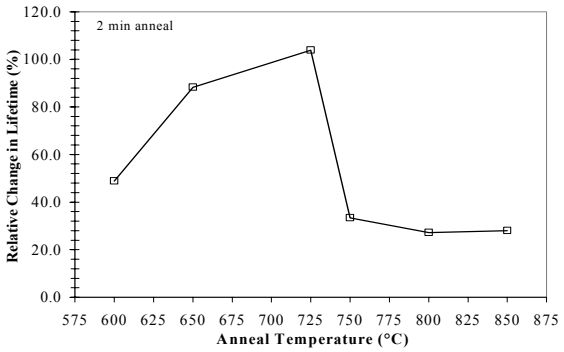

Fig. 4 Defect passivation from post-deposition anneal of PECVD SiN_x.

Fig. 4 shows that at anneal temperatures between 600^{o}C and 725^{o}C, the relative improvement in lifetime is greater than 50%, while in the temperature range of 750^{o}C-850^{o}C, the relative improvement drops to near 30%. The dramatic decrease in the effectiveness of hydrogen passivation above 725^{o}C shown in Fig. 4 may be due to the high temperature instability of hydrogen at defect sites in silicon. These results suggest that the hydrogen passivation of silicon defects may be proportional to the release of hydrogen from the PECVD SiN_x film as well as the ability of hydrogen to stick to defect sites in silicon.

PV-Reflectometer: a Process Monitoring Tool for Solar Cell Manufacturing

B. L. Sopori, W. Chen, and Y. Zhang

National Renewable Energy laboratory
1617 Cole Blvd., Golden, CO 80401

ABSTRACT

A new instrument is described for in-line monitoring of various process steps in silicon solar-cell fabrication. This system can rapidly measure a host of parameters that describe the front-surface and the back-surface properties of a wafer/cell. The measured parameters represent values averaged over the entire wafer/cell, making it suitable for monitoring process steps in a solar cell manufacturing facility.

1. Introduction

The photovoltaic (PV) industry is strongly interested in developing process monitoring tools to improve manufacturing processes, reduce product cost, and increase the product reliability. In a typical Si solar cell manufacturing facility, the prevalent process-control techniques are similar to those used in the past in the microelectronics industry. While the microelectronics industry has many new and sophisticated characterization-tools, those tools are not suitable for the PV industry. The PV industry needs process-monitoring techniques that can measure an entire large-area device, rapidly at a low-cost, and which are usable on rough and textured surfaces. Here we describe a new non-contact instrument, PV-Reflectometer, designed specifically for PV monitoring and measurement.

2. Principles of a PV-Reflectometer

A PV-Reflectometer measures the average reflectance (R) of an entire wafer or cell as a function of wavelength (□). The system operates in a broad spectral range that allows separation of the properties related to the front and the back surfaces. This information is used to determine various wafer and cell parameters. To illustrate how the parameters are derived from the reflectance data, Figure 1 shows a sketch of a typical reflectance plot of an antireflection (AR)-coated, textured cell with front and back metallization. In Figure 1:

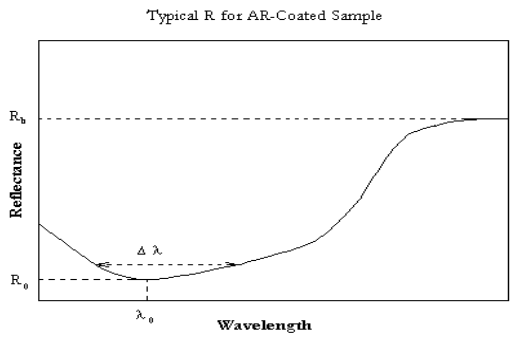

Figure 1. Illustration of parameters used for analysis of the reflectance curve.

- λ_0 (wavelength of minimum reflectance) determines the thickness of the AR coating.
- The value of R_0 (reflectance at λ_0) is used to determine the fraction of metallization. This assumes that, without front metallization, an AR-coated cell would exhibit a reflectance minimum (which is close to a null). Thus, the deviation from the zero implies that the cell is metallized. By calibrating the system, it is possible to relate this value to the fraction of the area covered by the metal.
- $\Delta\lambda$ is the width of the reflectance minimum, which is related to the surface scattering. For a given AR coating, $\Delta\lambda$ increases with an increase in the surface roughness. This parameter is used to calculate the roughness of the surface or the height of the texture (using PV Optics).
- The back-reflectance value can be derived from the reflectance at long wavelength, such as λ = 1.2 □m (using *PV Optics*).

Measurement of the reflectance curve of a large-area device is difficult. To overcome the difficulties intrinsic to the conventional methods of making R vs □ measurement, PV-Reflectometer uses a new concept based on the reciprocity principle in optics [1]. Figures 2(a) and 2(b) illustrate the reciprocity principle in that the two cases shown are optically equivalent. Figure 2(a) shows that the incident light is normal to the sample, and the reflected (scattered) light is collected through all the angles. Figure 2(b) shows that the light is incident from all the angles and collected normal to the sample. The approach of Figure 2(b) confers many advantages including ease of large-area illumination and simplification of the signal collection—features that can greatly enhance the S/N ratio to render a measurement quickly. The next section will show how this approach is made practical.

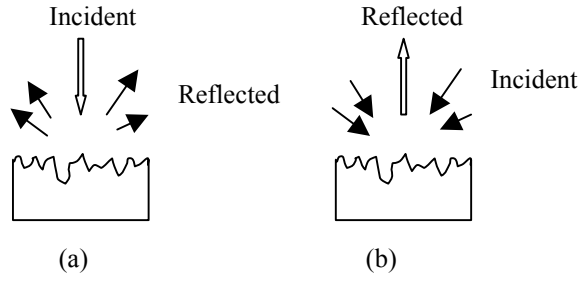

Figure 2. Illustration of the conventional illumination approach (a) and the reciprocal approach (b).

3. System configuration

Figure 3 is a schematic of the PV-Reflectometer. It consists of a highly-absorbing spherical dome, about 12 to 18 inches in diameter, with openings at the top and at the bottom. The bottom opening terminates in an optical baffle that houses a platform to support the test wafer. The dome has four sets of diverging lights located on the upper side that illuminate the test wafer. Separate controls balance the intensities of the lights. The entire system is designed to eliminate all possible scattering of the light except by the test wafer. The top-side of the dome has a lens and aperture assembly that couples the light reflected from the sample into a monochromator through an optical fiber. The monochromator drive, data taking/handling, calibration, and system control, are done by a computer that generates the reflectance (R) vs. wavelength (□) plot for the test sample.

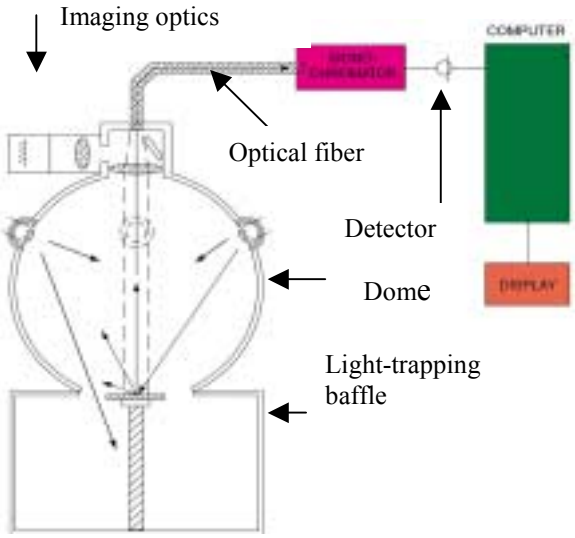

Figure 3. A schematic of the PV-Reflectometer.

4. Results

Figure 4 shows reflectance curves of three sets of samples, each having four wafers, taken at various stages of commercial Si solar cell fabrication—after sawing and pre-etch cleaning, after texture etching, and after AR coating. It is important to note that the reflectance values are in arbitrary units (AU), representing a scale that is much higher than the absolute scale. For comparison, the absolute reflectance of a typical textured mc-Si wafer is about 20%, and the minimum reflectance of an AR coated mc-Si wafer is <1%. Because of a high S/N ratio in a PV-Reflectometer, it is possible to rapidly scan the monochromator, and to achieve a good accuracy in measuring small shifts in the reflectance curve.

Figure 4 carries information, as outlined in the earlier section, which is automatically calculated by the computer. A detailed discussion is beyond the scope of this short paper. However, one can easily draw the following inferences:

- The measured thicknesses of the AR coating (TiO_2) ranges from 794 to 858 Å.
- There is very little variation in the sawn and cleaned samples. This is clearly expected if the sawing process is well controlled. We have found that in situations where sawing problems occur, the reflectance curve is typically shifted to higher values.
- The textured samples exhibit two interesting features. First, the average reflectance of the textured wafers is higher than the sawn wafers. This is because while texturing mc-Si wafers can reduce the reflectance of some grains, the reflectance of grains that have (111) orientation actually increases. Second, texturing introduces significant variation in the reflectance. This arises from the fact that the composition of the texturing bath changes continually as the etching proceeds, leading to variations in the texture quality within a batch as well as from batch to batch.
- The reflectance after AR coating is rather insensitive to variations in the texture, but is more controlled by the thickness of the AR coating (and its refractive index). This is rather fortunate because it greatly relaxes the degree of control needed for texturing bath.

Another unique feature of the PV-Reflectometer is its ability to measure both the fractional area and the thickness of the front metal contact. This is accomplished by making R VS□ measurements with two different illumination conditions. Details of this will be given in a forthcoming publication [2]. While a PV-Reflectometer can provide a variety of information for researchers, it provides powerful means of process monitoring and control on production lines.

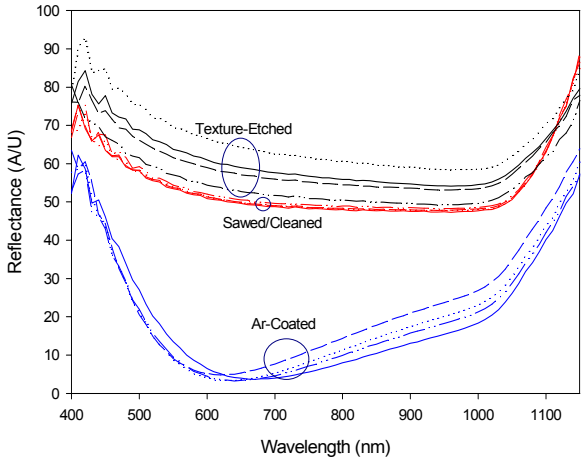

Figure 4. Reflectometer results on three groups of commercial PV-Si wafers (4.5 in. x 4.5 in.) at different stages of solar cell processing.

REFERENCES

[1] B. L. Sopori, "Principle of a new reflectometer for measuring dielectric film thickness on substrates of arbitrary characteristics," *Rev. Sci. Instrum.* **59(5)**, 725,1988.

[2] B. L. Sopori, W. Chen, Y. Zhang, and J. Madjdpour, 'Silicon Solar Cell Process Monitoring by a PV-Reflectometer," to be published.

Real time optics of p-type microcrystalline silicon deposition on specular and textured ZnO-coated glass surfaces

P. I. Rovira,[1] A. S. Ferlauto,[1] R. J. Koval,[1] C. R. Wronski,[1] R. W. Collins,[1] and G. Ganguly[2]

1 The Pennsylvania State University, Materials Research Laboratory and Center for Thin Film Devices, University Park, PA
2 BP Solarex, Thin Film R&D, Toano, VA

ABSTRACT

Using the guidance provided by real time spectroscopic ellipsometry (RTSE), we have optimized the plasma-enhanced chemical vapor deposition (PECVD) process to achieve high-density nucleation of single-phase microcrystalline silicon (μc-Si:H) p-type layers on specular zinc oxide (ZnO) coated glass at 200 °C. These optimized conditions have also been used in the fabrication of p-i-n solar cells on textured glass/SnO_2/ZnO substrates. We find that the time evolution of the microstructure and phase -- as well as the resulting dielectric functions -- all determined by RTSE, are similar for optimized μc-Si:H p-layers ~200 Å thick prepared on specular glass/ZnO and textured glass/SnO_2/ZnO surfaces.

1. Introduction

Previous RTSE studies have identified optimum PECVD processes for immediate high-density nucleation of p-type microcrystalline silicon (μc-Si:H) layers on H_2-plasma-treated intrinsic amorphous silicon (a-Si:H) surfaces at 200 °C using different dopant gases [1]. In the present study, we apply RTSE to identify the optimum gas flow conditions for immediate high-density nucleation of μc-Si:H p-layers on specular glass/ZnO substrates, focusing on $B(CH_3)_3$ as the dopant gas. As a result, different dopant gas flow ratios $D=[B(CH_3)_3]/[SiH_4]$ and H_2-dilution ratios $R=[H_2]/[SiH_4]$ are explored to obtain fully-coalesced μc-Si:H p-layers after 100 Å thickness. The optimum conditions of D and R for μc-Si:H p-layer deposition on specular glass/ZnO substrates are applied for the fabrication of p-i-n solar cells on textured glass/SnO_2/ZnO substrates. Of critical importance in the RTSE studies is a recently-developed multichannel ellipsometry technique based on the rotating-compensator principle [2], which has proven to be successful for evaluating the time evolution of the microscopic and macroscopic structure of a-Si:H p-i-n solar cells on textured surfaces, and for obtaining the optical properties of the component layers [3].

2. Experiment and results

The Si:H p-layers for RTSE studies were prepared by rf PECVD onto specular ZnO-coated Corning 7059 glass. The final intended thickness of the p-layers was ~1800 Å, the substrate temperature was 200 °C, and the rf plasma power was 0.23 W/cm^2. The first series of p-layers was deposited using R=200 and values of D ranging from 0 to 0.02 resulting in μc-Si:H films in all cases. In this series, we identified a minimum dopant flow ratio of D=0.02 for high p-layer conductivity [σ_{RT}>0.01 (Ω cm)$^{-1}$] in 200-300 Å layers. Furthermore, the RTSE data showed that as the $B(CH_3)_3$ gas flow ratio is reduced below D=0.02, much longer induction periods and lower crystallite nucleation densities are obtained. From these results, it is clear that $B(CH_3)_3$ acts as a catalyst for high-density nucleation of μc-Si:H. The second series of p-layers was deposited using D=0.02 and R varying from 30 to 300. The analysis of the

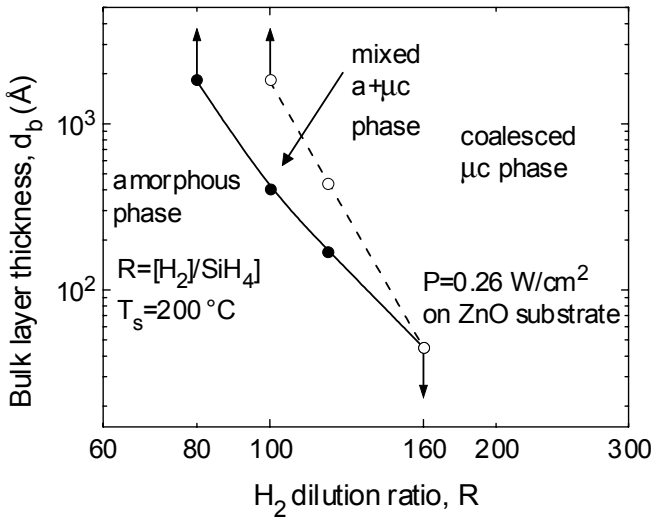

Figure 1. Evolutionary phase diagram for the deposition of Si:H p-layers at 200 °C on specular glass/ZnO substrates.

RTSE data for this series led to the evolutionary phase-diagram depicted in Fig. 1. As can be seen from Fig. 1, it is necessary to use R=160 or higher in order to obtain immediate nucleation of Si microcrystals on specular ZnO surfaces. A trade off exists, however, because higher dilutions lead to longer induction periods, lower nucleation densities, and lower deposition rates. Thus, it is preferable to operate at the lowest possible R, while avoiding the mixed-phase region.

An a-Si:H p-i-n solar cell was fabricated on top of a textured glass/SnO_2/ZnO substrate using a ~200 Å thick optimized μc-Si:H p-layer deposited with D=0.02 and R=200. In addition, the cell incorporated a ~5000 Å thick i-layer prepared using pure SiH_4 and a ~350 Å thick μc-Si:H n-layer. The time-dependent parameters that describe the p-layer evolution are (see inset in Fig. 2): (i) the volume fraction f_{i1} of p-layer material filling the substrate interface layer composed of SnO_2/ZnO/void; (ii) the volume fraction f_{i2} of p-layer material filling the substrate surface roughness layer composed of ZnO/void; and (iii) the volume fraction f_s and (iv) the thickness d_s, both describing the evolution of the microscopically rough p-layer that covers the substrate surface. In Fig. 2(c) the effective thickness, calculated as d_{eff} = (495 Å) [f_{i1}(μc-Si:H)] + (308 Å) [f_{i2}(μc-Si:H)] + [d_s(μc-Si:H)] [f_s(μc-Si:H)], is provided. For comparison, we also include in Fig. 2(c) the time evolution of d_{eff} for the p-layer on specular glass/ZnO deposited under the same conditions. The induction periods and deposition rates are similar in both cases, even though the substrates present very different structure. This suggests that only the chemical nature of the substrate controls the induction and nucleation behavior.

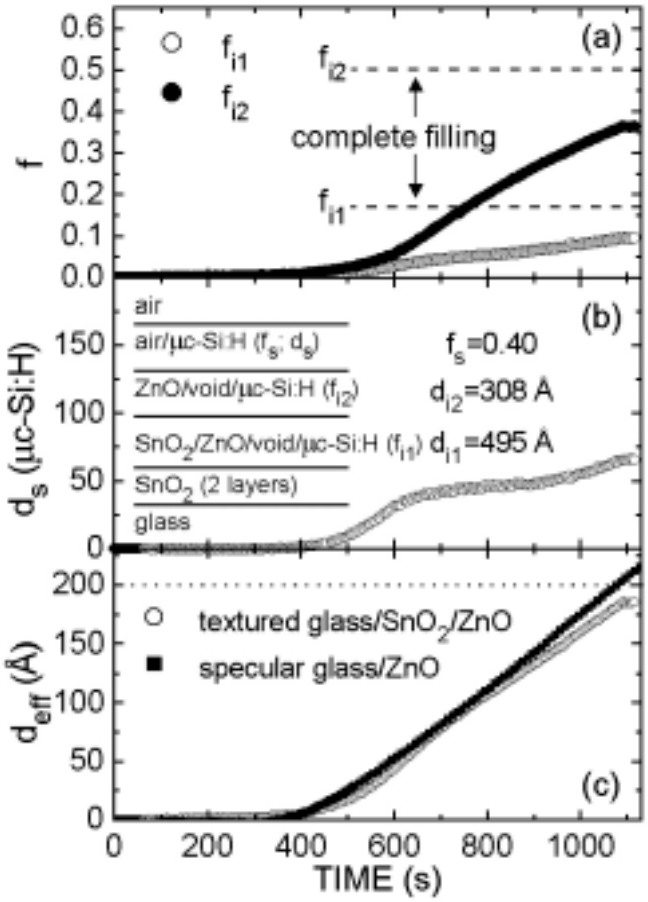

Figure 2. Time evolution of the microscopic structural parameters for a p-layer on textured glass/SnO_2/ZnO .

3. Acknowledgements

This work was supported by National Renewable Energy Laboratory (Subcontract No. AAD-9-18-668-16).

4. References

[1] Joohyun Koh, et al., J. Appl. Phys. **85**, 4141 (1999).

[2] J. Lee, P. I. Rovira, I. An, and R. W. Collins, Rev. Sci. Instrum. **69**, 1800 (1998).

[3] P. I. Rovira, A. S. Ferlauto, Ilsin An, H. Fujiwara, Joohyun Koh, R. J. Koval, C. R. Wronski, and R. W. Collins, Mater. Res. Soc. Symp. **557**, 719 (1999).

Structure and Effects of Extended Defects in Polycrystalline Si Thin Films

Y. Yan, M. M. Al-Jassim, T. H. Wang, and T. F. Ciszek

National Renewable Energy Laboratory

1617 Cole Blvd, Golden, CO 80401

ABSTRACT

The structure and effects of extended defects in rapid deposited polycrystalline Si thin films were studied using a combination of high-resolution transmission electron microscopy and first-principles total energy calculations. We found that the extended defects are mainly lamellar twins, and intrinsic and extrinsic stacking faults. The stacking faults were found to attract vacancies and produce energy barriers for oxygen diffusion, while lamellar twins have very little effect on the vacancies and oxygen impurities.

1. Introduction

Recently, high-speed deposition of large-grain polycrystalline silicon thin films on foreign substrates has been achieved using iodine vapor transport of silicon at atmospheric pressure with a vertical thermal gradient [1]. A consequential issue accompanying the high-speed deposition is the formation of a high-density of extended defects in the thin films. It is, thus, important to understand the atomic structure of these defects and their effects on the electronic properties of the films. In this paper we use a combination of high-resolution transmission electron microscopy (HRTEM) and first-principles total energy calculations to study the structure and effects of the extended defects in fast-grown polycrystalline Si thin films.

2. Experimental and theory

The polycrystalline Si thin films studied here were grown by a technique based on iodine vapor transport of Si at atmospheric pressure with a vertical thermal gradient [1]. Cross-sectional specimens were prepared for electron microscopy by first mechanical polishing to ~100 □m thickness, then dimpling the central portion of the specimens down to ~5 □m. The samples were subsequently thinned to electron transparency using a 4 kV Ar ion-beam at 14° inclination, then cleaned at a lower voltage (1.5 kV). A liquid N_2 cooling stage was used in order to minimize milling damage. HRTEM images were taken on a Philips CM30 microscope with a Cs = 2.0, operating at 300 kV. The image simulations were carried out using the EMS program package [2].

The total energy calculations were carried out using density-functional theory, local-density approximation (LDA) for exchange correlation, ultrasoft pseudopotentials, and plane waves [3]. The energy cutoff for the plane waves was set at 220 eV. We used supercell for defect calculations. Integration over the Brillouin zone was done using the Pack-Monkhost scheme with two irreducible k-points.

3. Results

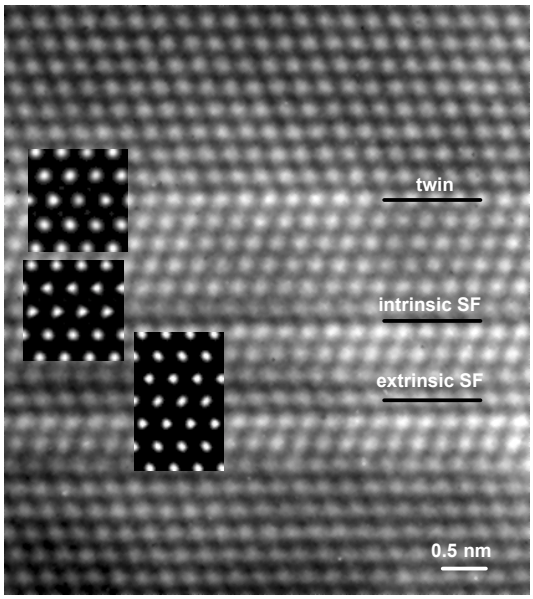

Fig. 1. A [$1\bar{1}0$] zone axis HRTEM image of lamellar twins, and intrinsic and extrinsic stacking faults in high speed deposited Si films. The insets are the simulated images of the determined structure shown in Fig. 2(b).

Our conventional TEM examinations revealed that the grain sizes of the polycrystalline Si thin films are in the range of 2 to 20 μm. A medium-density of extended defects, mainly planar defects, was observed in most grains.

Detailed analysis revealed that these planar defects are lamellar twins, and intrinsic and extrinsic stacking faults with a habit plane of {111}. The stacking faults often end at a partial dislocation inside the grains. The atomic structures of these defects were determined by HRTEM and image simulations. Figure 1 shows a HRTEM image taken from an area containing the three types of planar defects with the electron beam parallel to the $[1\bar{1}0]$ zone axis. The positions of the defects are indicated by black lines. The characters of the twins and the intrinsic and extrinsic stacking faults are clearly seen from the image.

In cubic materials, the possible structures of lamellar twins, and intrinsic and extrinsic stacking faults lying on {111} planes have been proposed [4]. Figure 2(a), (b) and (c) show the proposed structures for the lamellar twins, and intrinsic and extrinsic stacking faults, respectively. The arrows indicate the positions of the defects. The single and double lines at the defects indicate the bonding configuration across the defects. The open and black circles denote different heights. To demonstrate whether our observed planar defects have the same structure as the proposed, we performed through-focus and through-thickness image simulations. The inserts in figure 1 are the simulated images using the structures shown in figure 2 at a defocus of -60 nm for a thickness of 10 nm. There is no expansion or compression perpendicular to the twin boundary included in the structure. The good fitting demonstrates that the planar defects are indeed twins, and intrinsic and extrinsic stacking faults with the structures as shown in figure 2.

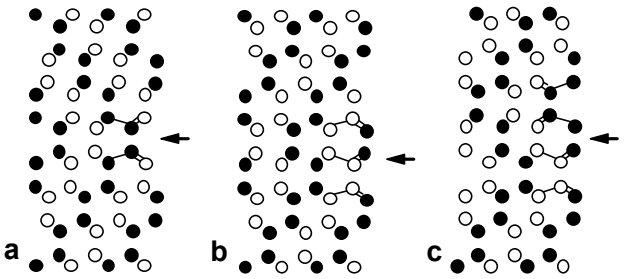

Fig. 2 $[1\bar{1}0]$ projections of the structures of: (a) a lamellar twin boundary; (b) an intrinsic stacking fault; (c) an extrinsic stacking fault.

We now turn to the effects of these planar defects on the properties of the thin films. First-principles calculations have shown that both intrinsic and extrinsic stacking faults produce some very shallow defect states [5]. However, no deep defect states were found. The main reason is that there are no wrong or dangling bonds across these defects. Nonetheless, these structural defects may interact with point defects and thus affect dislocation motion, vacancy migration, and impurity diffusion. Using first-principles total energy calculations, we studied the interaction between the planar defects and vacancies, and oxygen impurities. We first calculated the total energies of supercells containing a vacancy at the defects and at the bulklike region. We found that the formation energy of a vacancy at an intrinsic and an extrinsic stacking fault is lowered by 0.13 and 0.07 eV respectively, compared to that of the crystal site, while a lamellar twin does not change the formation energy. This indicates that stacking faults attract vacancies. Our result of the vacancy at the intrinsic stacking faults is consistent with a recently reported calculation [6].

We then calculated the differences in formation energies of oxygen interstitials in the bulk and at the defects. Oxygen is an important impurity in Si. Oxygen impurites are very mobile at temperatures in the 400 - 500 °C range and can form a family of distinct "thermal" double donor defects. The normal position of an oxygen interstitial in a Si lattice is shown in figure 3. We found that the formation energy of an oxygen interstitial at the intrinsic stacking faults is higher by 0.17 eV than that in the bulk; whereas it is 0.18 eV lower at the extrinsic stacking faults than that in the bulk. This means that intrinsic stacking faults will repel oxygen impurities, but the extrinsic stacking faults will attract oxygen. At the lamellar twin, the formation energy of an oxygen interstitial is only 0.08 eV higher than that in the bulk, indicating less interaction with oxygen impurities.

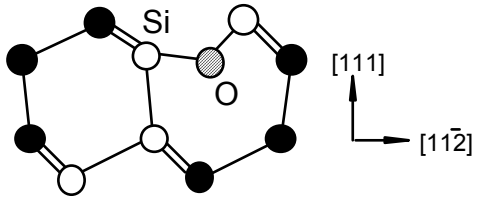

Fig.3 Projection of a Si lattice on a $(1\bar{1}0)$ plane showing the position of an O interstitial.

4. References

[1] T. H. Wang and T. F. Ciszek, J. Electrochem. Soc., **147**, 43 (2000).

[2] P. A. Stadelmann, Ultramicroscopy **21**, 131 (1987).

[3] G. Kresse and J. Hafner, Phys. Rev. B **47**, RC558 (1993).

[4] S. Amelinckx and J. Van Landhuyt, Diffraction and Imaging Techniques in Materials Science. Edited by S. Amelinckx, R. Gevers, and J. Van Landhuyt (North-Holland Publishing Company, Amsterdam, The Netherlands, 1978), p.107.

[5] M. Y. Chou, M. L. Cohen, and S. G. Louie, Phys. Rev. B **32**, 7979 (1985).

[6] A. Antoneli, J. F. Justo, and A. Fazzio, Phys. Rev. B **60**, 4711 (1999).

All Hot-Wire Chemical Vapor Deposition a-Si:H Solar Cells

E. Iwaniczko, Q. Wang, Y. Xu, B. P. Nelson, A. H. Mahan, R. S. Crandall, and H. M. Branz

National Renewable Energy Laboratory
1617 Cole Blvd., Golden, CO, 80401 USA

ABSTRACT

Efficient hydrogenated amorphous silicon (a-Si:H) nip solar cells have been fabricated with all doped and undoped a-Si:H layers deposited by hot-wire chemical vapor deposition (HWCVD). The total deposition time of all layers, except the top ITO-contact, is less than 4 minutes. On an untextured stainless steel (SS) substrate, an initial efficiency of 7.12% is reached, with a stable efficiency of 5.4% after 1000 hours 1 sun light soaking. This initial efficiency is reached by incorporating into the p/i interface about 60Å of intrinsic a-Si:H "edge" material grown at conditions near the transition to microcrystallinity. As a result, the cell's fill factor increases from 0.60 to 0.68 and the best open-circuit voltage is about 0.88 V. Using textured Ag/ZnO-coated SS supplied by United Solar Corporation, preliminary cell fabrications on textured SS have given an all-HWCVD initial efficiency record of 8.7 %.

1. Introduction

Increasing the throughput of efficient hydrogenated amorphous silicon solar cell fabrication is an important issue relating to production costs. One method to increase the factory throughput is to increase deposition rates. The best plasma enhanced chemical vapor deposition (PECVD) a-Si:H solar cells are currently fabricated at a deposition rate of about 1 Å/s, giving a total fabrication time of about 40 minutes (2300Å i-layer). Increasing the deposition rate beyond 1 Å/s has been attempted using PECVD [1] at 3-6 Å/s and HWCVD [1,2] at 18-20 Å/s. High deposition rates, in general, will reduce the device performance.

One of the advantages of HWCVD is the high deposition rate, not just for the intrinsic layer (i-layer) but also for all other dopant layers. In previous "hybrid" HWCVD solar cell research , all the dopant layers (n- and p-layers) were deposited by PECVD at about 1 Å/s and the i-layer by HWCVD at about 20 Å/s. For such "hybrid" solar cells, the throughput has already been increased by about a factor of 10 compared to those of PECVD devices, since the i-layer is by far the thickest device layer. However, when depositing all layers by HWCVD, the already shortened deposition time can be further reduced. In this work we describe the fabrication and properties of all-HWCVD a-Si:H nip solar cells made in less than 4 minutes, compared to the "hybrid" HWCVD cells with a total deposition time of 17 minutes.

2. Experimental and Results

A two-chamber load-locked system was used to fabricate all-HWCVD nip solar cells. One chamber (i-chamber) is used only for intrinsic a-Si:H deposition. The other chamber (dopant chamber) is used to grow the "edge" materials (e-layer) and both n- and p-type dopant layers. The details of this HWCVD reactor are reported elsewhere [3]. In both chambers, we use a spiral tungsten wire with a diameter of 0.5 mm, a length of 24 cm, and place it 5 cm below the substrate. The tungsten filament is heated to about 2000°C using an AC current. A process gas passes by the hot filament, dissociates on the filament, and leads to Si/H deposition on the substrate. With the aid of the load-lock chamber, the substrate can be transported without an air break between the two deposition chambers, thus ensuring the production of atomically clean interfaces.

The solar cell is deposited on a SS substrate with the structure SS/niep/ITO, where "e" denotes "edge" material. The n-layer is first made in the dopant chamber at a substrate temperature (T_{sub}) of ~300°C. The substrate is then transferred to the i-chamber for i-layer deposition at a T_{sub} of 320° to 360°C. Finally, the substrate is transferred back to the dopant chamber for e-layer and p-layer deposition at T_{sub} of 200°C. The thickness of each layer in a solar cell (see Table I) is estimated from the deposition rate of each layer grown on a glass substrate under the same deposition conditions. The top contact is 600 Å of indium tin oxide (ITO) deposited by reactive thermal evaporation, typically with a sheet resistance of 100 ohm/sq and 87% transmittance. The solar-cell performance is measured with a computer-interfaced JV station (XT-10) under 1-sun illumination (Xenon lamp). Light soaking of the solar cells is made under a 1- sun ELH light source.

We now describe the properties of the individual solar cell layers, which have been first evaluated using (thicker) films on glass or c-Si substrates. For the a-Si:H n-layer, PH_3 (3% in H_2) is used as the dopant gas which is mixed with SiH_4. Good n-layer properties with a conductivity of 2 $x10^{-2}$ S/cm and optical gap (E_{04}) of 1.88 eV are easily achieved with a high deposition rate of 11 Å/s. Also, the growth conditions for obtaining such good properties are quite broad. The film thickness used for the evaluation is about 2000 Å. The characteristics of HWCVD growth of a-Si:H are high T_{sub} (320 to 360°C), low pressure (12 mT), and high deposition rate (18-20Å/s) when compared to PECVD. Typical properties of this HWCVD i-layer are an

E_{04} of 1.89 eV, a low H-content of 3% to 6%, a low saturated defect density of 2 to 4 $x10^{16}$ (cm^{-3}), a dark conductivity $<10^{-10}$ S/cm, and a conductivity ratio (1-sun to dark) $> 10^5$. The film thicknesses used for these evaluations are between 0.5 and 1 μm.

The "edge" materials near the transition from a-S:Hi to μc-Si are made using high hydrogen dilution [4-8]. The film thickness used for the evaluation is about 2000 Å. Extensive measurements of material properties have been published elsewhere [9-11]. The phase (a-Si:H or μc-Si) of these materials can be easily determined from x-ray, Raman, or UV-reflectance spectroscopies. The structure and most of the properties of these materials are still a-Si:H like. The optimum growth conditions of these materials depends not only on the deposition parameters, but also on the film thickness and choice of substrate. It is worth noting that a-Si:H turns into μc-Si at the H_2 to SiH_4 ratio of 2 to 3 on a glass substrate when using HWCVD. This dilution is much lower than the transition ratio in PECVD, probably because a large amount of atomic hydrogen is generated by the filament during silane decomposition. The deposition rate of this edge material is 4 Å/s. Finally, for the HWCVD p-layer, TMB (5% in He) gas is used as the dopant gas. With an H_2 to SiH_4 ratio of 16, a series of p-layers was made by varying the TMB flow rate from 1 to 7 sccm. The film is μc-Si when the TMB flow is less than 3 sccm and turns to a-Si:H when the flow is greater than 4 sccm. The TMB flow we used was 6 sccm.

Table 1. Comparison of all HWCVD to "hybrid" devices

Layers	All-HWCVD phase•thk.•time•rate	"Hybrid" (HW- & PECVD) phase•thk.•time•rate
n	a-Si•200Å•20s•10Å/s	* a-Si•400Å•4m•1.7 Å/s
i	a-Si•2500Å•2.5m•20 Å/s	a-Si•2500Å•2.5m•20 Å/s
Interface	edge-Si•60Å•15s•4 Å/s	* H_2 Plasma•10min
p	edge-Si•130Å•30s•4.3 Å/s	* a-Si•100Å•1min•1.6 Å/s
Tot. Time	3.5 min	17.5 min

* = PECVD layers

Turning now to the solar cell results, Table 1 lists the material phase, thickness, deposition time, and deposition rate of all solar cell layers for the present all-HWCVD solar cell as well as the "hybrid" solar cell. As can be seen, our all-HWCVD solar cell takes advantage of the high deposition rate, and we achieved 3.5 minute total deposition time for all the layers that contain Si. It simplifies the process procedure by replacing the 10 minute PECVD H plasma treatment with a 15 second HWCVD e-layer deposition.

Table 2. HWCVD Solar Cell Performance on flat SS

Cell Type	LS State	V_{oc} (V)	FF	J_{sc} (mA/cm^2)	Eff.
All-HW	Initial	0.877	0.688	11.90	7.19
	1000 hr	0.817	0.572	11.74	5.48
Hybrid (HW-PE)	Initial	0.850	0.666	10.21	5.74
	1000 hr	0.830	0.572	10.20	4.86

Table 2 summarizes the best performance of both HWCVD nip solar cells on untextured, bare SS substrates. The best all-HWCVD cell has an initial efficiency of 7.19% with a V_{oc} of 0.88 V, a FF of 0.688, and a J_{sc} of 11.9 mA/cm^2. The best efficiency after 1000 hours 1-sun light soaking is 5.48%. When compared to the "hybrid" cell, the all-HWCVD cell demonstrates an improvement in all the initial cell performance parameters. We transferred the best recipe to a textured Ag/ZnO back-reflector substrate supplied by United Solar Corp., and obtained an all-HWCVD record initial efficiency of 8.7 %.

3. Summary

Efficient high throughput all-HWCVD a-Si:H niep solar cells have been demonstrated. All layers that contain Si were finished within 4 minutes. This reduction results from reducing the n-layer and p-layer deposition times as well as replacing a long PECVD hydrogen treatment at the p/i interface with a short deposition of "edge" a-Si:H layer material. Applying this e-layer to HWCVD solar cells is the key to the improvement of cell efficiency. Initial efficiencies of 7.12% and 8.7% were reached on untextured and textured SS substrates, respectively.

4. Acknowledgements

Authors would like to thank J. Yang and S. Guha at United Solar Inc for invaluable help. This work is supported by DOE subcontract DE-AC02-83CH10093.

5. Reference

[1] A. H. Mahan, R. C. Reedy Jr., E. Iwaniczko, Q. Wang, B. P. Nelson, Y. Xu, A. C. Gallagher, H. M. Branz, R. S. Crandall, J. Yang, and S. Guha., Mat. Res. Soc. Symp. Proc., Vol. **507**, p. 119 (1998).
[2] Q. Wang, E. Iwaniczko, Y. Xu, B. P. Nelson, and A. H. Mahan, Mat. Res. Soc. Symp. Proc., Vol. **557**, p. 163 (1999).
[3] B. P. Nelson, R. S. Crandall, E. Iwaniczko, A. H. Mahan, Q. Wang, Y. Xu, and W. Gao; Mat. Res. Soc. Symp. Proc., Vol. **557,** p. 97 (1999).
[4] J. Yang, S. Sugiyama, and S. Guha, Mat. Res. Soc. Symp. Proc., Vol. **507,** p. 157 (1998).
[5] D. V. Tsu, B. S. Chao, S. R. Ovshinshy, S. Guha, and J. Yang, Appl. Phys. Lett. **71**, 1317, 1997.
[6] L. Yang, L. Chen, S. Wiedemann and A. Catalano, Mat. Res. Soc. Symp. Proc., Vol. **283**, p. 462 (1992).
[7] J. Yang, and S. Guha, Mat. Res. Soc. Symp. Proc., Vol. **557**, p. 239 (1999).
[8] J. Koh, Y. Lee, H. Fujiwara, C. R. Wronski, and R. W. Collins, Appl. Phys. Lett. **73**, 1526, 1998.
[9] D. Han, G. Yue, J. D. Lorentzen,, J. Lin, H. Habuchi, and Q. Wang, J. Appl. Phys. in press 2000.
[10] Q. Wang, G. Yue, J. Li, and D. Han, Solid State Commun. **113**, p.175, 1999.
[11] G. Yue, J. D. Lorentzen, J. Lin, D. Han and Q. Wang, Appl. Phys. Lett., **75**, 492, 1999.

A Numerical Simulation of Hot-Wire Chemical Vapor Deposition of Si in SiH_4 and SiH_4:He Ambients

J. K. Holt, M. Swiatek, D. G. Goodwin, and Harry A. Atwater
Thomas J. Watson Laboratories of Applied Physics
California Institute of Technology
Pasadena, CA 91125

ABSTRACT

A numerical simulation is being used to determine the set of parameters optimal for high rate growth of high quality polycrystalline silicon via hot-wire chemical vapor deposition (HWCVD). The method used is direct simulation Monte Carlo (DSMC) [1]. Model predictions, such as species profiles, are found to be consistent with experimental observations.

1. Introduction

Synthesis of large-grained polycrystalline silicon at low temperatures and high throughput is critical to enabling a future thin-film silicon photovoltaics technology. To this end, a numerical simulation of the HWCVD reactor is being used explore mechanistic questions and to optimize growth conditions for speed, quality and uniformity. The simulation uses the DSMC technique, a particle-based (i.e. not individual molecule) method that is advantageous in low pressure regimes where gas mean free paths are smaller than the wire-to-substrate separation. In addition, the Chemkin [2] package is used to provide kinetic, thermodynamic, and transport properties.

2. One-dimensional Simulation

To concentrate on the relevant chemistry and transport involved in HWCVD, a simplified one-dimensional model was initially used, consisting of a hot-wire surrounded by a concentric cylindrical substrate. Although the model consists of a total of 15 species and 19 reversible reactions, a simplified chemistry scheme consisting of only bimolecular reactions was chosen, a portion of which is shown in Table 1.

Table 1. Bimolecular gas-phase chemistry included in the DSMC model. The rate constant is given by: $k = Aexp(-E_a/RT)$, with units given in moles, cm, and cal.

Reaction	A	E_a
(1) $SiH_4 + H \leftrightarrows SiH_3 + H_2$	7.8E14	4491
(2) $SiH_4 + SiH_2 \leftrightarrows H_3SiSiH + H_2$	1.3E13	0
(3) $SiH_2 + SiH_2 \leftrightarrows Si_2H_2 + H_2$	6.5E14	0
(4) $SiH + H_2 \leftrightarrows SiH_2 + H$	4.8E14	23640
(5) $Si + SiH_4 \leftrightarrows Si_2H_2 + H_2$	4.0E14	0

The simulated pressures were sufficiently low that collisional stabilization of 3-body reactions was considered negligible, and thus bimolecular reactions are likely the most important. Film growth is handled approximately via measured or estimated reactive sticking probabilities [3].

Fig. 1 shows selected species profiles for silicon growth in a He-diluted SiH_4 ambient, under conditions comparable to those reported by Molenbroek *et al.* [3] for growth of amorphous silicon (*a*-Si). SiH_4 is seen to be strongly depleted near the wire, while highly reactive species such as Si and H are depleted near the simulated substrate (located at 1.5 cm); such results are consistent with experiment. SiH_3 was

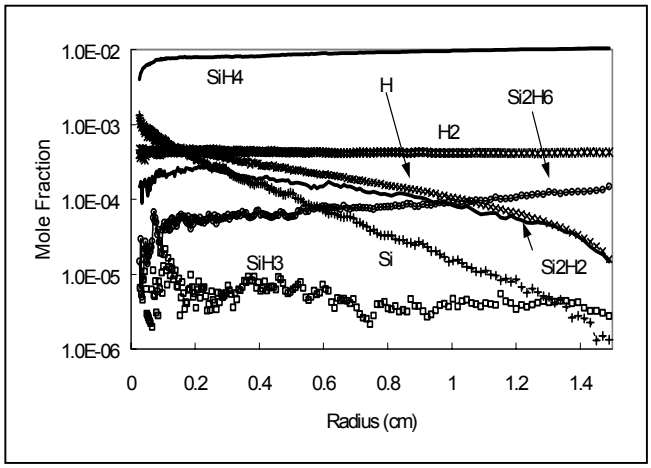

Fig. 1. Majority species profiles for 1-dimensional DSMC calculation at 40 Pa of 1% SiH_4 in He

included as it has been hypothesized as a low reactivity precursor to epitaxial film growth on hydrogenated Si (100) surfaces at temperatures as low as 195°C (dihydride surface) [4]; Si_2H_2 was also included, as it may play a similar role. Of the potential growth species, Si_2H_2 is seen to be greatest in abundance in the gas phase by a factor of 10 compared with Si. Si is a highly reactive and potentially lower quality film growth precursor at temperatures below 400°C on hydrogenated Si (100). Si has, however, been demonstrated to lead to epitaxy at temperatures in excess of 500°C, when complete H desorption occurs [5]. These results suggest that high quality film growth could result at these pressures, with an estimated growth rate of 1 Å/s, in fair agreement with experiments. At pressures substantially higher than 40 Pa, however, radical-radical recombination reactions could limit the availability of growth species and thus lower the growth rate. Thus there exists an optimal pressure regime in which pressures are high enough to form the desired low reactivity growth species with high flux, but also low enough to limit the extent of radical-radical recombination.

3. Two-dimensional Simulation

A two-dimensional DSMC code has also been used, which allows for a more realistic modeling of the near-wire region of the HWCVD reactor. In particular, the gas inlet nozzle-to-wire spacing was varied in an attempt to increase the depletion of SiH_4 and H_2; in the case of SiH_4, this should lead to higher film deposition rate. As seen in Table 2, a modest increase in depletion is observed as the nozzle is moved from its typical distance of 25mm from the wire to 1mm, a result of the higher incident flux of feed gases on the wire. The overall small depletion observed is due in part to the small physical cross-section of the wire, the dilution of SiH_4 by He, and operating in a diffusive rather than convective flow regime; these values are, however, comparable to experiment.

Table 2. Percentage depletion of feed gases

Nozzle-to-wire distance (mm)	H_2 depletion (%) (6.7 Pa H_2-13.3 Pa He)	SiH_4 depletion (%) (0.2 Pa SiH_4-16.8 Pa He)
1	2.4	3.3
25	1.8	2.1

It has been experimentally observed that deposited silicon films are of variable thickness, with the region nearest the wire being the thickest. Two-dimensional simulation can model this effect, and, in particular, for conditions of pure SiH_4 at a pressure of 75 Pa, and a wire-to-substrate separation of 2.5 cm, roughly a factor of 3 increase in SiH_3 (the dominant growth species at this pressure) flux

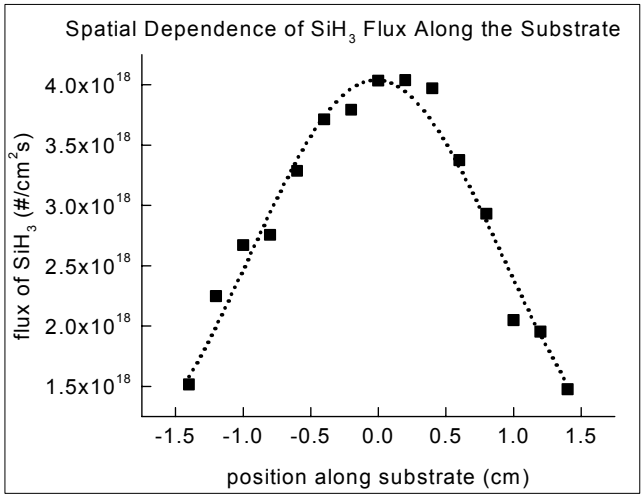

Fig. 2. SiH_3 flux under conditions of 75 Pa of pure SiH_4

is seen from the edge to the substrate center, located 1.5 cm away, as illustrated in Fig. 2. At wire-to-substrate distances much larger than the substrate diameter, the flux is more uniform, although the growth rate is lower as well (decreasing roughly as 1/r). In large-scale application of HWCVD, it would be desirable to eliminate such non-uniformity, while retaining a high growth rate.

Fig. 3 illustrates the distribution of SiH_3 in the near-wire region for conditions of pure SiH_4 at 1.3 Pa. SiH_3 is seen to be depleted near the substrate where it deposits, and its

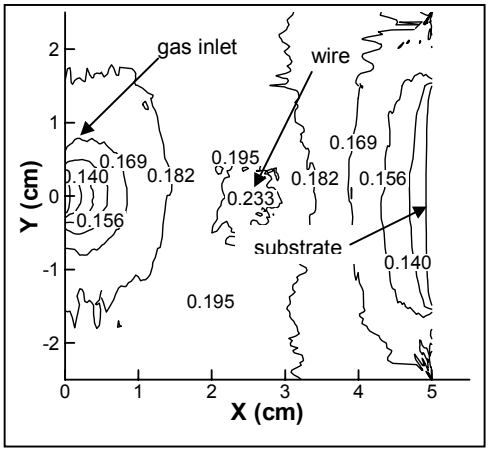

Fig. 3. Mole fraction of SiH_3 in the near-wire region, for a 1.3 Pa pure SiH_4 ambient

concentration remains substantial (~0.2 mole fraction) at theother two walls located at y = ±2.5 cm (where it is notassumed to stick). As mentioned previously, diffusive conditions prevail in the reactor, suggesting that it may be advantageous to place substrates along these other two walls.Alternatively, in the convective flow regime, a single substrateplaced downstream of the nozzle would allow for higher rategrowth in this direction, compared with the parallel walls.

4. Conclusions

The present modeling work has demonstrated that species suspected to play a role in polycrystalline or epitaxial growth are present under typical growth conditions. To increase the SiH_4 depletion and thus the growth rate in HWCVD silicon growth, a reduction in the gas nozzle-to-wire distance was found to be effective. In addition, spatial non-uniformity in growth species flux was modeled by the two-dimensional simulation. Finally, growth species profiles revealed that reactor flow is in the diffusive rather than convective regime, leading to uniform deposition on areas other than the substrate.

REFERENCES

[1] G. Bird, *Molecular Gas Dynamics and the Direct Simulation of Gas Flows* (Oxford University Press, 1994).
[2] R. Kee, F. Rupley, and J. Miller. "Chemkin-II: A Fortran Chemical Kinetics Package for the Analysis of Gas-Phase Chemical Kinetics". Technical Report SAND89-8009, Sandia National Laboratories.
[3] E. Molenbroek, A. Mahan, E. Johnson, and A. Gallagher, J. Appl. Phys. 79, 7278 (1996).
[4] J. Thiesen, E. Iwaniczko, K. Jones, A. Mahan, and R. Crandall, Appl. Phys. Lett. 75, 992 (1999).
[5] S. Wolff, S. Wagner, J. Bean, R. Hull, and J. Gibson, Appl. Phys. Lett. 55, 2017 (1989).

a-Si:H Grown by Hot-Wire CVD at Ultra-High Deposition Rates

Y. Xu, B.P. Nelson, A.H. Mahan, R.S. Crandall, E. Iwaniczko, Q. Wang

National Renewable Energy Laboratory

1617 Cole Blvd., Golden, CO 80401

D.L. Williamson

Colorado School of Mines

Golden, CO 80401

ABSTRACT

We increase the deposition rate of growing hydrogenated amorphous-silicon (a-Si:H) by the hot-wire chemical vapor deposition (HWCVD) technique by adding filaments (two) and decreasing the filament(s) to substrate distance. Increasing the deposition pressure, silane flow rate, and filament current also increases the deposition rate. However, an optimization procedure of these parameters, including the substrate temperature, is necessary to yield films with good electronic properties. We grow a-Si:H with photo-to-dark conductivity ratios exceeding 10^5 at deposition rates up to 130 Å/s. However, other electronic properties drop off at lower deposition rates. There is also a sharp increase in the void density, as measured by small-angle X-ray scattering (SAXS), when going from one to two filaments. However, both Raman and X-ray diffraction (XRD) measurements show no change in film structure with increasing deposition rates.

1. Introduction

Typical deposition rates of a-Si:H grown in commercial applications is normally less than 3 Å/s, below 10 Å/s. Increasing the deposition rate is important in order to decrease the manufacturing costs of a-Si:H devices. Increasing the deposition rates decreases the manufacturing time, which translates directly into reducing costs. Typical a-Si:H devices are based a p-i-n structure [1] where the intrinsic layer is much thicker than the doped layers. To accommodate this in an inline manufacturing process, the chambers where the i-layers are grown are usually made longer to allow for the requisite longer deposition times. Increasing the deposition rate of the i-layer growth can also lead to shorter deposition chamber length which translates into reduced capital equipment costs.

Since one early work in using HWCVD to grow a-Si:H [2] we have used the technique to grow films that have less light-induced degradation than similar films grown by plasma-enhanced CVD (PECVD) [3]. However, it is the ability to grow quality a-Si:H at very high deposition rates relative to PECVD-grown films that prompted this work.

2. Experimental Procedures

We grow a-Si:H by HWCVD in two types of reactors; a cross reactor and a tube reactor [4]. The cross reactor consists of a standard vacuum, six-way cross with an external substrate heater, room temperature chamber walls, and the filament perpendicular to the direction of gas flow. The tube reactor consists of a resistively-heated tube in a vacuum chamber that provides an isothermal heating zone at the substrate/deposition region, with the filament parallel to the direction of gas flow. Substrates must be loaded into the cross reactor by breaking vacuum each time. The tube reactors are equipped with a load lock to prevent exposing the chamber to air upon substrate loading.

The work reported in this paper was done entirely in one of our tube reactors. Our standard tube-reactor configuration has a single tungsten filament, 0.5 mm in diameter and approximately 16 cm long, in the center of the deposition region [4]. We can increase the deposition rate of this configuration by decreasing the filament to substrate distance (L) from 5 cm to 3 cm. By making this change, and increasing the silane flow rate and the chamber pressure we are able to obtain deposition rates up to 50 Å/s. However, to increase the deposition rate beyond 50 Å/s, we had to install a second filament. These filaments sit physically parallel and the current passes through them in parallel circuit. To maximize the thickness uniformity of the films, we try to keep the spacing between the filaments equal to L, but this was not physically possible for larger L. The two filaments are symmetric along the long axis of the tube-reactor. For this study, we have grown a-Si:H from pure silane, without dilution by hydrogen or other gases. More details of the chamber configuration and deposition conditions are in reference[5].

Deposition Parameter	Range
L—filament to substrate	5 to 3.2 cm
chamber pressure	10 to 75 mT
silane flow	10 to 75 sccm
filament current	14 to 16 amps/filament
substrate temperature	300 to 400°C

Table 1: Range of deposition conditions used to grow the a-Si:H reported on in this paper.

3. Results

Figure 1 shows how the photo-to-dark conductivity ratio of these films decreases as the deposition rate increases. The ambipolar diffusion length—as measured by the steady-state photo-grating technique—shows a similar decrease with increasing deposition rate from over 1,400 Å

at 17 Å/s to ~1,000 Å at 110 Å/s. The defect density (Nd_{CPM}) and Urbach energies (E_U) as measured by the constant photo-current method (CPM) do not reflect such a monotonic trend with deposition rate. Those films grown at <40 Å/s have similar Nd_{CPM} ($3\text{-}5 \times 10^{15}$ cm^{-3})and E_U (45-47 meV). There is then a big change and all the films grown at >40 Å/s also have similar Nd_{CPM} ($1\text{-}1.5 \times 10^{16}$ cm^{-3}) and E_U (52 meV). Rather than a monotonic change with deposition rate, these parameters seem to be in two groupings with the break being at 40 Å/s. For more details on the electrical properties of these materials, see reference [5].

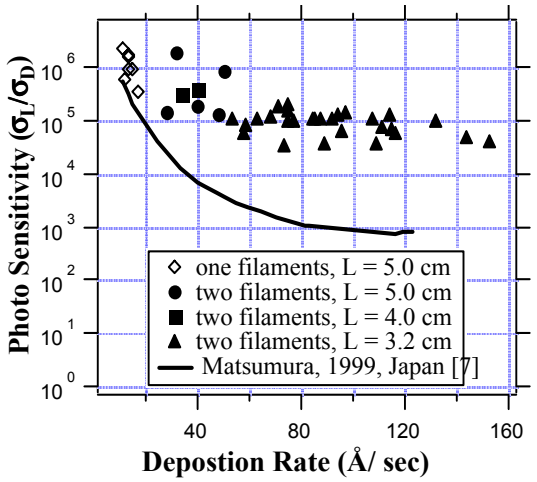

Figure 1: Changes in the photo response of a-Si:H grown at increasing deposition rates.

The degree of heterogeneity on nanometer scale as determined by SAXS follows a similar trend to the CPM measurements. That is, all films grown with two-filaments have an increase in the integrated-SAXS intensity by about a factor of 50 greater than those grown with a single filament at ~10 Å/s (from 0.05 to $\sim 2.5 \times 10^{24}$ eu/cm^3). Again, there is a clustering of the data in this range rather than a monotonic change with deposition rate. The degree of heterogeneity is associated with voids in the material; the larger the integrated SAXS intensity, the larger the void fraction of the film. Increasing the substrate temperature to 415°C can reduce the degree of heterogeneity in these high deposition-rate films by a factor of five, but does not reduce the single filament values. The void density of these high deposition-rate films amounts to about one percent.

The structural measurements as determined by other measurements do not show this trend of having a significant change when going to two filaments. Both XRD and Raman measurements show almost no change between films grown with one filament at deposition rates below 20 Å/s and those grown with two filaments at deposition rates over 130 Å/s. The full width at half maximum (FWHM) of the X-ray peak is related to the degree of medium-range order in the film. These films have a FWHM peak of 5.44° ± 0.05 of 2θ from 17 all the way up to 144 Å/s. These values are about 15% lower than those for state-of-the-art a-Si:H films grown by PECVD; indicating that these films have a higher degree of medium-range order. For more details on how the increase in deposition rate influences the structural properties of the resulting films, see reference [6].

4. Discussion

The dramatic change in some film properties at relatively low deposition rates (over the range investigated) indicates that there are significant differences in film growth below 40 Å/s and above that rate. However, these differences may not significantly limit the use of these high deposition rate materials in devices. The relatively small changes in some electronic properties (especially in the photo response) with increasing deposition rate is extremely encouraging.

The increase in void density as measured by SAXS does not correlate with the relatively small changes in the structure of the material as measured by both XRD and Raman. It may be that the growth mechanism responsible for void formation may not necessarily affect the tissue growth, giving rise to films with a high degree of medium-range order that have a high void density. If the tissue around the voids is of sufficient electronic quality, this technique may yield films adequate for device applications.

5. Conclusion

The results of this work are very encouraging. To maintain a photo-to-dark conductivity ratio in excess of 10^5 at deposition rates up to 130 Å/s is remarkable and far exceeds the results of any high deposition-rate research of which we are aware (see reference in Figure 1). Our future work will include further optimization of a-Si:H grown under these conditions as well as incorporating these materials into solar cells.

6. Acknowledgements

We gratefully acknowledge measurements made by John Perkins from National renewable energy Laboratory and Milan Vanecek from the Czech Republic. We also gratefully acknowledge the encouragement of Howard Branz to do this work. This work is supported by the U.S. Department of Energy under Contract No. DE-AC36-99GO10337.

7. References

[1] D.E. Carlson and C.R. Wronski, *Appl. Phys. Lett.* **28**, 671 (1976)
[2] A.H. Mahan, J. Carapella, B.P. Nelson, R.S. Crandall, and I. Balberg, Journ. Appl. Phys., 69, 6728 (1991)
[3] A.H. Mahan and M. Vanecek, Amer. Inst. of Phys. Conf. Proc. 234, (AIP, New York, 1991), p.195. .
[4] B.P. Nelson, R.S. Crandall, E. Iwaniczko, A.H. Mahan, Q. Wang, Y. Xu, and W. Gao, , *Mat. Res. Soc. Symp. Proc*. Vol. 557, MRS, Warrendale, PA, (April, 1999).
[5] B.P. Nelson, Y. Xu, A.H. Mahan, R.S. Crandall, E. Iwaniczko, and Q. Wang, Mat. Res. Soc. Symp. Proc. in press, MRS, Warrendale, PA, (April, 2000).
[6] A.H. Mahan, B.P. Nelson, Y. Xu, D.L. Williamson, M. Vanecek, R.S. Crandall, being submitted to Appl. Phy. Rev. Letters.
[7] Matsumura, CAT-CVD PVSEC satellite pre-workshop, Sept. 1999, unpublished.

Characterization for the Onset of Crystallization of Amorphous to Microcrystalline Silicon by Optical Spectroscopies

Guozhen Yue[1], Daxing Han[1], G. Ganguly[2], Qi Wang[3] Jeffrey Yang[4], and Subhendu Guha[4]

1. Dept of Physics & Astronomy, University of North Carolina at Chapel Hill, Chapel Hill, North Carolina 27599-3255, USA.
2. BP Solarex, 3601, LaGrange Parkway, Toano, VA 23168, USA. 3. National Renewable Energy Laboratory, 1617 Cole Blvd. Golden, CO 80401, USA. 4. United Solar Systems Corp., 1100W Maple Road, Troy, Michigan 48084, USA

ABSTRACT

We study the a- to μc-Si films made at three laboratories by using Raman, photoluminescence- and optical-absorption spectroscopies. Raman spectra show no signature of the c-Si peak in most samples. Whereas, low energy PL enhancement was observed in films containing small density μc-Si.

1. Introduction

To improve stability of a-Si:H, the edge material, i.e. amorphous (a) near the onset of microcrystalline (μc) has attracted attention.[1-3] Both PECVD with H-diluted gas and HWCVD have been used in the production of a-Si:H solar cell and thin-film transistors. Furthermore, evidence of μc-Si was found in films deposited with a high growth rate without H-dilution by PECVD.[4] To understand the correlation between deposition conditions, the film microstructure and its electronic properties, we studied numbers of the edge-films made by using Raman, photoluminescence- (PL) and optical-absorption spectra.

2. Samples and Results

Table I HWCVD samples deposited on glass

Sample ID	H_2/SiH_4(R)	XRD	Thickness(mm)	Dep. rate(Å/s)
1	1:1	a-Si	4.1	17.2
2	2:1	a-Si	3.0	12.5
3	3:1	a-+μc	1.7	7.1

Table II PECVD samples with H-dilution on ss

Sample ID	Substrate surface conditions	Thickness (μm)
10306	ss/i	0.5
10307	ss/n/i	0.5
10311	ss/n/i	1.5
10857	ss/textured Ag/ZnO/i	0.5
10859	ss/textured Ag/ZnO/n/i	0.5
10858	ss/textured Ag/ZnO/n/i	1.5
9883	ss/i	1.4

Table III PECVD samples deposited on c-Si and quartz

Sample ID	Substrate	H(sccm)	rf power (W)	d (μm)	Rate(Å/s)
12465	c-Si	none	100	2.33	16.2
12467	c-Si	none	60	1.60	10.3
12469	c-Si	none	10	1.69	2.8
12451	quartz	none	20	2.13	14.9
12464	quartz	120	100	2.10	15.22
12466	c-Si	120	60	1.90	10.55
12468	c-Si	120	20	1.64	2.5

Table I lists films deposited by HWCVD with H-dilution ratio 1≤R≤3. Films in Table II contain three structures which are identical to those edge materials studied by X-ray diffraction (XRD) and the transient photocapacitance (TPC) technique[1]. Table III lists films grown at high rates; μc- in the a-Si:H matrix was found by TPC measurements in most films[4]. Figs. 1(a) and (b) demonstrate the optical absorption and PL spectra for the a- to μc-Si transition materials listed in Table I. When the H-dilution ratio R= 1 and 2, no c-Si peak can be seen in both XRD and Raman. Meanwhile both the a(E) and PL spectra show a-Si:H-like features, whereas, an extra band at ~1.2 eV is clearly seen in the a(E) spectra as shown in Fig. 1(a). At R=3, XRD shown a c-Si component, the 520 cm^{-1} c-Si Raman peak appeared.[5] Meanwhile, a low energy PL band peaked at ~1.0 eV appears and the a(E) spectrum became poly-Si-like. The typical features of μc- are: a low energy PL band at~1.0 eV which is corresponding to the optical absorption band peaked at~1.2 eV.

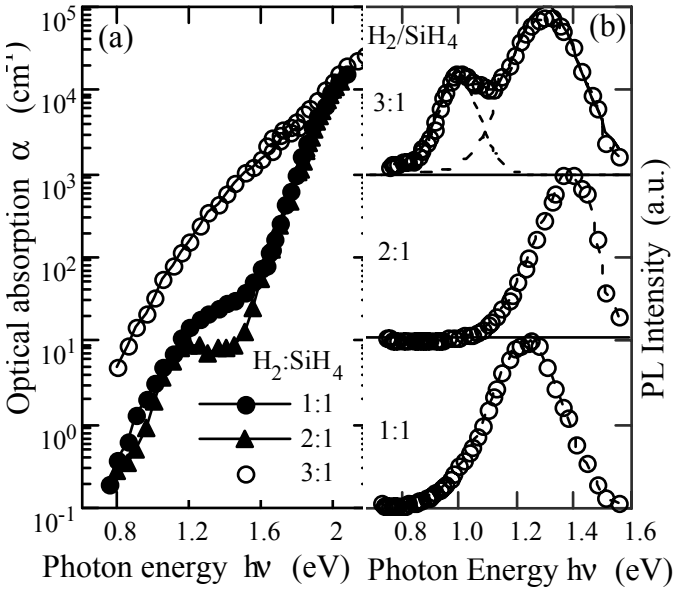

Fig. 1 (a) Optical absorption spectra and (b) PL for a-to μc-Si

For the edge materials listed in Tables II and III, we expected to see most of them contain the 520 cm^{-1} peak in Raman; the results in Fig. 2(a) showed only the a-Si:H peak centered at 480 cm^{-1} except for sample #9883 as shown in Fig. 2(b). We double checked the films listed in Table II by XRD.[6] In consistence with the Raman results, there was no c-Si peak in all six films but only film #9883 was.

However, we found μc-features in PL lineshape in above films. Fig. 3(a) shows the substrate effects, i.e. the low energy PL enhancement in the film grown on ss substrate. Fig. 3(b) shows thickness effects studied by varied PL excitation wavelengths on film #9883 which shows c-Si peak in Raman.The absorption depth is about 140, 600, 800 Å and

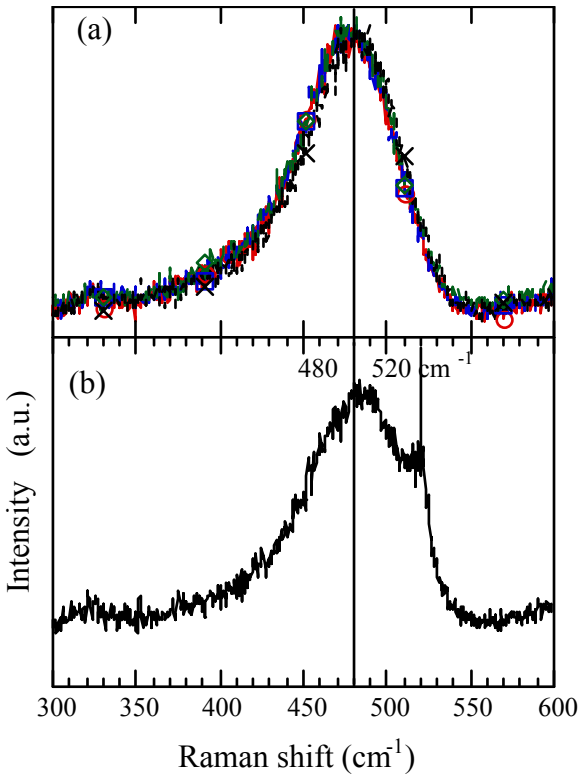

Fig. 2 Raman spectra (a) for all films listed in Tables II and III except (b) for #9883 listed in Table II

1 µm for the 325, 488, 514, and 632 nm laser in a-Si:H. As the examined layer moved to the top surface, the low energy PL was enhanced. The results imply that the structure tends to µc as the film grows thicker. Fig. 3(c) shows the PL spectra for the films deposited with the same H-dilution but varied deposition rate. The PL intensity decreases as the growth rate decreases due to µc. Meanwhile, the PL peak energy decreases from~1.3 to 1.18 eV in sample #12468, that is the film with highest µc in the TPC measurement[4].

3. Summary

For a number of a/µc films, Raman spectra showed no c-Si peak. Because that (a) growing near the a-µc transition, the resulting film properties are very sensitive to the film thickness and substrate material, so the results may not be the same unless one studies the same piece of sample; and (b) if the c-Si-grain volume fraction is only a few percentage or the grain size is ≤3 nm, it is below the technical limitation of Raman[7]. Whereas, low energy PL enhancement was observed in films containing small density µc-. The electronic density of states measured by PL and a(E) is more sensitive to the characterization of onset µç. Furthermore, the excitation wavelength dependence of PL can be used to study the non-uniformity along the growth direction.

Acknowledgments

The work at UNC and United Solar, was supported by NREL sub-subcontract under thin film PV partnership, XAK-8-17619-11, ZAK-817619-09, respectively. Wang is supported by DOE subcontract DE-AC02-83CH10093.

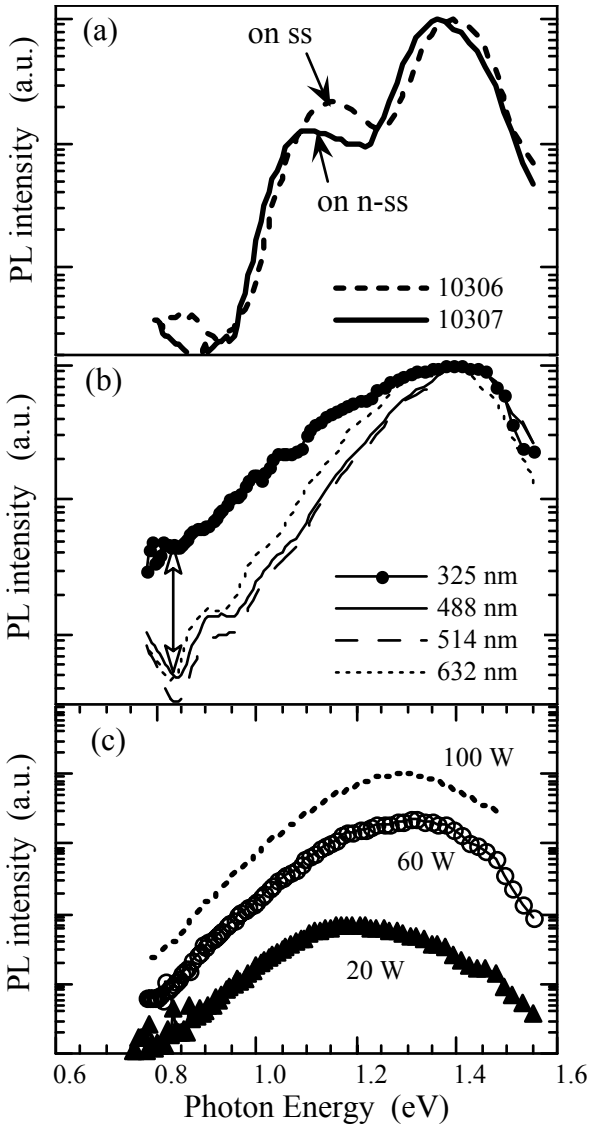

Fig. 3 PL spectra (a) for the 0.5-µm i-layer with and without an n-layer on ss substrate, (b) dependence on the excitation wavelength in a 1.4-µm thick a-/µc-Si film, and (c) as function of rf power for H-diluted films 12464, 12466, and 12468 listed in table III.

References

1. S. Guha, J. Yang, D.L Williamson, Y. Lubianiker, J. D. Cohen, A, H. Mahan, Appl. Phys. Lett., **74**, 1860 (1999).
2. J.Koh, A.S. Ferlauto, P.I. Rovira, C,R. Wronski, and R.W. Collins, Appl. Phys. Lett. **75**, 2286 (1999).
3. A.M. Brockhoff, E.H.C. Uiiersma, H. Meiling, F.H.P.M. Habraken, and W.F. van der Weg, Appl. Phys. Lett. **73**, 3244 (1998).
4. Y. Lubianiker, Y. Tan, J.D. Cohen and G. Ganguly, MRS Symp. Proc.(1999); ICAMS-18 (1999).
5. Daxing Han, Guozhen Yue, J. D. Lorentzen, Jing Lin, H. Habuchi, and Qi Wang, to be published in J.Appl. Phys. **87**, 1882 (2000).
6. XRD was examined by D.L. Williamson.
7 .S. Veprek, F.A. Sarott, and Z. Iqbal, Phys. Rev. **B36**, 3344 (1987).

Deposition of Device-Quality Amorphous Silicon Films with a New "Hot Wire" CVD Technique

Scott Morrison, Wenjie Song, Ken Coates, Arun Madan

MVSystems, Inc.

17301 W. Colfax Ave. Suite 305 Golden, CO, USA 80401

ABSTRACT

For the "Hot Wire" chemical vapor deposition technique (HWCVD) method to be applicable for photovoltaic applications, certain critical technical issues need to be addressed and resolved such as filament lifetime and reproducibility. We have developed a new approach (patent applied for) that addresses some of these problems, specifically longevity of the filaments and reproducibility of the materials produced. The new filament material used has so far shown no appreciable degradation even after deposition of 500 μm of amorphous silicon (a-Si). We report that this can produce "state-of-the-art" a-Si. These materials have been incorporated into p/i/n device structures, and are compared with similar films and devices deposited by the conventional HWCVD technique using tantalum wire. The development of microcrystalline silicon materials and devices is also discussed.

1. Introduction

"Hot Wire" chemical vapor deposition (HWCVD) technique has attracted a considerable amount of attention in the last few years because of, (1) the possibility of producing a low concentration of H in the SiH alloys with a view towards reducing or eliminating the instabilities in the material, (2) the possibility of obtaining a high deposition rate and (3), the fabrication of low temperature poly-crystalline silicon. The technique was first demonstrated by Matsumura [1], in which SiH_4 and H_2 gasses were decomposed by catalytic or pyrolytic reactions with a heated catalyzer placed near the substrate.

For the technique to be successful requires further developmental work, specifically in the following areas. (a) Filament: at present, the filament (usually W or Ta) diameter used is on the order of about 1 mm and its usefulness seems to be limited to about 20 μm of a-Si deposition and often less. (b) Reproducibility: its lack could result from the inevitable sag of the filaments. Further, the surface conditions and the temperature of the "Hot Wire" elements can be altered during deposition. These effects, amongst others compromise reproducibility.

We have developed a new HWCVD technique [2] which addresses some of the above concerns, and have so far deposited over 500 μm of silicon films without a noticeable change in the physical properties of the "Hot Wire" source. High quality a-Si films (intrinsic, n- and p-type) and preliminary intrinsic μc-Si films have been produced. Using SIMS technique, no significant contamination from the "Hot Wire" source has been found in the films. In this paper, we will describe the preparation and properties of the films and fabrication of devices.

2. Experimental Methods

Amorphous silicon (a-Si) films were produced in a commercially available PECVD/HWCVD system specifically designed for the thin film semiconductor market and manufactured by MVSystems,Inc. This chamber is capable of depositing in either the PECVD or the HWCVD mode of operation without breaking vacuum on 10 cm X 10 cm substrates situated on either the anode side of the RF electrode assembly (for the PECVD) or above the moveable HWCVD assembly.

In the HWCVD deposition mode, a-Si films were deposited with a silane gas flow rate of 20-100 sccm, deposition pressure in the range of 5-60 mTorr, and a substrate temperature of 240C. The "Hot Wire" elements were arranged in a grid fashion and the filament temperature was measured using a 2-color optical pyrometer to be in the range of 1650-1700 C. Microcrystalline silicon films were also deposited under conditions of high hydrogen dilution (>90%) and higher filament temperature (1900 C).

Simple solar cell structures of the type: Glass / SnO2 / p / buffer / i / n / Ag were employed. The p- and n-type materials were fabricated by the PECVD technique. The solar cell devices (with i layer fabricated using either the PECVD, HWCVD using a Ta filament or the new HWCVD technique) were deposited onto Asahi tin oxide coated glass with a transmission >80%. The Ag back contact was fabricated by thermal evaporation.

The opto-electronic, structure, and impurity properties were characterized by photo- (σ_{ph}) and dark conductivity (σ_d), FTIR, X-Ray diffraction, and SIMS techniques.

3. Results and Discussion

By using our new HWCVD technique, we have successfully and reproducibly fabricated high quality intrinsic a-Si films. Table 1 shows photo- and dark conductivity and gamma factor of films deposited by our new HWCVD technique, as well as a film deposited by a more conventional HWCVD technique using a Ta filament. The factor γ is derived from,

$$\ln(\sigma_{ph}) \alpha \gamma \ln(F) \qquad (1)$$

where F is the intensity of illumination. It should be noted that the recombination kinetics is dictated by the density of states (DOS) and as the DOS increases, γ decreases and vice versa [3,4]).

The two types of HWCVD a-Si:H films show similar characteristics, except in the FTIR measurements. The Ta-filament HWCVD film showed some slight indication of SiH_2 bonding, whereas the film deposited by the new technique showed no detectable SiH_2 bonding.

Measurement	Tantalum Filament	New Technique
Photoconductivity $(Ohm*cm)^{-1}$	8.2×10^{-5}	6×10^{-5}
Dark Conductivity $(Ohm*cm)^{-1}$	3×10^{-11}	1×10^{-10}
Gamma Factor	1.0	0.98
$E_C - E_F$ (eV)	0.82	0.81
FTIR	Detectable SiH_2 bonding	No detectable SiH_2 bonding
Hydrogen Concentration (from FTIR)	8% at.	9% at.

Table 1: Comparison of a-Si:H films deposited by two different HWCVD techniques.

The films deposited by the new technique also showed improved reproducibility when compared with films deposited by the Ta filament. Fig. 1 shows the normalized deposition rate as a function of total deposition time for both HWCVD using the new filament material and with a Ta filament. The Ta-filament-deposited films show a definite drop in deposition rate over time, and show no signs of reaching a steady-state condition even after 400 minutes of deposition. The new technique, however, shows an improved reproducibility, with the deposition rate after 250 minutes showing a steady-state deposition rate that is 90% of the initial deposition rate.

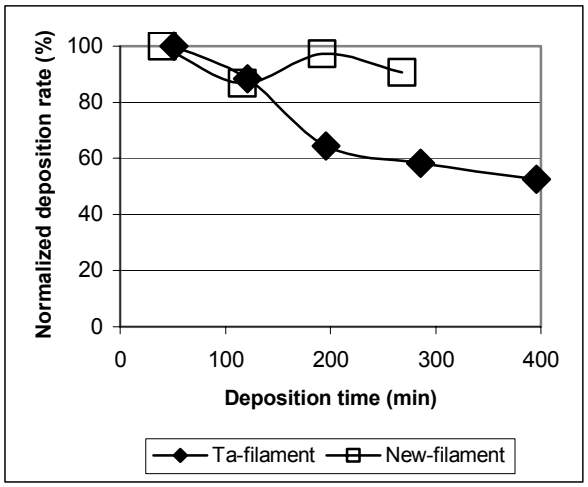

Fig. 1: Normalized deposition rate vs. total filament deposition time for HWCVD a-Si samples deposited with Ta filament (closed symbols) and new technique (open symbols)

Films deposited by both HWCVD techniques were incorporated into a simple p/i/n device structure. The results are shown in Table 2. The devices with the i-layer deposited by a Ta filament show a reasonable efficiency (7.96% as measured at NREL). A device with the i-layer deposited by the new technique shows an improved efficiency as compared with the Ta-deposited device, primarily in the V_{oc}. This indicates that the new technique is indeed capable of depositing device-quality amorphous silicon material.

	Ta filament-pin device (measured at MVS)	Ta filament-pin device (measured at NREL)	**New filament – pin device (measured at MVS)**
V_{oc} (mV)	780	825	**891**
J_{sc} (mA/cm^2)	16.41	15.65	**15.4**
FF	0.64	0.62	**0.63**
Eff.(%) (AM 1.5)	**8.19**	**7.96**	**8.64**

Table 2: Comparison of pin devices with i-layer deposited by HWCVD with Ta filament and with new material.

4. Microcrystalline Silicon Deposition

We have started work on microcrystalline silicon deposited using a Ta filament. The parameters varied so far are the hydrogen dilution and the substrate temperature, and the primary measurements made are of the average grain size and film orientation. For all of the substrate temperatures studied to date, as a function of hydrogen dilution, the amorphous-to-microcrystalline transition exhibits a strong (220) orientation in the deposited film. These films may be better for photovoltaic devices, since (220) orientation has been linked to a columnar grain structure in which the grains are oriented parallel to the primary direction of current flow.

5. Conclusions

We have shown that, using our new HWCVD technique, intrinsic amorphous silicon can be produced and their performance in simple pin structures is not too dissimilar from the corresponding Ta-filament HWCVD device. The major result here is that the films are reproducible and that in excess of 500um of deposition has been achieved without any discernible change in the "Hot Wire" source. This has a potential for large-scale development, which we are currently pursuing.

REFERENCES

[1] H. Matsumura: Jpn. J. Appl. Phys., **8B**, L1522, 1991
[2] A.Madan, J.Xi and S.Morrison, patent applied for.
[3] T. J. McMahon and A. Madan, Appl. Phys. Lett. **57**, 5302, (1985).
[4] A. Madan, and M.Shaw, The Physics and Applications of Amorphous Semiconductors (Academic Press, New York, 1988)

Development of VHF PECVD technique to prepare amorphous silicon-based multi-junction cells at high i-layer deposition rates.

S. J. Jones, T. Liu and M. Izu

Energy Conversion Devices, Inc.
1675 W. Maple Rd., Troy, MI 48084

ABSTRACT

Using a 70 MHz PECVD technique, amorphous silicon (a-Si:H) -based nip solar cells have been fabricated using i-layer deposition rates of 10 Å/s. Through optimization of a number of deposition conditions, 8.0% stable efficiencies have been achieved for single-junction a-Si:H devices. These efficiencies compare with 8.2% efficiencies obtained for devices of similar thickness made using the standard 13.56 MHz technique and the same deposition equipment. Also the performance of these devices remains relatively constant as the i-layer deposition rate is raised from 2 to 10 Å/s. Triple-junction cells with stable, total area efficiencies of 9% have been fabricated. The amount of light degradation for these cells was on average 12%, typical of what is observed for triple junction cells made using 1 Å/s i-layer deposition rates. The efficiencies for these cells are presently limited by the low currents for the amorphous silicon germanium (a-SiGe:H) bottom and middle cells.

INTRODUCTION

The benefits of using Very High Frequency (VHF) PECVD techniques to prepare amorphous silicon materials at rate as high as 10 Å/s are well documented. Several research groups [1-4] have reported higher efficiencies for cells made using frequencies of 70-100 MHz at i-layer deposition rates between 5 and 10 Å/s than for those prepared at the same rates using the rf deposition technique. The focus of this program is to test the feasibility of using a 70 MHz Very High Frequency (VHF) power signal to prepare high stable efficiency triple-junction devices at i-layer deposition rates near 10 Å/s. The 10 Å/s deposition rate is a significant increase over the 1-3 Å/s rates typically used in industry today using the rf 13.56 MHz power signal. Application of this high rate technique in ECD's roll-to-roll solar module manufacturing process will lead to reduced material costs and higher machine throughput, both of which will lower the production and product costs.

EXPERIMENTAL

The a-Si:H nip/a-SiGe:H nip/a-SiGe:H nip triple-junction solar cell structures were fabricated using a research scale, multi-chamber load locked deposition system. Stainless steel substrates coated with current enhancing Ag/ZnO back reflectors were used as the substrates for preparation of the semiconductor structures. Both the thin doped layers and the thin a-Si:H buffer layers, grown between the VHF deposited a-SiGe:H i-layers and the doped layers, were prepared using the conventional PECVD process in which a 13.56 MHz rf signal is used. The use of the lower rate process for the thin doped and buffer layers has only a small impact on the total fabrication time. To improve the cell properties, i-layer deposition conditions were altered including substrate temperature, hydrogen dilution, active gas flows and applied power.

After fabrication of the triple-junction structure, the devices were completed by depositing Indium Tin Oxide (ITO) conductive layers and then Aluminum collection grids. The cells had active and total areas of 0.25 and 0.265 cm^2, respectively. To complete light soaking studies, the cells were subjected to 600-1000 hrs. of one sun light with the cell temperature fixed at 50ºC.

RESULTS

a-Si:H

In Table I, data for single-junction a-Si:H nip cells whose i-layers were made using the VHF technique are compared with those for cells with the i-layers made using a 13.56 MHz frequency. These cells have similar i-layer thicknesses and were made without current enhancing back reflector layers. With increasing i-layer deposition rate to 10 Å/s, virtually no change in the initial cell efficiency (P_{max}) or the amount of degradation with 700 hrs. of light soaking is observed. Not shown in the table, a 5% drop in efficiency for thick a-Si:H cells made with the back reflector layers is observed due to a decrease in J_{sc}. In comparison, for the cells whose i-layers are made using the 13.56 MHz frequency, the cell efficiency decreases rapidly as the rate increases from 1 to 10 Å/s due to a sharp drop in fill factor.

Table I. Properties for a-Si:H cells.

Freq. (MHz)	Dep. Rate (Å/s)	FF	P_{max} (mW/cm^2)	% of Degr.
70	2.1	0.728	6.46	-
70	6.1	0.726	6.45	13
70	10.9	0.733	6.54	11
13.56	1	0.735	6.50	12
13.56	0.9	0.734	6.42	13
13.56	5	0.690	5.98	20
13.56	9.2	0.680	5.47	20

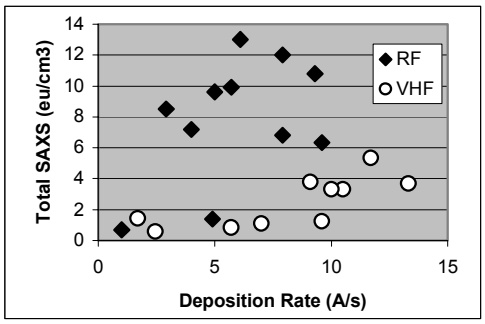

Figure 1. Small Angle X-ray Scattering as a function of deposition rate for a-Si:H films (RF=13.56 MHz, VHF=70 MHz). SAXS measurements were completed at the Colorado School of Mines.

The results from structural measurements of films made using the two different frequencies suggest that the deterioration in the fill factor with increasing deposition rate for the films made using the standard 13.56 MHz is related to changes in the film microstructure. In particular, Figure 1 shows that the Small Angle X-ray Scattering (SAXS) for the films made with the 13.56 MHz technique at deposition rates greater than 3 Å/s is on average larger than that for films made lower rates and the VHF produced films (both of which have high fill factors). The larger SAXS signals suggest that the films have larger void volume fractions.

For a-Si:H cells with Ag/ZnO back reflectors made using the VHF technique and i-layer deposition rates of 10 Å/s, initial cell efficiencies of 10.3% have been achieved. After 1000 hrs. of light soaking in white light, these cell efficiencies degrade by 20%, typical degradation percentages for cells of a similar i-layer thickness prepared by the standard rf PECVD technique at i-layer deposition rates of 1 Å/s. Presently, our best single-junction a-Si:H cell whose i-layer was prepared using the VHF process at 10 Å/s has a stable efficiency of 8.0% (V_{oc}=0.936 V, J_{sc}=14.3 mA/cm^2, FF=0.599).

a-SiGe:H

In Table II, data for a-SiGe:H cells whose i-layers were prepared using the VHF technique and the 10 Å/s i-layer deposition rate are compared with cells prepared using the standard 13.56 MHz, 1 Å/s conditions. The data was obtained using 630 nm filtered light in order to simulate absorption due to a top a-Si:H cell and a middle a-SiGe:H cell. While the cells made using the VHF technique have respectable efficiencies that are much larger than those obtained for cells made using the same 10 Å/s rate and the 13.56 MHz frequency, the efficiencies obtained thus far are lower than those obtained using the standard 13.56 MHz, 1 Å/s conditions. Comparing cells with similar V_{oc}, those made using the VHF technique have lower efficiencies due in most part to lower J_{sc} values. Increasing the currents further by using higher substrate temperatures and/or higher Ge contents leads to a loss in V_{oc} due to lower bandgaps and lower FF due to poorer material quality.

Table II. Properties for a-SiGe:H cells.

Freq. (MHz)	Dep. Rate (Å/s)	V_{oc} (V)	J_{sc} (mA/cm^2)	FF	P_{max} (mW/cm^2)
70	10	0.631	8.31	0.606	3.18
70	10	0.627	8.46	0.601	3.19
70	10	0.588	8.84	0.544	2.83
13.56	0.9	0.628	9.09	0.615	3.52
13.56	0.9	0.611	9.21	0.611	3.50

Triple-junction cells

The VHF technique has been used to prepare a-Si:H/a-SiGe:H/a-SiGe:H triple-junction cells with the i-layer deposition rates near 10 Å/s with representative cell data shown in Table III. Several cells with initial active area efficiencies near 11% and initial total area efficiencies of 10-10.3% have been fabricated. After 700 hrs. of light soaking, the cell efficiencies degrade to near 9.0% with a percentage of degradation from the initial value of 10-14%, a percentage typical of what is obtained for high efficiency triple-junction cells prepared using i-layer deposition rates near 1 Å/s. However, the stable efficiencies are presently lower than the 13% stable efficiencies obtained for cells made using the 1 Å/s rate[5].

Table III. Properties for triple-junction cells.

Soak Time (hrs.)	V_{oc} (V)	J_{sc} (mA/cm^2)	FF	P_{max} (mW/cm^2)	%. of Degr.
0	2.35	6.09	0.723	10.3	-
700	2.25	6.08	0.661	9.04	12.3

DISCUSSION

The efficiencies for the triple-junction cells prepared at the high i-layer deposition rates are presently limited by the performance of the a-SiGe:H layers and cells. Due to the current matching requirements for establishing the highest efficiencies for the triple-junction structures, the relatively low red-light currents for the a-SiGe:H cells limits the J_{sc} of the triple stack. Thus, further research will focus on increasing the J_{sc} values for the a-SiGe:H cells through modification of the fabrication processes while maintaining the V_{oc} and FF values.

ACKNOWLEDGEMENTS

The authors would like to recognize Don Williamson for his collaborative efforts in completing the SAXS studies and Helmutt Fritzsche and Standford R. Ovshinsky for discussions that helped guide the research program.

REFERENCES

1. H. Chatam et.al., Mat. Res. Soc. Proc. 149, 447 (1989).
2. A. Shah et. al., Mat. Res. Soc. Proc. 258, 15 (1992).
3. S.J. Jones et. al., Mat. Res. Soc. Proc. 507, 113 (1998).
4. J. Yang et. al., Mat. Res. Soc. Proc. 507, 157 (1998).
5. J. Yang et. al., Mat. Res. Soc. Proc. 557, 239 (1999).

Growth of Low Gap a-(Si,Ge) and Microcrystalline Si Devices

Vikram L. Dalal
Iowa State University
Dept. of Electrical and Computer Engineering, Ames, Iowa 50011

ABSTRACT

We describe the growth and properties of low gap a-(Si,Ge) and microcrystalline devices in the (Si,Ge) system. The devices were grown using a highly diluted remote plasma ECR system. It was found that low pressures (below 10 mT) were necessary in order to obtain high quality films and devices. The perofrmance of microcrystalline devices depended critically upon the interface between the p and n layers. Properly designed interfaces could improve the voltage by 25%.

1. Introduction

Both a-(Si,Ge) and microcrystalline Si are important material systems for tandem junction solar cells. While considerable work has been done on a-(Si,Ge) alloys with high bandgaps[1,2], it was always found that it was difficult to fabricate high quality devices in materials with Tauc gaps lower than 1.4-1.45 eV. In part, this has been ascribed to the low surface mobility of germane radicals compared to silane radicals during growth, resulting in a non-homogeneous film with highly defective microstructure. [3]. In this paper, we show that by using a remote ECR plasma at very low pressures, we can grow high quality a-(Si,Ge) devices with good fill factors and low Urbach energies. We have been able to make devices down to a gap of 1.25 eV. The design of these devices will be discussed.

Microcrystalline Si:H material has also become attractive recently as an alternative for the low gap material in a tandem cell.[4]. A critical factor in the design of microcrystalline cells is the selection of the top junction layer (p) and the interface between the p and the n. In this paper, we will show that this interface is critical in increasing the voltage in a microcrystalline Si:H cell.

2. Experimental Technique

The films and devices were grown using a remote, hydrogen diluted ECR plasma system.[5]. A highly diluted hydrogen-silane-germane plasma was used to deposit both amorphous and microcrystalline materials and devices. We discovered that it was essential to very low pressures (<10 mT) to obtain high quality devices. Typical growth rates were about 1 A/sec. To grow microcrystalline devices, the pressures were kept below 5 mT, and the dilution rate was increased to 20:1. Typical growth temperatures were between 275-350 C. The amorphous devices were of the p/i/n type, and micro Si devices were of p+/n/n+ type., both deposited on stainless steel substrates. Light entered from the p side, which was coated with either a semi-transparent Cr contact, or an ITO contact. For both amorphous and microcrystalline cells, the p layer was made from a-(Si,C).

3. Device Results

a. Amorphous (Si,Ge)

A typical I(V) curve for an a-(Si,Ge) device is shown in Fig. 1. The fill factor is 57%, and the bandgap is 1.28 eV. The quantum efficiency(QE) curves for this device are shown in Fig. 2, where we show the QE, and the QE ratio (QE at 0V/QE under forward bias) as functions of wavelength. The low QE ratio indicates good hole collecting properties

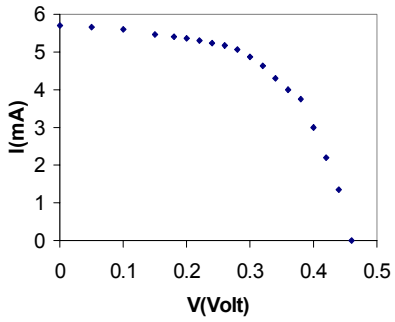

Fig. 1 I(V) curve of low gap a-(Si,Ge) cell

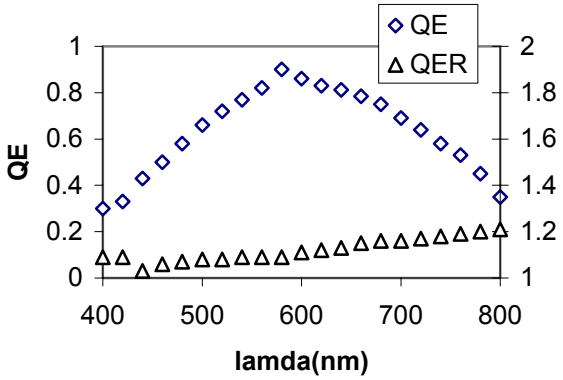

Fig. 2 QE(left) and QE ratio (right scale) for cell of Fig. 1

Further indication of device quality comes from measuring Urbach energy by doing a subgap QE vs. photon energy curve, which is shown in Fig. 3. The low Urbach energy value, ~45 meV, indicates good quality.

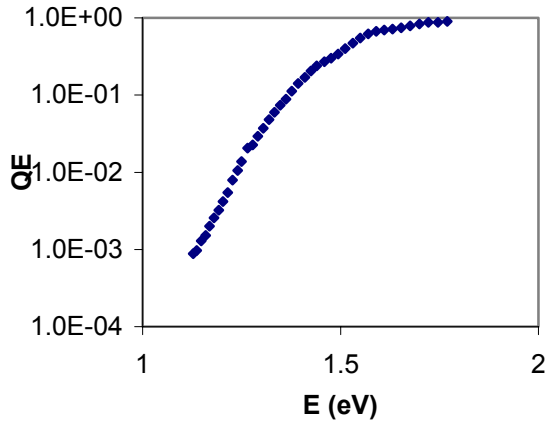

Fig. 3 Subgap QE of cell of Fig. 1

b. Microcrystalline Si

It was discovered that an appropriate graded-gap buffer layer was necessary between the p+ and n layers in micro Si:H cells in order to obtain both good voltages and good currents. This buffer layer was graded using a- (Si,Ge) alloy at the n-micro Si interface to an a-(Si,C) alloy at the p interface, thereby achieving a smooth interface matching for both conduction and valence bands. The grading introduced a further separation of light generated electrons and holes, thereby leading to an increase in voltage of about 0.1V (25%). The I(V) curve for a micro Si:H cell with the appropriate buffer layer grading is shown in Fig. 4. The excellent fill factor(>70%) and voltage indicate good material quality. Experiments to improve such cells are in progress. Note that the real intrinsic voltage is about 0.52 V, since only about 20% of the light passes through the Cr contact.

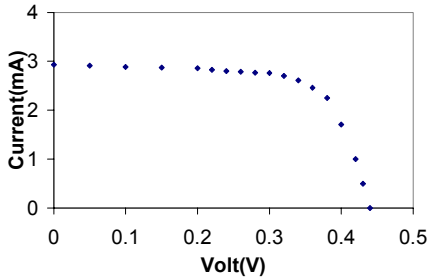

Fig. 4 I(V) curve of microcrystalline Si cell

4. Conclusions

In conclusion, we have shown that by using appropriate plasma chemistry, one can deposit high quality low gap a-(Si,Ge) cells. We have also shown that high quality micro Si:H cells can be deposited, and that appropriate buffer layers can achieve higher voltages and good fill factors.

5. Acknowledgements

This work was supported in part by NREL. I thank Kay Han, Z. Zhiyang and T. Maxson for their technical help.

6. References

1. A. Banerjee, J. Yang and S. Guha et al, Proc. Of Mater. Res.Soc., 557, 743(1999)
2. V. L. Dalal et al, to be published in J. Non-cryst) Solids (2000)
3. D. Williamson, Proc. Of MRS, 377,251(1995)
4. N. Wyrsch et al, Proc. Of 2nd. World Conf. On Photo-voltaic solar energy conversion, (Vienna,1998),p.467
5. V. L. Dalal et al, Appl. Phys. Lett. 64, 1862(1994)

Light-Induced Changes in Long-Ranged Disorder in Amorphous Silicon

D. Quicker, P. W. West and J. Kakalios

The University of Minnesota

School of Physics and Astronomy
Minneapolis, MN 55455

ABSTRACT

Experimental measurements of the thermopower and conductivity activation energies have been combined with that of the conductance 1/f noise in hydrogenated amorphous silicon in order to test non-local models for light induced conducance changes. Following extented light soaking, there is no change in the long range disorder in device quality amorphous silicon films, but preliminary results indicate that reversible changes in disorder do occur in films grown under non-optimal conditions.

1. Introduction

The standard model for the microscopic origin of light-induced conductance changes in hydrogenated amorphous silicon (a-Si:H), termed the Staebler-Wronski effect (SWE) involves the breaking of localized strained Si-Si bonds which create new dangling bond defects. However, recent experimental results and theoretical models have suggested that along with localized defect creation, the light induced damage involves changes in the long range disorder LRD (on length scales of ~ 10^3 Å of magnitude ~ 100 meV) already present in the a-Si:H. The previous emphasis on localized dangling bond creation is understandable, since these defects are the easiest to measure. Conventional transport measurements are not sensitive to the influence of LRD on the electronic properties in a-Si:H, since the inelastic scattering (phase breaking) length is ~ 5 Å at room temperature [1]. In order to determine whether the SWE effect involves long range as well as local changes in the defect structure, an experimental program to study the influence of long range disorder on the electronic properties of a-Si:H has been initiated.

2. Experimental Results

A series of r.f. glow discharge deposited n-type doped a-Si:H films for which the substrate temperature during film growth was varied from 25 C < T < 250 C for an rf plamsa power density of 3 W/50 cm^2 has been synthesized. Infra-red spectroscopy measurements of the hydrogen content and bonding microstructure (in particular the relative concentration of Si-H_2 bonds) for these films shows a nearly uniform increase as the deposition temperature is lowered, in agreement with prior studies by Bhattacharya and Mahan. [2] The long range disorder in these materials is quantified through measurements of the thermopower/conductivity activation energy difference. This activation energy difference, with the dark conductivity always displaying a larger value than observed in thermopwer measurements is due to the difference between open circuit (thermopower) and short circuit (conductivity) measurements and has long interpreted as a measure of the long range disorder at the mobility edges [2]. As shown in fig. 1, the activation energy difference also increases as the substrate deposition temperature is lowered, and when compared to the increasing concentration of Si-H_2 bonds, a nearly linear correlation is observed [4]. We therefore conclude that the conductivity/thermopower

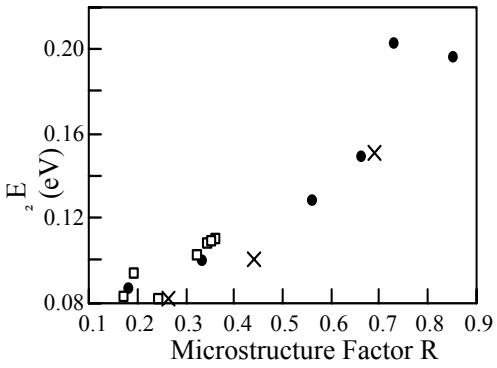

Fig. 1 Plot of the E□ the difference between the conductivity and thermopower activation energy against the concentration of Si-H□ bonds, as reflected in the ratio R of the infra-red absorption at 2100 cm-1 compared to the total

absorption from 2000 to 2200 cm-1 for a series of n-type doped a-si:H films deposited at substrate temperatures varying from 250 C down to room temperature.

activation energy difference can indeed be used as a quantitative measure of LRD in a-Si:H thin films.

However, a surprising result is that following 17 hours of light soaking with heat filtered white light from a tungsten-halogen lamp for an n-type a-Si:H film deposited at 250 C, there is no change in this activation energy difference, even though both the dark conductivity and thermopower display reversible light induced changes, as shown in fig. 2. This result suggests that the long range disorder is unaffected by light exposure, and that the changes in conductivity activation energy are due solely to shifts of the Fermi energy, and not to changes in the nature of the current carrying transport states [5]. This result is at odds with previous reports of significant changes in the activation energy difference following light exposure.[6] This discrepancy may be explained by the observation that there is a small but definite change in the activation energy difference for a film deposited at 60 C. This film has considerably more hydrogen microstructure, as reflected by infra-red spectroscopy measurements, indicating that any light induced changes in the LRD are sensitive to the degree of disorder already present in the annealied state.

The 1/f noise power spectra has also been measured for these films as a function of light soaking. After light exposure, the noise magnitude increases with illumination time, and is reversible upon annealing. This result, which agrees with independent reports by Verlag and Dijkhuis [7] is consistent with a decrease in the

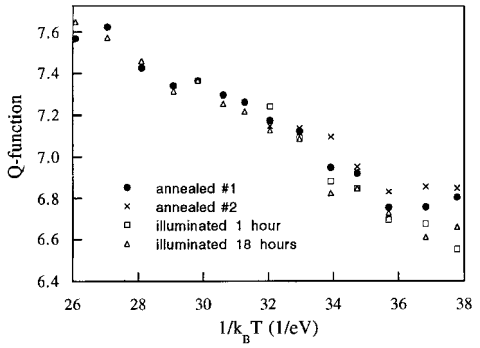

Fig.2 Temperature dependence of the Q function ($Q = \frac{e}{k_B}|S| + \ln(\sigma)$) in the annealed state and after several light exposures for an a-Si:H film doped with 4 x 10^{-4} PH_3 and deposited at 250 C.

noise magnitude due to ensemble averaging effects. Therefore the noise studies indicate that the defect density decreases following light more defects should lead to a decrease in the exposure, while the activation energy difference (as well as a host of other experimental evidence) suggests that the defect density increases. Clearly further studies on a broader
number of fluctuators giving rise to the current fluctuations. The conventional interpretation of the 1/f noise is that it arises from charge trapping and release from dangling bond defects, and thus range of samples is needed.

This work was supported by the University of Minnesota, the NSF DMR-9422772 and NREL/AAD-9-18668-13.

REFERENCES

[1] J. Kakalios and R. A. Street: "Electronic transport in doped amorphous silicon", Phys. Rev. B 34 (1986) 6014-6017.

[2] E. Bhattacharya and A. H. Mahan: "Microstructure and the light-induced metastability in hydrogenated amorphous silicon", Appl. Phys. Lett. 52 (1988) 1587-1589.

[3] H. M. Dyalsingh and J. Kakalios: "Thermopower and conductivity activation energies in hydrogenated amorphous silicon", Phys. Rev. B 54 (1996) 7630-7633.

[4] D. Quicker and J. Kakalios: "Influence of deposition conditions on long-range disorder in n-type doped hydrogenated amorphous silicon", Phys. Rev. B 60, 2449 (1999) 2449-2455.

[5] D. Quicker, P. W. West and J. Kakalios: "Long-range disorder and metastability in amorphous silicon", J. Non-Cryst. Solids (in press).

[6] D. Hauschildt, W. Fuhs and H. Mell: "Optically induced potential fluctuations in a-Si:H films", Phys. Stat. Solidi B 111 (1982) 171-174.

[7] P. A. W. E. Verlag and J. I. Dijkhuis: "Fluctuating defect density probed with noise spectroscopy in hydrogenated amorphous silicon", Phys. Rev. B 58 (1997) 3917-3921; "Generation-recombination noise studied in hydrogenated amorphous silicon", J. Non-Cryst. Solids (in press).

NMR Studies of Molecular Hydrogen in Hydrogenated Amorphous Silicon

T. Su[1], S. Chen[1], P. C. Taylor[1], R. S. Crandall[2], and A. H. Mahan[2]

[1]Department of Physics, University of Utah, Salt Lake City, UT 84112
[2]National Renewable Energy Laboratory, Golden, CO 80401

ABSTRACT

Using ^{1}H nuclear magnetic resonance (NMR), the concentrations of molecular hydrogen have been measured directly in hydrogenated amorphous silicon made by the hot wire chemical vapor deposition (HWCVD) technique. The NMR experiments employed a Jeener-Broekhaert three-pulse sequence. The molecular hydrogen concentrations are about an order of magnitude greater than those inferred from spin-lattice relaxation time measurements. The HWCVD samples have lower transition temperatures for freezing of the molecular hydrogen motion than those prepared by the plasma enhanced CVD method. This behavior is attributed to a more ordered silicon structure in the HWCVD samples.

1. Introduction

Hydrogen plays a crucial role in determining the structural and electronic properties of hydrogenated amorphous silicon (a-Si:H). In typical samples prepared by plasma enhanced chemical vapor deposition (PECVD), the hydrogen concentration is about 10 to 15 at. %. Most of the hydrogen atoms are bonded to silicon atoms. About 30 % of these bonded hydrogen atoms are isolated from one another (dilute); the rest of the bonded hydrogen atoms are clustered. These two different hydrogen environments can be distinguished by proton nuclear magnetic resonance (^{1}H NMR). In ^{1}H NMR the dilute hydrogen produces a narrow line (~ 4 kHz) that is best fitted by a Lorentzian function, while the clustered hydrogen produces a broader line (~ 25 kHz) that is best fitted by a Gaussian function [1,2].

The presence of a small amount of non-bonded molecular hydrogen in a-Si:H was first proposed by Conradi and Norberg to explain the temperature dependence of the spin-lattice-relaxation time (T_1) of bonded hydrogen [3]. From measurements of T_1 of bonded H, the concentration of H_2 is about 1 % of the total hydrogen in standard samples of a-Si:H made by the PECVD technique [2]. However, this model is based on the assumption that all ortho-H_2 molecules contribute to spin-lattice-relaxation of the bonded hydrogen atoms. Later experimental evidence has shown that this assumption is not correct [4].

It has been recently suggested that molecular hydrogen may play an important role in the metastable effects that are ubiquitous in a-Si:H [5]. Therefore, it is of importance to investigate the presence of hydrogen molecules in a-Si:H in more detail with new NMR techniques.

2. Experimental Details

Since the NMR lineshape of ortho-H_2 is very broad, the simplest NMR techniques, such as measurements of the free induction decay, are not useful. In order to obtain accurate and direct measurements of the ortho-H_2 we employed a Jeener-Broekhaert three-pulse sequence as described elsewhere [6]. By extrapolating the echo amplitudes to zero pulse separation between both the first and second pulses and the second and third pulses, one obtains a direct measure of the concentration of molecular hydrogen in the sample regardless of whether or not the molecules contribute to the spin-lattice relaxation of bonded hydrogen. Expedriments were performed on a standard pulsed NMR spectrometer using standard cryogenic techniques to achieve low temperatures [7].

3. Results

Figure 1 shows the low temperature (8 K) NMR lineshapes for three samples of a-Si:H made by the HWCVD technique and one sample made by the PECVD technique. In the PECVD sample the two peaks near ± 100

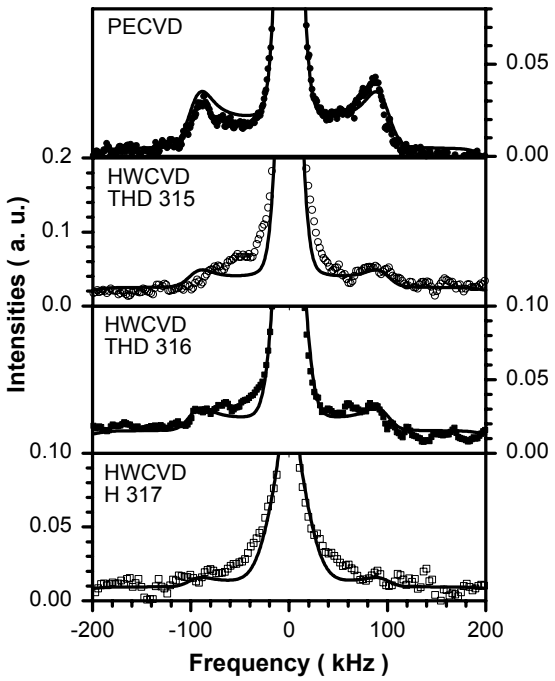

Fig. 1 NMR lineshape at 8 K in three samples of a-Si:H as described in the text.

kHz are due to ortho-H_2 molecules that are "frozen" into the ground rotational state (Pake doublet). The central region of the spectrum contains the two ^{1}H NMR signals due to bonded hydrogen in the dilute and clustered environments.

Note that in the three HWCVD samples the two Pake-doublet peaks due to molecular hydrogen are either less pronounced or absent. This narrowing occurs because the molecular hydrogen is tumbling rapidly even at 8 K in the HWCVD samples. Qualitatively, the tumbling rates increase for the bottom three samples in the figure (samples THD315, THD316, and H317). Sample H317 exhibits the fastest tumbling rate at 8 K. Samples THED315 and THD316 were made under similar conditions except that sample THD317 was made with a screen to protect the substrate from a direct view of the hot filament used to decompose the silane. Sample H317 is similar to those samples that have shown the lowest internal friction [8].

Figure 2 shows a direct comparison between the PECVD sample and the HWCVD sample (H317) at 8 K. Note the well defined Pake-doublet in the PECVD sample (solid circles) and the "motionally narrowed" molecular hydrogen contribution in the HWCVD sample (open squares.) The dashed line is a fit to the narrowed molecular hydrogen contribution to the NMR in the HWCVD sample. The width of this line is about 70 kHz (full width at half maximum).

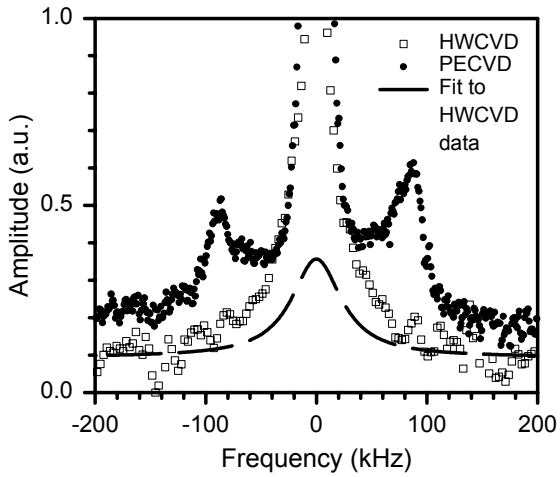

Fig. 2 Comparison of ortho-molecular hydrogen lineshapes in PECVD and HWCVD a-Si:H. See text for details.

4. Discussion

For both the PECVD and the HWCVD samples the concentrations of ortho-molecular hydrogen obtained from the direct measurements described above are one order of magnitude greater than those inferred from the spin-lattice relaxation time measurements, which probe the molecular hydrogen indirectly through their effect on the relaxation of the bonded hydrogen. This result establishes an accurate measurement of the concentration of H_2 for the first time.

The second important discovery is the much lower freezing temperature for H_2 in the HWCVD samples. Because the freezing temperature is controlled by the electric field gradient due to distortions in the silicon lattice, we infer that the HWCVD samples, and the sample with very low internal friction in particular, have a more ordered silicon lattice. This result is consistent with the conclusions drawn from the internal friction measurements [8].

5. Summary

The concentration of molecular hydrogen in a-Si:H is found to be about 10% of the total hydrogen concentration incorporated into both PECVD [9] and HWCVD samples. There are two types of sites for the molecular hydrxogen, one which is effective in relaxing the H NMR due to bonded hydrogen and one which is not. Comparison of the lineshapes at 8 K between the PECVD and HWCDVD samples suggests that the HWCVD samples have a more ordered silicon matrix.

6. Acknowledgements

Research at the University of Utah was performed as part of the Thin Film Partnership Program under support from NREL subcontract number XAK-8-17619-13.

RFEFERENCES

1. J. A. Reimer, R. W. Vaughan and J. Knights, Phys. Rev. Lett. **44**, 193 (1980); Phys. Rev. B**24**, 3360 (1981).
2. W. E. Carlos and P. C. Taylor, Phys. Rev. B**25**, 1435 (1982); Phys. Rev. B**26**, 3605 (1982).
3. M. S. Conradi and R. E. Norberg, Phys. Rev. B**24**, 2285 (1981).
4. J. B. Boyce, and M. Stutzmann, Phys. Rev. Lett. **54**, 562 (1985).
5. C. G. Van de Walle, J. Non-Cryst Solids **227-230**, 111 (1998).
6. J. Jeener and P. Broekaert, Phys. Rev. **157**, 232 (1967).
7. P. Hari, P. C. Taylor, and R. A. Street, Mat. Res. Soc. Symp. Proc. **336**, 293 (1994); Mat. Res. Soc. Symp. Proc. **377**, 185 (1995).
8. Xiao Liu, B. E. White, Jr., and R. O. Pohl, Phys. Rev. Lett. **78**, 4418 (1997).
9. T. Su, P. C. Taylor, S. Chen, R. S. Crandall, and A. H. Mahan, Appl. Phys. Lett. **76**, 565 (2000).

Open-Circuit Voltage Physics in Amorphous Silicon Based Solar Cells

L. Jiang, J. Lyou,[1] S. Rane, E. A. Schiff, Q. Wang,[2] and Q. Yuan

Department of Physics, Syracuse University
Syracuse, New York 13244-1130 USA

ABSTRACT

Results from a research project seeking to understand open-circuit voltages in amorphous-silicon based solar cells are given. Research includes drift-mobility and built-in potential measurements, as well as computer and analytical modeling of *pin* solar cells. A preliminary conclusion that the open-circuit voltage in optimized a-Si:H based cells is interface limited is discussed.

1. Introduction

The open-circuit voltage V_{oc} of amorphous silicon (a-Si:H) based *pin* solar cells remains the most ill-understood of its device parameters. This ignorance is remarkable, since the experimental behavior of V_{OC} is generally quite simple. V_{OC}: depends little upon the defect density or thickness of the intrinsic layer, and is generally proportional to the optical bandgap of this layer. Nonetheless, even the simplest question about it, which is whether V_{oc} is determined by intrinsic layer properties, or by the *p/i* or *n/i* interfaces, is not conclusively answered. Of course, this unsatisfactory state of affairs does leave open the tantalizing possibility of significant improvements in V_{oc} – if only device-makers could be pointed in a better direction.

In this short paper, we discuss our preliminary conclusion that V_{oc} in a-Si:H based *pin* solar cells is interface-limited even in "state-of-the-art" cells. This conclusion emerges from three areas of research conducted at Syracuse under subcontract with NREL. We make measurements of electron and hole drift mobilities, which establish essential parameters of the intrinsic layers. We have done extensive work to develop electroabsorption as a technique for estimating the built-in potential in *pin* cells. Finally, we are modeling solar cells exploiting the AMPS PC-1D program developed at Penn State University.

2. Voc isn't correlated with defect densities

It appears well accepted by device-makers that there is little correlation between V_{oc} and the density of deep levels N_D (usually presumed to be dangling bonds) in a-Si:H. One paper shows that light-soaking increased the defect density in intrinsic films nearly thirtyfold, while V_{OC} diminished by about 0.03 V[1].

When open-circuit voltages are determined by intrinsic layer properties, they may be equated to the separation between the electron and hole quasi-Fermi levels E_{fe} and E_{Fh}:

$$eV_{OC} = \left(E_{Fe} - E_{Fh}\right) , \quad (1)$$

where e is the electronic charge [2]. We illustrate the relation in Fig. 1 using an AMPS calculation with a-Si:H parameters described in the next section. For this calculation, interface effects are unimportant: the open-circuit voltage of 1.0 V matches the quasi-Fermi-level splitting of the intrinsic layer.

The changes in V_{OC} as the defect density changes may be calculated from the changes in the quasi-Fermi-levels for electrons and holes. The corresponding decline in the photoconductivity of a-Si:H films is roughly proportional to the reciprocal density [3]. Since the photoconductivity is electron-dominated, one may estimate the decline in the electron quasi-Fermi level ΔE_{Fe} simply:

$$\Delta E_{Fe} \Big/ kT = \ln\left(N_D^f \Big/ N_D^i \right) . \quad (2)$$

One obtains an expected decline of V_{OC} of about 0.09 eV due to this effect, which is substantially larger than the observed decline. An additional, smaller effect is also expected from changes in the hole quasi-Fermi-level E_{Fh} as

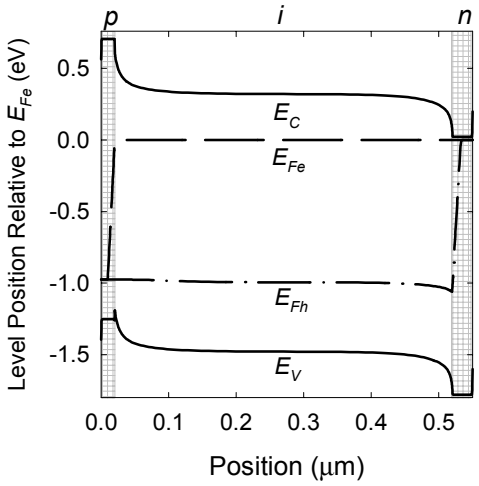

Fig. 1: Computer calculation of profiles for the conduction and valence bandedges and electron and hole quasi-Fermi levels in an a-Si:H based *pin* solar cell. The open-circuit voltage is precisely the value of E_{Fh} at the left interface ($x = 0$).

[1] Present address: Korea University, Chungnam, S. Korea.
[2] Present address: National Renewable Energy Laboratory, Golden,

the defect density rises.

It is clear that the myriad of photoconductivity measurements on a-Si:H have at best an uncertain relationship to V_{OC}. The alternative is that V_{OC} is determined by photoconductivity effects in the interface regions. The present argument favoring interface effects would be quite conclusive if defect density changes as large as those in films were observed in *pin* cells, but effects this large have not (to our knowledge) been reported.

3. Measured built-in potentials are too small to avoid interface effects

In Fig. 1 we present calculations of V_{oc} using the AMPS PC-1D computer program. Illumination was uniformly absorbed at the indicated photogeneration rates G. The intrinsic-layer parameters used to drive these calculations were chosen for consistency with fundamental measurements of electron and hole drift mobilities in a-Si:H; these are mostly parameters characterizing conduction and valence bandedges and exponential bandtails. Intrinsic layer defects were not incorporated, since V_{OC} is not much affected by them. The *n*-layer Fermi energy was set 0.1 eV below the conduction band; the *p*-layer Fermi energy was adjusted to yield the several values of the built-in potential shown in the figure.

The points calculated for V_{bi} =1.52 V approach the results of an independent analytical calculation for V_{OC} based on intrinsic layer properties alone [4]. The points for V_{bi} = 1.32 V fall away significantly from the intrinsic-layer limit due to interface limitation by the *p/i* interface. We note

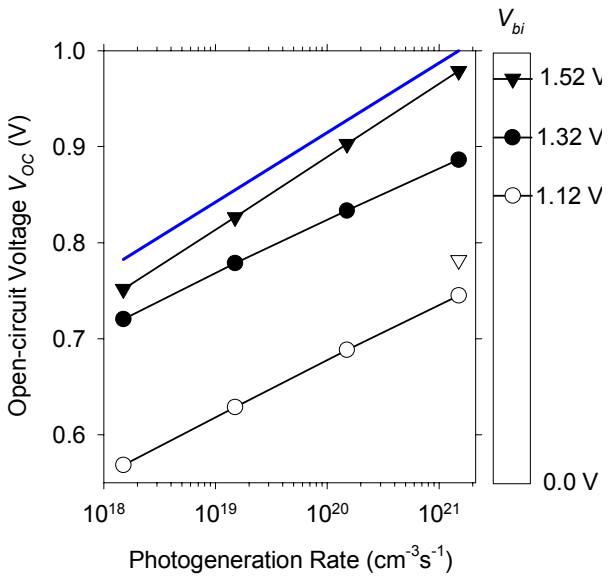

Fig. 1: Calculations of the dependence of the open-circuit voltage upon photogeneration rate for *pin* solar cells. The symbols plotted for different V_{bi} are based on computer calculations for varying Fermi-energies in the *p*-layer. The bold solid line is an analytical calculation based on intrinsic layer properties alone.

two aspects of this behavior. First, interface limitation is important even when V_{OC} is substantially (0.4 V) less than V_{bi}. Second, the power-law, functional form of the dependence of V_{oc} upon G gives little indication that V_{OC} has been reduced by the interface: the interface causes an extremely soft effect on V_{OC} and is stretched over many decades of generation rate.

To our knowledge, the best elaborated experimental estimates of V_{bi} in a-Si:H are based on the small, electroabsorption effect. This effect reduces the transmittance through a cell proportional to the electrostatic potential across the cell; by measuring this effect as a function of external potential, an estimate of the internal "built-in" potential is obtained. The actual interpretation of these measurements is somewhat more complicated than this description implies, but lead to a range $1.05 < V_{bi} < 1.25$ V in both the published and unpublished work of our laboratory [5,6]. These values are sufficiently small that, in conjunction with the calculations shown in the figure, they suggest that interface effects must be significantly reducing V_{OC} in current cells.

4. Discussion

Most of the results we have given above mount a case against the simple model that open-circuit voltages are determined solely by photoconductivity effects in the intrinsic layer. What is plainly required to advance open-circuit voltage physics is a satisfactory model for V_{OC} based on interface physics. In unpublished work, we have developed a fairly satisfactory account for the computer calculations of *p/i* interface effects in terms of electron thermionic emission from the intrinsic layer into the *p*-layer.

Experimentally, the simple models based on the bandtails inferred for thick, intrinsic films do not provide a satisfactory account for measured dependences of V_{OC} upon illumination intensity. In particular, measured V_{OC} vs. G relations for *pin* solar cells rise more steeply with G than any of the calculations in Fig. 1. We are, reluctantly, considering the possibility of more complex models for the *p/i* interface.

REFERENCES

[1] S. Wagner, X. Xu, X. R. Li, D. S. Shen, M. Isomura, M. Bennett, A. E. Delahoy, X. Li, J. K. Arch, J.-L. Nicque, and S. J. Fonash, in IEEE PVSC Proceedings, 1307 (1991).
[2] Despite the fact that this result is well-known, we are unaware of any conclusive proof which would indicate its limitations. We explore its validity in unpublished work (J. Goodisman and E. A. Schiff);
[3] F. Wang and R. Schwarz, *J. Appl. Phys.* **71**, 791 (1992).
[4] T. Tiedje, *Appl. Phys. Lett.* **40**, 627 (1982).
[5] L. Jiang, E. A. Schiff, Q. Wang, S. Guha, and J. Yang, *Appl. Phys. Lett.***69**, 3063 (1996).
[6] J.-H. Lyou, L. Jiang, E. A. Schiff, S. Guha, and J. Yang, NREL Annual Subcontract Report (1999).

Optimization of Protocrystalline Si:H Materials and Fabrication of Stable High-Performance Solar Cells

R.J. Koval, A.S. Ferlauto, P.I. Rovira, X. Niu, J. Pearce, R.W. Collins, and C.R. Wronski

The Center For Thin Film Devices and Materials Research Laboratory

The Pennsylvania State University, University Park, PA 16802, USA

1. Introduction

The importance of H_2-dilution of SiH_4 in plasma-enhanced CVD of i-layers for higher stability amorphous silicon (a-Si:H) based solar cells was established in several studies published from 1993 to 1994 [1-3]. In the same time frame, we established a guiding principle for optimum H_2-dilution of a-$Si_{1-x}C_x$:H i-layers for wide-gap p-i-n solar cells, specifically that the H_2-dilution ratio should be set at "the maximum value that can be sustained without entering the regime of microcrystallinity" [quotation from Ref. 4]. A few years later, this concept was reaffirmed for pure a-Si:H [5]. More recently, we recognized the complications of fabricating i-layers just within the amorphous side of the amorphous-to-microcrystalline (a→μc) boundary in preparation parameter space. These complications arise due to the high sensitivity of the a→μc transition to the accumulated Si film thickness and to the underlying substrate [6]. In order to quantify these effects, deposition phase diagrams were developed for various substrates that identified the thickness at which the a→μc transition occurs as a function of the H_2-dilution ratio $R=[H_2]/[SiH_4]$ [7]. The phase diagrams showed how the stabilized performance of p-i-n solar cells could be optimized using multi-step i-layers, including a so-called protocrystalline Si:H layer at the interface to the p-layer [6]. We applied the term "protocrystalline" to describe the more highly-ordered a-Si:H i-layers prepared at high R on amorphous p-layers that eventually evolve to a μc structure with increasing thickness. In this abstract, we extend the phase diagram concept for materials optimization and show how the features of the diagram are manifested in the p-i-n solar cell stability and overall performance.

2. Results and Discussion: An Extended Phase Diagram

Atomically-smooth c-Si substrates provide the highest sensitivity to surface roughness evolution in Si films by PECVD [6]. Thus, this substrate provides the highest sensitivity in deducing the evolutionary phase diagram by real time spectroscopic ellipsometry [7]. Here we enumerate four separate regimes in the extended phase diagram for c-Si substrates, as shown in Fig. 1.

(1) *Amorphous, stable surface.* In this regime, an amorphous phase grows and the surface either smoothens as a function of time or remains stable. The unique value of R is 10, in which case the surface remains stable throughout the growth of a 4000 Å film.

(2) *Amorphous, unstable surface.* In this regime, an amorphous phase grows but is roughening versus time. For all R≤30, there is an amorphous regime in which smoothening occurs as a result of nuclei coalescence. At the lower R values (R<10), however, this smoothening extends for a limited thickness range after which surface roughening then dominates.

(3) *Mixed-phase (a+μc).* This regime represents the thickness range over which microcrystallites are nucleating and growing within an amorphous phase. For 15<R<40, the μc phase dominates with increasing thickness, and this eventually leads to the development of a fully μc phase.

(4) *Coalesced microcrystalline.* In this regime, single-phase μc-Si:H film growth dominates. This phase can arise due to the nucleation and coalescence of crystallites from the amorphous phase, as occurs for 20≤R≤30, or it can arise from the coalescence of crystallites that nucleate immediately from the substrate, as occurs for R=40.

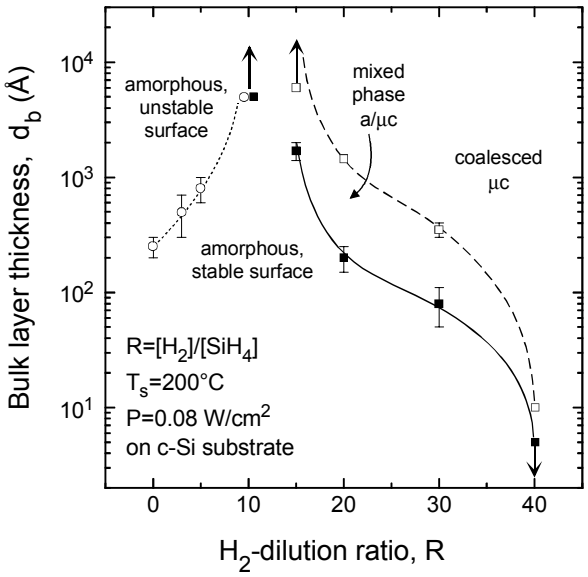

Fig. 1: Extended phase diagram for Si:H film growth on a native oxide-covered c-Si substrate.

3. Performance of Si:H Solar Cells—Role of the Evolutionary Phase Boundary

Guided by the corresponding evolutionary phase diagram for Si:H materials grown on R=0 a-Si:H substrate films, systematic studies have been carried out to assess the contributions of the protocrystalline region as well as the transition to microcrystallinity. In these studies the contribution of bulk intrinsic protocrystalline layers with R up to 20 in specular SnO_2/250Å p-a-SiC:H:B/ i-a-Si:H/ n-μc-Si:H:P/Cr solar cells were characterized by their effect on the FF [8]. The contribution of layers with R up to 80 were characterized by their effect on the open-circuit voltage (V_{oc}) when introduced as thin layers adjacent to the p/i interface in cells having the optimum (R=10) a-Si:H [9].

With p/i interface regions 100-200Å thick, a systematic increase in V_{oc} from 0.82 to 0.93V is obtained with an increase of R from R=0 to 40 and then a rapid decrease is obtained for R>40. [9]. The systematic increase in V_{oc} is attributed to the introduction of protocrystalline characteristics for the Si:H interface layers, and the decrease for R=40 layers with thicknesses greater than 200Å (as well as for the thinner layers of R=60 and 80) are due to the presence of a dominant microcrystalline phase as indicated by the RTSE/AFM results.

The transition to microcrystallinity in Si:H deposited with moderate R values (0≤R≤20) and its effect on bulk-dominated FF's was obtained from results on cells whose i-layer thicknesses were systematically changed. The effects of changing the bulk R value from 0 to 20 in p-i-n cells having i-layers up to 4000Å thick showed that for R≤10 the initial fill factors remain the same. However, for R>10 the initial FF's decrease significantly and such behavior begins to occur for the R=10 cells when the i-layer approaches a thickness of 1μm. The observed decreases in FF for cells having R>10 is not related to any adverse effects at the p/i interface since their inclusion leads to improved stable open-circuit voltages as discussed above. The decrease can be attributed however to changes in microstructure of the thicker i-layers, which may no longer be purely protocrystalline Si:H, but rather mixed-phase microcrystalline Si:H. This is illustrated in Fig. 2 with cells having R=10 i-layers as well as R=15 i-layers. In the latter material the phase transition occurs at a thickness of about 3000Å as indicated by RTSE results. The two thicknesses of the cells in Fig. 2 are 2400Å and 4000Å, and it can be seen that for the thicknesses of 2400Å identical FF's are obtained both in the initial state as well as the 1 sun degraded steady state. With a thickness of 4000Å, however, the onset of the microcrystalline phase transition region in the R=15 cell is evidenced by the significant lowering of the initial FF. Similar lowering of the FF is also obtained with R=20 material which occurs at a thickness of approximately 2000Å, again in agreement with RTSE results.

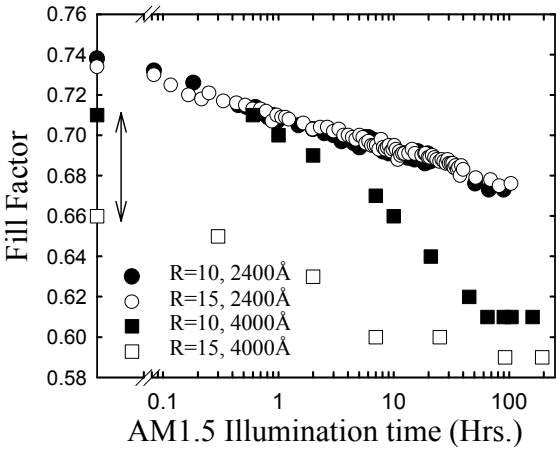

Figure 2. AM1.5 degradation of 2400Å and 4000Å p-i-n cells prepared with R=10 and R=15.

Results such as those discussed here, have established the role of protocrystallinity in optimizing solar cell performance and how RTSE can be employed to improve the performance of p-i-n solar cells systematically. Such results have also indicated the importance of the evolution with thickness of the transition from amorphous to microcrystalline phases in n-i-p cells where this transition in the i-layer occurs in the i/p region and thus has a very large effect on V_{oc} [10].

REFERENCES

[1] M. Bennett, K. Rajan, and K. Kritikson, *Conf. Record 23rd IEEE Photovoltaics Specialists Conference*, (IEEE, NY, 1993), p. 845.

[2] L. Yang and L.-F. Chen, Mater. Res. Soc. Symp. Proc. **336**, 669 (1994).

[3] J. Yang, X. Xu, and S. Guha, Mater. Res. Soc. Symp. Proc. **336**, 687 (1994).

[4] Y. Lu, S. Kim, M. Gunes, Y. Lee, C.R. Wronski, and R.W. Collins, Mater. Res. Soc. Symp. Proc. **336**, 595 (1994).

[5] D. Tsu, B. Chao, S. Ovshinsky, S. Guha, and J.Yang, Appl. Phys. Lett. **71**, 1317 (1997).

[6] J. Koh, Y. Lee, H. Fujiwara, C.R. Wronski, and R.W. Collins, Appl. Phys. Lett. **73**, 1526 (1998).

[7] J. Koh, A.S. Ferlauto, P.I. Rovira, C.R. Wronski, and R.W. Collins, Appl. Phys. Lett. **75**, 2286 (1999).

[8] R.J. Koval, J. Koh, R.W. Collins, and C.R. Wronski Appl. Phys. Lett. **75**, 1553 (1999)

[9] Y. Lee, A.S. Ferlauto, Z. Lu, J. Koh, H. Fujiwara, R.W. Collins and C.R. Wronski, *2nd World Conference on Photovoltaics Solar Energy Conversion,* (IEEE, Vienna, 1998), p.940.

[10] J. Yang, S. Guha (private communication).

SIMS Characterization of Amorphous-Silicon Solar Cells Grown by Hot-Wire Chemical Vapor Deposition on Stainless Steel

R.C. Reedy, Q. Wang, H. Moutinho, E. Iwaniczko, A.H. Mahan

National Renewable Energy Laboratory

1617 Cole Blvd., Golden, CO 80401

ABSTRACT

This poster is intended to be an overview of some of the challenges that must be overcome when characterizing amorphous-silicon solar-cell devices by the secondary ion mass spectrometry (SIMS) technique.

1. Introduction

SIMS is a mass-spectrometry technique that is highly prized for its sensitivity and ability to provide depth information. It is also one of the few techniques that can detect hydrogen. Much work has been performed with this technique to improve the quality of a-Si:H i-layers deposited by hot-wire chemical-vapor deposition (HWCVD) [1]. SIMS is also very useful in the characterization of a-SiGe:H materials [2,3]. Figure 1 shows a typical depth profile of a a-Si:H n-i-p device grown on a stainless-steel (SS) substrate at the National Renewable Energy Laboratory (NREL). The profile is actually a composite of three separate depth profiles. Hydrogen, carbon, and oxygen data were obtained by sputtering with our Cs^+ source at an impact energy of 14.5keV, analyzing negative secondary ions. Phosphorous data was obtained under similar conditions with the secondary optics optimized for high-mass resolution. Boron data was obtained by sputtering with our $O2^+$ source at an impact energy of 8keV, analyzing positive secondary ions.

SIMS depth profiles provide evidence of boron contamination in the n-layer and phosphorous in the p-layer which can most likely be attributed to the deposition of these materials in the same chamber. More important is the diffusion of dopants into the i-layer. Ideally, the growth of a-Si:H layers would conform to the substrate surface, and the sputtering during SIMS depth profiles would reproduce the original device surface. Since these ideal conditions are never completely met, it is important to determine the contribution of roughness to the apparent diffusion.

2. Mass Interferences

Mass interferences are common in SIMS because of the variety and intensity of the atomic and molecular ions species that are generated [4]. Mass resolution, $m/\Delta m$, is required to distinguish between two ions that have the same nominal mass, m, but differ in mass by a small value, Δm. The magnetic sector design of the dynamic SIMS instrument will normally provide unity-mass resolution, $m/\Delta m = 300$. High-mass resolution is achieved by physically limiting the amount of ions through the mass spectrometer by a set of mechanical slits. The mass resolution of the Cameca dynamic SIMS instrument can be varied up to 10,000, although transmission under these conditions is severely limited. Phosphorous requires a mass resolution of 3957 to separate $^{30}Si+^{1}H$ and is especially difficult in a-Si:H materials due to the high levels of hydrogen. While detection limits of 1E14 atoms/cm^3 can be easily achieved for boron under low-mass resolution, phosphorous background limits of 1E16 atoms/cm^3 require instrument parameters of the utmost precision.

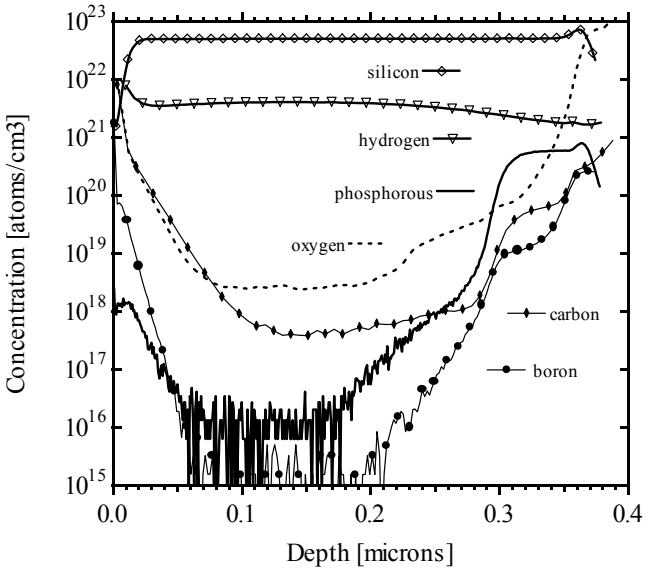

Figure 1. SIMS depth profile of a-Si:H n-i-p device deposited on un-polished stainless steel. Note the amount of boron in the n-layer and phosphorous in the p-layer.

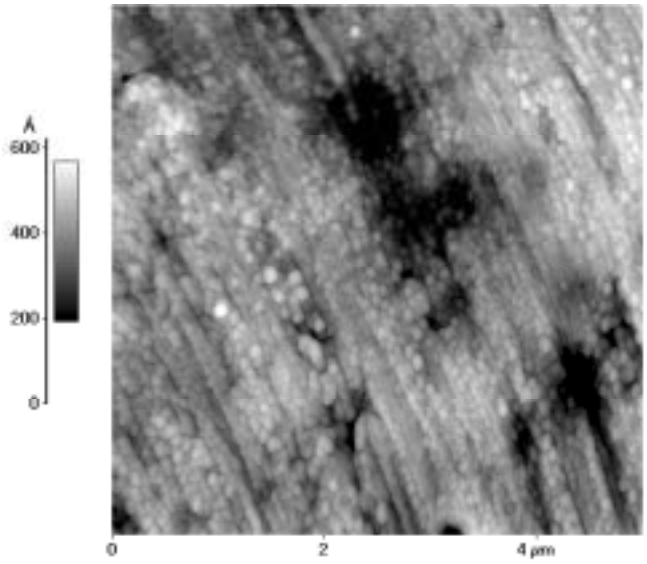

Figure 2. AFM image of standard stainless-steel surface roughness. Note that the typical SIMS analysis area has a diameter of 60 µm.

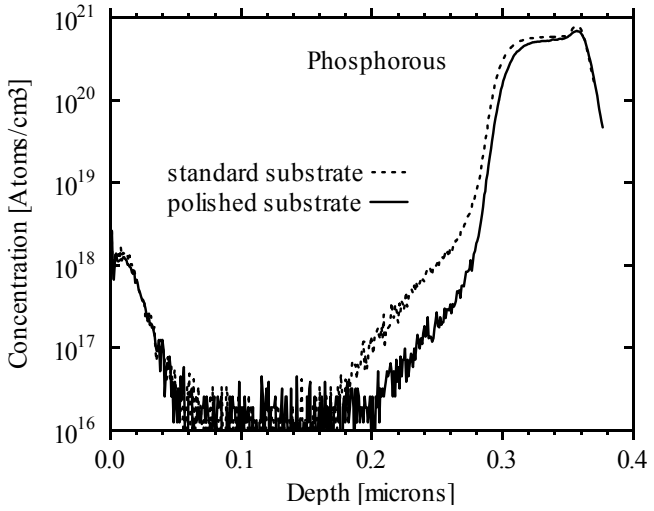

Figure 3. SIMS depth-profile comparison of phosphorous profiles, polished vs. standard SS substrates.

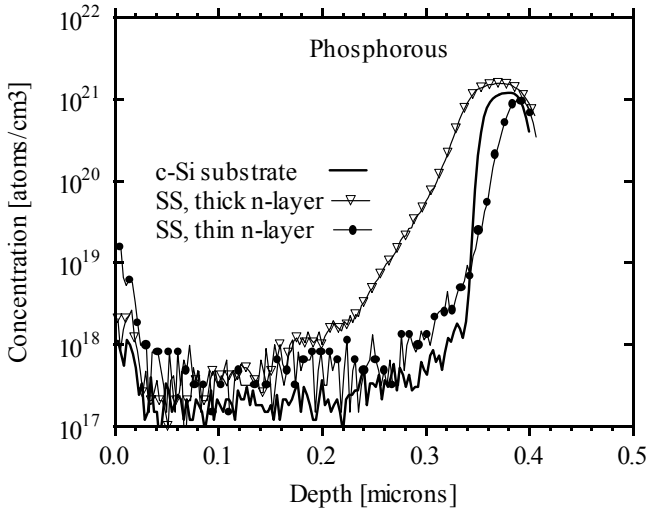

Figure 4. SIMS depth profile comparison of phosphorous profiles, single crystal silicon vs. SS substrates.

3. Roughness Issues

Substrate and surface roughness play a large role in affecting the depth resolution of SIMS depth profiles. Figure 2 is an atomic force microscopy (AFM) image taken from a typical NREL SS substrate. An attempt was made to polish a sample of substrate material and compare the SIMS depth profiles of a-Si:H n-i-p structures grown next to a standard substrate. Visually, the polished substrate appeared to be smoother than the standard, however the average roughness of both substrates, measured by AFM, was nearly identical at 80Å. Figure 3 is a comparison of phosphorous profiles and it clearly shows an improvement in depth resolution.

Comparisons can be made between smooth substrates e.g., glass and single-crystal silicon (c-Si). However, problems occur with adhesion to c-Si and charging effects associated with insulators. The thermal properties of different substrate materials may also influence growth of a-Si:H. Figure 4 is a comparison of a-Si:H n-i-p structures grown on SS and c-Si. There is evidence of approximately 1000Å of P diffusion in the c-Si substrate sample from the n to i-layer.

4. Summary

SIMS is a very powerful tool in the characterization of solar cell devices. Compromises are almost always necessary in detection limits, background levels, and depth resolution. It is imperative to understand the artifacts in measurements and sample preparation to determine the validity of resultant processed data.

REFERENCES

[1] A.H. Mahan; R.C. Reedy; E. Iwaniczko; Q. Wang; B.P. Nelson; Y. Xu; A.C. Gallagher; H.M. Branz; R.S. Crandall; J. Yang; and S. Guha: "H Out-Diffusion and Device Performance in n-i-p Solar Cells Utilizing High Temperature Hot Wire a-Si:H i-Layers", Materials Research Society Symposium Proceedings, Vol. 507, pp. 119-124 (1998).

[2] R.C. Reedy, A.R. Mason, B.P. Nelson, and Y. Xu, "SIMS Characterization of Amorphous Silicon Alloys Grown by Hot-Wire Deposition", Conference Proceedings of the 15th NCPV Photovoltaics Program Review, AIP 462, pp. 537-541

[3] B.P. Nelson, Y. Xu, J.D. Webb, A.M., R.C. Reedy, L.M. Gedivals, and W.A. Lanford, "Techniques for measuring the composition of hydrogenated amorphous silicon-germanium alloys", Journal of Non-Crystalline Solids, 5204, Article 6755 (2000).

[4] R.G. Wilson, F.A. Stevie, and C.W. Magee: "Secondary Ion Mass Spectrometry, A practical Handbook for Depth Profiling and Bulk Impurity Analysis", John Wiley & Sons, New York (1989).

Thin Polycrystalline Silicon Films by HWCVD

R. Aparicio[1], R. Birkmire[1], A. Pant[2], M. Huff[2] and M. Mauk[3]

[1]Institute of Energy Conversion, University of Delaware
[2]Department of Chemical Engineering, University of Delaware
[3]AstroPower Inc.

Newark, Delaware 19716

ABSTRACT

Thin polycrystalline silicon films with grain sizes between 10 to 50 nm and having (220) preferred orientation were deposited from pure silane onto 7059 Corning glass and crystalline silicon substrates by Hot-Wire Chemical Vapor Deposition (HWCVD). The effect of processing parameters, such as substrate temperature, silane flow rate and pressure, on the film properties, crystalline fraction and growth rate was investigated. The crystalline fraction was found to depend on the gas phase chemistry and substrate temperature at wire temperatures above 1815^{o}C.

1. Introduction

The goal of photovoltaic research and development is to reduce the cost per watt of solar electricity. Efforts are directed at either reducing the relatively high cost of c-Si wafer-based modules without sacrificing their performance, or increasing the relatively low performance of thin film modules without sacrificing their manufacturability over large areas. These conflicting themes can be resolved by combining the benefits of c-Si performance and stability in a low-cost monolithically integrated thin film module using thin Si devices on low cost substrates. A key requirement for such devices is a low temperature process which yields ~10 μm thick Si films, having a grain size of ~10 μm, good electronic properties and adequate light trapping. In this paper, results are presented on the growth of thin Si films deposited by hot wire chemical vapor deposition, HWCVD, a technique that has the potential to meet manufacturing as well as solar cell performance requirements. The relationship between processing parameters and resulting film properties is discussed with respect to gas phase chemistry.

2. Experimental

Thin silicon films were deposited from pure silane onto 1 in^2 7059 corning glass and single-crystal (100) silicon substrates. The depositions were carried out in a multi-wire HWCVD reactor which allows uniform deposition over a 6x6 in^2 area. The wire material was high purity Ta and its temperature was monitored with a dual-wavelength pyrometer focused onto the wire through a viewport. A quadrupole mass spectrometer was used to measure the concentration of the gas phase species during deposition. The depositions were performed at wire temperatures between 1815 to 1850^{o}C and reactor pressures between 25 to 700 mTorr. Independent heating of the substrates allowed the substrate temperature to be varied from 280 to 480^{o}C. The silane utilization efficiency (conversion) was calculated from the known inlet silane pressure and the outlet silane pressure measured by the mass spectrometer. The film growth rate was obtained both by measuring the film thickness and the weight gain on the substrates. The silicon film crystalline fraction was determined from Raman spectroscopy [1]. The films were also characterized by XRD, to determine the grain size and preferred orientation.

3. Results and Discussion

For both substrates used, the Si films had grain sizes between 10 to 50 nm and displayed a (220) preferred orientation. The crystalline fraction varied from 0 to 89 percent depending on the process conditions. As reported by Dusane et al. [2], these results, obtained with pure silane, demonstrate that crystalline films can be deposited without hydrogen dilution. At the wire temperatures used, the conversion of silane was approximately constant, ranging from 90 to 99 percent.

Film deposition in HWCVD proceeds through a series of reactions which occur simultaneously in the gas phase and at the wire and substrate surfaces. Table 1 lists a proposed set of reactions leading to Si film formation [3,4]. Silane radicals are produced by both reactions at the wire and in the gas phase, and equally contribute to film deposition. However, it has been previously proposed that the film crystallinity is controlled by the concentration of atomic hydrogen [5]. From Table 1, it is apparent that the concentration of atomic hydrogen, in turn, is determined by a balance of generation reactions at the wire and consumption reactions in the gas phase.

Figure 1 illustrates the effect of silane flow rate at two silane concentrations (pressures), irrespective of the film crystalline structure. The increase in growth rate with silane flow rate is the result of larger amounts of silane reacting to form larger amounts of radical precursors. As the pressure increases, the concentration of all radical species increases resulting in a higher growth rate. At the lower silane concentration, the growth rate becomes constant at flow rates greater than 18 sccm. This trend is attributed to a significant decrease in the residence time which leads to a decrease in the silane conversion.

Table 1. Reaction system in the deposition of Si films from silane.

silane cracking:	$SiH_{4(g)} \rightarrow Si_{(g)} + 4H_{(g)}$
hydrogen abstraction:	$SiH_{4(g)} + H_{(g)} \rightarrow SiH_{3(g)} + H_{2(g)}$
hydrogen cracking:	$H_{2(g)} \rightarrow 2H_{(g)}$
disproportionation:	$2SiH_{3(g)} \rightarrow SiH_{2(g)} + SiH_{4(g)}$
polymerization:	$SiH_{2(g)} + SiH_{4(g)} \rightarrow$ higher silanes
Film deposition:	$SiH_{x(g)} \rightarrow$ film + $(x/2)H_{2(g)}$

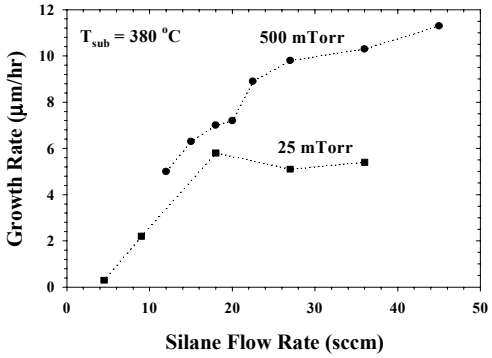

Figure 1. Effect of silane flow rate on the growth rate.

In Figure 2, the effect of residence time on the crystalline fraction is shown. The growth rate was also included for comparison. The residence time is a reactor independent parameter which represents the average time gas phase species spend in the reactor. It is proportional to the ratio of the silane pressure to the silane flow rate. The increase in crystallinity with increasing residence time is related to the efficiency with which the wire can produce atomic hydrogen. The longer the residence time, the greater the probability that silane and molecular hydrogen will interact with the wire and crack to form atomic hydrogen. For a given residence time, increasing the concentration leads to a decrease in crystallinity because higher pressures enhance the gas phase interactions, and thus the consumption of atomic hydrogen.

Figure 3 shows the dependence of crystalline fraction on the substrate temperature at two different conditions of residence time and concentration labeled 1 and 2 in Figure 2. These conditions were selected purposely to have starting points of high and low crystallinity, respectively. The effect of substrate temperature on the crystallinity is related to the mobility of the various species adsorbing onto the substrate surface. Interestingly, it has been postulated that atomic hydrogen has a similar effect of increasing the mobility of adatoms on the growing film [5]. Consequently, at condition 1, which is characteristic of enhanced atomic hydrogen production, the film crystalline fraction is insensitive to increases in mobility by the substrate temperature. On the other hand, at condition 2, where the contribution of atomic hydrogen is expected to be minimal, the substrate temperature plays a major role in determining the film crystalline fraction.

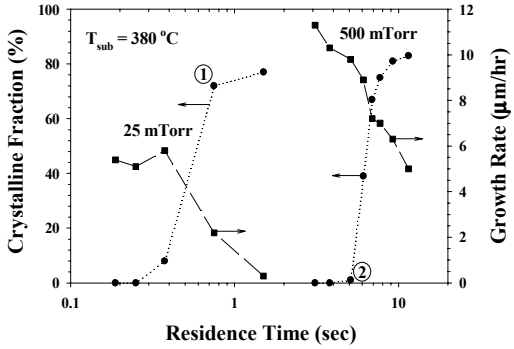

Figure 2. Effect of residence time on the crystalline fraction.

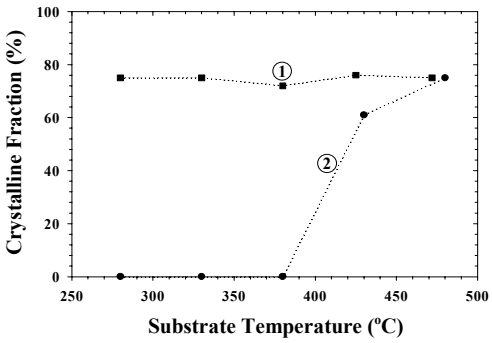

Figure 3. Effect of substrate temperature on the crystalline fraction.

4. Conclusions

Thin polycrystalline silicon films with grain sizes between 10 to 50 nm and (220) preferred orientation were deposited from pure silane onto glass and crystalline silicon substrates. This study demonstrates that highly crystalline silicon films can be deposited without hydrogen dilution. High growth rates can be obtained when high concentrations and flow rates of silane are used. High crystalline fractions result at high substrate temperatures and at concentrations and residence times which lead to relatively high concentrations of atomic hydrogen.

REFERENCES

1. Bustarret, E., Hachicha, M.A. and Brunel, M., *Applied Physics Letters*, **52** (20) 1988.
2. Dusane, R.O., Dusane, S.R., Bhide, V.G. and Kshirsagar, S.T., *Applied Physics Letters*, **63** (16) 1993.
3. Doyle, J., Robertson, R., Lin, G.H., He, M.Z. and Gallagher A., *Journal of Applied Physics*, **64** (6) 1988.
4. D.G. Goodwin, *Fundamental Gas-Phase and Surface Chemistry of Vapor-Phase Materials Synthesis,* ECS Symposium Proceedings, 1998.
5. C. Godet, N. Layadi, P. Roca i Cabarrocas, *Applied Physics Letters*, **66** (23) 1995.

ACKNOWLEDGEMENT

This work was supported in part by AstroPower, Inc. and the National Renewable Energy Laboratory under subcontract ZAK-8-17619-33.

Small-Angle Neutron Scattering Studies of a-Si:H and a-Si:D

D.L. Williamson[1], D.W.M. Marr[1], B.P. Nelson[2], E. Iwaniczko[2], J. Yang[3], B. Yan[3], and S. Guha[3]

[1]Colorado School of Mines, Golden, CO 80410

[2]National Renewable Energy Laboratory, Golden, CO 80401

[3]United Solar Systems Corp., Troy, MI 48084

ABSTRACT

The heterogeneity of hydrogen and deuterium on the nanometer scale has been probed by small-angle neutron scattering (SANS) from a-Si:H and a-Si:D films. Films were deposited by two techniques, plasma-enhanced chemical vapor deposition (PECVD) and hot-wire chemical vapor deposition (HWCVD) using conditions that yield high quality films and devices. Two important results are that no detectable light-induced changes were observed, in contrast with an earlier result, and that significant differences in SANS were observed between the samples made with various deposition conditions.

1. Introduction

Extensive small-angle x-ray scattering (SAXS) studies of a-Si-based materials have provided new information on the structure of these materials on the nanometer scale [1]. The purpose of this research is to complement the SAXS-based information with small-angle neutron scattering (SANS) measurements which are, in principle, much more sensitive to the hydrogen distributions [2]. Also, the possibility of substituting D for H allows additional information due to the large differences in scattering of neutrons by these two isotopes [2]. Although there has been previous SANS research with a-Si-based materials [3-5], there has been little documentation of the device quality of the material used in these investigations. Typically, good SANS signals were obtained with the poorer quality material. One intriguing result obtained in the mid-1980's was the observation of a light-induced change in the SANS [6], which could be explained only by a rather large-scale change in the H distribution [7]. We wanted to try to reproduce this result due to the implication for models of the Staebler-Wronski effect. We also wanted to test whether useful SANS data can be obtained from device-quality material using the high-flux SANS facility at the NIST Center for Neutron Research (NCNR) [8].

2. Experimental

The SANS measurements were done at the NCNR on beamline NG-3. Data were collected over a momentum transfer range from q = 0.05 nm^{-1} to 3 nm^{-1}, using neutrons with wavelength 0.6 nm and two detector positions (2 m and 13 m from the sample). Several special samples were prepared, some with deuterated gases (SiD_4, D_2) used in place of SiH_4 and H_2. Special, high purity FZ c-Si substrates were used with surface roughness below 0.5 nm (checked via AFM measurements) in order to prevent extra background scattering. Multiple films of 1 to 2 μm thickness were prepared to allow stacking of up to 20 layers. Four samples made under conditions that yield high quality material (high hydrogen or deuterium dilution in PECVD, and high substrate temperature in HWCVD) were examined in both a light-soaked state (300 h, AM1) and an annealed state (190°C, 1 h). The latter was done *in-situ* with a special annealing chamber and insured that no changes in measurement geometry occurred between the two states.

3. Results and Discussion

Example SANS data from two samples are shown in Fig. 1. Note the range of intensities over several orders of magnitude and the significant differences in the SANS intensities versus q for the PECVD and the HWCVD samples. Also note the good statistical quality of the data. The lower intensity at high q for the HWCVD sample is due to a much lower H content. We found significant differences in the SANS from the deuterated samples, partly due to the formation of microcrystalline material via the PECVD technique when using the high D_2 dilution condition. Fitting of the data with various models is underway to extract details of the H(D) nanostructure such as sizes of the scattering features and the variation in H(D) concentrations needed to explain the intensities observed. The latter is made possible by the use of absolute cross-section intensity units ($cm^{-1}ster^{-1}$) in processing the data.

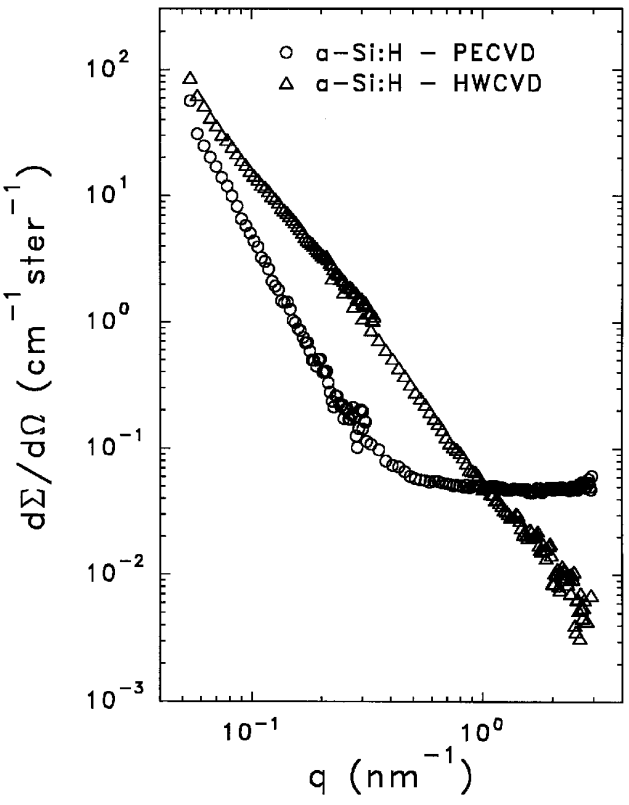

Fig. 1. Example SANS data from films of a-Si:H.

There was no obvious change in the SANS intensities caused by annealing the four light-soaked films. The previous result indicated an increase of 25% in the intensity at all q upon light soaking [6]. In order to examine our data more carefully, the ratio of light-soaked/annealed intensities was computed for each sample over all experimental q's. The ratios are unity within an experimental scatter range of about ± 2%.

4. Conclusions

The previous Staebler-Wronski-effect-induced change in nanostructure reported several years ago [6] could not be reproduced in the present study. No detectable changes were found. We also established that statistically-significant SANS data can be obtained from device-quality films. Analysis of such data should lead to improved understanding of the non-uniform H distributions and their ultimate connection with the opto-electronic properties.

REFERENCES

[1] D.L Williamson, Mat. Res. Soc. Symp. Proc. 377 (1995) 251.

[2] L.A. Feigin and D.I. Svergun, *Structure Analysis by Small-angle X-ray and Neutron Scattering* (Plenum, New York, 1987).

[3] A.J. Leadbetter, A.A.M. Rashid, R.M. Richardson, A.F. Wright, and J.C. Knights, Solid State Commun. 33 (1980) 973.

[4] R. Bellissent, A. Chenevas-Paule, and M. Roth, J. Non-Cryst. Solids 59&60 (1983) 229.

[5] C.A. Guy, A.F. Wright, R.N. Sinclair, R.J. Stewart, and F. Jansen, J. Non-Cryst. Solids 196 (1996) 260.

[6] A. Chenevas-Paule, R. Bellissent, M. Roth, and J.I. Pankove, J. Non-Cryst. Solids **77&78** (1985) 373.

[7] R. Bellissent, in *Amorphous Silicon and Related Materials*, Ed. by H. Fritzsche (World Scientific, Singapore, 1988) p. 93.

[8] C.J. Glinka, J.G. Barker, B. Hammouda, S. Krueger, J.J. Moyer, and W.J. Orts, J. Appl. Cryst. 31 (1998) 430.

Structural Ordering and its Correlation to the Optoelectronic Properties of a-Si:H Films

Jonathan Baugh[1], Daxing Han[1*], Alfred Kleinhammes[1], Qi Wang[2], and Yue Wu[1]

1. Dept of Physics and Astronomy, University of North Carolina, Chapel Hill, NC 27599-3255
2. National Renewable Energy Laboratory, 1617 Cole Blvd. Golden, CO 80401
*daxing@physics.unc.edu

ABSTRACT

Magnetic susceptibility (χ) was suggested theoretically to be sensitive to the overall structural order of a-Si:H. χ is measured precisely for various a-Si:H thin films using a new technique. The measured χ is shown to be sensitive to variations of the structural order and correlates well with the optoelectronic properties as well as the reversible conductivity changes, the SWE. Measurements of χ, H microstructure, and light-induced photoconductivity degradation on the same piece of thin film reveal clearly that the overall structural order plays an important role in the electronic properties including metastability of a-Si:H.

I. Introduction

The light induced defect creation was found to be smaller in a-Si:H films prepared by hot-wire chemical vapor deposition (HW-CVD) and by plasma-enhanced chemical vapor deposition (PE-CVD) under hydrogen dilution condition [1,2]. It was suggested that it is due to an improvement of the structural order[1-4]. This implies that the overall structure order of the film can be controlled and it has a direct impact to the metastability. Whereas, the electronic properties and its stability depends not only on deposition conditions but also sample thickness and substrate etc. The small difference of structural order among those device-quality films can hardly be detected by XRD and Raman spectroscopy [3,5]. Thus, more sensitive measures of overall structural order, especially those that could correlate with the SWE of a-Si:H, are highly desirable.

Previous studies have shown that the magnetic susceptibility χ is about a factor of 4.5 larger in a-Si than that in c-Si [6] due to structural deviations such as bond-angle and bond-length disorder[7]. In this work, we study χ in a series of HW a-Si:H films by using a new technique of NMR[8]. The goal is to detect possible differences in χ between device-quality a-Si:H films which exhibit different levels of metastability. Conventional techniques for measuring χ such as SQUID magnetometer, find some difficulties because of the small amount of sample (0.5 mg) and the irreproducibility of the background signal intensity after sample changes. In this work, the ^{1}H resonance frequencies are measured for sample orientations with the film surface both perpendicular and parallel to the external magnetic field. The change of the resonance frequency with such change of sample orientation gives a direct measure of χ.[8]. Theoretically, the structural order is measured by the contribution to the susceptibility per Si-Si bond [7]. Because of the possible existence of nanovoids, molar susceptibility, $\chi_{mol}=m\chi/4\pi\rho$ is a more appropriate measure of the local structural order, where ρ=2.300 g/cm^3 is the film's mass density and m =28 g/mol, is the silicon's molar mass.

II. Experimental and Results

1-μm thick a-Si:H films were deposited on 1.5x1.5 cm^2, 0.042 cm-thick quartz substrates by HWCVD with pure silane. A μc-Si sample #8 was prepared with H dilution. A single piece of sample is placed in a flattened NMR coil. The coil could be oriented so that the sample would be at any desired angle with respect to the external magnetic field. The NMR spectra were obtained in a field of 4.7 Tesla at room temperature. Since the films studied have low H contents, the home-made ^{1}H-NMR probe was specially designed to have very little or no ^{1}H background signal.

Table I
Sample preparation parameters and the measured χ_{mol}

Sample ID	T_S (^{o}C)	T_{fil} (^{o}C)	Growth Rate (Å/s)	C_H (at.%)	χ_{mol} (10^{-6}cm^3/mol)
1	280	1500	7.5	4.5	-13.27±0.49
2	310	1500	7.7	4.1	-13.76±0.59
3	340	1500	7.7	3.3	-13.72±0.64
4	360	1500	6.9	3.6	-12.72±0.48
5	380	1500	8.2	2.4	-13.92±0.54
6	380	1500	5.4	4.4	-11.62±0.56
7	380	1800	8.4	4.0	-13.73±0.53
8	220	1800	6.4	6.3	-6±0.8

The H microstructure were characterized by the NMR spectra which consist of a broad Gaussian line with a full width at half height (FWHH) of about 40 kHz (200 ppm) and a narrow Lorentzian line of about 3 kHz (15 ppm), due to clustered and isolated monohydrides (Si-H), respectively. The measured values of the molar susceptibility are listed in Table I. T_s and T_{fil} are the substrate and filament temperatures. χ_{mol} is in the cgs unit cm^3/mol. A μc-Si:H film yields a much smaller average χ_{mol}; here, the value of χ_{mol} implies a ~70% volume fraction of crystallites, which is consistent with the growth conditions.

Figure 1 shows the measured χ_{mol} vs. the growth rate for the films listed in Table I. The largest variation in χ_{mol}

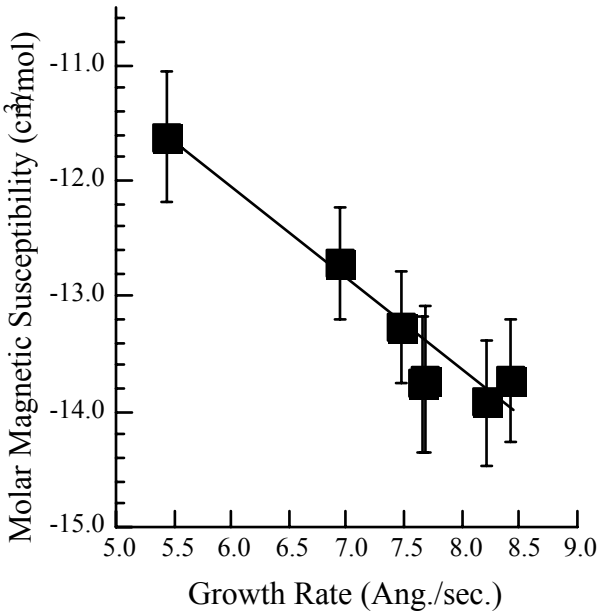

Figure 1
Measured χ_{mol} versus the growth rate for all the a-Si:H films listed in Table I.

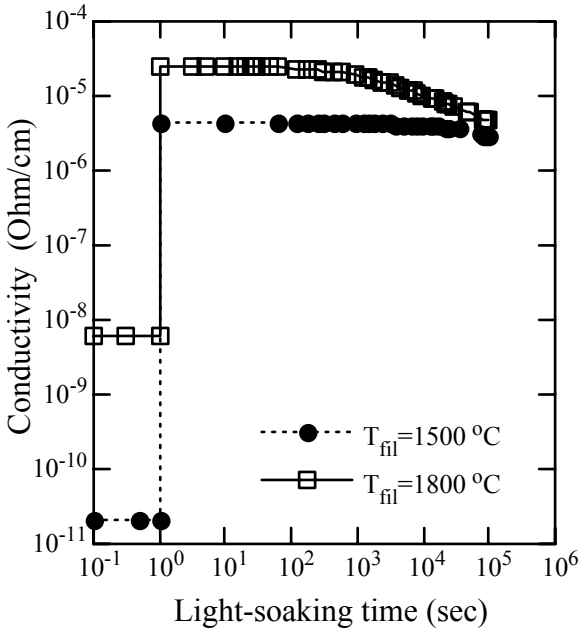

Figure 2
Dependence of the photoconductivity on light-soaking time for samples #6 and #7.

is about 17%. The data implies that in this growth parameter regime, a lower growth rate leads to a more ordered amorphous Si network. No such correlation is found between χ_{mol} and T_s or H content in this range of T_S (280 -380 ^{O}C). Fig. 2 shows the dependence of the phto-conductivity on light-soaking time, under 150 mW/cm^2 white light, in vacuum at 310 K, for films #6 and #7. For sample 6, which has the lowest χ_{mol}, photoconductivity decreases by only a factor of 1.5 at saturation of 28 hr. Sample 7, which has a χ about 15% larger than that of sample 6, is significantly less stable; its photo-conductivity decreases by a factor of 5.3 after the same illumination. The initial photo-sensitivity of sample 6 is 2.1x10^5 which is fifty times larger than that of sample 7.

III. Summary

The NMR method provides a unique tool for precise measurement of magnetic susceptibility χ in thin films. Measurements of χ, hydrogen microstructure, and photodegradation carried out on the same piece of sample suggest that the overall structural order plays an important role in both the initial photosensitivity and in the metastability of a-Si:H. The observation that growth rate correlates with the overall structural order in a-Si:H is not surprising, since it is well known that lower growth rates generally lead to lower defect densities in such films[9]. This unique tool allows for the unambiguous identification of the importance of the overall structural order on the metastability of a-Si:H in thin-film device structures.

Acknowledgments

This work is supported by NREL Thin Film PV partnership under the sub-subcontract XAK-8-17619-11, and NSF under the contracts DMR-9802101 and INT-9604915. Wang is supported by DOE subcontract DE-AC02-83CH10093. We thank C. Liu, G. Yue, and X.-P. Tang for helpful discussions and experimental assistance.

References

1. A. H. Mahan, J. Carapella, B. P. Nelson, R. S. Crandall, and I. Balberg, J. Appl. Phys. **69**, 6728 (1991).
2. S. Guha, J. Yang, D. L. Williamson, Y. Lubianiker, J. D. Cohen, A. H. Mahan, Appl. Phys. Lett. **74**, No. 13, 1860 (1999).
3. D. L. Williamson, Mat. Res. Soc. Symp. Proc. **557** (1999), in press.
4. Y. Wu, J. Todd. Stephen, Daxing Han, J.M. Rutland, R. A. Crandall, and H. Mahan, Phys. Rev. Lett., **77** (1996) 2049.
5. D. Han, G. Yue, J. Yang, and S. Guha, in this meeting.
6. R. Candea, S. Hudgens, M. Kastner, J. Knights, Phil. Mag. B **37**, 119 (1978).
7. T. Sahu and N. Das, Phys. Rev. B **45**, 13336 (1992).
8. J. Baugh, D. Han, A. Kleinhammes, Q. Wang, and Y. Wu, submitted to PRL, (2000).
9. G. Ganguly and A. Matsuda, Mat. Res. Soc. Symp. Proc. **258**, 39 (1992).

The chemical ordering in a-$Si_{1-x}C_x$:H thin films by vibrational spectroscopy and nuclear methods

D.Gracin[*1], J.M.Dutta*, V.Borjanovic*[2], B.Vlahovic*, I.Bogdanovic[1], M.Jaksic[1] and R.J.Nemanich[3]

* Physics Dept., North Carolina Central University, Durham, NC; [1] Rudjer Boskovic Institute, Zagreb, Croatia;

[2] Zagreb University, Zagreb, Croatia [3]; North Carolina State University, Raleigh, NC

ABSTRACT

The thin amorphous hydrogenated silicon-carbide films, a-$Si_{1-x}C_x$:H, were deposited in wide composition range and under various deposition conditions. The film composition and concentration of chemical bonding have been measured by RBS, ERDA, FTIR and Raman spectroscopy. The compatibility and accuracy of applied methods in quantitative analysis has been discussed and the degree of chemical ordering has been estimated.

1. Introduction

The degree of chemical ordering in composite systems is determined by the ratio of present to possible heteropolar bonds in material [1] and reveals the mutual positions of atoms of the constituents. It assumes the exact knowledge of the concentration of each type of bonds. This type of information is provided by the applications of IR and Raman spectroscopy, if the cross sections are well established. If working with amorphous alloys, which are not well defined, this assumption has to be verified by comparing the quantitative results obtained from vibrational spectroscopy with those obtained by other methods. Part of this verification procedure concerning Si-C bonds in a-$Si_{1-x}C_x$:H samples has already been demonstrated [2]. In this paper we report a quantitative analysis of Si-H, C-H and C-C bonds in the same type of samples.

2. Experimental

The 1 μm thick specimens were deposited by magnetron sputtering with carbon concentration between x=0.2 and x=1. The source of silicon atoms was magnetron cathode and working gas was argon-hydrogen mixture. Carbon was introduced in two ways: by co-sputtering of carbon and silicon and by decomposition of benzene vapor near the surface of growing film.

The RBS and ERDA measurements were done by using He ion beam from the 1.6 MV 5SDH Pelletron tandem accelerator at Johannes Kepler University in Linz, Austria. The procedure for performing and analysing IR results, has been already described in ref.[2]. Raman spectroscopy was performed by using a double grating spectrometer supplied with potomultiplier. For excitation, the 524.5 nm Ar ion laser beam was used.

3. Results and discussion

For testing the mutual compatibility of vibrational spectroscopy and nuclear methods, the sum of Si-H and C-H bonds concentrations is compared with total number of hydrogen atoms, C_H, measured by ERDA. As can be seen from Fig.1., the results agree inside the error bars (which are about 15% for ERDA and about 20% for FTIR [2]).

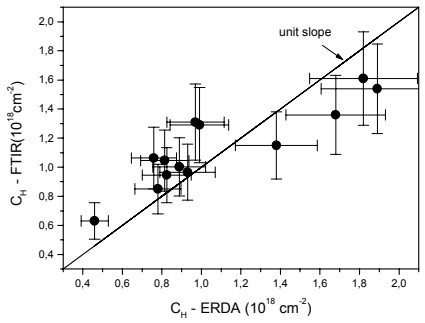

Fig.1. Hydrogen concentration, C_H, estimated from IR measurements versus C_H measured by ERDA

The spreading of mean values of data is most likely due to the slight change in cross sections for IR response, which is caused by the so called "solid state effect". In particularly, for higher hydrogen concentration, the underestimation of

hydrogen concentration by FTIR could be a consequence of the fact that part of the hydrogen in layer is not bonded either to carbon or silicon..

The quantitative analysis of C-C bonds by Raman spectroscopy needs some attention since generally, carbon appears as amorphous and microcrystalline, in sp^3 and/or sp^2 configuration, having cross-sections which differ by several orders of magnitude [3]. However, in our a-$Si_{1-x}C_x$:H specimens, the most of C-C bonds appear in sp^2

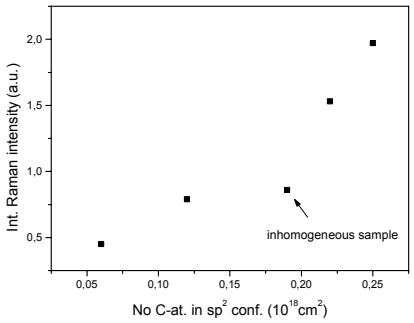

Fig.2. The integral intensity of Raman D and G bands versus number of C-atoms in sp^2 configuration estimated by combining IR and nuclear methods

configuration. For x≤0.5, the structure is amorphous (glassy) while at higher carbon concentrations, C-C bonds are in microcyistalline form, in about 5 nm large inclusions. All these facts should allow the direct correlation between the surface below Raman lines corresponding to C-C bonds and the number of C atoms which build C-C bonds in sp^2 configuration, estimated by combining IR spectroscopy and RBS results. As can be seen from Fig.2., there is good correlation between these quantities, allowing simple quantitative analysis.

Finally, after verifying quantitative aspect of vibrational spectroscopy, the degree of chemical ordering can be discussed. If the ratio of present to possible heteropolar bonds in material is close to one, alloy is considered to be completely chemically ordered [1]. In Fig.3. this kind of comparison has been done for Si-C bonds as a function of composition, x, for two series of a-$Si_{1-x}C_x$:H samples. The open circles represent samples deposited by cosputtering of

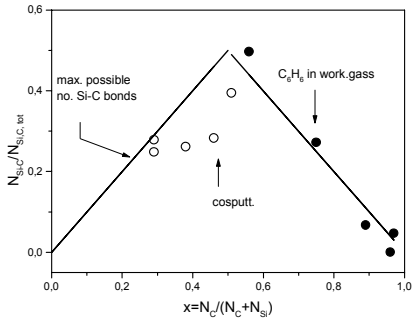

Fig.3. The ratio of Si-C bonds and total amount of Si and C atom bonds, $N_{Si-C}/N_{Si,C}$, versus composition, x;

Si and C while full circles are specimens where carbon is introduced by decomposition of benzene vapor. Full lines represent maximal possible $N_{Si-C}/N_{Si,C}$ ratio, e.g. perfect chemical ordering. As can be seen, for co-sputtered samples, as it can be expected, there is much less chemical ordering then for other type of deposition. This result verifies analyses procedure proposed above.

Summary

The possible way of analysing the chemical ordering of poly-phase alloys, combining vibrational spectroscopy and nuclear methods, has been demonstrated for a-$Si_{1-x}C_x$:H alloys. Usefulness of applied methods in quantitative analysis and theirs accuracy has been discussed.

Literature

[1] K.Mui and F.W.Smith, Phys Rev. B **35** (1987) 8080

[2] D.Gracin, M.Jaksic, C.Yang, V.Borjanovic and B.Pracek, Appl.Surface Science **144-145** (1999) 188

[3] R.E.Schroeder, R.J.Nemanich and J.T.Glass, Phys.Rev B **41** (1990) 3738

Acknowledgement: This work is partly supported by a grant from NREL, subcontract no. AAK-9-18675-03.

Ultrafast Dynamics of Photoexcited Carriers in HWCVD a-Si:H and a-SiGe:H

S. L. Dexheimer[1], J. E. Young[1], and Brent P. Nelson[2]

[1]Department of Physics, Washington State University, Pullman, WA 99163

[2]National Renewable Energy Laboratory, 1617 Cole Boulevard, Golden, CO 80401

ABSTRACT

We present femtosecond studies of photoexcited carrier dynamics in hydrogenated amorphous silicon and silicon-germanium alloys grown by the hot-wire assisted chemical vapor deposition (HWCVD) technique, which is promising for producing high-quality device-grade materials. We have used wavelength-resolved femtosecond pump-probe techniques to study the dynamics of photoexcitations in these materials. Femtosecond dynamics measurements have been carried out on thin film samples under experimental conditions with varying sensitivity to carriers in extended states or in band tail states. The relaxation dynamics of carriers associated with extended states show a strong dependence on excitation density and follow a bimolecular recombination law, consistent with a number of earlier studies on related amorphous materials. In contrast, measurements involving band tail states reveal significantly altered dynamics, characterized by a marked deviation from simple bimolecular recombination.

1. Introduction

Thin-film amorphous silicon and silicon-germanium alloys are promising materials for low-cost, high-efficiency solar cells, yet a range of issues relevant to their development and application as photovoltaic materials are not yet fully understood. Important unresolved issues include the detailed nature of the electronic states in these disordered semiconductors, and in particular, the relation of the band tail and extended states and their influence on the carrier dynamics. In this work, we investigate the dynamics of photoexcited carriers in a series of a-SiGe:H alloys. By varying the relative energy of the photoexcitation and the band gap, we selectively excite carriers into extended states or into progressively deeper band tail states, and we monitor the time evolution of the carrier distribution using femtosecond pump-probe techniques.

2. Experimental

Thin films of a-SiGe:H were grown on glass substrates by the hot-wire assisted chemical vapor deposition (HWCVD) technique [1]. For the experimental results presented in this paper, the Ge concentration of the films varied from 10 to 50 atomic percent. The optical band gap of the materials can be characterized in terms of the transition energy at which the absorbance reaches a value of 10^4 cm^{-1}, and this value corresponds to energies of 1.76 eV, 1.60 eV, and 1.42 eV for samples of 10, 30, and 50 atomic percent Ge, respectively. The samples were grown with a nonuniform thickness so that an optimal thickness for the thin film etalon response could be chosen for the time-resolved optical measurements [2]. Approximate sample thicknesses varied from ~ 350 nm for the 50% Ge sample to ~780 nm for the 10% Ge sample, giving optical densities at the pump wavelength of < 0.25.

Time-resolved measurements of the carrier dynamics were carried out using an optical pump-probe technique, in which a short pump pulse excites carriers in the sample and a time-delayed probe pulse measures the resulting change in the optical properties as a function of the pump-probe delay time. Measured changes in the transmission and reflectivity can be related to changes in the optical absorption coefficient and the index of refraction of thin film samples for comparison with theoretical models. In these initial measurements, the thin film samples were excited with pulses 35 fs in duration centered at a wavelength of 800 nm, corresponding to a transition energy of 1.55 eV. The pulses were generated by an amplified Ti:sapphire laser system operating at a repetition rate of 1 kHz. Probe pulses of variable wavelength were produced using a femtosecond white-light continuum generated by self-phase modulation in a sapphire plate, followed by prism dispersion compensation to give a temporal resolution typically < 50 fs.

3. Results

Measurements of the time-resolved change in transmission following excitation at 1.55 eV for a series of a-SiGe:H alloys are displayed in Figures 1-3 [3]. The data are presented as the negative of the differential transmittance, corresponding to an induced absorbance that results from the photoexcited carrier population. In all cases, the carrier response was probed at a detection wavelength of 900 nm.

The carrier response shows a nonexponential time dependence that is strongly dependent on excitation density. When carriers are initially excited into the extended states well above the band gap, as is the case for 1.55 eV excitation of the 50% Ge sample shown in Fig. 1, the relaxation dynamics can be well described by a bimolecular

recombination law, consistent with previous time-resolved measurements on similar systems at comparable excitation densities. Fits to the solution of a bimolecular rate equation $dn/dt = -kn^2$ are shown superimposed on the data traces, and give values for the bimolecular recombination constant $k \sim 5 \times 10^{-9}$ cm^3/s, consistent with previous work on a-Si:H in which carriers were excited into extended states at comparable energies relative to the band gap [4].

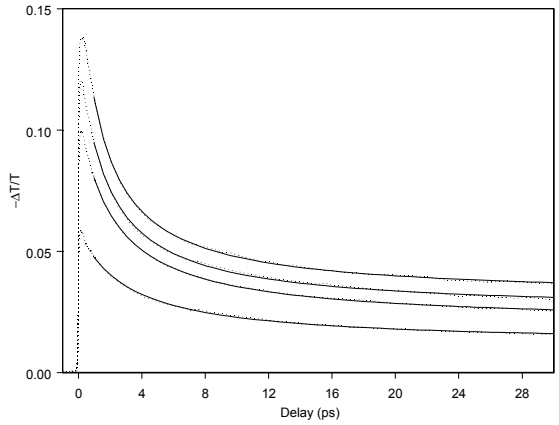

Fig. 1. Time-resolved negative differential transmittance of an a-Si_xGe_{1-x}:H thin film with x = 0.50. The data traces correspond to initial carrier densities of approximately 3 x 10^{20} cm^{-3}, 2.5 x 10^{20} cm^{-3}, 1.8 x 10^{20} cm^{-3}, and 9.2 x 10^{19} cm^{-3}.

In contrast, the time-resolved response for carrier excitation at lower energies relative to the optical gap exhibits a marked deviation from simple bimolecular recombination at short times. Representative responses for carriers excited progressively farther into the band tail states are presented in Figs. 2 and 3. For pump-probe delay times longer than ~ 1 ps, the response is well characterized by bimolecular recombination, as shown by the fits to the data traces. At early times, a significant delay is observed in the peak of the induced absorbance that becomes more pronounced for initial excitation farther into the band tail. (The sharp feature at t = 0 includes contributions from nonlinear effects due to the temporal overlap of the pump and probe pulses and is neglected in the interpretation of the carrier dynamics.) The short-time response provides evidence for a rapid thermalization process on a subpicosecond time scale.

Acknowledgments

We thank NREL for providing support for this work, and we thank Dick Crandall for facilitating the collaboration. Additional support was provided by the National Science Foundation and by Washington State University.

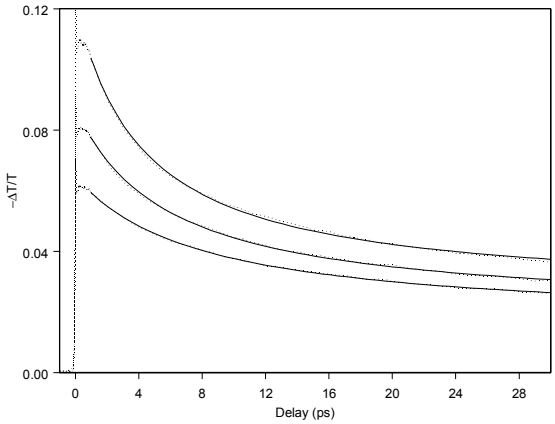

Fig. 2. Time-resolved negative differential transmittance of an a-Si_xGe_{1-x}:H thin film with x = 0.70 and initial carrier densities of approximately 5.5 x 10^{19} cm^{-3}, 4.4 x 10^{19} cm^{-3}, and 3.3 x 10^{19} cm^{-3}.

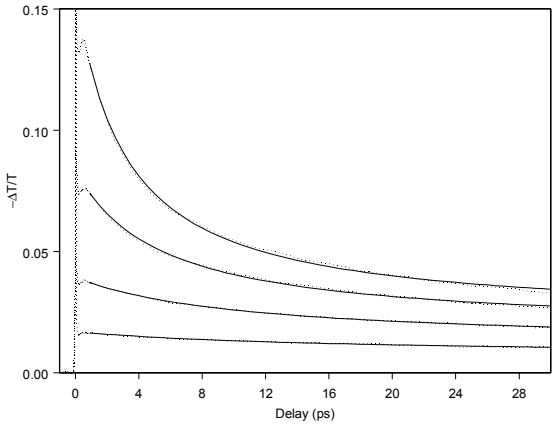

Fig. 3. Time-resolved negative differential transmittance of an a-Si_xGe_{1-x}:H thin film with x = 0.90 and initial carrier densities of approximately 6.6 x 10^{19} cm^{-3}, 4.4 x 10^{19} cm^{-3}, 2.6 x 10^{19} cm^{-3}, and 1.3 x 10^{19} cm^{-3}.

References

1. Nelson, B.P., *et al.*, Materials Research Society Symposium Proceedings (1998).
2. Moon, J.A. and J. Tauc,. J. Appl. Phys. (1993) **73**, 4571.
3. Young, J.E. and Dexheimer, S.L., to be published.
4. Esser, A., *et al.*, J. Appl. Phys. (1993) **73,** 1235, and references therein.

A Comparative Study of Chemical-bath-deposited CdS, (Cd,Zn)S, ZnS, and $In(OH)_xS_y$ Buffer Layers for CIS-based Solar Cells

C. H. Huang[a], Sheng S. Li[a], L. Rieth[b], A. Halani[1], Jiyon Song[a], T. J. Anderson[c], and P. H. Holloway[b]

a. Department of Electrical and Computer Engineering,
b. Department of Material Science and Engineering,
c. Department of Chemical Engineering,
University of Florida, Gainesville, FL 32611, USA
1. International Solar Electric Technology (ISET), Inc.
8635 Aviation Boulevard, Inglewood, CA 90301, USA

ABSTRACT

In this paper we report a comparative study of CdS, (Cd,Zn)S, ZnS, and $In(OH)_xS_y$ buffer layers grown by chemical bath deposition (CBD) on $Cu(In,Ga)(Se,S)_2$ films. X-ray Photoelectron Spectroscopy (XPS) analysis has been performed on these buffer layers. J-V characteristics of the CIGSS solar cells deposited with ZnS, (Cd,Zn)S, or $In(OH)_xS_y$ buffer layers were measured and compared to the cells deposited with CBD CdS buffer layers.

1. Introduction

The best performance CIGS solar cell with a total-area conversion efficiency of 18.8% employs the CBD CdS buffer layer. [1] Using wider band gap (E_g>2.4eV) materials as the buffer layers instead of CdS (E_g≈2.4eV) will improve the quantum efficiency at shorter wavelengths, resulting in increased short-circuit current. The (Cd,Zn)S buffer layer has a band gap energy greater than 2.4eV, and can provide a better lattice match to the CIGS absorber layer. Other alternative buffer layers were investigated to avoid using Cd due to its toxicity. Literature values for ZnS (E_g≈3.6eV) and $In(OH)_xS_y$ (E_g≈2.54eV) buffer layers on CIGS solar cells have achieved active-area conversion efficiencies of 16.9% and 15.7% respectively. [2-4]

2. Experimental

The CBD methods used for the deposition of CdS and $In(OH)_xS_y$ buffer layers on CIGS films have been described in the literature.[5,2] Acetic acid was added into the bath as a complexing agent to improve the quality of $In(OH)_xS_y$ films. The deposition of (Cd,Zn)S buffer layers was carried out by using the aqueous solution of $CdCl_2$, $ZnCl_2$, thiourea, NH_3, and NH_4Cl. A mixed solution of $ZnSO_4$, thiourea, NH_3, and hydrazine was used to deposit the ZnS films. The CdS, (Cd,Zn)S, ZnS, or $In(OH)_xS_y$ buffer layers were deposited on CIGSS samples provided by Siemens Solar Industries. The high and low resistivity ZnO bilayer films were then deposited by MOCVD on these samples at a substrate temperature of 150-200°C.

3. Results and Discussion

XPS analysis was conducted using a Physical Electronics 5100 ESCA equipped with a Mg Kα X-ray source. The compositions of ZnS, $In_x(OH,S)_y$, (Cd,Zn)S, and CdS films deposited on the CIGS samples were characterized. Carbon was initially present but became undetectable during sputter depth profiling, which revealed little carbon was incorporated in the films. Besides carbon the elements of metal (Cd, Zn, or In), sulfur, and oxygen were identified in the deposited films.

For the ZnS film, the deconvolution of Zn $2p_{3/2}$ binding-energy spectrum revealed one peak at 1022.0 eV. This is consistent with the energy peaks of ZnS and/or ZnO at 1022.0 eV and 1021.8 eV-1022.5 eV, respectively. [6] The oxygen 1s photoelectron binding energy spectra were fitted with Gaussian-Lorentzian curves both before and after sputtering the film. The XPS spectra can be represented by two peaks at about 530.6-530.1 eV and 531.6 eV, which correspond to the chemical bonds of Zn-O (530.4eV) and Zn-OH (530.9-532eV), respectively.[6] Thus the results suggest that the CBD ZnS films might be a mixture of ZnS, ZnO, and $Zn(OH)_2$. The estimated atomic concentration ratio of Zn, S, and O was about 5:3:2 after sputtering the film for 4 minutes.

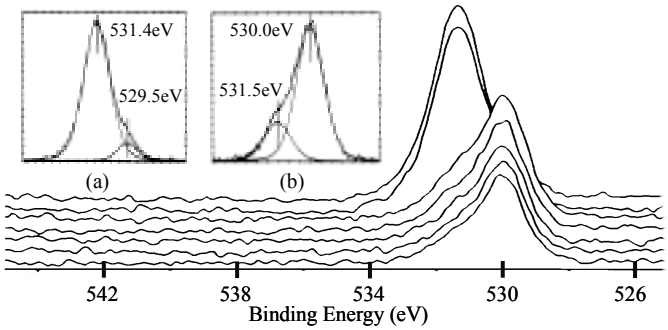

Figure 1 Montage of photoelectron binding energy spectra for a depth profile of an $In(OH)_xS_y$ film (view with surface curve in the background). The oxygen 1s photoelectron binding energy spectra in Figure 1 are (a) as-received surface and (b) after sputtering for 4 minutes.

For the $In(OH)_xS_y$ films, a binding energy peak of S $2p_{3/2}$ was found at about 161.24 eV, which can be assigned to the sulfide compound. A very weak binding energy peak around 168.96 eV suggests that the indium sulfate (169-171 eV) was also present. [6] After sputtering the film for 4 minutes no peaks were found in the range of 167-173 eV. We conclude that the sulfate compound only exists at the surface of the film. From Figure 1 the montage of binding energy distribution curves between 526 eV and 543 eV, it is evident that the shape of the spectra changes for the oxygen 1s peak during the depth profile. As shown in the inset of Figure 1(a), before sputtering the XPS spectra can be represented by two peaks at 531.4 eV and 529.5 eV, suggesting that the oxygen is present in the form of In-OH (531.8 eV) and In-O (529.8eV).

[6] As exhibited in the inset of Figure 1(b), likewise two fitted peaks at 531.5eV and 530.0eV are present in the curve after sputtering the film. This suggests that the film had more indium hydroxide than indium oxide at the near surface region. The estimated atomic concentration ratios of In, S, and O were about 49.9%:26.5%:23.6% after sputtering of 4 minutes.

Similarly the CdS and (Cd,Zn)S buffer layers include not only the sulfide compound but also the compounds of metal oxide and metal hydroxide. For the CdS film the estimated atomic concentration ratios of [Cd]/[S] and [S]/[O] were approximately 1.6 and 5.4, respectively. The XPS result indicated that a large amount of oxygen (around 40 %) and a small amount of zinc (around 2 %) were incorporated in the (Cd,Zn)S film. Since the precipitation of CdS is faster than that of ZnS during the CBD process, the deposited (Cd,Zn)S film only had a very small quantity of zinc even though the concentration of zinc source was one order of magnitude higher than that of cadmium source in the deposition bath.

Figure 2 illustrates the effect of ZnS buffer layer thickness on the performance of CIGSS solar cells. With the increase of ZnS buffer layer thickness the absorption of the incident light in the ZnS layer increases and thus the short circuit current of the cell decreases. And due to the high resistivity of ZnS buffer layer a thick buffer layer can increase the series resistance of the solar cells and causes a poor fill factor as shown in Figure 2. Since the band gap energy of ZnS is larger than that of CdS, the ZnS/CIGSS cell should have a higher short circuit current than CdS/CIGSS cell because of the higher quantum efficiency at shorter wavelengths. However, the highest short circuit current obtained in this study for the ZnS/CIGSS cell was only 27.74mA/cm^2. Thus further optimization of ZnS layer thickness is needed to reach the potential of CIS-based cells with ZnS buffer layers.

In our previous study [2], we conducted an investigation of $In(OH)_xS_y$ and CdS buffer layers on CIGS solar cells. The possible reason why the $In(OH)_xS_y$/CIGS cell has a higher V_{OC} than CdS/CIGS cell has been proposed in [4]. However, the $In(OH)_xS_y$/CIGS cell has a lower I_{SC} due to the lower spectral response than the CdS/CIGS cell at longer wavelengths [4]. By adding Acetic acid as a complexing agent into the chemical bath, a more adherent, reproducible, homogeneous, and better quality $In(OH)_xS_y$ film has been deposited on the CIGSS sample. [7] The performance of one $In(OH)_xS_y$/CIGSS cell is exhibited in Figure 3.

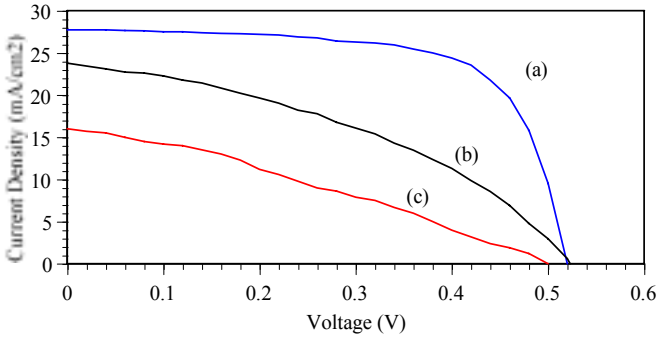

Figure 2 J-V characteristics of CIGSS solar cells using different thickness of CBD ZnS buffer layers deposited for (a) 10min, (b) 20min, and (c) 25min at 70℃.

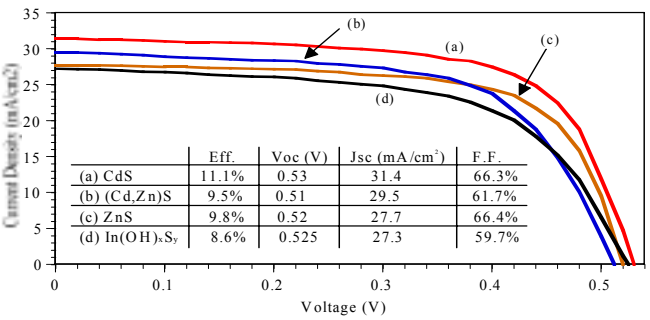

Figure 3 J-V characteristics of the CIGSS cells with CdS, (Cd,Zn)S, ZnS, or $In(OH)_xS_y$ buffer layers.

J-V characteristics of CIGSS solar cells with CdS, (Cd,Zn)S, ZnS, and $In(OH)_xS_y$ buffer layers grown by our CBD process are shown in Figure 3. The CIGSS solar cell with CdS buffer layer has the best conversion efficiency.

4. Summary

The XPS results revealed that CdS, (Cd,Zn)S, ZnS, and $In(OH)_xS_y$ films grown by CBD process were not completely pure. A small amount of carbon was incorporated in the first few atomic layers of the films. Also oxygen in the form of metal oxides and/or metal hydroxides was incorporated into the films during the deposition process. From the J-V characteristics obtained for the CIGSS solar cells with different buffer layers, the deposition conditions of CBD buffer layers need further optimization in order to realize the potential advantages of the alternative buffer layers.

Acknowledgements

This work has been funded by the DOE/NREL Thin Film PV Partnership Program and administrated by NREL under subcontract No. XAF-8-17619-32. The authors would like to thank Siemens Solar Industries and ISET, Inc. for generously providing the CIGSS and CIGS samples, respectively, used in this study, and Eric Lambers at the Major Analytical Instrumentation Center (MAIC) of the University of Florida for help with XPS analysis.

REFERENCES

[1] M.A. Contreras, B. Egaas, K. Ramanathan, J. Hiltner, A. Swartzlander, H. Hasoon, and R. Noufi, Prog. Photovolt: Res. App. 7 (1999) 311-316.

[2] C.H. Huang, Sheng S. Li, W.N. Shafarman, C.-H. Chang, J.W. Johson, L. Reith, S. Kim, B.J. Stanbery, and T.J. Anderson, Technical Digest of the 11th International Photovoltaic Science and Engineering Conference (1999) 855.

[3] T. Nakada, K. Furumi, and A. Kunioka, IEEE Transactions on Electron Devices 46 (1999) 2093-2097.

[4] D. Hariskos, M. Ruckh, U. Rühle, T. Walter, H.W. Schock, J. Hedström, and L. Stolt, Solar Energy Materials and Solar Cells 41/42 (1996) 345-353.

[5] C.-H Chang, A.A. Morrone, B.J. Stanbery, C. McCreary, M. Huang, C.H. Huang, Sheng S. Li, and T.J. Anderson, NCPV Photovoltaics Program Review: Proceedings of the 15th Conference, Denver, CO, USA (1998) 114-119.

[6] J.F. Moulder, W.F. Stickle, P.E. Sobol, and K.D. Bomben, Handbook of X-ray Photoelecttron Spectroscopy (1995) 45, 61, and 213-242.

[7] R. Bayon, C. Maffiotte, and J. Herrero, Thin Solid Films 353 (1999) 100-107.

AMPS Determination of Key CIGS Solar Cell Material Properties

Hong Zhu, Joseph D, Cuiffi and Stephen J, Fonash

Electronic Materials and Processing Research Lab

189 MRI Bldg, University Park, PA 16802

ABSTRACT

The computer simulation tool AMPS[1] has been used to gain insight into the operation of the CdS/CIGS solar cell. As a result of this study, we have determined which interface and bulk material parameters have the biggest impact on device performance. Through this device modeling, we can conclude that the CdS and the interface layer between CdS and CIGS absorber in this solar cell are critical to the cell efficiency.

1. Introduction

The CdS/CIGS thin film solar cell has demonstrated its potential to reach high efficiency with low cost. However, we believe further improvement can be achieved if more of the device physics can be understood for this complicated hetero-structure. A typical CIGS solar cell consists of a ZnO/CdS/interface and an OVC/CIGS absorber/Mo back contact. Many parameters are involved in describing such a complicated device structure and hence many parameters potentially can affect device performance. The difficulty is to know what parameters in which material are more important to device performance. If we had that information, the community's resources could be focused better on improving those parameters. The AMPS simulation tool provides the unique capability to provide just such information.

2. Device simulation

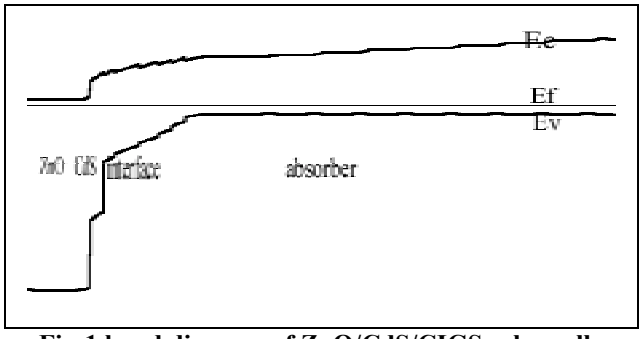

Fig-1 band diagram of ZnO/CdS/CIGS solar cell

Using AMPS, a user can build the device layer by layer by specifying material parameters such as bandgap, mobility, N_c, N_v, doping, defects, and absorption coefficients. AMPS also allows a user to specify operating temperature, voltage bias range and contact properties. With this information AMPS will generate I-V characteristics, QE under various light and voltage biasing, the band diagram, electric field, recombination profile, etc in either a graphic or text format.

AMPS modeling shows that many of the parameters needed to describe the structure seen in the band diagram of Fig-1 are not critical to device performance. However, some of the CdS, CdS/CIGS interface, and CIGS defect, mobility, and absorber parameters are critical. We explore this in the study discussed here. In Table-I we list the material parameters for these regions (i.e., mobility, recombination center density and doping) and in this report we determine which of these parameters are key to device performance. In this determination we have treated the CdS and interface as one region. In the absorber we will only change the p-type doping and in CdS/interface we will only adjust the donor concentration to demonstrate the criticality of these regions.

Table-I parameters used for cell sensitivity study

		CdS/interface	Absorber
Mobility cm^2/V-sec	μ_n	1-20	30-1000
	μ_p	0.3-3	30-300
Recombination centers #/cm^3		0-10^{18}	10^{15}-10^{17}
Doping #/cm^3		10^{14}-10^{17} (n type)	10^{15}-10^{17}(p-type)

Before we get into the discussion of our simulation results, certain transport mechanism can be clearly understood by just looking at the AMPS-generated band diagram in Fig-1. During the solar cell operation, free carriers are separated by the electric field in the pn junction depletion region (including the CdS layer) and collected by the n^+ ZnO layer. Any parameter that can affect the recombination rate before they can be collected is critical to cell efficiency. Unlike a single crystalline pin solar cell, this thin film heterojunction`s behavior is not straightforward. Defects, trapping centers and band offsets and their effects on transport make the device physics complicated as AMPS simulations demonstrate. For example, we know from our work that most of the band offset between CIGS and CdS is in the valance band even though we do not know the exact values. Therefore, under (dark) forward bias, few holes cross through CdS to the ZnO and their contribution to the current that is driven through the CdS is negligible. However, it is absolutely essential to know the ΔE_c between the ZnO and CdS because it controls the electron supply and the dark forward current. In this report we decouple the effects of band offsets by simply fixing the offsets at the

same values in all the cases we simulated. The numbers we use in the structure are carefully chosen to match the dark, light I-V and QE.

3. Results and discussion

First we will give the result of the impact of each parameter of Table I on cell efficiency.

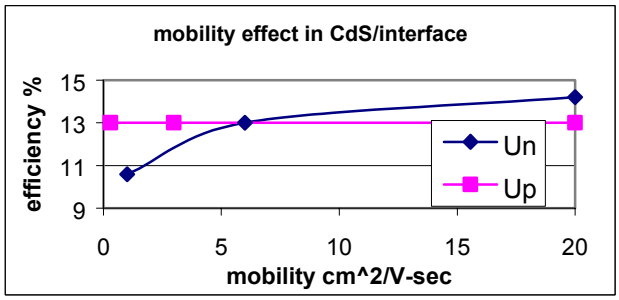

Fig-2 electron and hole mobility effect in the CdS/interface

In Fig-2 we can clearly see that the CdS/interface hole mobility of Table I has almost no effect on the cell efficiency, but that the CdS/interface electron mobility in this region can significantly alter device performance if that mobility falls below a threshold value.

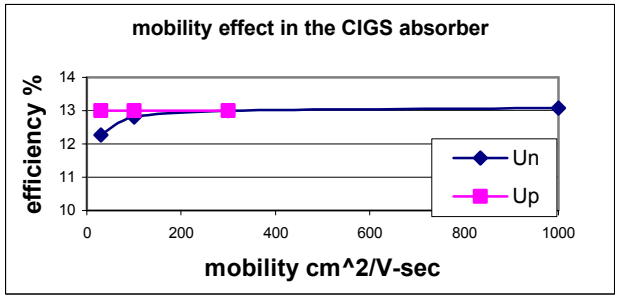

Fig-3 electron and hole mobility effect on the cell efficiency

However, over the range explored, we have found that neither electron nor hole mobility in the CIGS absorber is important to the cell efficiency, as seen in Fig-3. Here we vary the electron mobility from 30 to 1000 cm^2/V-sec and efficiency only increase from 12.3% to 13% and no effect from hole mobility change.

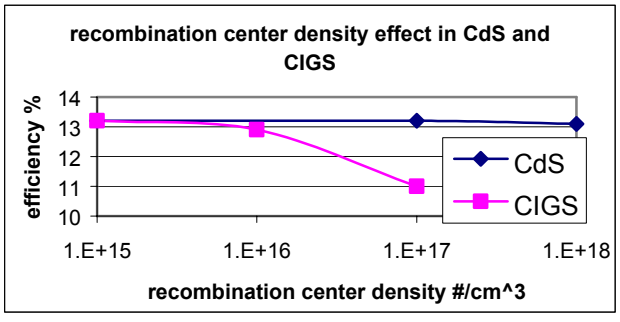

Fig-4 recombination center density effect on the cell efficiency

We have already established that trapped positive charge in the CdS layer can be important [2]. Consequently the CdS/interface recombination centers of Table-I are taken to be neutral in this report. Fig-4 shows that such neutral defects in the CdS layer are not important at all. However, without a doubt, defects in the absorber lower the efficiency but not with the sensitivity found in a-Si:H solar cells.

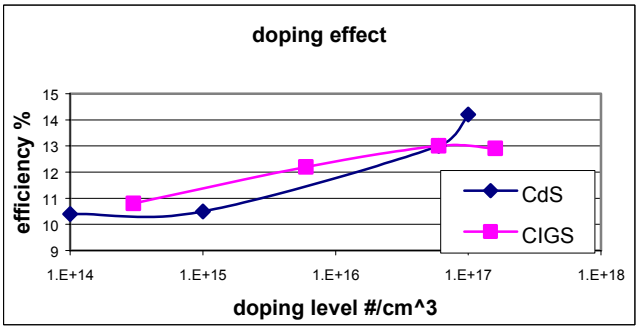

Fig-5 doping effect in the CIGS and CdS layer

In Fig-5 we demonstrate doping effects in the CdS and CIGS layers. It is clear that increasing donor doping in the CdS layer above a threshold level could significantly increase the cell efficiency even though it is only 30nm wide.

Although we can see that there are many ways to affect the cell efficiency, it is clear that some parameters are more sensitive than others. For example, cell efficiency is more sensitive to μ_n than μ_p and this sensitivity is different in the CdS/interface and bulk CIGS regions (see Fig-1 and 2). As another example, we note that doping level sensitivity is seen to be stronger in the CdS layer. We also note that the parameters of Table-I affect the efficiency in different ways. For example, μ_n and n-type doping in the CdS layer will change the efficiency mainly through FF. However, recombination centers in the absorber will affect V_{oc}, J_{sc} and FF. The physics behind those complicated behavior differences is easily understood through AMPS because we can view the change in device behavior at any given bias condition.

3. Conclusion

AMPS is a very powerful tool and can help users to visualize device operation. In this paper we use AMPS to conduct a sensitivity study on the device parameters to determine key interface and bulk CIGS solar cell material properties. As seen, the impact of CdS/interface layer is quantified and the most sensitive interface and bulk parameters are established. The results show that the same percentage of change in certain material parameters in the interface region can have stronger effects on the efficiency than the corresponding change in the bulk region.

4. References:

[1] P. J. McElheny, J. K. Arch, H. S. Lin, and S. J. Fonash, Journal of Applied Physics, 64, 1254 (1988)

[2] Applications of AMPS-1D for Solar Cell Simulation, National Conference Of Photovoltaic meeting P309-314, Sep, Denver 1998

CIS Carrier-Density Profiles Derived from Capacitance

P. Johnson and J. Sites

Dept. of Physics, Colorado State University

Fort Collins, CO 80523

ABSTRACT

This paper evaluates the use of capacitance-voltage (C-V) measurements on laboratory-scale polycrystalline thin-film CIS devices. In particular, the capacitance vs. frequency has been examined in a range spanning three decades, low temperature (- 50 ^{o}C) C-V measurements have been compared with room temperature (20 ^{o}C) measurements, and a variety of C-V pre-bias conditions have been compared. Also, C-V measurements made on devices with different buffer layers suggest that diffusion of cadmium from the window layer may cause greater compensation in the absorber.

1. Introduction

Earlier papers from our group discuss the measurement and interpretation of C-V measurements on polycrystalline thin-film CIS devices [1,2]. However, these were written when the typical efficiency for cells made from CIS was 8-10% [2]. Today, typical laboratory CIS cells are 14-16% efficient, and commonly include gallium and occasionally sulfur. Today's cells typically have carrier densities above 10^{16} cm^{-3}, compared to the 10^{15} cm^{-3} range for cells 10 years ago. In light of these higher efficiency cells with different dopant densities, the measurement technique and interpretation of C-V have been reevaluated.

Capacitance vs. frequency (C-F) measurements at four different bias voltages have been taken to confirm the validity of the use of the range of 1 kHz to 1000 kHz as standard practice. C-F and C-V have been measured at low temperatures, near room temperature, and various temperatures in between. C-V measurements have been taken after utilizing various pre-bias conditions to investigate the necessity for a 500 second reverse pre-bias. Finally, many measurements have been made on a variety of different CIS devices. We have chosen a small sample of these to present.

2. Measurement

The primary instrument used for measurements was a Hewlett-Packard 4192A LF Impedance Analyzer. Prior to all C-V measurements, C-F measurements were taken in the range of 1-1000 kHz within approximately 5 ^{o}C of the C-V measurement temperature. C-V measurements were taken with the voltage across the cell ranging from -2 V to 0.2 V. Unless otherwise noted, the cells were pre-biased for 500 seconds at a -2 V bias. All C-V measurements commenced at the pre-bias voltage. With the exception of the low temperature study, measurements were taken near 22 ^{o}C.

3. Results

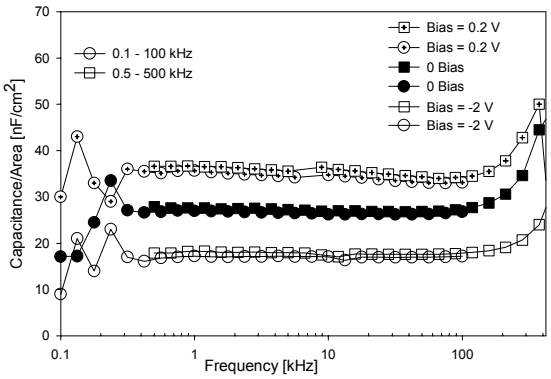

Fig. 1. C/A vs. F for a CIGSS/ CdS cell

C-F measurement results displayed in Figure 1 for the 1-400 kHz range are typical of most cells measured in that there is very little dispersion between 1 and 100 kHz. Below 0.5 kHz, a range not normally measured, there is significant scatter in the capacitance measurements. At frequencies near 200 kHz, the apparent capacitance increases, most likely due to the finite inductance of the measurement circuit [3]. Although moderate dispersion is occasionally present in C-F measurements, it can usually be attributed to shunting in the cell and is not a trait of well-behaved devices. Thus, for well-behaved devices we continue to see 1-1000 kHz as a reasonable range for standard C-F measurements.

Measurements taken incorporating variations of pre-bias duration and direction strongly suggest reverse-bias as the preferred pre-bias direction, but are not as conclusive regarding duration of the pre-bias. Reverse-bias was strongly indicated to be the preferred direction as a result of the curvature in the forward bias regime in the A^2/C^2 vs. V plots. For well-behaved diodes, the A^2/C^2 vs. V plots should have a voltage intercept approximately equal to the built-in voltage (V_{bi}), according to the following equation

$$A^2/C^2 = (2/q\varepsilon N)*(V_{bi}-V) \qquad (1)$$

Here q is the unit charge, ε is the dielectric constant of the absorber, and N is the carrier density of the more lightly doped material in the p-n junction [4]. However, as seen in Figure 2, plots extrapolated from C-V measurements made

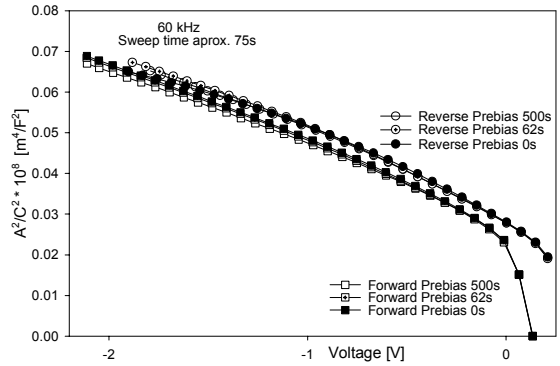

Fig. 2. C^2/A^2 vs. V from Reverse and Forward Prebias

after a forward pre-bias curved to zero at about 0.1 V, while the expected built-in voltage for CIS is between 0.5 and 1.0 V. Plots pertaining to measurements made after a reverse pre-bias on the same cell have a voltage intercept in the expected range of 0.5 to 1.0 V.

Investigations into C-V measurements made at low temperatures (- 50 ^{o}C) indicate several trends (Figure 3).

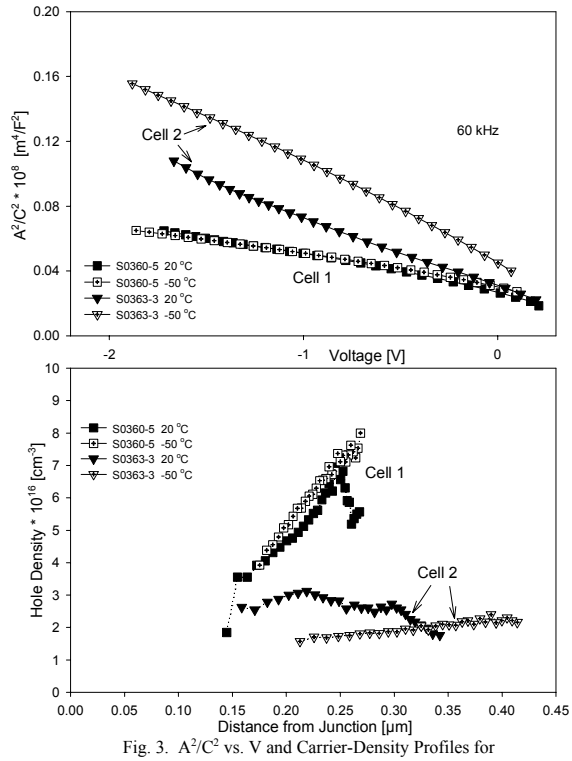

Fig. 3. A^2/C^2 vs. V and Carrier-Density Profiles for CIGSS Cells at Room and Low Temperature

Most significant is that between -50 ^{o}C and 20 ^{o}C, the overall carrier-density profile, which is calculated from the slope of the A^2/C^2 vs. V curve, did not change dramatically for any of the cells measured. Indeed, almost no dependence on temperature at all is seen for some cells. The low temperature and room temperature measurements in Figure 3 were taken on two CIS-based cells with NREL buffer layers made with slightly different processing steps. For these cells, more significant temperature variations exist when the capacitance at room temperature is lower. Note that even though the plots of A^2/C^2 vs. V seem to vary significantly with temperature in Figure 3 for cell 2, the carrier-density profiles are not dramatically different. This is consistent with low temperature measurements made on other CIS cells studied.

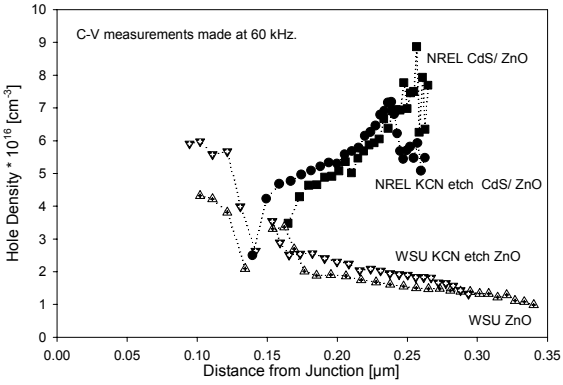

Fig. 4. Carrier-Density Profiles of CIGSS Thin-Film Devices

Finally, C-V measurements made on nominally identical CIGSS absorbers (Figure 4) suggest that compensation in completed devices with CdS buffer layers is smaller than that in the cadmium-free completed devices. This is perhaps due to diffusion of the cadmium from the buffer layer or the buffer layer deposition process into this CIGSS absorber [5].

4. Acknowledgements

We would like to acknowledge the National Renewable Energy Lab (NREL) for financial support, as well as discussions and samples. We would also like to acknowledge Siemens Solar Industries for providing absorber layers that were made into complete devices both by NREL and Washington State University in conjunction with the Institute of Energy Conversion. We are also grateful to J. Hiltner and K. Ramanathan for discussions.

REFERENCES

[1] H. Tavakolian and J. R. Sites, "Capacitance determination of interfacial states in CuInSe2 solar cells," Proc. 18th IEEE Photovoltaics Specialists Conf., pp. 1065-1068, October 1985.

[2] P. H. Mauk, H. Tavakolian and J. R. Sites, "Interpretation of thin-film polycrystalline solar cell capacitance," IEEE Trans. Electron Devices, vol. 37, iss. 2, pp. 422-427, 1990.

[3] J. H. Scofield, "Effects of Series Resistance and Inductance on Solar-cell Admittance Measurements," Solar Energy Materials and Solar Cells, vol. 37, no. 2, pp. 217-233, May 1995.

[4] A. S. Grove, *Physics and Technology of Semiconductor Devices*, New York: Wiley, 1967, p. 171.

[5] K. Ramanathan, Personal communication, January 2000.

$CuIn_{1-x}Ga_xSe$-Based Solar Cells Prepared from Electrodeposited and Electroless-deposited Precursors

W. K. Batchelor[a,b] and R.N. Bhattacharya[a]

[a]National Renewable Energy Laboratory, 1617 Cole Blvd., Golden, CO 80401, USA
[b]Department of Physics, Colorado School of Mines, Golden, CO 80401, USA

ABSTRACT

Three devices were fabricated from electrodeposited (ED) and electroless-deposited (EL) precursors. Compositions were adjusted with additional In and Ga by physical vapor deposition (PVD) for an ED and an EL device. A third, an ED device, was adjusted with only In. Auger analysis and grazing incidence X-ray diffraction (GIXRD) reveal a non-uniform Ga/(In+Ga) distribution when In and Ga are both added whereas a uniform distribution is observed when only In is added.

1. Introduction

Thin-film solar cell technology has proven to be a promising alternative to silicon solar cells popular today in many applications. $CuIn_{1-x}Ga_xSe_2$ (CIGS) has become one of the leaders in this field. Its large optical absorption coefficient, known long-term stability [1], and relatively good diffusion length has brought this material to the forefront. Electrodeposition (ED) and electroless deposition (EL) are two potential low-cost and scaleable techniques that have proven to yield high-quality CIGS thin-film solar cells. We have produced cells with efficiencies of 15.4% and 12.4%, respectively, from precursors deposited by ED and EL techniques. These completed cells have been examined and compared to 17.7% and 18.8% PVD cells by current voltage, capacitance voltage, and spectral response in previous articles [2,3].

2. Experimental

Both the ED and EL precursors are deposited from an acidic (pH~2) bath containing 0.02-0.05M $CuCl_2$, 0.04-0.06M $InCl_3$, 0.01-0.03M H_2SeO_3, 0.08-0.1M $GaCl_3$, and 0.7-1M LiCl dissolved in deionized water. Cu, In, Ga, and Se are codeposited at room temperature onto the substrate in a vertical cell; i.e., the electrodes are suspended from the top of the cell. The ED precursors are prepared in a three-electrode cell in which the reference is a platinum pseudo-reference, the counter is platinum gauze, and the working is the substrate. The substrate typically used is glass DC-sputtered with about 1 μm of Mo. A constant potential of -1.0 V is applied between the working and counter electrodes with a potentiostat. The EL precursor films are prepared by shorting the substrate to an oxidizing counter electrode such as Fe or Zn. Oxidation of the metal at the counter electrode causes a reduction of the Cu, In, Ga, and Se at the substrate. The precursors are subsequently rinsed in deionized water and dried in flowing nitrogen. The ED and EL films are nearly identical in precursor quality.

Compositions of the as-deposited precursors are determined by inductively coupled plasma (ICP) analysis. The as-deposited precursors are Cu-rich and additional In, Ga, and Se are added by PVD to adjust their final composition to $CuIn_{1-x}Ga_xSe_2$. During this step, the substrate temperature is maintained at 560°±10°C. The photovoltaic devices are then completed with a 50 nm layer of chemically deposited CdS, 50 nm of radio-frequency sputtered intrinsic ZnO, 350 nm of Al-doped ZnO, and bilayer Ni/Al top contacts deposited by e-beam. Finally, 100 nm of a MgF_2 layer is deposited to minimize reflection.

3. Results and discussion

Three different devices were examined: an EL cell to which 2500Å Ga and 5800Å In were added (S1283b), an ED cell to which 3000Å Ga and 7200Å In were added (S1285a), and an ED cell to which only 2300Å In was added (S1482a). The electrical characteristics of the finished devices are described in Table 1.

Table 1: Electrical Characteristics of ED and EL Devices

Cell	EL device S1283b	ED device S1285a	ED device S1482a
V_{oc} (V)	0.565	0.666	0.429
J_{sc} (mA/cm^2)	33.27	30.51	36.04
FF (%)	66.1	75.6	58.37
Efficiency (%)	12.4	15.4	9.0

The differences in device performance are likely due to the second-stage PVD addition. The addition of the In, Ga, and Se is observed to produce a non-uniform Ga/(In+Ga) distribution in cases where In and Ga are both added, whereas a uniform distribution is observed when only In is added. The gradient created in Ga composition can create a band-gap gradient, which can enhance the V_{oc}, fill factor and, in turn, the efficiency. Auger analysis of the cells can be seen in Figs. 1, 2, and 3.

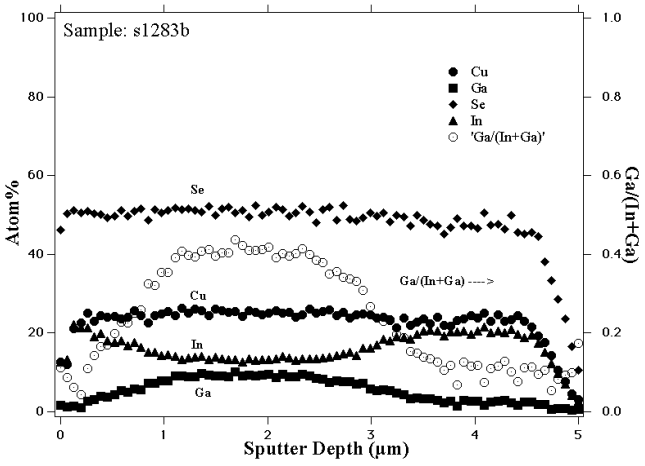

Fig. 1: Auger analysis of EL device S1283b

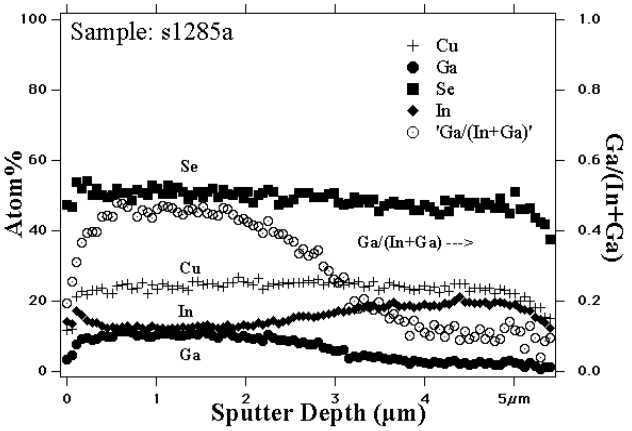

Fig. 2: Auger analysis of ED device S1285a

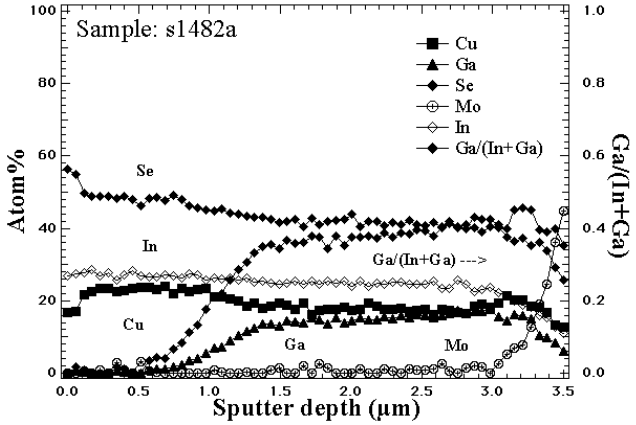

Fig. 3: Auger analysis of ED device S1482a

These observations were also confirmed using grazing incidence X-ray diffraction (GIXRD), observed in Figs. 4, 5, and 6. Normal penetration depths for different incident angles, □ are indicated for each scan. X-ray diffraction of S1283b and S1285a reveals a peak splitting in the (204/220) and (116/312) peaks of the CIGS that is not observed in S1482a. This indicates the existence of two phases of different compositions within the film when Ga is added by PVD. GIXRD has revealed only one phase on the surface of these films [4,5], correlating with the Ga hump in the Auger analysis. This is due to a material of higher Ga composition existing on the surface from the second-stage PVD addition.

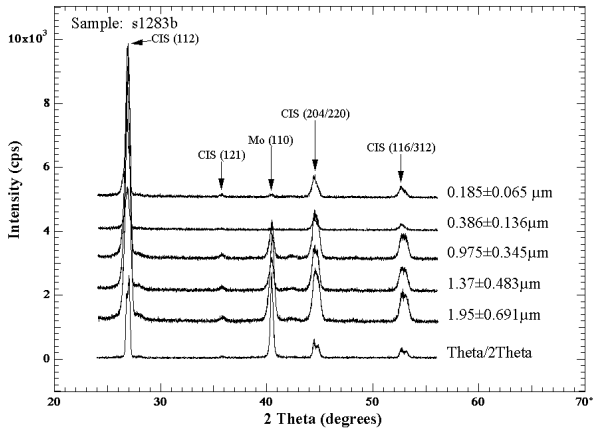

Fig. 4: GIXRD and Theta/2Theta of EL device S1283b

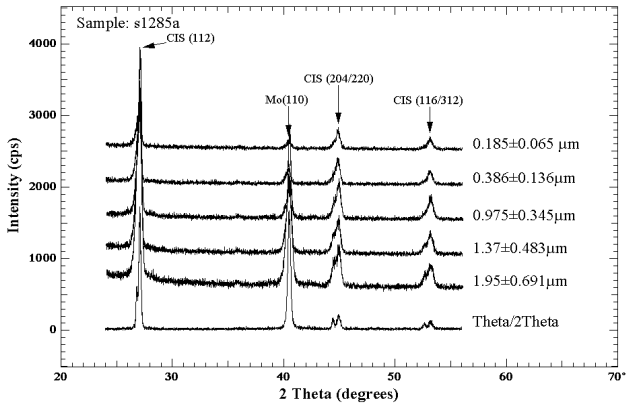

Fig. 5: GIXRD and Theta/2Theta of ED device S1285a

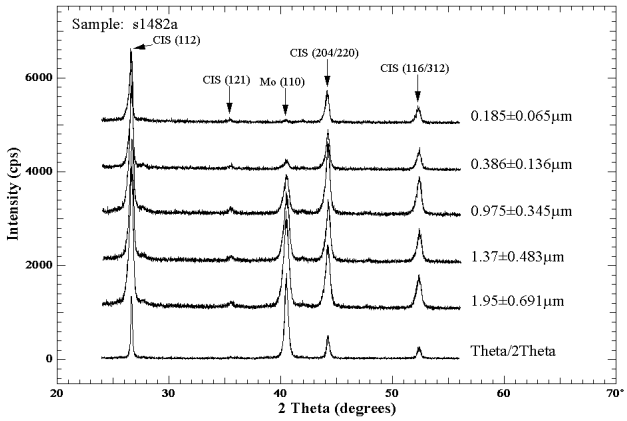

Fig. 6: GIXRD and Theta/2Theta of ED device S1482a

4. Conclusion

ED and EL are able to produce high-quality CIGS precursors for solar cell production. Second-stage PVD additions of In are uniformly incorporated into the precursors, but Ga is not as easily incorporated into the final polycrystalline structure, yielding gradients in Ga composition throughout the films that alters the device performance.

Acknowledgements

We would like to thank Amy Swartzlander and James Keane for their valuable contributions to this research. This work was supported by Davis, Joseph & Negley (California Corporation, Work-for Others Contract No. 1326). It was also partially supported by the U.S. Department of Energy under Contract No. DE-AC36-99-G010337.

REFERENCES

[1] H. S. Ullal, K. Zweibel, and B. Von Roedern, *Proceedings of the 26th IEEE PVSC, Anaheim, CA* (1997), pp. 301.

[2] R.N. Bhattacharya, J.F. Hiltner, W. Batchelor, M.A. Contreras, R.N. Noufi, and J.R. Sites, *Thin Solid Films* 361-362 (2000), pp. 396-399.

[3] R. N. Bhattacharya, W. Batchelor, J. F. Hiltner, and J. R. Sites, *Applied Physics Letters*, **75**, pp.1431-1433.

[4] A. Segmüller, I.C. Noyan, and V.S. Speriosu, *Prog. Crystal Growth and Charact.* (1989) **18**, pp.21-66.

[5] M.A. Contreras, Ph.D. thesis, Colorado School of Mines, (1996), pp. 96-100.

CVD ZnO Buffer Layers for SSI CIGSS Solar Cells

L. Olsen, F. Addis, L. Huang and P. Eschbach

Washington State University / Tri-Cities

2710 University Drive Richland, WA 99352

ABSTRACT

This paper describes investigations of cells based on Siemens Solar material, CIGSS, and highly resistive ZnO (i-ZnO) buffer layers grown by MOCVD. A process has been determined for growth of i-ZnO buffer layers on CIGSS that involves deposition of the film at 100°C, after heating the substrate to 250°C and using nitrogen as a carrier gas. Experimental results are reported that indicate that the use of a KCN etch of the CIGSS surface prior to growth of i-ZnO buffer layers is beneficial to cell performance. XPS studies show that the etching step removes oxygen from the substrate surface that had complexed with Se to form SeO_2. Cells that do not receive a KCN etch typically have shunted I-V curves leading to relatively low open circuit voltages, fill factors and efficiencies. A tentative model is proposed for the effect of KCN. Finally, one cell (using a KCN etch) exhibited a total area efficiency of 12.7 % with an open circuit voltage of 0.577 Volts.

1. Introduction

The work reported in this paper is part of a program to investigate alternative heterojunction partners for CIS-based solar cells, and to improve understanding regarding the effects of these buffer layers and related processing upon cell performance. ZnSe, ZnS and ZnO have been studied as buffer layers on substrates from industry and NREL. The II-VI compounds are grown by MOCVD. However, most of our work has concentrated on the use of highly resistive, CVD ZnO (i-ZnO) with CIGSS absorbers produced by Siemens Solar, Industries (SSI). Thus, this paper will focus on the ZnO buffer layer studies.

2. CIGSS Substrates and Surface Preparation

CIGSS (also referred to as Graded absorber) material has sulfur incorporated in the surface region such that the surface concentration is approximately CuInSeS, and Ga concentrated near the back contact with Mo [1]. CIGSS substrates used for cell fabrication consist of CIGSS absorber layer on Mo-coated glass. Substrates were typically 2 cm x 2 cm in size, and were diced from larger parts provided by SSI. Prior to MOCVD growth of i-ZnO buffer layers, all substrates were subjected to a cleaning process consisting of rinses in 1,1,1-trichlorethane, acetone, methanol and distilled water. In addition, some substrates were also etched with a 10% KCN solution preparation. As discussed below, superior cell performance is achieved with the KCN-etched substrates.

Surfaces of etched and unetched CIGSS were examined with XPS and AES to determine if any effects of the KCN etch could be observed. Results for the XPS studies are given in Figure 1. Photoelectron emission is observed for the unetched sample corresponding to Se apparently in its normal site, and also due to Se bonded to oxygen in the form of SeO_2. In the case of the etched sample , the SeO_2 line is completely removed. Thus, it is clear that one effect of the KCN etch treatment is to remove oxygen from the surface and probably grain boundaries near the substrate surface. Auger scans indicate that more than 50 % of the oxygen residing at the CIGSS surface is removed by the KCN etch. It is should be noted that the etched sample was exposed to air several hours between the time that the etching process occurred and when the XPS and Auger studies were carried out. Oxygen attached to Se at the surface would lead to Se vacancies at the surface, which constitute donors. Se vacancies should not be a problem at the interface with the buffer layer since the high donor density would tend to invert the CIGSS

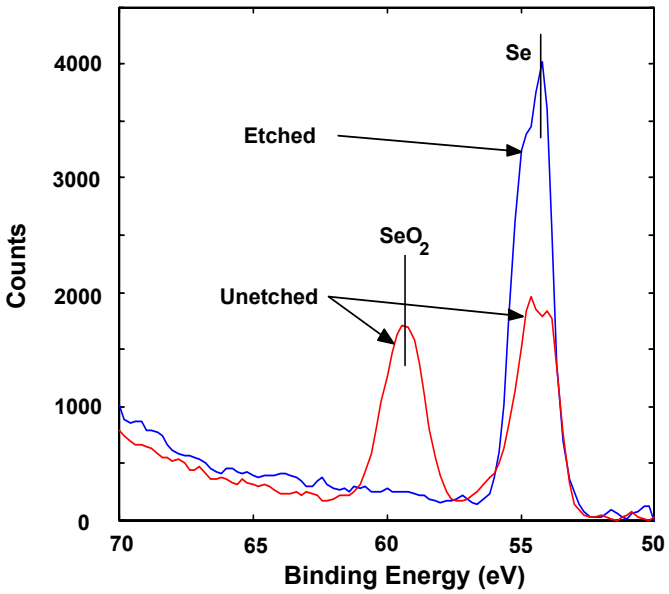

Figure 1. XPS spectra for two CIGSS substrates, one etched with KCN and one not etched.

surface. However, Se vacancies along Grain surfaces would tend to invert the grain boundaries resulting in excess recombination. Cahen and Noufi originally proposed that

heat treatment of CdS/CIGS cells in air resulted in neutralization of donors due to Se vacancies by oxygen at grain boundaries which resulted in improvement of cell properties [2]. In our case, it appears that we may have Se vacancies due to the formation of SeO_2 and KCN removes the oxygen thereby allowing Se to occupy the proper site. If this process is involved in cell improvement, it may be unique to the SSI material or the WSU situation, where CIGSS material is utilized that has been exposed to the atmosphere for a relatively long time between CIGSS growth and device processing.

3. ZnO Buffer Layer Growth and Characterization

Resistive ZnO buffer layers are grown by MOCVD by reacting a zinc adduct with tetrahydrofuran. Previous work with SSI CIS and NREL CIGS substrates involved the use of a two step process with hydrogen as a carrier gas [3]. In particular, the process consisted of growth of 100 Å at 250 °C followed by growth of 500 to 600 Å of i-ZnO at 100°C. We have determined that a modified procedure gives better results for the SSI CIGSS material. Instead of hydrogen, nitrogen is used as a carrier gas and although the sample is heated to 250°C, no film growth occurs until the sample is cooled to 100°C. An additional modification of our growth procedure involves adding water to the THF precursor. This approach results in a large VI/II ratio such that the Zn flow controls the growth rate. Furthermore, this process consistently yields very resistive i-ZnO films. Specifically, buffer layer resistivities on glass witnesses are typically > 1E4 ohm-cm.

4. Cell Completion and Performance

After growth of i-ZnO buffer layers, cells were completed by depositing n-ZnO TCO layers followed by deposition of Ni/Ag or Ni/Al collector grids. TCOs were deposited by RF sputtering at IEC and CVD at SSI. All collector grids for cells discussed in this paper were deposited at IEC. The cells have total areas of approximately 0.45 cm^2 , and two individual cells were formed on each 2 cm x 2 cm CIGSS substrate. Results tabulated in Table 1 represent the best individual cell on each substrate, and only cells with SSI CVD TCO layers. Similar results were obtained with IEC sputtered TCO layers. With the exception of cell 99-34, the cells fabricated on substrates that had not received a KCN etch exhibited poor performance. Without the KCN, devices typically exhibited lower values of FF, Voc and efficiency. Cell 99-52 which was processed with the KCN etch was sent to NREL for I-V characterization. The total area efficiency was 12.7 % and the open circuit voltage was 0.577 Volts. These values are comparable to results obtained for the CIGSS material with CdS buffer layers.

5. Aging Effects

Best results for cells with i-ZnO buffer layers are achieved if i-ZnO/CIGSS structures are exposed to air for several weeks before cell completion. Since the current process leads to highly resistive i-ZnO buffer layers, it does not appear that the aging is required for increasing the buffer layer resistivity. Cells that are fabricated in a relatively short time after buffer layer growth typically exhibit lower efficiencies than cells that have been allowed to 'age', because of an apparent light-induced current loss mechanism. Modeling calculations with PC-1D suggest that the low efficiency cells have a light-induced shunting mechanism and lower carrier lifetime in the depletion region. As i-ZnO/CIGSS structures are allowed to age, light-induced shunting is eliminated. Assuming the aging effect involves transport of oxygen to the i-ZnO/CIGSS interface, and along grain boundaries, it should be possible to introduce a heat treatment in air that will accomplish the requiring 'aging.'

6. Other Studies

In addition to the ZnO buffer layer effort, an approach has also been developed for MOCVD growth of ZnS. Highly resistive ZnS is grown by reacting a zinc adduct with hydrogen sulfide. Preliminary studies with test cells have resulted only in low efficiencies. These studies will continue. Procedures for sputter depositing low resistivity n-ZnO have been developed with a RF magnetron sputtering system acquired during this past year. We now are able to complete CIS-based cells after the buffer layer is grown on the absorber.

References

1. D. Tarrant and J. Ermer, 23rd IEEE PVSC, I-III- VI_2 Multinary Solar Cells Based On $CuInSe_2$", 23rd IEEE PVSC, 1993, pp. 372 - 378.
2. David Cahen and Rommel Noufi, "Surface Passivation of Polycrystalline, Chalcogenide Based Photovoltaic Cells, " Solar Cells 30 (1991) 53-59.
3. Larry C. Olsen, et al., "High Efficiency CIGS And CIS Cells With CVD ZnO Buffer Layers", 26th IEEE PVSC, 1997, pp 363 - 366.

Table 1 - Cell Results Wi th ZnO Buffer Layers

	Sample	Eff (%)	FF (%)	Voc (Volts)	Jsc (mA/sqcm)
KCN Etched	99-31	9.95	56.5	0.544	32.3
	99-45	11.04	63.3	0.561	31.1
	99-52	12.45	66.1	0.567	33.2
No KCN	99-34	10.10	61.9	0.511	31.2
	99-41	5.53	38.4	0.451	31.9
	99-44	2.69	30.8	0.282	30.9

Dependence of the Characteristics of Mo Films on Sputter Conditions

J. L. Alleman, H. Althani, R. Noufi, H. Moutinho, M. M. Al-jassim, F. Hasoon

National Renewable Energy Laboratory

1617 Cole Blvd Golden, Colorado 80401

ABSTRACT

The residual stress, resistance, orientation, and microstructure of sputtered Mo films were studied as a function of varied-deposition power and pressure. CIGS films were deposited by the three-stage process on the Mo films and their efficiency were related to the Mo films. The varied-deposition parameters of the Mo films produced CIGS device efficiencies from 13% to 17%.

1. Introduction

Mo thin films are used as an ohmic back contact for CIGS devices. Scofield [1] investigated deposition parameters for good adhesion. Here we revisit in more detail the deposited Mo-film characteristics: sheet resistance, residual stress, and adhesion to soda-lime glass. These properties are expected to influence the growth of the subsequent CIGS layer and, ultimately, the device performance.

2. Experimental

Films were sputtered using a 5" x 8" x 0.125" Mo target in a DC magnetron with a substrate to cathode distance of 78 mm. The 4" x 4" substrates were rotated into the path of the cathode and held stationary for the predetermined time to deposit a 0.75-µm-thick film. The base pressure in the vacuum system prior to deposition was less than 4 x 10^{-7} Torr. The soda-lime glass used for this experiment had a water-buff treatment performed by USPG on the float side of the glass. The water-buffing procedure uses CeO_2 slurry to polish the glass surface and remove imperfections. The matrix for this study consisted of Mo deposited in the constant-current mode at 1, 3, 5 and 7 amps. For each current setting, the pressure was 0.6, 0.7, 0.8 and 0.9 and from 1 to 16 mTorr in 1mTorr steps. The sheet resistance was measured diagonally across the substrate in three-equal distance steps using a four-point probe. The substrates were cut for XRD, thickness measurements, and SEM micrographs. CIGS films were deposited on a 3" x 3" portion of the Mo substrate.

3. Results

Power density was calculated using the target area. The power density for 1, 3, 5 and 7 current settings ranged 7~9, 21~29 and 38~50 and 66~82 W/in^2 respectively. The bulk resistance was calculated from the average of the sheet-resistance measurements and is shown in Figure 1. The bulk resistance decreases as deposition current increases. Figure 2 shows residual stress calculations made by the XRD Sin$^2\psi$ technique. Again, the curves shift with increase in current.

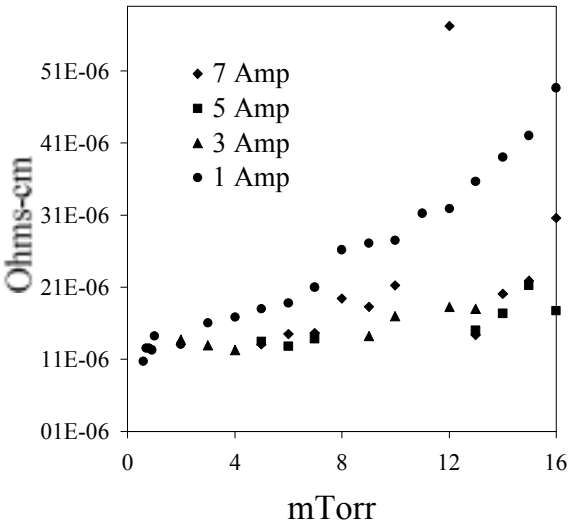

Fig. 1. Bulk resistance as a function of deposition pressure

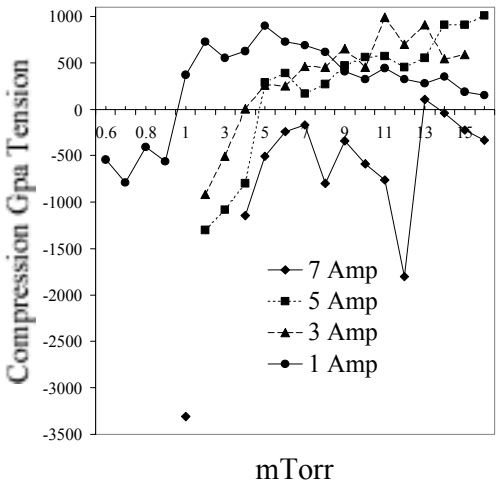

Fig. 2 Residual stress measured by the XRD Sin$^2\psi$ technique

XRD θ/2θ results of the films show a strongly-oriented 110 Mo film. The 211/110 ratio decreases as deposition pressure increases, as shown in Figure 3. The 211/110 ratio for powdered Mo is 0.31 [2]. A SEM micrograph of 0.8-mTorr-deposited film is surface shown in Figure 4. Figure 5 shows a SEM micrograph of a film deposited at 10 mTorr exhibiting increased grain size. The film sputtered at 0.8 mTorr was measured to be in compression and to have poor adhesion to the substrate while the 10-mTorr-sputtered film was under tensile stress and exhibited good adhesion using the tape test method [1].

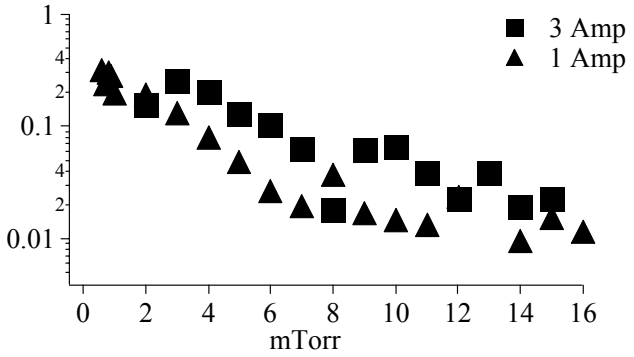

Figure 3 Normalized XRD 211/110 peaks

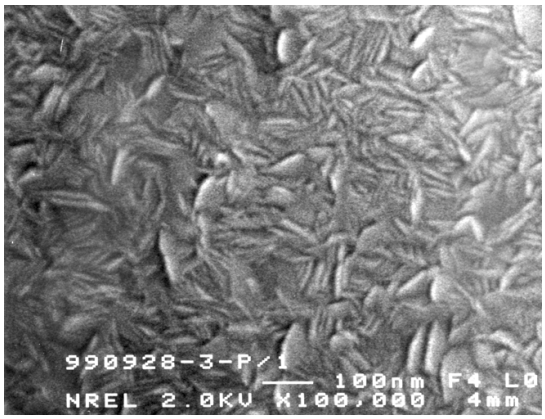

Fig. 4. SEM view of Mo surface deposited at 0.8 mTorr

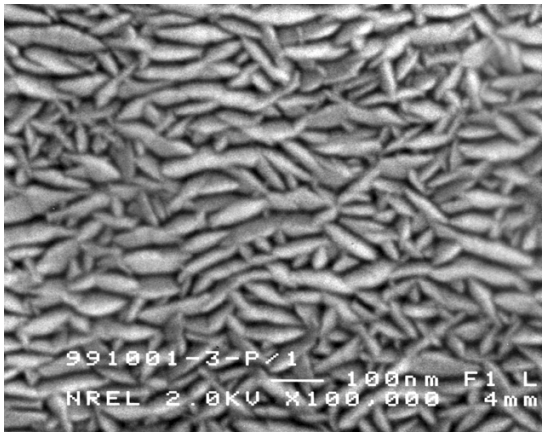

Fig. 5. SEM view of Mo surface deposited at 10 mTorr

Devices consisting of soda-lime glass/Mo/CIGS/CdS/ZnO were measured in the laboratory and results of the devices on Mo films sputtered at 1 amp are shown in Table 1.

mTorr	Voc (V)	Isc (ma)	FF (%)	EFF (%)
0.6	0.603	12.92	72.48	13.13
4.0	0.665	13.845	73.09	15.64
8.0	0.680	14.29	75.05	16.96

Table 1. Results of CIGS devices made on Mo films sputtered at power density of 7~9 W/in^2.

4. Discussion

The bulk resistance shown in Figure 1 shows a trend of lowered resistance as the deposition current increases. The shift is caused by the localized-pressure drop in front of the cathode where an increase in the current gives a larger plasma with greater heating effect. These conditions are also responsible for the shift in residual stress. The 7 amp residual stress and bulk-resistance values are skewed because the Mo target was replaced during the middle of the deposition set and the large amount of heat generated by the plasma. The break in period of the Mo target was not long enough and impurities on the target surface added to the changes.

5. Conclusion

Mo films were sputtered at different power densities and Argon pressure. The resulting films showed similar sheet resistance and intrinsic stress, taking into account the effect of localized heating around the plasma and lowering of pressure. The microstructure of the Mo film was shown to have greater ordering as the pressure was increased. The combined characteristics of the Mo films are shown to influence the CIGS films such that finished soda-lime glass/Mo/CIGS/CdS/ZnO device efficiencies ranged from 13% to 17%. The highest efficiency was obtained for devices made on Mo films deposited at 1 amp and 8 mTorr. The results will be reviewed in a future article in greater detail.

REFERENCES

[1] J. Scofield, A. Duda, D. Albin, B. L. Ballard, P. K. Perdecki : "Effects of Argon Pressure on the Properties of Sputtered Mo Films for CIS and CIGS Thin Film Solar Cell Back Contact Applications" 1st World Conf. on Photovolt. Energy Conv. Hawaii 1994

[2] JCPDS card 42-1120 Mo cubic a=3.1472

Deposition of $Cu(InGa)Se_2$ by Inline Evaporation

G. M. Hanket, P. D. Paulson, W. N. Shafarman, and R. W. Birkmire

Institute of Energy Conversion
University of Delaware
Newark, Delaware 19716

ABSTRACT

The deposition of $Cu(InGa)Se_2$ thin films by inline evaporation is described. In this process, a heated substrate is linearly translated over sequentially arranged elemental evaporation sources. A quantitative model based on the system geometry is used to predict the flux distribution at the substrate. This is experimentally verified by Auger electron spectroscopy which shows that the Cu is homogeneously distributed through the film but the Ga and In are graded as predicted by the flux model. A 13.1% efficient device was achieved for a 1.6 μm film deposited at a substrate temperature of 475ºC.

1. Introduction

Elemental in-line evaporation is a promising process for the fabrication of $Cu(InGa)Se_2$ thin films due to its potential to provide large-area, continuous deposition. The process, illustrated in Figure 1, involves the linear translation of a heated substrate over an array of sequential Cu, Ga, In, and Se evaporation sources. This type of system geometry inherently produces graded flux compositions at the substrate, allowing Ga/(Ga+In) grading in the films and Cu rich and deficient growth stages [1]. Thus, the inline evaporation process is useful for characterizing the effects of graded deposition as it applies to commercial-scale manufacture. The potential of inline evaporation has been previously demonstrated [2,3].

The Institute of Energy Conversion (IEC) has begun operation of a $Cu(InGa)Se_2$ inline evaporation system. The system has demonstrated good uniformity over a 6" wide substrate and the fabrication of a 13.1% efficient $Cu(InGa)Se_2$ device. A source effusion model couples the system design to the measured flux distribution at the substrate.

2. System description

The Cu, Ga, and In effusion rates are controlled using in-situ atomic absorption spectroscopy (AAS) [4]. Temperature control is used for selenium, which is uniformly delivered to the substrate throughout the deposition zone. The substrate can be translated at speeds up to 20"/min and is heated by two independently controlled heater platens.

Across the substrate width, the resultant $Cu(InGa)Se_2$ films are compositionally uniform within the energy dispersive spectroscopy (EDS) measurement error of 1 atomic %. However, with the present geometry, the film thickness decreases by 10% from the center to the edge of the substrate.

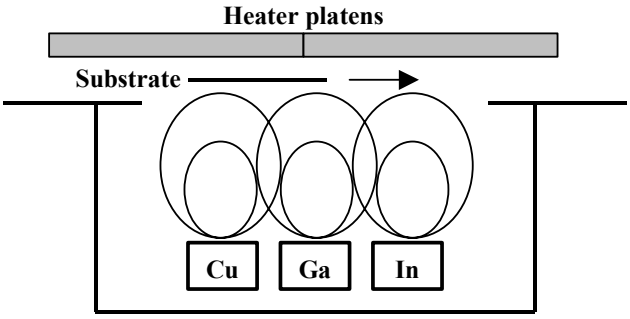

Figure 1. Schematic of inline evaporation system.

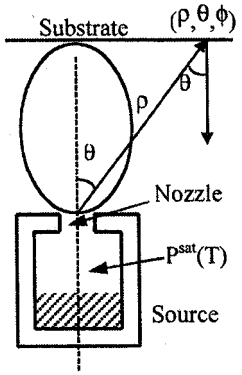

Figure 2. Variables for source effusion analysis.

3. Modeling

The flux profile from a single source, shown in Figure 2, is modeled using [5]:

$$f(\rho,\theta) = \frac{F(n+1)}{2\pi\rho^2}\cos^n\theta \qquad (1)$$

where n is an empirical fitting parameter describing the focusing of the molecular beam. The vector (ρ, θ) points from the source to a given point on the substrate. To describe the observed deposition rate at the substrate, an additional cos θ correction must be applied to account for the angle of incidence. F is the effusion rate of the source and, for free molecular flow, can be approximated by [6]:

$$F = \pi\Gamma^2 K P^{sat}(T)\sqrt{\frac{M}{2\pi RT}} \qquad (2)$$

where Γ is the nozzle radius, $P^{sat}(T)$ is the saturation pressure of the effusant, and K, which typically varies from 0.1 to 1, is an empirical function of the nozzle aspect ratio.

Using eqns. 1 and 2, elemental flux profiles through which the substrate moves are predicted. This is shown in Figure 3 for a typical source geometry using n = 2.

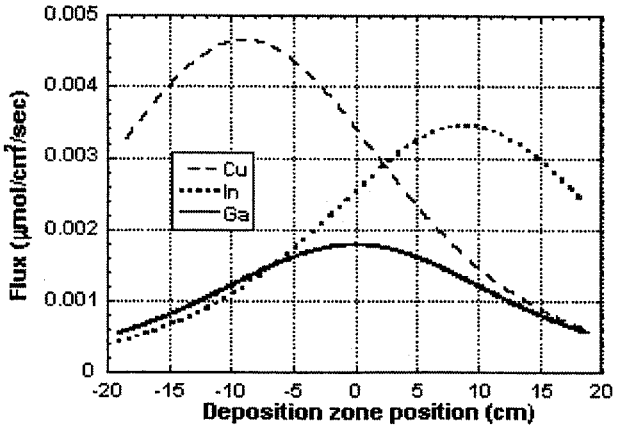

Figure 3. Elemental incident fluxes throughout the deposition zone.

Figure 4 shows an Auger compositional depth profile for a Cu(InGa)Se_2 film deposited at a substrate temperature of 475ºC under the flux conditions modeled above. The Cu is evenly distributed throughout the film while the Ga and In are graded. This indicates that Cu has a high mobility through the film, while Ga and In do not interdiffuse. This is consistent with films deposited in a stationary system with time-variant elemental fluxes [7].

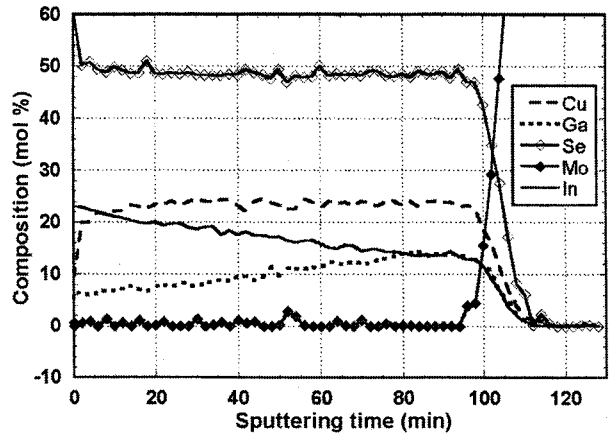

Figure 4. Auger depth profile of Cu(InGa)Se_2 film.

The measured compositional depth profile for Ga/(Ga+In) is compared to the modeled flux ratios in Figure 5, experimentally verifying the model's validity. This agreement between the deposition system geometry and film properties provides an engineering basis for the accurate design of graded deposition processes. Further results at different substrate temperatures and Ga/(Ga+In) ratios will be used to confirm whether Ga-In interdiffusion can be neglected when predicting film grading.

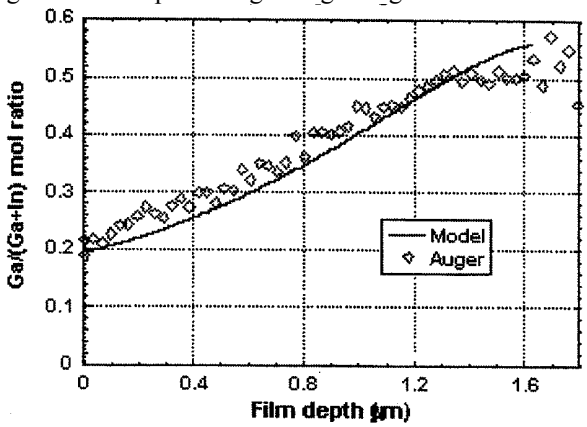

Figure 5. Auger depth profile of a Cu(InGa)Se_2 film deposited at 475 ºC.

4. Device results

Solar cells have been fabricated using Cu(InGa)Se_2 films produced by this process with the device structure glass/Mo/Cu(InGa)Se_2/CdS/ZnO/grid. The film characterized above has produced the best device to date. The current-voltage measurements, under 100mW/cm^2 AM1.5 illumination, yielded V_{OC} = 0.575 V, J_{SC} = 31.6 mA/cm^2, FF = 72.2%, and eff = 13.1%.

5. Conclusions

In conclusion, operation and modeling of an inline Cu(InGa)Se_2 process has been demonstrated. A quantitative model has been developed which successfully couples the deposition system design to the measured compositional profile in a Cu(InGa)Se_2 film. A solar cell fabricated from one such film has demonstrated a 13.1% efficiency. These results provide an engineering basis for the commercial-scale manufacture of Cu(InGa)Se_2 modules.

References

1. W. E. Devaney, W. S. Chen, J. M. Stewart, and R. A. Mickelsen, IEEE Trans. Elec. Devices **37**, 428 (1990).
2. J. Hedstrom and H. Ohlsen, 23rd IEEE PVSC, Louisville, KY, Louisville, KY, 364 (1993).
3. M. Powalla, G. Voorwinden, and B. Dimmler, 14th European Photovoltaic Solar Energy Conference, 1270 (1997).
4. C. Lu and Y. Guan, J. Vac. Sci. Tech. A **13(3)**, 1797 (1995).
5. S.C. Jackson, B.N. Baron, R.E. Rocheleau, and TWF Russell, J. Vac. Sci Technol. A3(5), 1916 (1985).
6. R. E. Rocheleau, B. N. Baron, and T. W. F. Russell, AIChE Journal **28(4)**, 656 (1982).
7. J.R. Tuttle, A.M. Gabor, M.A. Contreras, A.L.Tennant, K.R. Ramanathan, A. Franz, R. Matson and R. Noufi, AIP Conf. Proceedings **353**, 47 (1996).

(110) Epitaxial Growth and Devices

D. Liao and A. Rockett

Coordinated Science Laboratory and the Department of Materials Science and Engineering
1101 W. Springfield Ave., Urbana, IL 61801

ABSTRACT

Recent solar cell results suggests that a (110) orientation of CIGS thin films may have unique and possibly superior properties. We have deposited high-quality epitaxial (110)-oriented CIGS layers on GaAs (110). The surface consists of highly tilted terraces with large flat (112) facets alternating with rough (112) planes of opposite polarity. Temperature-dependent Hall effect showed up to a 20 fold decrease in carrier concentration relative to films grown with (112) and (100) orientations. Carrier compensation and other defects observed in the (100) and (112) oriented films, was eliminated. Changes in the hole mobility were also observed and are discussed. Theoretical modeling using the AMPS computer code demonstrates that the change in carrier concentration can potentially lead to dramatic improvements in device performances. Very preliminary results comparing different orientations of CIGS are presented to test this result.

1. Introduction

$CuIn_{1-x}Ga_xSe_2$(CIGS)/CdS heterojunction devices are promising candidates for photovoltaic devices when produced as polycrystalline materials. The recent record 18.8%-efficient device performance for a CIGS solar cell fabricated at the National Renewable Energy Laboratory (NREL) included the observation that the CIGS had a (110) preferred orientation. While many explanations for the exceptional device performance are important to consider, the result suggests that the (110) orientation of CIGS may have unique and possibly superior properties. We have the capability to test the orientation effect through the growth of epitaxial single crystals of CIGS on GaAs. This paper reports preliminary results of the study.

2. Experimental

Details of experimental procedures are given elsewhere.[1] Epitaxial CIGS films were deposited on both semiinsulating and highly conductive p-type (110), (100), and As-terminated (111) GaAs wafers using a hybrid sputtering and evaporation technique. This method generates In, Ga, and Cu fluxes by sputtering In and Cu-Ga alloy targets. Se is supplied in excess from an effusion cell. By the use of a Cu-Ga alloy target, diffusion of Ga from the substrate was suppressed. This improved adhesion of the films to the substrates by elimination of Kirkendall voids at the CIGS/GaAs interface. In addition, it reduced diffusion of Cu into the GaAs, leaving a conducting path through the substrates when conducting GaAs was used. Conducting GaAs was used for solar cell fabrication and insulating substrates with Au contacts were used for Hall-effect measurements. There was no detectable difference in films grown on insulating and conducting substrates. Thus, we believe that electrical measurements for films on insulating substrates are similar to films on conducting substrates. Growth temperatures were ~640°C for (100) and (110) orientations and 675°C for (111). Film thicknesses were ~0.75 μm. Compositions were determined by, EDS, XRD, and SIMS.

3. Results

The resulting films are high-quality epitaxial layers with the expected (110), (100), and (112) bulk grain orientations. The films on (100) had highly elongated ripples along one [110] direction and occasional rectangular pits with (112) facets. Films on $(111)_{As}$ substrates had very shallow triangular pyramidal facets on the surface with facet faces inclined at less than 5° with respect to the average (112) surface. By contrast, the (110) films had highly faceted surfaces where the surface planes themselves are (112) facets. These form spontaneously during growth. The result is a surface consisting of a highly tilted terraced structure (see Fig. 1.) Large, relatively-flat (112) facets alternate with very rough (112) planes. All of this is consistent with our previous results showing that the $(112)_{Se}$ surface is strongly preferred. The results here indicate that this surface is so strongly preferred that the (110) surface facets spontaneously to (112) planes. This has been found for all films and compositions grown to date on (110) GaAs.

Electrical properties of the resulting films were characterized and results showed a decrease by up to a factor of 20 in carrier concentration relative to similar films grown with (112) and (100) surface orientations (Fig 2). The reduction in carrier concentration was accompanied by a disappearance of evidence for a compensating donor and a second shallow acceptor observed in our non-(110) epitaxial layers. All films had a single acceptor state with a depth of ~150 meV with respect to the Valence band edge and a concentration of $\sim 8 \times 10^{15}$. The reduction in hole concentration and state densities is probably not a surface reaction controlled effect as the surfaces of both the (110) films are (112) planes.

The hole mobilities in the (110) films were reduced both at room temperature and below relative to the other orientations. In no case was the mobility observed to increase with decreasing temperature as was found in the non-(110) films. Rather, the mobility dropped as a power of the temperature, although the exponent of power law was found to vary dramatically from ~0.6 to ~2.5. Lower room temperature mobilities also dropped faster with decreasing temperature, although the carrier concentrations were almost identical. We believe that this indicates a transition to ionized impurity scattering at least in some films. This is consistent with a model we proposed recently for formation

of superclusters of defects. In the (100) and (112) films the concentration of defects is so high that we proposed that the dipole moments of the individual [$V_{Cu}In_{Cu}V_{Cu}$] defects cause these clusters to group into superclusters that reduce scattering. In the case of the (110) films we suggest that the defect concentration has dropped below a critical level necessary for clustering and consequently that the defect clusters are scattered throughout the material without alignment. This would explain the decreased mobility and change in temperature dependence as all of the acceptors are now free to scatter carriers.

To estimate the influence of these results on device performance, we are in the process of producing devices based on the (110) epitaxial layers in collaboration with both IEC at the University of Delaware and NREL. To date, devices have been produced with 8.5% efficiencies on (112)-oriented layers. Results for devices with comparable series and shunt resistances show superior performance in (110) devices. We have also conducted device simulations using the AMPS computer code developed at Penn State University by S. Fonash and coworkers. The AMPS simulation has been applied to modeling the results of the 18.8% NREL cell. In simulations ignoring the grading of the Ga content in the device, good fits to both the J/V and spectral response curves of the device have been obtained. Standard values for materials parameters were used when possible. The blue portion of the spectral response was found to depend strongly on the CdS properties and these were fit to this data. It was found necessary to introduce an n-type surface layer on the CIGS although a thickness of less than 10 nm was necessary to provide a good fit to the data. The red region of the spectral response data and the J/V curve were fit by adjusting the energy gap of the CIGS and the defect concentration in the CIGS. We then adjusted the hole concentration of the CIGS as a parameter. We conclude from this that significant improvements in device performance may result from the reduction in carrier concentration. We will provide experimental data as it becomes available to verify this.

4. Conclusions

CIGS films grown here with an average (110) bulk orientation have (112) surface facets, lower hole concentrations, and lower hole mobilities with modified temperature-dependences. Device simulations using the AMPS computer code suggest that lower carrier concentrations should yield better devices. This appears consistent with early device results on (110) epitaxial layers. The above suggests to us that while the NREL device films had strong (110) preferred orientation, they probably had (112) surface facets. We believe this is consistent with SEM images of the NREL device layers.

ACKNOWLEDGEMENTS

Support of this research by the Department of Energy and the National Renewable Energy Laboratory under contract DEFG02-91ER45439 and the Electric Power Research Institute are gratefully acknowledged. The materials characterizations were conducted in the Center for Microanalysis of Materials at the University of Illinois which is supported by the Department of Energy.

REFERENCES

[1] D.J. Schroeder, J.L. Hernandez, G.D. Berry, and A.A. Rockett, "Hole Transport and Doping States in Epitaxial Cu(In_xGa_{1-x})Se_2", J. Appl. Phys. **83(3)** (1998), 1519.

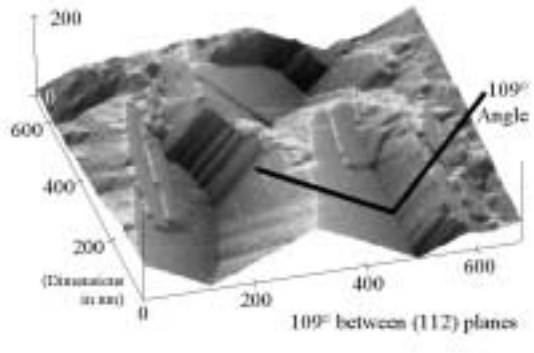

Fig. 1. An AFM image showing the surface facets on a typical (110)-oriented CIGS film.

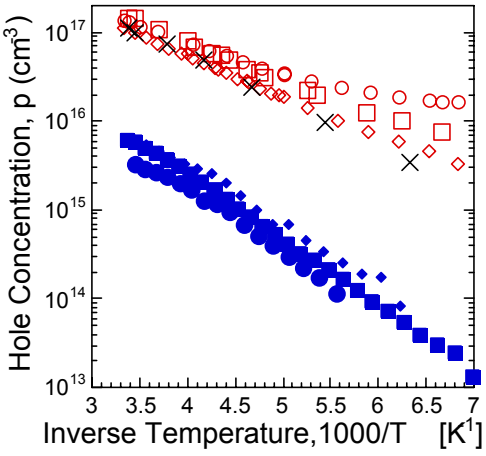

Figure 2: Hole concentration as a function of temperature. Values for (110) samples [closed points] are significantly below those for (112) [open] and (100) ["X"] samples.

Ga Incorporation Mechanisms in CIGS Solar Cells

P. Panse, H. Sankaranarayanan, R. Narayanaswamy, M. Shankaradas, Y. Ying,
C. S. Ferekides and D. L. Morel

Department of Electrical Engineering
Center for Clean Energy and Vehicles
University of South Florida
4202 E. Fowler Ave.
Tampa, FL

ABSTRACT

Advanced measurement techniques such as photo-capacitance are being combined with simulation models to advance our understanding of CIGS solar cells. Several complex defects have been identified. Through improved understanding of these defects we have been able to successfully incorporate Ga using our manufacturing-friendly 2-step solid source selenization process. High Jsc's and Voc's are now being attained in higher band gap devices.

Introduction

We have been developing a 2-step solid source selenization technique for the fabrication of CIGS solar cells. Our best devices have only trace quantities of Ga in the space charge layer and consequently band gaps below 1 eV. While we have produced state-of-the-art devices in this band gap range, higher efficiencies can be achieved at larger band gaps. In adding Ga to our films to increase Eg we have had difficulties in maintaining electronic properties. To help overcome this problem we have been developing simulation models based on AMPS and advanced measurement techniques such as photocapacitance. These are providing new insights to the defect properties of these films and are guiding our fabrication efforts to improve performance.

Another important aspect of our deposition process is that we can produce a matrix of 25 devices in a single run with intentional compositional gradients. This provides a close look at subtle compositional changes, while the large variety of device structures that we fabricate provides us with a rich data base of performance data.

Results and Discussion

An example of the effect of Ga on device performance is provided in figure 1. In depositing our devices the substrate is positioned in the center of the four sources. The Cu and In are across from each other as are the Ga and Se. Position 1 on the ordinate axis of figue 1 is nearest the

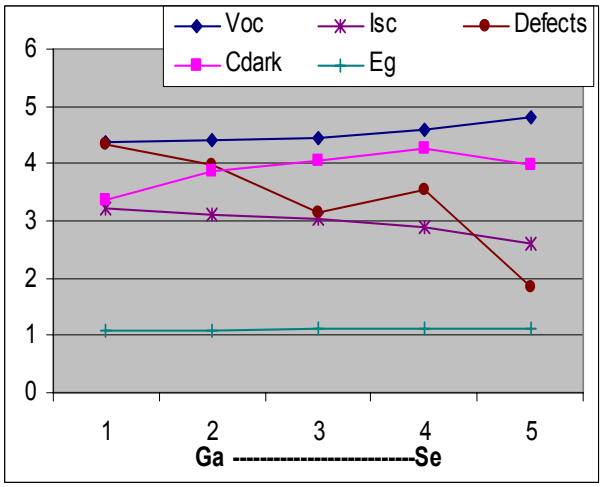

Figure 1. Various parameters plotted as a function of position along the Ga-Se gradient.

Ga source, while position 5 is farthest from Ga and closest to Se. Each data point is the average of 5 devices with the same Ga/Se composition. As can be seen, Voc increases with decreasing Ga, while the band gap holds constant. This is due to a decreasing defect density as shown. The

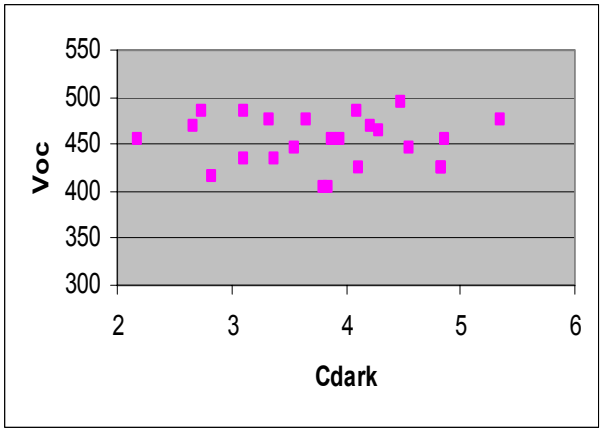

Figure 2. Voc as a function of dark capacitance for the devices of figure 1.

defect density is measured by a photocapacitance technique[1]. The increase in dark capacitance with decreasing Ga indicates an decreasing SC width in the dark that suggests some influence by an increasing acceptor concentration. However, as seen in figure 2, Voc is found to be independent of dark capacitance and hence acceptor concentration. The decrease in Isc as Ga is decreased , however, is in part directly attributable to the shrinking SC region. We attribute the reduction of defects in figure 2 to the increased Se flux[1]. Thus based on these insights we have learned how to incorporate Ga and control the associated defect structure.

We have also devoted considerable effort to the use of the Penn State/EPRI AMPS simulation program. As Ga is added to increase Eg, Jsc and Voc often go in opposite directions. The AMPS simulation in figure 3 of the recombination rate as a function of position at two representative band gaps indicates tradeoffs between bulk and surface recombination that can affect Jsc and Voc. The first peak at 0 microns is the CdS layer and indicates equal recombination for both band gaps. The second peak is a 100 nm thick CIGS region. To match the experimental data that accompanies these simulations the acceptor defect concentration in this region and in the rest of the bulk CIGS layer had to be raised significantly. The resulting recombination rates indicate the influence of Ga in the bulk and interface regions. Using these insights we have been able to achieve a one-for-one increase in Voc with Eg as shown in figure 4. Also shown is the defect level dependence on Eg as measured by photocapacitance. As seen, it remains constant or perhaps decreases slightly with increasing Ga. Although our Voc's are down shifted a bit due to factors other than the effect of Ga on Eg, the ability to add Ga and realize a one-for-one increase in Voc with Eg is a step forward.

As suggested by the simulations in figure 3, we have also had difficulties in maintaining current densities as we increase Eg. Detailed measurements indicate in some cases IV curves with significant slopes near the current axis, and QE responses with red-shifted or downshifted response as the band gap is increased. Again we have turned to AMPS to attempt to sort out the various influences on Jsc performance. Simulations suggest control by an acceptor/acceptor defect complex[1]. By learning to control this defect we are now able to achieve high Jsc's in higher Eg devices as shown in figure 5. We are now learning how to independently control these mechanisms so that Jsc and Voc can be optimized together to improve overall performance.

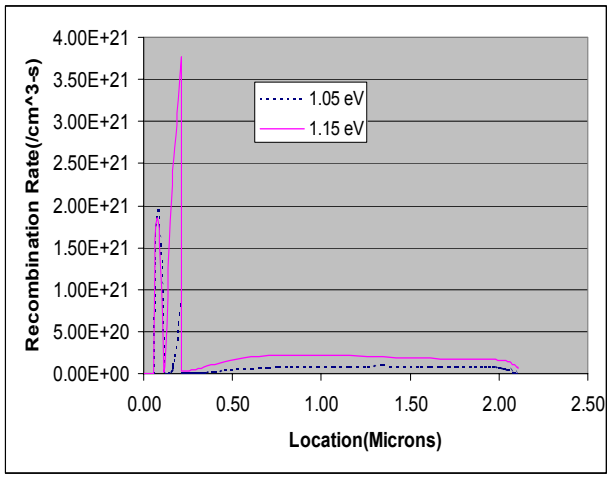

Figure 3. AMPS recombination rate simulation for devices with band gaps of 1.05 and 1.15 eV.

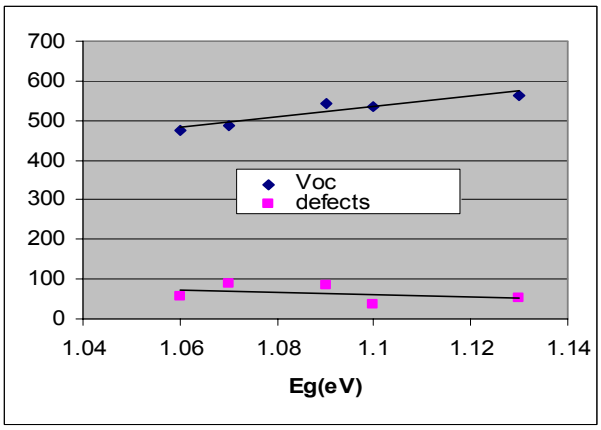

Figure 4. Dependence of Voc and defects on Eg .

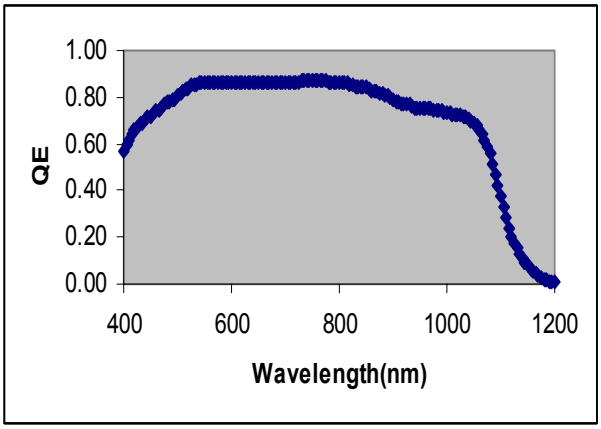

Figure 5. QE spectral response of a high current density(35.4 mA/cm^2) 1.09 eV band gap device.

References

1. M. Shankaradas, Y. Ying, H. Sankaranarayanan, P. Panse, C. S. Ferekides and D. L. Morel, "Photocapacitance Analysis of Defect Mechanisms in Cu(In, Ga)Se Solar Cells" , Submitted to the 28th IEEE PVSC.

Local Structure of $CuIn_3Se_5$

C.-H. Chang[1*]*, Su-Huai Wei[2], , N. Leyarovska[3], J.W. Johnson[1], S.B. Zhang[2], B.J. Stanbery[1], T.J. Anderson[1], R. Duran[1], and Grant Bunker[4]
University of Florida, Gainesville, FL 32611[1]
National Renewable Energy Laboratory, Golden, CO 80401[2]
Advanced Photon Source, Argonne National Laboratory, IL 60438[3]
Illinois Institute of Technology, Chicago, Illinois 60616[4]

ABSTRACT

The results of a detailed EXAFS study of the Cu-K, In-K, and Se-K edges $CuIn_3Se_5$ are reported. The Cu and In first nearest neighbor local structures were found to be almost identical to those in $CuInSe_2$. The Se first nearest neighbor local structures, however, are quite different. The fitted results indicated $CuIn_3Se_5$ consists of Se-centered tetrahedron with an average of 0.8 Cu and 2.4 In nearest neighbors. This result is consistent with first-principle total energy calculations for this system.

1. Introduction

The observed junction between α-$CuInSe_2$ and $CuIn_3Se_5$ appears to play an important role in the photovoltaic process. Several investigations have explored the structure of this compound; however, the reported structural solutions disagree significantly. To shed some light on this issue, we have studied the local structure of $CuIn_3Se_5$ using EXAFS measurement performed on the Cu, In, and Se K-edges. The first-principle total energy calculations are also performed to compare with experimental data.

2. Experiment

The samples were synthesized from Cu_2Se and In_2Se_3 powders placed in boron nitride (BN) coated evacuated quartz ampoules. These powder mixtures were slowly heated to ~ 150 °C above the melting temperature of In_2Se_3, then gradually cooled to 700°C and isothermally annealed for a week to reach equilibrium. The XAFS specimens were prepared by grinding the polycrystalline materials. Particle size analysis was done using a Horiba Capa-700 particle analyzer, which confirmed particles were less than ten microns in diameter. The fine powder was uniformly spread over a scotch tape. The XAFS measurements were performed on the MR-CAT beamline of the Advanced Photon Source (APS) at Argonne National Laboratory, which uses an APS undulator-A. The beamline optics incorporates a Si (111) double monochromator and a Rhodium coated harmonics-rejection mirror, which was set to reject second and higher harmonics. The X-ray intensities were monitored using ionization chambers, with Nitrogen and Argon respectively in the transmission and fluorescence ion chambers. Linearity was checked by attenuating the primary beam.

3. Results

The XAFS data were analyzed by standard methods using the WinXAFS package [1]. To obtain quantitative information, the standard EXAFS equation was used in the least square analysis:

$$\chi(k) = \sum_j \frac{N_j}{kR_j^2} S_0^2 F_j(k) \exp(-2k^2\sigma_j^2) \exp(\frac{-2R_j}{\lambda(k)}) \sin[2kR_j + \delta_j(k)]$$

In this equation N_j is the number of atoms in jth shell; R_j is the mean distance between the absorbing atom and the jth shell; $F_j(k)$ is the magnitude of the backscattering amplitude of the jth neighbor atom; $\delta_j(k)$ is the electronic phase shift due to the atomic potentials; σ^2 is the corresponding mean-square relative displacement; S_0 is the amplitude reduction factor representing central atom shake-up and shake-off effects, and $\lambda(k)$ is the photoelectron mean free path. The backscattering amplitude, $F_j(k)$, and phase shift, $\delta_j(k)$, for Cu and In K-edges were extracted from the $CuInSe_2$ spectra using the known structural data.

The isolated first shell Cu-K EXAFS spectra for $CuInSe_2$ and $CuIn_3Se_5$ are almost identical except the spectrum for $CuIn_3Se_5$ has a slightly larger damping coefficient. This indicates the first nearest neighbor local structures (i.e. the bond length, dCu-Se, and the number of nearest neighbors, N) around the Cu atoms in these two semiconductor alloys are nearly the same. The least-squares fit results are given in Table 1.

The isolated first shell In-K EXAFS spectra for $CuInSe_2$ and $CuIn_3Se_5$ are also found to be almost identical. The least square fitting results are given in Table 1. The fitting results confirmed the In-Se inter-atomic distance is conserved between $CuInSe_2$ and $CuIn_3Se_5$.

Table 1. Least square fitting results

	Coordination number	bond length (Å)
Cu-K edge	4±0.2	$R_{Cu\text{-}Se}$ 2.424±0.005
In-K edge	4±0.1	$R_{In\text{-}Se}$ 2.595±0.005

The isolated Se-K edge first shell spectra for $CuInSe_2$ and $CuIn_3Se_5$ are given in Figure 1. It is clear that the two spectra are very different. This indicates that the first nearest neighbor environment around Se atoms in these two semiconductor alloys is also very different. The ab intio multiple-scattering code FEFF7 [2] was used to calculate $F_j(k)$, $\delta_j(k)$, and $\lambda_j(k)$ to obtain quantitative

* Current address: Oregon State University, Chemical Engineering Department, Corvallis, OR 97330

estimates of the number of nearest neighbors and their distances. The least square fitting results are listed in Table 2. The fitted results show the Se-K edge data are consistent with the Cu and In K-edge data. The results confirm that $CuIn_3Se_5$ does belong to the defect-tetrahedral structure, which is characterized by vacant tetrahedral site in the Se-centered tetrahedron. The data are consistent with the models proposed by [3], which suggested that the structure of $CuIn_3Se_5$ consists of three types of local tetrahedral cationic clusters around each Se: V_{Cu}+Cu+2In (k=7), 2Cu+2In (k=8), and V_{Cu}+3In (k=9). How these different types of tetrahedron arrange themselves and form the long-range order structures (e.g., symmetry) needs further study by other techniques.

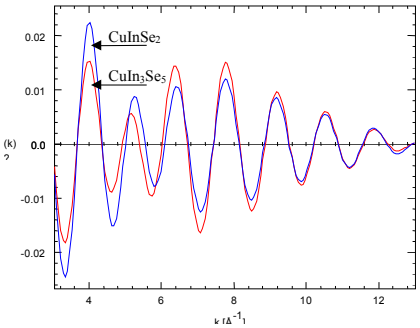

Figure 1. Fourier filtered EXAFS on the Se K edge for the first shell peaks in $CuInSe_2$ and $CuIn_3Se_5$.

Table 2. EXAFS analysis results for $CuIn_3Se_5$ Se-K edge data

	S_0^2	0.737
Cu-Se	N:	0.8
	R_{Cu-Se} (Å):	2.424
	σ^2 (Å^2) :	1.77×10^{-3}
In-Se	N:	2.4
	R_{In-Se} (Å):	2.598
	σ^2 (Å^2) :	4.22×10^{-3}

We have also studied the local crystal structures of various $CuInSe_2$, $CuIn_3Se_5$ and $CuIn_5Se_8$ compounds using the first-principles band structure method [4]. To choose the crystal structures, we have followed two guidelines: (a) The arrangement of atoms in the crystal has minimal deviations from the octet rule and (b) they have low Coulomb energy. Our total energy calculations show that the total energy differences between the six $CuIn_5Se_8$ structures being calculated are small, less than 8 meV/atom. Similar results are obtained for $CuIn_3Se_5$ and $CuInSe_2$. These results indicate that although the local environment of ordered vacancy compounds (OVCs) are well defined, containing weighted k=7, k=8 and k=9 clusters, the long range order of the OVCs may depend sensitively on growth kinetics, history of annealing, and the configuration entropies. This could explain why different crystal structures of $CuIn_3Se_5$ have been observed. For example, the crystal structure proposed by Hanada et al. [5] for $CuIn_3Se_5$ has a space

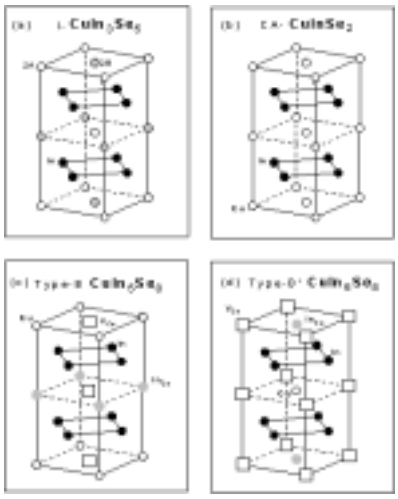

Figure 2. Structures for $CuIn_3Se_5$, $CuInSe_2$, and $CuIn_5Se_8$.

The model structure of Hanada et al. can be well described as a superposition of three single phases: (i) 20% of the CA-$CuInSe_2$ (Figure 2b.), (ii) 40% of the type-B $CuIn_5Se_8$ (Fig. 2c), and (iii) 40% of type-B' $CuIn_5Se_8$ (Figure 2d.), where type-B' $CuIn_5Se_8$ is identical to type-B $CuIn_5Se_8$ except that its origin is shifted by (1/2,1/2,1)a. The equilibrium bond lengths in the various OVCs were calculated. It was found that, within a calculation uncertainty of about 0.005 Å, the Cu-Se bond lengths in these OVCs are independent of the stoichiometry and atomic configuration. For the In-Se bonds, the bond lengths were found to increase linearly with k with RIn-Se(k=9) - RIn-Se(k=7) = 0.06 Å. The average In-Se bond lengths in $CuInSe_2$ and $CuIn_3Se_5$, however, are constant to within 0.01 Å, and decrease slightly as the Cu occupation decreases within the homogeneity range of the ß-phases (OVCs). The theoretical results are consistent with the present EXAFS measurements. The calculated standard deviation from the average In-Se bond lengths is ~ 0.03 Å. Temperature-dependent EXAFS measurements are needed to further clarify this difference.

The work at University of Florida was supported by the DOE/NREL Thin Film PV Partnership Program under subcontract XAF-5-14142-10.

REFERENCES

[1] T. Ressler, J. Physique IV, **7** (1997) C2-269.
[2] A.L. Ankudinov and J.J. Rehr, Phys. Rev. B. 52, 2995, 1995.
[3] S. B. Zhang, Su-Huai Wei, and Alex Zunger, H. Katayama-Yoshida, Phys. Rev. B. 57, 9642, 1998.
[4] S.-H. Wei and H. Krakauer, Phys. Rev. Lett. 55 1200 (1985)
[5] T. Hanada, A. Yamana, Y. Nakamura, O. Nittono, and T. Wada, Technical Digest: 9th International Photovoltaic Science and Engineering Conference (International PVSEC-9, Tokyo, 1996), p.595.

Modeling of Mass Flux and Platen Heat Distribution in a Molecular Beam Epitaxy Reactor for Deposition of CIS Precursor Films

Serkan Kincal, Suku Kim, Oscar D. Crisalle, and Tim Anderson

P.O Box 116005, Chemical Engineering Department
University of Florida
Gainesville, FL 32611-6005

1. INTRODUCTION

A Plasma Enhanced Migration Epitaxy (PMEE) reactor employed in the growth of $CuInSe_2$ (CIS) absorber layers at the University of Florida generates films on substrates placed on a rotating platen. The system uses thermal effusion sources with free evaporating surfaces for the deposition of the copper and indium metals, and a double-oven thermal cracker for the deposition of the selenium chalcogen. From a performance perspective, it is important to tightly control the ratio of Cu to In in the film. The selenium flux control is less important because it is supplied in stoichoimetric excess. In addition, the temperature of the substrate is critical because it defines the path of the surface reactions, and hence affecting the final efficiency of the solar cell. For improved process control it is thus necessary to develop models for (1) the flux distributions produced by the metal sources, and (2) the temperature profiles of the substrate.

2. FLUX MODELING

The flux from each metal source is controlled by regulating the power input to each effusion cell. A measure of the flux from each source is obtained from the signal detected by an individual electron impact emission spectrometer (EIES). There are several challenges that must be addressed before a reliable control strategy can be employed for the metal fluxes. First, the process is inherently non-linear because the flux increases exponentially with temperature. Second, the flux distribution on the entire substrate must be estimated from two measurements, namely the source temperature and the flux detected at a single point by the EIES sensor. Furthermore, the EIES calibration factor must be adjusted continuously as the melt height changes. Resolution of these issues requires the use of an accurate model that relates the temperature of the source to the flux distribution on the substrate, and to the flux incident on the EIES sensor. In addition to being accurate, this model should also be reasonably efficient if it is to be employed in real-time control strategies.

1.1. Approach

The flux modeling procedure is based on the merging and further refinement of two separate approaches available in the literature for the modeling of free evaporating surface effusion sources [1,2].

Figure 1 shows the flux distribution on the substrate as a function of position at nine different melt heights. This figure illustrates that as the melt level decreases, a region forms around the center of the substrate where the deposition rates are approximately constant at a given melt height. This is important from an operational point of view since it implies the existence of an optimum melt level that depends on the substrate size and on the desired level of uniformity through the film.

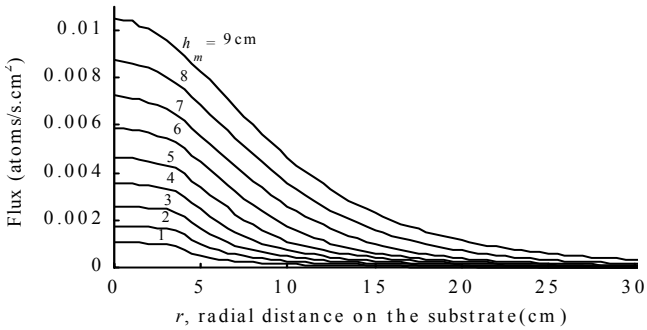

Figure 1. Incident flux (atoms/sec-cm^2) on the substrate at nine melt levels as a function of radial position (cm).

3. TEMPERATURE MODELING

The uniformity of the temperature distribution on the substrate is crucial to the growth of absorber layers with uniform film composition. The University of Florida reactor uses a rotating tungsten platen that successively exposes Mo-coated glass substrates to a heater. The substrate temperature is not measured directly since the only thermocouple available is located in the gap between the platen and the heater; therefore, a thermal model is needed to estimate the actual the temperature distribution on each substrate.

1.2. Approach

A two-dimensional model of the heat transfer on the platen can be developed based on a heat balance on the platen, namely [3]

$$\rho \hat{C}_p \frac{\partial T}{\partial t} = k\nabla^2 T + \phi_{rad} \qquad (1)$$

where ϕ_{rad} represents the combined radiative heat flux from the heater, the surrounding environment, and from the metal effusion sources; the remaining symbols are conventional. A second equation describing an energy balance on the

thermocouple located in the gap is also solved. Other thermal effects, such as convection, are ignored in this case since the pressure for the process is low (~10^{-8} torr). Time-varying view factors are employed to account for the fact that the platen rotates at a given angular speed. Symmetry considerations define the boundary conditions required for a full model formulation. Significant simplification is obtained by assuming blackbody radiation. This assumption that is reasonable given that the distance between the objects is much smaller than the dimensions of the objects.

The thermal contact between the substrate and the platen is poor [4]; hence, a thin thermal break-region of near-zero thermal conductivity is assumed to model the contact resistance. Modeling studies show that the existence of a thermal-break improves the temperature uniformity in the substrate region. Appropriate thermal conductivity, density, and heat capacity values are used to differentiate between the tungsten and glass domains. In the design of the rotating system, the platen and the substrates are locally heated and locally cooled. This creates some additional complexity and requires that the model be solved dynamically. The final temperature profiles are found numerically using a finite-element solver.

Figure 2 plots the calculated steady state temperature along the centerline of the substrate/platen. Either the platen or the glass substrate is exposed as the centerline is traversed. Since the glass substrate has a poorer thermal conductivity than the platen and a contact resistance exists between the two, a sharp increase in the centerline temperature is calculated when the centerline position moves from the platen to the substrate. The highest temperature occurs where the substrate exits the heating region (~230 ° position), and the lowest temperature at the point where the substrate enters the heating region. The model predicts that the maximum temperature difference between any two points on a single substrate at a given position is approximately 10°C (not shown in the figure). The temperature variation experienced by any single substrate throughout a complete revolution is no greater than 20°C when the highest temperature is approximately 490°C. Such temperature variations are relatively small compared with the peak temperature, and therefore the substrate temperature can be considered to be fairly uniform.

The thermal modeling results were validated by comparison to temperatures measured in a calibration experiment using selected eutectic films. Good agreement was obtained without adjusting model parameters.

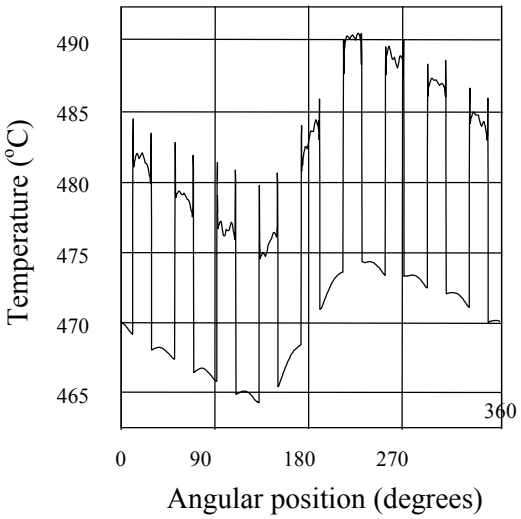

Figure 2. Steady state centerline temperature on the platen/substrate as a function of angular position.

4. CONCLUSIONS

The work on flux modeling is an improvement over previous studies in terms of efficiency of execution, accuracy, and applicability to control design. These improvements are realized by substituting analytical solutions for some of the numerical calculations proposed by Curless [1], hence reducing the numerical burden as well as increasing the accuracy. The procedure outlined by Grigor'ev et al. [2] is extended to include conical as well as cylindrical crucibles. Finally the presentation of the flux results in terms of look-up tables allows for the numerical simulations to be done off-line only once, making the entire strategy useful for model-based real-time control applications. The thermal modeling work shows that the reactor design is capable of achieving locally uniform temperature distributions.

5. REFERENCES

[1] Curless, J.A. (1985), *J. Vac. Sci. Tech.*, **B3**, 531.

[2] Grigor'ev, Y. N.; N. M. Sh. Shavalev, and V. P. Shapeev (1994), *Tech. Physics*, **39**, 759.

[3] Bird, R. B; W. E. Stewart, and E. N. Lightfoot (1960), *Transport Phenomena*, John Wiley & Sons, New York, 1960

[4] Kreith, F.; and M. S. Bohn (1993), *Principles of Heat Transfer*, West Publishing Co., St. Paul.

Monolithic Integration of CIGS based PV on Flexible Substrates

S. Wiedeman, J. Fogleboch, J. Muha, R.G. Wendt, J.S. Britt

Global Solar Energy L.L.C., 5575 So. Houghton Rd., Tucson, AZ, 85747
Tel: (520) 546-6313 Fax: (520) 546-6318

Abstract

An all-laser process for monolithic integration has been developed for Copper-Indium-Gallium-Diselenide (CIGS) based modules on flexible substrates. Results are presented including a selective laser process for front contact scribing and an ink-jet method for formation of insulating material over previously cut scribes. Robust, high speed processes with minimal scribe area loss have been demonstrated.

1. INTRODUCTION

Photovoltaic (PV) module fabrication based on flexible substrates enables the use of high speed, continuous roll-to-roll manufacturing processes. The potential for low cost, high volume manufacturing processes, coupled with inherent advantages in the resultant product such as durability, light weight and flexibility make the approach attractive. Monolithic integration is a crucial capability for cost-effective production of thin film PV. An excellent overview of thin film scribing techniques and requirements is given by Compaan[1]. Flexible substrates introduce several additional processing challenges and constraints, including special means to hold the substrate flat during laser processing. Also, processing must be performed from one side to avoid physical contact to the deposited PV layers. Mechanical scribing is problematic with flexible substrates, thus laser processes for all scribes are advantageous.

Thus, key goals include the development of high speed, all-laser processes to selectively cut thin film PV layers as required for back, front and interconnect scribes. The process used at GSE, described elsewhere[2], also requires controlled ink-jet deposition of insulating material into specific scribes. High speed, robust, all laser and ink-jet processing methods are required for high throughput.

2. ALL-LASER SCRIBING

To avoid scribe generated debris under the absorber layer that may lead to shunt formation, laser scribing is done after the back contact, CIGS and CdS layers have been deposited. Thus the back contact scribe must cut through the CIGS absorber layer and the CdS layer as well as the back contact material. The back contact scribe must be continuous, uniform and largely free from debris. Back contact scribes 100 microns wide have been routinely achieved. Continuous development to improve speed and robustness of processes and equipment has resulted in multiple beam scribing at a rate of 12-in./sec per beam. Fig. 1a shows representative high rate back contact scribes with exposing the polyimide substrate.

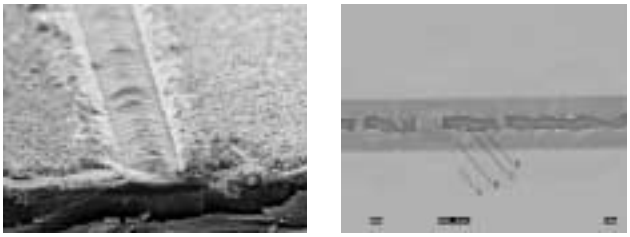

a) b)

Fig. 1 Micrograph of a) back contact scribe through CdS/CIGS/Mo on polyimide. and b) interconnect or via scribe in CdS/CIGS, both conducted at 12-in/min.

Interconnect or "via" scribes need not necessarily be continuous, but should be free of irregularities or edge defects that may create step coverage problems in the subsequent TCO deposition. Mechanical processes have been used, as well as laser methods for CIGS based PV on rigid substates [3]. GSE has developed a laser process for the interconnect scribe on flexible (polyimide) substrates. Progressively higher quality interconnect scribes have been developed (NREL TFP program), adapted and extended to high speed (12-in./sec), robust processes under the NREL PVMaT program.. A typical interconnect scribe, shown in Fig. 1b, is 100 microns wide with regular, uniform edges exhibiting little scribe generated debris. EDS analysis indicates undisturbed CdS/CIGS at location 'A' in Fig. 1b, which is largely removed with only a thin layer remaining at location 'B' inside the scribe. Locations 'C' and 'D' in Fig. 1b are exposed back contact and substrate material respectively. The low resistivity path is formed as the front contact material contacts regions 'B' and 'C'.

Front contact scribing requires selective removal of all the conductive TCO leaving the CIGS layer largely intact. Thermal or physical damage to the underlying CIGS or back contact layer that would result in shunt formation either across the scribe or between front and back contacts through the absorber thickness must be avoided.

At GSE we also have developed equipment and conditions to meet the requirements for front contact laser scribing. We have extended the capability and modified the conditions as required to reach a scribing rate of 12-in./sec per beam to address manufacturing throughput requirements. Fig. 2a and 2b show examples of a front contact scribe done at 12-in./sec on a device stack of TCO/CdS/CIGS/back contact/polyimide. In Fig. 2b the TCO (rough textured) layer appears to be removed in the scribe, as well as possibly some of the CIGS absorber.

Tab.1 shows EDS analysis (performed at a low energy to maximize surface sensitivity) indicating that the TCO, in this case ITO, has indeed been removed. Inside the scribed area essentially only the components of CIGS remain with residual CdS. Electrical tests have validated good electrical isolation across the front contact scribe without shunt formation from front to back contact. The process appears to be very robust.

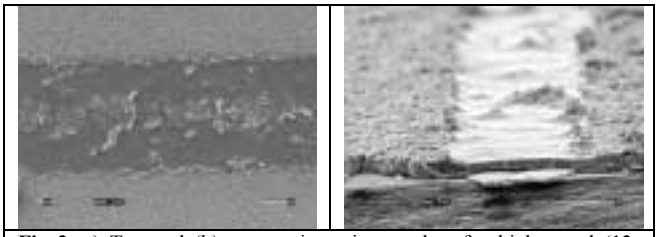

Fig 2. a) Top and (b) perspective micrographs of a high speed (12-in./sec) front contact laser scribe made on TCO/CdS/CIGS/Mo.

Tab. 1 EDS analysis showing elements present before and after ITO front contact scribing (10 keV Energy)

	Outside Scribe Area (elemental %)	Inside Scribe Area (elemental %)
Cu	0.45	24.16
In	80.46	19.93
Ga	0.25	6.15
Se	0.54	45.05
Cd	5.40	2.22
S	3.10	1.24
Sn	8.23	0.37

3.0 INK-JET DEVELOPMENT

To prevent direct shunt formation in the post-absorber approach, ink-jet technology has been developed at GSE to controllably print insulating material over the back contact scribes. Potential advantages of ink-jet over screen printing include reduced linewidths and increased registration accuracy, which would reduce module area losses and enable smaller segment widths. Additional benefits may include reduced labor and capital costs, greater flexibility in pattern generation and reduced set-up and clean-up time. Several types of ink-jet technology exist, each constrained by different limitations, such as speed, ultimate linewidth or fluid characteristics. Drying or curing time is important for the printed insulator materials to allow rapid processing.

Additional variables besides dispense parameters impact the above factors, notably fluid type and substrate type. Fig. 3a below shows an ink-jet printed line having the desirable features of uniformity, continuity and fairly small linewidth. The impact of fluid type is evident by comparison to Fig. 3b, which used another type of insulating material. A cross-sectional view of an ink-jet deposited line of insulating material is shown in Fig. 4. Material and processes have been identified at GSE that are compatible with subsequent processes and yield well-adherent, uniform and continuous lines of insulating material. Moreover, good registration of the printed insulator with the previously cut back contact scribe has been accomplished reproducibly.

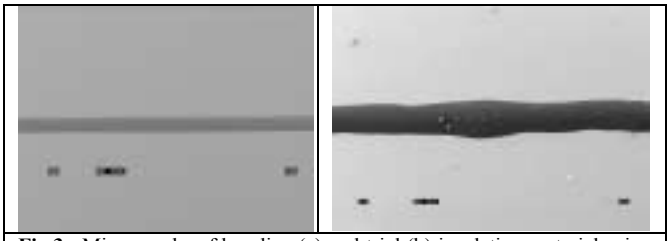

Fig.3. Micrographs of baseline (a) and trial (b) insulating material using a new adhesive, printed at 12-in./sec.

Figure 5 shows a complete module interconnect consisting of a front contact scribe, an interconnect scribe and a back contact scribe covered by an ink-jet printed line of insulating material (in sequence from left to right). For diagnostic purposes the scribes shown in Fig. 5 are not spaced tightly, nor is the printed insulator line centered over the back contact scribe.

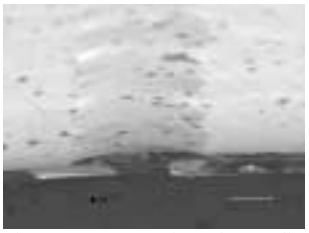

Fig. 4 Perspective view a line of insulating material ink-jet deposited over a back contact scribe on CdS/CIGS/Mo/polyimide.

Fig. 5 Micrograph of a functional module interconnect incorporating the high speed scribing and ink-jet printing processes.

4. CONCLUSIONS

GSE has successfully developed conditions and equipment for all-laser, high speed (12-in./sec) processes for the back contact, front contact and interconnect scribes for CIGS based modules on flexible polyimide substrates. High rate, selective thin film cutting has been confirmed for these processes using optical, SEM and electrical characterization. Ink-jet technology has been successfully adapted to print fine lines of insulating material over specific scribes, preventing shunting. The ink-jet process is also high speed and compatible with subsequent manufacturing steps.

5. Acknowledgements

The authors would like to acknowledge funding support from DARPA Agreement MDA972-95-3-0036, NREL contracts ZAK-8-17619-04 (NREL TFP), ZAX-8-17647-11 (NREL PVMaT), and Unisource Energy .

6. References

1 A. Compaan, *Laser Focus World*, (PenWell pub.) Jan. 2000, p.147-152.

2. S. Wiedeman, R.G. Wendt and J.S. Britt, *AIP Conference Proceedings Series #462* (1999)

3. J. Kessler, S. Wiedeman, L. Russell, S. Skibo, R. Arya and D. Carlson, "Cu(In,Ga)Se_2 Based Submodule Process Robustness",*Proc. of the 25th IEEE Photovoltaic Specialists Conference*, Wahsington, DC, 1996, p 813-816.

Non-vacuum, Particle-based Processes for $CuInSe_2$ Photovoltaics

C. Eberspacher, C. Fredric, K. Pauls and J. Serra

UNISUN
587-F North Ventu Park Road, PMB 124, Newbury Park, CA 91320 USA

ABSTRACT

This work is directed at developing low-cost, non-vacuum techniques for fabricating efficient photovoltaic (PV) modules based on thin-film $CuIn_{1-x}Ga_xSe_2$ (CIGS). The goal is to accelerate the commercialization of thin-film CIGS PV technology. Techniques based on nanoparticle technologies are shown to yield 11.7% cells and 5% monolithic multi-cell modules.

1. Introduction

Photovoltaics (PV) is a small but rapidly growing sector of the Nation's electrical power generation capacity. For PV to significantly impact the Nation's economy and quality of life, PV prices must fall by a factor of 2-3 and the capacity of the PV industry must expand multi-fold. Price reductions and capacity expansions require manufacturing cost reductions and higher returns on investment. One of the most promising strategies for lowering PV costs is the use of thin-film technologies, and one of the most promising thin-film PV absorber materials is $CuIn_{1-x}Ga_xSe_2$ (CIGS). Thin-film CIGS PV is comparable in efficiency and durability to commercial products based on crystalline silicon, but commercialization of CIGS PV is progressing slowly in large part due to the cost and complexity of the vacuum-based processes typically used to deposit PV thin films. The complexity and cost of the capital equipment needed for vacuum-based deposition complicate high-yield manufacturing and limit the overall cost savings possible.

The goal of this work is to develop low-cost, non-vacuum techniques for fabricating efficient CIGS PV modules. Non-vacuum deposition techniques such as spraying, printing, spin-coating, etc. can provide substantial operational and cost advantages relative to vacuum deposition and can result in higher overall return on investment. Non-vacuum thin-film technologies deliver a combination of lower costs, lower capital requirements, process simplicity and higher return on investment (ROI). The challenge is to fabricate efficient devices using functionally simple, non-vacuum techniques.

2. Experimental Methods

Unisun has pioneered techniques for preparing high-quality PV thin films from nanoparticle materials processed using simple, non-vacuum methods. The basic concept is to use simple non-vacuum techniques to deposit thin layers of sub-micron precursor powders and to convert the porous particulate layers into high-quality PV films by low-temperature sintering. The use of multinary particulate precursors simplifies composition control for multi-component materials like CIGS since key components (e.g. Cu, In, Ga, etc.) can be pre-mixed in the precursor particles. A typical composition for both particles and films is Cu/(In+Ga) = 0.9 and Ga/(Ga+In) = 0.1.

3. Cell Results

Individual solar cells are fabricated by depositing a particulate precursor layer on Mo-coated soda lime glass, sintering the particulate layer to form a dense CIGS film, coating the CIGS with CdS and ZnO, and depositing a metal grid. Mo-coated glass is provided by university and private sector collaborators. CIGS precursors and films are processed by Unisun. CdS, ZnO and grids are deposited by the Institute of Energy Conversion at the University of Delaware by solution deposition, rf sputtering, and evaporation, respectively.

Solar cells fabricated from particles-based CIGS films exhibit promising characteristics. Early results were highly variable; efficiencies up to 8.5% were measured, but cell-to-cell variation was large [1, 2]. Recent improvements in process control have substantially improved reproducibility (Fig. 1.) One contributing factor to the variation in past results was the time delay between CdS and ZnO deposition (Fig. 2.)

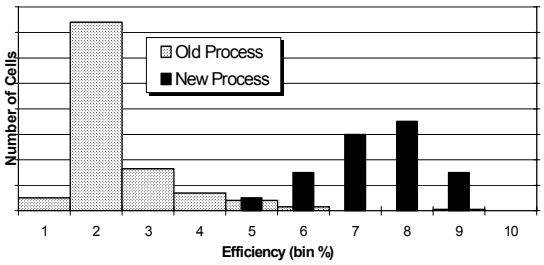

Fig. 1. Distribution of cell efficiencies for old and new "baseline" processes.

The best NREL-confirmed cell efficiency achieved to date is 11.7% (Fig. 3.) Given the relatively early stage of development, these results bode well for the future competitiveness of particle-based CIGS PV technology.

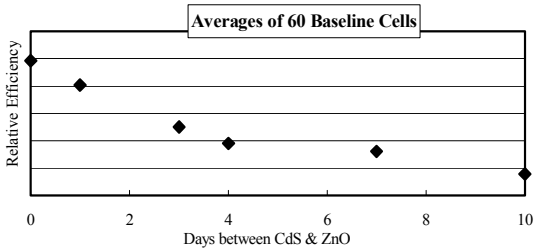

Fig. 2. Variation of cell efficiency as a function of time between CdS and ZnO deposition

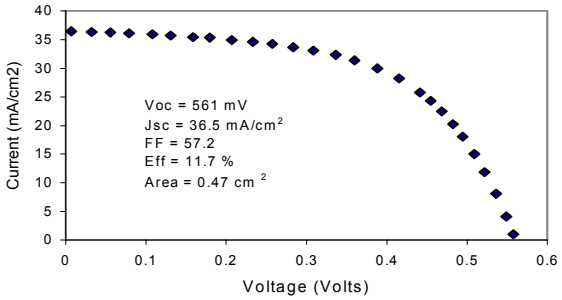

Fig. 3. Current-voltage response of ZnO/CdS/CIGS cell under simulated AM1.5 insolation at NREL.

At present, cell efficiencies appear to be limited by the quality of the CIGS film itself. Quantum efficiency measurements without light bias show a monotonic reduction of photocarrier collection efficiency at longer wavelengths, indicative of poor minority carrier diffusion. Quantum efficiency measurements with light bias show a wavelength-independent, voltage-dependent photocarrier collection, suggestive of recombination losses near the CIGS surface. High-frequency capacitance measurements suggest that hole densities are relatively high (e.g. ca. 10^{17} cm^{-3}) in the CIGS film and upwards of 10^{18} cm^{-3} near the CIGS surface. Cross-sectional scanning electron micrographs show reasonably dense CIGS films, but grain size varies considerably, e.g. 0.25 – 1 μm. These results suggest that cell efficiency improvements will accrue from improvements in CIGS film defect density, mass density, and grain size. Experiments are underway now to explore sintering process enhancements to will effect these improvements.

4. Module Results

Monolithic multi-cell modules were fabricated by depositing CIGS on patterned Mo-coated soda lime glass, coating the CIGS with CdS, patterning the CdS/CISG to expose the underlying Mo, depositing ZnO, and patterning the ZnO/CdS/CIGS to define separate cells. CIGS film processing and mechanical patterning were done by Unisun; CdS and ZnO deposition was done by IEC.

Early efforts were plagued by cracking, uplift and shunting near to the Mo patterns, due in part to interactions between the CIGS layer and the underlying Mo electrode, and were affected by high-resistance contact between the ZnO and Mo. Improvements in the CIGS sintering process, in the CdS/CIGS patterning procedure, and in the CdS and ZnO deposition schedules mitigated these problems.

The best NREL-confirmed module efficiency achieved to date is 5% (Fig. 4.)

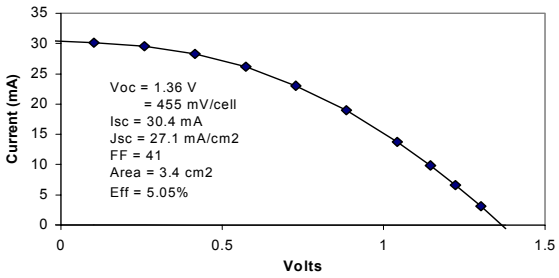

Fig. 4. Current-voltage response of ZnO/CdS/CIGS module under simulated AM1.5 insolation at NREL.

Recent work has focused on scaling up the process to larger areas. Unlike vacuum deposition processes, scaling non-vacuum processes to larger areas is relatively inexpensive and straight-forward. The first generation of 300 cm^2 monolithic module plates incorporated CIGS films deposited at Unisun and ZnO films deposited at NREL.

5. Conclusions

This work demonstrates the feasibility of using particulate precursor materials in a simple, easily-scalable, non-vacuum process for depositing CIGS films for large-area, low-cost PV modules. The process promises to halve the cost of a CIS film for a thin-film solar module, to increase the ROI for thin-film PV, and to significantly accelerate the large-scale commercialization of CIGS PV technology.

ACKNOWLEDGMENTS

This work was support in part by grant # DE-FG03-96ER823000 from the U.S. Department of Energy under its Small Business Innovation Research program. We are indebted to Jie Zhu and Bill Shafarman of IEC for cell fabrication and materials analyses, to Bob Gay of Siemens Solar for Mo-coated glass, to Rommel Noufi and Jim Keene of NREL for large-area ZnO deposition, to Pam Johnson and Jim Sites of Colorado State University for cell analyses, to Angus Rockett of the University of Illinois for additional materials analyses, and to Alan Fahrenbruch of Stanford University, Bob Birkmire of IEC, and Dave Ginley and Doug Schulz of NREL for valuable discussions on materials processing strategies and experimental equipment design.

REFERENCES

[1] C. Eberspacher et al., 2nd World Conference On Photovoltaic Solar Energy Conversion, Vienna (1998) 303.
[2] C. Fredric et al., NCPV Program Review Meeting, Denver (1998) 158.

Results From the Development of a Low-Cost, In-Situ, $CuIn_xGa_{1-x}Se_2$ Composition Sensor Based on X-Ray Fluorescence

I.L. Eisgruber, J.R. Engel, R.E. Treece, R.E. Hollingsworth
Materials Research Group, Inc.
12441 W. 49th Ave., Suite #2, Wheat Ridge, CO, 80033-1927

ABSTRACT

Yield and reproducibility issues remain an important challenge in $CuIn_xGa_{1-x}Se_2$ (CIGS) photovoltaic module fabrication. Development of sensors and controls for processing is therefore an important step towards realizing the potential of CIGS modules for cheap, large-scale power production. In-situ x-ray fluorescence (XRF) is under development to monitor composition and thickness of deposited layers. This paper describes advances in a number of areas that are necessary for in-situ composition measurements of CIGS: design of the sensor equipment, analysis of the x-ray signals, and deposition chamber installation issues.

1. System Design and Assembly

A low-cost XRF sensor was designed and assembled. The sensor is built entirely of commercially-available components. The choices made for a number of parts allow significant cost savings over traditional XRF sytems. A thermoelectrically-cooled Si PIN photodiode is used for x-ray detection. An x-ray tube with a relatively large spot size and Rh anode is used as an x-ray source. The use of a computer-integrated multi-channel buffer reduces cost as well as allowing data manipulation directly by custom software for closed-loop control.

Ex-situ measurements on the system demonstrated good agreement between measured and theoretical count rates in simple systems. For example, the data points in Figure 1 show the Cu-Kα emission as a function of thickness for thin Cu films. Error bars in the x-direction represent mechanical profilometer uncertainty. Error bars in the y-direction show the magnitude of fluctuation in the x-ray tube current. The line demonstrates the relationship expected from theory for the thicknesses shown. The agreement between theory and experiment can also be extended to very thick samples, within the uncertainty created by imprecise knowledge of the spectral distribution of the continuous radiation emitted from the x-ray tube.

2. Data Analysis

Compositions extracted from XRF measurements using the prototype sensor have shown good agreement with inductively coupled plasma (ICP) measurements, over a large variety of samples. An example of results of ex-situ XRF measurements are shown in Figure 2. The x-axis shows the ratio Cu/(In+Ga) as measured by ICP at the National Renewable Energy Laboratory (NREL). The y-axis shows Cu/(In+Ga) as measured by x-ray fluorescence. Error bars in the x-direction represent uncertainty in the ICP measurement, whereas error bars in the y-direction reflect noise in the XRF measurement and error due to sample nonuniformity. The range of elemental compositions in the samples of Figure 2 span high-efficiency CIGS samples by an appreciable percent. High efficiency CIGS devices typically contain about 3100 Å Cu, 5200 Å In, 1300 Å Ga, and 15000 Å Se. Cu thicknesses in the samples of Figure 2 range from 500 to 3600 Å, In

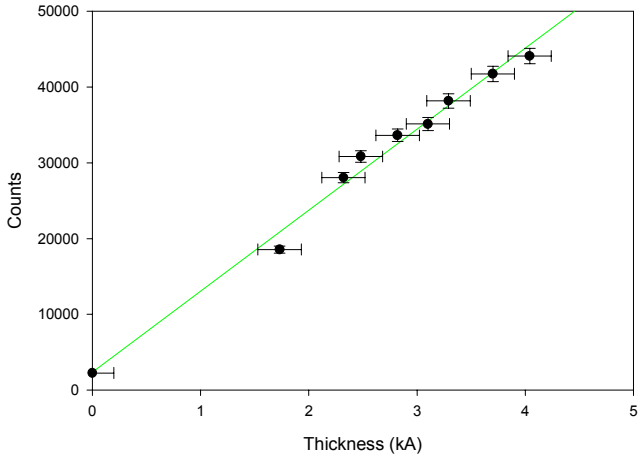

Figure 1: Counts from Cu emission as a function of Cu film thickness.

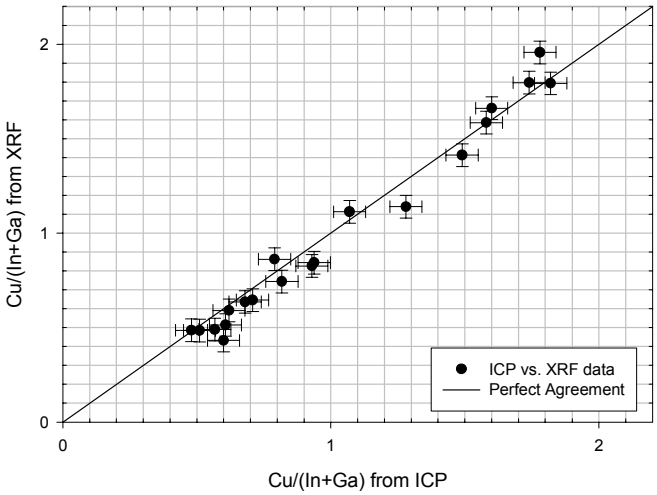

Figure 2: Comparison of the ratio Cu/(In+Ga) as measured by ICP and XRF.

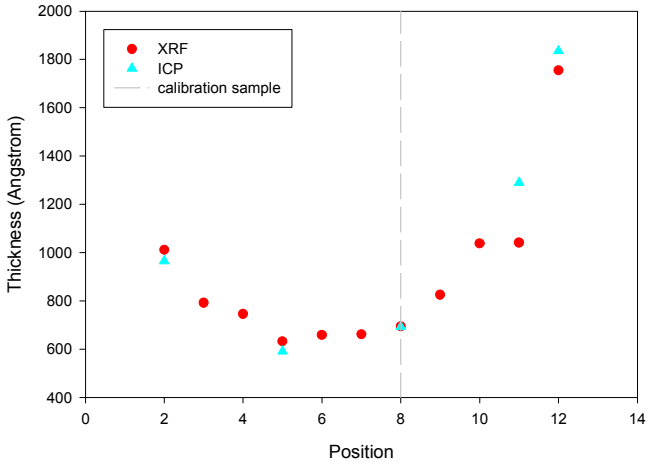

Figure 3: In thickness as a function of position on a large graded sample

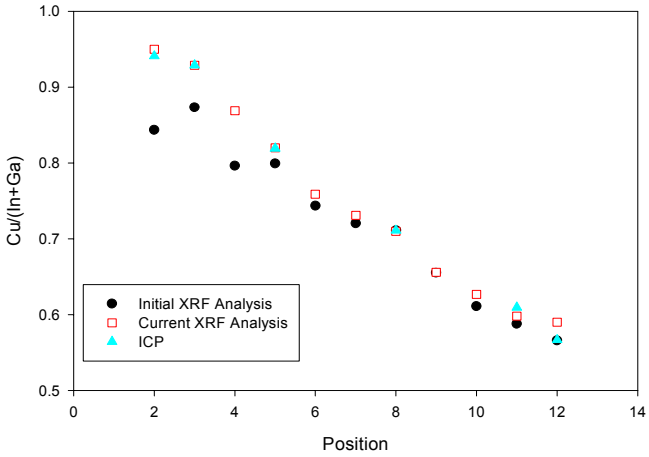

Figure 4: The ratio Cu/(In+Ga) as a function of position on a large graded sample.

thicknesses range from 600 to 16000 Å, Ga thicknesses range from 0 to 8400 Å, Se thicknesses range from 8100 to 31000 Å, and Mo thickness range from 2500 to 110000 Å. (XRF and ICP both measure atoms per sample area for each constituent element. For more intuitive reporting, atoms per sample area has been converted here to effective element thickness by use of the elemental density and atomic weight.)

Multiple levels of sophistication in the XRF interpretation improve the agreement between XRF and ICP measurements in Figure 2. Nonlinearities in counts versus thickness for each element are accounted for by first-principles calculations, performed before data acquisition. Full interpretation is completed by using a known back contact signal (or substrate signal, if steel substrates are used) to correct for fluctuations in x-ray tube intensity.

The use of low-cost x-ray sources and detectors introduces some complexity into the XRF measurement. Interpretation must be successful despite lower detector resolution and lack of higher energy x-rays. Correct assessments of the amount of In and Ga present can be particular challenges, since the high energy In-Kα peak is barely excited, and the Ga-Kα peaks and Cu-Kβ peaks overlap in energy. Data interpretation from the low-cost sensor has, however, accurately indicated the amounts of In and Ga in samples. For example, Figure 3 shows In thickness on a series of samples, as measured by XRF and ICP. Each sample was cut from a different position along a 12" graded CIGS piece. In Figure 3, triangles show the ICP results, while circles show the XRF results. The vertical line indicates the sample used for measurement calibration. The samples contain a variation in In thickness from 600 to 1800 Å. The amount of In in these samples is much less than the typical 5200 Å contained in a 2.5 μm CIGS film with a Ga/(In+Ga) ratio of 0.25. Nevertheless, the XRF and ICP measurements yield the same In thicknesses.

Figure 4 illustrates the improved sensitivity of Ga measurements through analysis of an alternate Ga emission line. The ratio Cu/(In+Ga) is shown versus position on the same sample set as in Figure 3. Triangles show ICP measurements, filled circles show XRF measurements made with the initial choice of Ga emission, and hollow squares show the improved interpretation results.

3. Installation Issues

A number of issues relating to installation of the sensor on the deposition chamber have been successfully addressed.

A critical aspect of installing the XRF sensor in-situ is protecting the sensor from Se and from thermal loads. Hardware has been designed and tested that allows the sensor to operate with ambient temperatures of 200 °C and Se pressure. The hardware is based on a heated outer envelope that drives off Se and a cooled inner envelope.

Another important concern is maintaining count rate when sensor to sample distance is increased. Measurement times around 60 seconds for in-situ configurations are achieved by increasing the x-ray tube current and allowing a slightly larger spot size than traditional XRF systems.

4. Conclusions

Several results from the development of a low-cost, in-situ, CIGS composition sensor have been demonstrated. These results include

- design and assembly of a low-cost XRF sensor suitable for in-situ use and real-time control;
- demonstration of agreement between theory and experiment for measurements on simple film systems using the XRF sensor;
- demonstration of agreement between ICP and XRF results over a wide variety of CIGS samples;
- design and testing of hardware protecting XRF sensor in heated, Se ambient; and
- demonstration of reasonable measurement time for in-situ configurations.

ACKNOWLEDGEMENTS

This research was supported by NREL through subcontract ZAK-8-17619-08. The authors thank Raghu Bhattacharya of NREL for ICP measurements and Craig Marshall of LMA for samples.

System Improvement for Preparation of $CuIn_{1-x}Ga_xS_2$ Thin Film Solar Cells

Neelkanth G. Dhere, Shashank R. Kulkarni and Shantinath R. Ghongadi

Florida Solar Energy Center

1679 Clearlake Road, Cocoa, FL, 32922-5703

ABSTRACT

Systems for the deposition of Mo, Cu-Ga, In, ZnO and ZnO:Al layers and sulfurization of metallic precursors have been improved for fabrication of complete CIGS and CIGS2 solar cells. Total area, AM1.5, PV parameters of the best AR coated CIGS2 thin film solar cell were: V_{oc} = 696 mV, J_{sc} = 20.59 mA/cm^2, FF = 64.88%, and η = 9.3%. AM 0 efficiency of 8.95% and QE cutoff at 800 nm, equivalent to CIGS2 bandgap of 1.55 eV showed an actual bandgap increase to the required optimum value for efficient AM0 PV conversion as a result of Ga incorporation. These represent the first measurements on CIGS2 solar cells under space conditions.

1. Introduction

The bandgap of $CuIn_{1-x}Ga_xS_2$ ($CuInS_2$) is near the optimum value for photovoltaic conversion of AM0 solar radiation in space. This paper describes the system improvement for preparation of complete CIGS2 thin film solar cells.

2. Experimental Technique

Metallic precursor could be sputter-deposited on only three substrates in a single run using an earlier rudimentary and potentially unstable sample rotation and positioning setup. A new high-vacuum compatible, rugged and convenient substrate mounting and rotation setup was designed and built in-house for deposition of eight 1 ¼" x 1 ½" substrates in a single run. Mo, Cu-Ga, and In thin films are being deposited routinely with reproducible characteristics.

Earlier a simple new sulfurization set up using H_2S gas diluted in argon was constructed and was set up in the FSEC Hydrogen Laboratory. It was shared with other FSEC groups. Recently a sulfurization unit was fabricated using a 4" diameter three zone furnace. The unit has been set up in the new fume hood in the PV Materials laboratory and is being used exclusively for sulfurization of CuGa/In precursors.

Earlier cadmium and tellurium thin films have been deposited at reasonably high rates by DC magnetron sputtering using target thickness up to 3/8" in a turbomolecular pumped vacuum system with a base pressure of $7x10^{-7}$ Torr. Hence RF magnetron sputter depositions were attempted using a ZnO:Al(2%) target having a total thickness of 3/8" including a copper backing plate. However, ZnO:Al films were highly resistive due to a low deposition rate in relation to the residual oxygen partial pressure. Deposition rate saturated at high RF power because of inefficient magnetron action. ZnO:Al films, RF-sputter deposited using the source fitted with existing magnet were highly transparent but at the same time highly resistive. It was realized that even though no oxygen was being supplied intentionally, ZnO:Al films were oxidized completely by the residual oxygen gas molecules incident on the substrate. Deposition rates did not increase sufficiently even with the use of a thinner (1/4") ZnO:Al target. After opening the magnetron gun, it was found that the old magnet assembly had deteriorated due to attack of circulating water. Therefore, old and weaker magnets were replaced with new and stronger magnets in both the sputtering sources. Now intrinsic ZnO and doped ZnO:Al films are being deposited at adequate rates by RF magnetron sputtering.

Cu-rich CIGS2 thin films were prepared by sulfurization of sputtered Cu:(In+Ga) precursor layers in a proportion of 1.4:1 on molybdenum-coated glass substrates in the new set up. Sulfurization was carried out at 475^o C for 60 minutes using Ar:H_2S(4%) flowing at a rate of 1000 sccm. Excess $Cu_{2-x}S$ segregated near the surface was etched away in dilute (10%) KCN solution. Solar cells were completed by deposition of CdS heterojunction partner layer by chemical-bath deposition, transparent-conducting ZnO/ZnO:Al window bilayer by RF sputtering, Ni/Al contact fingers by vacuum evaporation through metal mask and MgF_2 antireflection coating by vacuum evaporation. Because of problems with the RF sputtering system for ZnO/ZnO:Al deposition, earlier cells were completed at NREL. Now complete cells are being fabricated at FSEC. Current-voltage IxV and quantum efficiency, QE measurements were carried out NREL and NASA GRC.

3. Results and Discussion

$CuIn_{1-x}Ga_xS_2$ thin films were bluish, dark gray in color. Resistance measurement of CIGS2 films was used to verify if it was Cu-rich or Cu-poor. AES depth profile of unetched Cu-rich CIGS2 thin film showed segregation of excess copper at the surface possibly as a $Cu_{2-x}S$ layer. Excess $Cu_{2-x}S$ near the surface was etched away in dilute (10%) KCN solution for 3 minutes. Atomic proportions of Cu:In:Ga:S of typical Cu-poor CIGS2 films as measured by EMPA at 20 keV incident electron energy was 24.0:19.1:6.9:51.9, corresponding to formula $Cu_{0.92}In_{0.73}Ga_{0.27}Se_2$ thus very near the desired Cu content. Scanning electron microscopy revealed large (2-2.5 μm) compact-grain morphology for films sulfurized at and above the temperatures of 450^o C.

High deposition rates, attainable with the sputtering sources fitted with the stronger magnet assembly, made it possible to achieve a balance between incidence rates of the depositing ZnO:Al molecules and the residual oxygen molecules so as to obtain highly transparent and conducting ZnO:Al films (Figure 1). Table I shows the variation of optical transmittance and sheet resistance of ZnO:Al thin films with the sputtering power and deposition time.

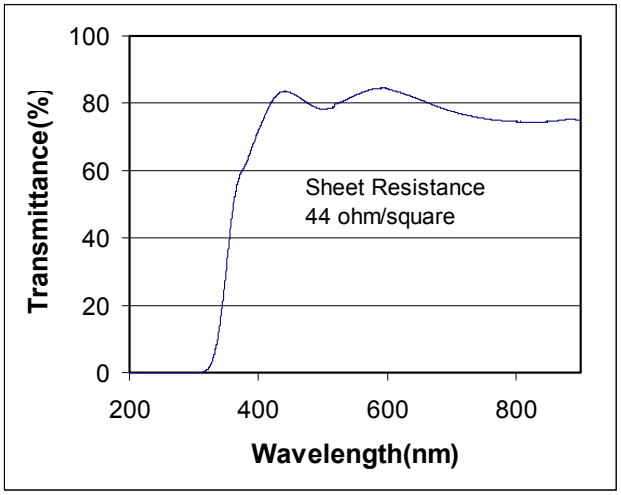

Figure 1. Optical transmittance spectrum of a ZnO:Al film.

All the cells showed PV conversion efficiency, η above 6%, most being over 7% (AM1.5, Total area). PV performance was uniform from one region to another, on the same substrate. AM1.5, total area, PV parameters of the best AR coated solar cell measured at NREL were as follows: V_{oc} = 696 mV, J_{sc} = 20.59 mA/cm^2, FF = 64.88%, and η = 9.3%, QE cutoff at 800 nm, equivalent to CIGS2 bandgap of 1.55 eV, showing an actual bandgap increase to the required optimum value for efficient AM0 PV conversion as a result of Ga incorporation (Figures 2, 3). PV parameters of the best solar cell measured under AM 0 conditions at the NASA Glenn Research Center were as follows: V_{oc} = 739 mV, J_{sc} = 26.01 mA/cm^2, FF = 63.7%, and η = 8.95%. To the best of our knowledge, these are the first measurements on CIGS2 thin film solar cells under the space conditions.

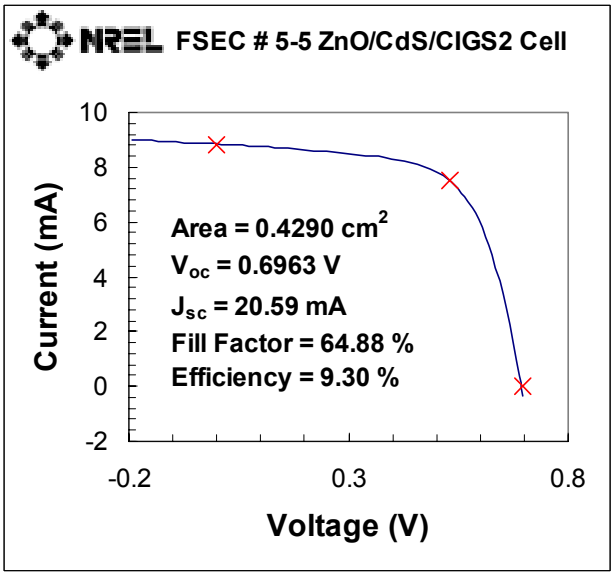

Figure 2. IxV characteristics of CIGS2 thin film solar cells under AM1.5 conditions.

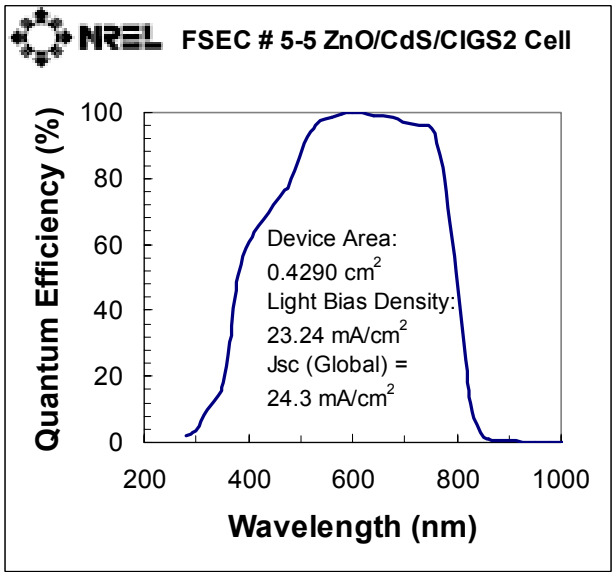

Figure 9. External quantum efficiency of CIGS2 thin film solar cells.

Power (W)	Time (min)	Sheet Resistance Ω/	Transmittance (%)
40	60	18.5	38.4
40	30	148	82.0
45	30	69	81.6
35	60	44	81.4
35	60	13.6	83.9
30	60	135	84.0

Table I. Variation of optical transmittance and sheet resistance of ZnO:Al thin films with sputtering power and deposition time.

4. Conclusions

Systems for sputter deposition of Mo, CuGa, In and ZnO/ZnO:Al layers as well as the sulfurization set-up have been improved. 9.3% (AM 1.5) and 8.95% (AM 0) CIGS2 thin film solar cells have been fabricated.

5. Acknowledgements

This work was supported by the National Renewable Energy Laboratory and the NASA Glenn Research Center. The authors are thankful to Keith Emery and Amy Swartzlander of NREL, for AM 1.5 IxV, QE and measurements, David Scheiman of Ohio Aerospace Institute for AMO measurements, and Dr. Kannan Ramnathan of NREL for help with cell fabrication and discussions.

REFERENCES

[1] N. G. Dhere, S. R. Kulkarni, S. S. Chavan and S. R. Ghongadi, "Cu(In,Ga)S_2 thin-film solar cells prepared by H_2S sulfurization of CuGa-In precursor", To be published in the Proc. NASA Space Power Conference (SPRAT), Cleveland, Ohio, Aug.-Sept. 1999.

AC Characterization of the Grain Boundary Electronic Properties in CdTe Thin Films

A. S. Gilmore, V. Kaydanov, U. Laor, A. Gupta, T. R. Ohno, B. McCandless[1]

Colorado School of Mines; Golden, Colorado

1. Institute of Energy Conversion; University of Delaware, Newark, Delaware

ABSTRACT

Results of characterizing CdTe films through AC electrical measurements are presented herein. Measurements were performed in the frequency range from 75kHz to 30MHz and with applied bias up to 30V. Grain boundary (GB) contribution dominates the in-plane film resistance both in dark and light although it is suppressed under one Sun intensity by orders of magnitude. The magnitude of the GB capacitance indicates a high doping level above $10^{18}cm^{-3}$ in the vicinity of the GB. Both the GB resistance and capacitance vary largely with bias due to the changes in electrical charge accumulated by the GB. Density of the GB electronic states was estimated from the $C(V_{bias})$ dependence. Preliminary investigations of the effects of sulfur and copper in CdTe diffusion on the GB electronic properties are presented.

1. Introduction

Better understanding of electronic properties of the GB and their dependence on processing procedure is important for further improving performance of the CdTe thin film polycrystalline solar cells. AC electrical measurements have the potential to be an informative characterization tool for the cells and the films within.

Measurements of frequency-dependent impedance/ admittance of CdTe thin films on insulating substrates presented here were aimed at determining the GB contribution to the in-plane film resistance as well as the specific GB capacitance. The former depends exponentially on the GB potential barrier height. The latter being measured at zero bias is determined by the GB depletion width and allows estimation of doping level in the vicinity of the GB. A significant increase observed in GB resistance and capacitance under applied bias is due to recharging of the GB electronic states. This effect can be utilized for characterization of the properties of these traps, in particular their density of states. Prior to the description and discussion of the experimental data (Sec. 3) we present the physical and electrical models our analysis was based on (Sec. 2).

2. Physical and electrical models

The potential barrier for the majority carriers (holes) provides the very high resistance of the GB. The so-called GB depletion or geometric capacitance arises from the semi-insulating properties of the depleted region adjacent to the GB. In the electrical model valid for zero bias, the GB resistance and capacitance are represented by a resistor R_{GB} and capacitor C_{GB} connected in parallel; resistance of the intragrain material is represented by resistor R_I connected in series with R_{GB} and C_{GB}. All three parameters can be derived from the film resistance and capacitance measured in the LCR "p" and "s" operating modes by fitting equations:

$$R_p=R_I+[R_{GB}/(1+\alpha)]\cdot\{1+\alpha/[1+(R_I/R_{GB})(1+\alpha)]\} \quad (1)$$

$$C_p=C_{GB}\cdot(1+\alpha)/\{[1+R_I/R_{GB}(1+\alpha)]^2+\alpha\} \quad (2)$$

$$R_s=R_I+R_{GB}/(1+\alpha) \quad (3)$$

$$C_s=C_{GB}\cdot(1+\alpha)/\alpha, \quad (4)$$

where $\alpha=(R_{GB}C_{GB}\omega)^2$. At low frequencies $R_p\approx R_s\approx R_{GB}+R_I$ and $C_p=C_{GB}$. In the high frequency range R_{GB} is shunted by C_{GB}, hence measured resistance tends to R_I, where R_s approaches R_I faster than R_p (see Fig.1).

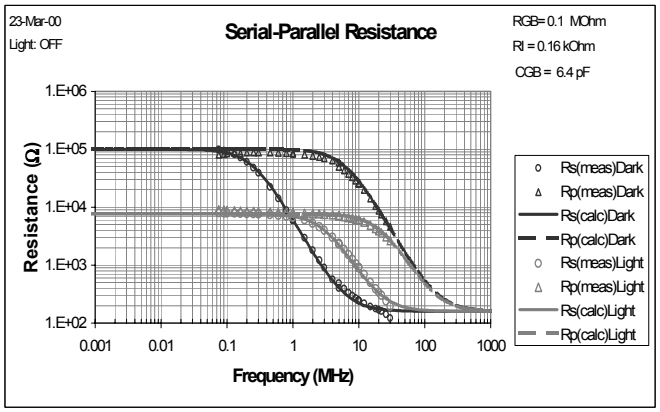

Fig.1. Resistance vs frequency measured experimentally and calculated from Eq 1 and 3 for a Cu treated CdTe thin film.

There are two major bias dependent contributions to the capacitance of each grain. The first is the geometry capacitance, which decreases due to the widening of the GB depletion region. This effect has been well established for e.g. Si, Ge and CdTe bicrystals [1,2,3]. The second contributor is due to the fact that the amount of trapped charge at a GB in general depends on the applied voltage [4]. AC voltage application leads to carrier transfer between the grain and the GB states which is out of phase with the voltage. This trapping-detrapping process can be modeled by a capacitor, C_t, in series with a resistor, R_t, which represents a finite probability for carriers incident on the GB to be trapped. The total AC current is a sum of grain-to-GB and grain-to-grain currents. Hence, the electrical model of the GB includes three branches connected in parallel: R_{GB}, C_{GB} and (C_t in series to R_t). Our experiments have shown that at intermediate frequencies the R_I influence is negligible and the capacitance measured in "p" mode can be written as:

$$C_p=C_{GB}+C_t/[1+(C_tR_t\omega)^2]. \quad (5)$$

The bias per grain boundary, V_{GB}, in our experiments was usually much smaller than the unbiased GB potential barrier height. Under this condition a simple approximate equation for the specific (per unit area of a single GB) capacitance, c_t, was obtained:

$$c_t=\{2c_{GB}(0)/[1+4c_{GB}(0)/q^2N_T]\}\times \tanh(qV_{GB}/2kT) \qquad (6)$$

where $c_{GB}(0)$ is the specific geometric capacitance at zero bias, $V_{GB}=V_{bias}d/l$, V_{bias} is the bias voltage applied between probes, l is the inter-probe distance, and d is an average grain size. The density of the GB traps, N_T, is assumed constant, because a small V_{GB} effects both the trap occupation and Fermi level position with respect to the trap band only slightly.

Thus the measured capacitance increases with bias until it reaches saturation at $V_{GB}>2kT$, then it may slowly decrease due to the geometry capacitance. Using this model, and allowing d and N_T to be fitting parameters, one can obtain information about average grain size and GB density of states:

$$N_T=(4/q^2)\times \beta/(2-\beta)\times c_{GB}(0);\ \beta=c_t^{sat}/c_{GB}(0) \qquad (7)$$

The average doping level in the GB depletion region can be calculated from above values as

$$N_{GB}=8\,[c_{GB}(0)]^2\,\phi_{GB}/(q\varepsilon) \qquad (8)$$

where ϕ_{GB} is the unbiased GB potential barrier height, and ε is the dielectric permittivity of the material.

3. Experimental results and discussion

CdTe films on the glass substrates were prepared at IEC with physical vapor deposition at a substrate temperature of 325°C. Some films were treated with $CdCl_2$ and doped with S and Cu at the CSM facilities. AC measurements of R_p, R_s, C_p, and C_s were performed in dark and under illumination. Measurements at zero bias and fitting data with Eqs. 1-4 were used to obtain R_{GB}, C_{GB}, and R_I values for each sample. Figure 1 shows typical measured R_p and R_s dependencies on frequency, as well as the fit used to determine R_{GB}, R_I, and C_{GB}. R_{GB} is orders of magnitude greater than the R_I for all films although the difference is smaller for the films doped with Cu. The estimated potential barrier height varied from 0.7 to 0.3 eV depending on post-deposition treatment. The decrease in barrier height caused by illumination achieved for some films 0.15-0.2eV. The doping level in the GB region estimated from c_{GB} using Eq. 8 is above $10^{18}cm^{-3}$ for all films, which is consistent with the estimates obtained with different method in ref.[5].

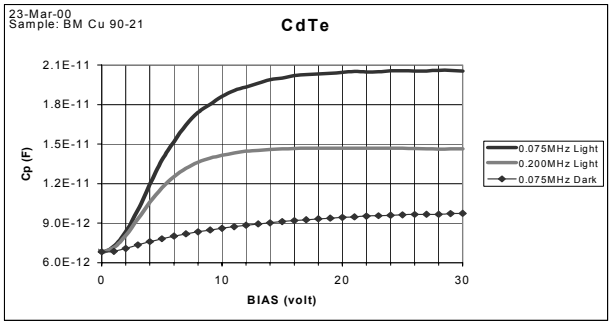

Fig. 2. Capacitance vs bias in dark and under 1 Sun illumination for a Cu treated CdTe thin film.

Figure 2 shows C_p versus bias for several frequencies at one Sun illumination. As expected (see Eq. 5), the increase in capacitance due to the trap charging and discharging lessened at higher frequencies, while a slow decrease in geometry capacitance is observed. From the fitting parameters determined in Figure 3, the average grain size was found to be 1.2μm, which is consistent with the estimates based on SEM and AFM images; N_T was found to be about $5\times10^{12}cm^{-3}eV^{-1}$.

Compared to as-deposited films, the different treatments on the films studied mainly effected R_{GB}. The $CdCl_2$ treatment lowered R_{GB} under illumination only. Sulfur diffusion lowered R_{GB} under illumination, but increased R_{GB} when in dark. Finally, copper diffusion into CdTe films was found to lower R_{GB} in both dark and under illumination by more than two orders of magnitude. The Cu treatment increased C_{GB} slightly. These results are preliminary, and future studies are planned to further our understanding.

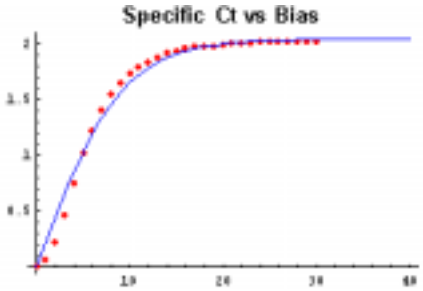

Fig. 3. c_t vs bias at 75kHz for a Cu treated CdTe thin film. Data and fit (solid curve) are both represented.

4. Conclusions

The results obtained are consistent with other measurements, as well as the theory derived above. These results are evidence that measuring frequency- and bias-dependent admittance/impedance holds promise as a future characterization technique for CdTe thin films. It can provide information on the GB electronic properties and their dependence on processing procedure.

5. Acknowledgements

This work was supported by the National Renewable Energy Laboratory under subcontract No. XAK-8-17619-28.

REFERENCES

[1] W. E. Taylor, N.H. Odell, and H.Y. Fan, Phys. Rev. 88, 1952, 867.

[2] C. H. Seager and G. E. Pike, Appl. Phys. Lett. 35, 1979, 709.

[3] T.P. Thorpe, Jr., A.L. Fahrenbruch, and R.H. Bube, J. Appl. Phys. **60**, 1986, 3622.

[4] C. H. Seager and G. E. Pike, Appl. Phys. Lett. 37(8), 1980, 747.

[5] L. M. Woods et al: "Electrical Characterization of CdTe Grain-Boundary Properties from as Processed CdTe/CdS Solar Cells" Proc. Of the 2nd World Conf. On PV Solar Energy Conversion, July 1998, Vienna, Austria, 1043.

Advances in Large Area Apollo® Module Development

D W Cunningham, K Davies, L Grammond, J Healy, E Mopas, N O'Connor, M Rubcich, M Sadeghi, D Skinner, T Trumbly

BP Solar, A Business Unit of BP Solarex

2300 North Watney Way, Fairfield, CA 94533

ABSTRACT

1. Introduction

BP Solar is introducing the Apollo® thin film CdTe technology at its new Fairfield, CA production plant. The plant is sized and equipped to produce 10 megawatts of Apollo® thin-film modules per annum. This production capability builds upon BP Solar's ten-year R&D program [1] to develop and characterize a stable 8% CdTe module on a 929cm^2 substrate. The Fairfield Apollo® process line is capable of producing both a 0.55m^2 and a 0.94m^2 monolithic CdS/CdTe module. The objectives of the BP Solar – NREL Thin-Film Partnership (Subcontract No. ZAK-7-17619-27) are to optimize CdTe electroplating and CdS chemical bath deposition operations, and to conduct process development experiments to enhance, device performance and module reliability.

2. CdS and CdTe deposition reactions.

Both semiconductor layers in the Apollo® process are deposited using wet chemistry methods. CdS is deposited from an aqueous solution reaction on to a commercially available transparent conducting oxide (TCO) substrate. The reduction/oxidation CBD reaction is as follows:

$$Cd^{2+}(complex)(aq) + (NH_2)_2CS(aq) + 2OH^-(aq) \rightarrow CdS(s) + H_2NCN(aq) + 2H_2O(l)$$

CdTe is deposited by electrochemical deposition. The cathode in the reaction is the CdS/TCO substrate. The reaction for the reduction of Cd and Te at the CdS/TCO surface is as follows:

$$Cd^{2+}_{(aq)} + HTeO_2^+{}_{(aq)} + 3H^+_{(aq)} + 6e^- \rightarrow CdTe(s) + 2H_20_{(l)}$$

The CdTe deposition occurs in a 40-plate electrodeposition tank (for the 0.55m^2 substrate), which is replicated eight times. The CdTe deposition equipment is completely automated with respect to plate handling and process control. Each 40-plate tank has two recirculation pumps that supply tellurium replenished solution to the plate cathodes. A computer-controlled potentiostat administers an applied voltage to the cathode plate and determines the total charge applied to the plate by integrating the plating current with time. The target charge is 1200C/sqft that produces approximately 1.6μm of CdTe film.

Figure 1. CdTe Deposition Equipment

3. CdTe Morphology.

CdTe samples were analysed to determine changes in morphology at various stages of the CdTe process. Of particular interest was the form of the CdTe directly after electrodeposition and subsequent heat treatments. Typically, low temperature depositions of CdTe such as electrochemical, physical vapour deposition, and sputtering produce small grain structures (<1μm). There is a considerable amount of strain incorporated in these films as deposited and the crystal structure has a predominant <111> orientation. Strain relief, is one of the aspects seen in the CdTe film after a 450C anneal in air, as is a change in orientation of the crystal unit cell. As well as the orientation change, grain growth can also occur when the heat treatment is performed in the presence of chloride. In the Apollo® electrochemical deposition of CdTe, chloride is incorporated into the film during the plating process. Two techniques were used to investigate the crystal structure namely atomic force microscopy (AFM) and x-ray diffraction (XRD).

Figure 2. AFM of post heat-treated CdTe

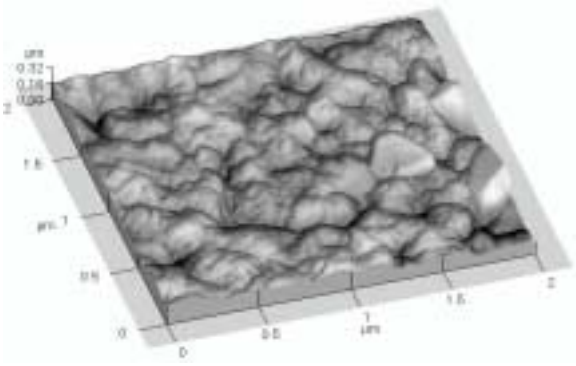

The typical grain size for as deposited CdTe is between 0.1µm and 0.2µm. Some grains exhibit faceted faces, which indicate that grain sizes could be smaller than 0.1µm. XRD data shows grain orientation at this stage was predominantly <111>. In Figure 2, the AFM image shows grain formation after heat treatment in air at 450C. Some grain growth and coalescing of the grain facets was observed. Also, the maximum grain dimension had increased to about 0.4µm from 0.2µm.

This data indicates that, while some gain growth occurred, it was not substantial and that the grain structure is held or pinned in some way.

4. Device Results.

Two 0.55m^2 modules made at Fairfield were sent to NREL as contract deliverables. The deliverable criterion was for an aperture efficiency >8% on a 14" x 61" module. Table 1 summarizes the results from measurements made at NREL. Spire 240A and outdoor measurements are shown for each module.

Table 1. 0.55m^2 Deliverables Measured at NREL

Module Number	Test System	Voc (V)	Isc (A)	FF (%)	Pmax (W)	Cell Eff. (%)
92030034	Spire 240A	24.7	2.53	0.61	38.2	8.1
92030034	Outdoors	24.7	2.55	0.63	40.0	8.4
92030041	Spire 240A	24.4	2.62	0.60	38.2	8.1
92030041	Outdoors	24.5	2.63	0.63	40.4	8.5

The cell (aperture) efficiency was calculated from the active area of each cell. The total active area was 153cm^2 per cell with 31 cells in series connection. This gave a total active (aperture) area of 0.474m^2. All modules satisfied the deliverable criteria of >8.0%.

Considerable effort was placed on large area development. One of the challenges for electroplating large areas is how to overcome voltage drop within the TCO. While potential drops in the contacting connections to the plate are minimal, lateral potential drops in the TCO between the connections can be substantial. If a substantial potential drop occurs in the TCO, then CdTe stoichiometry will vary, favouring Te rich or Cd rich CdTe deposits, depending on the extent of the drop within the plate. The Apollo® team worked with suppliers to obtain TCO films with sheet resistivities below 7Ω.sq to reduce potential drop in the 61" x 24" plate (0.94m^2). Initial results with the low resistivity TCO produced films with good composition uniformity. The electrical performance of the 0.94m^2 Apollo® modules were very encouraging, indicating a good robustness of the process towards large area scale up. The performance of two of the plates was verified at NREL and the results are summarised in Table 2.

Table 2. 0.94m^2 Module Measurements Made at NREL.

Module Number	Test System	Voc (V)	Isc (A)	FF (%)	Pmax (W)	Cell Eff. (%)
92440041	Spire 240A	44.92	2.476	.607	67.53	7.8
92440041	Outdoors	45.00	2.466	.623	69.08	7.9
92030054	Spire 240A	45.08	2.503	.615	69.43	8.0
92030054	Outdoors	45.19	2.477	.646	72.23	8.3

The electrical configuration of these modules consisted of 57 cells in series. The cell area was 152.3cm^2 giving an active area of 0.868m^2 and a total module area of 0.944m^2 All dimensional and electrical measurements were confirmed at NREL. The 72.23Wp Apollo® module is the highest power monolithic, thin film module to date.

5. Module Stress Testing.

Figure 3. Efficiency vs. Time for Voc, Isc, Pmax conditions

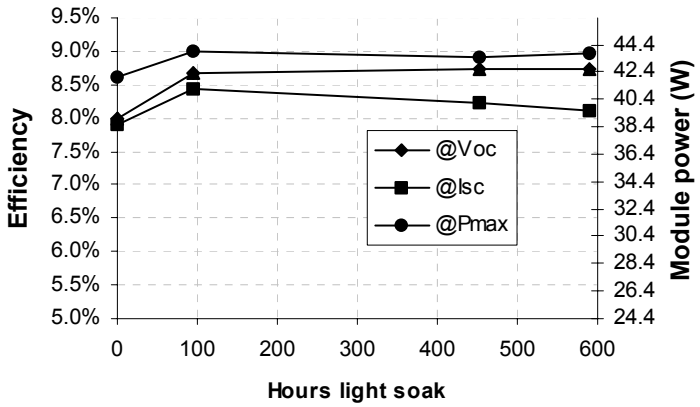

Stress testing is performed at Fairfield by continuous light soaking under various stress conditions. While under illumination, the modules are force cooled in air. Four 2kW metal halide lamps are used to illuminate the modules at 800W.m^{-2}. The temperature is monitored for each module and the light intensity is measured for uniformity using a 142cm^2 silicon cell. A CdTe reference module measures the overall average intensity for each of the five positions.

Figure 3 shows very similar performance for Apollo® modules under light soak at Voc, Isc and Pmax stress conditions. Module Isc and Voc show good stability at each stress condition. Moreover, we typically observe a decrease in the module series resistance in the first 100 hours gives rise to an increase in fill factor of about 5%. This effect is maintained throughout the light soak period. It is believed that this effect is evidence of the existence of traps within the absorber CdTe layer. Carriers passivate these traps once the module is illuminated.

Long-term exposure (>1500 hours continuous) also shows good stability with less than a 4% change over this period.

6. Summary.

The Apollo® team has made considerable progress in the implementation of a new technology in production. The efforts to date include a world record of 72.2Wp for the highest power of any thin-film monolithic module. Future work will continue to focus on increased conversion efficiency and module reliability of the Apollo® technology, with a performance target of a stable 10%, large area module (0.944m^2). BP Solar would like to acknowledge technical contributions from the Institute of Energy Conversion (University of Delaware) and NREL.

7. References.

[1] J M Woodcock et al, Proc. 12th EC PV Solar Energy Conf. (1994).

Analysis of Moisture and CO_2 Uptake in Anhydrous $CdCl_2$ Powders Used for Vapor $CdCl_2$ Treatment of CdS/CdTe PV Devices

T. Mazur[1], T. Gessert[1], G. Martins[2], and C. Curtis[1]

[1]National Renewable Energy Laboratory, 1617 Cole Blvd, Golden, CO 80401
[2]Colorado School of Mines, 1500 Illinois St, Golden, CO 80401

ABSTRACT

Water and CO_2 uptake in $CdCl_2$ powder precursors was investigated using thermogravimetric analysis/Fourier transform infrared spectroscopy (TGA/FTIR). Exposure of powders under ambient conditions shows that a steady-state hydration level near 9 % (by weight) is achieved after brief exposure to room air, with minimal absorption and/or adsorption of CO_2. TGA has also shown that storage in a desiccator with $Mg(ClO_4)_2$ preserves the anhydrous form. Water is rapidly devolved from hydrated powders, with the pure anhydrate reappearing at temperatures below 150°C under N_2 flow and a modest heating rate of 10°C/min. Water present in raw-powder precursors is shown to affect the appearance of source plates manufactured by the close-spaced sublimation (CSS) method.

1. Introduction

A number of techniques exist to make thin-film CdTe solar cells and the majority utilize cadmium chloride in a post-deposition heat treatment. The use of cadmium chloride in the various "heat treatments" is related to the experience-based expectation that it will lead to optimal performance of the n-CdS/p-CdTe heterojunction. In many cases, recrystallization and reduction of grain boundary area via grain growth have been associated with the chloride treatment. As such, the mechanisms associated with the role of cadmium chloride as a sintering aid (fluxing agent) are only qualitatively understood at the present time and more fundamental knowledge of basic properties of this compound is clearly needed.

CdS/CdTe devices produced at the National Renewable Energy Laboratory (NREL) currently use a vapor process for the $CdCl_2$ treatment. The process begins by depositing a thick $CdCl_2$ film (~1 mm thick) onto a 2" x 2" Corning glass plate (7059 or 7059 F) by CSS of $CdCl_2$ powders from a graphite boat. This glass substrate plate is then used in the same chamber as a source plate for vapor treatment of a CdS/CdTe device using a CSS-like process. Although this process works well, anecdotal evidence suggests that moisture may be an important and uncontrolled parameter of both the source-plate fabrication and vapor-treatment processes. Although this evidence is contrary to preliminary data [1], it should not be a surprise because $CdCl_2$ is a strongly hygroscopic material. Specifically, we have observed that source powders can erupt (decrepitate) from the graphite boat during source-plate fabrication if the moisture content of the powder is high. This decrepitation leads to considerable non-reproducibility during $CdCl_2$ source-plate production. Further, there appear to be significant differences between the source-plate films formed with old (hydrated) $CdCl_2$ powders and new powder sources. Finally, the vapor process appears to commence more rapidly when the laboratory humidity is high (i.e., the summer months). To isolate effects of moisture on the NREL vapor $CdCl_2$ process, this study uses TGA to measure the moisture content of $CdCl_2$ powders following controlled exposures to various environmental conditions. The $CdCl_2$ powders used at NREL are Alfa-Aesar products of 4N purity, anhydrous, and packed under argon. Two batches of the powders were investigated for this study. These batches were manufactured separately, and the major distinction between the two is the length of time they have been stored in the laboratory. Henceforth, any reference to "old" or "new" powders refers to these different batches.

2. Experimental Procedure

Anhydrous $CdCl_2$ powder samples were stored under controlled conditions including exposure to room air, storage in a desiccator charged with $Mg(ClO_4)_2$, and storage in a helium-filled glove box. For the air-exposed samples, an hygrometer was placed in the open container to monitor air humidity and temperature. Thermogravimetry, coupled with FTIR, was used to determine (in situ) species evolution and rate-of-loss when the powders were heated. A constant heating rate of 10°C/min from ambient to 500°C under an N_2 flow of 100 cc/min was used in all experiments.

3. Results and Discussion

As shown in Figure 1., fresh anhydrous powder and samples stored in protected environments exhibit little or no hydration. Regardless of exposure conditions, mass loss observed below 200°C is attributed to water evolution. This is demonstrated by real-time FTIR absorbance spectra correlating well with the TGA data. The steady "baseline" at intermediate temperatures is indicative of the pure anhydrate, and mass loss at temperatures above 450°C is due to sublimation of $CdCl_2$ (m.p. 568°C). CO_2 has been observed in some cases during the initial heating (low temperature) but at this time, it is uncertain if the CO_2 is present in the $CdCl_2$ or simply an artifact from the brief exposure of the TGA/FTIR system to the atmosphere during sample loading. No absorbance peaks are observed that correspond to the sublimation of $CdCl_2$ as it is an IR-inactive species.

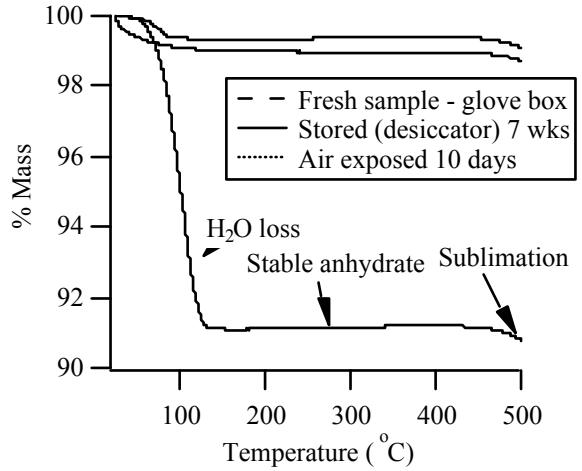

Figure 1. Thermogravimetric profiles of $CdCl_2$ stored under various conditions and heated at 10°C/min under N_2 flow.

Figure 2 shows the rate of hydration of $CdCl_2$ exposed to air. It is not clear at this time if the scatter in the data for exposure <5 days is related to some physical process. In any case, a steady-state value of ~9% (by weight) hydration was achieved after 1 week of exposure. This agrees well with preliminary analysis of the old powder source used to make source plates at NREL. In that case, no special precautions were used to preserve the anhydrous state of the powder and thermogravimetric analysis showed the water content to be ~8 wt.%. For reference, a fully hydrated compound ($CdCl_2 \cdot 2.5\ H_2O$, stable up to 34°C) contains ~20 wt.% H_2O.

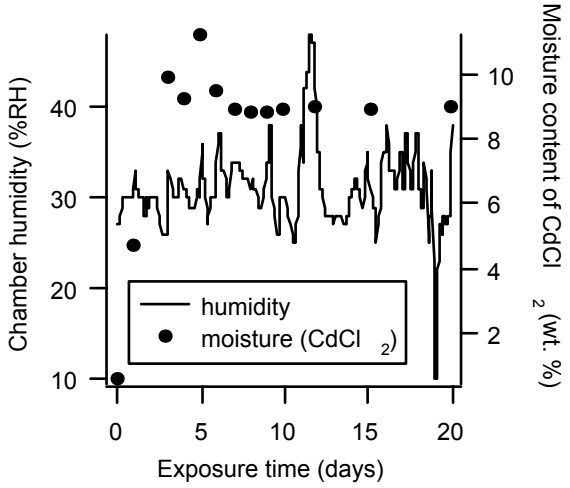

Figure 2. Moisture uptake in $CdCl_2$ exposed to ambient air.

The hydration level of $CdCl_2$ powder impacts the appearance of newly fabricated source plates. The old powder source (~8 wt.% water) produced more desirable source plates in the sense that the sublimated layer was thicker and more uniform as compared to plates made with the new powder (~2 wt.% water). However, as shown in Table 1, net-transfer efficiency (ratio of mass deposited on glass to total mass lost) was much lower with the old $CdCl_2$. In other words, though more material was deposited under the same conditions with the old powder, a correspondingly larger amount of the powder was simply wasted. It is believed that the old-source powder is forcibly expelled (decrepitation) from the boat during a rapid heating (ambient to 200°C in 2 minutes) portion of the source-plate manufacturing process. In that case, the rapidly-evolved water vapor could enhance the transport of $CdCl_2$ from the graphite boat in an aerosol at the low temperatures. Indeed, solid particles were observed in the deposition chamber to a much greater degree with the old powder. Further, it is speculated that the aerosol coats the glass substrate to an appreciable degree or at least nucleates the surface for more efficient transfer at higher temperatures where $CdCl_2$ vapor sufficiently exists (e.g. 500°C).

Table 1. Mass transfer of different $CdCl_2$ powders using the same time-temperature profile for source-plate fabrication.

Source Powder	Transfer Efficiency	Mass Distribution (% initial mass)		
		Glass	Boat Residue	System Loss
Old	54.3	20.2	62.8	17.0
Old	71.2	22.5	68.4	9.1
Old	54.3	21.3	60.7	18.0
Old	44.3	17.8	59.8	22.4
Old	58.6	23.9	59.2	16.9
Old	45.1	19.3	57.3	23.5
Old	31.2	16.9	45.9	37.2
New	75.5	8.2	89.1	2.7

4. Conclusions and Further Work

Water is readily absorbed by anhydrous $CdCl_2$ under ambient conditions. However, $CdCl_2$ source powders do not achieve full hydration. CO_2 absorption is minimal for the short-term exposure used in this study. The decrepitation phenomena will be further explored by controllably hydrating new material and assessing its impact on source-plate characteristics. An additional study will focus on the impact of water vapor in the process ambient when treating CdS/CdTe devices, with emphasis on chlorine diffusion into the device.

5. Acknowledgements

The author would like to thank Dave Albin for discussions related to this work. This research was supported by DOE Contract #DE-AC36-99GO10337.

REFERENCES

[1] Y. Mahathongdy, D.S. Albin, C.A. Wolden, and R.M. Baldwin, "Vapor $CdCl_2$ – optimization and screening experiments for an all dry chloride treatment of CdS/CdTe solar cells, AIP Conf. Proceedings #462, (AIP, New York) (1998) 236-241.

Analysis of Stress-Induced Degradation in CdS/CdTe Solar Cells

Steven S. Hegedus, Brian E. McCandless, Robert W. Birkmire

Institute of Energy Conversion

University of Delaware, Newark, DE 19711

ABSTRACT

Results and analysis of stress-induced degradation of CdS/CdTe solar cells are presented. Cells were thermally stressed in light and dark at different electrical bias points in different atmospheres using a new apparatus. These measurements, coupled with contact surface analysis and re-contacting procedures, allow junction and contact phenomena to be separated. At least two mechanisms exist to account for the measured changes in CdS/CdTe devices under thermal and electrical stress.

1. Introduction

CdTe/CdS modules under prolonged field testing are reported to be stable [1]. However, no clear correlation has been found between processing parameters and either of these stable existence-proof cases or those that changed in field testing. Recent work to accelerate these processes at the laboratory scale (stress testing) have shown that typically the V_{oc} and FF degrades, particularly for devices held at moderate forward or reverse bias [2]. The back contact process is strongly implicated in the stress-induced degradation especially with respect to the presence of Cu and its compounds, which are sensitive to small, localized fields, in both electrochemical and electromigration processes. In this paper, an analysis is presented of stress-degraded behavior, for devices made with and without intentional Cu in the process and stressed at different electrical bias points.

2. Experimental

Devices were fabricated using glass/SnO_2/ CdS/CdTe layers supplied by First Solar LLC and back contact processes developed at IEC. The contacting process consists of surface Te-enrichment, depositing 2-10 nm Cu, *in situ* heat treatment and application of carbon conductor [3]. Given the strong influence of the back contact processing on both initial and stressed performance [2,3], these devices are unique and are not representative of First Solar product with their contact. CdS/CdTe solar cells were stressed in an apparatus that allows controlled exposure to thermal, chemical, electrical, and illumination bias (Figure 1).

Figure 1. The Institute of Energy Conversion's four pod stress facility.

3. Separating Contact and Junction Behavior

A CdS/CdTe solar cell having an initial efficiency of 11.8% and V_{oc} = 0.82V was stressed at V_{oc} at 100°C for 6 weeks in air at 2 suns, which reduced the efficiency to 7.2% and V_{oc} to 0.73V (Figure 2). J_o increased ~30X, from 3 x 10^{-8} to 8 x 10^{-7} mA/cm^2, but there was no change in A-factor (~1.6), indicating that the magnitude, not the mechanism, for bulk recombination mechanism changed. This was confirmed with V_{oc}-T measurements before and after stress.

In addition, current-limiting behavior at forward bias in both dark and light JV characteristics developed after stress at forward bias, due to formation of a second diode (Figure 2). After stressing, the original carbon contact was peeled away, the CdTe surface was re-etched in weak bromine-methanol and a new C contact was applied. The second diode disappeared and FF increased significantly, and there was no change in V_{oc}, J_o and A, clearly demonstrating that the second diode is associated with the back contact.

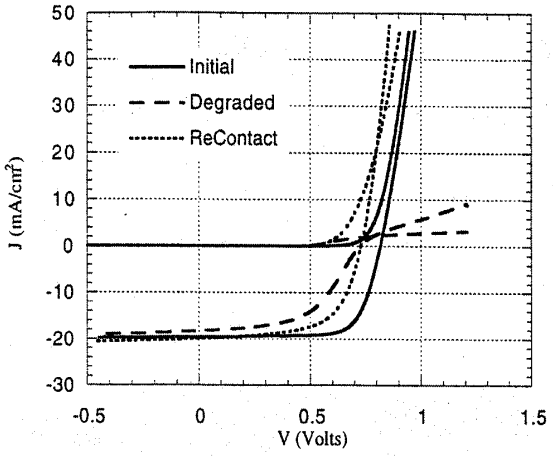

Figure 2. Light and dark JV curves for CdS/CdTe solar cell for initial, 6 week stress at 100°C at V_{oc}, and following re-contacting.

Figure 2. Light and dark JV curves for CdS/CdTe solar cell for initial, 6 week stress at 100°C at V_{oc}, and following re-contacting.

4. Effect of Electrical Bias

Based on a large number of samples and stress experiments, we found that devices biased at J_{sc} and $V < 0$ (V_{rev}) behave similarly, while those stressed at V_{MP}, V_{oc} and $V > V_{oc}$ (V_{fwd}) have a different but common degradation mode. To simplify the discussion, two bias points, V_{oc} and J_{sc} are considered. Devices stressed at J_{sc} have a smaller loss in V_{oc} (~50 mV) and FF (~5%) than those stressed at V_{oc} but develop a large cross-over between the light and dark curves, indicating formation of a photoconductive region. For devices stressed at V_{oc}, curvature in forward bias, indicative of a blocking contact, masks the photoconductive effect. This bias dependence indicates two different degradation modes whose impact appears to be minimal at the J_{sc} stress bias. Similar stress bias has been found for all cells processed with Cu in the contact, regardless of CdTe surface modification or stress ambient, for dry air, H_2/Ar or Ar.

Devices fabricated with 6 nm Cu in the contact and initial V_{oc} = 0.82V were stressed at J_{sc} and V_{fwd} in the dark at 60°C for 10 days. For stress at J_{sc}, the V_{oc} changed by ±15 mV, indicating their stability against a purely thermal mechanism at this bias point. For devices stressed at V_{fwd}, the V_{oc} decreased, with both magnitude and rate, in proportion to the forward bias potential; at stress bias V = +2.5V, V_{oc} decreased by ~200 mV after 10 days, and nearly half of the loss occurred in the first day. This relatively rapid change, together with the very small changes found after stress at J_{sc} suggests a mechanism involving field-driven diffusion of positively charged Cu ions along grain boundaries. Positively charged Cu^{++} is available under bias by the weakly favored reaction:

$$Cu_2Te - 2xe^- \rightarrow Cu_{2-x}Te + Cu^{++},$$
$$\Delta G_{100C} = -0.7 \text{ kcal/mol.}$$

The reduction of Cu_2Te to CuTe, measured using glancing incident x-ray diffraction of the CdTe-contact surface after removal of the C electrode from stressed devices, was only observed on devices stressed at forward bias.

To test the validity of the field-driven Cu^{++} hypothesis, *in situ* V_{oc} measurements were made during stress at 100°C at 1 sun in dry air or H_2/Ar under variable bias conditions. Devices having ~6 nm Cu with initial efficiencies ~11% and V_{oc}~0.80 V were stressed first at V_{oc} for 10 hours then switched to J_{sc}. The devices held at J_{sc} the entire time lost ~30 mV in the first 50 hours then remained stable for over 600 hours. The devices initially held at V_{oc} lost ~150 mV in the first 10 hours. After switching bias to J_{sc}, their V_{oc} slowly increased, leveling off after ~300 hours. The degradation and recovery rates were exponential, with recovery being >10X slower. The magnitude and rate of degradation and recovery were independent of oxidizing or reducing atmosphere. Devices stressed at V_{oc} for 1 hour recovered nearly all of the V_{oc} loss, while those stressed for 100 hours showed little recovery.

5. Summary and Phenomenological Model

At least two mechanisms are needed to account for the measured changes in these CdS/CdTe devices under thermal and electrical stress. One, which occurs in cells stressed at forward and reverse bias, increases J_o and is responsible for the onset of photoconductivity in the CdS or CdTe layer. The other, which occurs on the order of hours in cells stressed at forward bias, degrades the contact, greatly increases J_o and is partially reversible. Determination of the photoconductive region and detailed junction analysis is expected to reveal more about the bias-dependent mechanism. We propose that for stress at forward bias, Cu^{++} is easily liberated from the Cu_2Te contact layer by weak electric fields and subsequently diffuses or migrates along grain boundaries. Neutral Cu may also exist and thermally diffuse; the bulk diffusion coefficient at 100°C is ~3 x 10^{-13} cm^2/sec, yielding a characteristic diffusion length of ~0.3 micron in 1 hour, which is too small to account for the measured changes in junction behavior [4]. For an assumed grain boundary diffusion coefficient from 1 x 10^{-10} to 1 x 10^{-9} cm^2/sec at 100°C, the characteristic length could vary from 6 to 30 microns, which is a sufficiently large range to account changes at the junction.

REFERENCES

1. R. A. Sasala, R. C. Powell, G. L. Dorer, N. Reiter, *AIP Conf. Proc.* Vol 394, 1997, pp. 171-186
2. J. F. Hiltner, J. R. Sites, *AIP Conf. Proc*. Vol. 462, 1999, pp. 170-175
3. B. E. McCandless, Y. Qu, R. W. Birkmire, *Proc. 1st WCPEC*, 1994, p. 107-110.
4. H. H. Woodbury and M. Aven, *J. Appl. Phys*., 39(12) (1968) 5485-5488.

A Novel Cu –Free Back Contact For CdS/CdTe Thin Film Solar Cells

V.Viswanathan, B.Tetali, Z. Zhao, V.V. Komin, V. Palekis, N. Rao, D.L. Morel, and C.S. Ferekides

University Of South Florida
Center for Clean Energy and Vehicles
4202 East Fowler Avenue
Tampa, FL-33620

ABSTRACT

The fabrication of ohmic and reliable back contacts is one of the major challenges confronting the CdTe technology. The most successful contacts, predominantly Cu-based, appear to suffer from degradation associated with the migration of Cu to the junction [1]. This has resulted in the search for alternate contact materials. In this paper Ni_2P, mixed in graphite paste, is presented as a promising alternative. Experiments to determine the potential of this contact have been based on varying parameters such as contact anneal temperature, time, and Ni_2P concentration. Preliminary devices have yielded very encouraging results with V_{OC}'s in the 820-840mV range and FF of over 70%.

1. Introduction

Pseudo-ohmic contacts to CdTe have been fabricated using the common approach of doping the semiconductor adjacent to the contact highly p-type [2]. This is usually achieved by introducing elements like Cu or Au. However, these materials often lead to device degradation due to the ease with which they diffuse into the CdTe, eventually reaching the CdS/CdTe junction. They can create shunting paths and recombination centers that cause deterioration of the junction properties. The search for alternatives that provide ohmic or pseudo-ohmic contacts with long-term reliability, has gained increasing attention. Ni-P coatings have been found to provide ohmic contacts to CdTe, although the performance of the cells fabricated using this technology has not produced desired results [3]. In this work Ni_2P, mixed in graphite paste, is used for back contacts to CdS/CdTe solar cells. The performance of these contacts was studied by varying the contact annealing temperature, time, and the Ni_2P concentration.

2. Results

The cells used for this study were of glass/SnO_2/CdS/CdTe configuration. After a brief etch in Br_2/methanol, the cells were contacted using Ni_2P mixed in graphite paste. The cell performance, as a function of the contact characteristic, was obtained by varying the post application anneal temperature, time, and Ni_2P concentration.

Effect of Post application anneal temperature

The effect of post application anneal temperature was studied in the temperature range of 150-300ºC, maintaining the anneal time constant. Figure 1 shows the variation of V_{OC} and FF as a function of temperature. From the figure it can be seen that the V_{OC} and FF peak at 250ºC.At temperatures above 250ºC although the V_{OC} remains essentially constant, the FF decreases drastically. The improvement in these parameters is due to the reduced shunting and series resistance observed at higher temperature. The shunting is probably due to the presence free phosphorous that may be present at lower annealing temperatures. In addition, at low temperatures, the absence of a good contact increases the series resistance. Work done earlier on Ni-P contacts have revealed that the performance of the contact is dependent on the formation of a favorable phase of Ni-P(NiP_2) at the contact interface, that is characterized by a work function similar to that of gold. This helps formation of a good contact. It is believed that a similar process occurs in these cells.

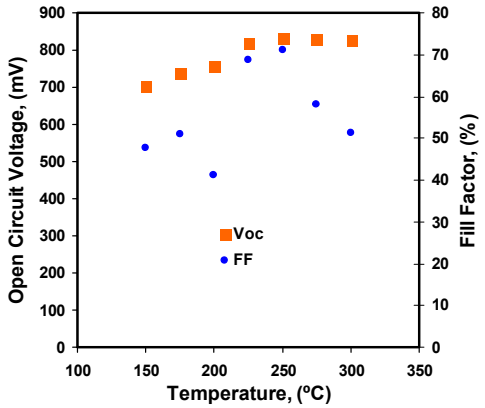

Figure 1 V_{OC} & FF as a function of annealing temperature

The reduction of FF's at temperatures above 250ºC is attributed to the onset of rectification at the back contact. This in-turn is possibly due to a change of phase, that promotes rectifying properties. Both these behaviors are clearly seen in the light I-V characteristics shown in figure 2.

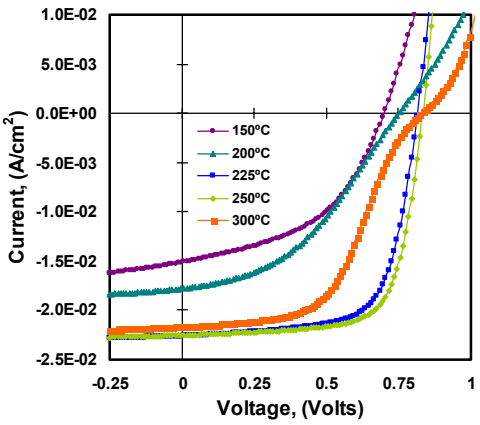

Figure 2 I-V characteristics of cells annealed at different temperatures.

Although, the above mentioned reasons could explain the observed contact behavior, no direct evidence is available at this time to verify this claim. Thus the CdTe surface

modified due to the contact application, needs to be studied for a better understanding of the effect of annealing temperature.

Effect Of Ni_2P Concentration

In order to study the influence of the Ni_2P concentration (wt% in graphite) on the contact performance, three different concentrations were experimented on cells, keeping all other parameters constant. Figure 3 shows the I-V characteristics of cells with different concentration of Ni_2P. From the figure, it is evident that the cell performance degrades at both "high" and "low" concentrations. It is however interesting to note that although the shunt characteristics are similar for all the three cells, the series resistance seems to increase at higher Ni_2P concentrations.

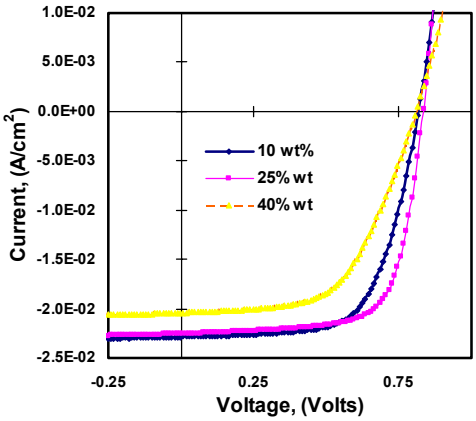

Figure 3 Effect of Ni_2P concentration on I-V curve

This behavior is most likely related to the different phases of Ni-P formed at the CdTe surface, and is a subject of future studies.

Effect of post application anneal time

The dependence of cell performance on the annealing time was determined in the range of 15-120 minutes. Table I summarizes the influence on V_{OC} and FF.

Table I: Effect of Anneal time on V_{OC} and FF

Annealing Time, min	Open Circuit Voltage, mV	Fill Factor, %
15	852	60.9
60	848	63.2
90	850	67.7
120	827	56.7

As the results in table I suggest, annealing times above 90 minutes prove detrimental to cell performance, affecting primarily the FF.

The observed decrease in the FF is due to the onset of rectification as illustrated in the I-V data in figure 4. The origin of this rectification with time is unclear, and requires a detailed study of the CdTe/contact interface.

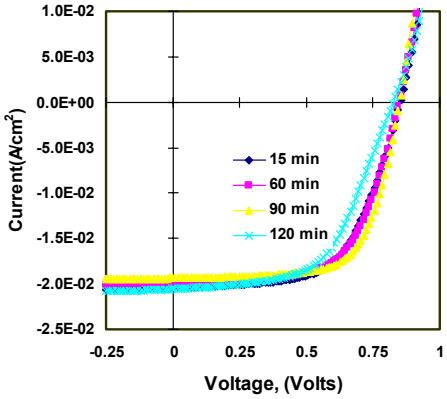

Figure 4 Effect of Anneal Time on I-V Curve

Initial results on Ni_2P contacts have thus been very promising. Additional studies of the interaction of the contact material at the CdTe interface and bulk could provide some explanations for some of the observed behavior and help improve the performance further. Some experiments currently being pursued is the SIMS profiling of the CdTe solar cells to obtain more information on the role of Ni and P diffusion, if any, in contact formation. These could be measured as a function of both annealing temperature and time to obtain a better knowledge on how these elements influence the cell performance. In addition, XRD of the CdTe interface at different conditions could provide valuable information on the favorable Ni-P phases for contact formation.

4. Conclusion

CdS/CdTe solar cells have been successfully fabricated using the Ni_2P/graphite contact with V_{OC}'s and FF's of up to 840mV and 70% respectively being obtained. Experiments on the effect of post application annealing temperature seem to suggest that the formation of different contact phases is probably responsible for the observed behavior of the back contact. The results obtained from the experiments on annealing time and Ni_2P concentration are not conclusive and need further studies to understand their effects. Future studies would need to involve stability tests to verify the reliability of the Ni_2P contact.

5. Acknowledgements

This work was supported by the National Renewable Energy Laboratory under sub-contract: ZAF-8-17619-29.

REFERENCES

[1] H.C. Chou, A. Rohatgi, "Effects of Cu on CdTe/CdS Heterojunction Solar Cells with Au/Cu Contacts" J. Electrochem. Soc., Vol 142, No. 1, Jan 1995, pg254-259

[2] Fahrenbruch, "Ohmic Contacts and Doping of cdTe", solar cells, 21, (1987), 399

[3] B. Ghosh, S. Purakayastha, "Formation of Stable Ohmic Contacts to CdTe Thin Films Through the Diffusion of P from Ni-P", Semicond. Sci. Tech., 10 (1995) 71-76.

Atmospheric Pressure Chemical Vapor Deposition of CdTe Films

Peter V. Meyers*, Colin Wolden†, James Kestner†, Laxminarayan Raja‡, Robert J. Kee‡

*ITN Energy Systems
12401 West 49th Ave.
Wheat Ridge, CO 80033

†Department of Chemical Engineering and ‡Engineering Division
Colorado School of Mines
Golden, CO 80401

ABSTRACT

Researchers are developing preliminary reactor designs and engineering principles for deposition of CdTe films by atmospheric pressure chemical vapor deposition (APCVD). CdTe deposition by APCVD employs the same reaction chemistry as has been used to deposit 16% efficient CdTe PV films[1,2], i.e., close spaced sublimation (CSS), but employs forced convection rather than diffusion as a mechanism of mass transport. Recent accomplishments include: design, fabrication and testing of a "simplified" APCVD reactor; deposition of the first dense, adherent APCVD CdTe films; and fabrication of the first APCVD CdTe PV devices.

1. Approach

Although there are many demonstrated methods for producing high-efficiency CdTe solar cells, large-scale commercial production of thin-film CdTe PV modules has not yet been realized.[3] An important contributor to the commercial production of thin-film CdTe will be development of advanced deposition reactors. APCVD combines proven CSS reaction chemistry with state-of-the-art engineering principles to enable design of thin film deposition reactors for the manufacturing environment. APCVD's anticipated advantages include:

- Low equipment cost compared to vacuum processing as equipment will need neither the structural strength nor the pumping systems of a vacuum chamber.
- Large area uniformity achieved through control of temperature and gas flow - both of which are subject to rigorous engineering design.
- Simplified process control and source replenishment because the source gas generation is physically separated from the deposition chamber.
- CdTe PV device fabrication process compatibility in that APCVD is presently used commercially to deposit transparent conducting oxide (TCO) films commonly used in CdTe solar cells. In fact, the processing sequence: deposit TCO, deposit CdS, deposit CdTe, dry $CdCl_2$ heat treatment and metalorganic CVD of electrodes could be performed in a continuous process.
- Low raw material costs as CdTe is used in its least expensive form - chunks.
- Simplified continuous processing because gas curtains replace load locks.

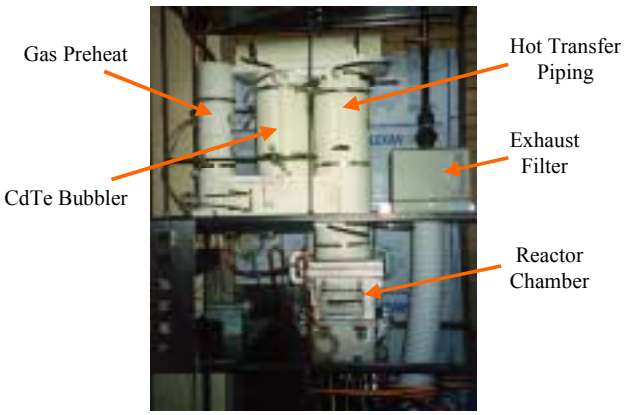

Figure 1. First generation APCVD reactor.

2. Premise Validation

Using design principles described earlier [4], an APCVD reactor, shown in Fig. 1, was designed, built and tested. A number of "dry runs", i.e., runs performed without CdTe in the bubbler, were successfully completed to establish reactor operating procedures and calibrate the substrate temperature. Subsequently, several CdTe deposition runs were performed. A key issue was to determine whether the ambient pressure and method of mass transport affect the nature of the deposited films. APCVD of CdTe is similar to CSS of CdTe in that both processes involve 1) sublimation of Cd and Te_2 gasses from hot CdTe, 2) transport of the source gasses to a hot substrate, and 3) deposition of CdTe films. The main difference between the two processes is step #2 - that in CSS mass transport of the source gasses is by diffusion whereas APCVD employs forced convection to transport the source gasses. A fundamental premise of the APCVD program has been that APCVD films have the same reaction chemistry as do CSS films, i.e., that the films with the same physical and electrical properties can be grown by either technique. If APCVD can indeed produce the same quality films as CSS, then the engineering advantages of APCVD can be used to make the same high efficiency devices obtained in laboratory scale CSS equipment but on a larger, industrial scale.

3. First APCVD CdTe Films

The first APCVD CdTe was deposited onto LOF SnO_2:F-coated sodalime glass. SEM photographs displayed in Figure 2 show that the first APCVD CdTe films have similar structure to films deposited at NREL by CSS on a

645°C substrate[5]. Substrate temperature during the first APCVD run had not yet been calibrated, but 645°C is within the range of reasonable estimates. The similarity in structure between the APCVD and CSS films strongly suggests that the reaction chemistry and growth of APCVD films are similar to those of CSS.

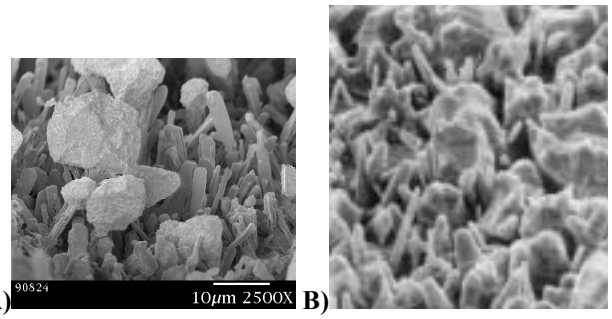

A) B)

Figure 2. Comparison of microstructure of first CdTe films grown A) by APCVD and B) by CSS at NREL at 645 ℃. Note that magnification of the CSS film is approximately 6X that of the APCVD film.

Additional films were deposited onto thin (~500 Å) CBD CdS-coated LOF glass. Film deposition rates ranged from 0.1 - 0.4 μm/min. A comparison of the film structure of a CdTe film deposited at 580 ºC by APCVD and a film from an NREL CSS reactor is displayed in Figure 3. X-ray diffraction data of the as-deposited film is shown in Figure 4. Despite the fine-grain structure observed in Fig. 3, the three dominant peaks confirm that the film composition is predominantly cubic CdTe. XPS analysis indicated that CdO was also present in the film. Presence of CdO may account for the fine grain structure of the APCVD film relative to CSS and some of the minor peaks observed in the XRD spectrum. As no intentional oxygen was in the source or carrier gasses, the presence of CdO in the films suggests that there were leaks in the reactor that allowed relatively humid room air to affect reactor performance. Modifications are presently underway to correct this deficiency.

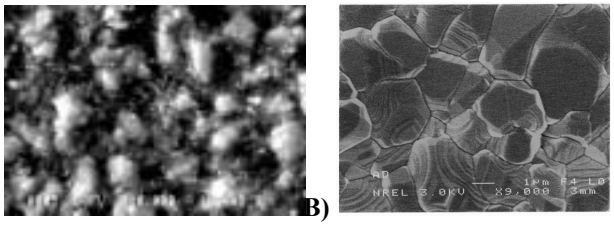

A) B)

Figure 3. Comparison of A) APCVD CdTe film deposited on 500 Å CBD CdS and B) CSS CdTe film deposited at NREL.

In spite of the preliminary nature of CdTe film deposition, devices were produced at Colorado School of Mines. Processing steps included a 20 min $CdCl_2$ heat treatment at 410 ºC and application of evaporated Au back contacts. Best device efficiency achieved was 3.8% (373 mV V_{oc}, 20.9 mA/cm^2 J_{sc} and 0.49 FF). Low V_{oc} is attributed to the thin CdS layer that appeared to be completely consumed during CdTe deposition and processing.

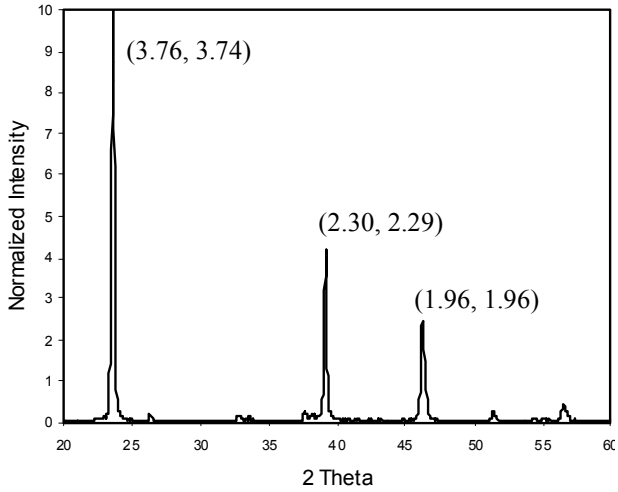

Figure 4. XRD spectrum of the film shown in Figure 3A. The three dominant peaks correspond to the 3 primary peaks associated with cubic CdTe. The numbers in parentheses correspond to the measured d spacing (Å) and reference values, respectively.

4. Conclusions and Next Steps

Data from initial CdTe deposition runs support the fundamental premise of the APCVD program and provide reason for continued optimism for the potential of APCVD in a manufacturing environment. Nonetheless, there are still significant deficiencies to be addressed in the APCVD reactor design and operation. Items to be addressed include: reduction in leakage of room air into the reactor, improved temperature and flow control, optimization of operating procedures, and identification and quantification of mass transport and film growth parameters.

ACKNOWLEDGMENTS

The authors gratefully acknowledge Tim Ohno, CSM, for providing XPS analysis, Rick Matson, NREL, and Brian Emerson, ITN, for taking SEM photos, J.R. Carter and John Bolster, ITN, for assistance with fabrication and operation of the APCVD reactor, and Ahklesh Gupta, CSM, for producing the APCVD CdTe PV devices.

REFERENCES

1 C. Ferekides and J. Britt, Solar Energy Mat. & Solar Cells 35 (1994) pp 255-262.

2 H. Ohyama, T. Aramoto, S. Kumazawa, H. Higuchi, T. Arita, S. Shibutani, T. Nishio, J. Nakajima, M. Tsuhi, A. Hanafusa, T. Hinino, K. Omura, and M. Murozono, Proc. 26th PVSC (1997) pp 343-346.

3 P.V. Meyers and R.W. Birkmire, Prog. in PV:Res. & Appl., Vol 3 (1995) pp 393-402.

4 P.V. Meyers, R.J. Kee, L. Raja, C.A. Wolden,and M. Aire , NCPV Review (1998), AIP Conf. Proc. CP462, M. Al-Jassim, J.P. Thornton and J.M. Gee, eds., pp 218-223.

5 X. Li et al., Proc. 25th IEEE PVSC, pp 933-936

Comparison of Degradation in Vapor Transport- and Electro- Deposited CdTe Solar Cells with ZnTe:Cu/Au and Cu/Au Back Contacts

A. Gupta, S. Townsend, V. Kaydanov and T. R. Ohno
Department of Physics, Colorado School of Mines, Golden, Colorado

ABSTRACT

Degradation has been studied of the CdTe solar cells fabricated with two different CdS/CdTe processing techniques and two different back contacts both involving copper. Degradation rates of cell efficiency and particular electrical parameters are found to be largely dependent on the bias applied during stress tests, CdS/CdTe processing and type of back contact.

1. Introduction

Almost all groups working on CdTe solar cells have used doping of CdS/CdTe solar cells with copper via back contact application. The positive effect of Cu mainly comes from enhancement of Voc and FF, the latter due to a significant decrease in the back contact resistance. While copper improves initial performance of CdS/CdTe solar cells, it was found in many studies to deteriorate the cell stability [1,2]. It is believed that one of the reasons is fast diffusion and electromigration of Cu in CdTe especially along grain boundaries in polycrystalline films. That leads to expectation that morphology of CdTe film should impact Cu migration and degradation process. Indeed, degradation rates under different stress conditions and their peculiarities reported by various groups are different depending on the processing techniques, type and application method of the back contact. Studies presented in this report were aimed at clarifying some of these issues.

2. Experimental

Two types of CdS/CdTe structures were used in this study. One was provided by First Solar, LLC, (FS). It contains about 300 nm thick CdS and wet $CdCl_2$ treated 3.5 to 4.0 μm thick CdTe prepared with the gas transport deposition method. The other type was prepared at Colorado School of Mines (CSM), containing 250 nm thick CdS (prepared with chemical bath deposition) and electrodeposited 3.3 μm thick CdTe. A wet $CdCl_2$ treatment was given to both CdS and CdTe [3].

Two types of back contacts were applied to the FS materials: ZnTe:Cu/Au and Cu/Au. For the first one, thin layers of Cu (7Å) and ZnTe (500Å) were evaporated on Br_2/methnol etched CdTe, and annealed in N_2 prior to evaporation of gold through mask to complete the back contact. For the second a thin Cu (30Å) was evaporated on the Br_2/methanol etched surface of CdTe and annealed in N_2. The excess Cu was removed by etching in Br_2/MeOH solution, and Au was evaporated to complete the back contact. Cells on the CSM material were completed with the Cu/Au back contact.

All three types of cells were stressed in dark at 100^0C in air under three bias conditions: open circuit (OC), forward bias of 0.55V (FB), and reverse bias of –1.2V (RB). Cells were periodically taken out of the oven and cooled down to room temperature before analyzing using I-V and C-V (at 100K Hz frequency) techniques.

3. Results

Fig. 1 shows the efficiency degradation under FB and RB conditions for the three types of cells: First Solar material with the first (ZnTe) and the second (Cu/Au) types of back contact, CSM electrodeposited (ED) CdTe with the Cu/Au back contact. Cells stressed under FB (with any back contact) demonstrate the least degradation. FS-ZnTe cells show a decrease in efficiency by only 3% in 590 stressing

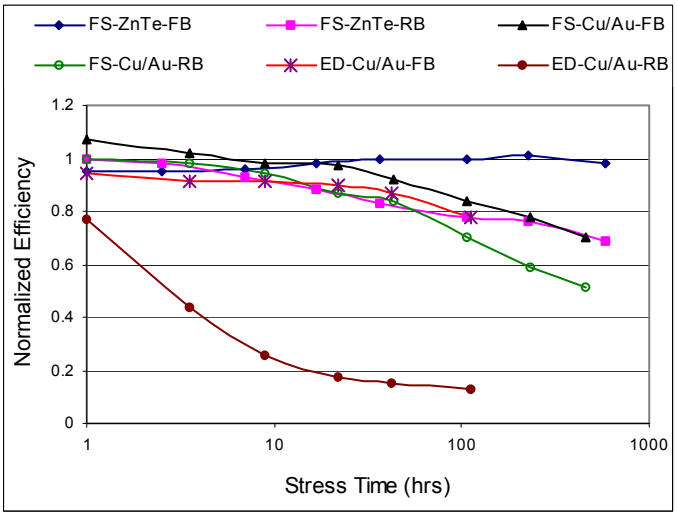

Fig. 1: Changes in normalized efficiency with stress time

hours while OC (not shown in the Figure) provided a 6% decrease for the same stressing time, and RB shows the most severe degradation of 33%. FS-Cu/Au samples show higher degree of degradation than that of ZnTe:Cu/Au contact, and different trend in efficiency change with time. Degradation is much more severe in ED-Cu/Au cells for all bias conditions, with the efficiency decreased by 80% under RB within 22 hours.

The trends in efficiency change in the initial hours of stressing are quite different for different back contacts (fig. 1 where stress time is plotted from 1 hour clearly shows this). FS-ZnTe cells stressed under FB, first showed a decrease in efficiency by 6% (higher than decrease in 590 hours), then an increase. The trend is opposite for the same

samples stressed under OC with the initial increase in efficiency followed by decrease. Cu/Au back contact on FS material manifest different trends. FB stressed cells show an initial increase in efficiency followed by a decrease, while OC-stressed cells show continuous decrease. Only reverse-biased cells showed almost the same trends of continuous decrease in both cases.

Pictograms in Fig.2 demonstrate visibly differences in degradation of Voc and FF for various cells due to different bias conditions.

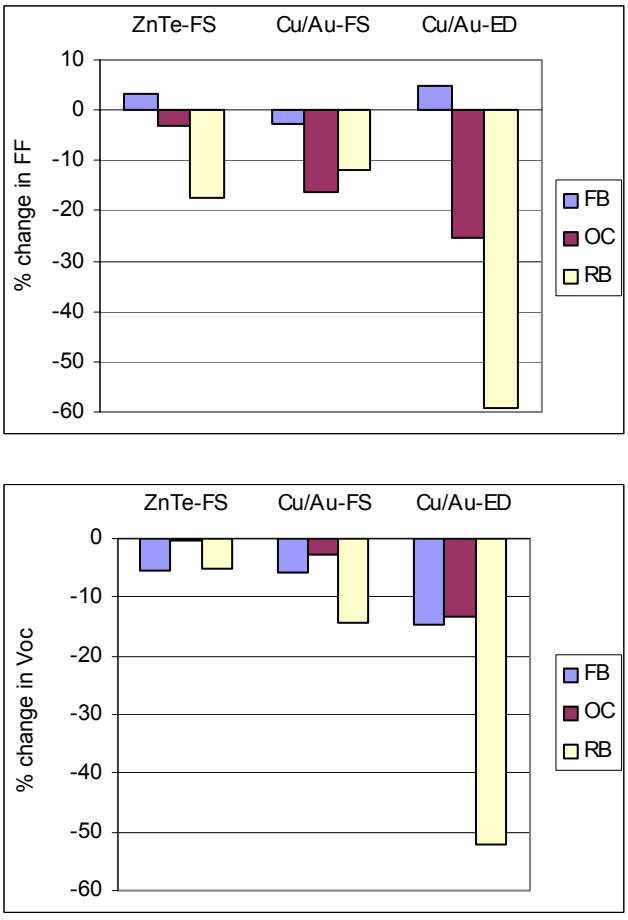

Fig. 2: Percentage change in FF and Voc after 110 hours of stressing

Differences in doping-depth profile changes after stressing correlate with the differences in degradation of the cell parameters. Fig. 3 shows some data for FS-ZnTe and ED-Cu/Au samples after 110 hours stressing as compared to the initial profiles.

The following major features are to be mentioned: (1) Doping density decreases after OC and FB stressing while it increases after RB stressing. This correlates with changes in the depletion width derived from the zero bias capacitance. (2) RB stressing causes a peak in doping profile just at the depletion layer edge.

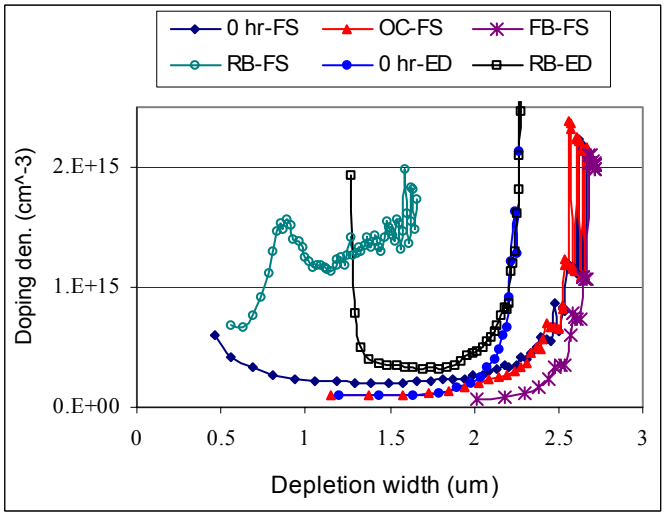

Fig. 3: Changes in doping profile after 110 hours of stressing to FS-ZnTe and ED-Cu/Au cells

4. Discussion and conclusions

Dependence of degradation process and changes in doping profile on the type of back contact indicates that the Cu-related degradation process depends on the back contact structure. The role of ZnTe interlayer is not limited to providing low back contact resistance.

For the same back contact, degradation varies with the CdTe processing. Probably it occurs due to difference in film morphology, grain boundary properties as well as in imperfection of the intra-grain material.

Degradation of cells is accompanied and caused at least partially by significant changes in doping profile which indicates spatial redistribution of electrically active defects.

A strong influence of the applied bias during stressing should be attributed to a significant contribution of electromigration to this redistribution and maybe also to transformation of the defects in strong electric fields.

ACKNOWLEDGMENT

The authors gratefully acknowledge First Solar, LLC. for supplying CdTe/CdS films for studies. This work was supported by National Renewable Energy Laboratory under subcontract No. XAK-8-17619-28.

REFERENCES

1. K. D. Dobson, I. V. Fisher, G. Hodes and D. Cahen Solar Energy Mater. Sol. Cells (in press)
2. J. Tang, D. Mao, T. R. Ohno, V. Kaydanov and J. U. Trefny Proceeding of 26th IEEE Photovoltaics Specialists Conference, Sept 30 – Oct. 3, 1997, Annaheim, CA, pp 439-442
3. W. Song, D. Mao, Y. Zhu, J. Tang and J. U. Trefny Proceeding of 25th IEEE Photovoltaics Specialists Conference, May 13-17, 1996, Washington, DC, pp 873-876

Cross-Section AFM and EFM Examination of Thin-Film Solar Cells

H.R. Moutinho, C. Ballif, M.M. Al-Jassim, R.G. Dhere, F.S. Hasoon, K. Ramanathan, and L.L. Kazmerski

National Renewable Energy Laboratory

1617 Cole Blvd., Golden CO 80401

ABSTRACT

We demonstrated the feasibility of analyzing cross sections of thin-film CdTe/CdS and CIGS/CdS solar cells using atomic force microscopy (AFM). The AFM images were compared with images obtained with the scanning electron microscopy (SEM), and the correspondence was very good. We also used electrostatic force microscopy (EFM) [1] to image the distribution of the electrical potential on cross sections of CdTe/CdS solar cells biased at different conditions. We were able to follow the potential drop at the junction, and the changes in the depletion width for different bias values.

EXPERIMENTAL

We used the following structures in this work: glass/SnO_2/CdS/CdTe and glass/Mo/CIGS/CdS/ZnO. The CdTe was grown by close-spaced sublimation, the CdS by chemical-bath deposition, the SnO_2 by chemical-vapor deposition, the CIGS by physical evaporation of Cu, In, and Ga in Se vapor, and the Mo and ZnO by sputtering. We prepared the cross sections by scratching one side of the structure (in general, the film side) and applying a pressure on the other side until the structure broke. All the devices were still working during the EFM analysis.

The AFM and EFM analyses were performed in an Autoprobe CP Research system, from ThermoMicroscopes. We used doped Si tips for the AFM and EFM analyses, and Co coated tips for some of the EFM analysis.

We obtained the EFM images by applying ac and dc voltages between the tip and the sample surface, and then monitoring the electrostatic force induced on the tip. To each EFM image, a simultaneous topographic image was also generated. The electrostatic force between the tip and the sample is given by the equation:

$$F = -\frac{1}{2}\frac{\partial C}{\partial z}\left[(V_{dc} - V_s)^2 + \frac{1}{2}V_{ac}^2\right]$$

$$-\frac{\partial C}{\partial z}(V_{dc} - V_s)V_{ac}\sin(\omega t) + \frac{1}{4}\frac{\partial C}{\partial z}V_{ac}^2\cos(2\omega t) \qquad (1)$$

where V_s is the the surface potencial, C the capacitance, and z the distance between the sample and the tip. V_{dc} is the dc bias, and V_{ac} and ω are the amplitude and frequency of the ac bias, respectively [2].

In this work we used a lock-in amplifier to analyze only the ω component (16 kHz) of the electrostatic force. The p-side of the device was grounded during analysis and the dc bias was applied to the n-side. From equation (1) we notice that the EFM images are a convolution of several parameters, and their interpretation is not always straightforward.

RESULTS AND DISCUSSION

Cross-Section AFM

In Figure 1, we observe the cross section of a CdTe/CdS solar cell. The CdS structure cannot be visually distinguished from the SnO_2 layer. The dynamic of the fracture in the CdTe film is such that the grain boundaries are not visible and several terraces, with different orientations, are formed. These features indicate intragranular fracture.

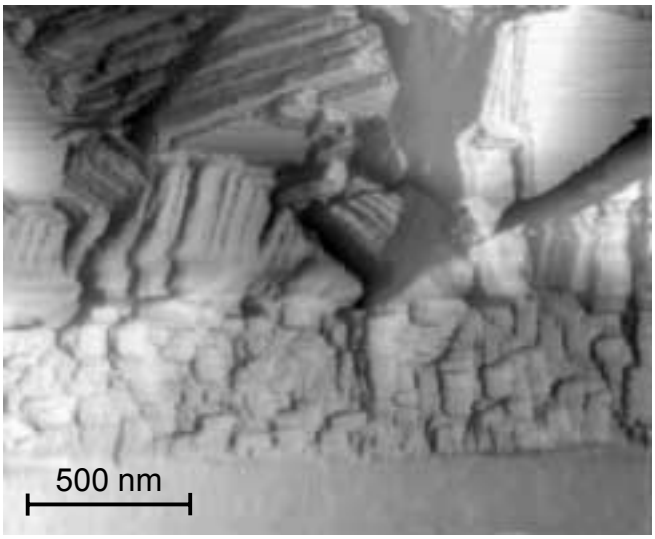

Figure 1 - AFM image of a glass/SnO_2/CdS/CdTe solar cell cross section.

The cross section of a CIGS/CdS solar cell is seen in Figure 2. Contrary to the CdTe case, the CIGS grains are easily distinguishable and present a regular form, which indicates that, in this case, the fracture process was intergranular. In Figure 2 we can also distinguish the columnar character of the Mo bi-layer.

We have also analyzed the cross-section structures with SEM. We were able to locate the same areas in the AFM

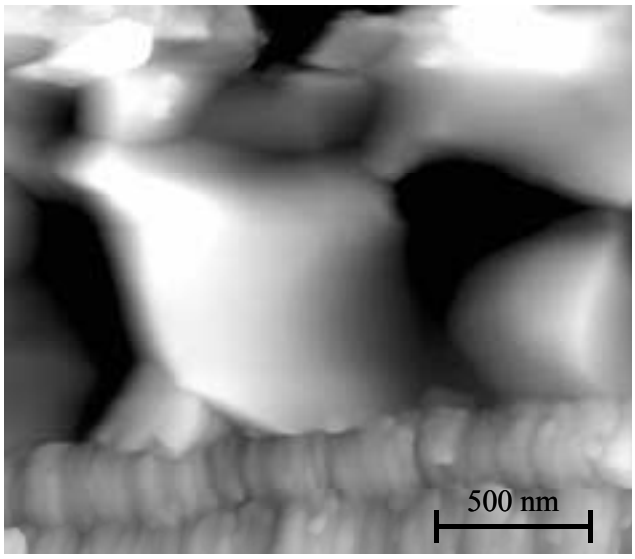

Figure 2 - AFM image of a glass/Mo/CIGS/CdS/ZnO solar cell cross section. The large grains belong to the CIGS film.

and SEM. The images were comparable, although we could, in general, obtain better resolution with the AFM.

Electrostatic-Force Microscopy

Figure 3 shows topographic and EFM images of a CdTe/CdS solar cell cross section. By convention, we use positive values for forward bias and negative values for reverse bias. The EFM signal shows that there is a sudden drop in electric potential at the CdTe/CdS junction. By comparing the topographic and EFM images, we notice that the drop in the EFM signal is located at the CdTe/CdS interface, indicating the presence of a heterojunction. As expected, the EFM contrast is inverted when we invert the polarization of the applied dc bias (Figures 3(b) and 3(c)). Figure 3(d) shows several line scans for the same device, with different applied bias. For direct bias, the signal drop is relatively sharp. As we polarize the junction in reverse bias condition, the signal change gets less abrupt and extends well into the CdTe layer. These results are associated with an increase in the depletion-region width as the reverse bias increases.

CONCLUSIONS

We showed the potential of the AFM for studying cross sections of polycrystalline semiconductor structures. The AFM provides better resolution than the SEM, and allows for real 3-dimensional manipulation and calculations in the images. EFM was applied to a CdTe/CdS solar cell and was able to map the drop in potential in the junction for different bias conditions. The results indicate that the CdTe/CdS solar cell is formed by a heterojunction between CdTe and CdS.

REFERENCES

[1] Y. Martin, D.W. Abraham, and H.K. Wickramasinghe, Appl. Phys. Lett. 52, 1103 (1988).
[2] Q. Xu and J.W.P. Hsu, J. Appl. Phys. 85, 2465 (1999).

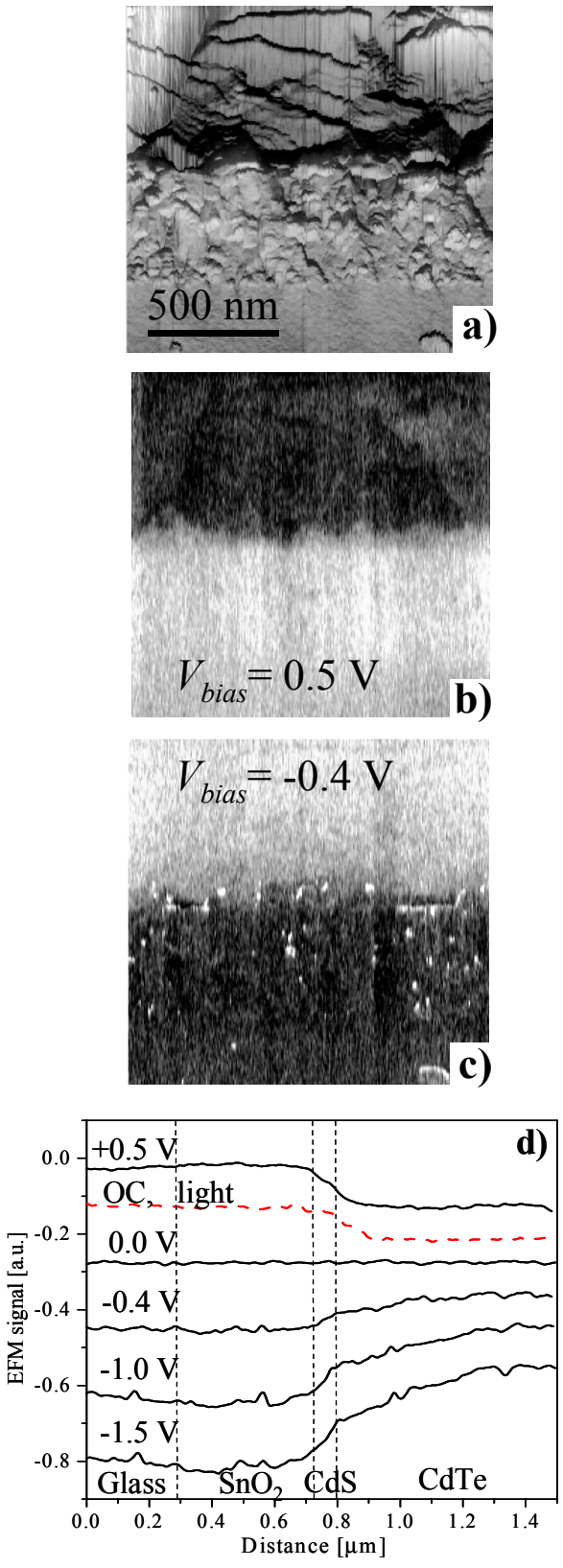

Figure 3 – AFM images of a CdTe/CdS solar cell cross section. (a) Topographic image. (b)(c) EFM images. (d) EFM line scans for different cell bias. OC denotes open-circuit configuration, i.e., device under illumination with no external voltage applied.

Determination of Cu Concentrations in CdTe/CdS Devices by High Mass Resolution Secondary Ion Mass Spectrometry

S.E. Asher, R.C. Reedy, Jr., R. Dhere, T.A. Gessert, M.R. Young

National Renewable Energy Laboratory

1617 Cole Blvd., Golden, CO 80401

ABSTRACT

We have used secondary ion mass spectrometry (SIMS) to quantitatively determine the concentration of Cu in CdTe/CdS devices. Empirical standards were fabricated by ion implantation of Cu into single-crystal and poly-crystalline CdTe and single-crystal CdS. Relative sensitivity factors were then generated from the measured implant profiles. Quantified profiles show that the apparent increase in Cu in the CdS is genuine, and not a sputtering artifact. This is the first quantified profile of Cu though CdTe/CdS device structures.

1. Introduction

Despite the technological significance of Cu in CdTe/CdS thin-film photovoltaic devices, little is known about the actual concentration of Cu in the devices. SIMS is a sensitive method for the analysis of trace elements in materials. However, SIMS is subject to artifacts caused by changes in secondary ion yield when profiling through different materials. It is possible to correct for these changes by preparing empirical standards of the element or matrix of interest. The simplest method to prepare standards is by ion implantation.

2. Experimental

SIMS depth profiles were obtained on a Cameca IMS-5F using an O_2^+ primary ion beam at 12.5 kV (8 kV impact energy) and detection of positive secondary ions. The mass spectrometer was tuned for mass resolution m/Δm≈4000 to separate the $^{63}Cu^+$ signal from mass interference from $^{126}Te^{2+}$. Device quality CdTe/CdS was supplied by First Solar Inc (FSI), as part of a back-contact study for the National Thin Film Partnership CdTe team. The CdTe was wet $CdCl_2$ processed at FSI. Contacts were applied by the National Renewable Energy Laboratory and the University of South Florida (HgTe:Cu graphite paste) and a ZnTe:Cu contact, also at NREL. Standards were fabricated by ion implantation of $^{63}Cu^{2+}$ at 400 kV, with a nominal dose of 1e15 at/cm^2 (actual measured dose was 9.68e14 at/cm^2). Multiple materials were implanted including polished single crystal CdTe and CdS, and polycrystalline CdTe (vapor $CdCl_2$ treated).

3. Results and Discussion

Figure 1 shows a typical high-mass-resolution (HMR) depth profile from a ZnTe/CdTe/CdS thin-film device structure. Each of the layers is clearly identified, although some broadening is observed due to topography. The profile also shows a substantial increase in the Cu signal in the CdS layer relative to the CdTe layer. To fully understand whether this increase represents a real change in concentration, it is necessary to correct for changes in ion yield between the CdTe and CdS matrices. To perform the correction, first a relative sensitivity factor (RSF) is generated from the implant standard. Then, the RSF is applied to the Cu signal in the unknown referenced to the matrix signal in the unknown.

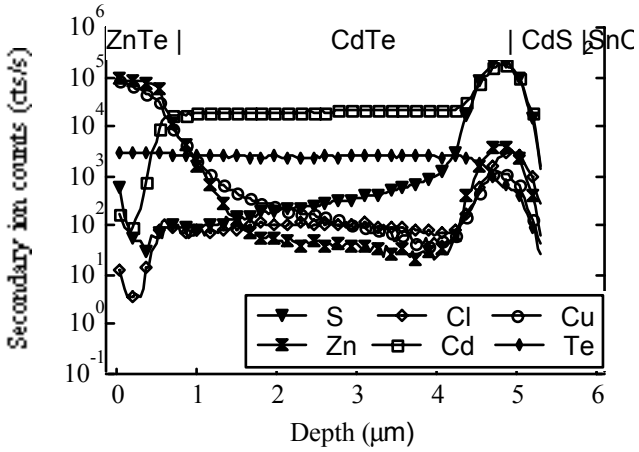

Figure 1. Unquantified depth profile from CdTe/CdS device.

The depth profiles shown in Figures 2-4 were obtained from the implant standards. Each standard was analyzed under low-mass resolution and again under high-mass resolution. For the case of CdTe, the dynamic range is significantly reduced for low-mass resolution. This shows the loss of sensitivity to Cu if low-mass resolution is used instead of HMR. No interference exists in the case of CdS, and the dynamic range is equal for the low- and high-mass resolution cases.

The Cu RSF's are referenced to the Cd matrix signals in the CdTe and CdS and to the Te signal in the ZnTe layer. The values of the RSF's must also be corrected for the isotopic abundance of ^{63}Cu to give the elemental concentrations of Cu in CdTe and CdS [1]. The RSF's generated in this study are shown in Table 1.

Table 1.

Matrix	RSF
CdTe	1.7e21
CdS	1.4e21

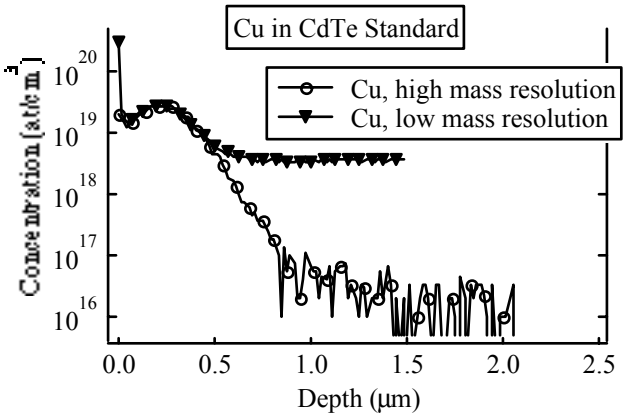

Figure 2. Depth profile of Cu in single crystal CdTe implant standard profiled with low- and high-mass resolution.

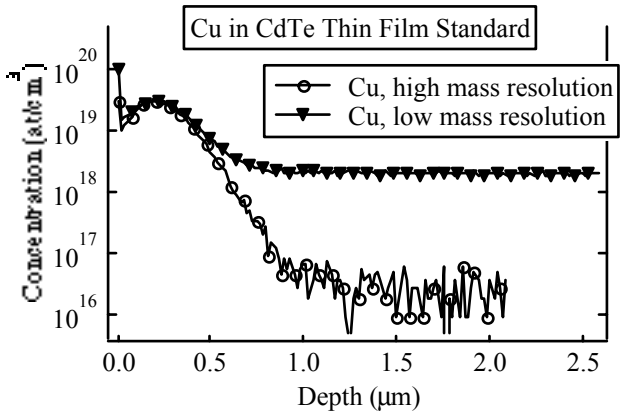

Figure 3. Depth profile of Cu in polycrystalline CdTe implant standard profiled with low- and high-mass resolution.

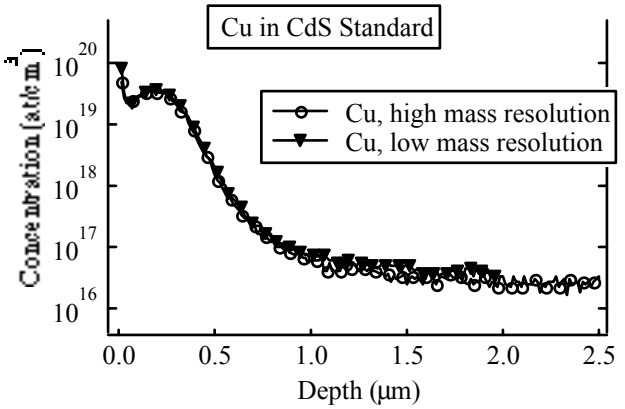

Figure 4. Depth profile of Cu in single crystal CdS implant standard profiled with low- and high-mass resolution.

Shown in Figure 5 are the raw Cu counts from depth profiles of one control device with no contact and three devices with different Cu-containing back contacts. Again, the increase in the Cu signal in the CdS is observed. Applying the RSF's shown in Table 1 to the profiles in Figure 5 yields the quantified data shown in Figure 6. It is now clear that the increase in Cu signal corresponds to a real increase in the Cu concentration in the CdS layer. Although the SIMS measurement does not distinguish between Cu at grains and Cu at grain boundaries, SIMS does show that

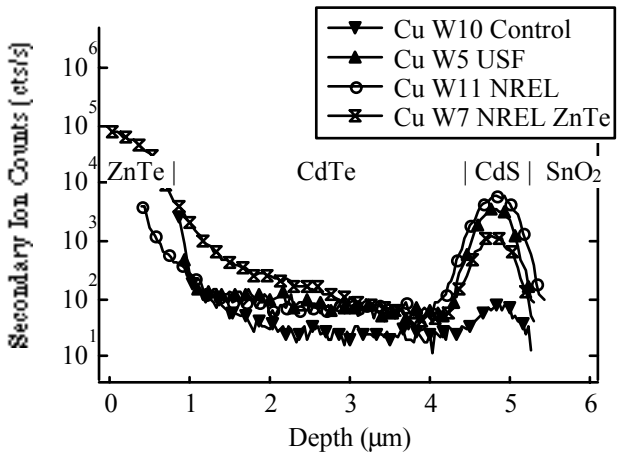

Figure 5. Raw Cu depth profiles from one un-contacted control device and three devices with different back contacts.

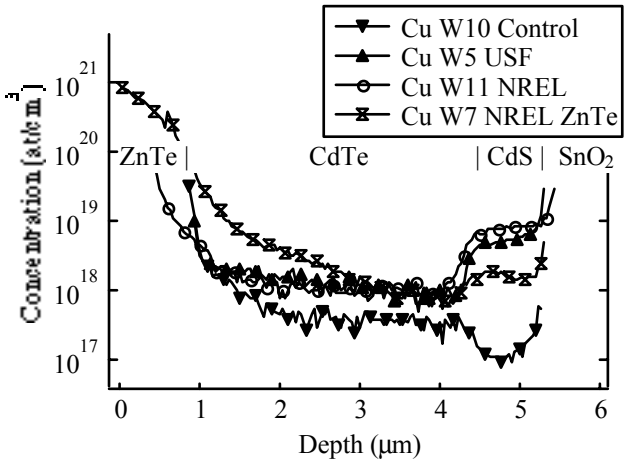

Figure 6. Quantified Cu depth profiles from four devices shown in Fig. 5.

there is still a real increase in the overall Cu concentration in the CdS layer .

4. Summary

High-mass-resolution depth profiling by SIMS has been used to study the distribution of Cu in CdTe/CdS. Ion implant standards have been fabricated to correct for changes in ion yield between the different matrices. Relative sensitivity factors have been calculated for Cu in CdTe and CdS. Quantified profiles of Cu through CdTe/CdS devices are shown for the first time.

REFERENCES

[1] R.G. Wilson, F.A. Stevie, C.W. Magee, "Secondary Ion Mass Spectrometry", John Wiley and Sons, New York, p. 3.1-1, NY,(1989).

ACKNOWLEDGEMENTS

This work was supported by the U.S. Department of Energy under contract No. DE-AC36-98-GO10337
The device structures were studied as part of the National Thin Film Partnership. Manuscript is in preparation.

Effects of Surface Composition on CdTe/CdS Device Performance

Dean Levi, David Albin, and David King

National Renewable Energy Laboratory

1617 Cole Blvd., Golden, CO 80401

ABSTRACT

The atomic composition of the back surface of the CdTe layer in a CdTe/CdS photovoltaic (PV) device has a significant influence on the quality of the electrical contact to this layer. This paper reports the results of a systematic study that correlates the composition of the back surface with pre-contact processing and device performance. We found that certain processing steps produce an oxide layer that degrades device performance by producing a metal-oxide-semiconductor (MOS) contact, rather than the intended metal-semiconductor, Schottky barrier contact. We also found that the as-deposited CdTe film is cadmium-rich for several hundred angstroms at the back surface. This n-type layer can impede current flow for majority holes, degrading device performance.

1. Introduction

An important issue in commercialization of CdTe-based thin-film solar cells is developing a method for making a stable, low-resistance back contact. Because no metal has a work function larger than the work function of p-type CdTe, a fundamental problem exists in forming low-resistance contacts. The standard method of producing low-resistance tunneling contacts by high doping of the surface is difficult because of the complexities in doping CdTe to high hole-densities.

There are various fabrication methods that produce high- efficiency polycrystalline CdTe/CdS PV cells. An essential step in all of these methods is exposure to $CdCl_2$ in conjunction with annealing. Most methods utilize either a solution-$CdCl_2$ (SCC) treatment, or a vapor-$CdCl_2$ (VCC) treatment. These treatments are followed by various types of surface-cleaning processes prior to back-contact application.

The National Renewable Energy Laboratory (NREL) CdTe device team has used both SCC and VCC treatments. In this study we have used X-ray photoelectron spectroscopy (XPS) to determine the atomic composition of the back surface at each step in the processing sequence for both SCC and VCC treatments. Devices have been fabricated from the films at each step of the processing in order to correlate back-contact performance with surface composition.

2. Sample Preparation

The polycrystalline CdTe/CdS thin films used in this study were deposited using close-spaced sublimation (CSS) at NREL. Samples used for surface characterization and device fabrication consisted of multi-layer CdTe/CdS/SnO_2/7059-glass structures typical of NREL CdTe/CdS devices[1].

We have studied two distinct processing "streams". The first one is the SCC treatment. First, the sample is placed in a boiling $CdCl_2$-methanol solution for 15-20 minutes. The sample is then annealed in air at 400^{o}C for 30 minutes. Following the annealing step, the samples are etched in a 350:4:140 mixture of HNO_3:H_3PO_4:H_2O, (NP etch). The samples are rinsed in running deionized (DI) water to halt the etch process. Following the rinse, a mixture of Cu-doped HgTe in Electrodag 114 is applied, and the sample is annealed in air for 30 minutes at 260^{o}C. Finally, silver paint is applied, and the device is annealed at 100^{o}C in air.

In the VCC treatment, the samples are exposed to $CdCl_2$ vapor at 400^{o}C in a modified CSS chamber in the laboratory ambient atmosphere. After this step, the samples are rinsed in flowing DI water, then etched in NP etch and rinsed again. The remainder of the contact application procedure is the same as above. NREL researchers regularly achieve devices with efficiencies of over 13% using either the SCC or the VCC treatments.

In addition to the standard conditions described above, we have also investigated the effects of annealing under vacuum, and of a weak nitric-acid solution. The vacuum annealing was performed at 10^{-3} torr and 400^{o}C for 10 minutes. The nitric acid etch consisted of 3 ml of 15.9 M nitric acid in 100ml of H_2O. Etch time was 60 seconds, followed by a DI rinse to halt the etching process.

3. Results

XPS sputter depth profiles were used to characterize the atomic composition of the near-surface region for each sample. The sputter rate was calibrated at 17 Å per minute. XPS data were collected with a sputtering interval of 20 seconds, which is equivalent to removal of 5.7 Å, or approximately two monolayers of material between XPS surveys. The atomic composition was profiled within 10 minutes sputter time (170 Å) of the surface. The atomic percentages of the elements tellurium, cadmium, oxygen, chlorine, sulfur, and carbon were measured. No other elements were present at levels detectable by XPS.

The atomic percent (at%) of oxygen in the surface region is strongly correlated with device performance. The oxygen depth profile is approximately linear, and is parameterized in Table 1 below. Much more detailed results are available in an upcoming publication[2].

Sample Processing	at% oxygen at surface	at% oxygen at 10 min., or depth at% < XPS limit
as deposited	20	3 min
SCC only	15	2 min
SCC/anneal	50	25
SCC/anneal/DI	49	20
SCC/anneal/vac.anneal	45	20
SCC/anneal/DI/HNO_3	10	0.5 min
SCC/anneal/DI/NPetch	6	6
VCC only	10	2
VCC/vacuum anneal	9	5
VCC/DI	30	5@4min 5@10min
VCC/DI/HNO_3	8	0.3 min
VCC/DI/NP etch	6	6

Table 1. Atomic percent oxygen at the surface, and the sputter time the oxygen at% goes below the XPS limit (<0.1%), or the at% after 10 minutes of sputtering.

We have also found that all of the samples, except the NP-etched samples, are cadmium rich in the near surface region. This has important implications for contact formation, as it is known that cadmium interstitials and tellurium vacancies both form shallow donors which could make the near-surface region n-type. Such an n-type region would impede the flow of majority-carrier holes through the metallic contact at the back surface, producing a relatively high-resistance back contact and limiting the efficiency of the solar cell.

4. Device Characterization

To correlate the back-surface composition with the quality of the back contact, we have fabricated devices from samples at each step of the processing. Considerable care has been taken to ensure that all of the devices are identical except for their back-surface processing. The primary measure of the quality of the back contact is the contact resistance, R_c. It is not practical to directly measure R_c in these devices; however, it is possible to determine the total series resistance of the device, R_S, using the following method. In forward bias, near V_{OC}, the series resistance, R_s can be expressed as the sum of the back-contact resistance plus the lumped resistance of the rest of the device, R_o:

$$R_s = R_o + R_c \quad , \qquad (1)$$

Because the devices in this study are essentially identical except for their back-surface treatments, we propose that changes in R_s are primarily due to changes in R_c.

Series resistance can be calculated from the J-V curve using an analytical technique established by Sites for the J-V analysis of polycrystalline solar cells[3]. Using the standard photodiode equation and assuming high shunt resistance (which is the case for the devices in this study), one can derive an equation of the form:

$$\left(\frac{dV}{dJ}\right) = R_S + \frac{AkT}{q}(J + J_{sc})^{-1} \quad , \qquad (2)$$

In the dark, the inverse current term reduces to J^{-1}. The series resistance is determined by taking the intercept of (dV/dJ) vs. J^{-1}. We have used this formalism to calculate values of R_s for each of the devices studied.

The efficiency and R_S values for the devices in this study are presented in Table 3. The values of R_S presented in the table are calculated from the dark J-V curves measured at 25° C.

Sample Processing	R_S(□-cm^2)	efficiency(%)
as deposited	5.0	8.7
SCC only	NA	NA
SCC/anneal	8.3	12.05
SCC/anneal/DI	8.6	12.35
SCC/anneal/ vac. anneal	4.7	11.9
SCC/anneal/DI/HNO_3	3.1	12.85
SCC/anneal/DI/NP etch	1.5	13.05
VCC only	2.3	13.1
VCC/vac. anneal	2.5	13.1
VCC/DI	4.5	12.25
VCC/DI/HNO_3	2.3	12.5
VCC/DI/NP etch	1.9	13.3

Table 2. Device R_S and efficiency for each processing condition. No device was fabricated for the SCC-only.

The relationship between R_S and oxygen at% is clearly illustrated in Figure 1. The line in the figure is a linear fit to the data points. It is clear that R_s, and hence R_c, are approximately linear functions of the oxygen content at the surface of the CdTe-absorber layer. This is consistent with formation of an MOS back contact for the devices with significant amounts of oxygen, and a metal-semiconductor Schottky barrier contact for those devices with very little oxygen.

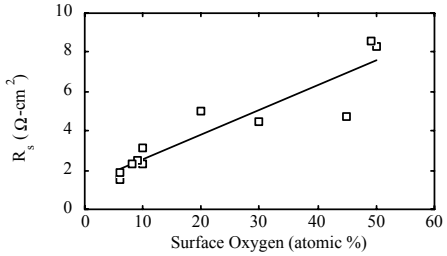

Figure 1. Dependence of R_S on oxygen atomic percent.

Acknowledgements

We wish to thank Yoxa Mahathongdy for assistance with vapor $CdCl_2$ treatments and device fabrication, and Rosine Ribelin for chemical bath deposition of the CdS layers. This work was supported by the US Department of Energy under Contract No. DE-AC36-99GO10337.

REFERENCES

1 . Rose DH, Hasoon FS, Dhere RG, Albin DS, Ribelin RM, Li X, Mahathongdy Y, Gessert TA, and Sheldon P, *Prog. Photovolt: res. Appl.* 7, 331-340 (1999).

2. Dean Levi, David Albin, and David King, submitted to *Prog. Photovolt. Res. Appl.,* Jan, 2000.

3. Sites JR, *Proc. of the. 20th IEEE Photovoltaic Specialists Conference*., Las Vegas, 1988, 1604-1608, IEEE, 1989.

Investigation of Deep Impurity Levels in CdTe/CdS Solar Cells

A. Balcioglu, F. Hasoon, D. Levi, and R. K. Ahrenkiel

National Renewable Energy Laboratory

1617 Cole Blvd. Golden CO 80401

ABSTRACT

We have studied deep impurity levels of CdTe/CdS solar cells by capacitance-voltage (C-V), deep-level transient spectroscopy (DLTS) and time-resolved photoluminescence (TRPL). CdTe/CdS devices were stressed under light soak of AM1.5 at 65°C for various lengths of time. C-V measurements indicate a high density of interface states. Using DLTS, a dominant electron (minority) and two hole (majority) trap levels were observed. These trap levels were labeled as E1 at Ec-0.28 to Ec-0.45 eV, H1 at Ev+0.35 eV, and H2 at Ev+0.45 eV. The H1 trap level is attributed to Cu substitutional defects. The E1 trap level is believed to be a deep donor. The calculated Shockley-Hall-Read (SHR) lifetime, using DLTS parameters, is about 0.85 ns, which is consistent with the lifetime values measured by TRPL. These results suggest that the E1 trap level is the lifetime-limiting defect.

Introduction

CdTe/CdS thin-film solar cells are one of the leading candidates for low-cost large-scale and terrestrial photovoltaic applications. The calculated maximum theoretical efficiency for single-crystal CdTe cells is close to 29% [1], but practically achieved results for polycrystalline CdTe/CdS heterojunction cells are around 16% [2]. Four problems appear to be dominant in polycrystalline CdTe/CdS thin-film solar cells: 1) recombination losses associated with the CdTe/CdS junction interface, 2) difficulty in doping the CdTe, 3) difficulty in obtaining low-resistance contacts to CdTe, and 4) degradation of the back contact [3].

Cu-doped ZnTe, HgTe, Cu_xTe and Au are currently being studied by various groups [4] as a back contact to CdTe thin-film solar cells in order to obtain low-resistance and a stable contact to the CdTe layer. Studies have shown [5] that Cu diffuses into the CdTe film during and subsequent to formation of the back contact. Uncontrollable Cu diffusion may severely reduce the stability of the devices and introduce deep-level impurities into the CdTe layer. In this paper, we study deep impurity levels of CdTe/CdS solar cells as a function of stress time. We discuss the origin of defects and their effect on the minority-carrier lifetime.

Experimental Procedure

The device structure of CdTe/CdS thin-film solar cells used in this study is described elsewhere [4]. A number of identical CdTe/CdS devices were prepared for stress testing. Devices were subjected to light soak under AM1.5 (1 Sun) at 65°C for various lengths of time.

The net carrier concentration (N_A-N_D) and the built in voltage (V_{bi}) of the devices were measured by using C-V measurements. C-V measurements were performed using an HP2474 multi-frequency LCR meter, at a frequency of 100 kHz on completed CdTe/CdS solar cells. The system used to measure the minority-carrier lifetime is described in reference [6]. DLTS is a powerful technique used to extract thermal properties of deep-level impurities such as the activation energy, capture cross section and the density of traps. Detailed information related to our DLTS system can be found in reference [7].

Experimental Results and Discussion

C-V measurements have revealed that the plot of (N_A-N_D) vs. applied bias (V) is not linear, indicating a nonuniform ionized impurity concentration with depth in the depletion layer. We have successfully fitted the data to two slopes, and the calculated doping densities are $8.2x10^{14}$ cm^{-3} at large reverse bias, which is associated with the bulk doping and $8.6x10^{13}$ cm^{-3} at forward bias that corresponds to the region near the CdTe/CdS interface. This reduction in net carrier concentration suggests a high density of surface or interface states due to compensation (deep donors) at the CdTe/ CdS junction.

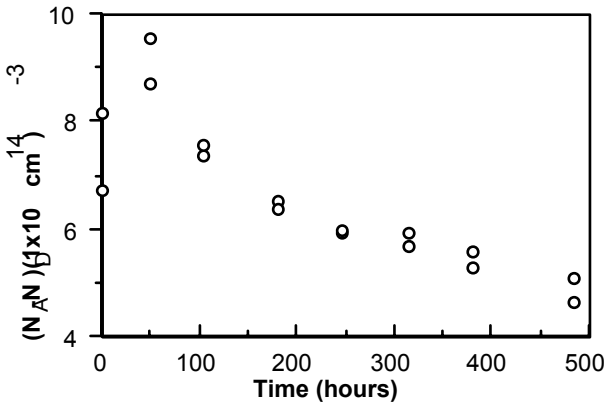

Figure 1 The net carrier concentration vs. stress time. The net carrier concentration was obtained from large reverse biases (from –2 V to –0.5 V).

We have monitored how the net carrier concentration was affected by stress time. Figure 1 shows that there is an improvement in carrier concentration upon the first 50 hours of stress which then decreases logarithmically. This

decrease in (N_A - N_D) is attributed to the presence of deep donors, which cause compensation that is likely to take place at longer stress times.

The DLTS data presented here were performed under identical bias conditions. Several trap levels were found in all samples in the temperature range of 80–300 K as shown in Figure 2. These trap levels are designated as E1, at E_C-0.28 eV to Ec-0.45 eV, H1 at E_V+0.34 eV, and H2 at E_V +0.45 eV. The trap concentrations of devices stressed about 500 hours are 1.5 x 10^{13}, 1.2 x 10^{13} and 8.5 x 10^{12} cm^{-3}, respectively.

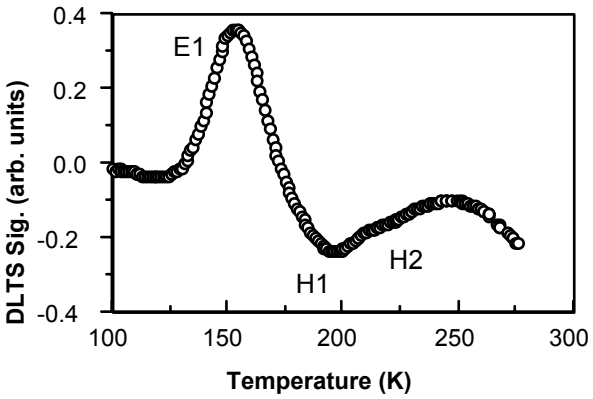

Figure 2 DLTS spectrum of an-as grown CdTe/CdS device.

Capture cross sections of E1 and H1 were not directly measurable with our system because, for the shortest reduced-bias pulse (≈1 μsec), all the levels were completely filled with the respective carriers. For this reason, the capture cross sections of the E1 and H1 trap levels were determined from the intercept of the Arrhenius plots. The values for devices stressed for 513 hours are $5x10^{-12}$ and $2x10^{-14}$ cm^2, respectively. The SHR lifetime of E1 trap level was calculated by using the appropriate values for thermal velocity, capture cross section, and trap concentration. The SHR lifetime is found to be about 0.85 ns for devices stressed for 513 hours, which is consistent with the lifetime values measured by TRPL as shown in figure 3. These results indicate that the E1 trap level is the lifetime limiting defect.

The H1 level observed here was previously reported to be associated with substitutional Cu impurities [5, 8]. Based on prior evidence [9–11] and the data presented here, we speculate that the E1 level is a deep donor due to the doubly ionized interstitial Cu (Cu_i^{++}) ions. C-V data suggests the presence of a high concentration of compensating donors that are responsible for compensation of net carrier concentration as shown in figure 1. We believe that the E1 level is responsible for the behavior of C-V data at low reverse biases, which corresponds to the interface.

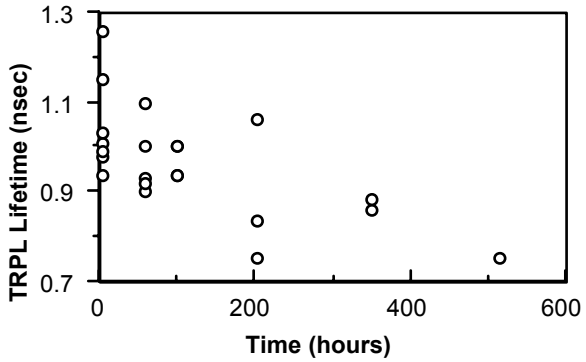

Figure 3 TRPL minority-carrier lifetime of several CdTe/CdS devices as a function of stress time.

In conclusion, the deep impurity levels and their effect on the minority-carrier lifetime in CdTe/CdS solar cells have been studied by C-V, DLTS, and TRPL. We have observed and identified a dominant electron trap, namely E1, that is an effective recombination center. The H1 level is attributed to the substitutional Cu impurities. The E1 level is likely to be a deep donor due to formation of Cu complexes near or at the interface and is the lifetime-limiting defect.

REFERENCES

[1] A. W. Brinkman, "Properties of Narrow Gap Cadmium-Based Compounds", edited by P. Capper, 10, 591 (IEEE, London 1994).

[2] T. L. Chu and S. S. Chu, Solid-State Elect., 38, 533 (1995).

[3] R. H. Bube, "Photovoltaic Materials", Imperial College Press (1998).

[4] D. H. Rose, F. S. Hasoon, R. G. Dhere, D. S. Albin, R. M. Ribelin, X. S. Li, Y. Mahathongdy, T. A. Gessert, and P Sheldon, Prog. Photovolt: Res. Appl., 7, 331 (1999).

[5] E. Kucys, J. Jerhot, K. Bertulis, and V. Bariss, Phys. Stat. Sol (a) 59, 91 (1980).

[6] R. K. Ahrenkiel and M. S. Lundstrom, "Semiconductors and Semimetals" 39, 65 (Academic Press).

[7] A. Balcioglu, R. K. Ahrenkiel and D. J. Friedman, Appl. Phys. Lett. (in press).

[8] S. S. Ou, A. Bindal, O. M. Stafsudd, and K. L. Wang, J. Appl. Phys., 55, 1020 (1984).

[9] Lyubomirsky, M. K. Rabinal, and D. Cahen, J. Appl. Phys., 81, 6684 (1997).

[10] C. M. Fortmann, A. L. Fahrenbruch, and R. H. Bube, J. Appl. Phys., 61, 2038 (1987).

[11] A. Balcioglu, R. K. Ahrenkiel and F. Hasoon, (to be published)

Micro-PL Studies of Polycrystalline CdS/CdTe Interfaces.

R.G. Dhere, H. Cheong, S. Smith, D.S.Albin, A. Mascarenhas, and T. A. Gessert

National Renewable Energy Laboratory

1617 Cole Blvd., Golden, CO 80401

ABSTRACT

We describe a technique of photoluminescence measurements with a resolution of microns. This technique is applied to examine the CdS/CdTe interface of CdTe solar cells. The devices were made using chemical-bath deposited CdS on SnO_2/glass substrates. The CdTe was deposited by close spaced sublimation and subsequently $CdCl_2$ treated and annealed. Micro-photoluminescence (micro-PL) analysis reveals sulfur accumulation at the grain boundaries and a graded CdS_xTe_{1-x} alloy at the interface. We have compared these results with measurements from a SnO_2/CdTe interface to make sure that the features observed in CdS/CdTe interface analysis are the result of CdSTe alloy and not other factors such as grain size or stress.

INTRODUCTION

Polycrystalline semiconductors are used in a number of device applications. Due to the inherent advantages of lower cost and ease of fabrication, polycrystalline thin film solar cells are prime candidates for commercialization. CdS/CdTe solar cells have demonstrated efficiencies of 15.8% in laboratory devices [1]. Due to its good stability and ease of fabrication, a number of groups are involved in development of this technology. There are however many issues that still need to be understood for successful scaling-up. In the case of polycrystalline semiconductors, grain boundaries can influence the properties of the material considerably. There has been extensive work done on the structural characterization of grain boundaries using microscopic techniques such as scanning and transmission electron microscopy. In the case of electronic devices, the effect of the grain boundaries on the electro-optical properties can be substantial and development of processing techniques to mitigate damaging effects are crucial for enhancing the performance of these devices. Most electro-optical analysis techniques give information on a macroscopic scale and the effect of grain boundaries can only be speculative based on comparison with equivalent single crystal samples. So far only Electron Beam Induced Current (EBIC) measurements have provided useful information on the properties of grain boundaries in CdTe based devices. In this paper, we describe a micro-PL technique, which can resolve the electrical properties of the grains and grain boundaries. CdS/CdTe samples are used as a test case to demonstrate the capabilities of this technique. The effect of grain boundaries and intra-grain structural defects on electro-optical properties is studied by micro-PL measurements.

EXPERIMENTAL DETAILS

Micro-PL measurements were performed at 4.2 K using a confocal spectroscopy setup. (Figure 1) About 130 W of the 514.5 nm excitation laser beam was focused onto the sample inside an Oxford Microstat He cryostat using a long-working distance reflective microscope objective. The objective lens has a capability to compensate for the spherical aberration due to the 500 µm-thick window of the

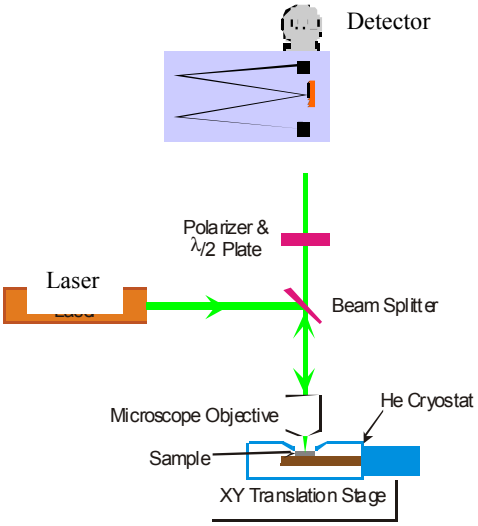

Figure1. Schematic diagram of micro-PL set-up

cryostat. The spot size on the sample is estimated to be 1–2 µm in diameter. The PL signal was collected and collimated by the same objective,and then focused onto the input slit of a Spex 0.6µm triple spectrometer. A charge-coupled-device (CCD) detector array was used to collect the spectra. The resolution of the system is estimated to be approximately 0.5 meV. In order to investigate the spatial variation of the PL spectra, the sample (and cryostat) was scanned in 1µm steps using an optically decoded translation stage. Although the spectrum changes significantly as a function of position, it varied little as a function of time at a given position. This indicates that the spatial stability of the sample was adequate. Details of the fabrication of CdS/CdTe samples are described elsewhere [2]

RESULTS AND DISCUSSION

Figure 2 shows the PL intensity as a function of position for a film that was released from the substrate, directly exposing the CdS/CdTe interface. The sample was

deposited at 610°C with a subsequent $CdCl_2$ heat treatment. In Figure 2, the peaks correspond to the center of the grains, and the valleys to the grain boundaries. The numbers above the arrows indicate the approximate distance between grain boundaries. PL intensity analysis from the CdTe side also shows similar behavior. PL spectra measured from the CdTe side and the CdS/CdTe interface side (for selected points in Figure 2 closer and away from grain boundaries) are presented in Figure 3. The PL spectra for measurements on the CdTe side show that, even though the intensity changes considerably from the center of the grain to the grain boundary, the peak position of the spectra remains at the same position (1.581 eV), corresponding to the CdTe bandgap. On the other hand, the PL spectra from the CdS/CdTe side show changes both in the intensity and the peak position. All of these spectra are shifted to lower

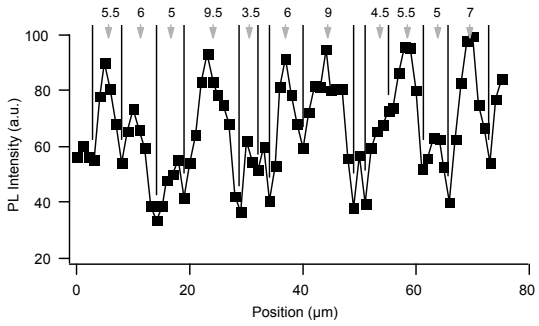

Figure 2. PL Intensity vs position for measurements from CdS/CdTe side.

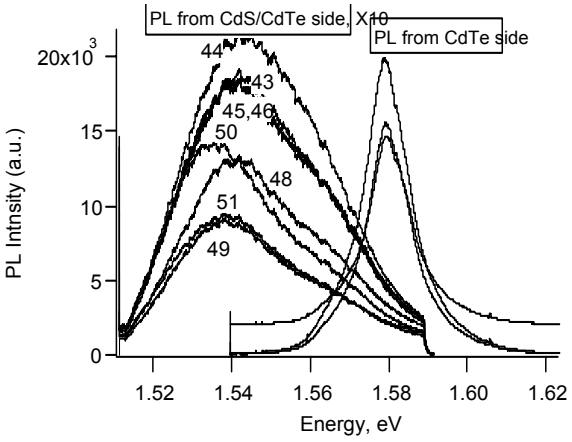

Figure 3. PL spectra measured at 4.2 K from the CdTe and the CdS/CdTe side. The numbers refer to the position in Figure 4.

energy and their bandwidth is much larger than that of the CdTe spectra seen from the backside. These spectra correspond to the alloyed region at the interface, which explains the peak shift to lower energies (expected for Te-rich CdS_xTe_{1-x} alloys)[3]. Peak-broadening is due to the superposition of spectra corresponding to the range of alloy compositions present in the alloyed layer. To substantiate this hypothesis, we also did these measurements on similar samples with SnO_2/CdTe structure from SnO_2 side. The spectra of PL intensity as a function of position for these samples were similar to spectra from CdTe side for CdS/CdTe samples. Peak position of these spectra also remained closer to CdTe bandgap (1.581 eV) and there was no peak broadening (Figure 4). Therefore the peak position shift and

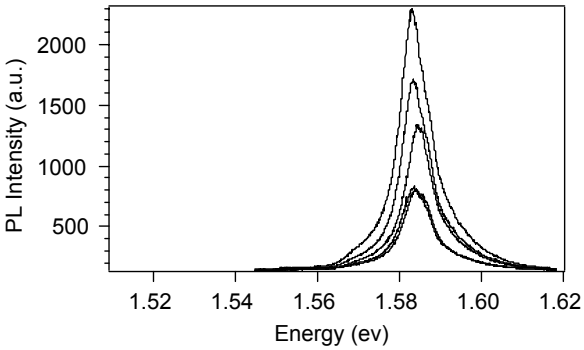

Figure 4. PL spectra from SnO_2 side of SnO_2/CdTe sample at 4.2 K at different positions.

peak broadening seen for PL spectra of CdS/CdTe samples can be uniquely assigned to the formation of CdS_xTe_{1-x} alloying. The spectra corresponding to the positions in the center of the larger grains (~9 μm) have higher intensities, with a peak position at 1.543 eV and symmetrical peak broadening in the range of 1.524 eV and 1.569 eV, corresponding to alloy composition range of x = 0.024 to 0.114. The spectra corresponding to the center position of a small grain (~2 μm) has a peak position at 1.535 eV and is asymmetrical, indicating the contribution predominantly from the lower gap alloys between 1.52 eV and 1.545 eV (x = 0.072 to 0.122). The peaks corresponding to the grain boundaries (lowest intensity peaks in the spectrum) have peak positions at 1.538 eV and also show predominant contribution from lower gap alloys. Previous work on Te-rich CdS_xTe_{1-x} alloys [3], indicates that the bandgap decreases as x increases from 0 to 0.25. Therefore, grain boundaries and heavily faulted small grains contain alloys with higher sulfur compositions as compared to the middle of the larger grains.

CONCLUSIONS

Micro-PL technique can determine electro-optical properties with microscopic resolution and give relevant information for the properties of grain boundaries in polycrystalline semiconductor device structures.

ACKNOWLEDGEMENTS

This research is supported by U.S. Department of Energy under contract No. DE-AC36-99GO10337.

REFERENCES

[1] J. Britt and C. Ferekides, *Proc. of the 11th European PVSC*, 276(1992).
[2] R.G. Dhere, Ph.D. Thesis, University of Colorado at Boulder, Boulder, CO (May 1997).
[3] K. Ohata, J. Saraie, and T. Tanaka, *Jap. J. of Appl. Phys*., **12**(10), 1641 (1973).

Modeling Results for CdS/CdTe Polycrystalline Thin Film Solar Cells

A. Fahrenbruch

ALF, Inc.

107 Montalvo Rd., Redwood City, CA 94062 alanf@stanford.edu

ABSTRACT

Using the AMPS modeling program, variations of J_{sc}, V_{oc}, ff, and efficiency with carrier density (N_a), lifetime, and CdTe layer thickness were calculated. Given the high J_{sc} exhibited by most experimental cells, these simulations show that the greatest potential for improvement of V_{oc} and ff is by increasing N_a. Variation of J_{sc}, V_{oc}, and ff with CdTe layer thickness demonstrates the strong influence of back contact barrier height, giving rise to the anomalies (V_{oc} shift, cross-over, and roll-over) that are commonly seen, particularly for stressed devices.

1. Introduction

The purpose of this modeling is to visualize the carrier transport properties such as fields, currents, recombination profiles, and the effects of illumination on transport in CdS/CdTe solar cells. It enables us to directly evaluate the effects of materials parameters (e.g., acceptor density) and design parameters (e.g., layer thickness) on cell operation.[1]

The following sections include discussions of AMPS-1D simulations of the effects of variation of acceptor density (N_a), minority carrier lifetime (□), and CdTe layer thickness (x_{CdTe}) on J_{sc}, V_{oc}, ff, and efficiency (Eff) (PV variables).

2. Influence of CdTe N_a and Lifetime

Modeling the effects of a variation of N_a and □ on the PV variables showed that [2]:

- Greater N_a gives higher efficiency.
- V_{oc} decreases strongly for decreasing N_a because the potential barrier faced by electrons diffusing across the junction to the right (the bucking current) collapses to a value determined by the back contact barrier height.
- Given the high J_{sc} values shown by most experimental cells, this modeling suggests that the effective carrier lifetime is already quite large and that further increases will only marginally increase V_{oc} and ff. The largest potential for improvement is in increasing N_a.
- For smaller CdTe layer thicknesses (≤ 2 μm, at $N_a = 10^{14}$ cm^{-3}), surface recombination at the back contact is a large part of the loss at V_{max}.

3. Variation of CdTe layer thickness

The variation of CdTe layer thickness yielded a surprising number of insights. For these cases, $N_a = 10^{14}$ cm^{-3} was used, with two extreme cases: the back contact barrier height $Ø_{bc}$ = 0.0 and 0.5 eV. Using $Ø_{bc}$ = 0.0 eV gives an accumulation region at the back contact which is both an ohmic contact and a minority carrier mirror, a most desirable condition but most likely never achievable in real cells. On the other hand, results for $Ø_{bc}$ = 0.5 eV show the typical anomalies which occur as a result of environmental stressing of experimental cells. Band diagrams for these cases are shown in Fig. 1; the resulting PV data are shown in Fig. 2.

J_{sc} is relatively insensitive to $Ø_{bc}$ and the drop-off in J_{sc} at smaller thicknesses is as expected, due to lessening of the absorption volume.

For $Ø_{bc}$ = 0, V_{oc} becomes larger for thinner CdTe because the recombination volume becomes smaller and the accumulation layer at the back contact reduces the surface recombination there to very small values.

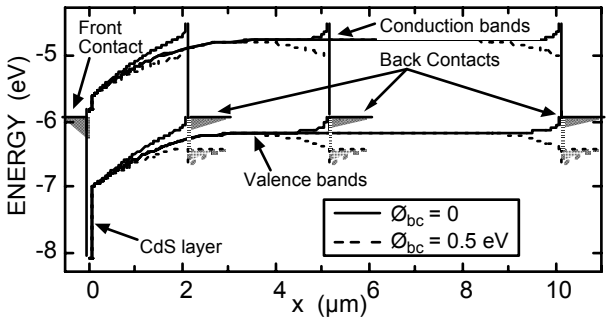

Fig. 1. Band diagrams for the CdTe thickness variation, for $Ø_{bc}$ = 0 and 0.5 eV (V = 0, dark).

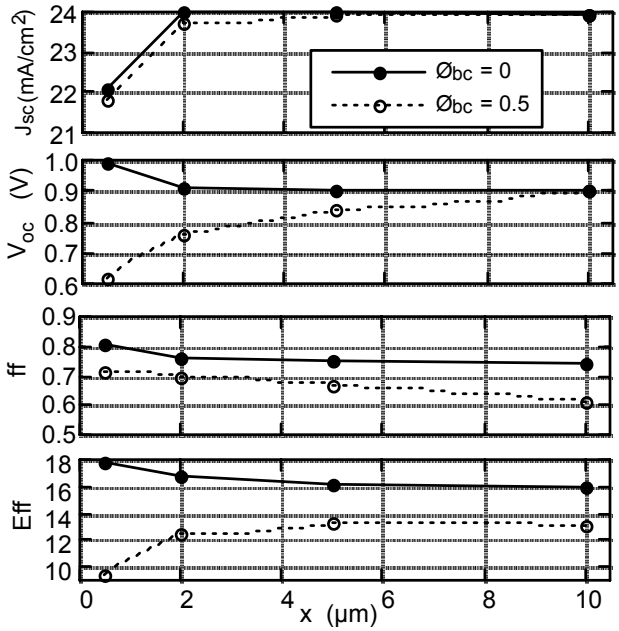

Fig. 2. PV variables for the CdTe thickness variation cases ($N_a = 10^{14}$, $\tau = 10^{-9}$ sec).

For $Ø_{bc}$ = 0.5 eV, V_{oc} is strongly reduced for thinner cells because the barrier to transport of electrons to the right (bucking current) collapses between 2 μm and 5 μm. In these cases, the reverse field at the back is lessened or nonexistent; thus there is no barrier to photogenerated holes, which strongly increases recombination loss at the back contact. The bulk recombination loss in the 2 μm CdTe case is smaller by a factor of 2 than that of the 5 μm CdTe case (smaller recombination volume). However, the surface recombination loss at the back contact is larger by a factor of 7 for the 2 μm cells. Thus the reverse field at the back essentially turns the back surface recombination on or off.

For a CdTe thickness of 0.5 μm, the J-V data in Fig. 3 show almost identical J_{sc} and similar ff values for both

$Ø_{bc}$ = 0 and 0.5 eV, but V_{oc} is shifted by almost 0.4 eV. The back contact barrier with $Ø_{bc}$ = 0.5 eV is not a barrier to photo-generated holes in this case, but just decreases the effective junction barrier of the cell. The light and dark curves do not cross for either value of $Ø_{bc}$.

For 2 and 5 μm and $Ø_{bc}$ = 0, Fig. 4, there is little difference between the light and dark JV curves and they do not cross. But for $Ø_{bc}$ = 0.5 eV, and x_{CdTe} = 2 μm, there is strong crossover of light and dark JV curves but no roll-over. Increasing the thickness to 5 μm causes a strong roll-over of the JV curves for V > V_{oc} because of the development of a barrier to photogenerated holes at the back contact.

The ff follows the variation of V_{oc}, as expected, for $Ø_{bc}$ = 0. However, for $Ø_{bc}$ = 0.5 eV, the ff actually increases for thinner CdTe layers because the collapse of the barrier for $x_{CdTe} \leq 2$ μm makes the back contact ohmic for photo-generated holes traveling to the right.

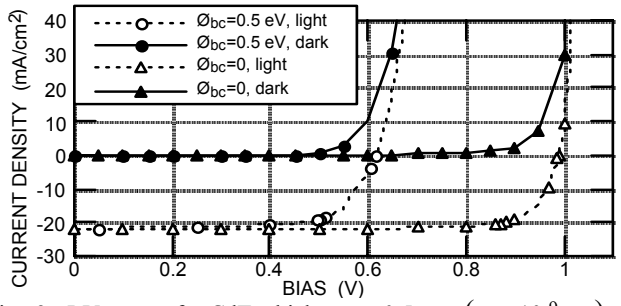

Fig. 3. J-V curves for CdTe thickness = 0.5 μm. (= 10^{-9} sec).

Since the depletion layer widths depend on N_a, the observed changes would take place for thicker (thinner) CdTe layers for lower (higher) N_a values. As with the N_a and , modeling, simultaneous targeting of V_{oc} and ff is not possible.

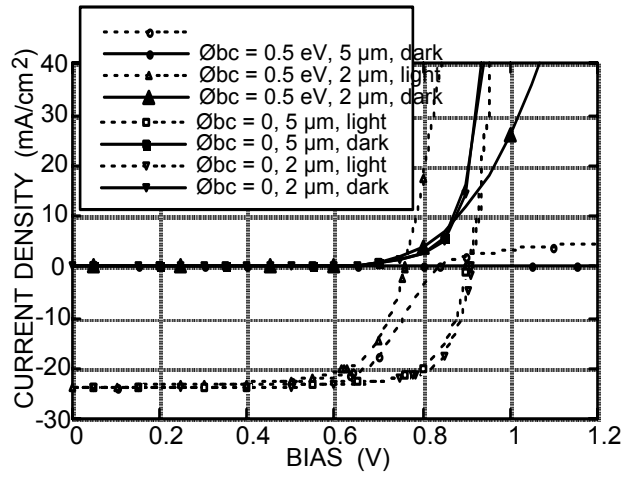

Fig. 4. J-V curves for x_{CdTe} = 2 and 5 μm. (= 10^{-9} sec).

The simulated J-V curves always show a bias-dependent light-generated current [$J_L(V)$] which lowers V_{oc} and ff from their ideal values. This breech of superposition of dark and light J-V curves is characteristic of all experimental CdS/CdTe cells. If the lifetime is increased to unreasonably high values for CdTe (10^{-5} sec), superposition is regained.

4. Introduction of a CdS_xTe_{1-x} alloy layer

The model was set up to include a CdS_xTe_{1-x} alloy layer (CdSTe) at the CdS/CdTe interface, resulting from inter-diffusion of S and Te, with x near the solubility limit. Such a layer is thought to be ª 0.1 μm thick with x ª 0.06 [3], giving E_g = 1.41 eV. The band offsets between CdSTe and CdTe were set to be entirely in the valence band.[4] The CdSTe lifetime $\tau = 10^{-9}$ sec and $N_a = 10^{14}$ cm^{-3} were kept the same as for the CdTe layers. In previous sections, the AMPS Lifetime (LT) mode was used, minimizing the effects of charged recombination centers. In this section, the AMPS Trap Density (TM) mode was used, recombination center properties were specified, and the effects of recombination center charge are now observed.

Remarkably, this simple modification allows a consistent set of PV variables to be targeted (Table 1). The use of the TM mode and the presence of the CdSTe layer lowers V_{oc}, but raises the ff, leaving the efficiency almost unchanged. By adjusting τ, V_{oc} can now be adjusted to the target value (0.850 V), leaving the ff slightly above the target value (0.750), with room for slight decreases by external series resistance. The increase in ff with the CdSTe layer is partly due to the movement of the generation distribution toward the junction interface, but mostly due to a decrease in V_{oc} because of the increased supply of holes for recombination near the junction interface for V = V_{oc}. The bulk recombination rate near the CdSTe layer increases dramatically between V_{max} and V_{oc}.

Table 1. CdS_xTe_{1-x} layer PV variables

CASE	Mode	J_{sc} (mA/cm^2)	V_{oc} (V)	ff	Eff (%)
no CdSTe	LT	23.9	0.893	0.742	15.9
no CdSTe	TM	24.1	0.852	0.770	15.8
CdSTe	TM	24.6	0.852	0.755	15.8

5. Conclusions

Variation of the CdTe layer thickness demonstrates the strong influence of back contact barrier height, giving rise to the anomalies (V_{oc} shift, cross-over, and roll-over) that are commonly seen in experimental devices, particularly for stressed devices.

With the use of the AMPS Trap Density mode and the addition of a CdSTe alloy layer, these rather simple AMPS models can duplicate the generic PV variable targets almost exactly, using a combination of experimental data and physically reasonable parameters.

6. Acknowledgements

The author acknowledges the support of Peter Meyers and ITN, Jim Sites and Colorado State University, the CdTe Team members, and NREL. Modeling results were obtained using AMPS-1D (Version 1,0,0,1), written under the direction of S. Fonash at Pennsylvania State University and supported by the Electric Power Research Institute.

REFERENCES

1. Representative AMPS case files will be sent by e-mail on request to the author <alanf@stanford.edu>.
2. These models used $Ø_{bc}$ = 0.3 eV, CdS thickness 0.1 μm, $N_{d,CdS} = 10^{17}$ cm^{-3}, and AMPS Lifetime Mode.
3. Brian E. McCandless, et al., "NREL/SNL Photovoltaics Program Review," AIP Conf. Proc. 394 (1996) p. 647.
4. Su-Huai Wei, S.B. Zhang, and Alex Zunger, J. Appl. Phys., **87**, 1304 (2000).

Novel CdTe Cell Fabrication Process with Potential for Low Cost and High Throughput

X. Wu and P. Sheldon
National Renewable Energy Laboratory, 1617 Cole Blvd., Golden, CO80401

Abstract

There are several production disadvantages inherent in the conventional SnO_2/CdS/CdTe manufacturing processes. In this paper, we report a novel manufacturing process for fabrication of polycrystalline Cd_2SnO_4/Zn_2SnO_4/CdS/CdTe thin-film solar cells that yielded a CdS/CdTe device with an NREL-confirmed efficiency of 14.0%. This process addresses undesirable manufacturing issues such as time-consuming and expensive heat-up and cool-down processes and generation of large amounts of liquid waste. CdTe cells prepared by this process have good performance, good uniformity, and excellent reproducibility. These results, coupled with the improved process manufacturability, can draw significant industrial interest.

Introdution

Cadmium telluride has been recognized as a promising photovoltaic material for thin-film solar cells because of its near-optimum bandgap of ~1.45 eV and its high direct-absorption coefficient. Commercial-scale modules with efficiencies of 6%-10% have been produced by several CdTe deposition techniques. However, performance and reproducibility of the CdTe modules have been limited by the conventional SnO_2/CdS/CdTe device structure used for many years. For example, higher short-circuit current density (J_{sc}) can be achieved by reducing the CdS thickness in CdTe cells. However, reducing the CdS thickness can adversely impact device open-circuit voltage (V_{oc}) and fill factor (FF). Hence, a thicker CdS layer has to be used in most CdTe module manufacturing processes, which results in low J_{sc} (~18 mA/cm^2). In addition, there are several undesirable production disadvantages in the conventional CdTe module manufacturing processes (see Figure 1). For example, the transparent conductive oxide (TCO) films are typically deposited at high temperatures using chemical-vapor deposition (CVD) or spray techniques. The CdS window layer is deposited at lower temperatures using chemical-bath deposition (CBD) or at high temperature using close-spaced sublimation (CSS) or CVD techniques.

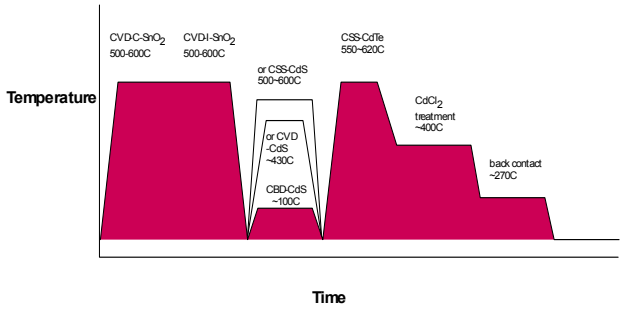

Figure 1. Conventional CdTe device manufacturing processes.

The high-temperature deposition process requires time-consuming and expensive heat-up and cool-down process segments. However, the treatment of a large amounts of liquid waste solution generated in wet processes can increase the manufacturing costs. Therefore, it is necessary to develop a more manufacturing-friendly process for fabricating CdTe modules. In this paper, we report a novel manufacturing process for fabricating CdTe solar cells with a modified device structure.

New Manufacturing Process

Figure 2 shows the new CdTe device manufacturing process. Compared to the conventional manufacturing processes, there are several new aspects in this CdTe device manufacturing process. First, the modified Cd_2SnO_4/Zn_2SnO_4/CdS/CdTe device structure developed at NREL has been used in the new process. In the modified device structure, the Cd_2SnO_4 (CTO) film replaces the conventional SnO_2 TCO film as a front-contact layer, and a Zn_2SnO_4 (ZTO) film is integrated into the device as a buffer layer. The device performance and reproducibility can be improved significantly by using the modified device structure. Second, the first three layers (including CTO TCO layer, ZTO buffer layer, and CdS window layer) are prepared by the same deposition technique – RF magnetron sputtering at room temperature. Third, the new process has only one heat-up segment in the entire device fabrication process. The recrystallization of the first three layers and the interdiffusion at the three interfaces (including the CTO/ZTO, ZTO/CdS, and CdS/CdTe interfaces) were completed during CdTe deposition by the CSS technique.

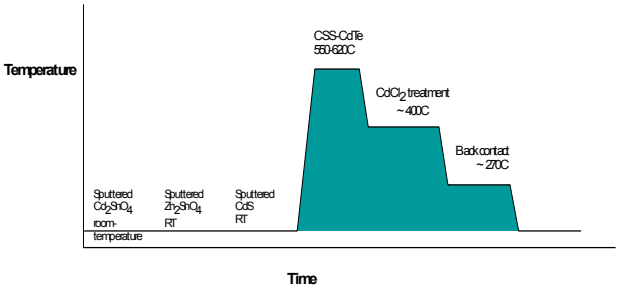

Figure 2. Novel CdTe device manufacturing processes.

Experimental

In this new process, the first three layers (CTO, ZTO, and CdS) were deposited at room temperature by the same RF magnetron sputtering technique. The CTO and ZTO layers were prepared in pure oxygen using commercial hot-pressed oxide targets, and the CdS film was deposited in pure Ar. The CdTe layer was deposited by the CSS technique at a substrate temperatures of 570°C-625°C for 3 minutes. Samples then received a vapor $CdCl_2$ treatment at 400°C-420°C for 15 minutes. Several techniques were used for

material and interface characterization, including Hall effect measurement, visible/near-UV spectrophotometry, X-ray diffraction (XRD), X-ray photoemission spectroscopy (XPS), and transmissiom electron microscopy (TEM). The standard current-voltage (I-V) curves, absolute external and internal quantum efficiencies, time-resolved photoluminescence, saturation dark-current density, and device diode factor have been measured for device performance analysis.

Results

In this process, the first three layers (CTO, ZTO, and CdS) were deposited at room temperature. Hence, all three as-grown films have an amorphous structure and very poor electrical and optical properties. After CdTe deposition at 570□C-625□C for 3 minutes, the three films were changed significantly in material structure, and in electrical and optical properties. We have done much work to understand these changes for the three materials. For example, the as-grown CTO film has an amorphous structure, very high resistivity (>25 Ω cm), and a low bandgap (~2.6 eV). After CdTe deposition at 620□C for 3 minutes, the CTO film structure changed to a spinel polycrystalline structure, and the material properties improved significantly. The post-heat-treated CTO film has a bulk resistivity (~$2.3x10^{-4}$ Ω cm) more than 5 orders of magnitude lower than the as-grown CTO film, and has a higher bandgap (~3.1 eV) and good transmission. We also investigated the interdiffusion among the four layers. For example, XPS and SIMS results show that the interdiffusion occurs at both the CTO/ZTO interface and at the ZTO/CdS interface. This feature can be used to improve device performance and reproducibility.

We have fabricated a Cd_2SnO_4/Zn_2SnO_4/CdS/CdTe solar cell with an NREL-confirmed efficiency of 14.0% (V_{oc} = 841.1 mV, J_{sc} = 22.28 mA/cm^2, fill factor = 74.95%) by this new process (see Figure 3). We believe that this is the highest NREL-confirmed efficiency ever reported for any thin-film solar cell with both the TCO and the CdS layer deposited at room temperature.

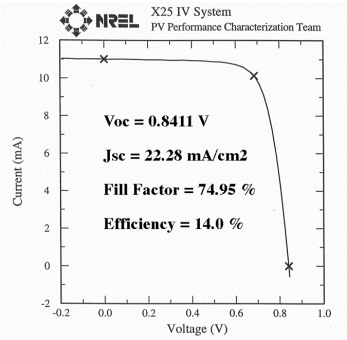

Figure 3. I-V curve of a Cd_2SnO_4/Zn_2SnO_4/CdS/CdTe cell prepared by the new process.

Our device results also demonstrated that CdTe cells prepared by this process have good uniformity and reproducibility, which is desirable for scaling-up a process. Table 1 shows the I-V data of four cells prepared from one substrate. We believe that this excellent device uniformity is from both the CSS and RF sputtering techniques. The good uniformity of devices can help reduce the efficiency gap between the small-area cells and the modules. Preliminary results of device reliability accelerated testing indicate that the CdTe cells prepared by the new process have similar behavior with NREL base-line CdTe cells and no extra degradation from the simplified process. The device was stressed at 100°C and in light of 2 suns, and the acceleration factor is 500-1000.

Table 1. Uniformity of CdTe cells prepared by the new process.

Device #	V_{oc} (mV)	J_{sc} (mA/cm^2)	FF (%)	η (%)
W331-A	840	22.9	73.3	14.1
W331-B	838	22.5	73.2	13.8
W331-C	835	23.3	72.9	14.2
W331-D	835	23.3	71.5	13.9

Potential Benefits from the New Process

1. This process can significantly reduce the thermal budget, because the first three layers are deposited at room temperature and the entire process has only one heat-up segment.
2. This process can significantly reduce the process time, thus increasing the throughput. Because the first three layers are deposited at room temperature, therefore no time is required for substrate heat-up and cool-down. In addition, because the first three layers are prepared by the same RF sputtering, thus no time is required for substrate loading and unloading.
3. This process can provide high yield, because all layers are prepared by two compatible deposition techniques: CSS and RF sputtering. Substrates can stay in vacuum through the entire process, and devices have very clean interfaces. In addition, devices prepared by the new process have no adhesion problems due to integrating the ZTO buffer layer.
4. This process can produce high-performance CdTe cells with good uniformity, good reproducibility, and acceptable device stability.

Conclusions

We have developed a low-cost manufacturing friendly process with the potential of high throughput for fabricating CdTe solar cells. CdTe cells prepared by this process have good performance, good uniformity, acceptable device stability, and excellent reproducibility. These results, coupled with the improved process manufacturability, will draw significant industrial interest. We also demonstrated the highest NREL-confirmed efficiency (14.0%) ever reported for any thin-film solar cell with both the TCO and the CdS layer deposited at room temperature.

Aknowledgments

The authors would like to thank all members of the NREL CdTe group for their technical support, and Prof. J. Sites and P. Johnson at CSU for device acceleration testing. This work is supported by U.S. Department of Energy under contract No. DE-AC36-99GO10337 to NREL.

Photoluminescence of CdTe:Cu and CdS:Cu Single Crystals

D. Grecu,[1] K. J. Price,[2] and A. D. Compaan[2]

[1]Present Address: First Solar, LLC, Toledo, OH
[2]The University of Toledo, Toledo, OH 43606

ABSTRACT

We have studied the photoluminescence (PL) of single crystal CdTe and CdS diffusion-doped with copper and annealed in various ambients in order to identify the behavior of Cu-related defect states active in recombination processes in the polycrystalline thin-films of these materials. The results help to identify the possible roles of Cu in some CdS/CdTe thin-film solar cells.

1. Introduction and Overview

Cu is often used in the formation of a back contact to CdTe/CdS solar cell devices. Recently, Asher has presented SIMS data indicating that in some cases, Cu can diffuse into both CdTe and CdS layers during device fabrication,[1] and understanding the behavior of Cu in these materials is important. Photoluminescence (PL) is a powerful technique to study the electrically active states in semiconductors. While CdTe/CdS devices are typically fabricated with polycrystalline films, PL in polycrystalline films is often difficult to interpret due to the presence of grain boundaries. We therefore present results of PL in CdTe:Cu and CdS:Cu single crystals doped by diffusion of thermally evaporated Cu.

In CdTe:Cu our results are consistent with some Cu atoms occupying substitutional positions on the Cd sublattice, and with others forming Frenkel pairs involving an interstitial Cu and a Cd vacancy. In addition, we find that Cu-related states in CdTe:Cu samples exhibit a significant reversible "aging" behavior. The reversible behavior is paralleled by changes in carrier concentration of polycrystalline CdTe:Cu films, and changes in open circuit voltage in CdTe/CdS devices, indicating that the observed Cu-related PL is related to metastable behavior in CdTe/CdS devices. In CdS:Cu, we show evidence of an exciton bound to a Cu-related site that is stable under short-term light illumination.

2. Sample Preparation

The single-crystal substrates used in this study were grown by the Bridgman method and were obtained from eV Products and Cleveland Crystals. Cu doping was achieved from a 15-20 nm thick, high-purity elemental Cu layer deposited on the surface of the crystals by thermal evaporation. Samples with and without a Cu layer were annealed at various temperatures in evacuated, sealed quartz tubes either alone (no overpressure) or with Cd, S, or $CdCl_2$ powder. Photoluminescence (PL) spectra were recorded at 10K. The excitation was achieved with the 752.5 nm line of a Kr laser or the 476.5 nm line of an Ar laser. Luminescence was collected using a triple-grating spectrometer and CCD detector. All spectra were corrected for the spectrometer/detector response.

3. PL of Copper-Doped CdTe

Figure 1 shows the 10K PL spectra of a CdTe sample before and after diffusion with Cu at 200 C for 1 hour, along with proposed assignments for several transitions. The spectrum of an undoped sample can be divided into three main regions: a) a cluster of bound exciton (BE) transitions in the region 1.58-1.60 eV; b) a strong donor-acceptor pair (DAP) transition at 1.55 eV and its phonon replicas at 1.53, 1.51, and 1.49 eV; c) a broad "defect" band ranging approximately from 1.40 to 1.52 eV and consisting of several shallow donor – deep acceptor transitions and phonon replicas. The strong DAP transition at 1.55 eV has been attributed to a transition between a hydrogenic donor and a Cd vacancy (V_{Cd}) acceptor state.[2]

After Cu diffusion, the PL spectrum is markedly different (Fig. 1). The BE region is now dominated by a transition at about 1.59eV, the transition at 1.55eV is strongly attenuated and a new strong "defect" band emerges at about 1.45eV. A bound exciton at 1.5896 eV (X, Cu_{Cd}) and a DAP transition at 1.45eV were previously attributed to Cu_{Cd}. In addition, when the PL spectrum is acquired shortly after diffusion with Cu, a new transition, at approximately 1.555eV can be observed. This transition is accompanied by 3-4 phonon side-bands which is indicative of a strong lattice coupling. Transitions with similar characteristics were observed in Ag[3] and Au[4] doped CdTe samples and tentatively assigned to the recombination of excitons bound to M_i-V_{Cd} or M_i-M_{Cd} complexes (where M = Ag, Au). The strong lattice coupling could be attributed to the lattice strain introduced by the interstitial atom.

We find that the intensity of Cu-related features in the PL spectrum decreases substantially after several days of room-temperature storage for both single crystal and polycrystalline[5] samples. We also observe a factor of 5 decrease in the carrier concentration in polycrystalline CdTe films and a drop in the open-circuit voltage of the CdS/CdTe solar-cell devices doped with Cu[5]. The

aging effect appears accelerated by exposing the samples to white-light radiation. Figure 2 illustrates the changes in the PL signal for a Cu- doped single crystal CdTe sample (1) immediately after diffusion (30 min., 200C), (2) after 90 hours of illumination (200W/cm^2) at room temperature and (3) after a re-anneal (30 min., 200 C).

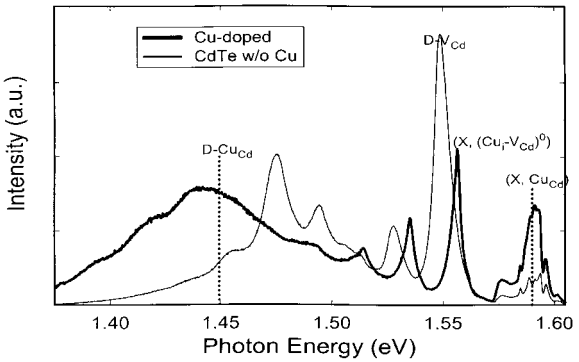

Figure 1. PL of CdTe without Cu, and CdTe:Cu immediately after Cu diffusion

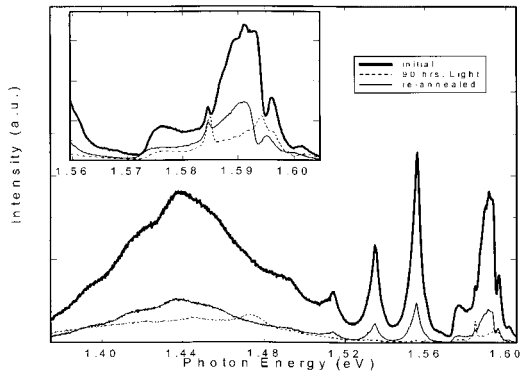

Figure 2. PL of CdTe:Cu immediately after diffusion, after 90 h light exposure, and after re-anneal

The illumination of the sample was achieved using a tungsten-halogen incandescent light source. In the light-soaked sample we note a major decrease of the PL signal including the intensities of the 1.45 eV band, the 1.59 eV bound exciton, and the complex line at 1.555eV. These aging effects are consistent with the dissociation of Cu_{Cd} and Cu_i+-V_{Cd}- states discussed previously. In addition, we attribute the overall decrease in the PL signal to the formation of Cu-related non-radiative recombination centers (possibly Cu precipitates). We find that the PL spectrum, carrier concentration, and open circuit voltage can be restored by re-annealing the samples. This effect is paralleled by a recovery of the open-circuit voltage of the CdS/CdTe devices.

4. PL of Copper-Doped CdS

CdS:Cu samples were diffused at 385 C for 1 hour and compared to as-grown CdS. PL from as-grown CdS was dominated by a bound exciton at 2.546 eV. After Cu diffusion, this center was replaced by a bound exciton at 2.542 eV. The Cu-related center appeared in all Cu-containing samples, whether the Cu diffusion was done with no overpressure, or in the presence of Cd, S, or $CdCl_2$ powder. Samples containing no Cu that were annealed under similar conditions did not exhibit the 2.542 eV feature.

The Cu-related center was tested for stability under short-term aging or light soaking. After several days at room temperature and atmosphere, no changes were observed in Cu-related PL. In addition, 15 hours of 1-sun light illumination did not affect the Cu-related PL.

5. Conclusion

We have observed emission due to Cu-related centers in CdTe:Cu and CdS:Cu. In CdTe:Cu, these centers are metastable under room-temperature aging or light-soaking, and these changes are correlated with a decrease in the open-circuit voltage in CdTe/CdS photovoltaic devices. In CdS:Cu, the Cu-related emission is stable under short-term aging and light-soaking.

6. Acknowledgments

We are pleased to acknowledge the support of NREL in this work. In addition, helpful advice has been received, *inter alia,* from Bolko von Roedern and from Doug Rose.

7. References

[1] S. Asher, presentation at National CdTe Team Meeting, Golden, CO, January, 2000.

[2] J.M. Figueroa, F. Sanchez-Sinencio, J.G. Mendoza-Alvarez, O. Zelaya, C. Vazquez-Lopez, and J.S. Helman, *J. Appl. Phys.* **60**, 452 (1986).

[3] J.P. Chamonal, E. Molva, J.L. Pautrat, L. Revoil, *J. Cryst. Growth* **59**, 297 (1982).

[4] E. Molva, J.M. Francou, J.L. Pautrat, K. Saminadayar, Le Si Dang, *J. Appl. Phys.* **56**, 2249 (1984)

[5] D. Grecu, A. D. Compaan, 15th NCPV Program Review Proceedings, p. 224, (1998)

Processing Effects on Junction Interdiffusion in CdS/CdTe Polycrystalline Devices

D. Albin, Y. Yan, D. King, H. Moutinho, K. Jones, R. Matson and M. Al-Jassim

National Renewable Energy Laboratory

1617 Cole Blvd., Golden, CO 80401

ABSTRACT

The performance of CdS/CdTe solar cells is strongly impacted by the process used to grow the CdS layer. CdS films grown by chemical-bath deposition (CBD) exhibit lower optical absorption than similar films grown by close-spaced sublimation (CSS). CBD-CdS films also form in a cubic phase structure while CSS-CdS films show a strong degree of hexagonality. During the initial growth by CSS, the CdTe structure is influenced by the CdS structure. Hexagonal CdS nucleates hexagonal CdTe. Similarly, cubic CdS favors the formation of cubic CdTe. Both polytypes show similar optical bandgaps. Alloying is not detectable during the initial stages of growth in either case. Auger Electron Spectroscopy (AES) depth profiles through the CdS/CdTe interface in finished CdTe devices, grazing-incidence x-ray diffraction (GIXRD) of the CdTe alloy region, transmission electron microscopy (TEM) with energy-dispersive x-ray (EDS) analysis, and scanning electron microscopy (SEM), are combined to show how CdS type impacts interdiffusion at the CdS/CdTe interface.

1. Introduction

Previously, we observed that changing the process used to grow CdS films (either CSS or CBD processes) had a serious impact on device performance [1]. Replacing CBD-CdS films with CSS-grown CdS resulted in open-circuit voltage, V_{oc}, drops of 100 - 150 mV. Because of the magnitude of this effect, it was believed that futher CdS/CdTe interfacial studies using these types of CdS were warranted in understanding how V_{oc} at the interface was affected.

In this paper, we combine previous results with new data obtained by TEM to arrive at a model for how interdiffusion occurs at the CdS/CdTe interface. These differences may explain differences in V_{oc} observed with these types of CdS.

2. Experimental Procedure

CBD CdS films of variable thickness were grown by a standard process involving the titration of Cd-acetate solutions with a thiourea base [2]. CSS-CdS films of similar thickness were grown by CSS in a helium ambient using a process previously described [1].

CdTe films were then deposited by CSS on 800-Å-thick CdS samples, using oxygen ambients of 0, 1, and 1.5 torr in 16 torr total ambients with He as the balance. CdTe source temperatures of 660°C and substrate temperatures of 620°C were used. *Thin-Layer* CdTe samples (100-400 nm) were made by decreasing deposition time to 1-5 seconds, depending upon oxygen level used. Higher oxygen concentrations required longer deposition times due to the growth-moderating effects of oxygen [3].

GIXRD measurements were performed on both as-grown CdS films and *thin-layer* samples to ascertain the CdS structure effects on CdTe growth. XRD scans were performed at angles near the critical angle (0.291° for CdTe) for total reflection as well as at higher angles up to 2.0° to probe structure as a function of depth. Optical reflection and transmission measurements were also performed on these samples to determine the optical gap of the deposited CdTe layer, and therefore the alloy composition that forms during initial film growth.

Device-representative thick samples (~8 microns; process terminated *before* the backcontact) were prepared for both lift-off analysis and TEM analysis. The lift-off technique involves epoxying a glass plate on top of the CdTe/CdS/TCO/7059 glass structures and then separating the glass layers. Such a method reveals the alloy region and CdS layers for direct analysis.

Finally, *device-representative* samples were prepared for electron microscopy by first mechanical polishing them to ~100 μm thickness, then dimpling the central portion of the specimens down to ~5 μm. The samples were subsequently thinned by using a 4 kV Ar ion-beam at 14° inclination. A liquid-N_2 cooling stage was used in order to minimize milling damage. TEM images were taken on a Philips CM30 microscope operating at 300 kV. The probe size was approximatly 60 nm.

3. Results and Discussion

Significant differences were observed in the optical and structural properties of as-grown CBD and CSS-CdS films. XRD data show only low intensity, broad peaks corresponding to the cubic phase of CBD-CdS. In contrast, CSS-CdS reflections are sharper, and show peaks corresponding to the hexagonal phase of CdS. Optical absorption in CSS-CdS films is higher. While the bandgap of CBD-CdS films decreases from 2.5 to less than 2.4 eV as film thickness increases, the bandgap for CSS-CdS films remains constant at about 2.42 eV. The grain size of CSS-CdS films was also found to be much greater (100 - 500 nm depending upon thickness) than CBD films (limited to ~30 - 50 nm).

GIXRD analysis of *thin-layer* CdTe deposited on different CdS substrates shows clearly that hexagonal CdTe nucleates when CSS-CdS is used, and cubic CdTe nucleates when CBD-CdS is used. The tendency for hexagonal CdTe to nucleate increases as oxygen in the growth environment increases. The dependence of CdTe nucleation on CdS type is intriguing in two regards. Recently, it has been predicted that differences in both valence and conduction band offsets can occur at CdS/CdTe interfaces depending upon which phase of CdS is present [4]. Also, if crystal field splitting is significant, so as to minimize thermalization effects, V_{oc} could be perturbed through differences in valence-band density of states which might exist between cubic and hexagonal CdTe.

XRD peak positions of *thin-layer* CdTe on different CdS films did not reveal either differences in initial alloying

behavior (i.e., contrasting CSS and CBD CdS) nor any alloying whatsoever. The optical bandgap of the *thin-layer* CdTe was determined to vary from 1.48 to 1.50 eV using $(\alpha h\nu)^2$ vs energy plots, again suggesting little initial alloying. No correlation between structure, oxygen, CdS type and bandgap was observed.

GIXRD analysis of lift-off samples prepared from both vapor $CdCl_2$ and non-$CdCl_2$ treated cells could not detect the presence of any hexagonal CdTe at the CdS/CdTe interface. It therefore appears that the initial hexagonal CdTe phase is transitory during growth.

TEM cross-sections of both types of interfaces did reveal a very unique difference between CSS and CBD-CdS films. As shown in Figure 1, the presence of the 80 nm (pre-CdTe measured) CBD CdS layer is clearly visible as a discrete layer between the SnO_2 and CdTe layers. However, the 70 nm (pre-CdTe measured) of CSS-CdS appears to be absent.

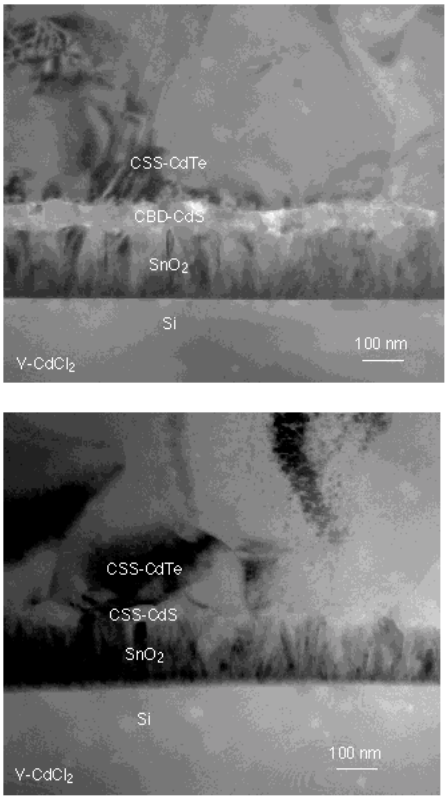

Fig. 1 TEM cross-sections of CBD CdS/CdTe (top) and CSS CdS/CdTe (bottom) devices.

This is a very interesting observation. Previous reports would support enhanced diffusion in smaller grained CBD CdS[1,5]. GIXRD data of lift-off samples clearly show, for example, that the degree of alloying at the CBD CdS/CdTe interface is much greater (~12 at.% S) than in the the CSS CdS/CdTe case (~2-3 at.%S) [1]. However, recent AES depth profiles shown in Figure 2 seem to indicate much greater penetration of S into the CdTe layer when CSS-CdS films are used [6]. Surface S levels of only 3 at.% (identified by GIXRD) and long-penetrating S "tails" identified by AES strongly suggest enhanced grain boundary diffusion for the CSS-CdS samples. This has now been substantiated by the TEM data. The penetration of S (and similar, albeit smaller, penetration of Te into CdS) is also a strong function of the

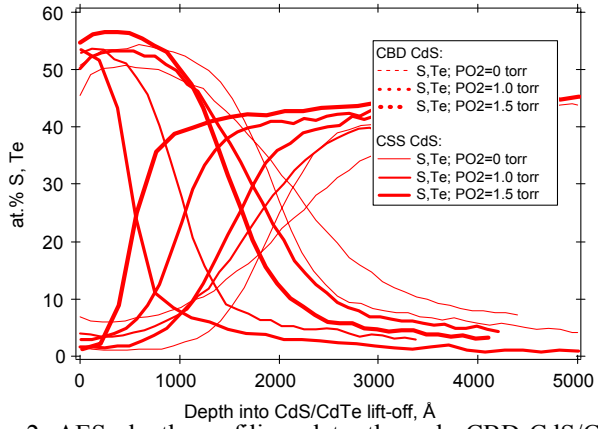

Fig. 2 AES depth profiling data through CBD-CdS/CdTe (dotted lines), and CSS-CdS/CdTe (solid lines) interfaces (lift-off samples)

oxygen present during the CSS growth of CdTe (as indicated in Figure 2). Increasing oxygen minimizes interdiffusion of

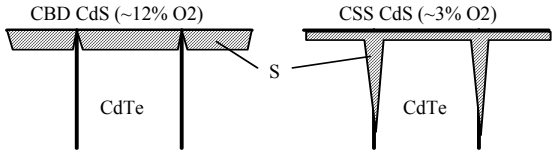

Fig. 3 Interdiffusion Models for CBD and CSS CdS/CdTe interfaces

both species. The reason why interdiffusion for CBD CdS is less than CSS CdS (in Fig. 2) may be that CBD CdS has much more residual oxygen (12 vs. 3 at.%) prior to CdTe deposition.

Combining data from GIXRD results [1], AES studies [6] and TEM (this study) suggests two consistent but different modes (dependent upon CdS type) for interdiffusion as shown in Figure 3.

In the case of CBD CdS, alloying is limited by bulk diffusion across the CdS/CdTe interface parallel to the substrate, possibly due to grain boundary oxides. In the CSS CdS case, less oxygen makes grain boundary diffusion the more favorable path, such that the same bulk diffusion is limited to only 3-4 at.% at the CdS/CdTe planer interface. The impact on V_{oc} will be different in both cases. In particular, total consumption of the CSS-CdS layer is problematic since TCO/CdTe interfaces are believed to be electrically inferior to TCO/CdS/CdTe interfaces.

4. References

1. D. Albin, D. Rose, R. Dhere, D. Levi, L. Woods, A. Swartzlander-Guest, and P. Sheldon, Proc. 26th IEEE Photovoltaic Specialists Conf., p. 367 (1997).
2. D. Rose, F. Hasoon, R. Dhere, D. Albin, R. Ribelin, X. Li, Y. Mahathongdy, T. Gessert, and P. Sheldon, Prog. Photovolt: Res. Appl. 7, p. 331 (1999).
3. D. Rose, D. Levi, R. Matson, D. Albin, R. Dhere, and P. Sheldon, Proc. 25th IEEE Photovoltaic Specialists Conf., p. 777 (1996).
4. S. Wei, and S. Zhang, submitted to Phys. Rev. (B).
5. C. Ferekides, K. Dugan, V. Ceekala, J. Killian, D. Oman, R. Swaminathan, and D. Morel, Proc. 24th IEEE - WCPEC, p. 99 (1994).
6. D. Albin, R. Dhere, A. Swartzlander-Guest, D. Rose, X.Li, D. Levi, D. Niles, H. Moutinho, R. Matson, and P. Sheldon, Mat. Res. Soc. Symp. Proc., vol. 485, p. 215 (1998).

Sputtered ZnTe:N Back Contacts to CdS/CdTe Solar Cells

K. Makhratchev, K.J. Price, X. Ma, D.A. Simmons, J. Drayton, A.D. Compaan
The University of Toledo, Department of Physics and Astronomy
Toledo, OH 43606

ABSTRACT

We report on the development of reactively-sputtered, nitrogen-doped back contacts for CdS/CdTe solar cells using Ar/N_2 mixtures as the process gas. We achieved reproducible *p-type* doping of the zinc telluride. The properties of both intrinsic and nitrogen-doped zinc telluride films were investigated. The conductivity of the doped films was about five orders of magnitude higher than that of intrinsic ones; the mobility of the doped films was less than 1 ohm-cm and carrier concentration, as measured by lateral Hall data, was in the high 10^{18} cm^{-3}.

These zinc telluride films were used as contacts for SnO_2/CdS/CdTe solar cells. The ZnTe/ZnTe:N/Ni based contacts showed slightly lower initial performance but improved stability (3000+ hours at 100 ^oC) compared to our evaporated Cu/Au contacts.

1. Introduction

The introduction of small partial pressures of N_2 with the Ar process gas in an rf plasma can lead to the production of atomic N which is known to be an excellent p-type dopant in II-VI semiconductors such as ZnTe and ZnSe. Although nitrogen doping has been quite successful with the use of plasma sources in molecular beam epitaxy,[1,2] to our knowledge nitrogen doping has not been reported in sputter deposition of these semiconductor materials.

In addition, Meyers[3] has shown that ZnTe can be used as part of a back contact structure for CdS/CdTe cells, and Gessert, *et al*[4] and Ohno, *et al*[5] have used ZnTe doped with copper for contact to CdTe. However, in the case of ZnTe:Cu, it has been shown that the Cu can diffuse into the CdTe and even through the CdTe into the CdS front heterojunction partner.[4]

2. Reactive sputtering for ZnTe:N

In this work we have extended some of our previous work on reactive sputtering of ZnTe with nitrogen in the process gas.[6,7] Here we provide details on the reactively sputtered ZnTe:N films with high p-type carrier concentrations and report on the successful use of this material for back contacts in CdS/CdTe solar cells. The properties of both intrinsic and doped ZnTe sputtered films were studied.

The undoped zinc telluride films approximately 0.8 μm thick had bulk resistivity in the range of 0.5 to 1.0 MΩ·cm. For increasing thickness, the resistivity of the undoped ZnTe films decreased, presumably due to the increasing grain size in the thicker films. That is, the resistivity was measured in the lateral direction with a parallel stripe geometry and as the films grow thicker there are fewer grain boundaries between contacts.

We used reactive sputtering with a N_2/Ar mixture to obtain the nitrogen-doped zinc telluride films. The lowest resistivity of the ZnTe:N films was about 5 Ω·cm; Hall measurements show *p-type* conductivity and carrier concentration of about $4 \cdot 10^{18}$ cm^{-3}.

The influence of several deposition parameters on the quality of the ZnTe:N films was investigated. The critical parameter is the substrate temperature; the film quality is unacceptable if the deposition was performed at temperatures below 200^0C. Another important parameter is the gas mixture flow—about 70 sccm is required to obtain highly doped films. The resistivity was not very sensitive to nitrogen concentration in the range of 1 – 4%. The resistivity data for N_2 fraction from 1.25% to 5% are presented in Fig. 1.

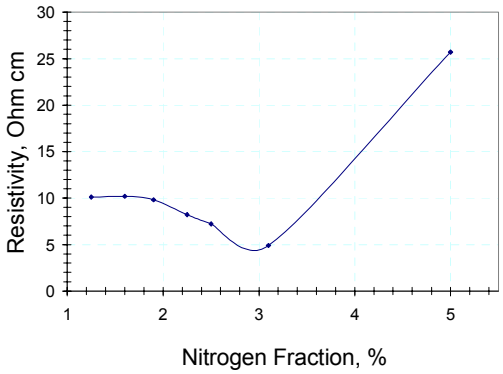

Fig. 1. Resistivity of ZnTe:N films vs. $N_2/(Ar+N_2)$ fraction

3. ZnTe:N for back contacts to CdTe

Nitrogen-doped zinc telluride films were used to contact solar cells on glass substrates with the typical SnO_2:F/CdS/CdTe structure. The schematics of the

solar cell structure with the ZnTe bilayer back contact is presented in Fig.2.

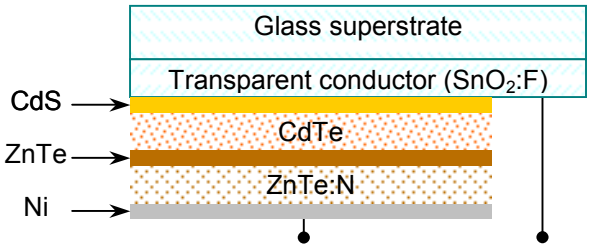

Fig. 2. Solar cell with ZnTe bilayer back contact.

We found that good solar cell performance could be obtained with a contact structure which utilized a bilayer ZnTe structure with an undoped ZnTe layer at the CdTe interface approximately 0.05 µm thick followed with a ZnTe:N layer approximately 0.1µm thick. This is analogous to the structure used by Gessert, *et al* [4] which, however, involved ZnTe doped with Cu.

The contact was completed with a layer of Ni deposited by dc sputtering at a power of 840 W from a six-inch magnetron.

Tests of initial performance (Table 1) and long-term stability (Fig. 3) were performed using an ELH lamp. We estimate this lamp results in I_{sc} and Eff values approximately 10% too high. The ZnTe-based contacts showed superior stability compared to Cu/Au ones although the ZnTe-contacted cells began with slightly lower initial performance. The stability results for a 3000-hour testing cycle at 100^0C in the dark are shown in Fig.3. The figure shows a representative subset of the data. There appears to be some initial rise in efficiency followed by a some short-term decrease and then stable performance. These structures are being tested further under a variety of stress conditions.

Table 1. Initial solar cell parameters: efficiency (Eff), open-circuit voltage (V_{oc}), short-circuit current (I_{sc}), and fill factor (FF) for Cu/Au and ZnTe:N back contacts. Due to lamp calibration, I_{sc} and Eff are approximately 10% too high.

Contact	Eff, %	V_{oc}, V	I_{sc}, mA	FF, %
Cu/Au A	9.6	0.788	3.58	61.7
Cu/Au B	9.3	0.791	3.56	59.7
ZnTe:N A	9.7	0.736	4.12	58.0
ZnTe:N B	9.6	0.738	4.02	58.4

We believe that the performance of these contacts may be limited by the lack of doping of the CdTe layer, which results in lower open circuit voltages compared to the samples with Cu/Au contacts.

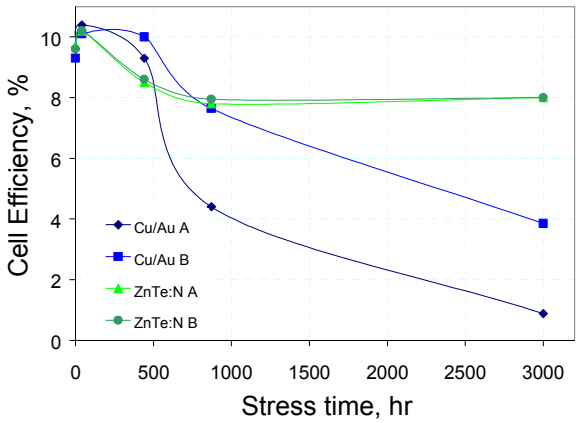

Fig. 3. Stability test results for Cu/Au and ZnTe:N based solar cells. Stress conditions: 100^0C, dark. Two samples for each contacting scheme are plotted (A and B).

4. Acknowledgment

The support of the National Renewable Energy Laboratory is gratefully acknowledged.

5. References:

1. T. Baron, K. Saminadyar, and N. Magnea, Appl. Phys. Lett. **83**, 1354 (1998)
2. S. Kijima, H. Okuyama, Y. Sanaka, T. Kobayashi, S. Tomiya, and A. Ishibashi, Appl. Phys. Lett. **73**, 235 (1998)
3. P.V. Meyers, "Polycrystalline CdS/CdTe/ZnTe n-i-p Solar Cell," 7th European PV Conference (1986).
4. C. Narayanswamy, T.A. Gessert, and S.E. Asher, "Analysis of Cu Diffusion in ZnTe-Based Contacts for Thin-Fiom CdS/CdTe Solar Cells," NCPV Photovoltaics Program Review, ed. by M. Al-Jassim, J.P. Thornton, and J.M Gee, (AIP CP462 p. 248, 1999)
5. D. MOrgan, J. Tang, V. Kaydanov, T.R. Ohno, and J.U. Trefny, "Degradation Mechanisms Studies in CdS/CdTe Solar Cells with ZnTe:Cu/Au Back Contact,"NCPV Photovoltaics Program Review, ed. by M. Al-Jassim, J.P. Thornton, and J.M Gee, (AIP CP462 p. 200, 1999)
6. R.G. Bohn, C.N. Tabory, C.Deak, M. Shao, A.D. Compaan, and N. Reiter, "RF Sputtered Films of Cu-Doped and N-Doped ZnTe," (First World Conference on Photovoltaic Energy Conversion, Hawaii Dec. 5-9, 1994), Proc. 24th IEEE Photovoltaic Specialists Conference 1994, pp. 354-356 (1995).
7. A.D. Compaan, X. Deng, R.G. Bohn, "High Efficiency Thin Film CdTe and a-Si Based Solar Cells", Annual Technical Report, 1999. NREL Contract No. ZAF-8-17619-14.

ZB/WZ Band Offsets and Carrier Localization in CdTe Solar Cells

S.-H. Wei and S. B. Zhang

National Renewable Energy Laboratory

1617 Cole Blvd., Golden, CO 80401

ABSTRACT

Using the first-principles band-structure method, we studied systematically the stability and electronic structure of Cd*X* (*X*=S, Se, and Te) semiconductors with the zinc-blende (ZB) and wurtzite (WZ) crystal structures. We find that the ground-state structure of CdS is WZ, whereas for CdSe and CdTe, it is ZB. However, the total energy differences between ZB and WZ Cd*X* are very small, less than 9 meV/2-atom. Cd*X* in the WZ structure has a larger band gap than the one in the ZB structure. The band alignment on the ZB/WZ interface is type-II, with holes localized on the WZ side and electrons on the ZB side. The predicted carrier localization in a mixed ZB/WZ system can significantly affect device transport properties.

1. Introduction

Unlike most III-V and II-VI semiconductors, Cd*X* (*X*=S, Se, and Te) compounds exist in both ZB and WZ structures or in mixed ZB/WZ phases [1]. Depending on the growth condition, one can stabilize one of the two crystal structures either by epitaxial strain on proper substrates or buffer layers, or by controlling the growth temperature. Understanding the effects of this additional structure freedom in Cd*X* is important for making more efficient and reliable solar cells. In this work, we systematically study the stability and electronic structure of Cd II-VI compounds in both ZB and WZ phases and at the ZB/WZ interfaces using the first-principles band-structure method based on the local density approximation (LDA) [2]. We calculated (a) the equilibrium crystal structures of ZB and WZ Cd*X* semiconductors, (b) the band offsets at the ZB/WZ interface for these Cd compounds, (c) the valence-band splitting at the top of the valence band of WZ Cd*X*, and (d) the carrier localization of valence-band maximum (VBM) and the conduction-band minimum (CBM) states in mixed ZB/WZ systems. In the following, we describe the method of our calculation and discuss the significant physics of the results.

2. Method of Calculations

The band structure and total energy calculations are performed using the LDA, as implemented by the full-potential linearized augmented plane wave (LAPW) method [2]. Large numbers of *k* points for the Brillouin-zone integration and high cut-off energies for the basis functions are used to ensure that the total energy differences between the WZ and ZB phases are converged to within 1 meV/2-atom. All the structural parameters are fully relaxed to minimize the total energy. The band structures are calculated at their respective equilibrium lattice constants [3].

The valence-band offsets ΔE_v(ZB/WZ) for compounds CdX are calculated using the standard approach similar to the photoemission measurement [4]. In this approach, the valence-band offset is given by

$$\Delta E_v(\mathrm{ZB/WZ}) = \Delta E_{\mathrm{VBM},C}(\mathrm{WZ}) - \Delta E_{\mathrm{VBM}',C'}(\mathrm{ZB}) + \Delta E_{C,C'}. \quad (1)$$

Here, $\Delta E_{\mathrm{VBM},C}(\mathrm{WZ})=E_{\mathrm{VBM}}(\mathrm{WZ})-E_C(\mathrm{WZ})$ is the core-level to valence-band maximum energy separations for Cd*X* in the WZ structure, and $\Delta E_{C,C'}=E_C(\mathrm{WZ})-E_{C'}(\mathrm{ZB})$ is the difference in core-level binding energy between Cd*X* in each side of the ZB/WZ interface. We find that, even though the ZB and WZ structures have very similar volumes and local structures, the core-level difference $\Delta E_{C,C'}$ makes a significant contribution to Eq. (1). Thus, it is necessary not only to calculate the bulk Cd*X* in the ZB and WZ phases, but also, to calculate the core-state alignment across the ZB/WZ interface. The conduction-band offsets can be obtained by using the relation $\Delta E_c=\Delta E_g+\Delta E_v$, where ΔE_g is the band-gap difference between the WZ and ZB phases.

3. Results

Although the ZB structure has the cubic space group and the WZ structure has the hexagonal space group, the two structures are in fact very similar; they start to differ only in their third-nearest-neighbor atomic arrangement. Our calculation [3] showed that for Cd*X* in the WZ structure, the calculated *c/a* ratios and the internal structure parameters *u* are very close to the ideal values of *c/a*=1.633 and *u*=0.375, respectively. Thus, the total energies and the direct band gaps at the Γ point for ZB and WZ Cd*X* are expected to be similar [5]. Table I gives the calculated total-energy differences ΔE(ZB/WZ), band-gap differences ΔE_g(ZB/WZ), valence-band and conduction-band offsets ΔE_v(ZB/WZ) and ΔE_c(ZB/WZ) between ZB and WZ Cd*X* compounds, and the valence-band splitting ΔE_{AB}(WZ). We find the following results:

(a) ΔE(ZB/WZ) is negative for CdS, but positive for CdSe and CdTe. These results indicate that at low temperatures CdS is stable in the wurtzite structure, whereas CdSe and CdTe are stable in the zinc-blende structure. However, the total energy differences between the WZ and ZB structures are very small. They are -2, 2, and 9 meV/2-atom. The increase of ΔE(ZB/WZ) as anion atomic number increases from S to Se to Te is consistent with the fact that as anion atomic number decreases, the compound becomes more ionic, thus stabilizing the WZ structure which has a larger Madelung constant than the ZB structure.

Due to the small energy differences between the ZB and WZ phases, the actual crystal structure of Cd compounds is highly dependent on the substrate orientation, growth temperature, and history of annealing. As a test, we calculated the total energy difference ΔE(ZB/WZ) of CdTe strained on a

Table I. Calculated total energy differences $\Delta E(ZB/WZ)$ (in meV/2-atom), band-gap differences $\Delta E_g(ZB/WZ)$, band offsets $\Delta E_v(ZB/WZ)$ and $\Delta E_c(ZB/WZ)$ and the valence-band splitting ΔE_{AB} in the WZ (all in meV).

Properties	CdS	CdSe	CdTe
$\Delta E(ZB/WZ)$	-2	2	9
$\Delta E_g(ZB/WZ)$	69	59	47
$\Delta E_v(ZB/WZ)$	46	35	18
$\Delta E_c(ZB/WZ)$	115	94	65
ΔE_{AB}	18	33	53

WZ CdS (0001) substrate. In this calculation, the lattice constants in the plane are fixed to the one for equilibrium bulk CdS, while the lattice constant perpendicular to the substrate is free to relax. We find that $\Delta E(ZB/WZ)$ is reduced from 9 meV/2-atom for bulk CdTe to zero for the epitaxial CdTe, suggesting that epitaxial CdTe can form more easily in the WZ structure than bulk CdTe can.

(b) The band gaps of the WZ structure are 69, 59, and 47 meV larger than those in the ZB structure for CdS, CdSe, and CdTe, respectively. The increase of the band gap in the WZ structure is due to lower symmetry in the WZ structure, which results in a coupling between the CBM Γ_{1c} state and the splitting VBM Γ_{1v} state [5]. The level repulsion between these two states leads to an upward shift of the CBM, thus, increasing the band gap of the WZ structure. The level repulsion also contributes to the crystal-field splittings at the VBM.

(c) The calculated valence-band splittings $\Delta E_{AB}(WZ)$ between the Γ_{9v} (A) and the Γ_{7v} (B) states are 18, 33, and 53 meV for CdS, CdSe, and CdTe, respectively. The increase of $\Delta E_{AB}(WZ)$ as anion atomic number increases can be explained by the fact that as anion atomic number increases, the band gap decreases; thus, the coupling between the CBM and the Γ_{7v} (B) state becomes larger, pushing the Γ_{7v} (B) state down. Our LDA calculated results can be compared with experimental values [1] of 15 and 25 meV for CdS and CdSe, respectively. It shows that LDA overestimate the splittings by about 25%, consistent with the LDA underestimation of the band gaps.

(d) Due to the crystal-field splitting in the WZ structure, the VBM of the WZ structure is higher than the VBM of the ZB structure. The calculated valence-band offsets between the ZB and WZ structures are 46, 35, and 18 meV, respectively, for CdS, CdSe, and CdTe, decreasing as anion atomic number increases. Using the calculated band-gap differences $\Delta E_g(ZB/WZ)$, the conduction-band offsets are 115, 94, and 65 meV, respectively, for CdS, CdSe, and CdTe. The CBM on the WZ side is higher. This type-II band alignment indicates that in a sample with mixed ZB and WZ phases, the hole state will localize on the WZ region, whereas the electron state will localize in the ZB region. The charge localization will be more significant for the VBM state because the hole effective mass is much larger than the electron effective mass. The degree of the carrier localization decreases as the anion atomic number increases, because $\Delta E_v(ZB/WZ)$ and $\Delta E_c(ZB/WZ)$ decrease from CdS to CdSe to CdTe. These expectations are confirmed [3] by examining our calculated plane-averaged charge distribution of the VBM and CBM of $(ZB)_6/(WZ)_6$ superlattice for CdS, CdSe and CdTe .

The predicted band alignment and carrier localization in a mixed ZB/WZ system are expected to have significant effects on the electronic and transport properties of Cd compounds and the affect their device applications. For example, in a p-CdTe/n-CdS solar cell, formation of a thin-layer WZ CdTe on the WZ CdS substrate (Fig. 1) can reduce the minority-carriers (electrons in CdTe and holes in CdS) collection, thus reducing the cell efficiency. This is because WZ CdTe has a higher VBM than ZB CdTe. Thus, holes generated in CdS will be trapped in WZ CdTe before they can be collected by ZB CdTe. On the other hand, ZB CdTe has a lower CBM than WZ CdTe. The electrons have to overcome an unfavorable spike before they can be collected by CdS. The effect of minority-carrier trapping will be even larger if the

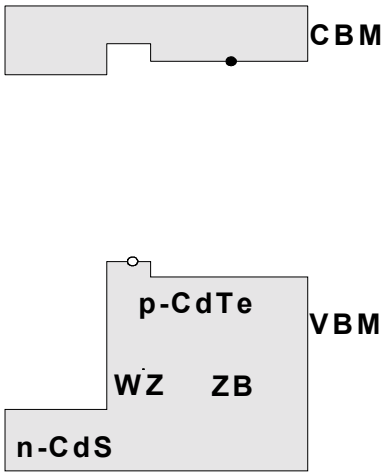

Fig. 1. Schematic plot of the band alignment at the n-CdS/p-CdTe interface.

WZ CdTe near the interface is strained on the WZ CdS substrate because the epitaxial strain will move up the VBM of WZ CdTe by 0.53 eV and the CBM by 0.30 eV, thus enhancing the energy barriers (Fig. 1).

REFERENCES

[1] Landolt-Bornstein: Numerical Data and Functional Relationships in Science and Technology, edited by O. Madelung, M. Schulz, and H. Weiss, Vol. **17b**, (Springer-Verlag, Berlin, 1982).

[2] S.-H. Wei, S. B. Zhang, and A. Zunger: First-principles calculation of band offsets, optical bowings and defects in CdS, CdSe, CdTe, and their alloys, *J. Appl. Phys*. **87**, 1304 (2000).

[3] S.-H. Wei and S. B. Zhang: Structure stability and carrier localization in Cd-based semiconductors, unpublished.

[4] S.-H. Wei and A. Zunger: Calculated natural band offsets of all II-VI and III-V semiconductors: chemical trends and the role of cation d orbitals, *Appl. Phys. Lett*. **72**, 2011 (1998).

[5] C.-Y. Yeh, S.-H. Wei, and A. Zunger: Relationships between the band gaps of the zinc-blende and wurtzite modifications of semiconductors, *Phys. Rev. B* **50**, 2715 (1994).

ADDENDUM TO THE PROCEEDINGS

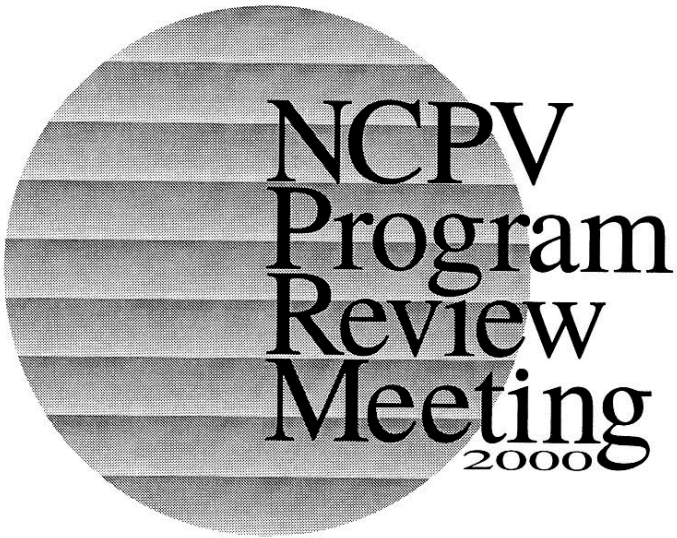

April 16–19, 2000

Adam's Mark Hotel

Denver, Colorado

NREL

Sandia National Laboratories

TABLE OF CONTENTS

A Perspective on International Photovoltaic Challenges & Opportunities for Rural Development

Roger W. Taylor

National Renewable Energy Laboratory

1617 Cole Blvd., Golden, Colorado 80401

ABSTRACT

International market opportunities for the sale and deployment of Photovoltaic (PV) systems abound and will continue to out-pace domestic, grid-connected opportunities for the foreseeable future. There are presently over 6 billion people on the planet; 4.8 billion, or 80%, live in developing countries. Over the next 25 years, the world's population is expected to grow from 6 billion to 8 billion. And 97% of of the growth will be in the developing world. The opportunity for tapping into this market is enormous, but it will require a multi-year, sustained commitment to a broad systematic approach.

1. Setting the Stage

Over 6 billion people presently inhabit the planet; 1.2 billion of these live in the U.S. and other developed countries while the other 4.8 billion, or 80% of the world's population live in developing countries. Three billion of them live on less than $2 per day. Two billion of them live in rural areas. And 2 billion of them do not have access to electric power and the applications powered by electricity. These 6 billion will grow to 8 billion people over the next 25 years, and 97% of these people will live in developing countries. Figure 1 dramatically depicts this increasing shift of the population balance.

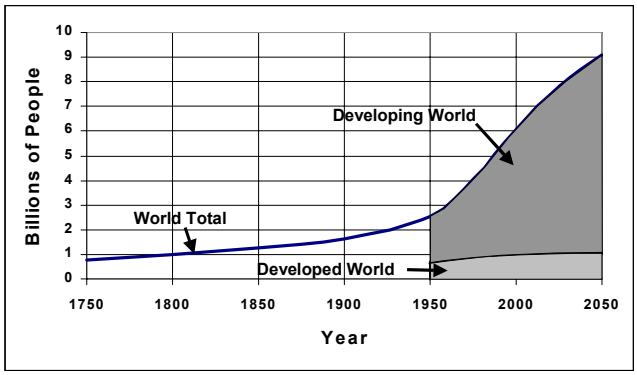

Fig. 1. World Population Growth and Projections (U.S. Census Bureau)

Given this population trend, and the coupled desire for development, at least three things are clear:

- The major market opportunities for renewable energy, PV in particular, are in the developing world,
- The reality of these markets will be constrained by the pace of development in these countries, and
- Accessing these markets will depend on defining and implementing sustainable product delivery pathways.

2. Key Market Sectors

The key market sectors for rural PV-based development include home systems, public-area lighting, schools, health clinics, water pumping and purification, micro-enterprise development, rural telecommunications, and diesel-hybrid power-system retrofits. PV is uniquely well positioned to make major inroads into all of these markets. However, more attention needs to be focused on productive uses (local enterprise development) and less on purely consumptive uses (home lighting) if rural economies are going to grow and be able to afford even larger and more productive PV applications. A systems approach that includes attention to policy and markets, as well at technology is required for success.

3. Business Challenges

Synergies between programs must also be pursued in order to build sustainable local-business capacity. The project opportunities for delivery of social programs (power for schools and health clinics) must be coupled with the additional vision of providing sales and financing to both individual households and businesses. One of the most important lessons learned over the past decade has to do with the relationship between business density and sustainability. The best current information suggests that the minimum business density (or "critical mass") is several thousand stand-alone installations in a geographically serviceable area (maybe 50 km).

Once this level of business density is achieved, a revenue stream can be created that can maintain the local service capacity. Unfortunately, programs are continuing that focus exclusively on highly dispersed schools or health clinics. While well intentioned, experience has shown that within usually 5 years), the inevitable battery failure, or other minor problems become a major issue without local service capability. NREL international program activities now advocate the delivery of social services as a kind of "anchor tenant" in development and implementation of sustainable delivery pathways. Every effort must be made to build local business capability as an integral part of every new rural PV-deployment program.

Business synergies are also becoming apparent, but we are still at the experimental stage in implementation. One of the most intriguing strategies at the moment is the

possibility of micro-enterprise development coupled with rapid expansion of e-commerce and advanced telecommunications. Rural e-commerce can bring cash into rural areas through access to global markets. Each element of this strategy requires power. Most often, PV power.

4. New Analysis Tools for Rural Electrification

From a national electrification perspective, a suite of new analysis tools are becoming available. Until now, rural electrification relied on either grid extension or installation of an isolated diesel engine-generator set. Now a suite of new renewable technologies are becoming available, but the tradeoffs and confusion about what is the best option to pursue can quickly become overwhelming. Even the analysis of retrofit options for rural diesel generators can be a challenge.

Over the past 5 years, the NREL PV program has contributed to the development of a family of computer-based analysis tools that help simplify this problem.

HOMER (the Hybrid Optimization Model for Electric Renewables) is a design optimization model that determines the configuration, dispatch, and load management strategy that minimizes the life-cycle costs for a particular site and application. It is fully functional to evaluate diesel-PV-wind-battery technology options. Code development is underway to include micro-hydro and biomass power.

ViPOR (the Village Power Optimization Model for Renewables) optimizes the power distribution system for a rural village and is being extended to assist with the question: "When should I stop extending the power grid and start considering village-scale hybrid power systems?"

Hybrid 2 is a tool designed to accurately predict the long term performance of a wide variety of power systems made up of conventional fuel generators, wind generators, PV, and energy storage through batteries. It is an engineering analysis tool that allows enormous system configuration flexibility, and the inclusion of company and model-specific technical characteristics.

These analysis tools are becoming increasingly important to the NREL PV and wind international program activities; programs which are now increasingly focused on technical assistance to developing countries. This assistance includes analysis of policy reforms, large scale project preparation, training, resource assessment, and implementation. Figure 2 depicts the multi-dimensional aspects of the NREL international programs.

5. Pathways to the Future

As the global experience in rural renewables-based rural electrification continues, it is increasingly apparent that

- Technology availability, cost, performance, and reliability are not the pacing issues, and
- Availability of project and program financing is not the pacing issue.

The pacing issues are clearly defining, developing and implementing the product delivery and revenue collection pathways. There must be a focus on sustainable energy enterprises. A number of increasingly large scale experiments focused on one or another of these sustainable enterprise pathways are underway throughout the world. Each pathway has its own pros and cons, which are different in each country due to cultural, regulatory, policy, financing, technical capability, and "starting point" differences. Possible pathway options include

- Individual retailers and entrepreneurs
- Traditional rural electric cooperatives
- Local village-based power associations
- Rural energy services companies
- Private voluntary organizations

Additionally, some of these pathways lend themselves to a possible franchise model (a "McSolar" type concept), and some may benefit from the concept of rural-geographic concessions that grant the exclusive right-to-serve in return for meeting certain responsibilities (like "universal access").

While we do not yet know which of these approaches will eventually dominate, we do know that the successful approaches will operate efficiently in both

- The delivery of high quality services (for a variety of applications ranging from homes to school to health clinics to local businesses), and
- They will find a way to effectively collect revenues, probably on a fee-for-service basis.

The wide range of services helps meet the business-density requirement, and the fee-for-service approach decouples the revenue from the traditional, often subsidized, low-perceived-cost kWh approach.

For those that figure out how to effectively meet these criteria in a manner that can be replicable and locally sustainable there are huge market opportunities for PV and other renewable technologies throughout the developing world

Fig. 2. The NREL International Programs Activities Cube

One-Year Performance Comparison of a Silicon Cell Concentrator Module to a Flat Plate Module in Northern California

P.J. Verlinden, A. Terao, S. Daroczi, R.A. Crane, W.P. Mulligan, M.J. Cudzinovic and R.M. Swanson

SunPower Corporation, 435 Indio Way, Sunnyvale, CA 94086
Tel: (408) 991-0900, Fax: (408) 739-7713
http://www.sunpowercorp.com

ABSTRACT

The objective of this paper is to report on a one-year field test comparison of a concentrator PV system to a fixed flat plate PV module. A concentrator PV module consisting of a Fresnel lens and a Point-Contact Silicon solar cell was mounted on a two-axis tracking system and tested over a one-year period in Northern California (Sunnyvale, CA). The results are compared to a multicrystalline Silicon flat plate module having a fixed southern orientation and tilt angle equal to the latitude (37 degrees).

1. Introduction

In a recently published paper [1], R.M. Swanson studied the history of concentrator PV and discussed the reasons why concentrator technology has so far not taken a larger segment of the PV market. Concentrator PV seems to be the least expensive alternative of all of the PV technologies for most of the locations in USA. There are many pre-conceived opinions about concentrator PV. One of them is that concentrators are reserved to very sunny locations, like the deserts in the Southwest US (New Mexico, Arizona), and that they do not produce enough energy in other locations where the amount of direct solar radiation is small compared to diffuse solar radiation [3]. The objective of this paper is to demonstrate that concentrators actually work very well, even in winter, in most of the US. Over a one year period, from October 1998 to October 1999, we compared the energy produced by a Fresnel lens concentrator module to a commercial flat plate module.

2. Available Solar Radiation

The annualized energy cost for a given PV system in a particular location is inversely proportional to the total amount of solar energy available per unit area at this location and to the conversion efficiency of such PV system. The concentrating receivers have a small acceptance angle and do not absorb diffuse light. Therefore, they have to track the sun. In theory, if the solar radiation were entirely direct, the gain in energy due to the 2-axis tracking would be about $\pi/2$, or 1.57. However, because of the low acceptance angle of the concentrator system and because the direct radiation is usually only 85% of the total solar radiation, the ratio between the direct solar radiation with 2-axis tracking and the global solar radiation with a fixed receiver is much lower than $\pi/2$, as Figure 1 shows. It varies between 0.61 and 0.97 in Seattle where the amount of direct radiation is quite small compared to diffuse radiation. In Albuquerque, however, the ratio varies between 0.97 and 1.2 [2]. This means that, in order to produce, every month, more energy with a concentrator than with a flat plate module of the same area, the concentrator PV system has to be at least 3% relatively more efficient than a flat plate PV system in Albuquerque, but about 63% relatively more efficient in Seattle.

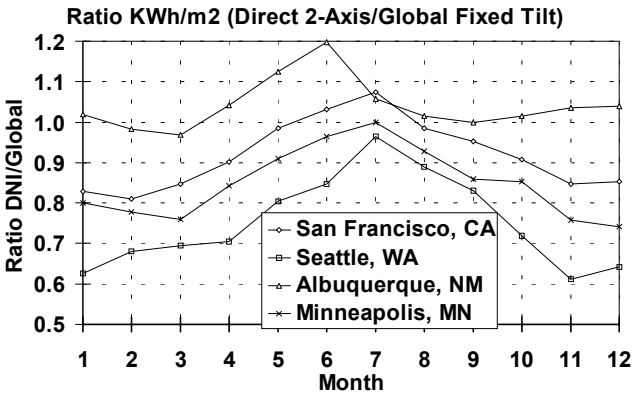

Fig. 1: Ratio of average monthly direct normal solar radiation (kWh/m^2) and global solar radiation for a fixed tilt angle equal to the latitude in four different locations [2].

Considering that the average flat plate module efficiency is around 12% (AM1.5, 25C), a concentrator PV modules should be at least 19.7% (AM1.5, 25C). This efficiency value is already achieved by most high-efficiency, high-concentration PV modules. For example, Point-Contact Silicon solar cells are up to 26.8% efficient at 100X and 25.5% efficient at 275X in a production environment [4]. Optical and interconnection losses are in the range of 15% and 5% respectively, resulting in a module efficiency of 21.6% and 20.6% at 100X and 275X respectively (AM1.5, 25C). We previously demonstrated such high efficiencies, up to 22.9% and 20%, for 88X and 250X concentration ratio respectively [4]. Therefore, with such efficiency, we should expect the concentrator module to outperform the flat plate module in any US location. The following experiment demonstrates it for one location.

3. Experimental Results

A data acquisition system was used to record parameters from both concentrator and flat plate modules every 5 minutes over a one-year period, from October '98 to October '99. The measured parameters were: short-circuit current (Isc), open-circuit voltage (Voc), maximum power current (Imp) and voltage (Vmp), ambient temperature (Ta), direct normal incident power density (DNI), global incident power density at the same angle as the flat plate module

(GIP), backside temperature of the flat plate module (Tfp) and heat-spreader (Tsp) temperature of the concentrator module. From these measured data, efficiencies, power and energy produced were calculated. For the purpose of comparison, the output power and energy were normalized to the module area. The flat plate module is a 145 W rated module, commercially available, consisting of 42 multicrystalline solar cells of 225 cm^2 each. The concentrator module is composed of one 650 cm^2 Fresnel lens concentrating 27.5 W/cm^2 onto a Silicon Point-Contact solar cell of 1.56 cm^2 in active area. The concentrator cell is soldered onto a ceramic substrate and is passively cooled.

The measured efficiencies of the concentrator and flat-plate modules were 16.5% and 10.7%, respectively, at operating temperature, and estimated 19% and 12.5% respectively at 25C cell temperature. Over the 1-year period, the cumulative energy production of the concentrator was more than 37% greater than the flat-plate module (Fig. 3). Surprisingly, even under relatively cloudy conditions, such as those of Northern California in the wintertime, the PV concentrator is superior to the flat-plate most of the time. Conventional wisdom says that concentrators will be effective only in geographic areas with exceptional direct solar resources, such as the desert southwest US. But testing in the relatively cloudy San Francisco Bay area showed that the PV concentrator outperformed the fixed orientation flat-plate module in all but 4 weeks of the year. On a monthly average basis, the concentrator outperforms the flat plate module every single month (Fig. 2). The explanation of this remarkable result is that while PV concentrator output is indeed near zero in cloudy weather, the output of the flat-plate module under the same conditions, while non-zero, is also extremely low. If there are even a few sunny hours in any given week, the performance advantage of the PV concentrator will more than compensate for the small advantage of the flat plate system in low-light cloudy weather.

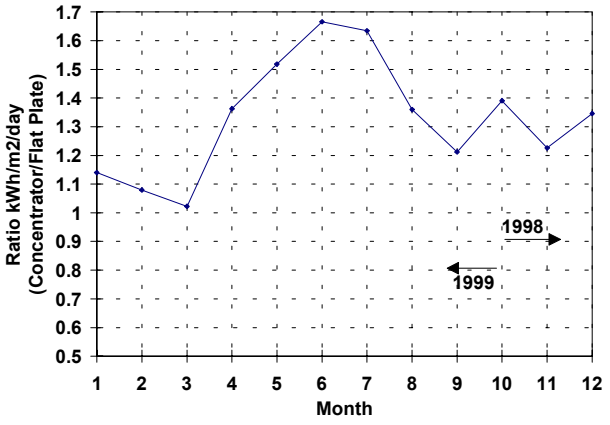

Fig. 2: Ratio of produced energy ($kWh/m^2/day$) by the concentrator and the flat plate module from October '98 to October 1999 in Sunnyvale, CA (month #1 is January 1999).

In the summer months, when demand for electricity is often highest, the concentrator outperformed the flat-plate by as much as 2 to 1 on a daily basis. The ratio of produced energy is greater than 1.65 in June. Because of tracking, the power production of the concentrator is much more level throughout the day than a fixed orientation flat-plate system. This not only leads to higher daily energy production and a higher capacity factor, but also has significant load matching advantages. For example, in sunny climates peak electric load due to air-conditioning occurs late in the afternoon rather than at solar noon.

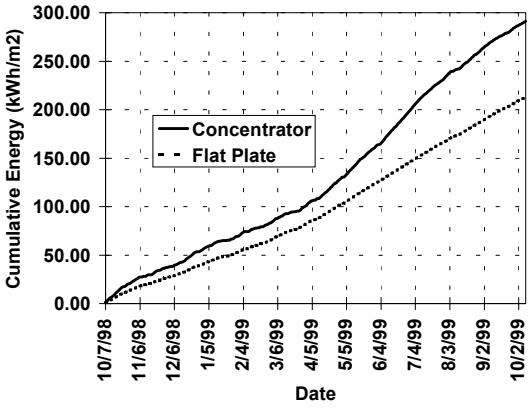

Fig. 3: Cumulative Energy Production (kWh/m2) over one year period in Sunnyvale, CA of a concentrator and a flat plate module.

We are currently in the process of replacing the single-lens concentrator module with a 12 lens concentrator module (120 W rating) populated with improved solar cells. The new concentrator module efficiency is now more than 18% at operating temperature. We will continue the comparison with the fixed flat-plate module. We expect the concentrator module will deliver about 50% more energy than the multicrystalline flat-plate module in Northern California, and even more in desert locations.

4. Acknowledgment

We would like to thank other members of SunPower for their contributions to this work, particularly Matt Piper.

REFERENCES

[1] R.M. Swanson, "The Promise of Concentrators", Progress in Photovoltaic Res. Appl., **8**, pp. 93-111, 2000

[2] "Solar Radiation Data Manual for Flat-Plate and Concentrating Collectors", NREL/TP-463-5607, April 1994

[3] A. Goetzberger and W. Stahl, "Global Estimation of available solar radiation and cost of energy for tracking and non-tracking PV systems, 18th IEEE Photovoltaic Specialists Conference, 1985, pp. 258-262

[4] P.J. Verlinden, R.M. Swanson, R.A. Crane, K. Wickham, J. Perkins, "A 26.8% Efficient Concentrator Point-Contact Solar Cell", 13th EC Photovoltaic Solar Energy Conference, Nice, October 23 -27, 1995, pp. 1582-1585.

ECD's PVMaT Progam: Efficiency and throughput advances in continuous roll-to-roll a-Si alloy PV manufacturing technology

Gennady Bondarenko, Joe Doehler, Tim Ellison, Eric Haggard, Masat Izu, Scott Jones, Rob Kopf, Arun Kumar, Art Myatt
Energy Conversion Devices, Inc.
1675 W Maple Rd., Troy MI 48084

Jon Call, Subhendu Guha, Kevin Hoffman, Mark Lycette, Gerard Pietka, Mike Walters, Jeff Yang
United Solar Systems Corp.
1100 W Maple Rd., Troy MI 48084

ABSTRACT

Energy Conversion Devices, Inc. (ECD) and United Solar Systems Corp. (United Solar) have been developing, testing, and implementing new technology to increase the performance of the present 5 MW production equipment. The 5 principal areas in this research and development program are: (1) improved web heating and temperature monitoring systems; (2) new online diagnostic systems; (3) testing and implementing reactive ZnO sputtering from Zn metal targets; (4) improved rf PECVD cathode designs; and (5) the development of new pinch valves. These new technologies are now well along in their development; most have been successfully tested or implemented in the present 5 MW production line. As a result of this success, these new technologies will be utilized in the new United Solar 25 MW line that is being built by ECD. In this paper we briefly review the problems being addressed and the solutions being developed.

INTRODUCTION

ECD has developed and built 6 generations of roll-to-roll amorphous silicon PV production equipment. A metal/oxide backreflector, a 9 layer a-Si/a-SiGe alloy triple junction solar cell, and top transparent conductive oxide coating are deposited onto 750 m long, 125 μm thick stainless steel webs in a series of three roll-to-roll deposition machines[1]. In the PVMaT 5A research program we are developing technology that will (1) result in efficiency and throughput increases in the present United Solar 5 MW production equipment and (2) be applicable for use in United Solar's next generation 25 MW production equipment.

HEATING and TEMPERATURE MONITORING

Web Heating. The stainless steel substrate has traditionally been heated using quartz envelope IR lamps. These lamps accumulate thermally decomposed material on their envelopes, which in combination with the unavoidable temperature cycles, eventually results in severe flaking and in physical stresses large enough to break the quartz envelopes resulting in downtime and expense.

We designed new low-temperature, long-lasting NiChrome resistance heaters as a replacement. After successful testing of the new design in United Solar's pilot machine, an improved version was installed in United Solar's 5 MW production equipment for long term testing (Fig. 1). This new system has demonstrated a factor of 5 increase in lifetime over the previous heater design and will be implemented in United Solar's 25 MW machine.

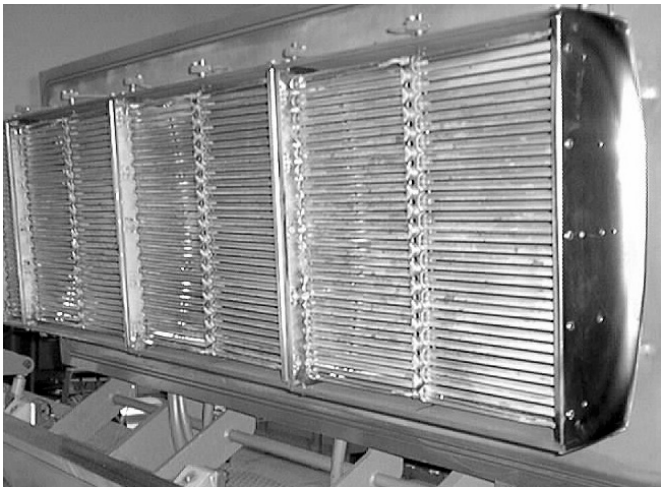

Fig. 1. New ribbon style heater assembly installed in United Solar's 5 MW production equipment.

Temperature Monitoring Systems. ECD has developed an accurate thermocouple temperature measurement system for the a-Si deposition machines. This system, based upon a high degree of thermal coupling to the web via the high conductivity hydrogen gas, however, does not work well in the Backreflector (BR) and ITO sputtering machines where the pressure is 1000 times lower and argon is the principal gas. We investigated and tested two new systems: an IR monitoring system and a rolling thermocouple system; we have chosen to continue to develop the latter due to its lower cost and demonstrated performance. This system is based upon the low thermal time constant, ≈ 1 ms, of the web. Consequently, the web immediately assumes the temperature of its supporting magnetic rollers when contact is made. The first generation design placed the thermocouple inside a roller making contact with the magnetic roller. The second generation system we are designing will place the thermocouple inside of a hollow magnetic roller. This new design will be tested and optimized in the 5 MW BR machine and used in the 25 MW BR and ITO machines.

ONLINE DIAGNOSTIC SYSTEMS

United Solar's production machines are very highly instrumented and automated. The present diagnostic systems principally use process control measurements for feedback. We are now developing a new set of online diagnostic systems that measure the PV device parameters.

These systems will allow immediate recognition of production problems and enable the operators, and eventually expert systems, to continuously optimize the process. These new capabilities will significantly reduce the commissioning time of the new 25 MW equipment.

BR Machine. Two new systems are being developed: a spectrometer system to monitor the thickness of the ZnO layer, and a scatterometer to measure the specular and diffuse reflectance of the metal layer. The spectrometer is already in use on the 5 MW BR machine and was used in the tests of the new reactive sputtering process, discussed below. The first generation scatterometer used a single photodiode mounted on a moving arm. The second-generation scatterometer, Fig. 2, uses a multi-element

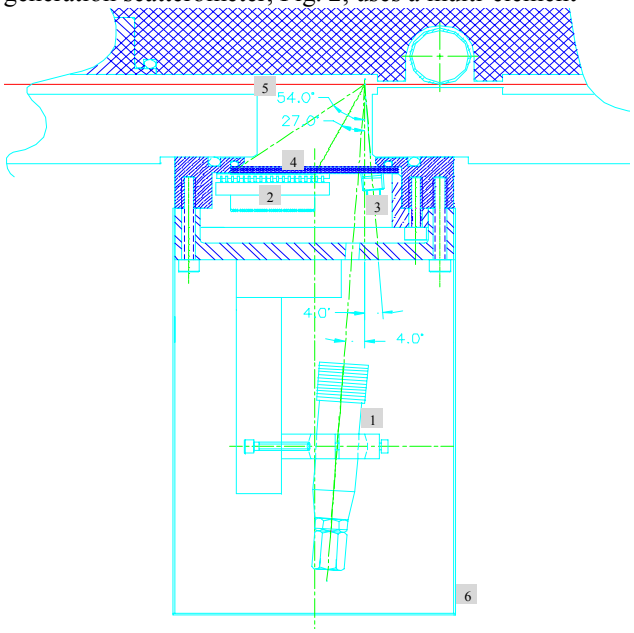

Fig. 2. Second generation scatterometer. (1) 635 nm laser; (2) photodiode array [diffuse]; (3) photodiode [specular]; (4) window; (5) web; (6) light enclosure.

photodiode array. This system is nearing completion and will be installed in the 5 MW BR machine for testing.

a-Si Machine. ECD is developing a PV Capacitive Diagnostic (PVCD) to measure the V_{OC}, J_{SC}, and *FF* of the PV material as it is being produced. A schematic of the system is shown in Fig. 3. A pulsed light source illuminates the PV material though a grounded grid and a sensor grid. The sensor grid is connected to a very high (> 10^{12} Ω) input impedance amplifier which outputs a voltage proportional to the PV voltage. The amplitude of the signal is directly proportional to V_{OC}; the waveform shape provides information on J_{SC}; and the amplitude vs. light intensity provides *FF* information. We are now in the final stages of the design of the 3rd generation system that will use an LED light source. With this system we hope to demonstrate measurement stability in the range of 10^{-3} to 10^{-4}.

NEW REACTIVE SPUTTERING PROCESS

The 5 MW BR machine sputters ZnO from ceramic targets. Zn metal targets are much lower in cost and offer the

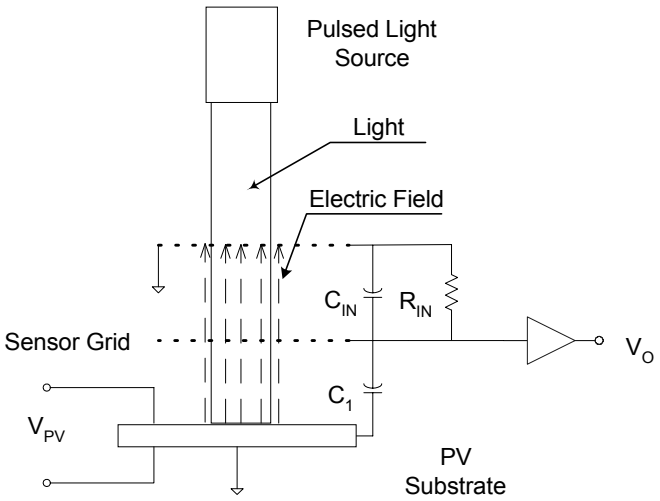

Fig. 3. Conceptual schematic of the PVCD.

possibility of higher sputtering rates and the use of rotating targets. In a batch system we demonstrated fabrication of cells on backreflector made from Zn metal targets with the same efficiency as those made on the production backreflector. More recently we have demonstrated the same performance in a test using this technique in the 5 MW production equipment.

IMPROVED CATHODE GEOMETRIES

The goal of this portion of the program is to develop new PECVD deposition chamber geometries that yield more uniform depositions over large areas for a wide range of deposition conditions. Three new geometries have been tested in a stand-alone set-up. Two of these system have also been implemented in United Solar's pilot roll-to-roll deposition machine for testing. We have developed new pumping and gas distribution systems that provide a much higher degree of deposition uniformity.

PINCH VALVES

A pinch valve system has been prototyped and tested. A second generation system has been designed and installed in the 5 MW a-Si machine. This system allows rolls of web to be changed at turn-around without letting up the deposition chambers to atmosphere. The system was recently successfully tested, resulting in an immediate 15 –20% reduction in turn around time, as well as other benefits. As machine operations are optimized around this device we expect further decreases in the machine turn-around time.

ACKNOWLEDGEMENTS

We thank Hellmut Fritzsche and Stanford R. Ovshinsky for their participation. We gratefully acknowledge the Dept. of Energy and the National Renewable Energy Laboratory for their support of this work is through the PV-Mat Program, Subcontract ZAX-8-17647-09.

REFERENCE

[1]. S. Guha, et al., Amorphous silicon alloy photovoltaic technology – from R&D to production. Proc. MRS Spring Mtg. (1994).

Nitrogen-induced evolution of $GaAs_{1-x}N_x$ studied by ballistic electron emission spectroscopy

V. Narayanamurti,[1] M. Kozhevnikov,[1] H.P. Xin,[2], C.W. Tu,[2] A. Mascarenhas[3] and Y. Zhang[3]

[1]Division of Engineering and Applied Sciences, Harvard University, 9 Oxford Street, Cambridge, MA 02138

[2] Electrical and Computer Engineering Department, University of California at San Diego, La Jolla, CA 92093

[3] National Renewable Energy Laboratory, 1617 Cole Boulevard, Golden, CO 80401

ABSTRACT

Giant bandgap reduction of dilute $GaAs_{1-x}N_x$ with nitrogen incorporation makes this material to be very attractive for conversion efficiency increase in multijunction, high efficiency solar cells. This paper reports on an experimental study of GaAsN band structure at low nitrogen concentrations by ballistic electron emission microscopy spectra. We present consistent results on the GaAsN conduction states evolution and a giant reduction of the Schottky barrier height as a function of the nitrogen concentration (up to x=0.021).

1. Introduction

In spite of the remarkable achievements in fabricating high-efficiency cells with III-V semiconductors, e.g. a high efficiency (>30%) monolithic GaInP/GaAs tandem cells [1], any further improvement will require incorporation of a third junction consisting of a semiconductor with a bandgap in the range of 0.95-1.1 eV. Giant bandgap reduction of dilute $GaAs_{1-x}N_x$ with nitrogen incorporation, by more than 0.4 eV at x~0.04, makes this material to be very attractive for conversion efficiency increase in multijunction, high efficiency solar cells. Despite the obvious progress in the experimental and theoretical study of GaAsN anomalies, little is known about the intrinsic electrical and optical properties of GaAsN surface and subsurface. To shed new light on the band structure we report here the first measurements of the electron transport in the conduction band of these alloys using the ballistic electron emission microscopy (BEEM) technique [2].

2. Samples and experimental approach

A 1000 Å undoped $GaAs_{1-X}N_X$ layer and 1000 Å n^+-GaAs buffer layer were grown on n^+ (001)-oriented GaAs substrates by gas source molecular beam epitaxy at 420°C [3]. A detailed analysis is presented here for the nitrogen compositions of x=0, 0.003, 0.005, 0.007, 0.012, 0.017 and 0.021. The details of the diode fabrication procedure have been published elsewhere [4]. The BEEM measurements were performed with a Surface/Interface AIVTB-4 BEEM/STM system using a Au tip. The tip-to-base voltage (V_t) was varied between 0.3 and 2.3 V to acquire the BEEM current (I_c) while keeping a constant tunneling current (I_t) of 4 nA.

3. Results

The room-temperature second derivative (SD)-BEEM spectra extracted from the experimental BEEM spectra by numerical differentiation with a 10 meV window are shown in Fig. 1. The SD-BEEM current is approximately the heterostructure transmission coefficient [5] and, therefore, allows an explicit energetic partitioning of the transport channels. Two main features (peaks) observed in the SD-BEEM spectra we associate with the Γ-like and *L*-like conduction minima in GaAsN [6]. As the nitrogen concentration increases, the low-energy threshold shifts towards lower voltages whereas the high-energy threshold shifts towards higher voltages The inset of Fig.2 shows that the relative *L*-like band contribution to the BEEM current reduces by two thirds as the nitrogen concentration increases from 0.3% to 2.1%.

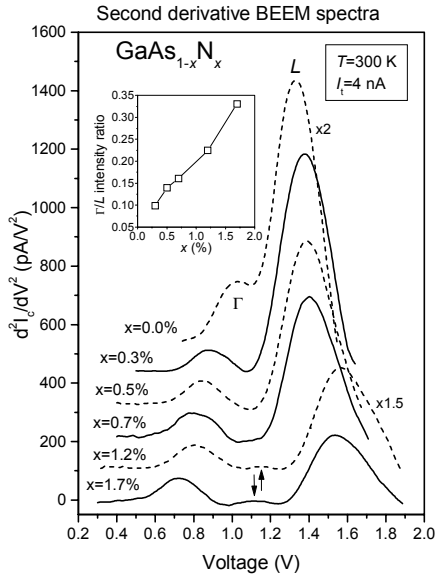

Figure 2. Room temperature SD-BEEM spectra for six different nitrogen compositions (from 0 to 0.017). For clarity, the SD-BEEM spectra are shifted along the vertical axis. The inset shows the ratio of the Γ-like peak to the *L*-like peak as a function of the nitrogen concentration.

The compositional dependencies of the thresholds observed in the SD-BEEM spectra are plotted in Fig. 2. While the Γ-like threshold decrease has a nearly linear compositional dependence up to x=2.1%, the *L*-like

threshold position increases initially at x≤1.2% and then is almost constant. The energetic separation between Γ-like and *L*-like transport channels as a function of the nitrogen composition is close to but exceeds slightly (<0.1 eV) the recently reported E_+-E_0 dependencies in optical experiments [7,8]. This difference between the *L*-like and E_+ energies above the conduction band edge is most likely due to the difference in the experimental techniques. In both the BEEM and optical techniques, the observed high-energy state is a weighted combination of the conduction states, but the BEEM weighting of the different bands is proportional to their DOS's [9], while the optical transition probability is defined by their Γ-character [8,10]. Since nitrogen substitution results in the splitting of the fourfold *L* valley into the $a_1(L_{1c})$ singlet and $t_2(L_{1c})$ triplet states [7,8] the *L*-like band in the BEEM experiments is mostly weighted on the $t_2(L_{1c})$ triplet state, and the E_+ transition is mostly weighted on the $a_1(L_{1c})$ singlet state.

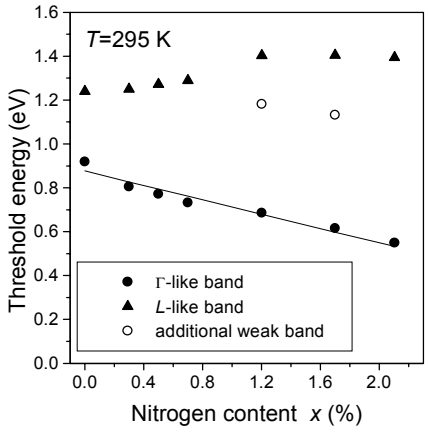

Figure 2. The compositional dependencies of the thresholds observed in the SD-BEEM spectra of $GaAs_{1-X}N_X$. The solid line is the best linear fit to the Γ-like threshold giving a slope of –16.4 eV.

The SD-BEEM spectra of two GaAsN samples, *x*=1.2 and 1.7 (see Fig. 1), reveal an additional weaker peak (indicated by the arrow), located ~0.40 eV and ~0.43 eV above the Γ-like state, respectively. This peak might represent the contribution from the $a_1(L_{1c})$ singlet state. The weaker amplitude of this peak matches the expected small DOS due to the increasing Γ-character of the $a_1(L_{1c})$ state in the alloy limit [10].

As the nitrogen concentration increases, the Au/GaAsN Schottky barrier (Γ-like threshold) decreases considerably, as shown in Fig. 2. The solid line in Fig. 2 is the best linear fit to the experimental data (with a slope of –16.4 eV). Using E_g(GaAs)=1.42 eV and E_g(GaN)=3.5 eV at room temperature, the same slope of E_g(GaAsN) would correspond to the bowing parameter of -18.9 eV. This value of the E_g bowing parameter is in a good agreement with the experimental estimates [11]. Thus we conclude that the nitrogen-induced Schottky barrier reduction accommodates most of the bandgap reduction in GaAsN. This result that is very important for device applications indicates that the effect of the nitrogen incorporation on the valence band is small.

4. Conclusions

The evolution of $GaAs_{1-X}N_X$ band structure at low nitrogen concentrations (up to *x*=0.021) was studied by BEEM. The SD-BEEM spectra of GaAsN show two main peaks, which we associate with the contribution of the Γ-like and *L*-like bands of GaAsN. As the nitrogen concentration increases, the energetic separation between these peaks increases as well, with a relative decrease of the *L*-like band contribution to the BEEM current. Another prominent effect of the nitrogen incorporation is a giant decrease of the Au/GaAsN Schottky barrier, from ~0.92 eV at *x*=0 down to ~0.55 eV at *x*=0.021. The observed Schottky barrier reduction follows approximately the bandgap reduction.

In future, we plan to extend our study to GaInAsN alloys that can be lattice matched to GaAs (Ge) by adjusting the In and N contents. It promises an additional controllable decrease of the bandgap, allowing the optimization of the solar cell efficiency.

The authors would like to thank Dr. N.A. Modine for helpful discussions. The support of the Midwest Research Institute under Department of Energy PV Program is gratefully acknowledged.

REFERENCES

[1] T. Takamoto *et al*.: "Over 30% effecient InGaAs tandem solar cells," Appl. Phys. Lett. 70 (1997) 381.
[2] L.D. Bell and W.J. Kaiser: "Observation of interface band structure by BEEM," Phys. Rev. Lett. 61 (1988) 2368.
[3] H.P. Xin and C.W. Tu: "GaInAsN/GaAs multiple quantum wells grown by gas-source MBE," Appl. Phys. Lett. 72 (1998) 2442.
[4] J.J. O'Shea *et al*.: "Ballistic-electron-emission spectroscopy of AlGaAs/GaAs heterostructures: Conduction-band offsets, transport mechanisms, and band-structure effects," Phys. Rev. B56 (1997) 2026.
[5] D.L. Smith and S.M. Kogan: "Theory of BEEM of buried semiconductor heterostructures," Phys. Rev. B54 (1996) 10354.
[6] M. Kozhevnikov *et al*.: "Evolution of GaAsN conduction states and giant Au/GaAsN Schottky barrier reduction studied by BEES," Phys. Rev. B61 (2000) R7861.
[7] W. Shan, *et al*.: "Effect of nitrogen on the band structure of GaInAsN alloys," J. Appl. Phys. 86 (1999) 2349.
[8] J.D. Perkins *et al*.: "Nitrogen-activated transitions, level repultion, and bandgap reduction in GaAsN with x<0.03," Phys. Rev. Lett. 82 (1999) 3312.
[9] D.L. Smith *et al*: "BEEM for nonepitaxial metal/semiconductor interfaces," Phys. Rev. Lett. 80 (1998) 2433.
[10] T. Mattila *et al*.: "Localization and anticrossing of electron levels in GaAsN alloys," Phys. Rev. B60 (1999) R11245.
[11] K. Uesugi and I. Suemune, "Bandgap enrgy of gaAsN alloys grown on (001) GaAs by MO-MBE," Jpn. J. Appl. Phys. 36 (12A) (1997) L1572.

Ultrafast Dynamics of Photoexcited Carriers in HWCVD a-Si:H and a-SiGe:H

S. L. Dexheimer[1], J. E. Young[1], and Brent P. Nelson[2]

[1]Department of Physics, Washington State University, Pullman, WA 99163

[2]National Renewable Energy Laboratory, 1617 Cole Boulevard, Golden, CO 80401

ABSTRACT

We present femtosecond studies of photoexcited carrier dynamics in hydrogenated amorphous silicon and silicon-germanium alloys grown by the hot-wire assisted chemical vapor deposition (HWCVD) technique, which is promising for producing high-quality device-grade materials. We have used wavelength-resolved femtosecond pump-probe techniques to study the dynamics of photoexcitations in these materials. Femtosecond dynamics measurements have been carried out on thin film samples under experimental conditions with varying sensitivity to carriers in extended states or in band tail states. The relaxation dynamics of carriers associated with extended states show a strong dependence on excitation density and follow a bimolecular recombination law, consistent with a number of earlier studies on related amorphous materials. In contrast, measurements involving band tail states reveal significantly altered dynamics, characterized by a marked deviation from simple bimolecular recombination.

1. Introduction

Thin-film amorphous silicon and silicon-germanium alloys are promising materials for low-cost, high-efficiency solar cells, yet a range of issues relevant to their development and application as photovoltaic materials are not yet fully understood. Important unresolved issues include the detailed nature of the electronic states in these disordered semiconductors, and in particular, the relation of the band tail and extended states and their influence on the carrier dynamics. In this work, we investigate the dynamics of photoexcited carriers in a series of a-SiGe:H alloys. By varying the relative energy of the photoexcitation and the band gap, we selectively excite carriers into extended states or into progressively deeper band tail states, and we monitor the time evolution of the carrier distribution using femtosecond pump-probe techniques.

2. Experimental

Thin films of a-SiGe:H were grown on glass substrates by the hot-wire assisted chemical vapor deposition (HWCVD) technique [1]. For the experimental results presented in this paper, the Ge concentration of the films varied from 10 to 50 atomic percent. The optical band gap of the materials can be characterized in terms of the transition energy at which the absorbance reaches a value of 104 cm 1, and this value corresponds to energies of 1.76 eV, 1.60 eV, and 1.42 eV for samples of 10, 30, and 50 atomic percent Ge, respectively. The samples were grown with a nonuniform thickness so that an optimal thickness for the thin film etalon response could be chosen for the timeresolved optical measurements [2]. Approximate sample thicknesses varied from - 350 nn for the 50% Ge sample to -780 nm for the 10% Ge sample, giving optical densities at the pump wavelength of < 0.25.

Time-resolved measurements of the carrier dynamics were carried out using an optical pump-probe technique, in which a short pump pulse excites carriers in the sample and a time-delayed probe pulse measures the resulting change in the optical properties as a function of the pump-probe delay time. Measured changes in the transmission and reflectivity can be related to changes in the optical absorption coefficient and the index of refraction of thin film samples for comparison with theoretical models. In these initial measurements, the thin film samples were excited with pulses 35 fs in duration centered at a wavelength of 800 *nn,* corresponding to a transition energy of 1.55 eV. The pulses were generated by an amplified Ti:sapphire laser system operating at a repetition rate of 1 kHz. Probe pulses of variable wavelength were produced using a femtosecond white-light continuum generated by self-phase modulation in a sapphire plate, followed by prism dispersion compensation to give a temporal resolution typically < 50 fs.

3. Results

Measurements of the time-resolved change in transmission following excitation at 1.55 eV for a series of a-SiGe:H alloys are displayed in Figures 1-3 [3]. The data are presented as the negative of the differential transmittance, corresponding to an induced absorbance that results from the photoexcited carrier population. In all cases, the carrier response was probed at a detection wavelength of 900 run.

The carrier response shows a nonexponential time dependence that is strongly dependent on excitation density. When carriers are initially excited into the extended states well above the band gap, as is the case for 1.55 eV excitation of the 50% Ge sample shown in Fig. 1, the relaxation dynamics can be well described by a

bimolecular recombination law, consistent with previous time-resolved measurements on similar systems at comparable excitation densities. Fits to the solution of a bimolecular rate equation dn/dt = -kn2 are shown superimposed on the data traces, and give values for the bimolecular recombination constant k -5 x 10-9 Cm3/s, consistent with previous work on a-Si:H in which carriers were excited into extended states at comparable energies relative to the band gap [4].

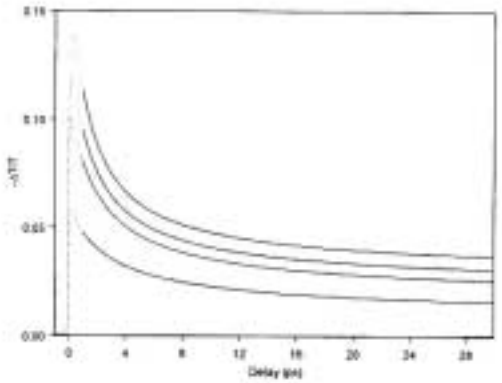

Fig. 1. Time-resolved negative differential transmittance of an a-Si_xGe_{1-x}:H thin film with x = 0.50. The data traces correspond to initial carrier densities of approximately 3 x 10^{20} cm^{-3}, 2.5 x 10^{20} cm^{-3}, 1.8 x 10^{20} cm^{-3}, and 9.2 x 10^{19} cm^{-3}.

In contrast, the time-resolved response for carrier excitation at lower energies relative to the optical gap exhibits a marked deviation from simple bimolecular recombination at short times. Representative responses for carriers excited progressively farther into the band tail states are presented in Figs. 2 and 3. For pump-probe delay times longer than - 1 ps, the response is well characterized bimolecular recombination, as shown by the fits to the data traces. At early times, a significant delay is observed in the peak of the induced absorbance that becomes more pronounced for initial excitation farther into the band tail. (The sharp feature at t = 0 includes contributions from nonlinear effects due to the temporal overlap of the pump and probe pulses and is neglected in the interpretation of the carrier dynamics.) The short-time response provides evidence for a rapid thermalization process on a subpicosecond time scale.

Acknowledgments

We thank NREL for providing support for this work, and we thank Dick Crandall for facilitating the collaboration. Additional support was provided by the National Science Foundation and by Washington State University.

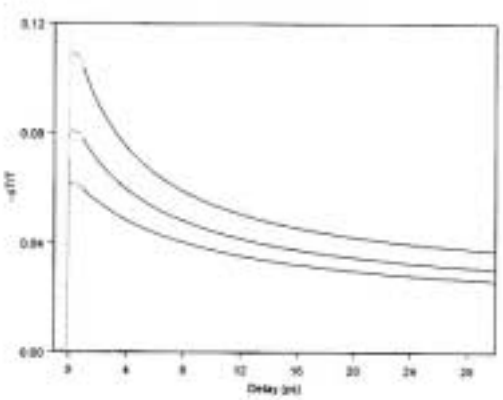

Fig. 2. Time-resolved negative differential transmittance of an a-Si_xGe_{1-x}:H thin film with x = 0.70 and initial carrier densities of approximately 5.5 x 10^{19} cm^{-3}, 4.4 x 10^{19} cm^{-3}, and 3.3 x 10^{19} cm^{-3}.

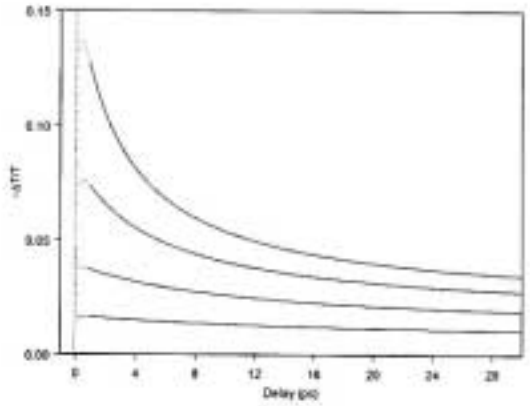

Fig. 3. Time-resolved negative differential transmittance of an a-Si_xGe_{1-x}:H thin film with x = 0.90 and initial carrier densities of approximately 6.6 x 10^{19} cm^{-3}, 4.4 x 10^{19} cm^{-3}, 2.6 x 10^{19} cm^{-3}, and 1.3 x 10^{19} cm^{-3}.

References

1. Nelson, B.P., *el al.*, Materials Research Society Symposium Proceedings (1998).
2. Moon, J.A. and J. Tauc., J. Appl. Phys. (1993) **73**, 4571.
3. Young, J.E. and Dexheimer, S.L., to be published.
4. Esser, A., et al., J. Appl. Phys. (1993) **73**, 1235, and references therein.

Light-Induced Changes in Long-Ranged Disorder in Amorphous Silicon

D. Quicker, P. W. West and J. Kakalios

The University of Minnesota

School of Physics and Astronomy
Minneapolis, MN 55455

ABSTRACT

Experimental measurements of the thermopower and conductivity activation energies have been combined with that of the conductance 1/f noise in hydrogenated amorphous silicon in order to test non-local models or light induced conducance changes. Following extented light soaking, there is no change in the long range disorder in device quality amorphous silicon films, but preliminary results indicate that reversible changes in disorder do occur in films grown under non-optimal conditions.

1. Introduction

The standard model for the microscopic origin of light-induced conductance changes in hydrogenated amorphous silicon (a-Si:H), termed the Staebler-Wronski effect (SWE) involves the breaking of localized strained Si-Si bonds which create new dangling bond defects. However, recent experimental results and theoretical models have suggested that along with localized defect creation, the light induced damage involves changes in the long range disorder LRD (on length scales of - 10' A of magnitude ~ 100 meV) already present in the aSi:H. The previous emphasis on localized dangling bond creation is understandable, since these defects are the easiest to measure. Conventional transport measurements are not sensitive to the influence of LRD on the electronic properties in a-Si:H, since the inelastic scattering (phase breaking) length is -5 A at room temperature [1]. In order to determine whether the SWE effect involves long range as well as local changes in the defect structure, an experimental program to study the influence of long range disorder on the electronic properties of a-Si:H has been initiated.

2. Experimental Results

A series of r.f. glow discharge deposited n-type doped a-Si:H films for which the substrate temperature during film growth was varied from 25 C < T < 250 C for an rf plamsa power density of 3 W/50 cm^2 has been synthesized. Infra-red spectroscopy measurements of the hydrogen content and bonding microstructure (in particular the relative concentration of Si-HZ bonds) for these films shows a nearly uniform increase as the deposition temperature is lowered, in agreement with prior studies by Bhattacharya and Mahan. [2] The long range disorder in these materials is quantified through measurements of the thermopower/conductivity activation energy difference. This activation energy difference, with the dark conductivity always displaying a larger value than observed in thermopwer measurements is due to the difference between open circuit (thermopower) and short circuit (conductivity) measurements and has long interpreted as a measure of the long range disorder at the mobility edges [2]. As shown in fig. 1, the activation energy difference also increases as the substrate deposition temperature is lowered, and when compared to the increasing concentration of Si-HZ bonds, a nearly linear correlation is observed [4]. We therefore conclude that the conductivity/thermopower

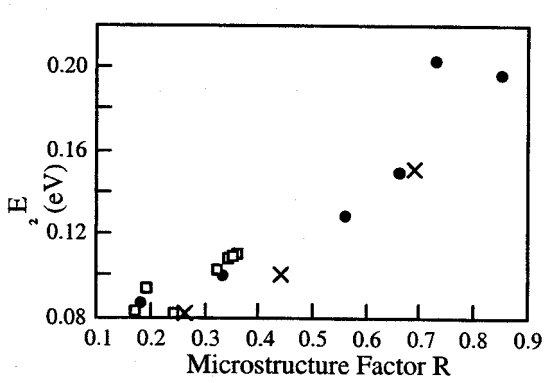

Fig. 1 Plot of the E_Δ the difference between the conductivity and thermopower activation energy against the concentration of Si-Hz bonds, as reflected in the ratio R of the infra-red absorption at 2100 cm-1 compared to the total absorption

from 2000 to 2200 cm-1 for a series of n-type doped a-si:H films deposited at 7.6 substrate temperatures varying from 250 C down to room temperature.
activation energy difference can indeed be used as a quantitative measure of LRD in a-Si:H thin films.

However, a surprising result is that following 17 hours of light soaking with heat filtered white light from a tungsten-halogen lamp for an n-type a-Si:H film deposited at 250 C, there is no change in this activation energy difference, even though both the dark conductivity and thermopower display reversible light induced changes, as shown in fig. 2. This result suggests that the long range disorder is unaffected by light exposure, and that the changes in conductivity activation energy are due solely to shifts of the Fermi energy, and not to changes in the nature of the current carrying transport states [5]. This result is at odds with previous reports of significant changes in the activation energy difference following light exposure.[6] This discrepancy may be explained by the observation that there is a small but definite change in the activation energy difference for a film deposited at 60 C. This film has considerably more hydrogen microstructure, as reflected by infra-red spectroscopy measurements, indicating that any light induced changes in the LRD are sensitive to the degree of disorder already present in the annealied state.

The 1/f noise power spectra has also been measured for these films as a function of light soaking. After light exposure, the noise magnitude increases with illumination time, and is reversible upon annealing. This result, which agrees with independent reports by Verlag and Dijkhuis [7] is consistent with a decrease in the more defects should lead to a decrease in the noise magnitude due to ensemble averaging effects. Therefore the noise studies indicate that the defect density decreases following light exposure, while the activation energy difference (as well as a host of other experimental evidence) suggests that the defect density increases. Clearly further studies on a broader number of fluctuators giving rise to the current fluctuations. The conventional interpretation of the 1/f noise is that it arises from charge trapping and release from dangling bond defects, and thus range of samples is needed.

This work was supported by the University of Minnesota, the NSF DMR 9422772 and NREL/AAD-9-18668-13.

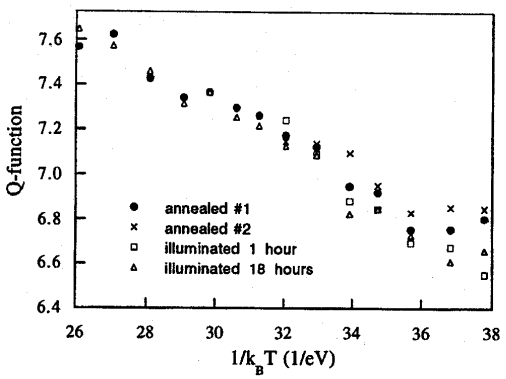

Fig.2 Temperature dependence of the Q function ($Q = \frac{e}{k_B}|S| + \ln(\sigma)$) in the annealed state and after several light exposures for an a-Si:H film doped with 4 x 10^{-4} PH_3 and deposited at 250 C.

REFERENCES

[1] J. Kakalios and R. A. Street: "Electronic transport in doped amorphous silicon", Phys. Rev. B 34 (1986) 6014-6017.

[2] E. Bhattacharya and A. H. Mahan: "Microstructure and the light-induced metastability in hydrogenated amorphous silicon", Appl. Phys. Lett. 52 (1988) 1587-1589.

[3] H. M. Dyalsingh and J. Kakalios: "Thermopower and conductivity activation energies in hydrogenated amorphous silicon", Phys. Rev. B 54 (1996) 7630-7633.

[4] D. Quicker and J. Kakalios: "Influence of deposition conditions on long-range disorder in n-type doped hydrogenated amorphous silicon", Phys. Rev. B 60, 2449 (1999) 24492455.

[5] D. Quicker, P. W. West and J. Kakalios: "Long-range disorder and metastability in amorphous silicon", J. Non-Cryst. Solids (in press).

[6] D. Hauschildt, W. Fuhs and H. Mell: "Optically induced potential fluctuations in aSi:H films", Phys. Stat. Solidi B 111 (1982) 171 174.

[7] P. A. W. E. Verlag and J. I. Dijkhuis: "Fluctuating defect density probed with noise spectroscopy in hydrogenated amorphous silicon", Phys. Rev. B 58 (1997) 3917-3921; "Generation-recombination noise studied in hydrogenated amorphous silicon", J. Non-Cryst. Solids (in press).

Amorphous Silicon Germanium Solar Cells And Thin Films Deposited Using Different Hydrogen Dilution

X. Deng, P. Agarwal, H. Povolny, and S. Han
Department of Physics and Astronomy, University of Toledo, Toledo, OH 43606

Abstract

In this report, we summarize our research study in two areas: 1) a-SiGe n-i-p solar cells and single-layer films deposited with different H dilution, R= $H_2/(GeH4+Si_2H_6)$, ranging from 1.7 to 240, and with a bandgap of around 1.5 eV; and 2) a-SiGe n-i-p solar cells and single-layer films having different Ge content in the i-layer. The results in the solar cell performance and film properties are compared. Light soaking degradation is performed for these sets of samples.

Introduction

To improve the efficiency of triple-junction a-Si based solar cells, it is important to have optimized narrow bandgap a-SiGe solar cells as the bottom component cell. In this work, we studied two sets of devices and films deposited with different H dilution and different Ge content for the optimization of bottom component cells.

Experimental

All samples and films are deposited in our laboratory using a ultra-high vacuum, multichamber, load-locked PECVD system. Mixtures of GeH_4, Si_2H_6 and H_2 are used for the a-SiGe layer deposition. While the H dilution, R, and the ratio of GeH_4/Si_2H_6 are changed, the other deposition conditions and all of the other layers remain unchanged. The deposition time is varied to obtain samples of the same thickness. Various device and film properties are tested.

Results

Table 1 shows the solar cell performance of a series of a-SiGe solar cells deposited using different H dilution, ranging from 1.7 to 240. The i-layer deposition time is changed so that the i-layer thickness is approximately the same. The V_{oc} increases from 0.64 V to 0.67 V with R up to 120, before it starts to decrease down to 0.64 V when R is further increased to 240. This may suggest that small amount of microcrystalline phase is formed at R=240. The J_{sc} is roughly unchanged within the experimental error which is approximately 5-10%. The J_{sc} is relatively low since no back-reflector is used for this study. The FF is highest for R=30, a moderate dilution, which is the condition that we used for the fabrication of the bottom cell of our 11% triple-junction solar cell [1]. The last column of Table 1 shows the degradation under 1 sun light soaking at 50 ^oC for 1000 hours. The degradation for sample GD429 at 1000 hours of soaking is unavailable since all of the test cells were shorted. The 300-hour soaking results shows a degradation of 21.1%, which is expected to be further increased at 1000 hours. It is found that the degradation is reduced with higher R, down from 20.9% for R=10 to 11.4% for R=120. Degradation of Samples GD451 and GD452 are not included here since they were fabricated later. From Table 1, one concludes that before light soaking, R=30 (GD425) shows the highest P_{max} while after light soaking, R=120 (GD427) shows the highest P_{max}.

To understand the i-layer materials made using different R, we deposit a set of single-layer films on a variety of substrates for measurements including FTIR, UV-Visible transmission, and H effusion. The results of these measurements for a set of films are summarized in Table 2. The refractive index and the bandgap are calculated from the transmission measurement. H content, [H], is calculated from the 640 cm^{-1} peaking in the FTIR, corresponding to the Si-H wagging mode absorption. Relative H content is also calculated from H effusion measurement. All films here have GeH_4/Si_2H_6 ratio of 0.72, which is the same as the i-layer in the n-i-p devices. From both the FITR measurement and the H effusion measurement, we find that the amount of H reduces when R is increased. The additional H in the low R samples is found to be mostly in SiH_2 mode, as reflected from the 2100 cm^{-1} peak in the IR absorption (FTIR figure not included here).

Comparing the device and film results, we find that i-layers deposited with higher R contain less H, however are more stable under light soaking.

Table 1.

Device No.	H dilution R	Time (min)	Thickness (nm)	V_{oc} (V)	J_{sc} (mA/cm^2)	FF (%)	Eff (%)	QE at 400nm	QE at 700nm	QE_{max}	Light Degrad. (%)
GD429	1.7	9.5	189	0.638	16.2	53.8	5.54	0.57	0.37	0.81	>21.1
GD428	10	19	190	0.640	17.7	53.1	6.02	0.58	0.42	0.83	20.9
GD425	30	36	189	0.656	17.4	59.1	6.76	0.59	0.43	0.83	21.6
Gd426	50	50	175	0.662	17.2	55.0	6.25	0.58	0.32	0.82	14.2
GD427	120	98	190	0.669	17.0	54.8	6.25	0.60	0.39	0.84	11.4
GD451	180	123	176	0.656	18.1	56.0	6.65	0.64	0.27	0.80	--
GD452	240	158	168	0.636	18.5	55.8	6.55	0.63	0.29	0.79	--

Table 2.

Sample No.	R	Thickness (nm)	Dep.rate (nm/sec)	n@600nm	E_g (eV)	[H] from IR (at.%)	H effusion relative
GD419	1.7	529	0.294	4.42	1.515	15.4	13.8
GD420	10	531	0.148	4.45	1.489	12.4	9.7
GD422	30	556	0.0772	4.36	1.479	10.9	13.2
GD423	50	608	0.0563	4.29	1.482	8.6	7.9
GD424	120	410	0.0285	4.48	1.516	11.6	7.6
GD449	180	492	0.0227	4.47	1.501	5.1	--
GD450	240	511	0.0177	4.53	1.482	4.7	--

Table 3 shows a set of a-SiGe n-i-p solar cells deposited using different GeH_4/Si_2H_6 ratio, ranging from 1.43 for narrow bandgap cell to 0 for a-Si top cell. Other deposition conditions are kept unchanged. The deposition time for the i-layer is adjusted to obtain the same i-layer thickness for the set of devices. Sample GD439, GD437, and GD435 are deposited under similar conditions as the top, middle and bottom cells of triple-junction solar cells. The motivation for this study is to 1) demonstrate the performance of the component cells used in our standard triple-junction solar cells and 2) find out whether a different Ge content in the bottom or middle cell would be more suitable for the triple cell. The device performance in Table 3 shows that as GeH_4/Si_2H_6 increases, V_{oc} and FF decrease. The J_{sc} increases up to GeH_4/Si_2H_6=0.72 and then remain approximately constant. The lack of further increase in J_{sc} is due to the low collection of carriers when the i-layer material quality is poorer.

The last three column of Table 3 shows the films properties of single-layer films deposited under the same conditions as the i-layer of the a-SiGe n-i-p solar cells. From this table, we find that both the bandgap E_g and the H content decrease with increasing Ge content. The table also shows that the bandgaps of the materials used as the i-layers of top, middle, and bottom cells are 1.84 eV, 1.65 eV and 1.50 eV, respectively, and that the H contents are 16.5 at.%, 15.0 at.% and 11 at.%, respectively.

Summary

The results from the devices and films deposited using different H dilution suggest that a high H dilution up to 120 could be used to deposited a-SiGe films with improved light stability. The results from devices and films with different Ge content in the i-layer show that the bandgap and H content for the top, middle, and bottom cells used for the 11% triple-junction solar cells reported previously [1], are 1.84 eV, 1.65 eV and 1.50 eV, respectively, for the bandgap and 16.5 at.%, 15 at.% and 11 at.%, respectively, for the H content. A further increase in GeH_4/Si_2H_6 from 0.72 to 1.0 for the i-layer does not yield solar cells with higher Jsc, yet the Voc and FF are significantly reduced.

Acknowledgements

The work is supported by NREL under Thin Film Partnership Program (No. ZAF-8-17619-14). The authors are grateful for the helps from our colleagues at ECD and United Solar.

References

1. X. Deng and X.B. Liao, S. Han, H. Povolny and P. Agarwal, *Solar Energy Mat. & Solar Cells*, 2000.

Table 3.

Device	Cell	GeH_4/Si_2H_6	V_{oc} (V)	J_{sc} (mA/cm^2)	FF (%)	Eff (%)		Sample	E_g	[H]
GD441		1.43	0.519	17.9	54.3	5.04		GD431	1.37	8.6
GD442		1.00	0.577	18.2	50.1	5.25		GD430	1.43	7.8
GD443	Bottom	0.72	0.660	17.4	55.3	6.36				
GD435	Bottom	0.72	0.666	19.1	54.3	6.91		GD357	1.50	10.5
GD436		0.50	0.744	14.1	63.9	6.72		GD358	1.57	11.9
GD437	Middle	0.36	0.810	16.1	61.8	8.05		GD359	1.65	15.0
GD438		0.18	0.849	12.0	63.1	6.44		GD360	1.72	18.1
GD439	Top	0.00	0.895	10.3	69.5	6.40		GD361	1.84	16.5

Characterization of Small particle Formation in the Preparation of Amorphous Silicon Solar Cells

Alan Gallagher and Karoly Rozsa

JILA, University of Colorado and KIST, Boulder, CO 80309-0440

ABSTRACT

This paper reports studies of particle formation in silane and related discharges used to produce hydrogenated amorphous silicon photovoltaics. Measurements of the location and size of particles within the quasi-neutral-plasma region of rf discharges, versus conditions and discharge operating time, are described. While particle growth rates are depend systematically on conditions, particle density and location undergoes a rich array of behavior e.g. particles smaller than 10 nn reside approximately midway between the electrodes, but with increasing size they spread into two layers closer to the electrodes. A plasma and chemistry model for particle formation and loss to the electrodes is also described briefly.

1. Introduction

Silicon-hydrogen based particles form in silane and related discharges that are used to produce hydrogenated amorphous silicon (aSi:H) photovoltaics. These particles tend to be negatively charged, and thereby trapped in the plasma by sheath potentials. This allows a fairly long time for particles to grow by Si atom addition, mostly due to radical collisions, but some particles are neutral and escape the plasma to become incorporated into the growing film. How this particle incorporation affects device properties is not well understood, as methods of systematically varying particle incorporation have not been developed. Nonetheless, it appears likely that particle incorporation has an important affect on the acceptable rates of growing device-quality films, and it may even limit the achievable electronic properties at low growth rates. This phenomena of particle growth in a film-deposition plasma is ubiquitous, as adjusting conditions to enhance film growth also enhances particle growth by the same processes.

In order to achieve a detailed understanding of particle growth and escape, and how to influence particle incorporation into devices, we have been studying particle behavior experimentally and with plasma-chemistry models. We have concentrated on the silane and silane/hydrogen rf, capacitively-coupled discharges most commonly used to produce a-Si:H films, and conditions appropriate to solar cell production. The following will summarize some of our observations and conclusions.

Z. Observations of Particles in the Plasma

We utilize a variety of techniques to detect the particles in the plasma and the films; here we will describe the results of light-scattering measurements of particle location and size in the discharge. We find that, as expected, most particles are suspended in the quasi-neutralplasma region, which fills 50-70 % of the electrode gap midway between the electrodes. However, the location of particles within this region is a very complicated function of the electrode shape and spacing, gas pressure, discharge power and particle size. Since particles escape to the electrodes from their location in the plasma, these locations are an important issue. By measuring versus discharge operating time (t), during which particle diameter grows nearly linearly, we observe particle behavior versus size. (Scattering by these very small particles is proportional to np rb, where r is the radius and np the density of particles, and we use afterglow diffusion to establish r. See Ref. l for details)

We find that the very small (<15 run diameter) particles that occur during the first few seconds are in a layer nearly midway between the electrodes, which is not the strongest glowing region for our asymmetric electrodes. A few seconds later, somewhat larger particles reside in two layers, considerably closer to the electrodes but again not in the strongest-glowing regions where they were expected. This change is attributed in part to a growing importance of the ion-wind force with increasing particle size. At later times particles > 50 nn in diameter are affected by gravity and largely settle into the lower layer near the rf electrode.

Particle densities decrease with discharge operating time, consistent with the escape of particles to the electrodes and the growing film. The data thus yields the particle fraction in the film (Ref 1). Changes in the rf electrode size, its distance from nearby grounded surfaces and adding an insulator at the periphery all

affect particle location, and thereby the quantity and size of particles that reach various parts of the substrate.

3. A Model for Particle Growth and Loss to Electrodes

We have modeled the growth of particles, from the initial radicals containing one Si atom through those with >10,000 Si that are observable by light scattering. During this growth most of the particles are negatively charged and trapped in the quasi-neutral-plasma, but a fraction are neutralized by ion collision and some of these diffuse to the electrodes before being recharged by electrons. This attrition competes with growth for every Si-atom addition, such that the density of larger (detectable) particles becomes an exponential fiuiction of discharge parameters. The fact that these discharges are in an attaching gas, as are almost all semiconductor deposition and processing plasmas, has a profound effect on the particle charge distribution. In particular, the negative ion density greatly exceeds the electron density, leading to an exceptionally large neutralparticle fraction and major particle escape to the electrodes. Another interesting result of the calculation is that particle densities depend on the discharge pressure (P), film growth rate (G) and electrode gap (L) in the combination Po.6GLi.s. Thus, particle incorporation into films is much more sensitive to electrode gap tan to gas pressure.

Details of these calculations and their results can be found in our NREL Reports of the last year.

4. Plans and Mitigation Techniques

Our studies have suggested a number of methods for minimizing particle incorporation into device films, or alternatively of deliberately introducing crystallized particles to initiate film crystallization. These methods include thermophoretic effects resulting from temperature differences between or along electrodes, plasma-potential variations due to electrode asymmetries and edges, and discharge transits. Quantitative studies of such phenomena in silane and silane/hydrogen discharges, to allow more certainty regarding how chamber and discharge design will effect particles, are planned and underway. To allow direct observation of how these methods affect particle incorporation into films, we have developed the capability of Transmission Electron Microscopy on films deposited on the substrate. This allows the observation of particles greater than about 4 run in size, as well as the density of particles in the films and their size distribution. It should also be capable of determining if particles are crystalline, although that has not yet been tested for these small particles.

This work is supported in part by NREL Contract DAD-8-18653-01

1) M.A. Childs and A. Gallagher, J. Appl. Phys. 87, 1076 (2000)

Summary Review of Silane Ignition Studies

V.M. Fthenakis
Environmental Research & Technology Division
Environmental Sciences Department
Brookhaven National Laboratory
Upton, NY 11973

1. Introduction

Accidental releases of silane present potentially serious consequences, since silane can ignite spontaneously, and under certain conditions explode, when released into the air. Silane related risks are illustrated by the number of incidents recorded in the semiconductor industry. A survey of 12 semiconductor manufacturers showed 36 silane incidents between 1997 and 1982. These included 15 fires in ducts and process tools; 6 fires from silane leaks in cabinets or gas supply systems; 5 explosions in ducts; and 3 explosions in cabinets or gas supply systems. Another survey reports 38 incidents during the period 1988-1993, and a further survey recorded 53 incidents between 1985 to 1993. These incidents involved different parts of a silane system from cylinder changing to emission control [1].

Articles 51 and 80 of the Uniform Fire Code (UFC) list protection guidelines applicable to indoor storage (in ventilated enclosures) and to outdoor storage of silane mixtures of 2% or higher concentration. These guidelines include requirements for ventilation inside an enclosure and requirements for restrictive flow orifices in supply lines. The UFC requirements appear to be applicable to only a narrow range of conditions. Recent studies by Union Carbide and by Factory Mutual Research improved our understanding of the behavior of silane ignition and allowed us to update existing safety guidelines, especially the requirements for ventilating cabinets. This paper is a synopsis of a comprehensive review of previous and recent experimental studies and protection guidelines applicable to the PV industry [7].

2. Previous Studies

Major experimental studies, conducted in the 1980's by Hazard Research Co, and the Southwest Research Institute, illuminated several aspects of the conditions under which silane explodes. These were discussed in a previous paper [2]; the major highlights are summarized below: 1) Slow discharges of 100% silane into ducts containing air, self-ignited only when the silane concentration reached about 3 to 4%; 2) Small (i.e., 40 lpm) leaks of 100% SiH4 in gas-storage cabinets purged with 500 cfm of air burned smoothly, without exploding; 3) A larger leak of SiH4 at 500 psi through a 1-mm (0.06") orifice, (flow rate of -330 lpm), into a storage cabinet resulted in a sudden explosion, even though the cabinet was continuously purged with 500 cfm air flow; 4) A leak in the upper part of the same cabinet where purging was more effective, produce neither an explosion nor a flame; 5) The same flow rates of silane discharged through N2-purged lines did not cause flames or explosions; 6) Discharges of mixtures of silane in nitrogen at concentrations of 5, 7.5, 10, and 15% in a ventilated gas cabinet showed that a 15% silane mixture produces an explosion even when released from a 50 psi source through a 1 mm flow restricting orifice; 7) Releases through the 4 mm orifice of silane/nitrogen mixtures at 50 psi and 500 psi, produced explosions of different magnitudes; 8) Unconfined outdoor discharge of 15% silane through a 4 mm orifice at 50 psi and at 500 psi, produced only small pops; 9) Unconfined outdoor discharge of 100% silane through 0.15 mm (0.006") flow-restricting valves, burnt smoothly without generating high

temperatures; 10) Releases through an open valve without an orifice generated flames that extended eight feet from the valve, and high temperatures (e.g., >1000°C).

3. Recent Studies

Experimental studies conducted by Union Carbide [3] show that 100% silane releases auto-ignite if the exit velocity is below a critical value, in the range of 10-50 m/s, depending on ambient temperature and orifice diameter. More recent studies by Factory Mutual Research (FMR) [4-6] showed auto-ignition starting at exit velocities greater than these values. This contradiction points out the need to account for the different types of ignition which are possible in ventilated enclosures of different geometry and ventilation patterns, in addition to the release conditions. FMR identified five possible ignition scenarios: prompt ignition, ignition during flow decay, ignition at shutoff, piloted ignition, and bulk auto-ignition. They found that the reactivity of silane depends on the volumetric concentration of the silane/air mixture (Xf) created from a release, as follows [4-6]:

Xf < 1.4%	Non-flammable mixtures
1.4% <Xf < .,4.1	Flammable and stable mixtures
Xf<-4.5%	Metastable mixtures

The identification of a lower explosive limit (LEL) of about 1.4% confirms what we knew from previous studies (about 2% LEL). However, the other two sets of conditions represent new knowledge that can be used in guidelines for preventing explosion. At concentrations equal to or greater than 4.5%, the mixtures were found to be metastable and ignited after a certain delay. In an accident, this event could be extremely destructive and protection provided by venting would be totally ineffective.

4. Conclusion and New Guidelines

Previous studies showed that storing silane in an open space reduces the risk of an explosion and that if silane is stored indoors in ventilated cabinets, the ventilation is effective in preventing the explosion of certain small releases through 1 mm orifices. Articles 51 and 80 of the UFC list requirements for ventilation inside an enclosure and for restrictive flow orifices, based on previous studies and a narrow set of conditions. The recent FMR studies show the need for establishing new requirements, which include, but are not limited to, the following: 1) To prevent bulk auto-ignition, limit to 1 % the maximum concentration of silane, resulting from a release in an enclosure. 2) Cabinet ventilation should be sufficient to keep below 0.4 % the average silane concentration resulting from mixing of a release with the ventilation air. These recommendations are additional ones to those previously published. For calculations, and a complete list of recommended safety guidelines, see the complete report [7].

REFERENCES

1. Silane Safety Improvement Report, SEMATECH Technology Transfer 94062405A-ENG.
2. Fthenakis V.M. and Moskowitz P.D., An Assessment of Silane Hazards, Solid State Technology, Jan. 1980, 81-85.
3. Britton l., Improve your Handling of Silane, Semiconductor International, April 1991.
4. Tamanini F, Chaffee J. L. and Jambar R.L., Reactivity and Ignition Characteristics of Silane/Air Mixtures, Process Safety Progress, 17(4), 243-258, 1998.
5. Factory Mutual Global, Property Loss Prevention Data Sheets, May 1999, revised January 2000.
6. Tamanini F. and Chaffee J.L., Ignition Characteristics of Releases of 100% silage, SEMATECH Technology Transfer 96013067AENG, March 7, 1996.
7. Fthenakis V.M., A Review of Silane Ignition Studies and Safety Guidelines, BNL report, in preparation.

Advances in CIGS PV Technology

A. Delahoy, J. Bruns, M. Akhtar, L. Chen, A. Ruppert, Z. Kiss

Energy Photovoltaics, Inc.
Princeton, NJ 08543

ABSTRACT

This paper reports breakthroughs in several areas that, taken as a whole, significantly contribute to the advancement of CIGS PV technology based on vacuum deposition. These results include the large area sputtering of Mo suitable for very high efficiency cells, a promising non-Cd buffer layer capable of vacuum deposition, and the improved delivery of Cu by linear source evaporation for large area vacuum deposition of CIGS.

1. Introduction

EPV is committed to developing manufacturing technology for CIGS PV modules based on vacuum deposition onto glass substrates. The promise of this technology is most clearly indicated by NREL's achievement of an 18.8% cell conversion efficiency using an R&D scale, 3-stage vacuum process. Under the Thin Film Partnership Program, EPV has striven to overcome impediments to commercialization of such technology. This brief paper reports advances in three critical areas: the back Mo electrode, the buffer layer, and means for forming CIGS over large areas.

2. Mo back electrode

It had earlier been conclusively demonstrated, through side-by-side CIGS depositions onto different Mo substrates, that the Mo can strongly affect cell efficiency. At the time, this comparison disfavored EPV Mo, and prompted a program to remedy the situation. We can now report that EPV has demonstrated large area sputtering of Mo capable of supporting very high efficiency cell processing. Using EPV Mo, NREL has deposited a 17.1% CIGS cell (no AR coating). The parameters of this cell are V_{oc} 644 mV, J_{sc} 35.7 mA cm^{-2}, FF 74.7% (see Table 1). The Mo was produced on EPV's 0.43 m^2 pilot line equipment. EPV further believes it can identify the signature of "good" Mo, and is currently exploring its sensitivity to sputtering parameters.

3. Non-Cd buffer layer

The highest efficiency CIGS cells are conventionally fabricated using a CdS buffer layer prepared by chemical bath deposition. This process is not viewed as being manufacturing-friendly because of the liquid waste and the use of cadmium. To solve these problems, EPV has investigated ternary compounds that can be deposited by vacuum evaporation as potential buffer layer materials. Since Zn is an n-type dopant in CIS, and since In and Se are already present in CIS or CIGS, we contemplated the use of $ZnIn_xSe_y$ (ZIS) as a buffer material. (This material was first applied to CIGS by co-evaporation by Konagai [1]. At sufficiently high substrate temperatures the defect chalcopyrite $ZnIn_2Se_4$ is obtained).

ZIS films were deposited over a range of substrate temperatures and characterized according to composition, conductivity, and bandgap. For a thickness of about 0.5μm, reasonable properties were obtained for T_s = 270-300°C: $\sigma_d = 1.5 \times 10^{-4}$ $(\Omega\ cm)^{-1}$, $\sigma_{ph} = 4.9 \times 10^{-4}$ $(\Omega\ cm)^{-1}$ (1 sun), and from a plot of $(\alpha h\nu)^2 \sim (h\nu - E_g)$ a bandgap E_g of 1.9–2.0 eV was deduced.

Another possible ternary buffer material is $ZnGa_xSe_y$ (ZGS). EPV has explored several possible material compositions, with variable results. One material, however, has proved promising and consistently provides reasonable cell efficiencies. Using this material, designated "ZIS", as a buffer layer in the configuration ZnO/ZIS/CIGS/Mo/glass, an 11.5% cell has been achieved with V_{oc} 560 mV, J_{sc} 32.1 mA cm^{-2}, and FF 64.3% (see Figure 1 and Table 1).

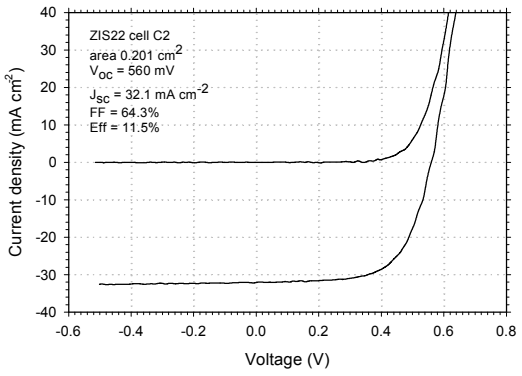

Fig. 1. I-V curve for an 11.5% CIGS cell with vacuum-deposited, non-Cd, ternary buffer layer

These cells can be fabricated with no dark-light crossover of the I-V curves (not true for all ternary buffers). Furthermore, no light soaking effects are seen,

unlike the strong increase in V_{oc} exhibited by ZnO/CIGS devices where the ZnO is prepared by the *ROMEAO* process [2]. The spectral response of this 11.5% cell is shown in Fig. 2, and is compared to that of a good CIGS cell from EPV's R&D system that uses CBD CdS as the buffer layer. The ZIS cell is shown to have a superior quantum efficiency for wavelengths less than 520 nm.

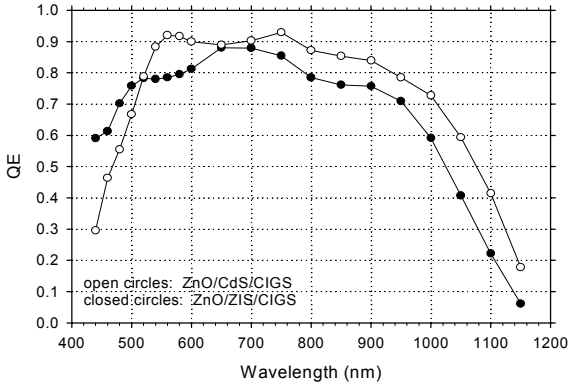

Fig. 2. Spectral response for CIGS cells with CdS and ZIS buffer layers

4. Large area CIGS deposition

To prepare CIGS over a large area (currently 0.43 m^2) EPV delivers materials from line sources to a substrate that is translated in a direction perpendicular to the axis of the source. In particular, a linear evaporation source for Cu delivery has been developed. This technological "tour de force" allows EPV to build large area CIGS systems possessing considerable process flexibility, and capable of implementing either the EPV *FORNAX* process [3], or the NREL 3-stage process. The figure below shows the thickness distribution of CIGS prepared in the pilot line across the width of the glass substrate i.e. in the direction of the source axes.

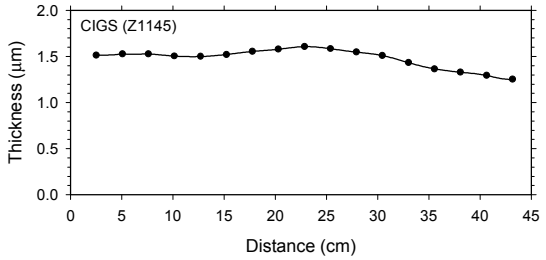

Fig. 3. Thickness distribution for CIGS in the direction of the linear sources

To monitor the quality of CIGS prepared in the pilot line, small sections of the substrate are processed through the R&D scale CdS/ZnO stations. Figure 4 shows the I-V curve of a 12.0% cell with 581 mV V_{oc} prepared using pilot line CIGS; the PV parameters are also given in Table 1. This result demonstrates that high quality CIGS can be prepared by linear source evaporation.

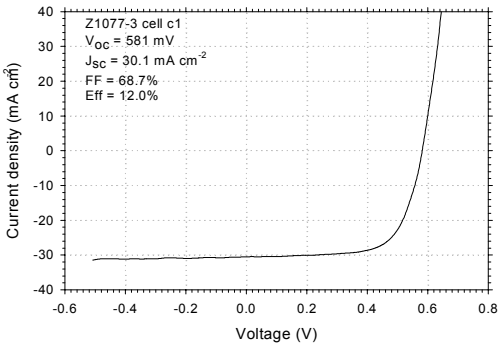

Fig. 4. I-V curve for 12.0% cell prepared using pilot line CIGS

Table 1. Summary of cell parameters

CIGS source	Comm.	Buffer Layer	V_{oc}	J_{sc}	FF	Eff.
NREL	EPV Mo	CdS	644	35.7	74.7	17.1
R&D	2-stage	CdS	560	34.7	67.7	13.2
Pilot-Line	Cut;small area proc.	CdS	581	30.1	68.7	12.0
R&D	3-stage	"ZIS"	560	32.1	64.3	11.5

5. Future work

EPV will continue to document the performance of various types of Mo, optimize the non-Cd, ternary buffer layer by applying it to CIGS routinely produced by a simple 2-stage process (see Table 1), and will add novel control methods to its linear source based CIGS machines. EPV has committed to scale up its CIGS technology and is building a new pilot line capable of coating substrates 0.79 m^2 in area. The new technology described above will be utilized in this line. In addition to upscaling experience, it is planned that limited commercial CIGS product will result from this line.

ACKNOWLEDGMENTS

The authors thank the other members of EPV's technical staff who contributed to this work, Dr. Miguel Contreras of NREL for advice and CIGS deposition onto EPV Mo, and the US DOE for support under subcontract ZAK-8-17619-21 with NREL.

REFERENCES

[1] M. Konagai, Y. Ohtake, and T. Okamoto, MRS Symp. Proc. Vol. 426 (1996) 153-163.
[2] A.E. Delahoy, A.F. Ruppert, and M. Contreras, *Thin Solid Films* 361-362 (2000) 140-144.
[3] A.E. Delahoy, D. Chorobski, F. Ziobro, Z.J. Kiss, AIP Conf. Proc. Vol. 462 (AIP, NY, 1999) 144-151.

Photoluminescence of CdTe:Cu and CdS:Cu Single Crystals

D. Grecu,[1] K. J. Price,[2] and A. D. Compaan[2]

[1]Present Address: First Solar, LLC, Toledo, OH
[2]The University of Toledo, Toledo, OH 43606

ABSTRACT

We have studied the photoluminescence (PL) of single crystal CdTe and CdS diffusion-doped with copper and annealed in various ambients in order to identify the behavior of Cu-related defect states active in recombination processes in the polycrystalline thin-films of these materials. The results help to identify the possible roles of Cu in some CdS/CdTe thin-film solar cells.

1. Introduction and Overview

Cu is often used in the formation of a back contact to CdTe/CdS solar cell devices. Recently, Asher has presented SIMS data indicating that in some cases, Cu can diffuse into both CdTe and CdS layers during device fabrication,[1] and understanding the behavior of Cu in these materials is important. Photoluminescence (PL) is a powerful technique to study the electrically active states in semiconductors. While CdTe/CdS devices are typically fabricated with polycrystalline films, PL in polycrystalline films is often difficult to interpret due to the presence of grain boundaries. We therefore present results of PL in CdTe:Cu and CdS:Cu single crystals doped by diffusion of thermally evaporated Cu.

In CdTe:Cu our results are consistent with some Cu atoms occupying substitutional positions on the Cd sublattice, and with others forming Frenkel pairs involving an interstitial Cu and a Cd vacancy. In addition, we find that Cu-related states in CdTe:Cu samples exhibit a significant reversible "aging" behavior. The reversible behavior is paralleled by changes in carrier concentration of polycrystalline CdTe:Cu films, and changes in open circuit voltage in CdTe/CdS devices, indicating that the observed Cu-related PL is related to metastable behavior in CdTe/CdS devices. In CdS:Cu, we show evidence of an exciton bound to a Cu-related site that is stable under short-term light illumination.

2. Sample Preparation

The single-crystal substrates used in this study were grown by the Bridgman method and were obtained from eV Products and Cleveland Crystals. Cu doping was achieved from a 15-20 nm thick, high-purity elemental Cu layer deposited on the surface of the crystals by thermal evaporation. Samples with and without a Cu layer were annealed at various temperatures in evacuated, sealed quartz tubes either alone (no overpressure) or with Cd, S, or $CdCl_2$ powder. Photoluminescence (PL) spectra were recorded at 10K. The excitation was achieved with the 752.5 ran line of a Kr laser or the 476.5 nm line of an Ar laser. Luminescence was collected using a triple-grating spectrometer and CCD detector. All spectra were corrected for the spectrometer/detector response.

3. PL of Copper-Doped CdTe

Figure 1 shows the lOK PL spectra of a CdTe sample before and after diffusion with Cu at 200 C for 1 hour, along with proposed assignments for several transitions. The spectrum of an undoped sample can be divided into three main regions: a) a cluster of bound exciton (BE) transitions in the region 1.58-1.60 eV; b) a strong donor acceptor pair (DAP) transition at 1.55 eV and its phonon replicas at 1.53, 1.51, and 1.49 eV; c) a broad "defect" band ranging approximately from 1.40 to 1.52 eV and consisting of several shallow donor ─ deep acceptor transitions and phonon replicas. The strong DAP transition at 1.55 eV has been attributed to a transition between a hydrogenic donor and a Cd vacancy (V_{Cd}) acceptor state.[2]

After Cu diffusion, the PL spectrum is markedly different (Fig. 1). The BE region is now dominated by a transition at about 1.59eV, the transition at 1.55eV is strongly attenuated and a new strong "defect" band emerges at about 1.45eV. A bound exciton at 1.5896 eV (X, Cu_{Cd}) and a DAP transition at 1.45eV were previously attributed to Cu_{Cd}. In addition, when the PL spectrum is acquired shortly after diffusion with Cu, a new transition, at approximately 1.555eV can be observed. This transition is accompanied by 3-4 phonon side-bands which is indicative of a strong lattice coupling. Transitions with similar characteristics were observed in Ag[3] and Au[4] doped CdTe samples and tentatively assigned to the recombination of excitons bound to M; VCd or M; MCd complexes (where M = Ag, Au). The strong lattice coupling could be attributed to the lattice strain introduced by the interstitial atom.

We find that the intensity of Cu-related features in the PL spectrum decreases substantially after several days of room-temperature storage for both single crystal and polycrystalline[5] samples. We also observe a factor of 5 decrease in the carrier concentration in polycrystal-

line CdTe films and a drop in the open-circuit voltage of the CdS/CdTe solar-cell devices doped with Cu[5]. The aging effect appears accelerated by exposing the samples to white-light radiation. Figure 2 illustrates the changes in the PL signal for a Cu- doped single crystal CdTe sample (1) immediately after diffusion (30 min., 200C), (2) after 90 hours of illumination (200W/cm^2) at room temperature and (3) after a re-anneal (30 min., 200 C).

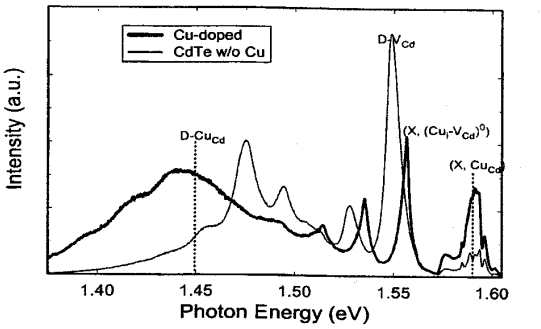

Figure 1. PL of CdTe without Cu, and CdTe:Cu immediately after Cu diffusion

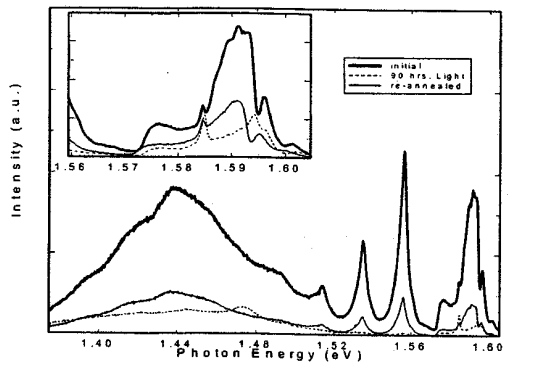

Figure 2. PL of CdTe:Cu immediately after diffusion, after 90 h light exposure, and after re-anneal

The illumination of the sample was achieved using a tungsten-halogen incandescent light source. In the light-soaked sample we note a major decrease of the PL signal including the intensities of the 1.45 eV band, the 1.59 eV bound exciton, and the complex line at 1.SSSeV. These aging effects are consistent with the dissociation of CuCa and Cu;+-V_{Cd-} states discussed previously. In addition, we attribute the overall decrease in the PL signal to the formation of Cu-related non-radiative recombination centers (possibly Cu precipitates). We find that the PL spectrum, carrier concentration, and open circuit voltage can be restored by re-annealing the samples. This effect is paralleled by a recovery of the open-circuit voltage of the CdS/CdTe devices.

4. PL of Copper-Doped CdS

CdS:Cu samples were diffused at 385 C for 1 hour and compared to as-grown CdS. PL from as-grown CdS was dominated by a bound exciton at 2.546 eV. After Cu diffusion, this center was replaced by a bound exciton at 2.542 eV. The Cu-related center appeared in all Cu containing samples, whether the Cu diffusion was done with no overpressure, or in the presence of Cd, S, of $CdCl_2$ powder. Samples containing no Cu that were annealed under similar conditions did not exhibit the 2.542 eV feature.

The Cu-related center was tested for stability under short-term aging or light soaking. After several days a' room temperature and atmosphere, no changes were ob served in Cu-related PL. In addition, 15 hours of 1-su light illumination did not affect the Cu-related PL.

5. Conclusion

We have observed emission due to Cu-related centers in CdTe:Cu and CdS:Cu. In CdTe:Cu, these centers are metastable under room-temperature aging or light-soaking, and these changes are correlated with a decrease in the open-circuit voltage in CdTe/CdS photovoltaic devices. In CdS:Cu, the Cu-related emission is stable under short-term aging and light-soaking.

6. Acknowledgments

We are pleased to acknowledge the support of NREL in this work. In addition, helpful advice has been received, inter alia, from Bolko von Roedern and from Doug Rose.

7. References

[1] S. Asher, presentation at National CdTe Team Meeting, Golden, CO, January, 2000.

[2] J.M. Figueroa, F. Sanchez-Sinencio, J.G. Mendoza Alvarez, O. Zelaya, C. Vazquez-Lopez, and J.S Helman, *J. Appl. Phys.* **60**, 452 (1986).

[3] J.P. Chamonal, E. Molva, J.L. Pautrat, L. Revoil, *J.*Cryst. Growth **59**, 297 (1982).

[4 E. Molva, J.M. Francou, J.L. Pautrat, K. Saminadayar, Le Si Dang, *J. Appl. Phys.* 56, 2249 (1984)

[5] D. Grecu, A. D. Compaan, 15th NCPV Program Review Proceedings, p. 224, (1998)